Ecological Studies 229

Thomas Foken *Editor*

Energy and Matter Fluxes of a Spruce Forest Ecosystem

Springer

Ecological Studies

Analysis and Synthesis

Volume 229

Ecological Studies is Springer's premier book series treating all aspects of ecology. These volumes, either authored or edited collections, appear several times each year. They are intended to analyze and synthesize our understanding of natural and managed ecosystems and their constituent organisms and resources at different scales from the biosphere to communities, populations, individual organisms and molecular interactions. Many volumes constitute case studies illustrating and synthesizing ecological principles for an intended audience of scientists, students, environmental managers and policy experts. Recent volumes address biodiversity, global change, landscape ecology, air pollution, ecosystem analysis, microbial ecology, ecophysiology and molecular ecology.

More information about this series at http://www.springer.com/series/86

Thomas Foken
Editor

Energy and Matter Fluxes of a Spruce Forest Ecosystem

Springer

Editor
Thomas Foken
Universität Bayreuth
Bayreuth Center of Ecology
and Environmental
Research (BayCEER)
Bayreuth, Germany

Additional material to this book can be downloaded from http://extras.springer.com.

ISSN 0070-8356 ISSN 2196-971X (electronic)
Ecological Studies
ISBN 978-3-319-49387-9 ISBN 978-3-319-49389-3 (eBook)
DOI 10.1007/978-3-319-49389-3

Library of Congress Control Number: 2017933974

Printed on acid-free paper

This Springer imprint is published by Springer Nature
The registered company is Springer International Publishing AG
The registered company address is: Gewerbestrasse 11, 6330 Cham, Switzerland

Foreword

Ecosystems function on ecosystem time scales, spanning hours, days, seasons, years, and decades. Consequently, if one is to understand fully the structure and function of an ecosystem and how it interacts with its variable and changing environment, one needs to invest in long-term studies, lasting decades and longer. Long-term ecological studies are relatively rare. But when and where they exist, they can provide a treasure trove of information. For example, long-term ecological studies are natural laboratories that detect how ecosystem processes respond to a wide range of varying and interacting biophysical forcings. Hence, they serve as a powerful case study about ecosystem-atmosphere interactions.

The Waldstein forest in Germany has been the focus of integrated ecological, micrometeorological, and air pollution research for over 20 years. Data compiled from this site produces an important case study on the functioning of a temperate, evergreen conifer forest. In this book, a team of scientists from Bayreuth University have compiled the lessons learned from this research.

One of the strengths of a long-term field study is that ample data can be collected on the properties of the forest, its soil, air, and climate. This provides the opportunity for such a site to be a benchmark for model development, testing, and application. A second strength of a long-term ecological study site is that it can evolve with the development of instruments and methods and the discovering of new and pressing scientific questions. In the early days (1980s), there was much concern about "Waldsterben," forest dieback, from air pollution and soil acidification. So this site was home to some of the early pollution deposition and soil chemistry studies. As we learned more about pollution, scientists also started to hone in on the effects of volatile organic carbon emissions from trees, like terpenes, and their role on photochemical pollution. Because the trees are both sinks and sources for many pollutants and pollutant precursors, one needed to understand the role of stomatal control and transpiration. Such concerns also prompted efforts on the ecophysiology of trees. Development of methods measuring transpiration by sap flow were made and deployed at this site. By the late 1990s, development in commercial sonic anemometers and infrared gas analyzers enabled this team to apply their micrometeorological skills and measure integrated fluxes of water,

energy, and carbon over short to long time scales. The interpretation of such data led to much efforts on flux footprint climatology and flux footprint theory. And, to this day, this site remains an important node in the global FLUXNET network. In fact, few sites in the FLUXNET network have colocated data on pollution and carbon and water fluxes. In fact, one of the pressing questions with global change is the degree to which forest function and structure will change in a warming world, with more CO_2 and nitrogen deposition. Sites like this can help answer that question.

Coordinator of FLUXNET Dennis Baldocchi
October 2016

Preface

As a result of the forest decline in Central Europe in the 1980s and 1990s of the last century, a forest research station was established in a large area of spruce in the Fichtelgebirge Mountains in Germany. It is the aim of the book to summarize the scientific results obtained over the last 20 years at the FLUXNET station DE-Bay (Waldstein-Weidenbrunnen). While many of these results have already been published, others–including those in many as-yet unpublished master's theses and some PhD theses–are presented here for the first time. Work presented in early papers also needs a revision in light of the most recent investigations. Because the main focus of the research in recent years has been on the turbulent exchange conditions and turbulent energy and matter fluxes, the book is different to studies that are otherwise similar but more ecology-based. The book does, however, seek to convey an understanding of the functioning of the ecosystem as a whole by highlighting processes in the atmosphere. The Waldstein-Weidenbrunnen site is, alongside sites like Duke Forest, Niwot Ridge, and Hyytiälä, one of the best-investigated FLUXNET sites, with a strong focus on exchange conditions.

The opening chapter describes the history of the site and the research carried out in different types of projects and larger experiments beyond the continuously running observation program. From this, the reader can appreciate how the results in the book came together as a mosaic of many individual projects. The next chapter provides site documentation together with an appendix of the permanent instrumentation of the site, as well as the instrumentation used during special experiments. This allowed us to reduce the site descriptions in the individual chapters to their most important parts. Chapters 3 and 4 provide analysis of the monitoring data for climate, air pollution, water, and carbon fluxes on a scale of hours to years, and they describe the environment for all other research topics. The data are available on a monthly basis in an appendix. Chapters 5–14 mainly describe experimental case studies conducted on a much smaller scale in time and space. The authors used references between the chapters to show the strong interaction of these individual process studies. Model studies conducted from the catchment scale up to a high-resolution large eddy simulation are presented in a similar manner in Chaps. 15–18. Chapter 19 serves to bring everything together. Highlighting some special

problems, it assembles the results of the different chapters–the pieces of the puzzle–and formulates necessary research for the future and recommendations for possible networks similar to FLUXNET.

I am eager to express my acknowledgment of all who supported this research, in particular the European and German funding agencies, the authorities of the University of Bayreuth, and the technicians, mainly Jörg Gerchau, Johannes Olesch, and Gerhard Müller, without whom the intensive measuring program would not be possible. Furthermore, I want to thank Richard Howes for the language editing of many of the chapters. The book was also written in memoriam of Dr. Peter Werle, who supported many optical measurements.

Together with all authors, I hope that the book is not only a documentation of the Waldstein sites but also an interesting account of the generation of a deeper understanding of the turbulent exchange conditions of tall vegetation and that it will contribute ideas for further research.

Bischberg, Germany Thomas Foken
October 2016

Contents

List of Abbreviations

ACASA	Advanced Canopy-Atmosphere-Soil Algorithm model
AMERIFLUX	Network of PI-managed sites measuring ecosystem CO_2, water, and energy fluxes in North, Central, and South America
AOT40	Accumulated ozone exposure over a threshold of 40 ppb
ARW	Advanced Research WRF
BAHC	Biospheric Aspects of the Hydrological Cycle (of IGBP)
BayCEER	Bayreuth Center of Ecology and Environmental Research
BEWA 2000	Regional biogenic emissions of reactive volatile organic compounds (BVOC) from forests
BITÖK	Bayreuth Institute of Terrestrial Ecosystem Research
BMBF	German Federal Ministry of Education and Research
BVOC	Biogenic VOC
CACHE	Canopy-Chemistry model
CARBOEUROFLUX	An investigation on carbon and energy exchanges of terrestrial ecosystems in Europe
CARBOEUROP-IP	Assessment of the European terrestrial carbon balance
CEST	Central European Summer Time
CET	Central European Time
CUE	Carbon-Use Efficiency
DFG	German Science Foundation
DWD	German Meteorological Service (Deutscher Wetterdienst)
EC	Eddy-covariance
EGER	ExchanGE processes in mountainous Regions
EOF	Empirical Orthogonal Function
ET	Evapotranspiration
EUROFLUX	Fluxes of carbon, water and energy of European forests
FLAME	Forest-Land-Atmosphere-ModEl
FLUXNET	A global network: integrating worldwide CO_2, water and energy flux measurements

FOR 562	Research Group No. 562 of DFG "Dynamics of soil processes under extreme meteorological boundary conditions"
GLOBOENET	Global Biogenic Organic Emissions Network
GPP	Gross Primary Production
HMMS	Horizontal Moving Measuring System
HREA	Hyperbolic Relaxed Eddy Accumulation
IGBP	International Geosphere-Biosphere Programme
INTAS	International association for the promotion of cooperation with scientists from the independent states of the former Soviet Union
IOP	Intensive Observation Period
IPCC	Intergovernmental Panel on Climate Change
LAI	Leaf-Area Index
LES	Large Eddy Simulation
LLJ	Low Level Jet
MAE	Mean Average Error
MBE	Mean Bias Error
MLC-CHEM	Multi-Layer Canopy Chemistry exchange model
NCAR	National Center for Atmospheric Research
NEE	Net Ecosystem Exchange
PAD	Plant-Area Distribution
PAI	Plant-Area Index
PAK 446	Package Project No. 446 of DFG "EGER"
PALM	PArallelized Large-eddy simulation Model
PCA	Principal Component Analysis
PROXEL	Process-oriented Pixel model
RASS	Radio Acoustic Sounding System
REA	Relaxed Eddy Accumulation
RMSE	Root Mean Square Error
SCM-ECHAM4	Single-Column Model of the coupled chemistry-climate model ECHAM4
SFB 137	Collaborative Research Centre No. 137 of DFG
SODAR	SOund Detecting And Ranging
STANDFLUX	Process-based simulation model, describes canopy water vapour and carbon dioxide exchange
STANDFLUX 3D	Three-dimensional STANDFLUX
SVAT-CN	Soil-Vegetation-Atmosphere Transfer model for Carbon dioxide and Nitrogen
TA-Luft	Technical instructions on air quality control
TK2, TK3	"Turbulence Knight": Eddy-covariance calculation programme of the University of Bayreuth
VOC	Volatile Organic Compounds

VPDB	Vienna Pee Dee Belemnite
WALDATEM-2003	WAveLet Detection and Atmospheric Turbulence Exchange Measurements
WHNSIM	Water Heat and Nitrogen SImulation Model
WMO	World Meteorological Organization
WRF	Weather Research and Forecasting
WUE	Water-Use Efficiency

Part I
Introduction

Chapter 1
History of the Waldstein Measuring Sites

Thomas Foken and John Tenhunen

1.1 Introduction

The development of the ecological measurement sites in the Waldstein area is closely connected with the foundation of the Bayreuth Institute of Terrestrial Ecosystem Research (BITÖK). The activities of this institute came after a decade of acid rain research that had identified sulfur deposition in combination with nitrogen deposition as the main cause for forest decline. The initial studies at the Waldstein site had a stronger focus on plant ecology than on air quality and micrometeorology. In 1994, the air-quality station Oberwarmensteinach-Wagenthal (in operation since 1986) was moved to the Waldstein area (Pflanzgarten), and 1996 saw the start of the carbon dioxide flux measurements at the Waldstein-Weidenbrunnen site within the first European-funded EUROFLUX project that focused on ecosystem flux measurements. This was the beginning of a very intensive period of ecosystem-atmosphere interaction research. After the end of the funding of BITÖK in 2004 and until the present day, there have always been several projects running. This

T. Foken (✉)
Am Herrgottsbaum 28, 96120 Bischberg, Germany

Bayreuth Center of Ecology and Environmental Research, University of Bayreuth, Bayreuth, Germany
e-mail: foken@micrometeorology.de

J. Tenhunen
Bayreuth Center of Ecology and Environmental Research, University of Bayreuth, 95440 Bayreuth, Germany

T. Foken: Affiliation during the work at the Waldstein sites—University of Bayreuth, Department of Micrometeorology, Germany
J. Tenhunen: Affiliation during the work at the Waldstein sites—University of Bayreuth, BITÖK, Chair of Plant Ecology, Germany

T. Foken (ed.), *Energy and Matter Fluxes of a Spruce Forest Ecosystem*,
Ecological Studies 229, DOI 10.1007/978-3-319-49389-3_1

chapter will give the reader an overview of the history and development of the sites, particularly those used for atmospheric measurements.

1.2 The Foundation of BITÖK and the Establishment of the Waldstein Sites

The University of Bayreuth was founded in 1975 with "experimental ecology" as a focus for research and education, as recommended by the founding committee. Building upon the ecological research of the first years at the University of Bayreuth, the ecology of hedgerows started in 1976, and the Collaborative Research Centre (SFB 137) of the German Science Foundation started in 1980 (Schulze 1994). In response to forest decline, a Bavarian project of "forest toxicology" was initiated in the middle of the 1980s. Consequently, on July 30, 1986, the Senate of the University of Bayreuth followed the recommendation of the Federal Ministry of Education and Research (BMBF) and founded the Bayreuth Institute of Terrestrial Ecosystem Research (BITÖK), which was officially opened on November 5, 1990, at the University of Bayreuth. The foundation of BITÖK can also be seen in the light of large international programs like the International Geosphere-Biosphere Programme (IGBP) and its core project Biospheric Aspects of the Hydrological Cycle (BAHC, Kabat et al. 2004), with some special research topics in Bayreuth (Sturm et al. 1998; Tenhunen et al. 1998; Culf et al. 2004). Meteorological and climatological investigation was not a main topic of the scope of both the SFB 137 and the forest decline project. While the SFB concentrated on fluxes in plants and soil without the investigation of fluxes between the atmosphere and the ecosystem, the investigations of the forest decline (Schulze et al. 1989) needed additional measurements in the atmosphere, mainly of air pollution (Eiden et al. 1989); therefore, the Department[1] of Meteorology at the University cooperated on these topics. The importance of atmospheric measurements and research became increasingly obvious, and in the middle of the 1990s, the Department of Climatology at the BITÖK was established.

From 1989 to 1992, several start-up projects for the new institute on the basis of established postdoctoral projects began. Projects which are relevant to the topic of this book are listed in Table 1.1. In 1993 the first official project period of BITÖK, of only 2 years duration, started. The following three funding periods had a duration of 3–4 years up to 2004. In the first two periods, the measuring sites near the Waldstein in Fichtelgebirge (see Chap. 2), located in the Lehestenbach catchment, were established. The first of these was the Coulissenhieb site, which was used for biogeochemical research. The air pollution station of the Bavarian Environmental Agency at Oberwarmensteinach-Wagenthal (1984–1993) was incorporated into the BITÖK at the Waldstein-Pflanzgarten site and has been permanently running since that time (Klemm and Lange 1999, see Chap. 3). In 1994 the 32 m high walk-up

[1]The German department (Abteilung) is comparable with a laboratory or a research group.

scaffold tower with balcony-like platforms in the crown level of the forest, called the "Main Tower" (MT), was erected as well (see Chap. 2). This tower allowed plant ecological measurements in the crown, such as chamber measurements and sap flow measurements (Alsheimer et al. 1998), and deposition modeling on the basis of deposition velocities (Peters and Bruckner-Schatt 1995). Direct flux measurements started at the end of 1996 with carbon dioxide flux measurements (station "GE1") as part of the EUROFLUX program (Bernhofer et al. 2003). This station of the FLUXNET program (Baldocchi et al. 2001) "DE-Bay" is one of the oldest and, although unfortunately not directly funded after the EUROFLUX period, has always been maintained parallel to other research projects.

This book brings together a selection of the results of the research regarding the topic "Energy and Matter Fluxes of a Spruce Forest Ecosystem" and only covers a part of the much wider research activities of BITÖK documented in the book by Matzner (2004). The specific flux topic was under the scientific leadership of Prof. Ernst-Detlef Schulze (up to 1997; later on at Max-Planck-Institute for Biogeochemistry, Jena), Prof. John D. Tenhunen, Prof. Thomas Foken (since 1997, coming from the German Meteorological Service, following on from Prof. Eiden), and, for fluxes in the soil, Prof. Bernd Huwe. Funding for plant ecology research after 2000 was mainly directed to work on beech forests on larger scales and no longer to the research conducted at the measuring sites at Waldstein, with the consequence that since 2000 the plant ecological measuring program has been significantly reduced. Administration of the relevant research for this book was carried out by two chairs of plant ecology (Prof. Schulze at the University of Bayreuth and Prof. Tenhunen as part of BITÖK, since 2000 at the University), the Department of Soil Physics at the University (Prof. Huwe) and the Department of Micrometeorology at the University and the Department of Climatology as part of BITÖK, both headed by Prof. Foken.

After the end of the BITÖK funding in 2004, the new Bayreuth Center of Ecology and Environmental Research (BayCEER) was founded. Only one Chair of Plant Ecology was available, and the staff of the Department of Climatology was merged into the Department of Micrometeorology. BayCEER was set up with an umbrella function, but it offers some support in management of the measuring sites, chemical analysis, and handling of the data transfer and of the database.

1.3 Research and Measuring Programs

1.3.1 BITÖK Research Projects

The BITÖK research projects were organized in four funding periods (1993–1994, 1995–1997, 1998–2000, and 2001–2004), initially for the topics "nitrogen," "sulfur," "water," and "modeling," which were later on separated for different processes and scales. The research projects related to the context of this book "Energy and Matter Fluxes of a Spruce Forest Ecosystem" were mainly organized

under the topics "sulfur" and "water." In the first two funding periods, the relevant projects came mainly from the plant ecological groups and in the second two funding periods from the micrometeorological group. An overview of all relevant projects is given in Table 1.1.

The plant ecological measurements were focused on the understory, with chamber measurements for evapotranspiration (Wedler et al. 1996) and sap flow measurements (see Chap. 5) for the forest stand (Köstner et al. 1996; Alsheimer et al. 1998). However, comparisons of eddy covariance fluxes in the trunk space with chamber measurements and the data of the FLUXNET station (Subke et al. 2004; Subke and Tenhunen 2004) were also carried out. Most of the research was focused on the modeling of the water and carbon dioxide fluxes. The fundamental papers of the development of the relevant models are from the BITÖK research, including Falge et al. (1997), Köstner et al. (1998), or Sturm et al. (1998), which were the basis for Chaps. 5 and 16 of this book. Furthermore, a model with transilient closure was adapted to the site (Berger et al. 2004). Also, the first Lehstenbach catchment studies (Ostendorf and Manderscheid 1997) - relevant for Chap. 15 - are from this period.

In all four funding periods, projects related to air pollution and climate were realized, and these formed the basis of the establishment of the permanent measuring program (see Sect. 1.3.4 and Chap. 3). This research was also supported by the German Science Foundation (DFG) within a project investigating fog deposition (Wrzesinsky and Klemm 2000; Wrzesinsky et al. 2004, see Table 1.3).

In the first two periods, the influence of leaf wetness and water films on spruce needles on the deposition was investigated within special projects, unfortunately without any significant results. It was the logical consequence of earlier investigations on thin water films on needles and their influence on the deposition process (Burkhardt and Eiden 1994) and the development of a needle wetness sensor (Burkhardt and Gerchau 1994), which was also used in the following years (see Chap. 9).

In the last two funding periods, fluxes of the stable ^{13}C carbon isotope were measured above the forest to separate respiration and assimilation fluxes, even at daytime. Two different relaxed accumulation systems were therefore developed (Wichura et al. 2004). A synthesis of these results is given in Chap. 10. It was found that the coupling between the trunk space and the atmosphere above the crown is relevant to the exchange process of a forest. As a consequence, a special project was established in the last funding period. Its results (Thomas and Foken 2007a, b) had a significant influence on the research of the following 10 years, and this is reviewed in Chap. 6.

Furthermore, Schlather and Huwe (2005) developed models for three-dimensional flow patterns in the forest soil, which are applied for the Waldstein-Weidenbrunnen site in Chap. 7.

BITÖK and the Waldstein-Weidenbrunnen site hosted in 2001 and 2002 two experiments of the project BEWA 2000 "Regional biogenic emissions of reactive volatile organic compounds (BVOC) from forests", which were funded within the German atmospheric research program (AFO 2000). Two experiments took place in 2001 and 2002 (09.07.2001–03.08.2001 and 24.06.2002–02.08.2002,

Table 1.1 Projects within the BITÖK funding

Period	Title	**Principal investigator**, Co-workers	See Chapter
1989–1992 Start-up period	Determination of air pollution of spruce forests by dry deposition of aerosol particle and dew formation (special funding)	**R. Eiden,** K. Peters, J. Burkhardt	3
	Mathematical modeling of the deposition of aerosol particles in a spruce forest	**R. Eiden,** K. Peters	
	Investigation of the deposition process of atmospheric particles at plant surfaces	**R. Eiden,** J. Burkhardt	
1993–1994 Period A	Dry deposition of sulfur compounds to spruce forests in the Fichtelgebirge	**R. Eiden,** K. Peters	3
	The formation of water films on plant surfaces and their influence on the deposition of atmospheric trace gases	**R. Eiden,** N. Kanchanakanti	9
	Exchange processes at the vegetation-atmosphere interface: canopy transpiration and conductance as key variables in forests of different structures	**J. Tenhunen,** B. Köstner	5
	Characterization of spatial heterogeneity in transpiration from different spruce stands	**J. Tenhunen,** M. Alsheimer	5
	Evapotranspiration and CO_2-gas exchange in the understory in forest ecosystems	**J. Tenhunen,** M. Wedler	16
	Development of a physically based spatial model of gas exchange in forest ecosystems at the catchment scale	**J. Tenhunen,** B. Ostendorf	16
	Soil water availability effects on transpiration and canopy conductance of *Pinus silvestris*	**J. Tenhunen,** M. Sturm	7, 16
	Sources of NH_4 emission in the Fichtelgebirge	**E.-D. Schulze,** G. Bruckner-Schatt	3

(continued)

Table 1.1 (continued)

Period	Title	**Principal investigator**, Co-workers	See Chapter
1995–1997 Period B	Concentrations and deposition of particulate and gaseous sulfur and nitrogen in the Fichtelgebirge	**R. Eiden,** O. Klemm	3
	The formation of water films on plant surfaces and their influence on the deposition of atmospheric trace gases	**R. Eiden,** N. Kanchanakanti	9
	Evapotranspiration from understory in forest ecosystems	**J. Tenhunen,** M. Wedler	16
	Exchange processes at the vegetation-atmosphere-interface: canopy transpiration and conductance as key variables in forests of different structure	**J. Tenhunen,** B. Köstner	5, 16
	PROXEL–development of a model for landscape level simulations of vegetation-atmosphere exchange	**J. Tenhunen,** U. Joss	16
	Analysis of factors affecting landscape variation in transpiration from spruce stands	**J. Tenhunen,** M. Alsheimer	5
	Soil water availability effects on transpiration and canopy conductance of *Pinus silvestris*	**J. Tenhunen,** M. Sturm	7, 16
	Coupled transport of water, heat, and soil gases in forest soils: measurement and simulation	**B. Huwe,** M. Haubold	7
	Investigation of the sulfur dynamics in the groundwater	**M. Hauhs,** G. Lischeid	15

1998–2000 Period C	Influences of the leaf wetness on the deposition velocity of water-soluble gases	**T. Foken, O. Klemm,** O. Klemm	9
	Phase distribution of nitrogen compounds in the near-surface atmosphere	**O. Klemm,** T. Wrzesinsky, A. Held	9
	Climatology and air pollution in the Fichtelgebirge	**O. Klemm,** O. Klemm, T. Foken	3
	Pools and fluxes of the stable carbon isotope 13C between soil, vegetation, and atmosphere	**T. Foken, N. Buchmann,** B. Wichura	10
	Dynamically induced pattern of transport processes in forest soils	**B. Huwe,** M. Schlather	7
	Analysis of hydrological and hydro-chemical time series with multivariate and non-linear methods	**M. Hauhs,** G. Lischeid	15
	Hydraulic and hydro-chemical cross-linking of leakage water, surface water, and ground water-episodes and long-term trends	**M. Hauhs,** G. Lischeid	15
2001–2004 Period D	Climatology and deposition of air pollutants in the Fichtelgebirge	**O. Klemm (from 2003: T. Foken),** O. Klemm, T. Foken, J. Lüers	3
	Influences of coherent structures on the energy and matter exchange of tall canopies	**T. Foken,** C. Thomas	6, 12
	Measurement of turbulent fluxes of carbon dioxide and of the stabile ^{13}C carbon isotope above plant communities with the relaxed eddy accumulation method	**T. Foken,** J. Ruppert	10, 12
	Dynamically induced pattern of transport processes in forest soils	**B. Huwe,** M. Schlather	7
	Temporal development and spatial dynamics of the mass balance of two catchments	**E. Matzner,** G. Lischeid	15

Table 1.2 Larger experimental activities at Waldstein-Weidenbrunnen site, see also Chap. 2

Short name	Title	Reference	See Chapter
BEWA-Experiment 2001	Regional biogenic emissions of reactive volatile organic compounds (BVOC) from forests: process studies, modeling, and validation experiments (BEWA 2000)	Steinbrecher et al. (2004), Klemm et al. (2006)	9
BEWA-Experiment 2002			
WALDATEM-2003	Wavelet detection and atmospheric turbulence exchange measurements	Thomas et al. (2004)	6, 10, 12
EGER-IOP1 2007	Exchange processes in mountainous regions (EGER), intensive observation period 1 (IOP1)	Foken et al. (2012)	3, 4, 5, 6, 8, 9, 11, 12, 14, 16, 18
EGER-IOP2 2008	Exchange processes in mountainous regions (EGER), intensive observation period 2 (IOP2)		
EGER-IOP1 2011	Exchange processes in mountainous regions (EGER), intensive observation period 3 (IOP3)	This volume	3, 4, 6, 8, 9, 11, 13, 14, 16, 17

see Table 1.2); for process studies and model validation, the results have been completely published, e.g., with overview papers by Steinbrecher et al. (2004) and Klemm et al. (2006). For the first time, particle fluxes were measured (Held and Klemm 2006). An overview of the installations is given in Appendix A and a summary of the results in Chap. 9.

Furthermore, in 2003 a large experiment was created to investigate ^{13}C fluxes and the coupling within the forest canopy, running from April 28 to August 03, 2003, named WALDATEM-2003 (Wavelet Detection and Atmospheric Turbulence Exchange Measurements) (Thomas et al. 2004). An overview of the installations is given in Appendix A and results are included in Chaps. 6, 10, and 12.

1.3.2 European Research Projects

A main milestone in the measurement of the energy and matter exchange at the Waldstein-Weidenbrunnen site was the participation in the European EUROFLUX program (Table 1.3). Within this project the FLUXNET site GE1 (now DE-Bay)

Table 1.3 Projects funded by the European Community

Period	Title	**Principal investigator,** Co-workers	See Chapter
1996–1998	Long-term carbon dioxide and water vapor fluxes of European forests and interactions with the climate system (EUROFLUX)	**J. Tenhunen**, C. Rebmann	4
2000–2003	An investigation of carbon and energy exchange of terrestrial ecosystems in Europe (CARBOEUROFLUX)	**T. Foken**, C. Rebmann, M. Göckede	4, 12
2000–2003	Random walk models for the footprint problem in the turbulent atmosphere (INTAS)	**T. Foken**, M. Göckede	12
2003–2008	Assessment of the European terrestrial carbon balance (CARBOEUROPE-IP)	**T. Foken**, M. Göckede, M. Mauder	4, 12

was installed with eddy covariance measurements at 32 m on the Main Tower and occasionally also at 21 m. A book about the project was published (Valentini 2003), and the site-specific results given by Matteucci et al. (2000), Bernhofer et al. (2003), and Rebmann et al. (2004) are also part of Chap. 4. Besides the installation of a permanent carbon and water flux-monitoring program, the methodology for eddy covariance measurements within monitoring programs was also supported (Aubinet et al. 2000, 2003).

In the following funding period of 2000–2003 under the CARBOEUROFLUX project, funding was only provided for methodical aspects of the measuring method and not for the FLUXNET station itself and supporting research programs. Since 2000, PhD as well as postdoctoral students of related projects supported the maintenance of the station and the scientific analysis of the data. A first report, which covered the years 2000 and 2001 in addition to the EUROFLUX period 1997–1999, was published by Rebmann et al. (2004). Chapter 4 gives a full overview of the measurements up to 2014. Unfortunately, due to the shortfall in funding, all plant ecological studies ended in 2000, and the station only operated with a micrometeorological focus.

The CARBOEUROFLUX project and an INTAS project (support of scientists of the former Soviet Union; see also Table 1.3) were orientated on the development of footprint modeling in data quality control of FLUXNET stations. The developed method (Foken et al. 2004; Göckede et al. 2004) was applied to European FLUXNET sites (Rebmann et al. 2005). More details are given in Chap. 12. With the follow-up project CARBOEUROPE-IP, the method was updated with a Lagrangian footprint model (Göckede et al. 2006) and again applied to European FLUXNET sites with tall and low vegetation (Göckede et al. 2008). This study was combined with a comparison of available software packages for eddy covariance data (Mauder et al. 2008).

1.3.3 German Research Projects

Still within the BITÖK funding period, two projects funded by the German Science Foundation (DFG) and the German Federal Ministry of Education and Research (BMBF), see Table 1.4, supported the research on fog deposition and the two experiments of the BEWA-2000 project (see Table 1.2). The BMBF also supported the development of data quality tools for long-term measuring programs where the Waldstein-Weidenbrunnen site was one of the Anchor stations (Table 1.4).

After the end of the BITÖK funding, the scientists of the newly founded BayCEER proposed the establishment of a Collaborative Research Centre (SFB) with the title "Nonlinear Processes in Ecosystems" (SFB 1971). Unfortunately, the overall funding failed but selected parts of the proposal were funded. The research group (FOR 562) of DFG "Dynamics of soil processes under extreme meteorological boundary conditions" worked from 2005 to 2011 at the Coulissenhieb-II site (identical with Weidenbrunnen-II site) between the Waldstein-Weidenbrunnen and Pflanzgarten sites with soil manipulation experiments (Muhr et al. 2009) and at the Schlöppnerbrunnen temperate fen site (Wunderlich and Borken 2012). In accordance with the topic of this book, only the soil flux part of this project is included as Chap. 7.

A second research group (FOR 658) "Exchange Processes in Mountainous Regions" (EGER) was only partly funded (the modeling part was not covered) as single projects in 2006–2009 and as a package project (PAK 446) in 2010–2013 (see Table 1.4). The project combined researchers from BayCEER and the Max-Planck Institute of Chemistry at Mainz and the University of Hannover (second phase only). Within the project, three large experimental activities took place, with the last of these being in 2011 with international partners from the USA and the European Community. The main topics of the experiments in 2007 (autumn) and 2008 (summer) were related to the interaction between atmospheric turbulence and chemistry, with a strong focus on the coupling from the ground through the canopy up to the atmosphere and its relation on the Damköhler number (Foken et al. 2012). The third experiment had a focus on the forest edge and related vertical and horizontal structures as the experimental part and on a three-dimensional modeling with classical models and large eddy simulations. The results of the EGER project are of relevance for nearly all chapters. Within the EGER project, an international workshop "Atmospheric Transport and Chemistry in Forest Ecosystems" was organized in the Castle of Thurnau (October 5–8, 2009), with about 100 participants from 24 countries on five continents (Lüers and Foken 2009; Foken et al. 2011).

1.3.4 Permanent Measuring Program

The air pollution measuring program has one of the longest measuring series since 1984 (including the former station Oberwarmensteinach-Wagenthal), with SO_2-,

Table 1.4 Projects funded by German science foundation (DFG) and the German Federal Ministry of Education and Research (BMBF)

Period	Title	**Principal investigator,** Co-workers	See Chapter
1999–2002	Quantification of the atmospheric input of water and nutrients to a forest ecosystem through fog deposition (DFG: KL 623/4–1)	**O. Klemm,** T. Wrzesinsky	3
2001–2004	Regional biogenic emissions of reactive volatile organic compounds (BVOC) from forests: process studies, modeling, and validation experiments (BMBF: AFO-2000/BEWA 2000)	**O. Klemm,** A. Held	9
2001–2004	Vertical transports of energy and trace gases at Anchor stations and its spatial and temporal extrapolation under complex natural conditions (BMBF: AFO-2000/VERTIKO)	**T. Foken**, M. Göckede, C. Liebethal, M. Mauder	12
2005–2008	Changing flow paths in soils (DFG: FOR 562, TP5)	**B. Huwe**, C. Bogner	7
2008–2011	Response of flow systems in soils (DFG: FOR 562, TP10)	**B. Huwe**, K. Müller	7
2006–2009	Turbulence and stand-scale modeling (DFG: FO 226/16–1)	**T. Foken**, A. Serafimovich, K. Staudt (Köck), L. Siebicke	4, 6, 11, 12, 14, 16, 18
	Reactive trace gases and plant ecology (DFG: ME 4100/4–1)	**F. X. Meixner**, E. Falge	3, 5, 8, 9, 16
	Heterogeneous processes (DFG: ZE 792/4–1)	**C. Zetzsch**, M. Sörgel	8, 9
2010–2013	Exchange processes in mountainous regions (DFG: PAK 446)	**T. Foken, F.X. Meixner, S. Raasch,** A. Serafimovich, J. Hübner, E. Falge, L. Voß, F. Kanani (Kanani-Sühring)	3, 4, 6, 8, 9, 11, 13, 14, 16, 17
2011–2014	Nitrous acid (HONO) source and sink processes in a disturbed forest ecosystem - interactions of heterogeneous chemistry and turbulent transport (DFG: HE 5214/4–1, related to PAK 446)	**A. Held,** M. Sörgel	8, 9

NO-, NO_2-, and O_3-concentration measurements at the Waldstein-Pflanzgarten site. Since 1995/1996, a climatological measuring program has been installed together with the EUROFLUX station, with wind measurements at eight levels, temperature and humidity at four levels, and global radiation and net radiation at the top of the tower. Since 2000 the program has been extended, and better sensors have been installed, especially for the radiation measurements. Details about the permanent program are given in Appendix A. Since 2007, the wet deposition has also been permanently measured. A first scientific analysis was presented by Eiden et al. (1989). The site was included in a climatological study of northeast Bavaria and northwest Bohemia (Foken 2003). The final results of the BITÖK-period are given by Klemm (2004) and Foken (2004). These findings were updated up to 2014 (Chap. 3). The Bavarian Environment Agency uses these data partly for environmental control, and the rain gauge has been included since 2012 in the Bavarian flood warning system to monitor precipitation events in the spring catchment of the rivers Main, Saale, Eger (Ohre), and Naab.

1.4 Conclusions

The founding of the BITÖK was a successful and sustainable initiative to establish a forest research site with now more than 20 years of intensive research activities. The impressive book about the BITÖK research (Matzner 2004) was a first summary of the long list of publications. Since 2005, under the umbrella of BayCEER, not only could the long-term measuring program of climatology and air pollution and the FLUXNET station DE-Bay be stabilized, but also a long list of projects and publications on the topic of "Energy and Matter Fluxes of a Forest Ecosystem" was realized in the last 10 years. While at the beginning of the BITÖK, the research was very focused on the forest decline and on plants and soils, the climate impact and processes between the atmosphere and ecosystem became more and more important. The results could not be imagined without the enthusiastic work of many technicians, bachelor, master, and PhD students as well as postdoctoral students. Therefore, the work on the sites was closely related to education in geoecology and biology at the University of Bayreuth. Many of the former students are now well-known scientists in Germany and other countries.

This chapter provides more than a historical list of projects, funding, and experiments and is relevant not only for scientists involved in the research at the Waldstein sites. The chapter helps the readers to find the circumstances and the periods of specific research topics at the site and to combine these with the specific studies in Chaps. 5–18. As highlighted in Chap. 19, funding periods, projects, and responsibilities also constitute important metadata for long-term measuring programs (Chaps. 3, 4). Gaps or periods with missing data can also be explained by such more or less administrative criteria. Therefore, this chapter is essential for a better understanding and interpretation of the measurements and is an example of how to prepare such data as the metadata of a research site.

The authors of this book have prepared a comprehensive overview of the research of the last 20 years at the Waldstein measuring sites, with some outlooks into the future. The chapters give an inventory of the many results of this period but also have a strong methodological aspect, which makes the book interesting in addition to the historical aspect, and show the influence of the Waldstein research on many research projects beyond Bayreuth and Germany.

Acknowledgments The research at the Waldstein sites were funded by the Federal Ministry of Education, Science, Research and Technology, the European Community, the German Science Foundation, and others. For details and relevant project numbers, see the chapters of the book. The authors acknowledge Dr. Thomas Gollan for his support with historical documents and his helpful discussion.

Reports

Results of the implementation and four research periods of BITÖK:

1989–1992 BITÖK Forschungsbericht 1989–1992, Bayreuth 1993, 180 S.

1993–1994 BITÖK Forschungsbericht 1993, BITÖK, Bayreuth 1994, 249 S.; BITÖK Forschungsbericht 1994, Bayreuther Forum Ökologie No. 15, 1995, 266 S.

1995–1997 BITÖK Forschungsbericht 1995–1997, Bayreuther Forum Ökologie No. 56, 1998, 256 S.

1998–2000 BITÖK Forschungsbericht 1998–2000, Bayreuther Forum Ökologie No. 84, 2001, 382 S.

2001–2004 BITÖK Forschungsbericht 2001–2004, BITÖK, Bayreuth 2005, 306 S. (unpublished). The meteorological projects are published in: Foken, T. (Ed.): Klimatologische und mikrometeorologische Forschungen im Rahmen des Bayreuther Institutes für Terrestrische Ökosystemforschung (BITÖK) 1989–2004. Arbeitsergebnisse, Universität Bayreuth, Abt. Mikrometeorologie, No. 29, 2005, 105 S. (ISSN: 1614–8916).

References

Alsheimer M, Köstner B, Falge E, Tenhunen JD (1998) Temporal and spatial variation in transpiration of Norway spruce stands within a forested catchment of the Fichtelgebirge, Germany. Ann Sci For 55:103–123

Aubinet M, Clement R, Elbers J, Foken T, Grelle A, Ibrom A, Moncrieff H, Pilegaard K, Rannik U, Rebmann C (2003) Methodology for data acquisition, storage and treatment. In: Valentini R (ed) Fluxes of carbon, water and energy of European forests, ecological studies, vol 163. Springer, Berlin, pp 9–35

Aubinet M, Grelle A, Ibrom A, Rannik Ü, Moncrieff J, Foken T, Kowalski AS, Martin PH, Berbigier P, Bernhofer C, Clement R, Elbers J, Granier A, Grünwald T, Morgenstern K, Pilegaard K, Rebmann C, Snijders W, Valentini R, Vesala T (2000) Estimates of the annual net

carbon and water exchange of forests: the EUROFLUX methodology. Adv Ecol Res 30:113–175

Baldocchi D, Falge E, Gu L, Olson R, Hollinger D, Running S, Anthoni P, Bernhofer C, Davis K, Evans R, Fuentes J, Goldstein A, Katul G, Law B, Lee XH, Malhi Y, Meyers T, Munger W, Oechel W, Paw U KT, Pilegaard K, Schmid HP, Valentini R, Verma S, Vesala T (2001) FLUXNET: a new tool to study the temporal and spatial variability of ecosystem-scale carbon dioxide, water vapor, and energy flux densities. Bull Am Meteorol Soc 82:2415–2434

Berger M, Dlugi R, Foken T (2004) Modelling the vegetation atmospheric exchange with transilient model. In: Matzner E (ed) Biogeochemistry of forested catchments in a changing enivironment: a German case study. Ecological studies, vol 172. Springer, Berlin, pp 177–190

Bernhofer C, Aubinet M, Clement R, Grelle A, Grünwald T, Ibrom A, Jarvis P, Rebmann C, Schulze E-D, Tenhunen JD (2003) Spruce forests (Norway and Sitka spruce, including Douglas fir): carbon and water fluxes and balances, ecological and ecophysiological determinants. In: Valentini R (ed) Fluxes of carbon, water and energy of European forests. Ecological studies series 163. Springer, Berlin, pp 99–123

Burkhardt J, Eiden R (1994) Thin water films on coniferous needles: a new device for the study of water vapour condensation and gaseous deposition to plant surfaces and particle samples. Atmos Environ 28:2001–2011

Burkhardt J, Gerchau J (1994) A new device for the study of water vapour concentration and gaseous deposition to plant surfaces and particle samples. Atmos Environ 28:2012–2017

Culf AD, Foken T, Gash JHC (2004) The energy balance closure problem. In: Kabat P et al (eds) Vegetation, water, humans and the climate. A new perspective on an interactive system, Springer, Berlin, pp 159–166

Eiden R, Förster J, Peters K, Trautner F, Herterich R, Gietl G (1989) Air pollution and deposition. In: Schulze E-D et al (eds) Forest decline and air pollution, vol 77. Springer, Berlin, pp 57–103

Falge EM, Ryel RJ, Alsheimer M, Tenhunen JD (1997) Effects on stand structure and physiology on forest gas exchange: a simulation study for Norway spruce. Trees 11:436–448

Foken T (2003) Lufthygienisch-Bioklimatische Kennzeichnung des oberen Egertales. Bayreuther Forum Ökologie 100:69+XLVIII

Foken T (2004) Climate change in the Lehstenbach region. In: Matzner E (ed) Biogeochemistry of forested catchments in a changing enivironment, a German case study. Ecological studies. Springer, Berlin, pp 59–66

Foken T, Aubinet M, Finnigan J, Leclerc MY, Mauder M, Paw U KT (2011) Results of a panel discussion about the energy balance closure correction for trace gases. Bull Am Meteorol Soc 92:ES13–ES18

Foken T, Göckede M, Mauder M, Mahrt L, Amiro BD, Munger JW (2004) Post-field data quality control. In: Lee X et al (eds) Handbook of micrometeorology: a guide for surface flux measurement and analysis. Kluwer, Dordrecht, pp 181–208

Foken T, Meixner FX, Falge E, Zetzsch C, Serafimovich A, Bargsten A, Behrendt T, Biermann T, Breuninger C, Dix S, Gerken T, Hunner M, Lehmann-Pape L, Hens K, Jocher G, Kesselmeier J, Lüers J, Mayer JC, Moravek A, Plake D, Riederer M, Rütz F, Scheibe M, Siebicke L, Sörgel M, Staudt K, Trebs I, Tsokankunku A, Welling M, Wolff V, Zhu Z (2012) Coupling processes and exchange of energy and reactive and non-reactive trace gases at a forest site—results of the EGER experiment. Atmos Chem Phys 12:1923–1950

Göckede M, Foken T, Aubinet M, Aurela M, Banza J, Bernhofer C, Bonnefond J-M, Brunet Y, Carrara A, Clement R, Dellwik E, Elbers JA, Eugster W, Fuhrer J, Granier A, Grünwald T, Heinesch B, Janssens IA, Knohl A, Koeble R, Laurila T, Longdoz B, Manca G, Marek M, Markkanen T, Mateus J, Matteucci G, Mauder M, Migliavacca M, Minerbi S, Moncrieff JB, Montagnani L, Moors E, Ourcival J-M, Papale D, Pereira J, Pilegaard K, Pita G, Rambal S, Rebmann C, Rodrigues A, Rotenberg E, Sanz MJ, Sedlak P, Seufert G, Siebicke L, Soussana JF, Valentini R, Vesala T, Verbeeck H, Yakir D (2008) Quality control of CarboEurope flux data—part 1: coupling footprint analyses with flux data quality assessment to evaluate sites in forest ecosystems. Biogeosciences 5:433–450

Göckede M, Markkanen T, Hasager CB, Foken T (2006) Update of a footprint-based approach for the characterisation of complex measuring sites. Bound Lay Meteorol 118:635–655

Göckede M, Rebmann C, Foken T (2004) A combination of quality assessment tools for eddy covariance measurements with footprint modelling for the characterisation of complex sites. Agric For Meteorol 127:175–188

Held A, Klemm O (2006) Direct measurement of turbulent particle exchange with a twin CPC eddy covariance system. Atmos Environm 40(Supplement 1):92–102

Kabat P, Claussen M, Dirmeyer PA, Gash JHC, de Guenni LB, Meybeck H, Pielke RA Sr, Vörösmarty C, Hutjes RWA, Lütkemeier S (eds) (2004) Vegetation, water, humans and the climate. A new perspective on an interactive system. Springer, Berlin, 566 pp

Klemm O (2004) Trace gases and particles in the atmospheric boundary layer at the Waldstein site: present state and his historic trends. In: Matzner E (ed) Biogeochemistry of forested catchments in a changing enivironment, a German case study. Ecological studies, vol 172. Springer, Berlin, pp 45–58

Klemm O, Held A, Forkel R, Gasche R, Kanter H-J, Rappenglück B, Steinbrecher R, Müller K, Plewka A, Cojocariu C, Kreuzwieser J, Valverde-Canossa, Schuster G, Moortgat GK, Graus M, Hansel A (2006) Experiments on forest/atmosphere exchange: climatology and fluxes during two summer campaigns in NE Bavaria. Atmos Environ 40(Supplement 1):3–20

Klemm O, Lange H (1999) Trends of air pollution in the fichtelgebirge mountains, Bavaria. Environ Sci Pollut Res 6:193–199

Köstner B, Alsheimer M, Tenhunen JD (1996) Water fluxes in a spruce forest ecosystem: tree canopy transpiration at different sites. Verh Ges Ökol 26:61–68

Köstner B, Falge EM, Alsheimer M, Geyer R, Tenhunen JD (1998) Estimating tree canopy water use via xylem sapflow in an old Norway spruce forest and a comparison with simulation-based canopy transpiration estimates. Ann For Sci 55:125–139

Lüers J, Foken T (2009) Proceedings of the international conference of "Atmospheric Transport and Chemistry in Forest Ecosystems", Castle of Thurnau, Germany, Oct 5 to Oct 8, 2009. Arbeitsergebn, Univ Bayreuth, Abt Mikrometeorol, ISSN 1614–8916, 40, 70pp

Matteucci G, Dore S, Stivanello S, Rebmann C, Buchmann N (2000) Soil respiration in beech and spruce forests in Europe: trends, controling factors, annual budgets and implications for the ecosystem carbon balance. In: Schulze ED (ed) Carbon and nitrogen cycling in European forest ecosystems. Springer, Berlin, pp 217–236

Matzner E (ed) (2004) Biogeochemistry of forested catchments in a changing environment, a German case study. Springer, Berlin, 498 pp

Mauder M, Foken T, Clement R, Elbers J, Eugster W, Grünwald T, Heusinkveld B, Kolle O (2008) Quality control of CarboEurope flux data—part 2: inter-comparison of eddy-covariance software. Biogeosciences 5:451–462

Muhr J, Borken W, Matzner E (2009) Effects of soil frost on soil respiration and its radiocarbon signature in a Norway spruce forest soil. Glob Chang Biol 15:782–793

Ostendorf B, Manderscheid B (1997) Seasonal modelling of catchment water balance: a two-level cascading modification of TOPMODEL to increase the realism of spatio-temporal processes. Hydrol Process 11:1231–1242

Peters K, Bruckner-Schatt G (1995) The dry deposition of gaseous and participate nitrogen compounds to a spruce stand. Water Air Soil Pollut 85:2217–2222

Rebmann C, Anthoni P, Falge E, Göckede M, Mangold A, Subke J-A, Thomas C, Wichura B, Schulze ED, Tenhunen J, Foken T (2004) Carbon budget of a spruce forest ecosystem. In: Matzner E (ed) Biogeochemistry of forested catchments in a changing enivironment, a German case study. Ecological studies, vol 172. Springer, Berlin, pp 143–160

Rebmann C, Göckede M, Foken T, Aubinet M, Aurela M, Berbigier P, Bernhofer C, Buchmann N, Carrara A, Cescatti A, Ceulemans R, Clement R, Elbers J, Granier A, Grünwald T, Guyon D, Havránková K, Heinesch B, Knohl A, Laurila T, Longdoz B, Marcolla B, Markkanen T, Miglietta F, Moncrieff H, Montagnani L, Moors E, Nardino M, Ourcvial J-M, Rambal S, Rannik U, Rotenberg E, Sedlak P, Unterhuber G, Vesala T, Yakir D (2005) Quality analysis

applied on eddy covariance measurements at complex forest sites using footprint modelling. Theor Appl Climatol 80:121–141

Schlather M, Huwe B (2005) A stochastic model for 3-dimensional flow patterns in infiltration experiments. J Hydrol 310:17–27

Schulze ED (ed) (1994) Flux control in biological systems. Academic Press, San Diego, NY, 494 pp

Schulze ED, Lange OL, Oren R (eds) (1989) Forest decline and air pollution, vol XVIII. Springer, Berlin, 475 pp

Steinbrecher R, Rappenglück B, Hansel A, Graus M, Klemm O, Held A, Wiedensohler A, Nowak A (2004) Vegetation-atmospheric interactions: the emissions of biogenic volatile organic compounds (BVOC) and their relevance to atmospheric particle dynamics. In: Matzner E (ed) Biogeochemistry of forested catchments in a changing enivironment, a German case study. Ecological studies, vol 172. Springer, Berlin, pp 215–235

Sturm N, Köstner B, Hartung W, Tenhunen JD (1998) Environmental and endogenous controls on leaf- and stand-level water conductance in a Scots pine plantation. Ann Sci For 55:237–253

Subke J-A, Buchmann N, Tenhunen JD (2004) Soil CO_2 fluxes in spruce forests—temporal and spacial variation, and environmental controls. In: Matzner E (ed) Biogeochemistry of forested catchments in a changing enivironment, a German case study. Ecological studies, vol 172. Springer, Berlin, pp 127–141

Subke J-A, Tenhunen J (2004) Direct measurements of CO_2 flux below a spruce forest canopy. Agric For Meteorol 126:157–168

Tenhunen JD, Valentini R, Köstner B, Zimmermann R, Granier A (1998) Variation in forest gas exchange at landscape to continental scales. Ann Sci For 55:1–11

Thomas C, Foken T (2007a) Flux contribution of coherent structures and its implications for the exchange of energy and matter in a tall spruce canopy. Bound Lay Meteorol 123:317–337

Thomas C, Foken T (2007b) Organised motion in a tall spruce canopy: temporal scales, structure spacing and terrain effects. Bound Lay Meteorol 122:123–147

Thomas C, Ruppert J, Lüers J, Schröter J, Mayer J-C, Bertolini T (2004) Documentation of the WALDATEM-2003 experiment April, 28th to August, 03rd 2003. Arbeitsergebn, Univ Bayreuth, Abt Mikrometeorol, ISSN 1614–8916, 24, 57 pp

Valentini R (ed) (2003) Fluxes of carbon, water and energy of European forests. Ecological studies, vol 163. Springer, Berlin, 270 pp

Wedler M, Köstner B, Tenhunen J (1996) Understory contribution to stand total water loss at an old Norway spruce forest. Verh Ges Ökol 26:69–77

Wichura B, Ruppert J, Delany AC, Buchmann N, Foken T (2004) Structure of carbon dioxide exchange processes above a spruce forest. In: Matzner E (ed) Biogeochemistry of forested catchments in a changing enivironment, a German case study. Ecological studies, vol 172. Springer, Berlin, pp 161–176

Wrzesinsky T, Klemm O (2000) Summertime fog chemistry at a mountainous site in central Europe. Atmos Environ 34:1487–1496

Wrzesinsky T, Scheer C, Klemm O (2004) Fog deposition and its role in biogeochemical cycles of nutrients and pollutants. In: Matzner E (ed) Biogeochemistry of forested catchments in a changing enivironment, a German case study. Ecological studies, vol 172. Springer, Berlin, pp 191–202

Wunderlich S, Borken W (2012) Partitioning of soil CO_2 efflux in un-manipulated and experimentally flooded plots of a temperate fen. Biogeosciences 9:3477–3489

Chapter 2
Description of the Waldstein Measuring Site

Thomas Foken, Pedro Gerstberger, Katharina Köck, Lukas Siebicke, Andrei Serafimovich, and Johannes Lüers

2.1 Introduction

The measuring sites of the Bayreuth Center of Ecology and Environmental Research (BayCEER) at the Waldstein area in the Fichtelgebirge Mountains (Fig. 2.1) have a well-documented history over a period of more than 20 years (see Chap. 1). The most comprehensive description of each of the measurement sites can befound in Gerstberger (2001) and Gerstberger et al. (2004). Between the two mountains "Großer Waldstein" (879 m a.s.l.) and the "Bergkopf" (857 m a.s.l.) is located the

T. Foken (✉)
Am Herrgottsbaum 28, 96120 Bischberg, Germany

Bayreuth Center of Ecology and Environmental Research, University of Bayreuth, Bayreuth, Germany
e-mail: foken@micrometeorology.de

P. Gerstberger
University of Bayreuth, Chair of Plant Ecology, 95440 Bayreuth, Germany

Bayreuth Center of Ecology and Environmental Research, University of Bayreuth, Bayreuth, Germany

K. Köck
Schulstraße 14, 95032 Hof, Germany

L. Siebicke
Georg-August-University Göttingen, Bioclimatology, Büsgenweg 2, 37077 Göttingen, Germany

A. Serafimovich
Helmholtz Centre Potsdam, GFZ German Research Centre for Geosciences, Telegrafenberg, Haus A 6, 14473 Potsdam, Germany

T. Foken (ed.), *Energy and Matter Fluxes of a Spruce Forest Ecosystem*,
Ecological Studies 229, DOI 10.1007/978-3-319-49389-3_2

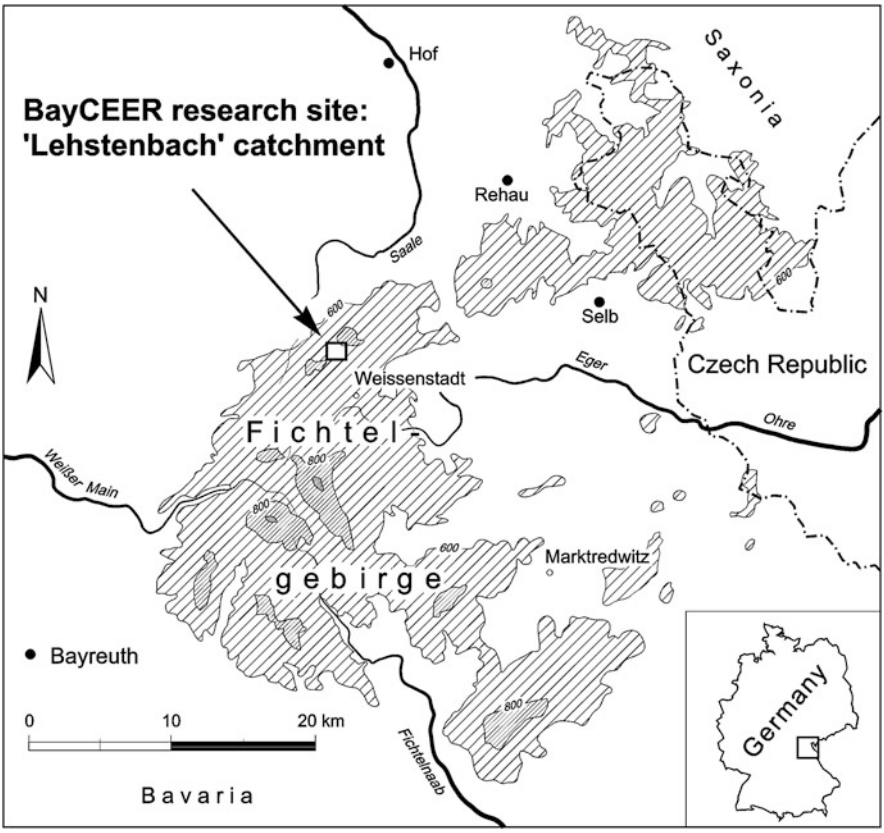

Fig. 2.1 Fichtelgebirge Mountains with the location of the Lehstenbach catchment; the contour lines are 600, 800, and 1000 m a.s.l. (Gerstberger et al. 2004, published with kind permission of © Springer-Verlag Berlin, Heidelberg, All rights reserved)

"Lehestenbach Catchment," with several measuring sites (Fig. 2.2). The present documentation is mainly for the Pflanzgarten site, with air quality and some climatological measurements, and the Weidenbrunnen site with forest climate measurements and the FLUXNET station (DE-Bay). Both sites were established in 1994. Furthermore, in some of the chapters of this volume, the Weidenbrunnen II

J. Lüers
Bayreuth Center of Ecology and Environmental Research, University of Bayreuth, 95440 Bayreuth, Germany

T. Foken, K, Köck, L. Siebicke, A. Serafimovich, and J. Lüers: Affiliation during the work at the Waldstein sites – University of Bayreuth, Department of Micrometeorology, Germany

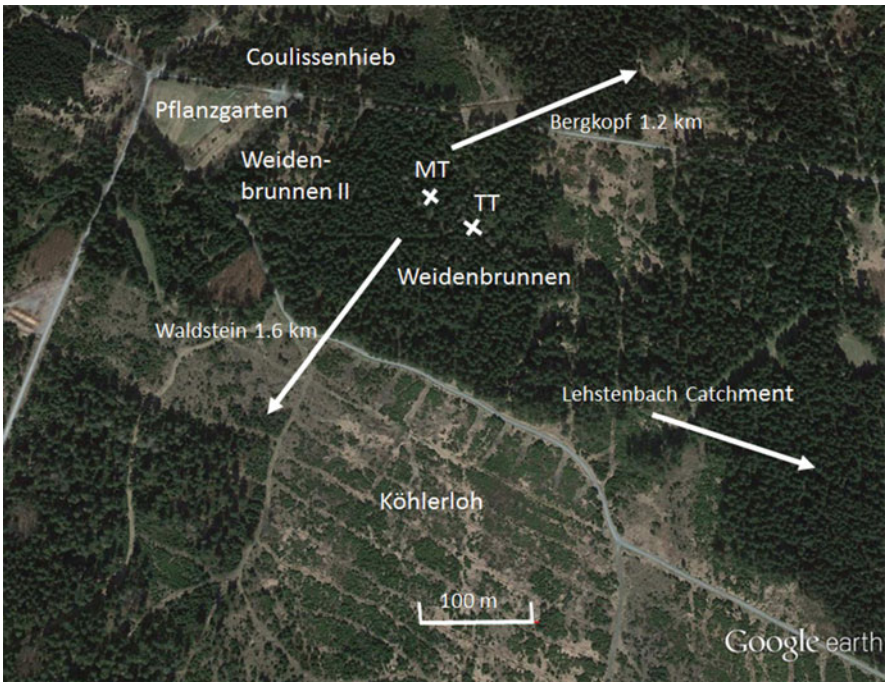

Fig. 2.2 Aerial view of the Waldstein sites in the Lehstenbach catchment (photograph from April 19, 2015, showing nearly no changes since 2007), with the different measuring sites and distances to relevant hills in the surrounding landscape (Published with kind permission of © Google earth, 2015, All rights reserved), MT: Main Tower, TT: Turbulence Tower

site (later on called Coulissenhieb II), the Schlöpnerbrunnen site, and the Köhlerloh site are also included in the analysis. The necessary details of these sites are given in the relevant chapters. The main site for ecological and soil research, Coulissenhieb, has no relevant atmospheric measurements and is not included in this book. Many details have been published in a separate book (Matzner 2004) and later on by Muhr et al. (2009).

In the period of the existence of the Bayreuth Institute of Terrestrial Ecosystem Research (BITÖK) from 1994 to 2004 and of the European EUROFLUX project (see Chap. 1), all the Waldstein sites were worked on by many researchers and were the subjects of a great number of scientific and popular scientific publications including site documentations. Staudt (now Köck) and Foken (2007) made a comparison of all published data and selected recommended values, and this constituted a major step toward providing harmonized and quality-controlled consistent data. In this chapter, we follow this documentation.

2.2 The Waldstein Area

The densely forested Fichtelgebirge Mountains located in the northeast of Bavaria (Fig. 2.1) originated from a large granitic pluton surrounded by metamorphic rock series such as gneiss, mica schists, and phyllites. The highest summits are "Schneeberg" (1053 m) and "Ochsenkopf" (1023 m) and do not reach the timberline. In the Pleistocene, the Fichtelgebirge was not glaciated, but erosion and solifluction occurred, leaving behind typical "woolsack" rock formations of granite (e.g., the Waldstein, Rudolphstein). The region was, for several decades, heavily influenced by air pollution, mainly SO_2 (see Chap. 3) and reactive nitrogen.

The long-lasting pollution of the region resulted in severe acidification of the already acid soils, and forest decline at higher altitudes (above 800 m) of the Fichtelgebirge occurred in the 1980s (Schulze et al. 1989). Today the input of sulfur has dropped dramatically. However, the input of nitrogen compounds (as NO_x and NH_4^+) is still high and shows no decreasing trend (Matzner 2004); the continuing high levels of NO_2 are given in Chap. 3.

The main experimental plots are located in the Lehstenbach catchment, which has an area of 4.5 km^2 and an altitude of 695 m to 877 m a.s.l., with the Waldstein-Weidenbrunnen site at 875 m. The annual precipitation is 1.162 mm and the mean temperature 5.3 °C (Foken 2003, updated in Chap. 3) for the period 1971–2000. Most of the measurement sites are in the vicinity of the Weidenbrunnen site (Fig. 2.2). All sites, with the exception of the Weidenbrunnen site, were limed in the 1990s using dolomitic lime. The Weidenbrunnen site, due to a later liming, was therefore the most affected by acidification of all sites, with characteristic yellowing of the older needles of Norway spruce (*Picea abies*) and more than 30 % needle loss (Gerstberger 2001). However, it was decided in 2001 to lime this site as well and to stop any investigations of the forest decline in the period after the acid rain. In the following years, the forest regained its green color and had a growth similar to the whole forest (see Chap. 4). A description of all forest stands in this area can be found in Alsheimer (1997). The potential natural vegetation of the area is a beech-fir-mixed forest (Reif 1989).

The forest structure was severely disturbed by two storm events: Kyrill on January 18, 2007 and Emma on February 29, 2008. Kyrill mainly destroyed large parts of the Köhlerloh site, with a wind throw of about 1.5 km length in that site, and parts in the Weidenbrunnen II site (Fig. 2.2). For the Waldstein area, we should therefore separate a period with a widely intact forest site before 2007, with the exception of some degradations due to acid rain before 2002 for the Weidenbrunnen site, and a period with large areas destroyed by windfall and bark beetle infestation since 2007. An overview of the characteristic data of all sites is given in Table 2.1.

Table 2.1 Main characteristics of the different sites

	Weidenbrunnen	Pflanzgarten	Köhlerloh
Latitude	50°08′31″ N (MT) 50°08′30″ N (TT)	50°08′35″N	50°08′22″N
Longitude	11°52′01″ E (MT) 11°52′03″ E (TT)	11°51′49″E	11°52′02″E
Elevation	775 m (MT) 773 m (TT)	765 m	749 m
Forest	Norway spruce (*Picea abies*) Age: 60 years (2013)	–	–
Understory	*Calamagrostis villosa, Deschampsia flexuosa, Vaccinium myrtillus, Dryopteris dilatata, Oxalis acetosella, Dicranum scoparium* cover: 60–80 %	Mown grass meadow, scrub	*Deschampsia flexuosa, Picea abies, Vaccinium myrtillus* (together 60 %); *Calamagrostis villosa,* (9 %); *Juncaceae, Cyperaceae* (together 3 %); others: dead wood, bare soil
References	Staudt and Foken (2007)		Serafimovich et al. (2011)

MT Main Tower, TT Turbulence Tower

Table 2.2 Time-dependent characteristics of the forest stand

Year	Canopy height in m	Leaf area index in m^2 m^{-2}	Reference
1993	16.1	5.3	Alsheimer (1997)
1995	17.8		Mund (1996)
2003	19	5.2	Thomas et al. (2004) and Thomas and Foken (2007a)
2008	25	4.8	Foken et al. (2012)
2011	27		Serafimovich et al. (2011)

2.3 Specific Details of the Measuring Sites

2.3.1 Waldstein-Weidenbrunnen

2.3.1.1 Forest Stand

The Norway spruce forest (*Picea abies* (L.) KARST.) has an age of 60 years (2013) with 60–80 % understory (Table 2.1). Because of beetle attacks and storm events, the forest has become more and more heterogeneous in the last 10 years with a lower tree density, which was about 1000 ha^{-1} at the end of the 1990s. The tree height and the leaf area index are given in Table 2.2. Measurements of the horizontal distribution of plant area index (PAI) were made with two optical area meters (Plant Canopy Analyzer, LAI2000, LiCor, USA) and are available for 2003 (Thomas and Foken 2007a) and 2008, with 5.6 ± 2.1 m^2 m^{-2} for the overstory trees and 3.5 m^2 m^{-2} (LAI 0.5 m^2 m^{-2}) for the understory (Foken et al. 2012); both are shown in Fig. 2.3. For the spatial distribution of the plant parameters and its use in

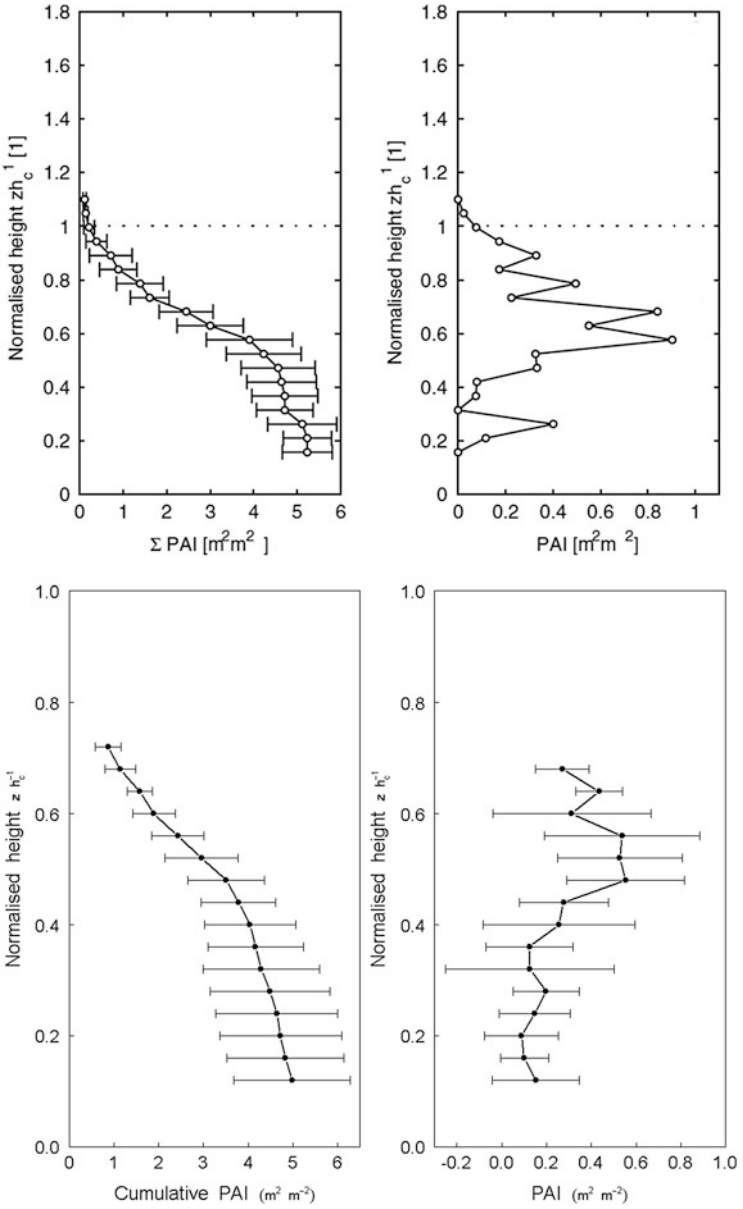

Fig. 2.3 Vertical profile of the (left) cumulative and (right) absolute overstory plant area index (PAI) of the Waldstein-Weidenbrunnen site for 2003 (above Thomas and Foken 2007a) and 2008 (below Foken et al. 2012). The height is normalized by a canopy height according to Table 2.2. Published with kind permission of (above) © Springer-Verlag Berlin, Heidelberg, and (below) © Copernicus publications, distributed under the Creative Commons Attribution 3.0 Licence. 2012, All rights reserved

modeling approaches, see Chap. 16. The distribution of the understory in 2008 is shown in Fig. 2.4 (Behrendt 2010), with more understory in the northeastern part and a higher tree density in the southwestern part. The corresponding distribution of the plant area index is given in Fig. 2.5, which corresponds to the mean vertical profile in Fig. 2.3 (below).

The podzolic soils of the upper parts of the Fichtelgebirge developed from deeply weathered (up to 30 m) granite or gneiss bedrock. The forest floor is moor type and well stratified and consists of a litter (Oi), a fermented (Oe), and a humified (Oa) horizon. The soil texture is sandy loam to loam (US Soil Taxonomy), with a relatively high clay content in the Bh horizon. The content of rock fragments is about 10–25 % vol. in the A and B horizons and increases in the C horizon (deeper than 55 cm) to 50–75 % vol. Detailed information about soil texture and soil chemistry are available for the Coulissenhieb site (Gerstberger et al. 2004; Staudt and Foken 2007). During the installation of a new measuring profile for soil temperature and moisture at the Weidenbrunnen site, a soil profile was obtained to a depth of 2 m and is shown in Fig. 2.6.

2.3.1.2 Instrumentation

The main installation of the measuring site is the 32 m high walk-up scaffold tower (Fig. 2.7) with balcony-like platforms in the crown level of the forest, called the "Main Tower" (MT). This tower was erected in 1994 to allow plant ecological measurements in the crown and is still in use. Starting at the end of 1996, carbon dioxide fluxes were measured as part of the EUROFLUX program (see Chap. 4). From that point on, additional meteorological instrumentation was successively installed, such as for short period flux measurements at two levels above the crown (Rebmann 2003), or implemented as long-term standard measurements of temperature, humidity, wind velocity, and radiation components.

After the closing down of the Bayreuth Institute of Terrestrial Ecosystem Research (BITÖK) and the establishment of the Bayreuth Center of Ecology and Environmental Research (BayCEER) in 2004 (see Chap. 1), the full responsibility for the Waldstein-Weidenbrunnen site moved to the Department of Micrometeorology. From that time, the instrumentation was stepwise renewed and upgraded when necessary (Appendix A, Table 2.3), with no significant changes in the last 10 years. This standard measurement program also offered the possibility of testing sensors under the harsh environmental conditions of the site occurring mainly in winter, with fog and heavy frost. For instance, the heating system of the two-dimensional sonic anemometer of Adolf Thies GmbH & Co. KG, Göttingen was tested as well as a ship rain gauge (Eigenbrodt GmbH & Co. KG, Königsmoor) for precipitation measurements above the canopy. A good agreement found between precipitation above the forest and that obtained by a standard rain gauge at the Waldstein-Pflanzgarten site and the data analysis yielded the finding that the wind speed was not so strong above the forest that a correction for rain on a vertical and horizontal collector was necessary.

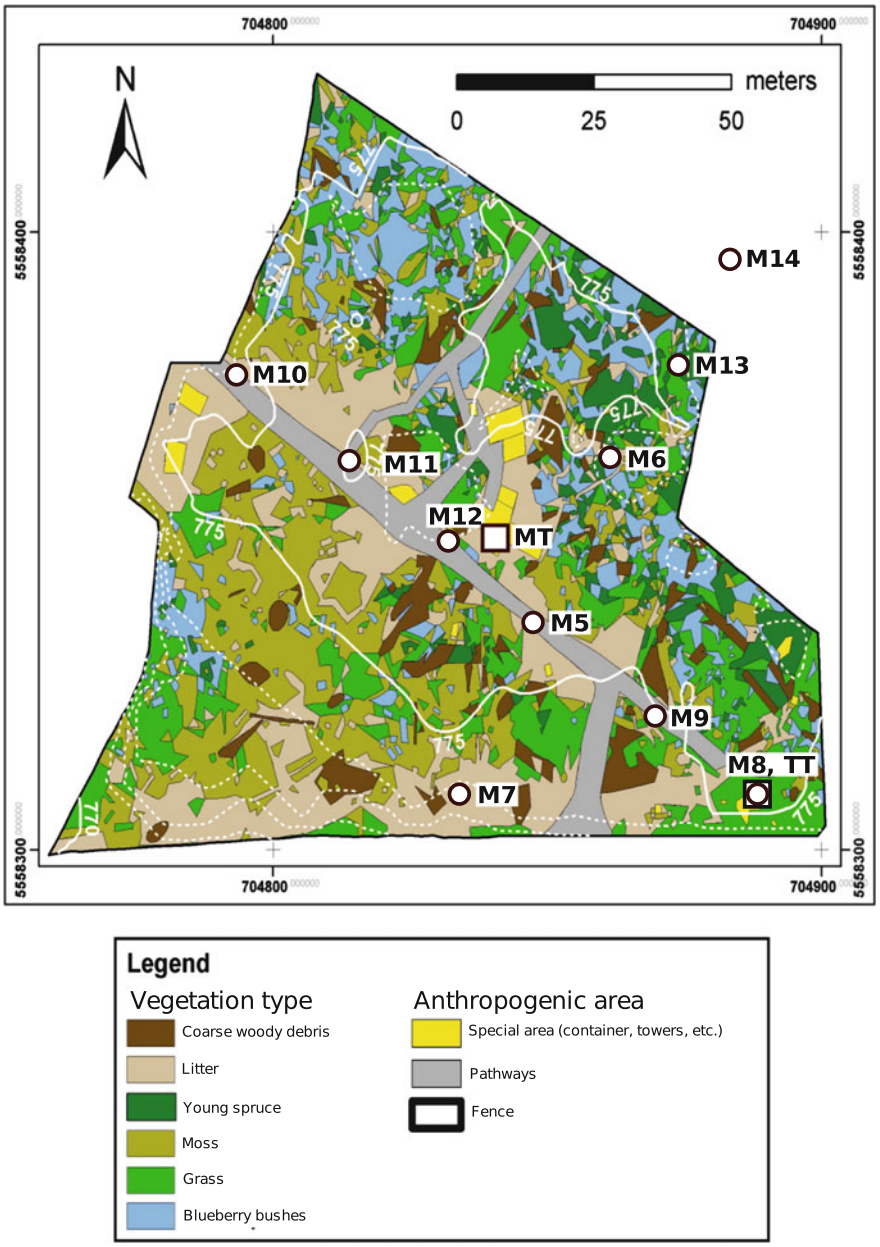

Fig. 2.4 Understory vegetation and topography (shown as *white isolines*). Equidistance of *dashed lines*, 1 m. *Circles* indicate position of 2 m masts after Siebicke (2011), see Table 2.5, and *squares* indicate position of tall towers: "Main Tower" (MT) and "Turbulence Tower" (TT) during the EGER-IOP 1 and EGER-IOP 2 (see Appendix A). Understory vegetation data and graphics produced by Behrendt (2010)

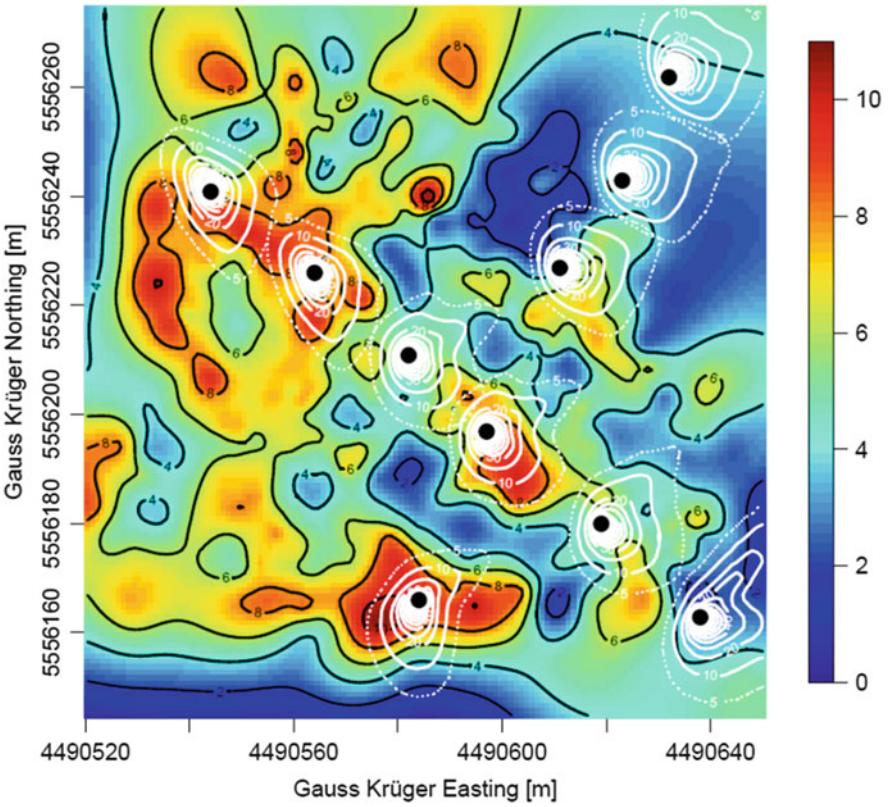

Fig. 2.5 Map of plant area index given as *colors and black contour lines*. *Black points* show the positions of the towers for sub-canopy measurements; see Table 2.5. X- and Y-axis are distances in meters in the Gauss-Krüger coordinate system. *White isolines* show the relative flux contribution of the corresponding footprint area in 10 % intervals for stable cases only (2008). The outermost, *dashed isoline* indicates the area where 95 % of the flux originates. Raw data of PAI were provided by E. Falge (Siebicke 2011)

With the help provided by the funding of several large research projects by the German Science Foundation between 2006 and 2013, it was possible to erect a 36 m slim tower (Fig. 2.8) for turbulence measurements only. From the end of 2007, this so-called "Turbulence Tower" (TT) hosted a second carbon dioxide flux measurement complex in addition to the device on the Main Tower. Flux profile measurements (Foken et al. 2012) were possible on the Turbulence Tower with a much better quality than in an earlier experiment in 2003 that used just the Main Tower (Thomas and Foken 2007b). Furthermore, the power supply was stabilized with a separate transformer near the site (2011), which allowed more extensive chemical and remote sensing measurements, even at the Köhlerloh site. At the top of both towers, the carbon dioxide flux measurements within the FLUXNET program (Baldocchi et al. 2001) have been running since 1996 as station DE-1

Fig. 2.6 Soil profile up to 2 m depth near the Main Tower in 2007 (Photograph: J. Lüers)

(EUROFLUX), later DE-Wei, and now DE-Bay. The main land cover was classified as Evergreen Needleleaf Forest (ENF). Nineteen percent of all measurements had more than 95 % of the target area in the footprint of the measurements, while 65 % of all measurements had more than 80 % (Göckede et al. 2008). The remaining flux contribution originated from the Pflanzgarten clearing and other small clearings nearby. After the storm event Kyrill in January 2007, the measurements for southerly winds, mainly for stable stratification, were significantly influenced by the Köhlerloh clearing. This is shown in Fig. 2.9 for the Main Tower and the Turbulence Tower, where the Turbulence Tower is slightly more affected (Siebicke 2008).

Besides the FLUXNET measurements and the meteorological routine program, both towers served as platforms for many short-term research projects, such as

Fig. 2.7 Main Tower at Waldstein-Weidenbrunnen site (2008, Photograph T. Foken)

the work on fog deposition (Wrzesinsky and Klemm 2000, see Chap. 3) or studies of ^{13}C-isotope fluxes (Chap. 10). Furthermore, large experiments, sometimes with international participation, were realized at the Waldstein-Weidenbrunnen site (Table 2.4). During these 2–3-month-long experiments, several additional devices operated at the towers. An overview is given in Appendix A. Additional towers were erected during the EGER experiments: in IOP 1 and IOP 2 a 40 m tower about 80 m westward of the Main Tower and a network of small towers in the trunk space, which can be seen in Figs. 2.4 and 2.5. During IOP 3 the 40 m tower was installed at the forest edge south of the Turbulence Tower, and the network of small towers was relocated to form a line along the forest edge and in the Köhlerloh clear-cut. It should be mentioned that these experiments made the site more visible in the

Table 2.3 Basic instrumentations at Waldstein-Weidenbrunnen site (Main Tower); for details, see Appendix A, and for flux measurements, see Chap. 4

Height in m	Parameter	Sensor
2, 21, 31	Temperature, moisture	Pt100, capacitive sensor, unventilated
0, 2, 5, 12, 21, 31	Temperature, moisture	Psychometer (ventilated, moisture only April–October)
2, 5, 10, 16, 18, 21, 25, 32	Wind speed	Cup anemometer
32	Wind speed and direction	2D sonic anemometer
30	Short- and long-wave radiation balance	
31	Precipitation	Ship rain gauge
33	Turbulent fluxes	3D sonic anemometer, gas analyzer
21	Visibility, weather code	Present weather sensor
−0.02, −0.05, −0.1, −0.2, −0.5, −0.7, −1.0, −2.0	Soil temperature	Pt100
−0.1, −0.5	Soil humidity	TDR
−0.1 (2x)	Soil heat flux	Soil heat flux plate

scientific literature than did the continuously running programs. For an overview of all towers and their operation times, see Table 2.5.

2.3.2 *Waldstein-Pflanzgarten*

The Waldstein-Pflanzgarten site is now a forest clearing cultivated mainly as a meadow. Prior to more than 10 years ago, it was used as a nursery. The current clearing has a size of approximately 0.5 ha and is, in main parts, only meadow. Since 1994 concentrations of trace gases like SO_2, NO, NO_2, and O_3 have been measured. Short-term observations of NH_3 have only shown significant concentrations during days of fertilization with liquid manure in the agricultural area about 2 km westward. Since 2007, permanent wet deposition measurements of cationic and anionic atoms or molecules and heavy metals have been running. The results are reported in Chap. 3. An overview of the site is given in Fig. 2.10.

The site is furthermore equipped with standard meteorological instrumentation to obtain temperature, humidity, wind, radiation, and precipitation. All measuring parameters are shown in Appendix A and Table 2.6. During large experiments (Table 2.4), the site was also used for additional chemical measurements, like aerosol measurements (Held et al. 2004). During all three EGER campaigns, a sodar-RASS system was in operation to characterize the wind field above the forest.

The wet deposition measurements have also been used since 2007 by the Bavarian State Office for Environment for environmental control. It is the highest-

Fig. 2.8 Turbulence Tower at Waldstein-Weidenbrunnen site (2008, Photograph T. Foken)

situated station in Northern Bavaria. Furthermore, the rain gauge has been included since 2012 in the Bavarian flood warning system to control precipitation events in the spring catchment of the rivers Main, Saale, Eger (Ohre), and Naab. The site fulfills – together with the trunk space measurements of the Waldstein-Weidenbrunnen site – all criteria for a so-called forest climate station (Dietrich et al. 2006).

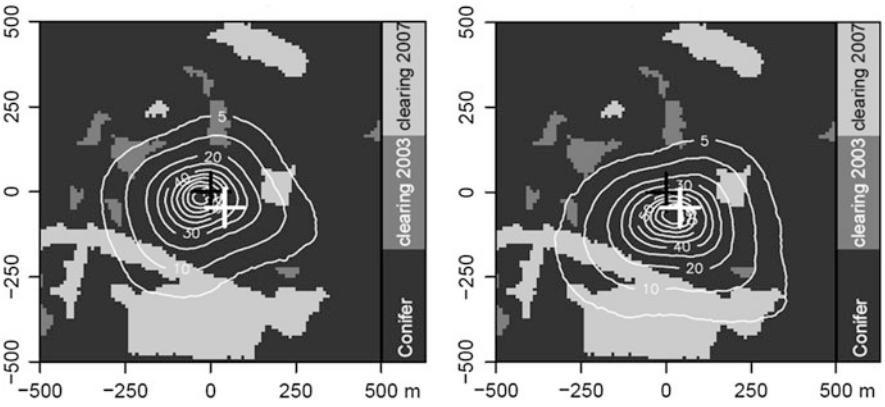

Fig. 2.9 Footprint climatology of the towers of the Waldstein-Weidenbrunnen site (*left figure and black cross*, Main Tower; *right figure and white cross*, Turbulence Tower) on the basis of the data set from September 06 to October 07, 2007 (Siebicke 2008)

Table 2.4 Micrometeorological and air chemistry experiments at Waldstein-Weidenbrunnen site (see Chap. 1)

Date	Experiment	Aim of the experiment	Documentation/reference
09.07.2001–03.08.2001	BEWA* 2001	Emissions of reactive biogenic volatile organic compounds	Klemm et al.(2006)
24.06.2002–02.08.2002	BEWA* 2002		
28.04.2003–03.08.2003	WALDATEM** 2003	Intensive investigation of coherent structures and carbon fluxes within and above a tall spruce forest	Thomas et al. (2004)
06.09.2007–07.10.2007	EGER***–IOP1	Energy and trace gas transport in and above a tall spruce forest	Serafimovich et al. (2008a) and Foken et al. (2012)
01.06.2008–15.07.2008	EGER***–IOP2		Serafimovich et al. (2008b) and Foken et al. (2012)
13.06.2011–26.07.2011	EGER***–IOP3	Interaction between a forest and a clearing	Serafimovich et al. (2011) and this volume

*Regional biogenic emissions of reactive volatile organic compounds (BVOC) from forests: process studies, modeling, and validation experiments
***WALD* WAveLet Detection, *ATEM* Atmospheric Turbulence Exchange Measurements
***Exchange processes in mountainous regions, *IOP* Intensive Observation Period

Table 2.5 Overview of the tower installations at Waldstein-Weidenbrunnen site

Tower	Operation time	Purpose	Further references
Main Tower (MT), 32 m high, see Table 2.1 and Figs. 2.2 and 2.7	Since 1997	Micrometeorological standard program	Table 2.3; Appendix A, Table A1
	Since 1997	FLUXNET station	Chap. 4; Appendix A, Table A2
	BEWA 2001, 2002, see Table 2.4	Air chemistry measurements	Chap. 9; Appendix A, Table A4
	WALDATEM 2003, see Table 2.4	Micrometeorological and carbon flux studies	Chaps. 6 and 10; Appendix A, Table A5
	EGER, IOP 1,2 in 2007 and 2008, see Table 2.4	Micrometeorological and air chemistry measurements	Chaps. 8, 9, and 12; Appendix A, Table A6
Turbulence Tower (TT) 36 m high see Table 2.1 and Figs. 2.2 and 2.8	Since 2007	Additional FLUXNET station	Chap. 4; Appendix A, Table A3
Bio-tower, 80 m westward of MM 40 m high	EGER, IOP 1,2 in 2007 and 2008, see Table 2.4	Sap flow and plant ecological measurements	Chaps. 5 and 16
Forest-edge tower (M3), south of TT 40 m high	EGER, IOP 3 in 2011, see Table 2.4	Micrometeorological and air chemistry measurements	Chaps. 9 and 13; Appendix A, Table A8 and Fig. A3
Network of small towers	WALDATEM 2003, see Table 2.4	Micrometeorological and carbon flux studies	Chap. 6; Appendix A, Table A5
	EGER, IOP 1 in 2007, see Table 2.4	Micrometeorological and air chemistry measurements	Chaps. 8, 9, and 12; Appendix A, Table A6 and Fig. A1
	EGER, IOP 2 in 2008, see Table 2.4	Micrometeorological and air chemistry measurements	Chaps. 8, 9, and 12; Appendix A, Table A7 and Fig. A2
	EGER, IOP 3 in 2011, see Table 2.4	Micrometeorological and air chemistry measurements	Chaps. 9 and 13; Appendix A, Table A8 and Fig. A3

2.3.3 Köhlerloh

As a large forest clearing, the Köhlerloh provides an interesting subject of research, especially since the storm event "Kyrill" in January 2007. In particular, the edge between forest and clearing was part of a deep investigation during the EGER-IOP 3 campaign in 2011. The southern region of this forest was managed by the administration beforehand (felling in 2006), but the north area of the forest was also heavily affected by the severe storm "Kyrill" (Fig. 2.11). During EGER-IOP 3 the site was equipped with a 40 m tall tower and several smaller ones along the

Fig. 2.10 Waldstein-Pflanzgarten site in 2008 with the measurement container (on the top radiation measurements and 10 m wind measurements); in the background the wet-only sampler is visible. Additional instrumentation during EGER-IOP 2 with a measuring container for additional trace gas measurements and a sodar-RASS system in the foreground (2008, Photograph T. Foken)

Table 2.6 Basic instrumentations at Waldstein-Pflanzgarten site; for details, see Appendix A, and for concentration measurements, see Chap. 3

Height in m	Parameter	Sensor
2	Temperature, moisture	Pt100, capacitive sensor, unventilated
10	Wind speed and direction	Cup anemometer, wind vane
4	Down-welling shortwave and diffuse radiation	Pyranometer, shadow ring
1	Precipitation	Tipping bucket and weighing rain gauge
2	Air pressure	Capacitive sensor
1	Wet deposition	Wet only precipitation collector
3	O_3 concentration	Gas analyzer
3	SO_2 concentration	Gas analyzer
3	NO and NO_2 concentration	Gas analyzer

forest edge and on the clear-cut. In addition a sodar system and laser scintillometer pathways were in use. The land cover with the different plant species is shown in Table 2.7.

Fig. 2.11 Köhlerloh clear-cut in 2011 with a mixture of bare soil, deadwood, grass, and small trees. During EGER-IOP 3 the site was equipped with additional measuring systems (View to south with the Waldstein in the background in 2011, Photograph T. Foken)

Table 2.7 Land cover of the Köhlerloh site (Serafimovich et al. 2011), updated

Vegetation	Ground cover in %	Height in m	PAI in $m^2\ m^{-2}$
Deschampsia flexuosa	21.7	0.17 ± 0.05	2.65 ± 1.08
Picea	21.4	1.21 ± 0.50	8.67 ± 2.29
Vaccinium	15.9	0.27 ± 0.10	3.46 ± 1.05
Calamagrostis, Agrostis	9.0	0.42 ± 0.10	3.43 ± 1.07
Carex	3.1	0.74 ± 0.13	1.77 ± 0.60
Other *herbaceous*	1.6		
Moss	0.9		
Dead grass, bare soil	7.2		
Dead wood (harvest residuals)	18.8		
Water	0.2		

2.4 Conclusions

The Waldstein-Weidenbrunnen and Waldstein-Pflanzgarten sites have been used for observing air pollutants and meteorological parameters for more than 20 years and trace gases, such as carbon dioxide, for nearly two decades. The duration of measurements and the instrumentation are comparable with stations like Duke Forest, Niwot Ridge (both the USA), and Hyytiälä (Finland); however, the focus was mainly on micrometeorological measurements and less on plant ecological measurements. Therefore, the site is only barely represented in the large FLUXNET

overview papers (see Appendix C). Many data quality issues were tested at this site and have led to now standard methods in the community. The large experiments all had a special focus. They would be scarcely imaginable without the well-equipped sites with their infrastructure and basic measurements.

This offered the possibility of a wide range of scientific investigations in addition to the climate and air pollution studies (Chap. 3) and the water and carbon fluxes (FLUXNET, Chap. 4), with many methodological studies (Chaps. 6 and 12) and investigation of the influences of boundary layer phenomena on these fluxes (Chap. 11). Over short periods, sap flow (Chap. 5), fluxes in the soil (Chap. 7), isotope fluxes (Chap. 10), and catchment fluxes (Chap. 15) were studied. After 2007, fluxes at the heterogeneous site (Chaps. 12, 13, and 17) became a dominant issue of research, as did the related microclimate (Chap. 14). The air chemistry measurements (Chaps. 8 and 9) could be controlled by micrometeorological measurements. And last but not least, several models were tested and applied at these sites (Chaps. 15, 16, 17, and 18).

Acknowledgments The operation of the site was funded by the Federal Ministry of Education, Science, Research and Technology (PT BEO-0339476 B, C, D), the European Community (EUROFLUX), the German Science Foundation (FO 226/16-1, FO 226/22-1), and the Oberfranken Foundation (contract 01879). This work was only possible with the enthusiasm and hard work, sometimes under harsh weather conditions, of so many technicians, students, PhD candidates, and motivated scientists.

References

Alsheimer M (1997) Charakterisierung räumlicher und zeitlicher Heterogenität der Transpiration unterschiedlicher montaner Fichtenbestände (*Picea abies* (L.) KARST.) durch Xylemflußmessungen. Bayreuther Forum Ökologie 49:143 p

Baldocchi D, Falge E, Gu L, Olson R, Hollinger D, Running S, Anthoni P, Bernhofer C, Davis K, Evans R, Fuentes J, Goldstein A, Katul G, Law B, Lee XH, Malhi Y, Meyers T, Munger W, Oechel W, Paw U KT, Pilegaard K, Schmid HP, Valentini R, Verma S, Vesala T (2001) FLUXNET: a new tool to study the temporal and spatial variability of ecosystem-scale carbon dioxide, water vapor, and energy flux densities. Bull Am Meteorol Soc 82:2415–2434

Behrendt T (2010) A small-scale geostatistical analysis of the variability of soil properties. An example from the Weidenbrunnen (Fichtelgebirge) research area. Master Thesis, University of Mainz

Dietrich H-P, Raspe S, Schulz C (2006) Waldklimastationen-Säule forstlicher Umweltbeobachtung. AFZ/Der Wald 61:972–974

Foken T (2003) Lufthygienisch-Bioklimatische Kennzeichnung des oberen Egertales. Bayreuther Forum Ökologie 100:69+XLVIII

Foken T, Meixner FX, Falge E, Zetzsch C, Serafimovich A, Bargsten A, Behrendt T, Biermann T, Breuninger C, Dix S, Gerken T, Hunner M, Lehmann-Pape L, Hens K, Jocher G, Kesselmeier J, Lüers J, Mayer JC, Moravek A, Plake D, Riederer M, Rütz F, Scheibe M, Siebicke L, Sörgel M, Staudt K, Trebs I, Tsokankunku A, Welling M, Wolff V, Zhu Z (2012) Coupling processes and exchange of energy and reactive and non-reactive trace gases at a forest site – results of the EGER experiment. Atmos Chem Phys 12:1923–1950

Gerstberger P (2001) Die BITÖK-Untersuchungsflächen im Fichtelgebirge und Steigerwald. Bayreuther Forum Ökologie 90:193 p

Gerstberger P, Foken T and Kalbitz K (2004) The Lehstenbach and Steinkreuz catchments in NE Bavaria, Germany. In: Matzner E (ed), Biogeochemistry of forested catchments in a changing enivironment, a German case study. Ecological Studies, vol 172. Springer, Berlin, Heidelberg, pp 15–41

Göckede M, Foken T, Aubinet M, Aurela M, Banza J, Bernhofer C, Bonnefond J-M, Brunet Y, Carrara A, Clement R, Dellwik E, Elbers JA, Eugster W, Fuhrer J, Granier A, Grünwald T, Heinesch B, Janssens IA, Knohl A, Koeble R, Laurila T, Longdoz B, Manca G, Marek M, Markkanen T, Mateus J, Matteucci G, Mauder M, Migliavacca M, Minerbi S, Moncrieff JB, Montagnani L, Moors E, Ourcival J-M, Papale D, Pereira J, Pilegaard K, Pita G, Rambal S, Rebmann C, Rodrigues A, Rotenberg E, Sanz MJ, Sedlak P, Seufert G, Siebicke L, Soussana JF, Valentini R, Vesala T, Verbeeck H, Yakir D (2008) Quality control of CarboEurope flux data – part 1: coupling footprint analyses with flux data quality assessment to evaluate sites in forest ecosystems. Biogeosciences 5:433–450

Held A, Nowak A, Birmili W, Wiedensohler A, Forkel R, Klemm O (2004) Observations of particle formation and growth in a mountainous forest region in central Europe. J Geophys Res D109:D23204

Klemm O, Held A, Forkel R, Gasche R, Kanter H-J, Rappenglück B, Steinbrecher R, Müller K, Plewka A, Cojocariu C, Kreuzwieser J, Valverde-Canossa J, Schuster G, Moortgat GK, Graus M, Hansel A (2006) Experiments on forest/atmosphere exchange: climatology and fluxes during two summer campaigns in NE Bavaria. Atmos Environ 40(Supplement 1):3–20

Matzner E (ed) (2004) Biogeochemistry of forested catchments in a changing environment, a German case study. Springer, Berlin, Heidelberg, see impressum of the book, 498 pp

Muhr J, Borken W, Matzner E (2009) Effects of soil frost on soil respiration and its radiocarbon signature in a Norway spruce forest soil. Glob Chang Biol 15:782–793

Mund M (1996) Wachstum und oberirdische Biomasse von Fichtenbeständen (*Picea abies* [L.] KARST.) in einer Periode anthropogener Stickstoffeinträge. Diploma Thesis, Universität Bayreuth

Rebmann C (2003) Kohlendioxid-, Wasserdampf- und Energieaustausch eines Fichtenwaldes in Mittelgebirgslage. Dissertation, Universität Bayreuth, Bayreuth, 149 pp

Reif A (1989) The vegetation of the Fichtelgebirge: origin, site conditions, and present status. In: Schulze ED et al (eds) Forest decline and air pollution. A study of spruce (*Picea abies*) on acid soils. Springer, Berlin, pp 8–22

Schulze E-D, Lange OL, Oren R (eds) (1989) Forest decline and air pollution, vol XVIII. Springer, Berlin, 475 pp

Serafimovich A, Siebicke L, Staudt K, Lüers J, Biermann T, Schier S, Mayer J-C and Foken T (2008a) Exchange processes in mountainous Regions (EGER): documentation of the Intensive Observation Period (IOP1), September, 6th to October, 7th 2007. Arbeitsergebn, Univ Bayreuth, Abt Mikrometeorol, ISSN 1614-8916, 36, 145 pp

Serafimovich A, Siebicke L, Staudt K, Lüers J, Hunner M, Gerken T, Schier S, Biermann T, Rütz F, Buttlar JV, Riederer M, Falge E, Mayer J-C and Foken T (2008b) Exchange processes in mountainous Regions (EGER): documentation of the Intensive Observation Period (IOP2) June, 1st to July, 15th 2008. Arbeitsergebn, Univ Bayreuth, Abt Mikrometeorol, ISSN 1614-8916, 37, 180 pp

Serafimovich A, Eder F, Hübner J, Falge E, Voß L, Sörgel M, Held A, Liu Q, Eigenmann R, Huber K, Duarte HF, Werle P, Gast E, Cieslik S, Liu H and Foken T (2011) Exchange processes in mountainous Regions (EGER): documentation of the Intensive Observation Period (IOP3) June, 13th to July, 26th 2011. Arbeitsergebn, Univ Bayreuth, Abt Mikrometeorol, ISSN 1614-8916, 47, p 135

Siebicke L (2008) Footprint synthesis for the FLUXNET site Waldstein/Weidenbrunnen (DE-Bay) during the EGER experiment. Arbeitsergebn, Univ Bayreuth, Abt Mikrometeorol, ISSN 1614-8916, 38, 45 pp

Siebicke L (2011) Advection at a forest site – an updated approach. PhD Thesis, University of Bayreuth, Bayreuth, 113 pp

Staudt K and Foken T (2007) Documentation of reference data for the experimental areas of the Bayreuth Centre for Ecology and Environmental Research (BayCEER) at the Waldstein site. Arbeitsergebn, Univ Bayreuth, Abt Mikrometeorol, ISSN 1614-8916, 35, 35 pp

Thomas C, Foken T (2007a) Flux contribution of coherent structures and its implications for the exchange of energy and matter in a tall spruce canopy. Bound Lay Meteorol 123:317–337

Thomas C, Foken T (2007b) Organised motion in a tall spruce canopy: temporal scales, structure spacing and terrain effects. Bound Lay Meteorol 122:123–147

Thomas C, Ruppert J, Lüers J, Schröter J, Mayer J-C and Bertolini T (2004) Documentation of the WALDATEM-2003 Experiment April, 28th to August, 03rd 2003. Arbeitsergebn, Univ Bayreuth, Abt Mikrometeorol, ISSN 1614-8916, 24, p 57

Wrzesinsky T, Klemm O (2000) Summertime fog chemistry at a mountainous site in central Europe. Atmos Environ 34:1487–1496

Part II
Studies of Long-Term Measurements

Chapter 3
Climate, Air Pollutants, and Wet Deposition

Johannes Lüers, Barbara Grasse, Thomas Wrzesinsky, and Thomas Foken

3.1 Introduction

One main topic of scientific and public interest regarding the Waldstein research site (see Chap. 2 and site documentation by Staudt and Foken 2007) continues to be the high-quality observation of weather that captures the meteorology and climate of this particular site and the neighboring regions. These reach from the Eger (Ohře) river basin in the east (town of Weißenstadt) to the Saale river valley in the west, and the Weißer Main river in the south to the Waldstein range of the Fichtelgebirge, with the middle mountain) summits of Schneeberg (1051 m a.s.l.), Großer Waldstein (877 m a.s.l.), and Großer Kornberg (827 m a.s.l.), to the north.

J. Lüers (✉)
Bayreuth Center of Ecology and Environmental Research, University of Bayreuth, Bayreuth, Germany
e-mail: johannes.lueers@uni-bayreuth.de

B. Grasse
CDM Smith, Neue Bergstr. 13, 64665 Alsbach, Germany

T. Wrzesinsky
Stettener Str. 11, 88709 Meersburg, Germany

T. Foken
Am Herrgottsbaum 28, 96120 Bischberg, Germany

Bayreuth Center of Ecology and Environmental Research, University of Bayreuth, Bayreuth, Germany

J. Lüers and T. Wrzesinsky: Affiliation during the work at the Waldstein sites before 2005–University of Bayreuth, Bayreuth Institute of Terrestrial Ecosystem Research (BITÖK), Department of Climatology, Germany

J. Lüers, B. Grasse, and T. Foken: Affiliation during the work at the Waldstein sites–University of Bayreuth, Department of Micrometeorology, Germany

T. Foken (ed.), *Energy and Matter Fluxes of a Spruce Forest Ecosystem*,
Ecological Studies 229, DOI 10.1007/978-3-319-49389-3_3

Based on meteorological measurements made at the Waldstein facility (see Chap. 1 and Sect. 2.3) from 1994 to the present and on weather data from nearby stations operated by the German Meteorological Service (Deutscher Wetterdienst, DWD), several studies—mainly of air temperature, precipitation, and air quality (air pollutants)—were conducted over the last 15 years. The latest (Foken and Lüers 2015b) describes the regional characteristics of climate change in Oberfranken (Ofr., Upper Franconia), whereby the strong global rise of the Earth's basic air temperature takes a more moderate course in Franconia. This is mostly a consequence of the cool-temperate climate effect of higher than average altitudes of the Waldstein area between 600 m and 1100 m a.s.l. compared to the Central European lowlands (below 200 m a.s.l.).

On the other hand, the already continental location within the Central European climate zones, in combination with a heterogeneous landscape with high relief intensity and imposed local orographic wind circulation systems (wind- and leeward or mountain-valley cycles), will increase and reinforce diurnal and seasonal amplitudes and the spatial variety of basic meteorological elements and will possibly induce a higher risk of local extreme weather (climate) events (Foken and Lüers 2013). Especially the change of the seasonal distribution of precipitation events impacts the water balance in Franconia and the Waldstein Mountain Range negatively, considering (fresh) drinking water supply or the water demand of forests, grasslands, and agriculture. As already mentioned in 2003 by Foken and Lüers (2003) and confirmed by Lüers (2012) and Foken and Lüers (2015b), the amount of precipitated water over Franconia has been showing a significant decrease during the late-winter and early-summer seasons, observed as one to three dry periods, each of at least 4 or 5 weeks of duration, occurring anytime between February and May but with different start dates over the past 20 years. These dry periods are interrupted by single—or short but heavy and severe—rain (or occasional snow) events, often causing local flooding, between the otherwise low water runoff times. This spring- and summertime loss of precipitation water and the change of characteristics from steady front-borne rain to short and severe convective events has, for most of the last 20 years, not been compensated enough by steady rain and snow falling during the autumn and winter to enable, for example, recharge of the local groundwater storage. Assuming that this situation will prevail, the water availability may become inadequate for the habitat requirements of the current dominant coniferous (spruce) Upper Franconian forests. A survey (not included in this volume) of snow height and cover and possible impacts to tourism and winter recreation activities was recently conducted by Foken and Lüers (2015b) and showed a strong decreasing trend of the number of days on which there was a closed snow cover with a snow height of $\geq$15 cm or $\geq$30 cm. Kittler et al. (2011) considered the already limited current and future snow conditions in the Fichtelgebirge Mountains. An update containing quality-checked, corrected, and gap-filled climate values of air temperature and precipitation and their statistics can be found in Sect. 3.3.1.

Regarding air quality, Klemm and Lange (1999) were the first to describe trends of air pollution in the Fichtelgebirge Mountains, investigating 13 years (1985–1997) of SO_2, NO_x, and O_3, measurements from Waldstein and vicinity. They were able

to confirm the remarkably strong Europe-wide decrease of atmospheric SO_2 and the connected reduction of acid rain deposition for the Waldstein forest between 1987 and 1989 that has resulted from the enforcement of air pollution control strategies in Germany.

Continuing the research on climate trends, Foken (2003) published a detailed investigation on air quality and bioclimatic relevance of the Waldstein region including the upper Eger river basin, based on data collected up to the end of 2000. His work confirms the overall reduction of SO_2—and partly of NO_x—concentration in the boundary layer of the atmosphere. But it showed a slight increase of ozone (especially of the background level) during the years 1985–2000, with a peak in 1998. The ozone situation at the Waldstein location in particular received attention. Klemm and Mangold (2001) and Klemm et al. (2004) reported on measured and modeled ozone deposition fluxes, with the conclusion that the modeled O_3 fluxes tended to underestimate the measured values. The work by Barbara Grasse (Lüers and Foken 2010) and the update by Foken and Lüers (2015a), having a main focus on the development of ozone episodes at the Waldstein, and the results are presented in Sect. 3.3.2. In conjunction with a 1-year observation period in 2001/2002, Wrzesinsky et al. (2004) wrote about fog deposition fluxes and gave an insight into fog chemistry and the collection of fog droplets and fog water samples (see Sect. 3.3.3). The ongoing determination of wet deposition at Waldstein started at the end of 2007. Sections 3.2.3 and 3.3.4 represent a complete revision and reevaluation of the Waldstein measurements of the amount and concentration of trace elements (including heavy metals) and dissolved ions deposited by precipitation water and replace the previous documentation (Lüers and Foken 2010; Foken and Lüers 2015a).

3.2 Material and Methods

3.2.1 Main Meteorological Elements and Climatological Observations

The meteorological measurements at Waldstein conform to the international and national standards and guidelines of the World Meteorological Organization (WMO 2008) and of the technical administrative regulation TA-Luft (TA-Luft 2002) and the attendant standards of the Association of German Engineers (VDI). The complete list and operational history of instruments in use since the start of measurements in 1994 at Waldstein by the University of Bayreuth can be found in Appendix A. Besides the main focus on air temperature and precipitation, data sets of wind, air humidity, short- and longwave radiation, air pressure, visibility, and soil temperature and moisture are available but not quality checked and gap filled. To gain reliable air temperature and precipitation time series suitable for climate analysis, an extensive examination was necessary. Especially the cold season winter precipitation data

needed to be corrected (errors were caused by snowfall or icing of the tipping rain gauge). For value analysis (e.g., outliers) and gap filling of the original Waldstein temperature and precipitation measurement, a comparison and cross-check with independent observations was used. Concerning air temperature, the data of the climate station Fichtelberg/Oberfranken-Hüttstadl (operated by the German Meteorological Service, DWD), located 20 km southward from and 110 m lower than Waldstein, was applicable. And to cross-check and complete the Waldstein precipitation time series, data recorded by the DWD precipitation station Weißenstadt (7 km distance) during the years 1971–2005, and data collected by the DWD climate station Fichtelberg- Oberfranken-Hüttstadl (the same station as above) from 2006 to the present, could be used.

3.2.2 Air Pollution Measurements

The presence of air pollutants (as trace gases or aerosols) is usually measured as an immission (deposition) or actual mass concentration per air volume. All trace gas data of ozone, sulfur dioxide, and nitrogen oxides are given in pressure- and temperature-independent ppb units (parts per billion), which means a volume (or molar) fraction or mixing ratio on the order of 10^{-9}. However, a part of the trace gas observation at the Waldstein region was recorded using the mass unit $\mu g\ m^{-3}$ based upon a volume of air under standard conditions (1013 hPa, 273 K or 293 K). For these cases, the condition-specific values in $\mu g\ m^{-3}$ were converted to corresponding ppb mixing ratios.

The first air quality monitoring station in the Fichtelgebirge was set up in 1985 at a remote forest site close to the village of Warmensteinach at an altitude of 760 m a.s.l. After operating at that site until 1993, the station was moved approximately 20 km northward to its current position at the research site Waldstein-Pflanzgarten (765 m a.s.l.). That move led to a data gap of 8 months during the 1993/1994 turn. Klemm and Lange (1999) applied statistical tests to find indications of whether the relocation of the monitoring station in 1993/1994 produced any systematic bias in the data. They found that it is fully appropriate to combine both time series. Therefore, air quality measurements are now available for the Waldstein area for SO_2 and NO_x starting in 1985 and ending in 2008, or running until the present for ozone (as of 2013). All air pollution measurement is conducted using a standard Bavarian Environment Agency (LfU) measurement container (mobile transport container, Fig. 2.10), which shelters the gas analyzers, power supply and data logger. The inlets for taking the air samples are attached at the top of the container roof at 3 m height. The Waldstein-Pflanzgarten clearing, an area of close to 100 × 200 m surrounded by 80- to 130-year-old spruce trees, is part of a rural, forested middle mountain range which is only disturbed by a low-traffic-volume road that connects the villages of Weißenstadt and Sparneck from east to west and passes at a distance of about 1.5 km south of the clearing (see Chap. 2, Eiden et al. 1989; Gerstberger et al. 2004).

To measure tropospheric ozone at Waldstein, an O_3 analyzer MLU ML 8810 M (Monitor Labs) was in use until 2008. It was necessary to replace this old, outdated device and between January 2008 and July 2012 a UV-absorption O_3 analyzer MLU-400 (API Inc.) was in service, followed by the new UV-photometric version MLU Model 49i (Thermo Scientific Inc.) from summer 2012 until today. NO_2 and NO concentrations were determined using a chemiluminescence NO/NO_x analyzer ECO CLD 700 AL (Eco Physics Inc.) between 1985 and 2008. SO_2 was measured with a trace level pulsed fluorescence SO_2 analyzer Model 43C (Thermo Environmental Instruments Inc.) during the years 2008–2012 and prior to this with a MLU ML 8850 S from Monitor Labs.

Both of the SO_2 and NO_x devices (built between 1980 and 1985) were already outdated during their operation at Waldstein, and from 2007 the manufactures were no longer able to provide maintenance and necessary calibration. This meant that the measurement of nitrogen oxides finally had to be terminated in 2008 and later, in 2012, that of sulfur dioxide. However, the SO_2 data from 2008 to 2012 was too incomplete and of not high enough reliability to be considered for scientific analysis. Detailed operating information about the air pollution measurement at Waldstein-Pflanzgarten can be found in Appendix A (Table A1).

To provide a time series analysis and appropriate trend detection, the original 10-min time resolution was aggregated to half hourly values. In the case of air temperature and precipitation data, it is common to employ simple linear regression methods (correlation with time) to find, for example, monotonically increasing or decreasing tendencies of the scalar in time (Schönwiese 2013). To ensure impartial determination of possible trend reversal points within longer time series, the use of a polynomial spline regression of at least the second or third degree was suitable. If not otherwise stated, the nonparametric significant test following Mann (1945) and Kendall (1975) was applied.

3.2.3 Wet Deposition

To capture gravitational wet deposition or atmospheric hydrometeors as raindrops and snowflakes, the use of a so-called "wet-only" precipitation sampler is necessary. This instrument is equipped with an automatized coverlid for a wet-only application. This lid is opened only during precipitation events; it otherwise remains closed to prevent the contamination of the collection funnel by dry deposits (e.g., dust). During a precipitation event, the water collected by the funnel flows through drainpipes and silicone hoses into polyethylene sampling bottles. At the Waldstein-Pflanzgarten site, the "wet-only" precipitation sampler NSA 181/KHS developed by the Eigenbrodt GmbH & Co. KG (Eigenbrodt 2007) started its routine operation at the end of 2007. This sampler is equipped with a rotating ninefold sample insert (daily switch mode) and a bottle tray with nine separate polyethylene sampling bottles. The gauge's funnel has a 500 cm^2 collecting surface and is heated during

the cold winter season. The sampling room is temperature balanced by an automatic climate control system (4–6 °C).

In accordance with the procedure of the Bavarian Environment Agency (LfU), the water for each set of chemical analyses was taken from precipitation water collected over 4-week periods. This resulted in a possible maximum of 13 4-weekly periods for each year. However, the start and end dates of each period differ slightly from year to year. To simplify the statistical evaluation of the chemical analyses, the average of the 4-week periods 1–13 of each year was considered even when the start and end dates of a single period did not exactly correspond every year.

The laboratory of the Bavarian Environment Agency (LfU) in the city of Augsburg was responsible for the chemical analyses. Running an inductively coupled plasma mass spectrometer (ICP-MS), the following content could be detected: aluminum (Al), arsenic (As), bismuth (Bi), calcium (Ca), cadmium (Cd), cobalt (Co), chrome (Cr), copper (Cu), iron (Fe), potassium (K), magnesium (Mg), manganese (Mn), molybdenum (Mo), sodium (Na), nickel (Ni), lead (Pb), antimony (Sb), titanium (Ti), vanadium (V), and zinc (Zn). Ion chromatography was used for the detection of the following ions in the precipitation water: chloride, nitrite, nitrate, phosphate, sulfate, sodium, ammonium, potassium, magnesium, and calcium. The results are given as concentration rates in milligrams per square meter (mg m^{-2}) by considering the collected water amount. To check the precipitation amount obtained by the 4-weekly wet-only sampling, this data was compared with the standard meteorological precipitation gauge measurement nearby. For most of the periods, the respective water amounts from both collectors are in the same range (Fig. 3.1). For the periods 1 (Dec/Jan), 6 (Jun/Jul), 12 (Oct/Nov), or 13 (Nov/Dec), a larger

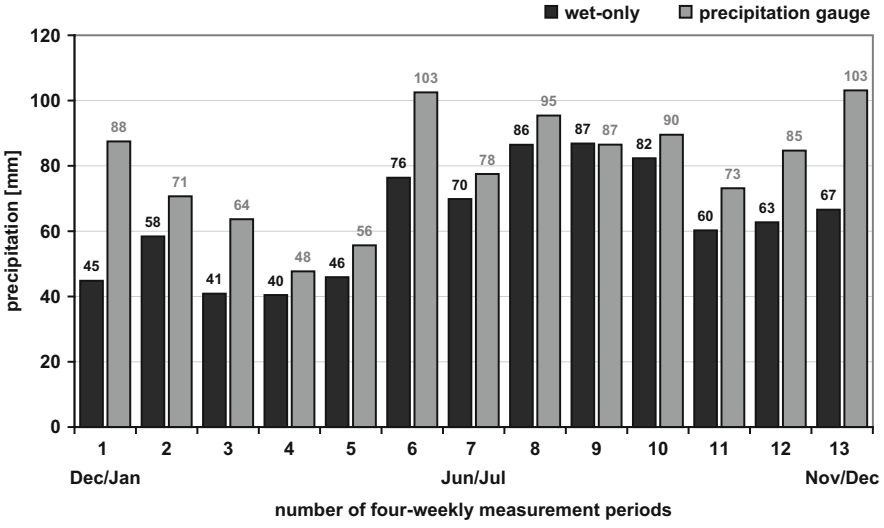

Fig. 3.1 Mean water amount in [mm] for each wet-only 4-week collecting period (*black bars*) and mean precipitation obtained by a standard gauge within each corresponding 4-week period (*gray bars*). For both instruments, the average of the 6 years 2008–2013 for each period is used

difference occurred. This was caused by several errors, for example, a different funnel collecting surface (thus different wind and wetting and evaporation effects) and a different performance during snowfall, or, in some cases, by severe errors made in the collection of the 4-week wet-only water samples. Figure 3.1 also shows the typical bimodal precipitation distribution, with a drier late-winter to early-summer season and a wetter summer and midwinter (Foken 2003). The methods used and detailed results of the chemical analyses running the inductively coupled plasma mass spectrometer (ICP-MS) and ion chromatography can be read in the work reports of Lüers and Foken (2010) and Foken and Lüers (2015a). It should be mentioned that due to an error made in these two documentations, the allocation between the sample number and corresponding date now has to be changed to the correct manner (especially for 2011, 2012, and 2013).

For the first samples collected at the onset of measurement in 2007, the concentration values of the heavy metals were unexpectedly high. That could be an artifact caused by the brand-new, maybe contaminated, NSA 181 wet-only collector. Similar unrealistically high values of chrome, copper, iron, and nickel could also be found in the 4-week sample numbers 11 and 13 in 2012. The cause was corrosion inside the collecting funnel. The too-high values of cobalt in sample number 3 and copper in samples 7 and 13 in 2009 remain unexplained; therefore these values were not considered. For the whole investigation period 2008–2013, only two other total sample periods (No. 9 in 2012 and No. 1 in 2013) are unavailable. In the case of the ion chromatography, it can occur that the analysis results are below the limit of detection. These possibly uncertain values are still included in the plots shown in Sect. 3.3.4. On the one hand, this can cause some slight overestimation, while on the other hand, it will eliminate all existing variance below the respective fixed determination levels.

The Bavarian Environment Agency (LfU) has changed the measurement procedure from wet-only to the bulk deposition method (wet deposition plus water-soluble dry deposits). This complicates the direct comparison between the Waldstein-Pflanzgarten observation and the LfU-network. The nearest LfU station is the Naila (Selbitzer Berg) station located 25 km to the north of Waldstein. A short investigation comparing the data from Naila with Waldstein-Pflanzgarten data from 2008 did not show any significant differences in behavior. In addition, this station ceased operation in 2012, leaving only the data from the LfU stations located at Hof and Kulmbach (both 30 km away), which are however of very limited relevance due to a strong urban influence. Therefore, Waldstein is the only rural site providing wet deposition observations in the northern Bavarian mountains.

3.3 Results and Discussion

As already mentioned in the introduction and as described in Chap. 2 and Appendix A, a huge number of routine or specialized meteorological elements, as well as energy and trace gas fluxes, soil and plant parameters either were or are still under

observation and investigation at Waldstein during the last 20 and more years. The aim of this chapter is to give an insight into the basic climatology (represented by air temperature and precipitation), the air pollution situation with a main focus on ozone, and wet deposition caused by precipitated water.

3.3.1 Climatology

The German-Franconian region—including the Fichtelgebirge Mountains—as part of the Central European Variscan Mountain Range is, if following the effective classification system after Köppen-Geiger (Kottek et al. 2006; Peel et al. 2007), classified as a "Cfb" mid-latitude (warm) temperate "C," fully humid "f" climate zone with a warm summer period "b." However, especially for North America and Europe, that older Wladimir Köppen system (around 1900) is not specific enough. Trewartha and Horn (1980) suggested a modified version to address the problem of separating subtropical from mid-latitude and maritime from continental climate zones better than Köppen. Thus, the Köppen-Trewartha climate classification (Hendl 1991; Belda et al. 2014) regrouped the temperate climates into a subtropical group "C" and a temperate group "D" and locates the boundary of the maritime oceanic type ("Do," coldest monthly air temperature mean is 0 °C or higher) and the continental type ("Dc," coldest monthly mean below 0 °C) diagonally across Central Europe and Germany.

The Waldstein region is now located at this edge and is influenced by those two major sources of air masses: the oceanic (Atlantic, Mediterranean Sea) and the continental (Eurasia) zones. That means that during wintertime, air mass advection transports either temperate, humid air (fronts carrying rain or snow) from northwest to southeast or cold, dry air from north to east to Upper Franconia. During late spring, summer, or early autumn, these progressions of cold and warm are reversed. Frontal weather systems associated with Atlantic depressions coming from westerly directions cause fast and short cool-temperate weather or storm events on the one hand, while (strong) anticyclonic high-pressure conditions on the other produce a (warm, hot, convective) continental weather characteristic. However, forced by the rapidly changing global climate, these typical synoptic atmospheric circulation patterns have already altered perceptibly. The frequency and intensity of such weather-changing situations has increased during the last three or four decades in parallel with the span and the unpredictability of extreme weather conditions. Depending on which Europe-wide circulation system (zonal or meridional pattern) takes control, such an air mass boundary can be stationary for a few days or moving fast as a front across the country. Both patterns are now commonly attended by severe weather: heavy rain or snow, wind- or thunderstorm events. The observed increase of air temperature and a significant change of the intra-annual precipitation variability in Upper Franconia and the Waldstein Mountain Range is the reason that during the last years, in many cases, a shift has already occurred from a fully humid "f" climate to one with at least one or more dry seasons, as well as a possible climate

shift from warm summer "b" ("Dcb") to a hot summer "a" ("Dca"). The following two subchapters will present that situation in brief.

3.3.1.1 Air Temperature

The measurement of air temperature conducted at Waldstein by the University of Bayreuth has a history going back to 1994. To obtain a robust statistic that includes time series from 2015 to 1994 and extends back to the year 1971, monthly data was generated using the air temperature observations of the DWD-Station Fichtelberg/Oberfranken (at 20 km distance) as a reference. Both the Waldstein and Fichtelberg data overlap for the years 1994 until 2015. For each pair of matching monthly values in this time period, the difference between the Fichtelberg reference value and that from Waldstein was calculated and the resulting differences averaged for each calendar month, obtaining a mean monthly correction factor. Applying this correction value month by month, it is possible to reconstruct the missing Waldstein data back to the year 1971 from the reference data.

The monthly and the annual long-term averaged air temperature statistics are presented in Fig. 3.2, Table 3.1, and Appendix B. With altitudes above 750 m a.s.l., the Waldstein area can be seen to be a cool-temperate version of the actual warmer Central European climate zone. Compared to lower altitudes, which mostly have

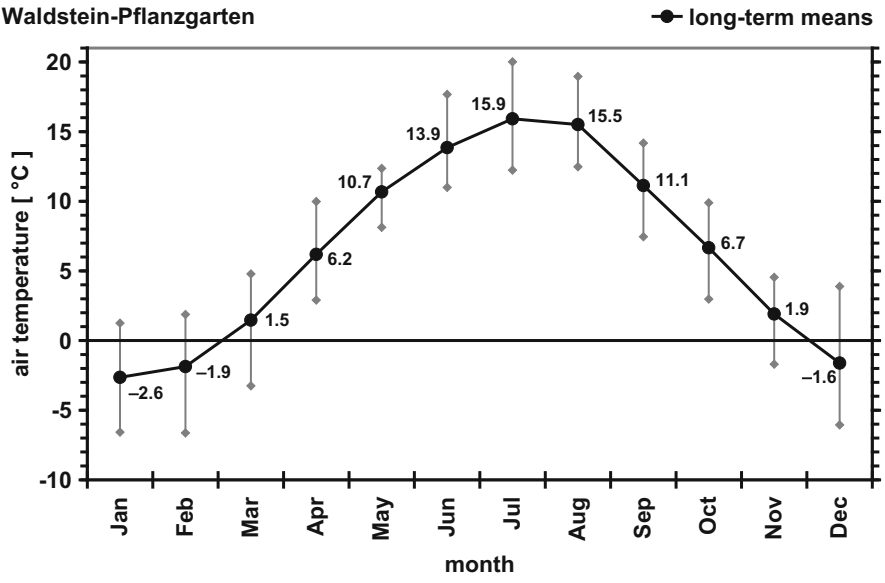

Fig. 3.2 Long-term averaged monthly air temperature at 2 m above ground (meadow) in [°C] and span of coldest and warmest years (*gray bars*), based on data from years 1994 to 2015, Waldstein-Pflanzgarten

Table 3.1 Long-term averaged monthly air temperature at 2 m above ground (meadow) in [°C] and values of coldest and warmest years, based on data from years 1994 to 2015, and the 30-year climatological periods 1971–2000 and 1981–2010 based on the generated time series, Waldstein-Pflanzgarten (WPf)

Waldstein-Pflanzgarten: air temperature 2 m [°C]													
	Month												Year
	Jan	Feb	Mar	Apr	May	Jun	Jul	Aug	Sep	Oct	Nov	Dec	Annual mean
Waldstein-Pflanzgarten only: long-term 1994–2015													
Coldest one	−6.6	−6.6	−3.2	2.9	8.1	11.0	12.2	12.5	7.5	3.0	−1.7	−6.1	**(1996) 4.0**
Mean	**−2.6**	**−1.9**	**1.5**	**6.2**	**10.7**	**13.9**	**15.9**	**15.5**	**11.1**	**6.7**	**1.9**	**−1.6**	**6.5**
Warmest one	1.3	1.9	4.8	10.0	12.4	17.7	20.0	19.0	14.2	9.9	4.5	3.9	**(2015) 8.0**
Waldstein-Pflanzgarten: (1971–1993 generated, reference DWD Fichtelberg Ofr.) 1994–2015 original WPf													
Generated long-term 1971–2000	−3.3	−2.5	0.9	4.6	9.9	12.6	14.9	14.8	10.8	6.0	0.6	−1.9	**5.6**
Generated long-term 1981–2010	−3.1	−2.4	1.0	5.5	10.4	13.2	15.5	15.2	11.0	6.4	1.2	−2.0	**6.0**

only 1 month (January) with a long-term air temperature (barely) below zero degree Celsius, the three winter months December, January, and February show clearly negative values. In the warmest month, July, the mean does not exceed 16 °C, and the annual value is just above 6 °C, which is around 2 K lower than the current nationwide average for both cases. The largest amplitude between the warmest and coldest occurrences of a given month during the years 1994–2015 occurred in February (8.5 K) and December (9.9 K), indicating a strong interannual variability of cold versus warm weather periods during these 2 months (Fig. 3.2). The lowest variation can be seen—surprisingly—in May (4.2 K) and, as expected, in November (6.2 K). In the case of 1996, the Europe-wide coldest year since 1990, the annual mean of 4.0 °C was also the coldest observed in the last 35 years at Waldstein. And in agreement with the globally warmest year of 2015, the annual average at Waldstein exceeded—for the first time—the 8 °C mark (Table 3.1). With respect to the earlier investigation by Foken (2003), it is true that the global warming effect is acting through all months and seasons. Comparing the climatological period 1971–2000 with the last 22 years 1994–2015 (see Table 3.1), a warming shift of above 1 K for the months April (1.6 K), November (1.3 K), June (1.2 K), and July (1.1 K) and below 1 K for the other months between 0.3 K (September) and 0.8 K (May) is observable. It is no longer true that only the winter season is showing strong warming trends. The result of the global temperature development and changing macro-patterns of atmospheric circulation during the last 10–15 years is that the biggest impact is now visible in spring (Apr), summer (Jun, Jul) and autumn (Nov). Especially April is remarkable (see Fig. 3.3a), containing a 100% significant warming trend of 0.8 K per 10 years, which is continuing without interruption. The annual linear warming trend representative for the whole Waldstein and adjacent region is a continuous air temperature increase of 0.4 K per decade. With exception of the 2 cold years 1996 and 2010, the trend is steady, with the absolute warmest years in 2014 and 2015 ever observed so far (see Fig. 3.4). Besides this trend, Fig. 3.4 renders visible exceptional warm or cold episodes that sometimes occur 20 or

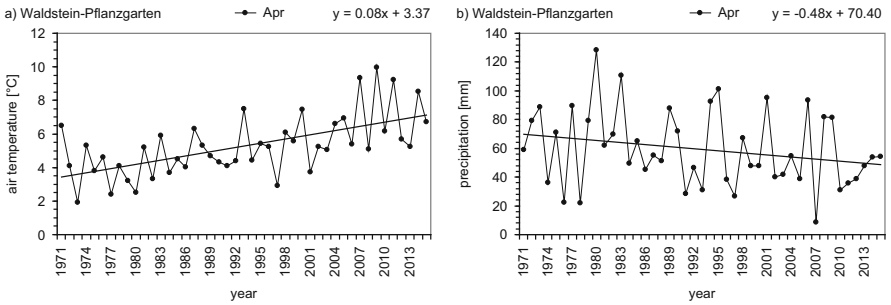

Fig. 3.3 Linear regression trend analysis of (**a**) April's monthly means of air temperature in [°C] and (**b**) April's monthly sums of precipitation in [mm]. Both based on data from 1971 to 1993 using adjacent DWD stations as reference to reconstruct the Waldstein time series and data from 1994 to 2015 originally measured at Waldstein-Pflanzgarten

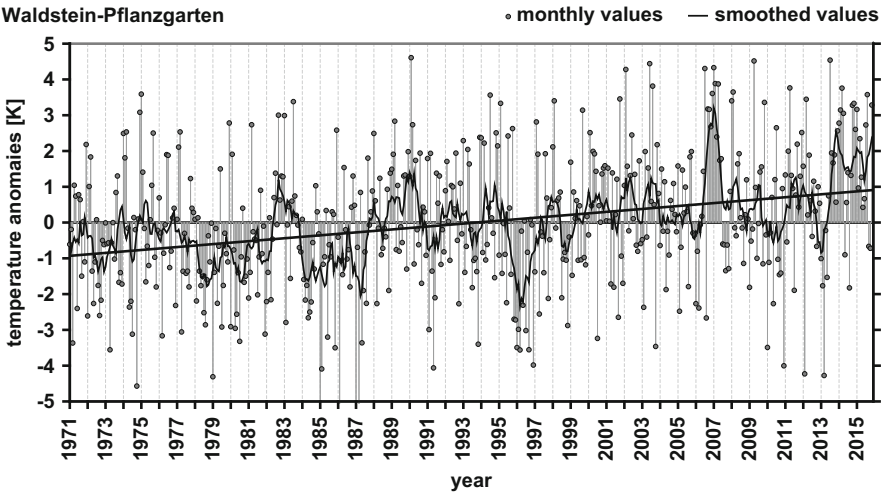

Fig. 3.4 Anomalies of monthly means of air temperature (*gray dots*), their smoothed values (running average, *bold black graph*), and linear trend (*straight line*). Differences of each monthly value from the corresponding long-term average (climatological period 1981–2010), based on data from 1971 to 1993 obtained using adjacent DWD stations as references to reconstruct the Waldstein time series and data from 1994 to 2015 originally measured at Waldstein-Pflanzgarten

even more than 30 months in succession. The last two long and continuous warm phases occur (not only at Waldstein) during the 14 months from May 2006 to June 2007 and lately for the 31 months from June 2013 to December 2015.

3.3.1.2 Precipitation

Congruent to the procedure for prolonging the air temperature time series from 1993 back to 1971, the precipitation data measured at Waldstein from 1994 to 2015 were also extended back to the year 1971 by reconstructing the monthly data, this time using as a reference the records of the DWD-Station Weißenstadt just 7 km away from the Waldstein research site. Both the Waldstein and Weißenstadt data are overlapping for the years 1994 until 2005. Instead of a subtraction of reference and Waldstein data, both precipitation sets were divided, and the mean quotient was used as mean correction factor for each month. The monthly and the annual long-term averaged precipitation sums are presented in Fig. 3.5, Table 3.2, and Appendix B.

The mountain ridge location, with altitudes between 750 m a.s.l. and 877 m a.s.l. (Großer Waldstein), causes this area to show either an advective relief-rainfall or orographic-lift effect (including orographic (cloud) fog formation) or typical convective-induced precipitation (e.g., shower or thunderstorms). The advective mode appears when maritime air masses, mostly transporting moist air, are forced

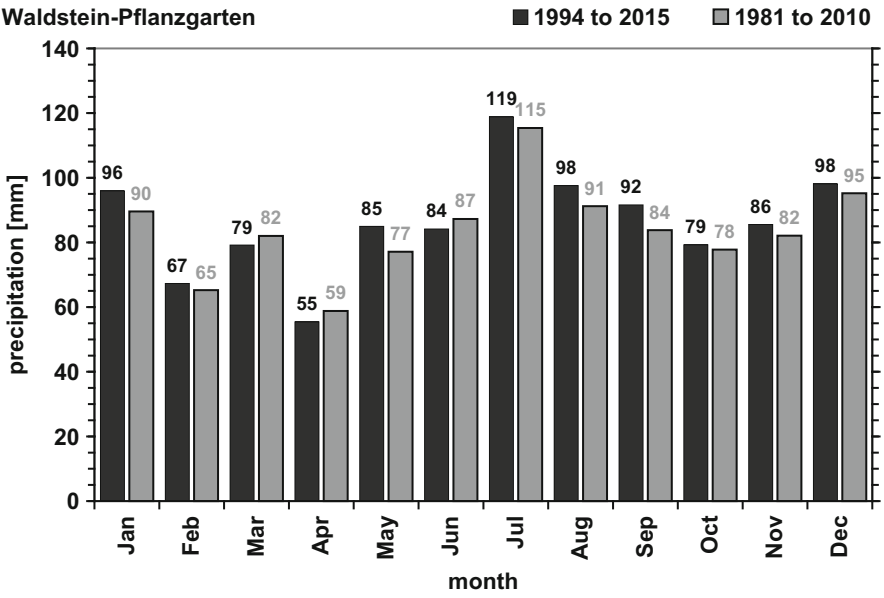

Fig. 3.5 Long-term averaged monthly precipitation sums at 1 m above ground (meadow) in [mm]. (**a**) Based on data from the latest years 1994–2015 (*dark gray bars*). (**b**) Based on the 30-year climatological period 1981–2010 (*light gray bars*); Waldstein-Pflanzgarten

to move over the rising terrain of the Fichtelgebirge range. Two major types of these mesoscale synoptic patterns can occur. Throughout the year, the macro atmospheric circulation pattern of the northern hemisphere can force a maritime Atlantic air mass transport of warm and moist air from the NW to SW sector. During spring, summer, and autumn times, the second maritime type appears in addition to or as replacement of this and is characterized by a transport of maritime hot and moist air from SE to NE that is caused by a strong, stationary deep-pressure cyclone over Eastern Europe moving air from the Mediterranean Sea to Germany. The convection-driven precipitation is connected to the start or end phases of Central European high-pressure systems or to fast moving frontal low-pressure disturbances. Both rain-bringing situations alternate with dry periods caused by anticyclonic blocking action patterns.

As shown in Fig. 3.5 and Table 3.2, on average, more rain or snow falls during December and January (in a steady form and of maritime origin) or during July and August (as short, convective heavy rain events). During the transition seasons of spring and autumn, it is obvious that neither the maritime advection nor the convective processes deliver as much precipitation. As mentioned above (Sect. 3.1), over the last 20 years, the duration and frequency of those dry periods have been increasing, and 4 or 5 rainless weeks are alternating with short and severe weather changes bringing heavy rain, hail, snow, and/or strong windstorms. Projecting the global climate change, it seems strongly possible that this kind of unpredictable

Table 3.2 Long-term averaged monthly precipitation sums at 1 m above ground (meadow) in [mm] and values of driest and wettest years, based on data from years 1994 to 2015, and the 30-year climatological periods 1971–2000 and 1981–2010 based on the generated time series, Waldstein-Pflanzgarten (WPf)

Waldstein-Pflanzgarten: precipitation [mm]													
	Month												Year
	Jan	*Feb*	*Mar*	*Apr*	*May*	*Jun*	*Jul*	*Aug*	*Sep*	*Oct*	*Nov*	*Dec*	Annual sum
Waldstein-Pflanzgarten only: long-term 1994–2015													
Driest	3	18	13	8	23	25	43	19	15	17	2	22	**(1997) 544**
Mean	**96**	**67**	**79**	**55**	**85**	**84**	**119**	**98**	**92**	**79**	**86**	**98**	**1038**
Wettest	201	215	169	101	199	165	190	264	198	242	170	215	**(1994) 1348**
Waldstein-Pflanzgarten: (1971 to 1993 generated, reference DWD Weißenstadt) 1994–2015 original WPf													
Generated long-term 1971–2000	81	56	69	62	69	92	116	82	74	77	74	95	**948**
Generated long-term 1981–2010	90	65	82	59	77	87	115	91	84	78	82	95	**1005**

precipitation pattern of long dry phases and short heavy rain caused by the clash of air masses of different humidity and temperature across Germany will encompass the whole northern hemispheric summer circulation mode from March to October. In addition—and already happening—are short but heavy snowfall events that can occur into late spring or commence in early autumn, when northerly (or NE) air that is still (or already) very cold and dry collides with already warm (or hot) and humid air originating from the Mediterranean Sea.

A significant tendency for an either decreasing or increasing annual precipitation amount is not yet detectable (see Fig. 3.6). But keeping in mind the strong temperature trend in April, April is easily identifiable as the month with the strongest precipitation trend, showing a clear decrease of precipitation of around 4 mm per decade (see Fig. 3.3b). All other months show either a slight, nonsignificant increase or no change at all with the exception of September, where a reliable positive trend is visible (increase of 8 mm 10 a^{-1}). Also discernible are longer dry or wet periods of several months in length. The remarkably dry episode lasting over two full years from October 1995 to May 1998 followed the extremely wet and over 22 months long period from December 1993 to September 1995. The driest year so far was 1997 (544 mm, 52% of the normal sum) and not 2003 (653 mm) as many would have expected. The wettest year was indeed 1994 (1348 mm, 130% of normal) followed by 1998 and 2007 (both about 1300 mm). Figure 3.6 shows in addition—and contrary to the temperature behavior—the high variability of precipitation and

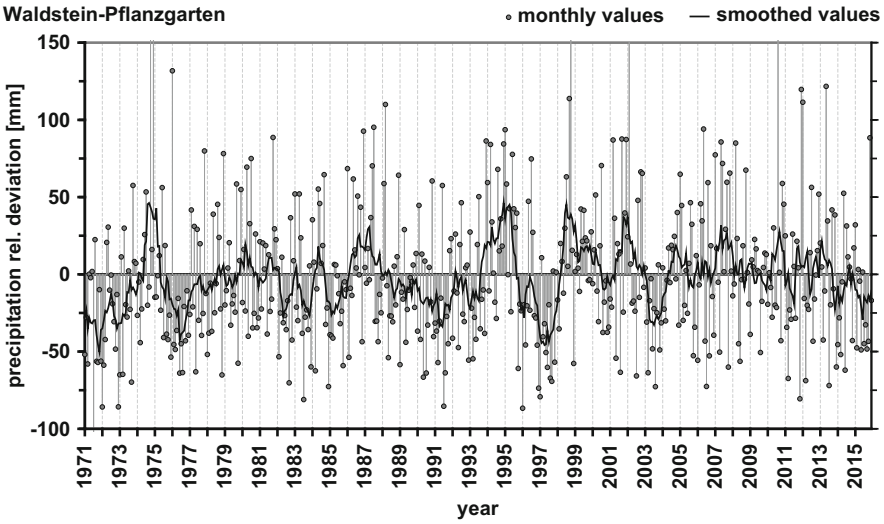

Fig. 3.6 Relative anomalies of monthly mean sums of precipitation (*gray dots*) and smoothed values (running average, *bold black line*). Difference of each monthly value from the corresponding long-term average (climatological period 1981 to 2010); based on data from 1971 to 1993 using adjacent DWD stations as references to reconstruct the Waldstein time series and data from 1994 to 2015 originally measured at Waldstein-Pflanzgarten

quick changes from dry to wet events (especially during springtime), with some prominent long and extreme seasons as described.

3.3.2 Air Pollutants O_3, SO_2, and NO_x

3.3.2.1 Ozone

Tropospheric ground-level ozone, with its risk of health hazards to humans, animals, and plants, is still a current issue and may be more relevant for rural recreation areas in Germany than for urban, inhabited, or industrialized regions. Especially the constant stress acting upon (spruce) trees caused by a high background level of ozone at the Waldstein (or comparable) forests has not disappeared and has, in combination with other factors (extreme weather and pest infection), a negative impact on the growing conditions. Taking into account the previously outlined change of weather conditions at Waldstein (Sect. 3.3.1), it is of great interest to follow the levels of ozone and its formation, depletion, and transport processes and impacting factors. The next subchapters will give an abridged account of the air pollution research done at Waldstein (Foken and Lüers 2015a).

3.3.2.2 Trend Analysis

The background, constant and extreme stress for plants, or low, medium, and high levels of tropospheric ozone concentration (and later SO_2 and NO_x) can be best examined by calculating a quantile (or percentile) as a measure of location of a certain percentage of observations ranked by frequency distribution. For example, the 10% quantile means that all data points of the frequency distribution with a value (score) below the cut point of 10% are considered. Fifty percent (half of data points below and half above the cut point) is equal to the median, and above the 95% quantile are all data points with the 95% highest values (ranks). Figure 3.7 shows all three concentration levels encompassing full years. The annual background or low level (10%) has, on average, a mixing ratio of around 10 ppb but not exceeding 20 ppb. The constant stress level (50%) for plants ranges between 20 ppb and 35 ppb and the extreme stress level touches 70 ppb (years 1993–1995) but varies, on average, around 55 ppb. For all levels, there seems to be a slight increase of the annual values during the 10-year period 1985–1995 followed by a nonsignificant reduction until 2003 and then a weak rise of the ozone concentration again. As a result of the missing data in 2006 and 2007, the last third of the time series is too short for a reliable scientific statement. Forced by the change of mesoscale atmospheric circulation patterns (Sect. 3.3.1) effecting sunshine duration, air temperature and air humidity, wind, and date and duration of precipitation (all of them important players in the formation or destruction of near-surface ozone) at Waldstein, it is hard to predict which month or season will show distinct trends over

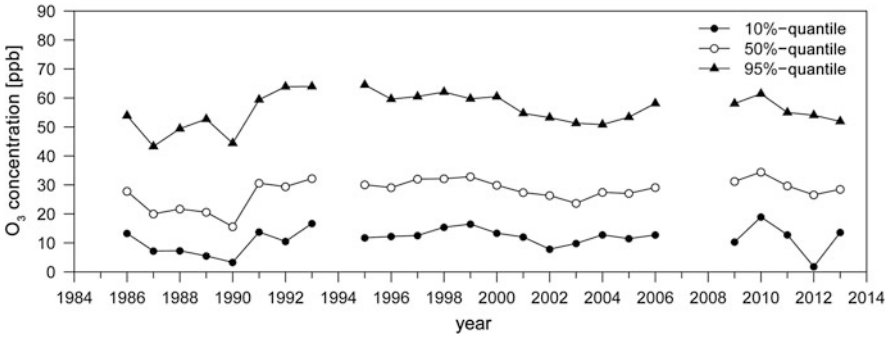

Fig. 3.7 O_3 concentration based on 30-min values in [ppb]; annual 10, 50, and 95 % quantiles (low, medium, and high level). Data for the years 1985–1993 from the LfU station Oberwarmensteinach-Wagenthal and years 1995–2013 from Waldstein-Pflanzgarten. Insufficient data (below 75 % coverage) for 1994, 2006, and 2007

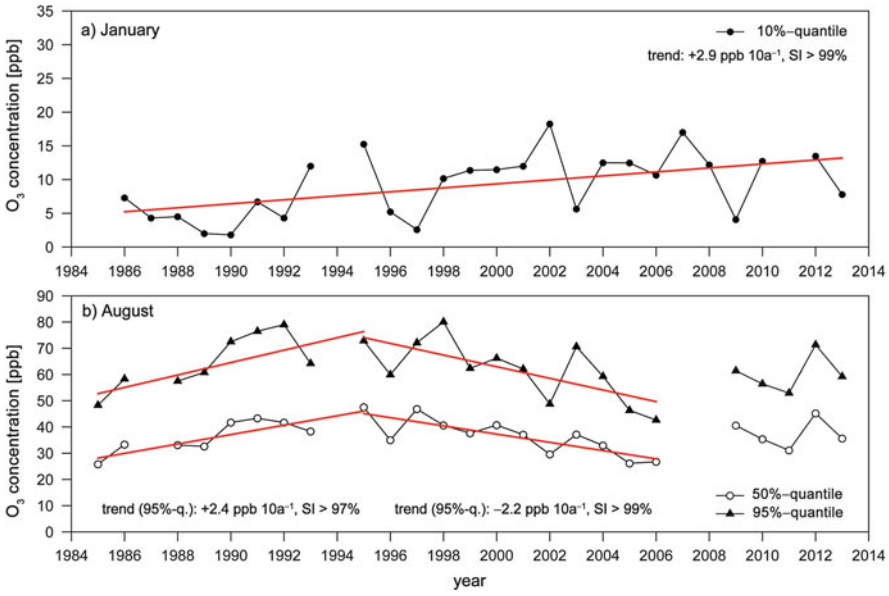

Fig. 3.8 O_3 concentration based on 30-min values in [ppb]. (**a**) January: monthly 10% quantile (low level) of ozone and temporal trend. (**b**) August: monthly 50% and 95% quantiles (medium and high level) of ozone and corresponding partial trends for the 95% quantile. Trends (*straight lines*): linear regression in [ppb per 10 years] and significance (SI) in % (Mann 1945; Kendall 1975). Data for the years 1985–1993 from the LfU station Oberwarmensteinach-Wagenthal and years 1995–2013 from Waldstein-Pflanzgarten. Insufficient data (below 75% coverage) January 1994 and 2011; August 1994, 2006, 2007

the past and future times. As an example, the 2 months with the biggest change so far can be seen in Fig. 3.8.

Surprisingly, during the last 25 years, the background ozone level of the main winter month January recorded the strongest increase of all months. More (cold), calm and sunny weather conditions may have played a role in at least the background concentration showing, in certain years, a visible reaction. For example, the peak of nearly 20 ppb in 2002 could be caused by an 18-day long, sunny, rain/snowfall-free but very cold period during the first 3 weeks of January. A significant increasing trend in August, starting in the early 1980s and ending around 1998, is replaced by an ozone decrease running until at least 2006 (Fig. 3.8b). The peak in August 1998 was caused by a nearly 3-week-long hot, sunny, and ozone-rich episode at Waldstein. The observed interim of relatively weak ozone stress in August between 1999 and 2006 goes along with either quite cold temperatures and heavy rain events once a week and/or (convective) cloud formation during noon and afternoon that cut off the daily ozone peak exactly at that time of day where the main secondary photochemical ozone production would otherwise have taken place.

3.3.2.3 Annual O_3 Variation and the Accumulated Exposure Over a Threshold of 40 ppb (AOT)

To investigate the eco-toxicological impact of ozone on plants, especially trees (forests) and crops, the measure of the exposure of a plant (or forest or crop field) to ozone, expressed as the accumulated ozone exposure over a threshold of 40 ppb (AOT40), was issued in 2004 and required by law under the German Federal Immission Control Act (Bundes- Immissionsschutzgesetz, BImSchG) and the current 39th Immission Protection Ordinance. The intention of this threshold is to have a measure of the risk of a toxic effect or a reduction of the plant (forest or crops) biomass gain caused by constant ozone exposure. It is not designed to express health risks for humans or animals. Thus, in this Air Quality Directive, the medium-term exposure target value for protection of vegetation is set to 18,000 μg per cubic meter during daylight hours (μg m^{-3} h) or 9000 ppb h, averaging the cumulative measurements from May to July over 5 years, while the overall long-term objective is set to 6000 μg m^{-3} h or 3000 ppb h, respectively. Karlsson et al. (2004), however, proposed a lower target value between 2000 ppb h and 5000 ppb h because some ozone-sensitive tree species already respond to this constant stress level with a 3–6% reduction of their biomass production. Different specific plant-orientated AOTx indexes are still in discussion (Karlsson et al. 2003; Mohammed et al. 2011). The plotted AOT40 sums in Fig. 3.9a show values around 7000 ppb h during the 1980s—below the official 9000 ppb h threshold but above the long-term prevention goal of 3000 ppb h. However, during most years between 1991 and 2010, the medium-term protection target of 9000 ppb h was clearly surpassed or even doubled, for example, in 1992 or 1995 (more than 20,000 ppb h), but interrupted by a 4-year long period (2001–2004) with lesser ozone stress. The same phases of lower stress occurred during the last three examined years 2011–2013.

Figure 3.9b gives, for each year, the start and end date on which the ozone concentration exceeded for the first time or for the last time, respectively, the

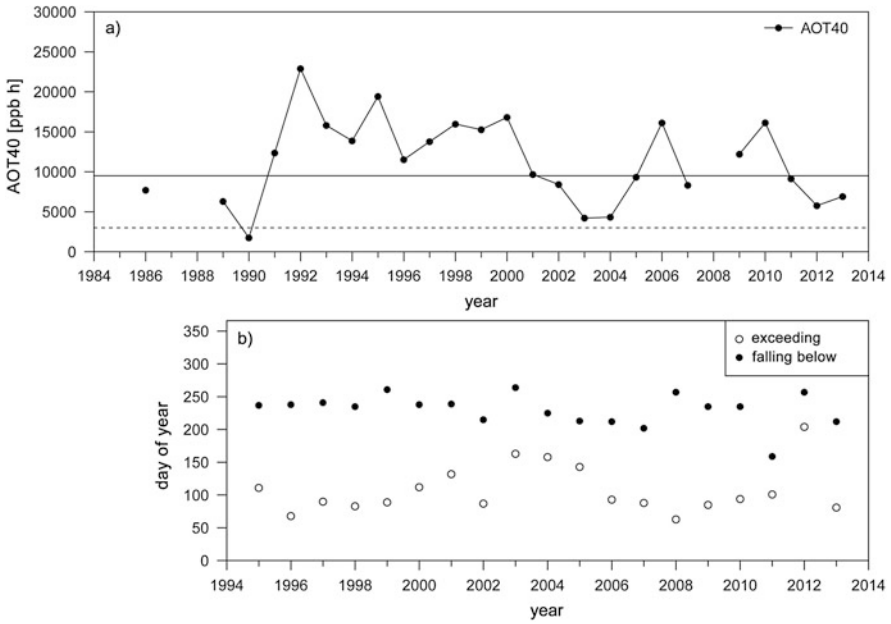

Fig. 3.9 AOT40 (accumulated ozone exposure over a threshold of 40 ppb). (**a**) Year-by-year cumulative sum of 1 h means of ozone exceeding the threshold of 40 ppb between May and July; based on data from 1986 to 2013. *Straight line*: target value of 9000 ppb h. *Dotted line*: long-term target of 3000 ppb h according to the 39th German Federal Immission Protection Ordinance. (**b**) Start dates (*open circles*) on which the ozone concentration exceeded for the first time and end dates (*closed circles*) on which O_3 exceeded for the last time the threshold of 40 ppb for each year. Dates are given as day of year, counting from 1 (1st of Jan), 100 (10th of Apr), and 250 (7th of Sep) to 365 (31st of Dec). Data based on low-pass smoothed ozone values (21-day window filter) years 1994–2013, Waldstein-Pflanzgarten

threshold of 40 ppb. Remembering that the official AOT40 index only considered daylight O_3 values of the season May to July and keeping in mind the strong warming effect (Fig. 3.3a) and the trend to more sunny and dry conditions (Fig. 3.3b)—especially during springtime—this period no longer covers the growing season and raises the question of whether the current AOT40 is still the best method for quantifying the ozone risk to the Waldstein spruce forests. In addition, it seems to be true for many plants that during the early stages of exponential growth, the young or mid-age leaves (or needles) are more vulnerable to O_3 damage and that the developmental or physiological age is an important factor in ozone sensitivity (Kasana 1991). With the exception of the years 2003, 2004, 2005, and 2012 (where extremely dry springtimes delayed plant growth), the onset of critical ozone levels already started, at the earliest, at mid-March, and mostly early April has been strongly connected with long-lasting warm, clear-sky weather and strong ozone episodes at Waldstein. Enduring high ozone stress at the early stages of the annual development phase of a plant (or tree) could increase the risk, especially in

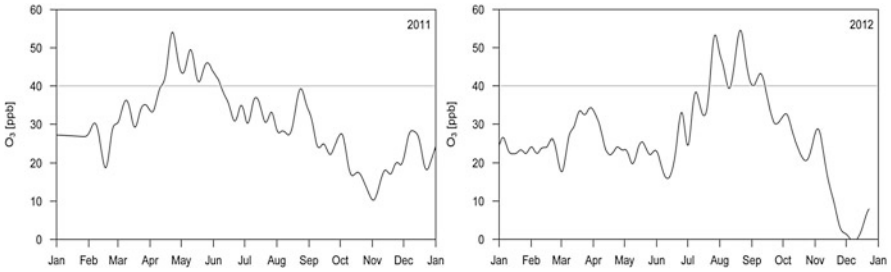

Fig. 3.10 Ozone variation in [ppb] based on low-pass smoothed ozone values (21-day window filter), for the years 2011 and 2012. *Straight line*: threshold (target) value of 40 ppb ozone, Waldstein-Pflanzgarten

combination with water shortage. The end dates where the ozone stress drops below the threshold have shifted mostly into September, and it is still unclear whether this causes an additional risk.

Noticeable are the years between 2001 and 2005 and 2011 and 2012. The earlier period shows a quite short annual ozone period with a late onset (mid-May) and early end (beginning of August). Compared to the years before (1995–2000) or after (2006–2010), with an average duration of 154 days, the annual ozone period is halved. In addition, it could be observed that until 1999, regular, long-lasting periods of exceeded threshold occurred, but beginning around 2000, only occasional and intermittent ozone-rich episodes appeared, reflecting the increasing variability of the weather conditions, i.e., clear versus overcast skies. Figure 3.10 shows examples of two totally different annual ozone patterns with extreme ozone stress conditions during a sunny and dry spring (full 2 months April and May) and no ozone risk in a rainy summer and autumn in 2011, and the opposite in 2012 with no ozone hazards during a rainy spring and early summer but with extreme stress between mid-July and mid-September (very dry and sunny August). Obviously the weather conditions of April and August are triggering the annual ozone pattern. Considering the shift to more unpredictable atmospheric macro- and mesoscale circulation patterns affecting the weather in Central Europe due to the global climate change, it will be difficult to forecast whether we will have conditions promoting the buildup of a distinct, long, and high-level ozone episode or conditions that inhibit such a situation in spring and/or midsummer.

3.3.2.4 SO_2 and NO_x

The trace gas sulfur dioxide (SO_2) enters the atmosphere as a result of both anthropogenic activities and natural processes, where the anthropogenic combustion of fossil fuels (especially brown coal) causes the biggest emission followed by oxidation of organic material in soils, volcanic eruptions, and biomass burning. SO_2 emissions are a precursor to acid rain and atmospheric aerosols (Chap. 9). The

Waldstein region was, like many forested areas in Germany, heavily impacted by acid rain (Matschonat and Vogt 1998; Thalmann et al. 2002) and is still suffering from that man-made pollution input. NO_x is a generic term for the combination of the reactive mono-nitrogen oxides NO and NO_2. The major natural sources of the fast-reacting nitric oxide NO (forms the longer living NO_2) are lightning, the nitrogen fixation by soil microorganisms, and natural wildfires. Most prominent anthropogenic sources for NO and NO_2 are internal combustion engines (motor vehicles) and thermal power stations. Both NO and NO_2, as well as SO_2, play an important role through the formation of secondary inorganic aerosols, where the aerosol compounds such as sulfate, nitrate, or ammonium have been partitioned into the particle phase by chemical reaction of precursor gases SO_2, NO_x, and NH_3 (see Chap. 9). And finally, the (photo)chemical reactions of the $NO/NO_2/O_3$ triad are the main players in forming and depleting atmospheric ozone in the troposphere.

Figure 3.11 shows the remarkable decrease of the high-level, extreme stress concentration of SO_2 at Waldstein (95% quantile), which is representative for the entire Europe and is caused by efficient flue-gas desulfurization of all of the currently operating coal power stations. Typical for this kind of source (combustion), the course of the SO_2 gas concentration follows either the emission of nearby SO_2-containing exhaust or is connected to advection of SO_2-loaded air masses as observed during northeast to southeast winds at Waldstein (sources: coal power plants of the Czech Republic). The SO_2 background level (50% quantile) is otherwise very low and close to the detection limit.

A not such sharp and nonsignificant decreasing trend is visible for the NO_x concentration (Fig. 3.12), but reasons are unclear. Neither an upward nor downward shift of NO is provable for Waldstein. The only directly man-made source is the low-traffic road (around 2100 cars per day on workdays, Foken et al. 2012) at approximately 1.5 km distance from the measurement site. The daily NO

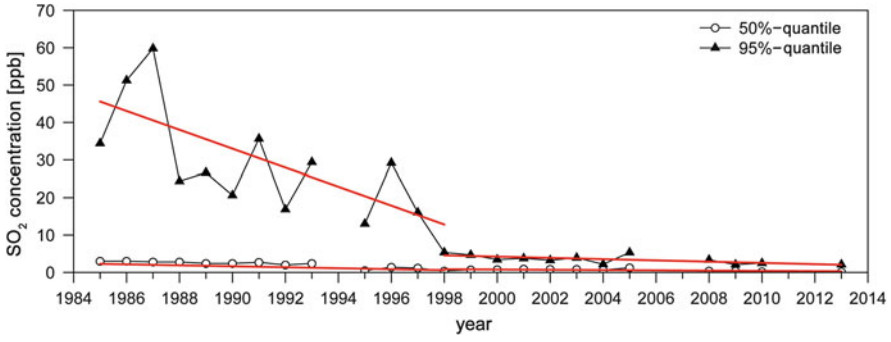

Fig. 3.11 Annual 50% and 95% quantiles (medium and high level) of the SO_2 concentration based on 30-min values in [ppb] and partial linear regression (*red lines*). Years 1985 to 1993 are data from the LfU station Oberwarmensteinach-Wagenthal and years 1995–2013 from Waldstein-Pflanzgarten. No data available for 2006 and 2007 and insufficient data (below 75% coverage) for 1994, 2011, and 2012

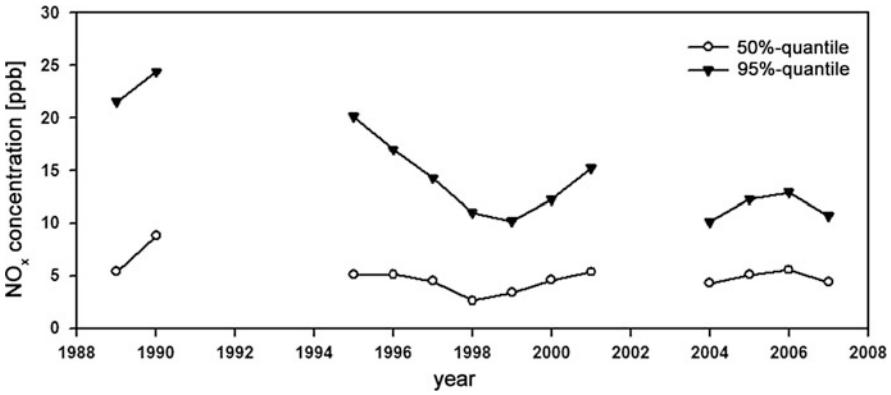

Fig. 3.12 Annual 50% and 95% quantiles (medium and high level) of the NO_x concentration based on 30-min values in [ppb]. Years 1989–1990 are data from the LfU station Oberwarmensteinach-Wagenthal, and years 1995–2007 from Waldstein-Pflanzgarten. Insufficient data (below 75% coverage) for years 1991–1994 and 2002 and 2003

concentration follows the daily traffic emissions (Foken et al. 2012), but no long-term trend can be derived. Considering the NO_x decrease, it seems that a reduction of NO_2 has to be responsible. It is possible that either the frequency of NO_2-loaded air mass advection to Waldstein or the amount of NO_2 within that air itself has decreased over the last 20 years.

3.3.3 Fog Deposition Fluxes

Due to its elevated location at 775 m above sea level, the Waldstein site is prone to fog, that is, the presence of an aerosol with liquid droplets in the diameter range of a few to several tens of μm dispersed in air having direct contact with the ground. Wrzesinsky et al. (2004) reported 223 fog days in a 1-year observation period in 2001/2002, which is slightly more than the long-term average of 200 fog days per year. Thus, the deposition of fog (occult deposition) is a non-negligible input path of water as well as nutrients and pollutants for the Waldstein site. Interestingly, the contribution due to the sedimentation of fog droplets is only a small fraction of the total water input by fog. In 2001 and 2002, sedimentation of fog droplets was 17 kg m^{-2} a^{-1}, whereas the turbulent deposition of fog droplets was 108 kg m^{-2} a^{-1} (Wrzesinsky et al. 2004). Although this is around 10% of the average precipitation at the Waldstein site (1038 mm; see Sect. 3.3.1), the net fog deposition of inorganic ions is extremely important because ion concentrations are typically enhanced in fog water compared to rainwater. For example, during a field experiment from June to December 2000 (Thalmann et al. 2002; Wrzesinsky et al. 2004), the rain-bound deposition of NH_4^+ (6.5 kg ha^{-1} a^{-1}) and NO_3^- (16.2 kg ha^{-1} a^{-1}) was smaller

than the fog-bound deposition of NH_4^+ (7.1 kg ha^{-1} a^{-1}) and NO_3^- (17.2 kg ha^{-1} a^{-1}). This emphasizes the important role of fog deposition for nutrient and pollutant fluxes in the Waldstein forest ecosystem.

Similar to reactive trace gases and aerosol particles, fog droplets cannot be considered as conserved atmospheric scalars, because chemical reactions and phase transitions may change the number concentration, size distribution, and chemical composition of fog droplets. Surface heating may lead to evaporation of fog droplets occurring simultaneously with fog deposition. Indeed, vertical flux divergences of the liquid water content, probably caused by condensation and evaporation of fog droplets, have been observed at the Waldstein site (Burkard et al. 2002). Also, Wrzesinsky et al. (2004) reported simultaneous emission of fog droplets with diameters smaller than 7 μm and deposition of fog droplets with diameters larger than 7 μm. Overall, net deposition of fog water prevails, with typical fog deposition fluxes ranging from −1.86 to +0.02 kg m^{-2} per individual fog event (Wrzresinsky et al. 2004). Table 3.3 and Fig. 3.13 give an insight into the fog chemistry at the Waldstein site. During a half-year investigation in 1997, Wrzresinsky and Klemm (2000) collected 56 fog samples between April and October 1997, with volumes of 2 ml to 1000 ml (mean 315 ml) of fog water being retrieved. Both the absolute concentration levels (Table 3.3) and the relative contributions (Fig. 3.13) of various ions to the ion load are highly variable. The total equivalent concentration ranges from 149 to 6760 μeq l^{-1} (median: 1870 μeq l^{-1}). Not surprisingly, ammonium (NH_4^+), nitrate (NO_3^-), and sulfate (SO_4^{2-}) are the dominating ions. Together, they make up approximately 85% of the total ion charge of the fog water at Waldstein. The precursors of these ions are predominately emitted from animal farming (86% of NH_3 emissions in Germany; UBA 1997); combustion of gasoline and other fossil fuels in road traffic, power plants, and industry (92% of the NO_x emissions); and the combustion of sulfur-containing fuel such as lignite in power plants and industrial plants (82% of SO_2 emissions). The logarithmic (base 10) pH value—used as a measure of the activity of the hydrogen ion and as a scale for specifying the acidity or basicity of an aqueous solution—indicates a medium acid solution between 3.3

Table 3.3 Statistical characterization and composition of solute ions based on 56 fog water samples collected at Waldstein between April and October 1997 in equivalent concentration μeq l^{-1}

Waldstein	pH	H^+	Na^+	K^+	NH_4^+	Mg^{2+}	Ca^{2+}	Cl^-	NO_3^-	SO_4^{2-}
		μeq l^{-1}								
x_{mean}	4.3	89	65	11.5	669	19.5	69	54	481	497
X_{med}	4.3	52	30	9.7	547	10.0	40	31	409	421
x_{log}	4.3	51	39	13.8	547	14.8	46	46	342	376
x_{min}	3.3	2	<9	<6.7	<21	<4.6	<11	<13	20	55
x_{max}	5.7	513	664	68.5	2580	152	493	389	1740	1800

Less than (<) indicates a value below the given determination limit; x_{mean} is the arithmetic mean; x_{med} is the median; x_{log} is the mean derived from the logarithm; x_{min} is the minimum; x_{max} is the maximum

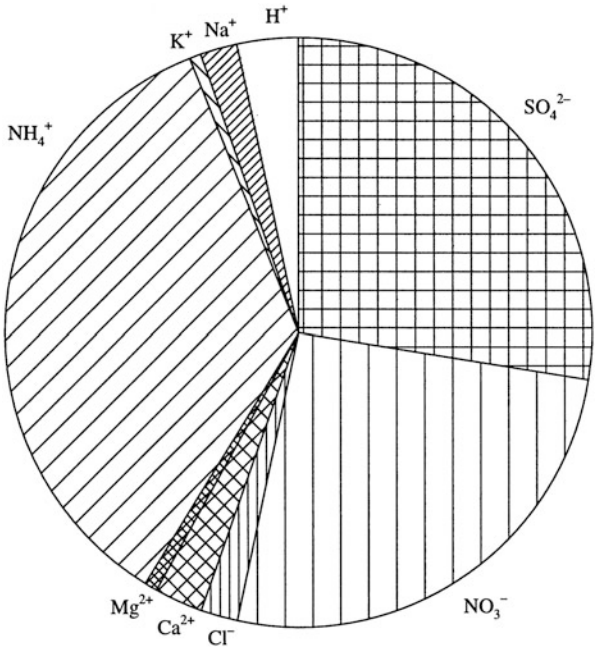

Fig. 3.13 Mean relative equivalent concentration of solute ions based on fog water samples collected at Waldstein between April and October 1997 from Wrzesinsky and Klemm (2000) (compare Table 3.3). Published with kind permission of © Elsevier Science AG Oxford 2000; All rights reserved

and 5.7 (mean 4.3), which is, in most cases, within the range for acid rain (pH < 5.0). The cation loads of sodium, potassium, and calcium salts and the anion chloride have a wide span, varying between the determination limit and quite high values. The Na^+ and Cl^- salt ions, for example, could reach high equivalent concentrations of around 650 and 400 $\mu eq\ l^{-1}$, respectively, which are strongly related to the sea-salt load originating from the North Atlantic and North Sea and transported with air mass advection from the west.

3.3.4 Wet Deposition

There are two main mechanisms by which rainwater obtains its content of salts, cations and anions, metallic trace elements, or organic matter: first by the dilution of particulate materials (e.g., cloud condensation nuclei) in the atmosphere during the water condensation process and second when the waterdrops themselves dissolve particles or gases from the atmosphere. Depending on geography (above oceans or coastal or land areas), regional geology, and human activity, the content of

diluted particles, salts, and dissolved gases varies significantly from place to place. Likewise, the concentration of gaseous nitrogen and sulfur compounds (as sources for acids and bases), the concentration of (heavy) metals and ions from dust and salts, or the group of volatile organic compounds are now to a large extent a function of anthropogenic activity such as technical combustion or chemistry (traffic, electricity, heat, or other industrial production), construction activity (dust), or agriculture (use of synthetic fertilizers).

The operation of a wet-only sampler is not capable of addressing all of these points of interest in their entirety, but it will provide a good overview of the wet deposition of the main rainwater components at the Waldstein site. Figure 3.14 itemizes the average deposition amounts of the main ions and trace elements during the years 2008 and 2013 and confirms the concentrations found in fog water (compare Fig. 3.13). As expected, nitrate (NO_3^-), sulfate (SO_4^{2-}), and ammonium (NH_4^+) make up by far the biggest ion fraction and are mostly caused by anthropogenic emission of NO_x (traffic), SO_2 (fossil combustion), and NH_3 (fertilizers). Two-thirds of all dissolved elements are calcium (Ca), mostly of geological origin and dust-bound, and sodium (Na), of maritime origin, present in more or less the same fraction. These are followed by potassium (K), which is mostly of organic origin. Looking at these numbers, it is obvious—and typical for times with a huge human impact—that the majority of the dissolved mass deposited by rainwater is nitrogen and sulfur, both of which strongly affect the nutrient cycle of the Waldstein ecosystems (eutrophication, acidification). The mass input varies from year to year, mainly corresponding to the amount of precipitated water and/or human activity or synoptic mesoscale weather patterns (humid or dry air mass advection loaded with or without precursors or stable/turbulent exchange conditions). Which

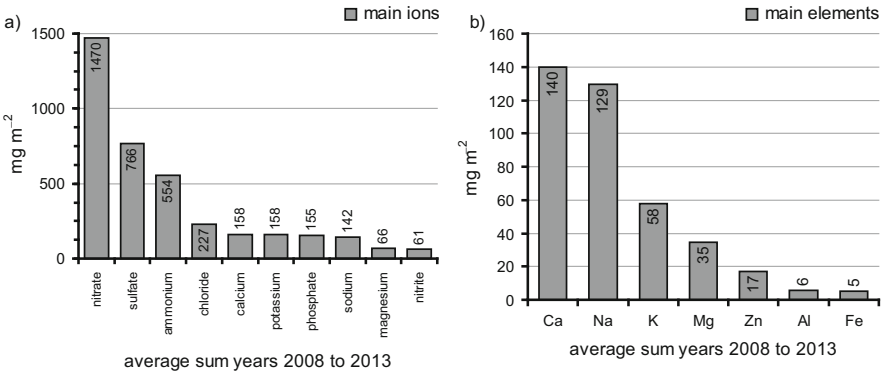

Fig. 3.14 Wet-only deposition in [mg m^{-2}]. (**a**) Average annual sum of **main ions**: nitrate (NO_3^-), sulfate (SO_4^{2-}), ammonium (NH_4^+), chloride (Cl^-), calcium (Ca^{2+}), potassium (K^+), phosphate (PO_4^{3-}), sodium (Na^+), magnesium (Mg^{2+}), and nitrite (NO_2^-); (**b**) average annual sum of **main trace elements**. Both based on years 2008–2013; (**a**) ion chromatography and (**b**) mass spectrometer conducted by Bavarian Environment Agency (LfU), water samples from Waldstein-Pflanzgarten collected by the University of Bayreuth (wet-only sampler)

combination of these factors is responsible for the actual deposition is difficult to determine. The annual wet-deposited sums of the acid residues nitrate and sulfate and the alkaline cation ammonium are shown in Fig. 3.15, and of the trace elements calcium, sodium and potassium in Fig. 3.16, for the years 2008–2013.

The ion fraction clearly points to an expected correlation with the mass of precipitated water, and the variance of all three major ions seems to be explained mostly by

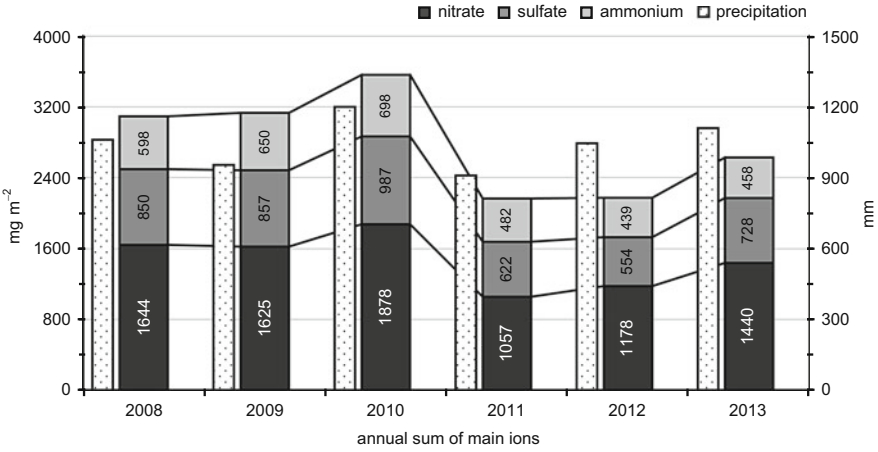

Fig. 3.15 Annual sum of **main ions** in [mg m^{-2}] and corresponding precipitation in [mm] for the years 2008–2013: nitrate (NO_3^-), sulfate (SO_4^{2-}), and ammonium (NH_4^+) ions. Ion chromatography conducted by Bavarian Environment Agency (LfU); water samples from Waldstein-Pflanzgarten collected by the University of Bayreuth (wet-only sampler)

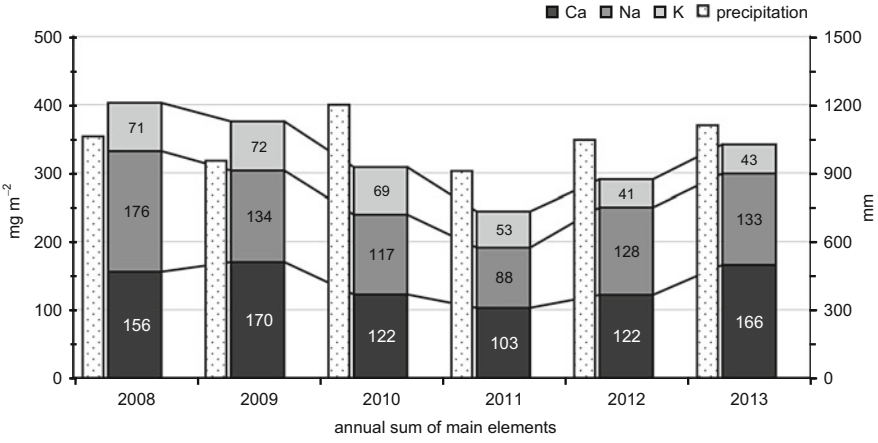

Fig. 3.16 Annual sum of **main trace elements** in [mg m^{-2}] and corresponding precipitation in [mm] for the years 2008 to 2013: calcium (Ca), sodium (Na), and potassium (K) atoms. Mass spectrometry conducted by Bavarian Environment Agency (LfU); water samples from Waldstein-Pflanzgarten collected by the University of Bayreuth (wet-only sampler)

the variability of deposited rainwater. That means—considering a quantity-adjusted correction—a more or less constant amount of nitrogen and sulfur entering the ecosystem at Waldstein during the last years. Conspicuous are the values for 2010, with a very cold winter and spring, a cold and extremely wet August (more than 250 mm) and a cold autumn, resulting in the biggest nitrogen and sulfur input so far. Not so easy to explain is the total mass of the major Ca, Na, and K atoms contained in the rainwater (Fig. 3.16).

No real connection to the annual rainwater mass can be discerned. Reasons for this could be the fact that (a) for some water samples, the concentration of those elements was under the detection limit of the mass spectrometer and therefore an overestimation is possible and (b) the water amount obtained with the wet-only collector was always below the real precipitated mass (see Fig. 3.1). Another plausible factor could be a year-to-year variation of dust load and/or human activity such as agricultural or construction-linked sources, or winter traffic management (amount of deicing salts: Na, Mg, or K). For example, the extreme dry and hot August in 2009 and the equally dry and hot July in 2013 could have caused the peaks of calcium. Or likewise, the quite warm and wet winter and early spring, and rainy and cold summer and autumn, with a lot of air mass advection from the Atlantic in 2008 could have caused the Na peak.

Figures 3.17, 3.18, and 3.19 contain the results of the 13 4-weekly collecting periods averaged over the 6 years (2008–2013), giving a view of the intra-annual variation of dissolved ions and elements in the precipitation water falling at Waldstein. Most of the atmospheric nitrogen (NO_3^- and NH_4^+) and sulfur

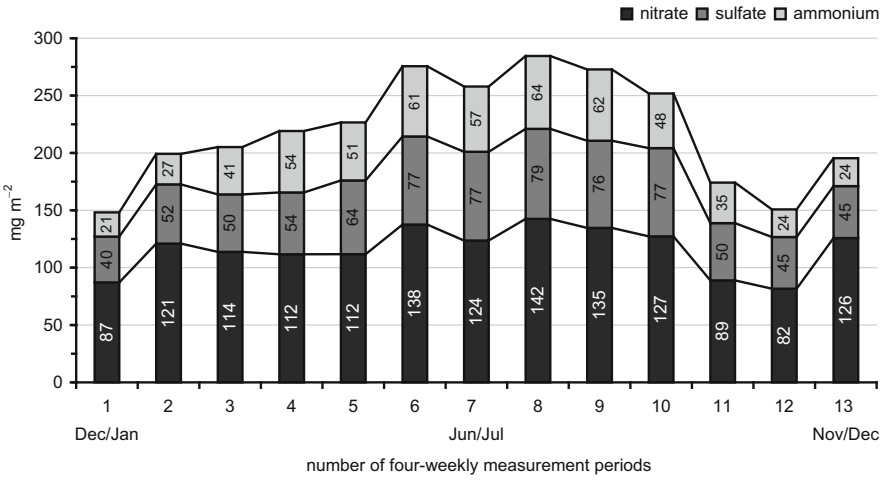

Fig. 3.17 Average annual cycle of **main ions** in [mg m^{-2}] based on years 2008–2013: nitrate (NO_3^-), sulfate (SO_4^{2-}), and ammonium (NH_4^+). Ion chromatography conducted by Bavarian Environment Agency (LfU); water samples from Waldstein-Pflanzgarten collected by the University of Bayreuth (wet-only sampler)

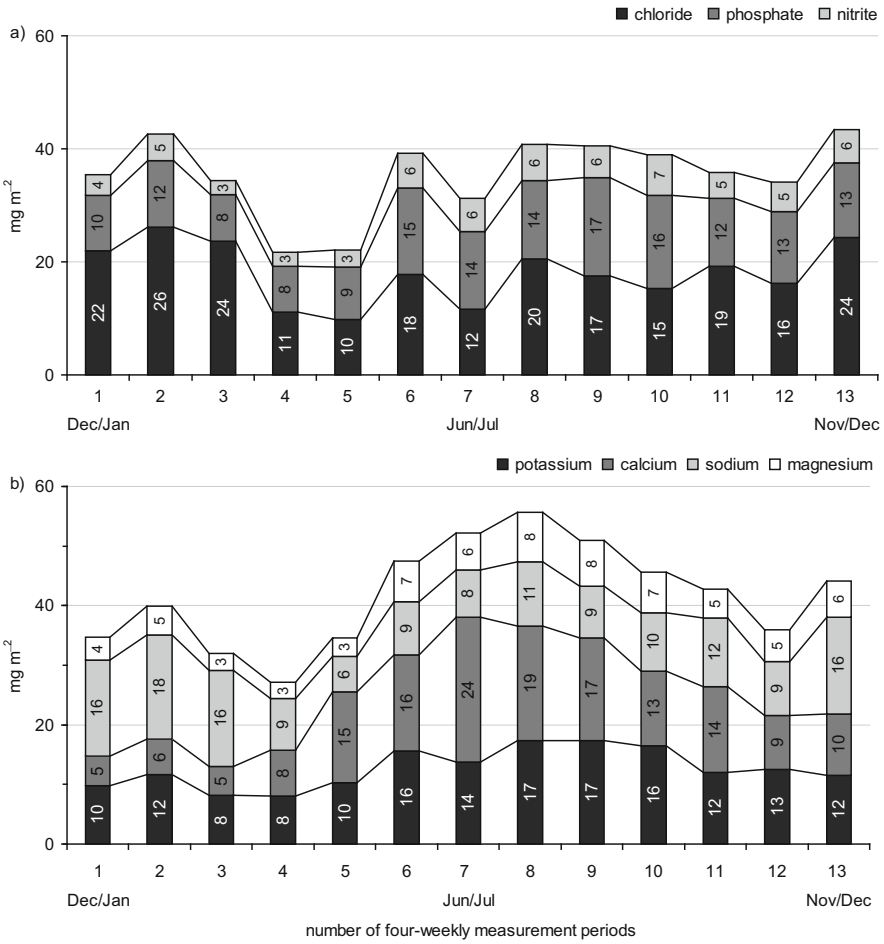

Fig. 3.18 Average annual cycle of dissolved ions in [mg m^{-2}]. (**a**) **anions** chloride (Cl^-), phosphate (PO_4^{3-}), and nitrite (NO_2^-); and (**b**) **metallic cations** potassium (K^+), calcium (Ca^{2+}), sodium (Na^+), and magnesium (Mg^{2+}). All based on years 2008 to 2013. Ion chromatography conducted by Bavarian Environment Agency (LfU); water samples from Waldstein-Pflanzgarten collected by the University of Bayreuth (wet-only sampler)

(SO_4^{2-}) entered the ecosystem via the rainwater during May/Jun (period 6) and Sep/Oct (period 10, Fig. 3.17). That was caused by the more reactive (enhanced photochemical) condition of the tropospheric atmosphere and the presence of ozone and hydroxyl radicals (OH^- ions) during summer or times of clear skies and strong shortwave radiation.

Looking at the main anions (Fig. 3.18a), chloride (Cl^-), phosphate (PO_4^{3-}), and nitrite (NO_2^-), and metallic cations (Fig. 3.18b), potassium (K^+), calcium (Ca^{2+}) sodium (Na^+), and magnesium (Mg^{2+}), different seasonal inputs are observable.

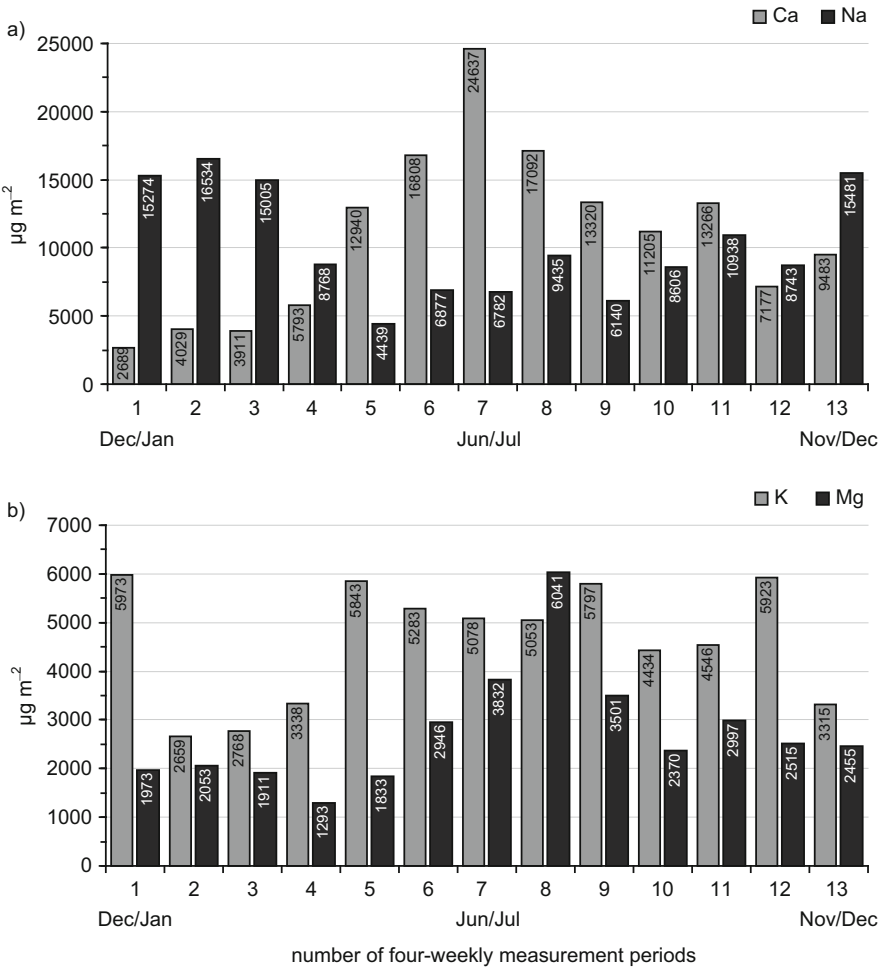

Fig. 3.19 Average annual cycle of **dissolved trace elements** in [µg m^{-2}] for the years 2008–2013: calcium (Ca), sodium (Na), potassium (K), and magnesium (Mg) atoms. Mass spectrometry conducted by Bavarian Environment Agency (LfU); water samples from Waldstein-Pflanzgarten collected by the University of Bayreuth (wet-only sampler)

The source of chloride during the wintertime (Nov to Mar) is mainly man-made, caused by the use of NaCl as deicing salt. A maritime source (i.e., the Atlantic or the North Sea) is unlikely, because during the long transportation from the ocean to Upper Franconia, the hydrochloric acid completely reacts to nitric acid. The smallest depositions of anions and cations occur during April and mid-June due to the occurrence of long rain/snowfall-free times in spring. Peaks of potassium input again occurred between May/Jun (period 6) and Sep/Oct (period 10, Fig. 3.18b) but also during November to February (Fig. 3.19b). This was caused by fertilizer

application (mostly potassium nitrate) and biomass combustion (commercial power generation from biogas) throughout the year and by the burning of wood during the wintertime heating period (Hartmann and Turowski 2010). The enhanced calcium deposition occurring during the extended summer period (Figs. 3.18b and 3.19a), with a peak in June/July, is mostly caused by Ca-rich minerals suspended as dust aerosols during turbulent, convective exchange conditions and washed out by summery rainfall. The sodium (Na) shows a distinct winter peak (Figs. 3.18b and 3.19a). As said, in addition to the maritime source of Na, the application of NaCl as deicing salt results in high deposition rates during the cold season.

3.4 Conclusions

The huge list of measured meteorological elements, including hydrometeors and key aerosols, and basic air chemistry above a free area (Pflanzgarten) as well as within the forest sub-canopy or above the trees (Weidenbrunnen), enables a large variety of environmental investigations using data from the Waldstein research site. The changed weather, climate and air pollution conditions, and their predicted future trends presented in this chapter will help in the interpretation of the energy and matter fluxes, the response of vegetation and microorganisms, the change of soils, and the impact to the carbon, water, and nutrient cycles of this spruce forest ecosystem. Especially the climatological location at the border between two major climate zones—the maritime- and the continental-influenced regions of Central Europe—makes the Waldstein interesting and special not only for climate impact studies but also for a comparison of spatial, gridded 2D/3D weather or climate model calculations with single plot measurements. Beyond the presented characterization of air temperature and precipitation, it will be possible with the available information about horizontal and vertical wind profiles, short- and longwave radiation, and atmospheric visibility and fog occurrence, to broaden the approach of climate classifications and to move away from an all-year perspective (as is solely applied nowadays) to a seasonal, weather-pattern-based classification.

Still enduring the aftermath of a century-long acidification of European soils and both running and lentic waters caused by anthropogenic sulfur emissions and the following wet deposition (acid rain), the growing conditions of our forests or, in general, the environmental conditions of mountain ecosystems are furthermore affected by an increasing risk of damage caused by a continuous high background ozone level or by periods of long, extreme ozone stress. This, in combination with an increasingly inconvenient accumulation of stressful weather events (drought, excessive wetness, stronger windstorms, extreme heat, or frost) and ongoing nitrogen eutrophication, is weakening the ecosystem resilience and likelihood of resistance. It will also enhance the risk of bacterial or virus plant diseases and massive and severe infection by invasive pests (e.g., bark beetles). With all of these factors in mind, it is necessary to make adjustments to the Franconian forest ecosystems to put them on the right track for the future.

Acknowledgments The operation of the site was funded by The Federal Ministry of Education, Science, Research and Technology (PT BEO-0339476 A, B, C, D) and the Oberfranken Foundation (contract 01879). Many thanks go to the Bavarian Environment Agency (LfU), which was responsible for all of the chemical analyses. This work was only possible with the enthusiasm and hard work, sometimes under harsh weather conditions, of very many technicians, students, PhD candidates, and motivated scientists.

References

Belda M, Holtanová E, Halenka T, Kalvová J (2014) Climate classification revisited: from Köppen to Trewartha. Clim Res 59:1–13. doi:10.3354/cr01204

Burkard R, Eugster W, Wrzesinsky T, Klemm O (2002) Vertical divergence of fogwater fluxes above a spruce forest. Atmos Res 64(1–4):133–145. doi:10.1016/S0169-8095(02)00086-8

Eiden R, Förster J, Peters K, Trautner F, Herterich R, Gietl G (1989) Air pollution and deposition. In: Schulze ED, Lange OL, Oren R (eds) Forest decline and air pollution. Ecological studies. Springer, Heidelberg, pp 57–103

Eigenbrodt (2007) Betriebs- und Wartungsanleitung Automatischer Niederschlagssammler NSA 181/KHS. Eigenbrodt GmbH & Co. KG, Königsmoor

Foken T (2003) Lufthygienisch-Bioklimatische Kennzeichnung des oberen Egertales. Bayreuther Forum Ökologie 100:69+XLVIII

Foken T, Lüers J (2003) Klimawandel in Oberfranken. Terra Nostra 6:129–135

Foken T, Lüers J (2013) Regionale atmosphärische Prozesse und ihre raumzeitliche Ausprägung. Ann Meteorol 46:25–29

Foken T, Lüers J (2015a) Abschlussbericht zum Förderprojekt 01879 Untersuchung der Veränderung der Konzentration von Luftbeimengungen und Treibhausgasen im hohen Fichtelgebirge: 2007 bis 2014. Universität Bayreuth, Abt. Mikrometeorologie, Arbeitsergebnisse 61, ISSN 1614-8916, 97 pp

Foken T, Lüers J (2015b) Regionale Ausprägung des Klimawandels in Oberfranken. In: Obermaier G (ed) Folgen des Klimawandels. Bayreuther Kontaktstudium Geographie, vol 8, pp 33–42

Foken T, Meixner FX, Falge E, Zetzsch C, Serafimovich A, Bargsten A, Behrendt T, Biermann T, Breuninger C, Dix S, Gerken T, Hunner M, Lehmann-Pape L, Hens K, Jocher G, Kesselmeier J, Lüers J, Mayer JC, Moravek A, Plake D, Riederer M, Rütz F, Scheibe M, Siebicke L, Sörgel M, Staudt K, Trebs I, Tsokankunku A, Welling M, Wolff V, Zhu Z (2012) Coupling processes and exchange of energy and reactive and non-reactive trace gases at a forest site—results of the EGER experiment. Atmos Chem Phys 12:1923–1950

Gerstberger P, Foken T, Kalbitz K (2004) The Lehstenbach and Steinkreuz chatchments in NE Bavaria, Germany. In: Matzner E (ed) Biogeochmistry of forested catchments in a changing environment, a German case study. Ecological studies, vol 172. Springer, Heidelberg, pp 15–41

Hartmann H, Turowski P (2010) Feinstaubemisionen aus Holzheizungen. Bayerisches Landesamt für Wald- und Forstwirtschaft. LWF-aktuell 74:10–12

Hendl M (1991) Globale Klimaklassifikation. In: Hupfer P (ed) Das Klimasystem der Erde. Akademie-Verlag, Berlin, pp 218–266

Karlsson PE, Selldén G, Pleijel H (eds) (2003) Establishing ozone critical levels II. UNECE workshop report, IVL report B 1523. Gothenburg, IVL Swedish Environmental Research Institute

Karlsson PE, Uddling J, Braun S, Broadmeadow M, Elvira S, Gimeno BS, Le Thiec D, Oksanen E, Vandermeiren K, Wilkinson M, Emberson L (2004) New critical levels for ozone effects on young trees based on AOT40 and simulated cumulative leaf uptake of ozone. Atmos Environ 38:2283–2294

Kasana MS (1991) Sensitivity of three leguminous crops to O_3 as influenced by different stages of growth and development. Environ Pollut 69:131–149
Kendall MG (1975) Rank correlation methods, 4th edn. Charles Griffin, London
Kittler F, Lüers J, Nauß T, Foken T (2011) Möglichkeiten der künstlichen Beschneiung im gegenwärtigen und zukünftigen Klima im Fichtelgebirge. Der Siebenstern 80(5):240–243
Klemm O, Lange H (1999) Trends of air pollution in the Fichtelgebirge mountains, Bavaria. Environ Sci Pollut Res 6:193–199
Klemm O, Mangold A (2001) Ozone deposition at a forest site in NE Bavaria. Water Air Soil Pollut Focus 1:223–232
Klemm O, Mangold A, Held A (2004) Turbulent deposition of ozone to a mountainous forest ecosystem. In: Matzner E (ed) Biogeochmistry of forested catchments in a changing environment, a German case study. Ecological studies, vol 172. Springer, Heidelberg, pp 203–213
Kottek M, Grieser J, Beck C, Rudof B, Rubel F (2006) World map of the Köppen-Geiger climate classification updated. Meteorol Z 15:259–263. doi:10.1127/0941-2948/2006/0130
Lüers J (2012) Wasser in Oberfranken. Wie viel Wasser brauchen wir und wo wird es gewonnen? Spektrum, 1–2012, Universität Bayreuth, pp 26–31.
Lüers J, Foken T (2010) Jahresbericht 2009 zum Förderprojekt 01879, Untersuchung der Veränderung der Konzentration von Luftbeimengungen und Treibhausgasen im hohen Fichtelgebirge. Universität Bayreuth, Abt. Mikrometeorologie, Arbeitsergebnisse 43, ISSN 1614–8916, 59 pp.
Mann HB (1945) Non-parametric tests against trend. Econometrica 13:163–171
Matschonat G, Vogt R (1998) Significance of the total cation concentration in acid forest soils for the solution composition and the saturation of exchange sites. Geoderma 84(4):289–307. doi:10.1016/S0016-7061(98)00009-3
Mohammed NI, Ramli NA, Yahya AS, Ghazali NA, Ul-Saufie AZ (2011) Relationship between AOTX indices and crops response towards ozone concentration in Malaysia. Int J Appl Sci Technol 1(1):36–44
Peel MC, Finlayson BL, McMahon TA (2007) Updated world map of the Köppen-Geiger climate classification. Hydrol Earth Syst Sci 11:1633–1644. doi:10.5194/hess-11-1633-2007
Schönwiese CD (2013) Praktische Statistik für Meteorologen und Geowissenschaftler. 5. Aufl. ed. Borntraeger, Stuttgart, 319 S
Staudt K, Foken T (2007) Documentation of reference data for the experimental areas of the Bayreuth Centre for Ecology and Environmental Research (BayCEER) at the Waldstein site. Universität Bayreuth, Abt. Mikrometeorologie, Arbeitsergebnisse 35, ISSN 1614–8916, 35 pp
TA-Luft 2002 Erste Allgemeine Verwaltungsvorschrift zum Bundes-Immissionsschutzgesetz (Technische Anleitung zur Reinhaltung der Luft—TA Luft) vom 24. Juli 2002, GMBl 2002 S. 511–605
Thalmann E, Burkard R, Wrzesinsky T, Eugster W, Klemm O (2002) Ion fluxes from fog and rain to an agricultural and a forest ecosystem in Europe. Atmos Res 64(1–4):147–158. doi:10.1016/S0169-8095(02)00087-X
Trewartha GT, Horn LH (1980) Introduction to climate, 5th edn. McGraw Hill, New York, NY
UBA U (ed) (1997) Daten zur Umwelt. Erich Schmidt Verlag, Berlin, 570 pp
WMO (2008) Guide to meteorological instruments and methods of observation. World Meteorological Organization, WMO Note 8, CIMO-Guide 7th edn
Wrzesinsky T, Klemm O (2000) Summertime fog chemistry at a mountainous site in Central Europe. Atmos Environ 34:1487–1496
Wrzesinsky T, Scheer C, Klemm O (2004) Fog deposition and its role in biogeochemical cycles of nutrients and pollutants. In: Matzner E (ed) Biogeochmistry of forested catchments in a changing environment, a German case study. Ecological studies, vol 172. Springer, Heidelberg, pp 191–202

Chapter 4
Long-Term Carbon and Water Vapour Fluxes

Wolfgang Babel, Johannes Lüers, Jörg Hübner, Corinna Rebmann, Bodo Wichura, Christoph K. Thomas, Andrei Serafimovich, and Thomas Foken

4.1 Introduction

Long-term flux measurements of water vapour and carbon dioxide, as structured within networks like FLUXNET (Baldocchi et al. 2001), are of strong interest for the scientific community for ecosystem level process studies (e.g. Valentini et al. 2000), derivation of regional to global budgets (e.g. Jung et al. 2009) or to evaluation of land surface models (e.g. Bonan et al. 2011).

The Waldstein–Weidenbrunnen site (DE-Bay) has been intensively studied for more than 20 years, starting with the first carbon dioxide flux measurements in 1996. A history of the site including the main activities during the last two decades is given in Chap. 1. The climate at the Waldstein–Weidenbrunnen site is warm-temperate

W. Babel (✉) • C.K. Thomas
Micrometeorology Group, University of Bayreuth, 95440 Bayreuth, Germany
e-mail: wolfgang.babel@uni-bayreuth.de

Bayreuth Center of Ecology and Environmental Research, University of Bayreuth, Bayreuth, Germany

J. Lüers
Bayreuth Center of Ecology and Environmental Research, University of Bayreuth, 95440 Bayreuth, Germany

J. Hübner
Uhl Windkraft Projektierung GmbH & Co. KG, Max-Eyth-Str. 40, 73479 Ellwangen, Germany

C. Rebmann
Computational Hydrosystems, Helmholtz Centre for Environmental Research UFZ, Permoserstraße 15, 04318 Leipzig, Germany

B. Wichura
Deutscher Wetterdienst, Climate and Environment Consultancy, Regional Office Potsdam, Postfach 600552, 14405 Potsdam, Germany

T. Foken (ed.), *Energy and Matter Fluxes of a Spruce Forest Ecosystem*,
Ecological Studies 229, DOI 10.1007/978-3-319-49389-3_4

in the sense of FLUXNET conventions, and the climate type is Cfb according to Köppen–Geiger classification (Kottek et al. 2006). It has been included in the EUROFLUX sites (Valentini et al. 2000), with eddy-covariance-measured carbon and water fluxes obeying the EUROFLUX methodology (Aubinet et al. 2000, 2003). The site took part in the development of quality standards, especially with respect to eddy-covariance data quality (see Chap. 12), footprint (Rebmann et al. 2005; Göckede et al. 2002, 2008) and gap-filling (Rebmann et al. 2004; Ruppert et al. 2006) for eddy-covariance-measured carbon and water fluxes of the EUROFLUX project.

The first flux data sets from 1997 to 2001 were published by Rebmann (2004), Rebmann et al. (2004), the data has been used for site-specific process studies of carbon and water cycling (e.g. Valentini et al. 2000; Matteucci et al. 2000; Bernhofer et al. 2003). A long-term data set has now been compiled for the Waldstein–Weidenbrunnen site. The present study adds the analysis of the data from 2002 up to 2014. We show the long-term behaviour of the site with respect to evapotranspiration and net carbon uptake, as well as gross primary production and ecosystem respiration derived by flux partitioning algorithms. Furthermore, we investigate the inter-annual variation of evapotranspiration with respect to the Budyko framework, which is a non-dimensional characterization of a region by the relationships between evapotranspiration, potential evaporation and precipitation, and compare our data with the results of Williams et al. (2012). Finally, we put our measurements into the regional context and compare our results to selected examples from related studies.

4.2 Methods

4.2.1 Site Description and Measurement Set-up

The long-term observations of carbon dioxide and water vapour fluxes have been conducted above a Norway spruce forest in the Fichtelgebirge, at the Weidenbrun-

A. Serafimovich
German Research Centre for Geosciences GFZ, Helmholtz Centre Potsdam, Telegrafenberg, Haus A 6, 14473 Potsdam, Germany

T. Foken
Am Herrgottsbaum 28, 96120 Bischberg, Germany

Bayreuth Center of Ecology and Environmental Research, University of Bayreuth, Bayreuth, Germany

W. Babel, J. Lüers, J. Hübner, C. Rebmann, B. Wichura, C.K. Thomas, A. Serafimovich, T. Foken: Affiliation during the work at the Waldstein sites: Department of Micrometeorology, University of Bayreuth, Bayreuth, Germany

C. Rebmann (up to 2002) Affiliation during the work at the Waldstein sites: Chair of Plant Ecology, University of Bayreuth, Bayreuth, Germany

Table 4.1 Selection of instruments used for the long-term budgets

Parameter	Manufacturer, device	Location	Period
Flux measurements			
Wind vector	Gill, R2 sonic (until May 19, 2003)	MT[a], 33 m	1997–2003
	Gill, R3 sonic	MT[a], 33 m	2003–2006
Water vapour and CO_2	Li-Cor, Li6262 (until April, 2002)	MT[a], 33 m	1997–2002
	Li-Cor, Li7500	MT[a], 33 m	2002–2006
Wind vector	Metek, USA1	TT[b], 36 m	2007–2014
Water vapour and CO_2	LiCor Biosci., Li7500	TT[b], 36 m	2007–2014
Meteorological measurements			
Short-wave radiation	Kipp&Zonen, CM14	MT[a], 30 m	1998–2014
Long-wave radiation	Kipp&Zonen, CG2	MT[a], 30 m	1998–2014
Air temperature	Friedrichs, Frankenberger Psychrometer	MT[a], 31 m, 2 m	1998–2014
and humidity	Vaisala, HMP 45A		
Present weather detector	Vaisala, PWD11	MT[a], 21 m	2002–2014
Precipitation	OMC 212, tipping bucket	Pfl[c], 1 m	1994–2014
	Ott, Pluvio2	Pfl[c], 1.5 m	2012–2014

For a complete instrumentation list of the main tower and Pflanzgarten site see Appendix A
[a]Waldstein–Weidenbrunnen, main tower
[b]Waldstein–Weidenbrunnen, turbulence tower
[c]Waldstein–Pflanzgarten

nen site in the Waldstein measurement area. Chapter 2 provides details about this site including information about location, climate and vegetation. The eddy-covariance set-up has been in operation on the 32 m high walk-up scaffold tower, henceforth called Main Tower or MT (see Chap. 2, Figs. 2.2 and 2.7) since 1996, with a change of instrumentation in 2001 and 2007. A second eddy-covariance complex has been established on a 36 m high slim tower, henceforth called Turbulence Tower or TT in 2007 (see Chap. 2, Figs. 2.2 and 2.8). In this chapter we analyse the data from 2002 up to 2014, with the relevant instrumentation summarized in Table 4.1, while additional information about further routine set-up is given in Appendix A.

4.2.2 Data Processing

4.2.2.1 Turbulent Flux Processing

Turbulent fluxes of carbon dioxide and latent heat have been calculated with the internationally compared software package TK2/TK3 (Mauder and Foken 2011, 2015), obeying micrometeorological standards with respect to corrections and data quality control (Foken et al. 2012). Coordinate rotation has been carried out with the planar-fit method (Wilczak et al. 2001) for each month separately, based on an analysis by Siebicke et al. (2012). The net ecosystem exchange *NEE* is then

the sum of the eddy-covariance carbon dioxide flux and the change in storage of the air column below the sensor. As CO_2 profile measurements were only available during intensive observation periods, the storage flux has been calculated from mean CO_2 concentrations at the top of the tower for the whole period. Ruppert et al. (2006) showed for the Waldstein site, that this method captures the canopy storage reasonably well, as long as unrealistic values of the open-path gas analyser were rejected. The evapotranspiration *ET* in mm is the water equivalent of the eddy-covariance latent heat flux.

The flux data has been quality controlled with a flagging system ranging from 1 to 9, combining tests for stationarity and integral turbulence characteristics (Foken and Wichura 1996; Foken et al. 2004). Therefore a u_*-filtering on *NEE* flux measurements has not been applied (Ruppert et al. 2006, see Chap. 12). We kept flux data of best and intermediate data quality (1–6) for the long-term budgets, while the parameterization of the gap-filling routine (this section) was done with data of best quality (1–3) only. In addition, all data during rain or fog events and the following hour have been discarded due to steamed up windows of the open-path gas analyser. No quality checks in terms of advection have been applied, as the relationship between advection and diagnostics of the eddy-covariance flux is still unclear. Especially the night-time u_*-criteria was shown to be not consistent with advection (Aubinet et al. 2010). More details about advection at Waldstein–Weidenbrunnen is given in Chaps. 6, 12 and 14.

The footprint of the eddy-covariance data has been calculated with a Lagrangian stochastic forward model (method presented by Göckede et al. 2006). The calculations for 2003 (Göckede et al. 2008, before Kyrill) and for the IOPs in 2007 and 2008 (Siebicke 2008, after Kyrill) showed that although this significant wind-throw destroyed large forest areas in the further vicinity of the sensors, the contribution from the forest to the flux is in the range of 80–97% (main tower: nearly all of the data; turbulence tower: approx. 75% of the data) and is therefore even slightly larger than the contribution in 2003. This can be explained by the canopy height of a growing forest (2003: 19 m, 2008: 25 m, see Chap. 2), diminishing the average footprint extent. The differences between the footprints of the main tower and the turbulence tower can be attributed to the fact that the turbulence tower is slightly closer to the Köhlerloh clearing (showing larger contribution), and further from the Pflanzgarten clearing (showing less contribution). Twenty-five percent of the data at TT is still not exceeding 80% target contribution, but within a range of approximately 74–80%. All in all, we judged the contribution of the target area as sufficient for the calculation of long-term budgets and did not exclude data on the basis of footprint issues.

4.2.2.2 Meteorological Data

The meteorological data, comprised of the radiation balance (four components) and air temperature, has been used as input for the gap-filling routine, while additional measurements of the precipitation and weather code served for quality checks

(Table 4.1). After visual plausibility checks of the data, gaps have been filled (where possible) by linear regression from measurements at other heights or at the Waldstein–Pflanzgarten site.

4.2.2.3 Gap-Filling

As a last quality check, a multi-step error filter as used by Lüers et al. (2014) has been performed on the meteorological data, the mean CO_2 and H_2O densities as well as on the fluxes. Besides fixed thresholds, adjustable quantile and standard deviation filters have been applied in order to remove physically non-plausible outliers from the data. In addition to the quality checks mentioned earlier in this section, this procedure removed 2.4% of measured *NEE* and 1.3% evapotranspiration records. After all quality checks, and due to longer periods of sensor malfunction and power failures, remaining measured *NEE* (*ET*) in 2007 and 2010 were only 4.1% (4.0%) and 17.4% (17.5%), respectively (Table 4.2). Therefore, these 2 years have been discarded from further analysis. Available measured *NEE* (*ET*) for the remaining years range from 26.5% (26.6%) to 58.4% (56.2%).

Gap-filling of the *NEE* data was then performed with non-linear regression: The Lloyd–Taylor function (Lloyd and Taylor 1994) is used for night-time respiration with the air temperature as the explanatory variable and a Michaelis–Menten type function (Michaelis and Menten 1913) for day-time *NEE*, binned in temperature

Table 4.2 Percentages of observations available for the annual budgets of *NEE* and evapotranspiration after all quality checks (measured), percentages of data gapfilled with non-linear regression (nonlin reg, Ruppert et al. 2006) and percentages of data filled with the half-hourly ensemble average of all years (ens avg); *2007* and *2010* were discarded from further analysis due to low data coverage

	ET			*NEE*		
Year	measured (%)	nonlin regr (%)	ens avg (%)	measured (%)	nonlin regr (%)	ens avg (%)
2002	33.8	60.7	5.5	32.8	62.2	5.0
2003	51.1	47.1	1.8	49.0	50.0	1.0
2004	44.1	53.3	2.6	43.6	54.7	1.7
2005	43.5	55.6	0.9	39.4	60.6	0.1
2006	30.7	65.4	3.9	29.5	69.4	1.1
2007	*7.0*	*76.9*	*16.1*	*7.2*	*70.1*	*22.7*
2008	26.6	66.4	7.0	26.5	71.5	1.9
2009	45.2	50.7	4.0	45.5	53.0	1.6
2010	*17.5*	*71.2*	*11.3*	*17.4*	*76.6*	*6.0*
2011	33.3	42.8	23.9	33.5	55.9	10.5
2012	47.9	48.3	3.8	48.7	48.7	2.6
2013	36.8	52.4	10.8	37.7	53.1	9.2
2014	56.2	41.4	2.4	58.4	41.3	0.3

classes of 2 K width and using global radiation as the explanatory variable. The procedure is explained in detail by Ruppert et al. (2006), and they showed with a data set from 2003 that the explanatory variables used explain most of the variability of *NEE* at the Waldstein site.

Gaps in *ET* measurements have been filled with the help of Priestley–Taylor potential evaporation E_p (Priestley and Taylor 1972). Measured net radiation as well as air temperature was used to calculate E_p, with the ground heat flux being 5% of the net radiation (Rebmann et al. 2004). For gap-filling, E_p has been scaled to measured *ET* by linear regression.

Large gaps in the data in winter-time lead to an under-representation of training data for these conditions. Therefore, regressions have not been performed on an annual basis but for two periods only: 2002–2006 (measurements at the main tower) and 2008–2014 (measurements at the turbulence tower). Further adjustments include a temperature threshold for winter-time assimilation, preventing the occurrence of unrealistic carbon uptake during winter-time. Reasons for these adjustments, and their impact, are presented in Sect. 4.3.2.

After this procedure, some gaps were still left due to missing meteorological input data. Filling these gaps by mean diurnal variation as reviewed by, for example, Falge et al. (2001) seems to be not appropriate, as the gaps occur in larger blocks (due to instrument failures or power outages). An ensemble average annual cycle has therefore been calculated for 2002–2014 on half-hourly basis, and used to fill these gaps. A summary of data availability and gap-filling gives Table 4.2, and a detailed list on a monthly basis is in Appendix B of this book.

4.3 Results and Discussion

4.3.1 Energy Balance Closure of EC Measurements

The non-closure of the observed surface-energy balance introduces a systematic error to the long-term flux measurements (Foken 2008). We calculate the energy balance closure ratio *EBR* as the slope of the geometric mean regression of turbulent fluxes vs. available energy ($R_n - Q_G$, with $Q_G = 0.05 \cdot R_n$). The average closure for the whole period is 81.3 ± 5.2% (mean and standard deviation), while the *EBR* significantly changes from the first to the second period: *EBR* at the main tower (2002–2006) was 75.4 ± 1.9%, while *EBR* at the turbulence tower (2007–2014) increases to 84.9 ± 2.2%. A summary of annual *EBR* is given in Table 4.3, and exemplary scatterplots are displayed in Fig. 4.1. The energy balance closure for the period 1997–1999 was 72.6% (Aubinet et al. 2000), which is similar to the closure from 2002 to 2006. Recent hypotheses as to the reasons for the unclosed energy balance suggest that the missing flux is mainly attributed to the sensible heat flux (Charuchittipan et al. 2014, see Chap. 12). We therefore decided not to correct the latent heat flux (and *NEE*) for missing turbulent energy.

Table 4.3 Annual energy balance closure ratios *EBR* of eddy-covariance data

Tower	Year	*EBR* (slope)	Offset (W m^{-2})	R^2
MT	2002	0.724	8.3	0.74
	2003	0.753	4.0	0.90
	2004	0.762	3.5	0.87
	2005	0.774	6.6	0.90
	2006	0.755	6.9	0.90
		0.754 ± 0.019 (mean ± std)		
TT	2007	0.849	1.3	0.89
	2008	0.828	5.6	0.84
	2009	0.840	5.7	0.80
	2010	0.824	1.0	0.89
	2011	0.840	8.8	0.92
	2012	0.863	7.9	0.75
	2013	0.858	2.9	0.76
	2014	0.892	10.4	0.76
		0.849 ± 0.022 (mean ± std)		
	All	0.813 ± 0.052 (mean ± std)		

4.3.2 Adaptations of the Gap-Filling Method for NEE

With the given set-up, however, the long-term measurements face specific problems during winter-time: data availability is very low due to frequently steamed windows of the open-path gas analyser, and the heating of the sonic anemometer often failed to prevent icing of the sensor head. Moreover, the remaining winter-time data showed carbon uptake in many cases, which is at least not representative for winter-time, and most likely not true, as the respiration components might be subjected to advection, leaving the measured (Reynolds-) flux as an incomplete representation of *NEE*. Utilizing this data for the gap-filling routine (Sect. 4.2.2) would significantly underestimate winter-time respiration. The following adjustments have therefore been made:

Multi-annual parameterization In order to enlarge data coverage in winter-time, non-linear regressions have been performed only for the two periods with different sensor set-up (instead of a parameterization for each year): 2002–2006 and 2008–2014. In order to reduce scatter and to preserve the relative weight of the lower temperature regimes, the regression has been performed on the median of temperature classes (2 K width). All necessary equations and parameters are listed in Table 4.4

Temperature threshold Winter-time assimilation (November–April) is only accepted when the air temperature is above 6 °C. Otherwise, assimilation is set to zero and only parameterized ecosystem respiration is used. A similar method has been applied at a disturbed spruce forest site in the Bavarian Forest by Lindauer et al. (2014), who set *GPP* to zero from December to March, as *GPP* from measurements in this period are zero on average. This is not the

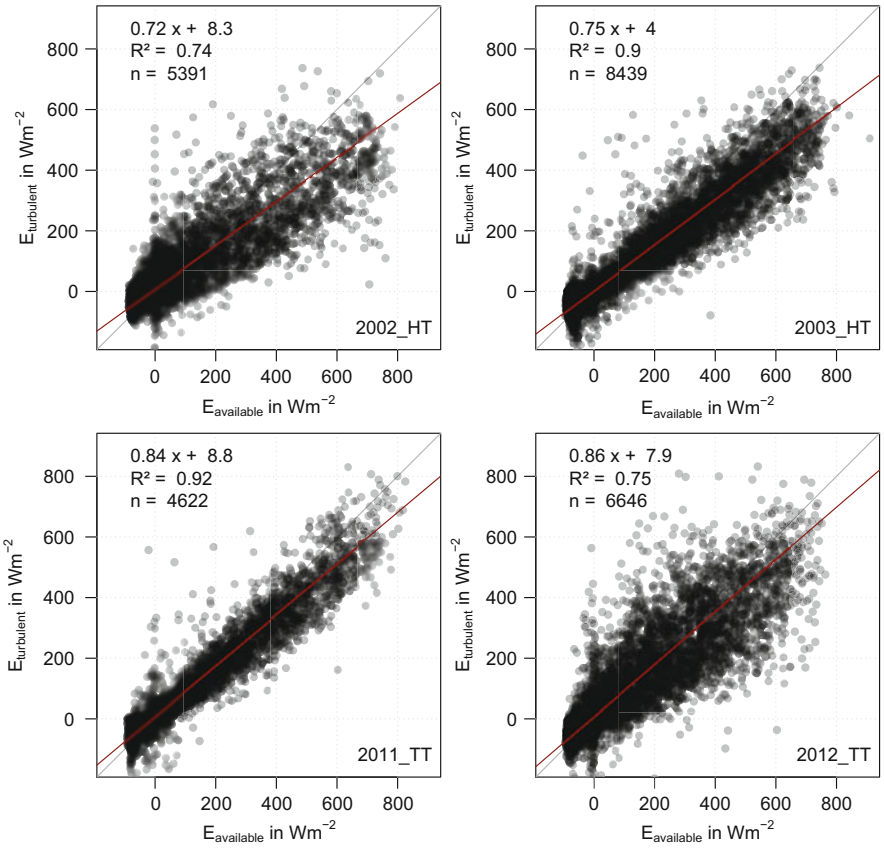

Fig. 4.1 Energy balance closure ratio from available energy ($R_n - Q_G$) vs. turbulent fluxes for 2002/2003 at main tower and 2011/2012 at turbulence tower

case here, as the rare measurements with the open-path gas analyser show, on average, assimilation for November–April. However, these measurements are only available under dry, clear-sky conditions, which are not representative of average winter-time conditions. Excluding these data diminishes annual net carbon uptake ($-NEE$) by $74 \pm 50\,\mathrm{g\,C\,m^{-2}\,a^{-1}}$, on average, in the period 2002–2014.

4.3.3 Carbon and Water Vapour Fluxes

The ecosystem fluxes of net ecosystem exchange *NEE*, gross primary production *GPP* and ecosystem respiration R_{eco} as well as evapotranspiration *ET* and potential evaporation E_p for the calculated period from 2002 up to 2014, as well as the results by Rebmann et al. (2004) from 1997 to 2001, are summarized as annual budgets

Table 4.4 Parameterization of the non-linear regression functions for gap-filling of *NEE* and latent heat Q_E, upper part: Michaelis–Menten type function (Michaelis and Menten 1913) for daytime *NEE*; middle part: Lloyd–Taylor function (Lloyd and Taylor 1994) for ecosystem respiration R_{eco}; lower part: coefficient for Priestley–Taylor function (Priestley and Taylor 1972); grey values displayed in italic type were discarded from the analysis due to low data coverage

Michaelis–Menten: $NEE_{day} = \frac{a \cdot R_G \cdot F_{C,sat}}{a \cdot R_G + F_{C,sat}} + R_{eco,day}$ with global radiation R_G as predictor						
	2002–2006			*2007–2014*		
t_{air} class (°C)	$R_{eco,day}$ ($\mu mol\ m^{-2}\ s^{-1}$)	$F_{C,sat}$ ($\mu mol\ m^{-2}\ s^{-1}$)	a ($\mu mol\ J^{-1}$)	$R_{eco,day}$ ($\mu mol\ m^{-2}\ s^{-1}$)	$F_{C,sat}$ ($\mu mol\ m^{-2}\ s^{-1}$)	a ($\mu mol\ J^{-1}$)
0	1.18	−8.5	−0.085	4.99	−12.7	−0.919
2	1.69	−10.4	−0.130	0.48	−12.6	−0.152
4	2.84	−17.0	−0.125	0.74	−16.8	−0.110
6	3.08	−22.4	−0.099	2.15	−23.5	−0.108
8	3.18	−25.6	−0.094	3.32	−25.2	−0.151
10	4.13	−27.5	−0.099	3.10	−29.2	−0.117
12	4.60	−27.8	−0.100	4.36	−30.1	−0.125
14	5.10	−31.9	−0.086	5.01	−29.0	−0.131
16	5.75	−27.4	−0.100	5.93	−31.1	−0.106
18	5.21	−25.5	−0.086	6.10	−29.4	−0.099
20	5.28	−24.5	−0.069	8.42	−29.0	−0.117
22	5.21	−22.4	−0.052	5.91	−28.9	−0.058
24	4.28	−20.3	−0.033	10.48	−26.5	−0.097
26	2.23	−21.8	−0.015	9.09	−32.1	−0.047
Lloyd–Taylor: $R_{eco} = F_{R,10} \cdot \exp\left(E_0 \cdot \left[(283.15\,K - T_0)^{-1} - (T_{air} - T_0)^{-1}\right]\right)$						
	2002–2006			*2007–2014*		
	$F_{R,10}$ ($\mu mol\ m^{-2}\ s^{-1}$)	E_0 (K)	T_0 (K)	$F_{R,10}$ ($\mu mol\ m^{-2}\ s^{-1}$)	E_0 (K)	T_0 (K)
	2.973	282.3	227.13[a]	3.004	285.4	227.13[a]
Priestley–Taylor: $Q_E = \alpha \cdot Q_{E,p} = \alpha \cdot \alpha_{PT} \cdot \frac{s_c \cdot (R_n - Q_G)}{s_c + \gamma}$, $s_c = \frac{dq_s}{dT}$, $\gamma = \frac{c_p}{\lambda}$, $\alpha_{PT} = 1.25$						
	2002–2006: $\alpha = 0.396$			*2007–2014*: $\alpha = 0.481$		

[a]Not optimized, but original value taken as done in Ruppert et al. (2006)

in Table 4.5. We analyse these fluxes in more detail in the next sections. Monthly budgets were provided in Appendix B. In the following the data is partly analysed in its whole length, but due to changes in instrument set-up (Table 4.1) and availability of measurements (Table 4.2), three periods were discriminated as well:

1997–2001 MT, Gill R2, LiCor Li6262, data analysis: Rebmann et al. (2004).
2002–2006 MT, Gill R2/R3, LiCor Li7500, data analysis: this chapter.
2008–2014 TT, Metek USA1, LiCor Li7500, data analysis: this chapter.

Table 4.5 Annual budgets of net ecosystem exchange *NEE*, gross primary production *GPP* and ecosystem respiration R_{eco} as well as evapotranspiration *ET* and potential evaporation E_p (Priestley and Taylor 1972); italic values were discarded from the analysis due to low data coverage

Year	*NEE* ($g\,C\,m^{-2}\,a^{-1}$)	*GPP* ($g\,C\,m^{-2}\,a^{-1}$)	R_{eco} ($g\,C\,m^{-2}\,a^{-1}$)	*ET* (mm)	E_p (mm)
1997	−55	−1257	1203	301	–
1998	−41	−1265	1224	299	–
1999	−35	−1314	1279	321	–
2000	−146	−1947	1802	254	–
2001	−24	−1663	1639	211	–
2002	−238	−1271	1033	352	774
2003	−288	−1356	1068	413	946
2004	−377	−1337	960	415	794
2005	−354	−1333	979	412	808
2006	−301	−1329	1027	407	878
2007	*−497*	*−1544*	*1047*	*443*	897
2008	−492	−1510	1018	435	851
2009	−491	−1563	1072	491	852
2010	*−443*	*−1378*	*935*	*408*	771
2011	−608	−1659	1051	488	835
2012	−652	−1726	1075	570	697
2013	−508	−1605	1097	497	757
2014	−692	−1842	1150	562	780

4.3.3.1 Carbon Exchange

The annual sums of *NEE* show a net uptake of carbon throughout the whole time series and a clear trend towards larger uptake (Table 4.5, Fig. 4.2). The three periods differ significantly from each other in both flux magnitudes and variance: 1997–2001 shows low values and variation with $40 \pm 12\,g\,C\,m^{-2}\,a^{-1}$ on average, except for the year 2000 with an uptake of $146\,g\,C\,m^{-2}\,a^{-1}$. The net carbon sink in 2002–2006 ranges from 238 to $377\,g\,C\,m^{-2}\,a^{-1}$, and finally reaches a range of 491–$692\,g\,C\,m^{-2}\,a^{-1}$ in 2008–2014. The highest uptakes were observed for 2011–2014, with $615 \pm 79\,g\,C\,m^{-2}\,a^{-1}$ on average. In comparison with a mean biome flux of $398 \pm 42\,g\,C\,m^{-2}\,a^{-1}$ for evergreen humid temperate forests from a global database (Luyssaert et al. 2007), our numbers seem to be in the same range on average, but low for 1997–2001 and very high in 2008–2014. Nevertheless, all values are within the range for temperate forest sites shown by Luyssaert et al. (2010).

While the trend is significant over the whole period and specifically for 2002–2014 (Mann–Kendall trend test, $p < 0.05$), it is reflected in the latter two sub-periods, but is not significant for 2002–2006 ($p = 0.46$) and is only a tendency for 2008–2014 ($p = 0.13$). This implies a superposition of a real trend and site-specific effects related to the sub-periods, which will be discussed later. The flux partitioning estimates suggest that this increase in carbon uptake can be mainly attributed to an

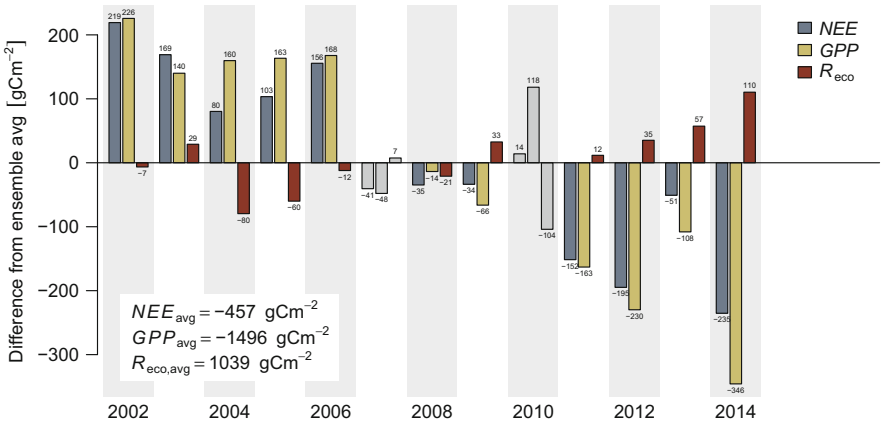

Fig. 4.2 Annual sums of carbon flux components, displayed as absolute deviations from the ensemble average for the whole period; positive values for *NEE* (*GPP*) indicate less net (gross) uptake than on average, positive R_{eco} indicate higher respiration than on average

enhancement in *GPP*, while R_{eco} is increasing as well but to a lesser extent than does *GPP*: a linear regression of R_{eco} vs. *GPP* gives a slope of 0.21, indicating that a rising *GPP* causes an increase in *NEE* by 79% of this growth, while only 21% is consumed by R_{eco} (Fig. 4.3). The coherence between *GPP* and R_{eco} seems to be robust, and is reasonable in an ecophysiological sense as observed for many sites (Fernández-Martínez et al. 2014; Kutsch and Kolari 2015), although to some extent this coherence must be attributed to a spurious correlation resulting from the calculation for $GPP = NEE - R_{eco}$ as a balance residual, see Vickers et al. (2009) and the follow-up discussion (Lasslop et al. 2010; Vickers et al. 2010).

These changes in *NEE*, *GPP* and R_{eco} are reflected in the seasonal patterns as presented in cumulative time series and monthly sums (Fig. 4.4). The ensemble average *NEE* shows net respiration during winter-time from the beginning of November until mid-March, while net uptake takes place in the other months. All years are similar in the winter-time respiration, but the latter periods 2002–2006 and 2008–2014 exhibit subsequently stronger uptake from April to October, especially June, July and August for 2008–2014. The extraordinarily large carbon uptake in 2011, 2012 and 2014 are mainly characterized by an earlier change from net respiration to uptake in March and even stronger uptake from July to October. The time of maximum net uptake shifts from May (1997–2001) to June (2008–2014). Such a shift is reflected in *GPP* (maximum gross uptake in 2002–2006 mainly in June to mainly in July for the period 2008–2014) as well as in R_{eco} (maximum respiration from mainly July to July/August).

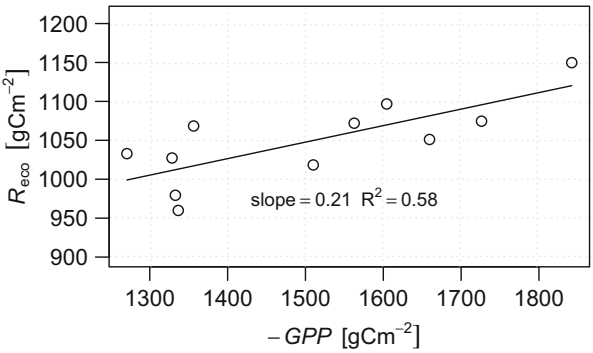

Fig. 4.3 Annual R_{eco} vs. $-GPP$

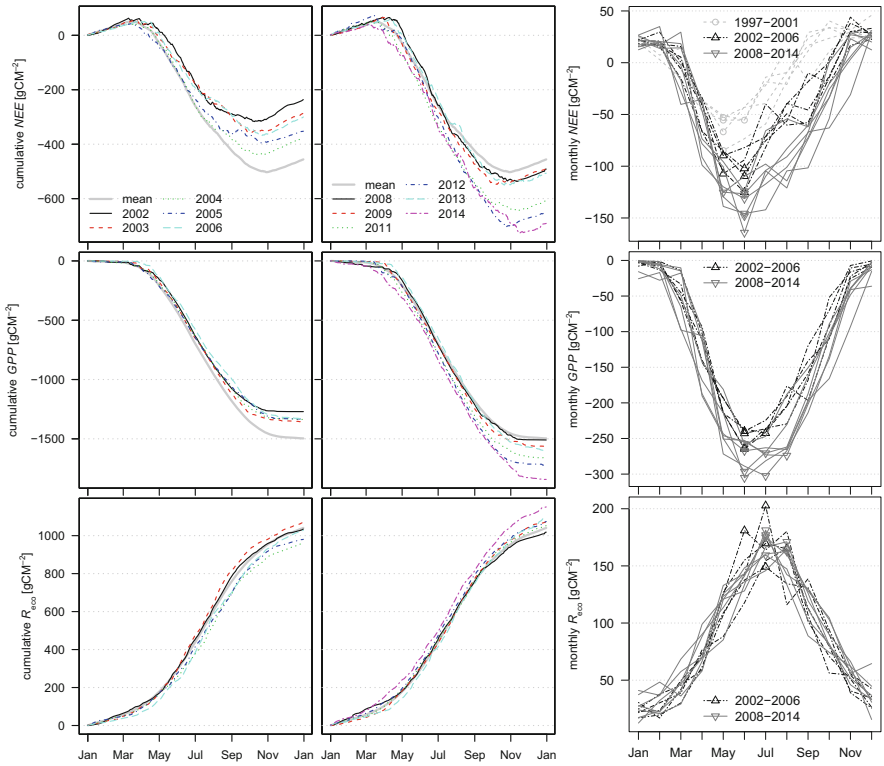

Fig. 4.4 Seasonal carbon exchange at Waldstein–Weidenbrunnen, *left panels*: Cumulative sums of daily net ecosystem exchange *NEE*, gross primary production *GPP* and ecosystem respiration R_{eco} for the period 2002–2006 (*left*) and 2008–2014 (*middle*); the *thick grey line* shows the cumulative sum of the ensemble average for the whole period 2002–2014. *Right panel*: Monthly sums of *NEE*, *GPP* and R_{eco} for 1997–2001 (*light grey*), 2002–2006 (*black*) and 2008–2014 (*darkgrey*); the symbols represent the month with the highest uptake/respiration within the respective year

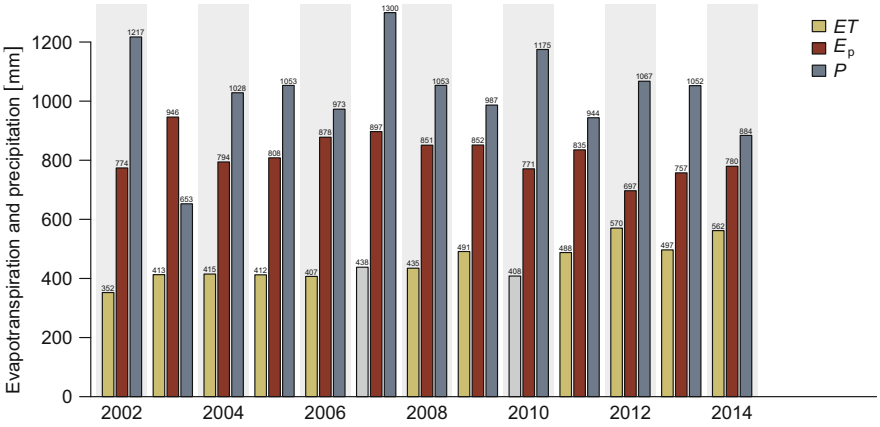

Fig. 4.5 Annual sums of *ET*, E_p and precipitation *P*

4.3.3.2 Water Vapour Fluxes

The annual sums of *ET* show a distinct increase for the whole time series (Table 4.5, Fig. 4.5), with values ranging from 211 to 301 mm a^{-1} (1997–2001), from 352 to 415 mm a^{-1} (2002–2006) and from 435 to 570 mm a^{-1} (2008–2014). The average fluxes increase from 277 ± 44 mm a^{-1} for 1997–2001 to 493 ± 60 mm a^{-1} for 2008–2014. Similar to *NEE*, the trend is significant for the whole period, with no trend visible for 2002–2006 and a tendency apparent for 2008–2014 ($p = 0.13$). Thus the patterns for annual *ET* and *NEE* for all years are consistent, with high correlation ($R^2 = 0.9$). Such increase, however, is not reflected in the potential evaporation E_p, nor in precipitation, which both show variability but no trend, suggesting that *ET* is (still) not strongly limited by these factors.

Budyko (1974) provides an appropriate framework to examine relationships between *ET*, E_p and precipitation with non-dimensional numbers: evaporative index (*ET*, normalized with precipitation) vs. dryness index (E_p, normalized with precipitation). In Fig. 4.6, dashed straight lines denote the supply limit ($ET = P$) and the demand or energy limit ($ET = E_p$). Within this framework, annual values at the Waldstein site suggest not only a trend towards the energy limit (driven by the *ET* trend, while E_p shows no trend), but also a large variability (caused mainly by the variability in *P*, which is not reflected by *ET* or E_p). Although a trend to drier spring seasons has been detected (see Chap. 3), annual *ET* is still not limited by precipitation. Williams et al. (2012) conducted such an analysis for a global set of flux stations. We compared our values with a corresponding subset of numbers from warm-temperate evergreen coniferous forest sites and found a similar range, and the inter-annual variability at the Waldstein site also nearly covers the variation of the station subset chosen from Williams et al. (2012).

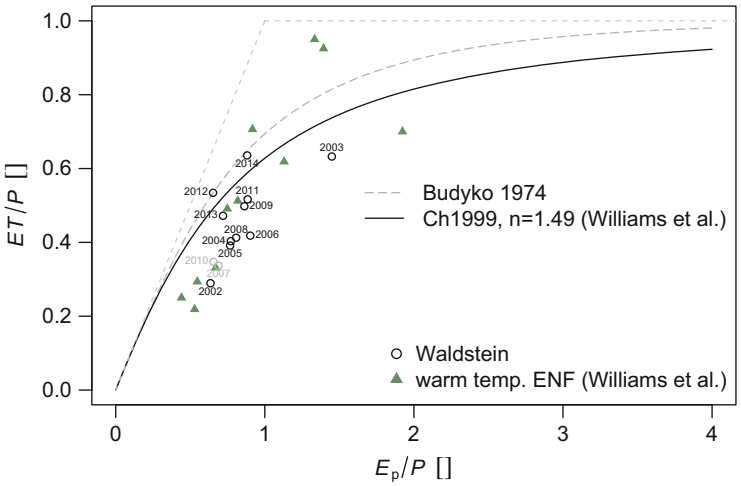

Fig. 4.6 Annual potential evaporation, normalized with annual precipitation vs. normalized evapotranspiration according to the Budyko framework. The *grey dashed line* is the original parameterizations according to Budyko (1974), the *red line* according to Choudhury (1999) with an exponent $n = 1$ and the *black line* also according to Choudhury (1999), but with an exponent $n = 1.49$ as proposed for the sites examined by Williams et al. (2012) (Adapted and completed with kind permission of © John Wiley and Sons 2012, All rights reserved)

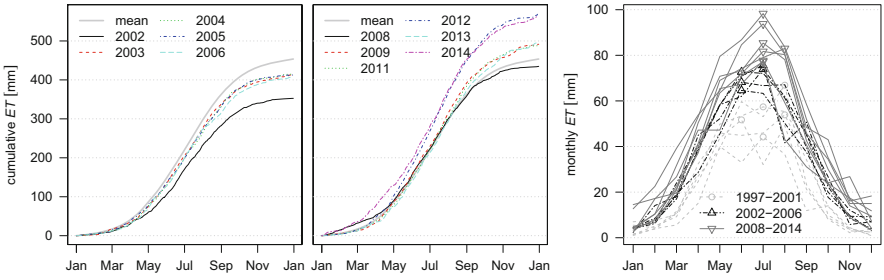

Fig. 4.7 Seasonal water vapour exchange at Waldstein–Weidenbrunnen, *left panels*: Cumulative sums of daily evapotranspiration *ET* for the period 2002–2006 (*left*) and 2008–2014 (*middle*); the *thick grey line* shows the cumulative sum of the ensemble average for the whole period 2002–2014. *Right panel*: Monthly sums of *ET* for 1997–2001 (*light grey*), 2002–2006 (*black*) and 2008–2014 (*darkgrey*); the symbols represent the month with the highest *ET* within the respective year

The inter-annual seasonal variations of *ET* follow the patterns found for *NEE* (Fig. 4.7): a subsequent increase of *ET* from April to October, and only minor changes in winter-time. For *ET*, only 2012 and 2014 were extraordinarily large.

4.3.4 *Factors Influencing the Carbon and Water Vapour Exchange*

In Sect. 4.3.3 we showed remarkable trends of carbon and water vapour exchange with a large range in flux magnitude. There are many possible reasons, which may be attributed either to a gradual shift, or to step changes after breakpoints. Some of them, like instrument set-up and location, are rather local effects, and variations due to these factors are not related to the flux variability of the ecosystem that we wish to characterize and therefore add to the uncertainty of the measurements. The history of the forest's state is site-specific as well, but is certainly relevant for the ecosystem flux. Other factors may have regional to global implication, as, for example, climate change.

4.3.4.1 Development of the Spruce Forest at Waldstein Site

The Norway spruce forest at the Waldstein site has undergone tremendous changes, partly described in Chap. 2, with obvious implications for ecosystem performance. The most important steps are:

- forest visibly suffering from forest decline, with nearly no growth and only slight increase in canopy height from 17.8 m (1995) up to 19 m (2003).
- reconvalescence after a liming application in 2001: re-greening of needles observed and increase in canopy height up to 25 m (2008) and 28 m (2011).
- Increase in heterogeneity of the forest after the wind-throw in 2007 due to the storm "Kyrill", with a clearing south of the site and a reduced tree density west of the site (see Chap. 7), although the percentage of forest in the footprint estimates were not changed significantly. The trees from the blowdown have been removed.

It is obvious that regeneration is accompanied by a large carbon uptake as well as enhanced *ET*. The latter is in agreement with findings in sap-flow measurements (see Chap. 5). Their measurements show that both stand-scale sapwood area and sap flow increased at the Waldstein site, which might be attributed to the effect of liming. The sap-flow measurements made in 1995 at the Waldstein–Weidenbrunnen and five other sites in the area (Alsheimer et al. 1998) always had fluxes below 3 mm d^{-1}, while the measurements in 2007 and 2008 (Chap. 5) also had fluxes larger than 3 mm d^{-1}. The implications of heterogeneity are discussed in a broader perspective in Chap. 19.

4.3.4.2 Instrumental and Methodological Issues

The annual trends of *NEE* and *ET* show distinct jumps in magnitude between the periods 1997–2001, 2002–2006 and 2008–2014. The breakpoints coincide with a change in measurement set-up as summarized at the beginning of Sect. 4.3.3. A potential problem related to the low fluxes in 1997–2001 might arise from the 12-bit

digitalization done within the Li6262 in contrast to the 16-bit digitalization within the Li7500. Such digitalization problems also existed for the Gill R2 and R3 sonic anemometer up to 2003 (Foken et al. 2004).

Furthermore, we investigated the impact of the change from R3 to the Metek USA1 sonic anemometer through a comparison of the integral turbulence characteristics for the vertical wind velocity $\sigma_w u_*^{-1}$, as its stability dependence is quite weak in the near-neutral range (Thomas and Foken 2002). Monthly averaged values (March–October, 2002–2014) yield an average $\sigma_w u_*^{-1} = 1.32 \pm 0.026$ for 2002–2006 (R2/R3) and 1.20 ± 0.026 for 2008–2014 (USA1). A larger number indicates a lower momentum flux for the same observed variance σ_w^2 and therefore a possible underestimation of fluxes with the R2/R3. Or, from another perspective, a larger fraction of the variance in R2/R3 observation must be attributed to random noise, which does not contribute to the momentum flux (which likely has an impact on $\overline{w'q'}$ and $\overline{w'c'}$ as well). An exemplary time series is shown for R3, June 2006 and USA1, June 2008 (Fig. 4.8). There is no remarkable difference between R2 and R3 or between the USA1 at the Main Tower and the USA1 at the Turbulence Tower (not shown). The latter indicates that the move of the instrumentation to the Turbulence Tower in 2007 has, at least, no effect with respect to flow distortion by tower elements. On the other hand, the energy imbalance decreased since measurements have been performed on the turbulence tower (Sect. 4.3.1). This suggests that the increase in fluxes is only weakly connected to differences in the sonic anemometer, but might be related to the increased heterogeneity since 2007, which is discussed in Chap. 19.

Another problem arises from the methodological differences between the calculation and gap-filling of the fluxes for 1997–2001 (Rebmann 2004; Rebmann et al.

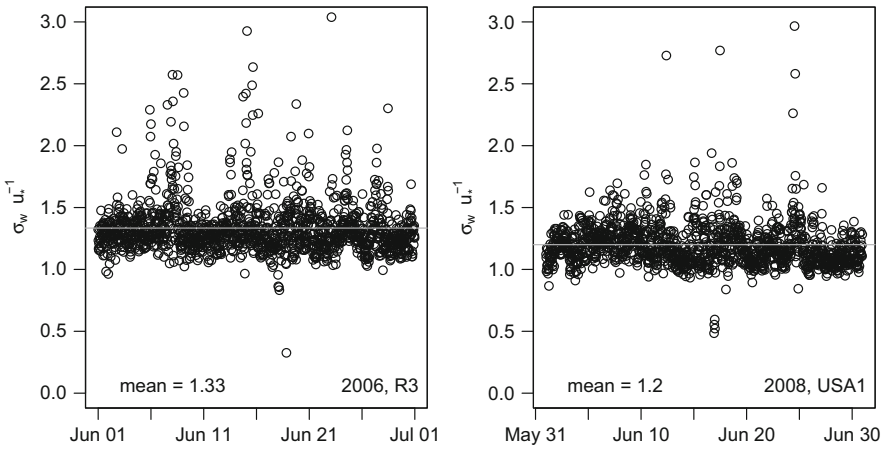

Fig. 4.8 Integral turbulence characteristics for vertical wind velocity $\sigma_w u_*^{-1}$ from ultrasonic anemometer measurements, *left*: June 2006, Main Tower, Gill solent R3; *right*: June 2008, Main Tower, Metek USA1

2004) and the procedure conducted in this chapter. In flux quality assessment, for instance, Rebmann et al. (2004) used the u_*-criterion, while in this chapter the integral turbulence characteristics were utilized. Although similar equations have been used for flux partitioning, parameterization differs in the selection of data subsets for individual regressions. We therefore compared both methods with the data of 2002 (very large fraction of parameterized fluxes, see Appendix B), yielding $NEE = -238\,\mathrm{g\,C\,m^{-2}\,a^{-1}}$ for the methods used here and $NEE = -326\,\mathrm{g\,C\,m^{-2}\,a^{-1}}$ with the methods by Rebmann et al. (2004). While this difference is surely not negligible, it shows that the distinct jump in flux magnitude is reproduced and therefore not a matter of methodological differences. Flux partitioning, however, is affected much more, with differences of $490\,\mathrm{g\,C\,m^{-2}\,a^{-1}}$ for ecosystem respiration. This can be partly explained with a potential overestimation of night-time respiration (and therefore also extrapolated day-time respiration) due to the usage of the u_*-criterion (see Chap. 12), and underlines the huge variability among different approaches.

Although different locations and instrumentations may be one reason for the behaviour of the fluxes in the three periods, modelling approaches in 1998, 2003, 2007, 2008 and 2011 with the ACASA model (see Chap. 16) show similar results of comparisons, at least for day-time data of *NEE* between modelled and measured fluxes in all years. This suggests that the fluxes were reasonable and the differences, attributed either to changes in forest structure or climate, can be reproduced with a process-based model. Also R_{eco} seems to be realistic, as Rebmann et al. (2004) compared the respiration measured using the eddy-covariance method with the sum of the soil efflux (chamber measurements, Subke and Tenhunen 2004) and the modelled wood and foliage respiration for the years 1997–1999, and found good agreement.

4.3.4.3 Influential Factors of Regional Relevance

Another reason for the trends found that has regional relevance is, of course, climate change. It is shown in Chap. 3 that the site is affected by climate change, mainly through an increase of the temperature in all months and drought periods occurring mainly in spring, while the annual precipitation sum is nearly constant. We have observed the largest increase in fluxes in summer, where no significant trend in precipitation could be found. It is reasonable to assume that higher temperatures in summer could increase carbon uptake in this well-watered region, where the mean temperature for the period 1971–2000 is 5.3 °C. On the other hand, the parameterization coefficient α, which we used to scale E_{p} to *ET* in order to gap-fill the measured *ET* series, was 0.396 for 2002–2006 and 0.481 for 2007–2014. This, together with the fact that E_{p} shows no trend (which is also true for summer only), suggests that the increase in *ET* seems to be unrelated to environmental conditions.

Keenan et al. (2013) attribute an observed positive trend of *NEE* to an increasing carbon dioxide concentration. They were able to show an increase in water use efficiency as leaf intercellular CO_2 concentrations rise, which may cause a higher carbon uptake. The authors showed a significant increase of *NEE* for five North

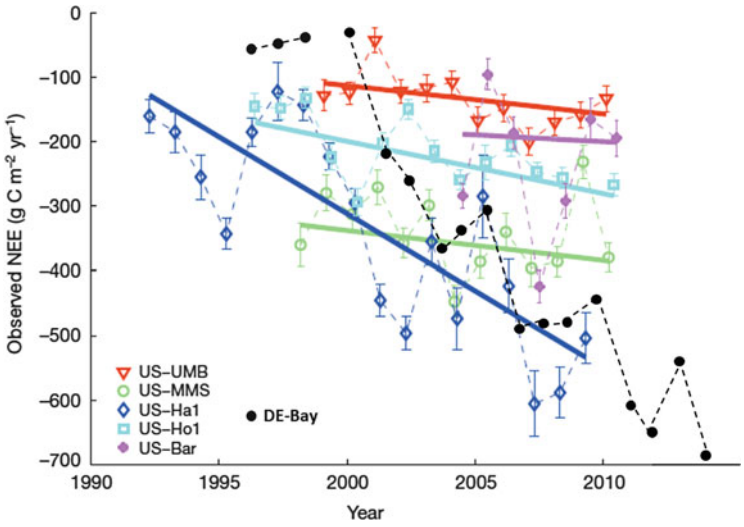

Fig. 4.9 Long-term increase in net ecosystem exchange *NEE* at five natural forest sites in the north-eastern USA according to Keenan et al. (2013) and at the Waldstein–Weidenbrunnen site (DE-Bay). Remark: only the station (US-Ho1, Howland Forest) is an evergreen coniferous forest, the others are deciduous broad-leaf forests (Published with kind permission of © Nature Publishing Group 2013, All rights reserved)

American stations, and the Waldstein–Weidenbrunnen data also fits with their data (Fig. 4.9). Therefore, an increase of the atmospheric carbon dioxide concentration at Waldstein–Weidenbrunnen from 360 to 400 ppm (1997–2015) could potentially contribute to rising fluxes. We assume that the growth at Waldstein–Weidenbrunnen is not limited by nitrogen availability, as this was the case at the beginning of the time series (Matzner 2004), and atmospheric concentrations decreased only slightly (see Chap. 3). We calculated the ecosystem-scale water use efficiency $WUE = GPP/ET$, using only data from April to September, using only measured *ET* (and *GPP* was inferred from measured *NEE* only), and rainy days as well as the days after were excluded to ensure that measured *ET* mainly accounts for transpiration. *WUE* for 2002–2014, however, ranges from 3.5 to 4.2 g C $(\text{kg H}_2\text{O})^{-1}$ with no visible trend, and even a vague decreasing tendency. Similar to the method used by Keenan et al. (2013), we also calculated the inherent water use efficiency by multiplying *WUE* with E_p in order to eliminate the influence of atmospheric demand, but this does not change the situation. This means that reasons other than rising CO_2 levels play an important role.

A very conservative parameter is the carbon use efficiency (*CUE*)—the ratio of net ecosystem exchange and gross primary production. Kutsch and Kolari (2015) made a re-analysis of the investigations by Fernández-Martínez et al. (2014) and found that nutrient availability has some influence on *CUE* (not as large as postulated by Fernández-Martínez et al. 2014), and a strong dependence on the heterogeneity (in altitude) of the area in the vicinity of the station. They further

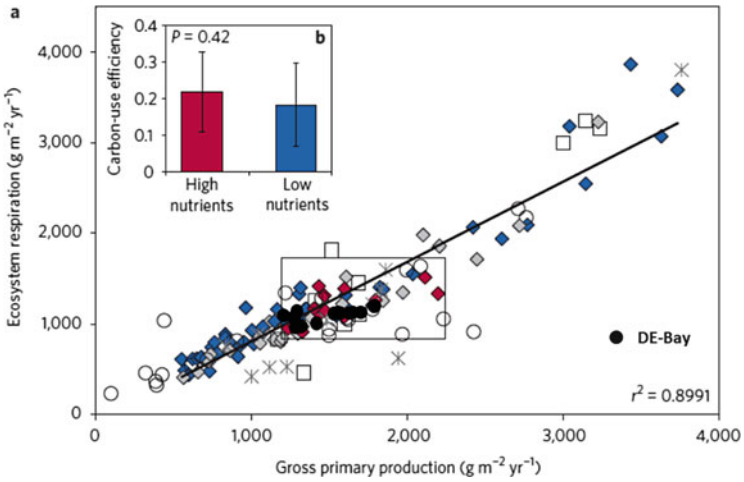

Fig. 4.10 Ecosystem respiration R_{eco} plotted vs. *GPP* for the remaining 82 sites according to Kutsch and Kolari (2015) and for the Waldstein–Weidenbrunnen site (DE-Bay). (**a**) *Red*: sites with high nutrient availability. *Blue*: sites with low nutrient availability. *Grey*: sites with medium nutrient availability. *Open squares*: sites removed owing to bad data quality and unclosed carbon balance that could not be corrected. *Open circles*: removed sites younger than 15 years. *Grey stars*: removed sites with complex terrain. (**b**) Average CUE for sites with low and high nutrient availability with a *GPP* between 1200 and 2300 g C m^{-2} a^{-1} (Published with kind permission of © Nature Publishing Group 2015, All rights reserved)

conclude that a reasonable range of *CUE* is between 0 and 0.3 and a strong relationship exists between *GPP* and R_{eco}. In Fig. 4.10 we add the Waldstein–Weidenbrunnen data to the figure of R_{eco} vs. *GPP* by Kutsch and Kolari (2015). The data from 2002 to 2006 fit well in the relationship found by Kutsch and Kolari (2015), and the data from 2008 to 2014 are still within the observed range, and closer to the data from sites which are rich in nutrients. *CUE* increases significantly at the Waldstein site, with $CUE = 0.23 \pm 0.04$ (2002–2006) and $CUE = 0.34 \pm 0.03$ (2008–2014). This implies that an increase of the heterogeneity in 2007 caused by the wind-throw, and perhaps subsequently enhanced nutrient availability could be responsible for the rising *NEE* and *CUE* at the Waldstein site.

4.4 Conclusion

A long-term data set of eddy-covariance measurements of carbon dioxide and water vapour exchange has been compiled for the Waldstein–Weidenbrunnen site (DE-Bay). While measurements from 1997 to 2001 have already been published, we analysed the years from 2002 until 2014 in a uniform manner with respect to data selection and quality control, processing and gap-filling. Within the latter, gross

primary production *GPP* as well as ecosystem respiration R_{eco} has been estimated with standard flux partitioning algorithms.

The Waldstein–Weidenbrunnen site was a carbon sink in all years, while magnitude and variance of net uptake (−*NEE*) increased significantly from values around 40 g C m^{-2} a^{-1} for 1997–1999 up to 615 ± 79 g C m^{-2} a^{-1} for 2011–2014. This is related to a strong increase in *GPP*, while R_{eco} is slightly enhanced. Evapotranspiration *ET* follows the *NEE* trend coherently, with average fluxes ranging from 277 ± 44 mm a^{-1} (1997–2001) up to 493 ± 60 mm a^{-1} (2008–2014), while atmospheric demand does not drive the change.

We discussed various potential drivers for this development, namely instrumentation issues, forest stand history and climate change. Instrumental and methodological problems seem to play a minor role and could not explain the huge flux variability. Climate variability and change do indeed play a role at the site, as warming and rising CO_2-concentrations are consistent with the observed trend. The effects, however, cannot be disentangled from site-specific changes such as the recovery from forest decline after liming and an increase in heterogeneity after a wind-throw, as well as structural change within the under-storey, which are likely primarily responsible for the harsh changes in the observed dynamics. This attempt has been made here using only the flux data as the information source, with a more general discussion given in Chap. 19. Although "know thy site" is already a commonplace aphorism regarding long-term flux stations, there is a more general problem behind it, as a transition from an "ideal" to a disturbed or heterogeneous site is surely not a singular occurrence and therefore a systematic bias in regional studies using multiple sites is likely.

The presented data set suffers from problems in the measurements, creating large and systematic gaps in the winter-time and raising the need for assumptions about a temperature threshold for winter-time assimilation, which cannot be proved with the current data set. The uncertainty in *NEE* measurements therefore by far exceeds the 50 g C m^{-2} a^{-1} error proposed by Baldocchi (2003) for ideal sites. Nevertheless, the visible variation and trends should be robust due to consistent data processing, and the comparisons with other sites show that our estimates are realistic.

The Waldstein–Weidenbrunnen site has been intensively studied for a long time and large, detailed data sets exist from intensive observation campaigns. A long-term flux data set as presented in this chapter offers the opportunity to put these experiments in a temporal context and therefore create a better connection among those campaigns. The data set provides a comprehensive basis for water balance studies (see Chap. 15). Despite the trend found in the series there is a high inter-annual variability in the fluxes of *NEE* and *ET*, presumably following climatic drivers, which should be investigated in more detail. Seasonal trends of precipitation as detected in Chap. 3, however, do not influence the annual *ET* budgets. Furthermore, model studies can be deployed with varying climate and stand structure to quantify the influence of the different drivers at the Waldstein site. Such investigations could bring more generality into a case study at a unique location, having a special history.

Acknowledgements The operation of the site was funded by The Federal Ministry of Education, Science, Research and Technology (PT BEO-0339476 B, C, D), the European Community (EUROFLUX), the German Science Foundation (FO 226/16-1, FO 226/22-1) and the Oberfranken Foundation (contract 01879). This work was only possible with the enthusiasm and hard work, sometimes under harsh weather conditions, of so many technicians, students, PhD candidates and motivated scientists.

References

Alsheimer M, Köstner B, Falge E, Tenhunen JD (1998) Temporal and spatial variation in transpiration of Norway spruce stands within a forested catchment of the Fichtelgebirge, Germany. Ann Sci 55(1–2):103–123. doi:10.1051/forest:19980107

Aubinet M, Grelle A, Ibrom A, Rannik U, Moncrieff J, Foken T, Kowalski A, Martin P, Berbigier P, Bernhofer C, Clement R, Elbers J, Granier A, Grünwald T, Morgenstern K, Pilegaard K, Rebmann C, Snijders W, Valentini R, Vesala T (2000) Estimates of the annual net carbon and water exchange of forests: the EUROFLUX methodology. In: Advances in ecological research, vol 30. Academic, New York, pp 113–175. doi:dx.doi.org/10.1016/S0065–2504(08)60018–5

Aubinet M, Clement R, Elbers J, Foken T, Grelle A, Ibrom A, Moncrieff J, Pilegaard K, Rannik U, Rebmann C (2003) Methodology for data acquisition, storage, and treatment. In: Valentini R (ed) Fluxes of carbon, water and energy of European forests. Ecological studies, chap 2, vol 163. Springer, Berlin, Heidelberg, pp 9–35. doi:10.1007/978-3-662-05171-9_2

Aubinet M, Feigenwinter C, Heinesch B, Bernhofer C, Canepa E, Lindroth A, Montagnani L, Rebmann C, Sedlak P, Gorsel EV (2010) Direct advection measurements do not help to solve the night-time {CO2} closure problem: evidence from three different forests. Agric For Meteorol 150(5):655–664. doi:10.1016/j.agrformet.2010.01.016. Special issue on advection: {ADVEX} and other direct advection measurement campaigns

Baldocchi D (2003) Assessing the eddy covariance technique for evaluating carbon dioxide exchange rates of ecosystems: past, present and future. Glob Chang Biol 9(4):479–492. doi:10.1046/j.1365-2486.2003.00629.x

Baldocchi D, Falge E, Gu L, Olson R, Hollinger D, Running S, Anthoni P, Bernhofer C, Davis K, Evans R, Fuentes J, Goldstein A, Katul G, Law B, Lee X, Malhi Y, Meyers T, Munger W, Oechel W, Paw U KT, Pilegaard K, Schmid HP, Valentini R, Verma S, Vesala T, Wilson K, Wofsy S (2001) Fluxnet: a new tool to study the temporal and spatial variability of ecosystem-scale carbon dioxide, water vapor, and energy flux densities. Bull Am Meteorol Soc 82(11):2415–2434. doi:10.1175/1520-0477(2001)082<2415:FANTTS>2.3.CO;2

Bernhofer C, Aubinet M, Clement R, Grelle A, Grünwald T, Ibrom A, Jarvis PG, Rebmann C, Schulze ED, Tenhunen J (2003) Spruce forests (Norway and sitka spruce, including douglas fir): carbon and water fluxes and balances, eco-logical and ecophysiological determinants. In: Valentini R (ed) Fluxes of carbon, water and energy of European forests, ecological studies, chap 6, vol 163. Springer, Berlin, Heidelberg, pp 99–123

Bonan GB, Lawrence PJ, Oleson KW, Levis S, Jung M, Reichstein M, Lawrence DM, Swenson SC (2011) Improving canopy processes in the community land model version 4 (clm4) using global flux fields empirically inferred from fluxnet data. J Geophys Res 116(G2):G02,014. doi:10.1029/2010JG001593

Budyko M (1974) Climate and life. Academic, New York

Charuchittipan D, Babel W, Mauder M, Leps JP, Foken T (2014) Extension of the averaging time in eddy-covariance measurements and its effect on the energy balance closure. Bound-Layer Meteorol 152(3):303–327. doi:10.1007/s10546-014-9922-6

Choudhury B (1999) Evaluation of an empirical equation for annual evaporation using field observations and results from a biophysical model. J Hydrol 216(1–2):99–110. doi:10.1016/S0022-1694(98)00293-5

Falge E, Baldocchi D, Olson R, Anthoni P, Aubinet M, Bernhofer C, Burba G, Ceulemans R, Clement R, Dolman H, Granier A, Gross P, Grünwald T, Hollinger D, Jensen NO, Katul G, Keronen P, Kowalski A, Lai CT, Law BE, Meyers T, Moncrieff J, Moors E, Munger JW, Pilegaard K, Rannik U, Rebmann C, Suyker A, Tenhunen J, Tu K, Verma S, Vesala T, Wilson K, Wofsy S (2001) Gap filling strategies for defensible annual sums of net ecosystem exchange. Agric For Meteorol 107(1):43–69. doi:10.1016/S0168-1923(00)00225-2

Fernández-Martínez M, Vicca S, Janssens IA, Sardans J, Luyssaert S, Campioli M, Chapin III FS, Ciais P, Malhi Y, Obersteiner M, Papale D, Piao SL, Reichstein M, Rodà F, Peñuelas J (2014) Nutrient availability as the key regulator of global forest carbon balance. Nat Clim Chang 4(6):471–476. doi:10.1038/nclimate2177

Foken T (2008) The energy balance closure problem: an overview. Ecol Appl 18(6):1351–1367. http://www.jstor.org/stable/40062260

Foken T, Wichura B (1996) Tools for quality assessment of surface-based flux measurements. Agric For Meteorol 78(1–2):83–105

Foken T, Göckede M, Mauder M, Mahrt L, Amiro B, Munger J (2004) Post-field data quality control. In: Lee X, Massman W, Law B (eds) Handbook of micrometeorology: a guide for surface flux measurement and analysis. Kluwer, Dordrecht, pp 181–208. doi:10.1007/1-4020-2265-4_9

Foken T, Leuning R, Oncley SR, Mauder M, Aubinet M (2012) Corrections and data quality control. In: Aubinet M, Vesala T, Papale D (eds) Eddy covariance: a practical guide to measurement and data analysis. Springer atmospheric sciences. Springer, Netherlands, pp 85–131. doi:10.1007/978-94-007-2351-1_4

Göckede M, Rebmann C, Foken T (2002) Characterisation of a complex measuring site for flux measurements. Work Report University of Bayreuth, Department of Micrometeorology, ISSN 1614-8916, 20, 21pp. http://epub.uni-bayreuth.de/996/

Göckede M, Markkanen T, Hasager CB, Foken T (2006) Update of a footprint-based approach for the characterisation of complex measurement sites. Bound-Layer Meteorol 118(3):635–655. doi:10.1007/s10546-005-6435-3

Göckede M, Foken T, Aubinet M, Aurela M, Banza J, Bernhofer C, Bonnefond JM, Brunet Y, Carrara A, Clement R, Dellwik E, Elbers J, Eugster W, Fuhrer J, Granier A, Grunwald T, Heinesch B, Janssens IA, Knohl A, Koeble R, Laurila T, Longdoz B, Manca G, Marek M, Markkanen T, Mateus J, Matteucci G, Mauder M, Migliavacca M, Minerbi S, Moncrieff J, Montagnani L, Moors E, Ourcival JM, Papale D, Pereira J, Pilegaard K, Pita G, Rambal S, Rebmann C, Rodrigues A, Rotenberg E, Sanz MJ, Sedlak P, Seufert G, Siebicke L, Soussana JF, Valentini R, Vesala T, Verbeeck H, Yakir D (2008) Quality control of carboeurope flux data – part 1: coupling footprint analyses with flux data quality assessment to evaluate sites in forest ecosystems. Biogeosciences 5(2):433–450. doi:10.5194/bg-5-433-2008

Jung M, Reichstein M, Bondeau A (2009) Towards global empirical upscaling of fluxnet eddy covariance observations: validation of a model tree ensemble approach using a biosphere model. Biogeosciences 6(10):2001–2013. doi:10.5194/bg-6-2001-2009

Keenan TF, Hollinger DY, Bohrer G, Dragoni D, Munger JW, Schmid HP, Richardson AD (2013) Increase in forest water-use efficiency as atmospheric carbon dioxide concentrations rise. Nature 499(7458):324–327. doi:10.1038/nature12291

Kottek M, Grieser J, Beck C, Rudolf B, Rubel F (2006) World map of the Köppen-Geiger climate classification updated. Meteorol Z 15(3):259–263. doi:10.1127/0941-2948/2006/0130

Kutsch WL, Kolari P (2015) Data quality and the role of nutrients in forest carbon-use efficiency. Nat Clim Chang 5(11):959–960. doi:10.1038/nclimate2793

Lasslop G, Reichstein M, Detto M, Richardson AD, Baldocchi DD (2010) Comment on Vickers et al.: self-correlation between assimilation and respiration resulting from flux partitioning of eddy-covariance CO_2 fluxes. Agric For Meteorol 150(2):312–314. doi:10.1016/j.agrformet.2009.11.003

Lindauer M, Schmid H, Grote R, Mauder M, Steinbrecher R, Wolpert B (2014) Net ecosystem exchange over a non-cleared wind-throw-disturbed upland spruce forest – measurements and simulations. Agric For Meteorol 197(0):219–234. doi:10.1016/j.agrformet.2014.07.005

Lloyd J, Taylor JA (1994) On the temperature dependence of soil respiration. Funct Ecol 8(3):315–323. doi:10.2307/2389824

Lüers J, Westermann S, Piel K, Boike J (2014) Annual CO_2 budget and seasonal CO_2 exchange signals at a high arctic permafrost site on Spitsbergen, Svalbard archipelago. Biogeosciences 11(22):6307–6322. doi:10.5194/bg-11-6307-2014

Luyssaert S, Inglima I, Jung M, Richardson AD, Reichstein M, Papale D, Piao SL, Schulze ED, Wingate L, Matteucci G, Aragao L, Aubinet M, Beer C, Bernhofer C, Black KG, Bonal D, Bonnefond JM, Chambers J, Ciais P, Cook B, Davis KJ, Dolman AJ, Gielen B, Goulden M, Grace J, Granier A, Grelle A, Griffis T, Grünwald T, Guidolotti G, Hanson PJ, Harding R, Hollinger DY, Hutyra LR, Kolari P, Kruijt B, Kutsch W, Lagergren F, Laurila T, Law BE, Le Maire G, Lindroth A, Loustau D, Malhi Y, Mateus J, Migliavacca M, Misson L, Montagnani L, Moncrieff J, Moors E, Munger JW, Nikinmaa E, Ollinger SV, Pita G, Rebmann C, Roupsard O, Saigusa N, Sanz MJ, Seufert G, Sierra C, Smith ML, Tang J, Valentini R, Vesala T, Janssens IA (2007) CO_2 balance of boreal, temperate, and tropical forests derived from a global database. Glob Chang Biol 13(12):2509–2537. doi:10.1111/j.1365-2486.2007.01439.x

Luyssaert S, Ciais P, Piao SL, Schulze ED, Jung M, Zaehle S, Schelhaas MJ, Reichstein M, Churkina G, Papale D, Abril G, Beer C, Grace J, Loustau D, Matteucci G, Magnani F, Nabuurs GJ, Verbeeck H, Sulkava M, van der Werf GR, Janssens IA, Members of the Carboeurope-IP Synthesis Team (2010) The European carbon balance. part 3: forests. Glob Chang Biol 16(5):1429–1450. doi:10.1111/j.1365-2486.2009.02056.x

Matteucci G, Dore S, Stivanello S, Rebmann C, Buchmann N (2000) Soil respiration in beech and spruce forests in Europe: trends, controlling factors, annual budgets and implications for the ecosystem carbon balance. In: Schulze ED (ed) Carbon and nitrogen cycling in European forest ecosystems. Springer, Berlin, Heidelberg, pp 217–236

Matzner E (ed) (2004) Biogeochemistry of forested catchments in a changing environment - a German case study. Ecological studies, vol 172. Springer, Berlin, Heidelberg. doi:10.1007/978-3-662-06073-5

Mauder M, Foken T (2011) Documentation and instruction manual of the eddy-covariance software package TK3. Work Report University of Bayreuth, Department of Micrometeorology, ISSN 1614-8916, 46, 58pp. http://epub.uni-bayreuth.de/342/

Mauder M, Foken T (2015) Documentation and instruction manual of the eddy-covariance software package TK3 (update). Work Report University of Bayreuth, Department of Micrometeorology, ISSN 1614-8916, 62, 64pp. http://epub.uni-bayreuth.de/2130/

Michaelis L, Menten ML (1913) Die kinetik der invertinwirkung. Biochem Z 49:333–369

Priestley CHB, Taylor RJ (1972) On the assessment of surface heat flux and evaporation using large-scale parameters. Mon Weather Rev 100(2):81–92. doi:10.1175/1520-0493(1972)100<0081:OTAOSH>2.3.CO;2

Rebmann C (2004) Kohlendioxid-, Wasserdampf- und Energieaustausch eines Fichtenwaldes in Mittelgebirgslage in Nordostbayern. Bayreuther Forum Ökologie, 106, 140pp

Rebmann C, Anthoni P, Falge E, Göckede M, Mangold A, Subke JA, Thomas C, Wichura B, Schulze ED, Tenhunen J, Foken T (2004) Carbon budget of a spruce forest ecosystem. In: Matzner E (ed) Biogeochemistry of forested catchments in a changing environment. Ecological studies, chap 8, vol 172. Springer, Berlin, Heidelberg, pp 143–159. doi:10.1007/978-3-662-06073-5_8

Rebmann C, Göckede M, Foken T, Aubinet M, Aurela M, Berbigier P, Bernhofer C, Buchmann N, Carrara A, Cescatti A, Ceulemans R, Clement R, Elbers JA, Granier A, Grunwald T, Guyon D, Havrankova K, Heinesch B, Knohl A, Laurila T, Longdoz B, Marcolla B, Markkanen T, Miglietta F, Moncrieff J, Montagnani L, Moors E, Nardino M, Ourcival JM, Rambal S, Rannik U, Rotenberg E, Sedlak P, Unterhuber G, Vesala T, Yakir D (2005) Quality analysis applied on eddy covariance measurements at complex forest sites using footprint modelling. Theor Appl Climatol 80(2–4):121–141

Ruppert J, Mauder M, Thomas C, Lüers J (2006) Innovative gap-filling strategy for annual sums of co2 net ecosystem exchange. Agric For Meteorol 138:5–18. doi:10.1016/j.agrformet.2006.03.003

Siebicke L (2008) Footprint synthesis for the FLUXNET site waldstein/weidenbrunnen (DE-Bay) during the EGER experiment. Work Report University of Bayreuth, Department of Micrometeorology, ISSN 1614-8916, 38, 45pp. https://epub.uni-bayreuth.de/540/

Siebicke L, Hunner M, Foken T (2012) Aspects of co_2 advection measurements. Theor Appl Climatol 109:109–131. doi:10.1007/s00704-011-0552-3

Subke JA, Tenhunen JD (2004) Direct measurements of CO_2 flux below a spruce forest canopy. Agric For Meteorol 126(1–2):157–168. doi:http://dx.doi.org/10.1016/j.agrformet.2004.06.007

Thomas C, Foken T (2002) Re-evaluation of integral turbulence characteristics and their parameterisations. In: 15th conference on turbulence and boundary layers, Wageningen, NL, 15–19 July 2002. American Meteorological Society, Boston, MA, pp 129–132

Valentini R, Matteucci G, Dolman AJ, Schulze ED, Rebmann C, Moors EJ, Granier A, Gross P, Jensen NO, Pilegaard K, Lindroth A, Grelle A, Bernhofer C, Grunwald T, Aubinet M, Ceulemans R, Kowalski AS, Vesala T, Rannik U, Berbigier P, Loustau D, Gu[eth]mundsson J, Thorgeirsson H, Ibrom A, Morgenstern K, Clement R, Moncrieff J, Montagnani L, Minerbi S, Jarvis PG (2000) Respiration as the main determinant of carbon balance in European forests. Nature 404(6780):861–865. doi:10.1038/35009084

Vickers D, Thomas CK, Martin JG, Law B (2009) Self-correlation between assimilation and respiration resulting from flux partitioning of eddy-covariance CO_2 fluxes. Agric For Meteorol 149(9):1552–1555. doi:10.1016/j.agrformet.2009.03.009

Vickers D, Thomas CK, Martin JG, Law B (2010) Reply to the comment on Vickers et al. (2009) Self-correlation between assimilation and respiration resulting from flux partitioning of eddy-covariance CO_2 fluxes. Agric For Meteorol 150(2):315–317. doi:10.1016/j.agrformet.2009.12.002

Wilczak J, Oncley S, Stage S (2001) Sonic anemometer tilt correction algorithms. Bound-Layer Meteorol 99:127–150. doi:10.1023/A:1018966204465

Williams CA, Reichstein M, Buchmann N, Baldocchi D, Beer C, Schwalm C, Wohlfahrt G, Hasler N, Bernhofer C, Foken T, Papale D, Schymanski S, Schaefer K (2012) Climate and vegetation controls on the surface water balance: synthesis of evapotranspiration measured across a global network of flux towers. Water Resour Res 48(6). doi:10.1029/2011WR011586

Part III
Experimental Studies of Energy and Matter Fluxes

Chapter 5
Sap Flow Measurements

Barbara Köstner, Eva Falge, and Martina Alsheimer

5.1 Introduction

Sap flow measurements in trees are today the most common method to determine transpiration of the forest canopy (E_c), when separation from other evaporation components and independent measurements for flux comparison and model validation are required. Sap flow is only detected when the canopy is dry; therefore canopy interception can be excluded by sap flow. Agreement could be demonstrated between the sum of tree sap flow scaled up to the forest canopy and evaporation determined by eddy covariance technique when evaporation from the soil and forest floor was included (Granier et al. 1993, 1996; Köstner et al. 1992, 1998b). After this, sap flow measurements became a standard tool of ecosystem research (e.g., Tenhunen et al. 1998). Ecophysiological and micrometeorological methods were

B. Köstner (✉)
Chair of Meteorology, Institute of Hydrology and Meteorology, Technische Universität Dresden, 01062 Dresden, Germany
e-mail: barbara.koestner@tu-dresden.de

E. Falge
Thünen-Institute, Institute of Climate-Smart Agriculture, Bundesallee 50, 38116 Braunschweig, Germany

M. Alsheimer
Stückackerweg 18, 97218 Gerbrunn, Germany

B. Köstner, M. Alsheimer, and E. Falge: Affiliation during the work at the Waldstein sites—University of Bayreuth, BITÖK, Chair of Plant Ecology

E. Falge (from 2005): Affiliation during the work at the Waldstein sites—Max Planck Institute for Chemistry, Hahn-Meitner-Weg 1, 55128 Mainz, Germany

T. Foken (ed.), *Energy and Matter Fluxes of a Spruce Forest Ecosystem*,
Ecological Studies 229, DOI 10.1007/978-3-319-49389-3_5

combined with modeling of soil-vegetation-atmosphere transfer to simulate fluxes up to the landscape and continental scale. Both different sap flow techniques and scaling procedures were compared (e.g., Hatton and Wu 1995; Köstner et al. 1998b; Granier et al. 2000). Sap flow techniques are also used to derive canopy conductance and to assess trace gas uptake of trees (Köstner et al. 2008). The thermometric sap flow techniques basically belong to three different principles with heat being used as a marker of sap flow: heat pulse velocity methods, heat dissipation methods using constant heating, and methods using controlled variable heating to determine the heat carried away by the sap. The thermal signal is transferred to water flux by the physical heat capacity of water or by empirical calibration (e.g., Smith and Allen 1996; Burgess et al. 2001). Scaling is required from the sensed spot within tree sapwood to the tree and from sample trees to the forest stand. Scaling errors are related to the determination of representative flux rates (flux density, flux velocity) in the conducting sapwood area of sample trees and the use of proxies like stem circumference or diameter at breast height, projected crown area, leaf area, or stem basal area to establish biometric relationships for scaling from tree to stand level (see review by Wullschleger et al. 1998).

In the Waldstein region, studies of water fluxes at the tree and forest canopy level have started in 1993 at the 140-year-old Norway spruce (*Picea abies* L. KARST.) site Coulissenhieb I within the frame of forest ecosystem research of BITÖK (Bayreuth Institute of Terrestrial Ecosystem Research). The Waldstein region includes the Lehstenbach catchment which was addressed to study water and matter fluxes at the ecosystem level (Tenhunen et al. 2001b, Chap. 1). The catchment comprised an area of approx. 4 km^2 and consisted of a mosaic of individually managed stands differing in age. Previous studies of Norway spruce in the Fichtelgebirge had focused on water use of younger trees without scaling to the forest canopy level (Schulze et al. 1989). It was necessary to understand the importance of leaf area, tree biometry and age for scaling up, and modeling fluxes at stand and catchment level (Tenhunen et al. 2001a). The sap flow technique allowed to determine whole tree transpiration without scaling up from the leaf level. This has led to successful comparisons of E_c derived at the tree level by sap flow and E_c derived from spatial simulation of leaf CO_2 exchange of trees (Köstner et al. 1998a; Falge et al. 2000).

A comparative study of different sites was performed to understand spatial heterogeneity (Alsheimer et al. 1998) as well as atmospheric controls and flux partitioning between trees and vegetation or litter of the forest floor (Köstner et al. 2001). These studies had a strong influence on water balance research at BITÖK as well as on research of age dependencies and hydraulic adaptation of trees (McDowell et al. 2002; Köstner et al. 2002; Ryan et al. 2006). In the following years, the research was focused on a broad-leaved forest catchment dominated by European beech and sessile oak (Köstner et al. 2004). At the spruce site Waldstein-Weidenbrunnen, measurements of water fluxes were continued by eddy covariance technique (Chap. 4). While studies during the initial research phase have especially

focused on horizontal variation between individual stands in the Lehstenbach catchment, an intensive study on vertical variation of evapotranspiration components was performed within the EGER project in 2007. A vertical profile had been installed for complementary studies of canopy sap flow and eddy covariance measurements to demonstrate and simulate different pathways of water vapor fluxes by 1D and 3D multilayer modeling (Staudt et al. 2011, Chap. 16). In parallel to the EGER project, a joint research project on soil processes using artificial roofs below the canopy of Coulissenhieb II took place from 2006 to 2008 (Borken and Matzner 2009).

5.2 Material and Methods

5.2.1 Study Sites

The Waldstein-Weidenbrunnen and Coulissenhieb measuring sites are located in the Lehstenbach catchment in the mountainous region Fichtelgebirge in South Germany. The altitude of both sites is 775 m above sea level. Mean annual temperature is 5.3 °C, and mean annual precipitation amounts 1162 mm (1971–2000, Foken 2003) on the basis of a synthetic climate data set. For the years 2001 to 2010, mean annual temperature reached 6.5 °C and mean annual precipitation 1064 mm (Waldstein-Pflanzgarten, Chap. 3); for further details, see Chap. 2. An overview of sites and measurements is given in Table 5.1. The site Coulissenhieb II with soil treatment plots was heavily destroyed by the storm Kyrill in January 2007

Table 5.1 Sap flow measurements at the Waldstein-Weidenbrunnen and Coulissenhieb I and II measuring sites. April/May to October represents the main growing season at the site. In January 2007 the site Coulissenhieb II was heavily damaged by the storm Kyrill

Site	Measurement period	Stand age	Number of trees	Number of levels
Weidenbrunnen	May–Oct 1994 April–Oct 1995	40	10	1
Schlöppner Brunnen (boggy site)	April–Oct 1995	40	10	1
Schanze (NE exposure)	April–Oct 1995	40	10	1
Süßer Schlag	April–Oct 1995	70	10	1
Gemös	April–Oct 1995	90	10	1
Coulissenhieb I	May–Oct 1993/1994 April–Oct 1995	140	13 13	1 1
Coulissenhieb II	June 2006–Jan 2007 July 2007–June 2008	145 146	18 9	1 1
Weidenbrunnen	Sep–Oct 2007 May–July 2008	54 55	2 1 6	6 6 1

and had to be reconstructed. Tree density within the study area was 338 and 197 trees/ha before and after the storm, respectively.

5.2.2 Sap Flow Measuring Technique

Overall three different sap flow techniques have been applied at the study sites. Measurements started at the site Coulissenhieb I with a controlled variable heating system (Kucera et al. 1977; Schulze et al. 1985). The method maintains a constant temperature difference between a defined spatial sector of sapwood and reference probes in the sapwood by electronic control using the variable electric heating power of the controller as the primary signal to quantify sap flux via the heat capacity of water. In 1994/1995 additional sap flow sensors constructed according to Granier (1985) were installed at Coulissenhieb I and the younger sites in the Lehstenbach catchment (Alsheimer et al. 1998). Needle-type heating and sensing elements were inserted into the trunks at breast height, one above the other ca. 15 cm apart, and the upper element was heated with constant power. The temperature difference sensed between the two elements was influenced by the sap flux density in the vicinity of the heated element. Sap flux density was estimated via empirical calibration factors established in the laboratory (Granier 1985). No systematic differences in flux densities derived from both methods were found (Köstner et al. 1998a, b). Cross-sectional sapwood area was determined by increment borer and computer tomography in living trees and by stem disks of harvested trees (Alsheimer et al. 1998).

During the second study phase, sap flow sensors according to Granier were installed at the site Coulissenhieb II in soil treatment and reference plots of the roof experiment. This experiment was focused on soil and root studies (Gaul et al. 2008a, b). The "heat ratio method" (HRM) was applied for profile studies at the Weidenbrunnen site. The method allows the local measurement of sap flux in woody parts of tree trunks and branches and the derivation of transpiration estimates for trees and stands (Green et al. 2003; Burgess et al. 2000). Sap flux velocity probes (HMR-30, ICT International Pty Ltd., Armidale, Australia) were installed at six levels of two spruce trees close to the 36 m-high scaffolding (bio) tower (Staudt et al. 2011). Eddy covariance measurements were additionally conducted at a slim tower (mast) of 35 m height in a distance of 70 m. More details about the comparison of eddy covariance and sap flux estimates of in-canopy profile and stand transpiration are described in Chap. 16.

5.2.3 Modeling

The STANDFLUX model consists of a leaf or branch gas exchange module; a three-dimensional, single-tree light interception and gas exchange module; and the three-dimensional forest stand gas exchange model. It describes canopy water vapor

and carbon dioxide exchange based on rates calculated for individual trees and as affected by local gradients in photon flux density (PFD), atmospheric humidity, atmospheric carbon dioxide concentration, and air temperature. Direct, diffuse, and reflected PFD incident on foliage elements is calculated for a three-dimensional matrix of points superimposed over the canopy. The model was used to calculate forest radiation absorption, net photosynthesis and transpiration of single trees, and gas exchange of tree canopies of a series of Norway spruce stands (see Table 5.1). Stand-specific parameterization included information on vertical and horizontal leaf area distribution, tree positions and tree sizes, and species-specific leaf physiological characteristics (Falge et al. 2005; Staudt et al. 2011). The modeling of the 1995 data was performed with an earlier version of the model (Falge et al. 1996).

5.2.4 Eddy Covariance Measurements

Evapotranspiration was determined by the eddy covariance method during the second study phase at the Waldstein-Weidenbrunnen site, from 2002 to 2006 at the "Main Tower" and at the "Turbulence Tower" from 2007 until today. For the comparison with in-canopy profile measurements of sap flux-derived stand transpiration, five "golden" days of IOP1 of the EGER project were used (Staudt et al. 2011). For more details about instrumentation, eddy covariance processing, quality control, and gap filling, see Chap. 4.

5.3 Results and Discussions

5.3.1 Tree Sap Flow and Canopy Transpiration

Measurements of tree sap flow were connected with extensive biometric studies to establish allometric relationships between simple measures of tree size, e.g., tree circumference or tree diameter at breast height and physiologically functional parameters like cross-sectional sapwood area or needle area. Needle area was derived by whole tree harvest of selected trees representing the size classes in the stand (Tenhunen et al. 2001b; Mund et al. 2002). Cumulative stand sapwood area represented the scaling factor for sap flow (Köstner et al. 1998a, b), while spatial distribution of leaf area was the scaling factor for the gas exchange model (Falge et al. 1996, 2000). Different relationships of sapwood area at breast height to sapwood area below live crown and between sapwood area and leaf area of the 40-year-old and older stands indicated functional adaptation along with growth and aging (Köstner et al. 2002, Table 5.2). This adaptation is obviously expressed in a similar range of sap flux densities of canopy trees independent of tree size and age, while subcanopy trees exhibited significantly lower flux densities. Hence, bulk sap flux of trees increased continuously with tree size and cross-sectional sapwood

Table 5.2 Biometric functions derived from tree measurements and harvests for scaling up from the sensed sapwood to tree and stand level and for investigation of structure-function relationships. For conversion of projected leaf area to all-sided leaf area, a general factor of 2.6 was used (data after Alsheimer 1997; Tenhunen et al. 2001b; Köstner et al. 2002)

Age (years)	Parameters	Biometric function	R^2	n
40 70–140	Sapwood area at breast height, A_{sbh} (cm^2)	$A_{sbh} = 553.5 * cbh^{2.20}$ $A_{sbh} = 317.1 * cbh^{1.75}$	0.94 0.74	15 15
40 70–140	Sapwood area below live crown, A_{sblc} (cm^2)	$A_{sblc} = 432.4 * cbh^{2.69}$ $A_{sblc} = 191.5 * cbh^{1.71}$	0.94 0.61	15 15
40–140	Sapwood area below live crown, A_{sblc} (cm^2)	$A_{sblc} = 0.64 * A_{sbh} + 1.79$	0.89	35
40–140	All-sided leaf area, A_{fa} (m^2)	$A_{fa} = 356.2 * cbh^{2.38}$	0.93	35
40 70/110 140	All-sided leaf area, A_{fa} (m^2)	$A_{fa} = 1.21 * A_{sblc} - 15.34$ $A_{fa} = 1.66 * A_{sblc} - 0.99$ $A_{fa} = 3.30 * A_{sblc} - 118.65$	0.90 0.84 0.95	15 10 9
140	Projected crown area, A_{cra} (m^2)	$A_{cra} = 13.07 * cbh^{3.096}$	0.99	6

A_{sbh} sapwood area at breast height (cm^2), A_{sblc} sapwood area below live crown (cm^2), A_{fa} all-sided leaf area (m^2), A_{cra} projected crown area (m^2), *cbh* circumference at breast height (m)

area of trees (Fig. 5.1a, b). However, sap flux per leaf area decreased with tree size, indicating less functional leaf area of older trees (Fig. 5.1c). This was confirmed at the stand level by simulations of the 3D structure-dependent stand gas exchange model STANDFLUX (Falge et al. 1996, 2000). A decline of intercepted photon flux density with increasing leaf area index (*LAI*) of the stands was simulated based on measured stand structure (Fig. 5.2a). Accordingly, E_c scaled up from sap flow did not depend on *LAI* within the range of the investigated stands (projected *LAI*: 5.3–7.9 $m^2\ m^{-2}$, Fig. 5.2b). Obviously, needle clumping at higher *LAI* had a stronger negative effect on light interception than the expected increase of light interception with increasing needle surface when the needles are homogeneously distributed (Beer's law). This has to be considered when *LAI* is used as a scaling factor in SVAT models, especially for coniferous species with a larger number of needle age classes.

Atmospheric controls of transpiration were studied at the forest canopy level. Daily E_c strongly depended on vapor pressure deficit (D) of the air, saturating between a daytime average D of 1–1.5 kPa (Fig. 5.3a). Further variation between individual days was explained by PFD (Alsheimer et al. 1998). Each stand reached a typical maximum rate of E_c (E_{cmax}), which was highest at the site Schlöppner Brunnen, a boggy site in one of the main drainage areas of the catchment (map in Tenhunen et al. 2001a), where soil water availability was high and atmospheric demand by D lowest compared to the other sites. The curvilinear dependencies were similar between sites for relative E_c (E_c/E_{cmax}, Fig. 5.3b). The strong control of transpiration is explained by decreasing canopy conductance with increasing D and

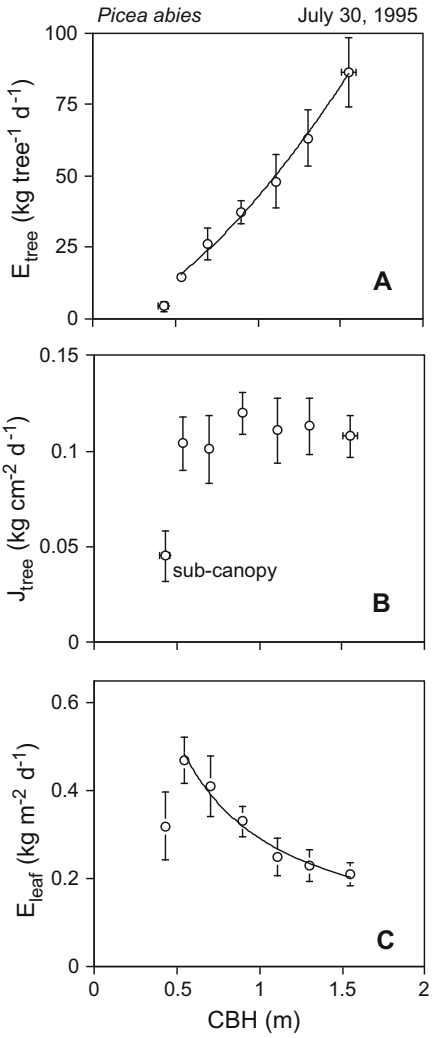

Fig. 5.1 Relationship between tree circumference at breast height, CBH (m) and (**a**) daily tree sap flux per tree, E_{tree}; (**b**) tree sap flux per sapwood area (sap flux density), J; and (**c**) daily sap flux per leaf area of trees, E_{leaf} (Köstner 1999, published with kind permission of © Author 1999, All rights reserved)

most pronounced vegetation-atmosphere coupling in older stands (Köstner et al. 2001).

In 2007 and 2008 sap flux-derived estimates of E_c were measured at the site Weidenbrunnen (in 1995 40 years old), and the above analysis of the dependence on D of the air repeated (Fig. 5.4). Interestingly, the site showed now much higher daily sums of E_c (maximum of 3.56 mm) than 12–13 years ago. Solving the regression lines for an average daytime D of 1 kPa, the values of E_c almost doubled (from 1.57 in 1995 to 3.05 mm d^{-1} in 2007/2008). This finding is supported by the observed increase in evapotranspiration derived from the continuous eddy covariance measurements at the site over the period from 2002 until now, discussed

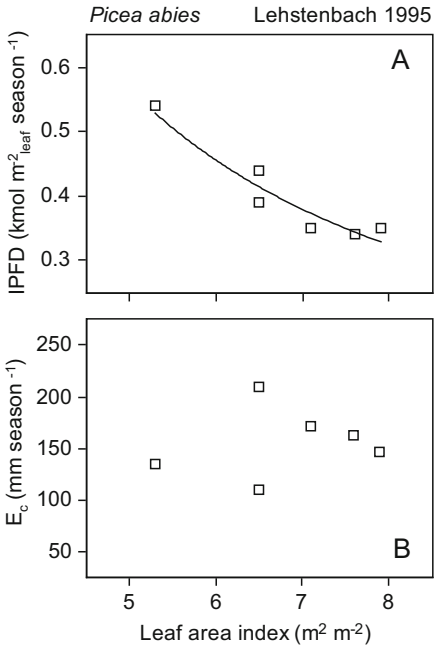

Fig. 5.2 Relationship between projected leaf area index (LAI) of forest stands and (**a**) intercepted photon flux density (IPFD) simulated by the 3D STANDFLUX model and (**b**) seasonal canopy transpiration of stands (April–Oct) determined by tree sap flow (Köstner 1999, published with kind permission of © Author 1999, All rights reserved)

in Chap. 4. At the same time, sap flow was measured in trees of the older Coulissenhieb II site. Trees showed a similar increase with *D*, however, with lower maximum values of E_c (2.1 mm d^{-1}) compared to the Weidenbrunnen site. For the Coulissenhieb II site, canopy transpiration was referred to projected crown area of the trees. Scaling up to the whole ground area of the stand by biometric relationships would have resulted in lower E_{cmax} (1.3 mm d^{-1}) due to reduced tree density after the storm Kyrill. Further, sample trees of treatment plots (soil drought, soil freezing) at this site showed reduced sap flow for the same period, reaching 1.3 and 1.2 mm d^{-1} (per projected crown area) for the drought and freezing plot, respectively. In contrast to the Weidenbrunnen site, less difference was found between earlier measurements at Coulissenhieb I in 1995 when compared to the adjacent site Coulissenhieb II in 2007/2008. But these older sites have not been fertilized. Similar relationships to atmospheric conditions could be described for 110-year-old Norway spruce at the Tharandt site in the Lower Ore Mountains of eastern Germany (Clausnitzer et al. 2011). At the Tharandt site, it was also demonstrated that comparably low sap flux rates of old trees agreed with the amount of local water extraction measured in the soil (Schwärzel et al. 2009).

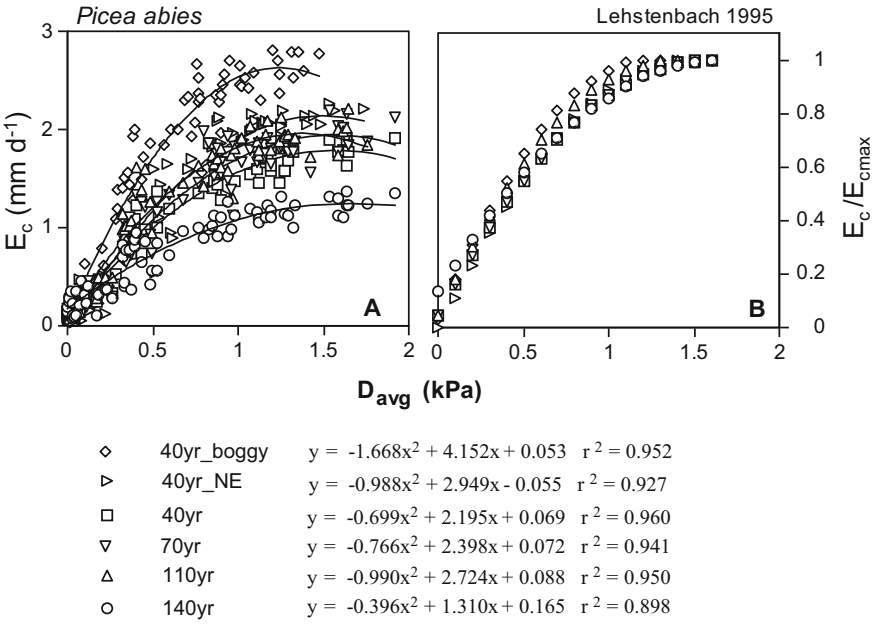

Fig. 5.3 Relationship between daytime average vapor pressure deficit of the air (D, measured between 0600 and 1800 h) and canopy transpiration, E_c, and (**a**) canopy transpiration, E_c, and (**b**) relative E_c/E_{cmax} for the 40–140-year-old stands in the Lehstenbach catchment (from Köstner et al. 2002). Published with kind permission of © Oxford University Press 2002, All rights reserved)

5.3.2 Tree Profile Measurements

Models as well as sap flow and eddy covariance measurements allow the study of the partitioning of (evapo)transpiration within canopy profile. For a comparison experiment (Staudt et al. 2011, Chap. 16), five eddy covariance systems were positioned within the canopy; the highest eddy covariance system, 11 m above the canopy, at the top of the tower can be taken to represent canopy top measurements assuming a constant flux layer above the canopy. Simultaneously, xylem sap flow sensors were installed in five heights within the canopy and at breast height in the trunk of two trees. As sap flow measurements integrate over the transpiration taking place above the installation point, the measurements in breast height represent the total transpiration of the tree and scaled that of the forest canopy. Adding forest floor evaporation and neglecting interception loss, the latter corresponds to the evapotranspiration data from the highest eddy covariance system. The difference in sap flux estimates between adjacent installation heights represents the transpiration flux occurring within the respective canopy layer. The comparison with eddy covariance flux estimates of in-canopy profile is discussed in detail in Staudt et al. (2011) and summarized in Chap. 16.

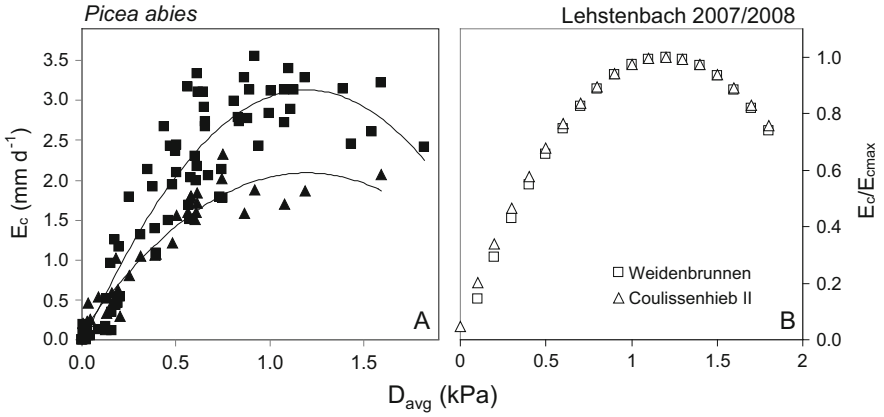

Fig. 5.4 Relationship between daytime average vapor pressure deficit of the air (D, measured between 0600 and 1800 h) and canopy transpiration, E_c, for the stand Weidenbrunnen (40 years in 1995, 52–53 years in 2007/2008; squares, $y = -2.237x^2 + 5.348x - 0.064$; $r^2 = 0.872$) and Coulissenhieb II (145 years; triangles, $y = -1.395x^2 + 3.335x + 0.1$; $r^2 = 0.904$). Periods are for Weidenbrunnen Sep 9–Oct 6, 2007, and May 26–July 11, 2008; for Coulissenhieb II Sep 7–Oct 6, 2007, and May 31–June 8, 2008

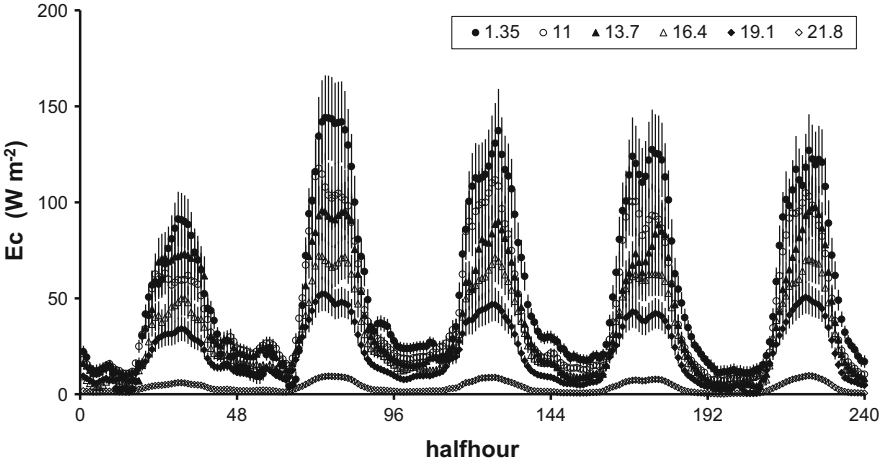

Fig. 5.5 Diurnal courses of cumulative transpiration from xylem sap flux in six heights above ground in a *Picea abies* tree near the Bio Tower for JD 263–267 of 2007. Sap flux rates were measured with the heat pulse method (ICT), scaled to the forest stand, and converted to the energy equivalent for comparison with latent heat fluxes from kg h^{-1} to Wm^{-2} by multiplication with the latent heat of evaporation (2.45 MJ kg^{-1} at 20 °C). For this comparison and the estimation of sap flux errors, see explanations in the Appendix of Staudt et al. (2011)

Figure 5.5 shows for the five golden days of the EGER IOP1 experiment diurnal courses of tree transpiration scaled to the forest stand for the different installation heights. The biggest contribution to the total E_c (measured at installation height 1.35 m) is found in the sun crown, between 19.1 and 21.8 m. Estimated mean relative

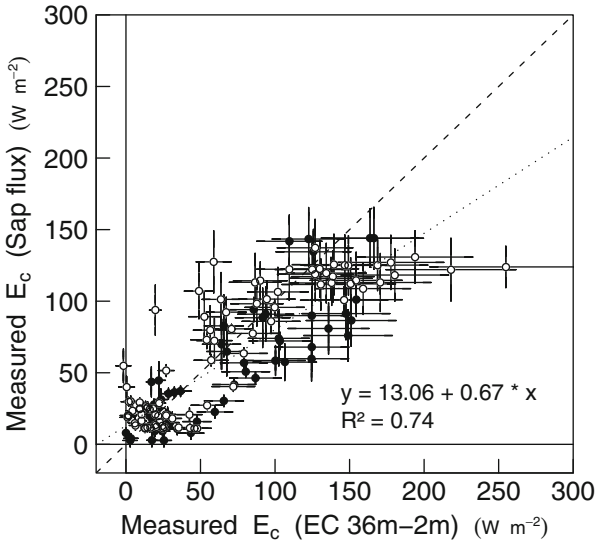

Fig. 5.6 Scatter plot for the comparison of transpiration (E_c) measured with sap flux versus transpiration (E_c) measured with eddy covariance (EC, 36–2.25 m) with its errors for DOY 263–264 (*filled circles*) and DOY 265–267 (*open circles*) ($N = 125$). For eddy covariance measurements, an error of 20 % is added to the data for comparison (Mauder et al. 2006). For the estimation of sap flux errors, see explanations in the Appendix of Staudt et al. (2011). (Adapted from Staudt et al. 2011, published with kind permission of © Elsevier, 2011. All rights reserved)

errors for sap flux measurements were 16–18 % for daytime. At night, largest errors were estimated for total E_c (26 %) and within the canopy errors were between 13 % and 16 %.

The scatter plot in Fig. 5.6 illustrates the underestimation of E_c derived from sap flux measurements compared to eddy covariance estimates during the first two of the five golden days of the EGER IOP1 experiment. For the last 3 days, the behavior changed to an overestimation. Staudt et al. (2011) discussed as potential reasons a change in wind direction and subsequent preferential sampling of different footprint areas by the eddy covariance measurements; alternatively, fog and a wet canopy at the beginning of the period might have had an influence on the agreement of both methods. Under such conditions, the difference of above and in-canopy eddy covariance measurements might not only represent E_c but also include canopy interception.

5.4 Conclusions

Sap flow measurements have importance in ecological and hydrological research because they represent an integrated measure of tree transpiration and therefore separate between the physiologically controlled plant process and physical evaporation

from soil and interception. They contribute to the analysis of atmospheric controls and allow the derivation of canopy conductance without impact of other flux components. Further they enable to establish structure-function relationships between tree/forest biometric and flux parameters. Results of the presented studies also improved the understanding of functional change along with aging or long-term stand recovery after fertilization (Chap. 19). Sap flow measurements support the interpretation and plausibility of total evaporation estimates by vertical flux partitioning within the canopy and between forest floor and tree canopy. They also support the interpretation of horizontal contributions from different local patches in heterogeneous terrain. Sap flow measurements in the canopy profile have the potential for cross validation of independent measurements of water fluxes (derived from the water equivalent of latent heat fluxes from eddy covariance technique). This holds especially for periods where evaporation from interception pool or soil surface is low, or adequate independent estimates of evaporative fluxes are available. Nevertheless, for a direct comparison, differences in temporal and spatial integration of sap flow and micrometeorological techniques have to be kept in mind. Xylem sap flow data lag in time and are dampened due to water storage changes in needles/leaves and sapwood over the diurnal cycle. Further, scaling procedures of sap flow cannot fully correspond to variable source areas of micrometeorological measurements.

Separation of flux components is further important for model validation because evaporation and transpiration in most of the models are parameterized in different ways. Sophisticated micrometeorological methods with isotope fluxes or the separation of eddies with a different moisture signal (Thomas et al. 2008, Chap. 6) is too complicated for the generation of longer data sets.

Acknowledgment This research was funded by the German Ministry of Education and Technology within the first two funding periods of BITÖK (PT BEO 51-0339476 A, B) and during the second phase within the German Science Foundation (DFG) projects FO 226/16-1 and ME 2100/4-1 to the University of Bayreuth and FE 504/2-1-2 to Technische Universität Dresden.

References

Alsheimer M (1997) Xylemflussmessungen zur Charakterisierung raum-zeitlicher Heterogenitaten in der Transpiration montaner Fichtenbestande (*Picea abies* (L.) KARST.). PhD Thesis, Bayreuther Forum Okologie 49

Alsheimer M, Köstner B, Falge E, Tenhunen JD (1998) Temporal and spatial variation in transpiration of Norway spruce stands within a forested catchment of the Fichtelgebirge, Germany. Ann Sci For 55:103–123

Borken W, Matzner E (2009) Reappraisal of drying and wetting effects on C and N mineralization and fluxes in soils. Glob Chang Biol 15:808–824. doi:10.1111/j.1365-2486.2008.01681.x

Burgess SSO, Adams MA, Bleby TM (2000) Measurement of sap flow in roots of woody plants: a commentary. Tree Physiol 20:909–913

Burgess SSO, Adams M, Turner NC, Beverly CR, Ong CK, Khan AA, Bleby TM (2001) An improved heat pulse method to measure low and reverse rates of sap flow in woody plants. Tree Physiol 21:589–598

Clausnitzer F, Köstner B, Schwärzel K, Bernhofer C (2011) Relationships between canopy transpiration, atmospheric conditions and soil water availability—analyses of long-term sap-flow measurements in an old Norway spruce forest at the Ore Mountains/Germany. Agric For Meteorol 151:1023–1034

Falge E, Graber W, Siegwolf R, Tenhunen JD (1996) A model of the gas exchange response of *Picea abies* to habitat conditions. Trees 10:277–287

Falge E, Tenhunen JD, Ryel R, Alsheimer M, Köstner B (2000) Modelling age- and density-related gas exchange of *Picea abies* canopies in the Fichtelgebirge, Germany. Ann Sci For 57:229–243

Falge E et al (2005) Comparison of surface energy exchange models with eddy flux data in forest and grassland ecosystems of Germany. Ecol Model 188:174–216

Foken T (2003) Lufthygienisch-Bioklimatische Kennzeichnung des oberen Egertales. Bayreuther Forum Ökologie. 100:69+XLVIII

Gaul D, Hertel D, Borken W, Matzner E, Leuschner C (2008a) Effects of experimental drought on the fine root system of mature Norway spruce. For Ecol Manag 256:1151–1159

Gaul D, Hertel D, Leuschner C (2008b) Effects of experimental soil frost on the fine-root system of mature Norway spruce. J Plant Nutr Soil Sci 2008(171):690–698. doi:10.1002/jpln.200700284

Granier A (1985) Une nouvelle méthode pour la mesure du flux de sève brute dans le tronc des arbres. Ann Sci For 42:193–200

Granier A, Biron P, Köstner B, Gay LW, Najjar G (1996) Comparisons of xylem sap flow and water vapour flux at the stand level and derivation of canopy conductance for Scots pine. Theor Appl Climatol 53(1–3):115–122

Granier A, Biron P, Lemoine D (2000) Water balance, transpiration and canopy conductance in two beech stands. Agric For Meteorol 100:291–308

Granier A, Bobay V, Gash JHC, Gelpe J, Saugier B, Shuttleworth WJ (1993) Vapour flux density and transpiration rate comparisons in a stand of Maritime pine (*Pinus pinaster* Ait.) in Les Landes forest. Agric For Meteorol 51:309–319

Green S, Clothier B, Jardine B (2003) Theory and practical application of heat pulse to measure sap flow. Agron J 95:1371–1379

Hatton TJ, Wu H-I (1995) Scaling theory to extrapolate individual tree water use to stand water use. Hydrol Process 9:527–540

Köstner B (1999) Die Transpiration von Wäldern—Quantifizierung als Xylemsaftfluß und Faktorenabhängigkeit von Teilflüssen. Universität Bayreuth, Habilitationsschrift

Köstner B, Falge EM, Alsheimer M, Geyer R, Tenhunen JD (1998a) Estimating tree canopy water use via xylem sapflow in an old Norway spruce forest and a comparison with simulation-based canopy transpiration estimates. Ann For Sci 55:125–139

Köstner B, Falge E, Tenhunen JD (2002) Age-related effects on leaf area/sapwood area relationships, canopy transpiration, and carbon gain of *Picea abies* stands in the Fichtelgebirge/Germany. Tree Physiol 22:567–574

Köstner B, Granier A, Cermák J (1998b) Sap flow measurements in forest stands: methods and uncertainties. Ann Sci For 55:13–27

Köstner B, Matyssek R, Heilmeier H, Clausnitzer F, Nunn AJ, Wieser G (2008) Sap flow measurements as a basis for assessing trace-gas exchange of trees. Flora 203:14–33

Köstner B, Schmidt M, Falge E, Fleck S, Tenhunen JD (2004) Atmospheric and structural controls on carbon and water relations in mixed-forest stands of beech and oak. In: Matzner E (ed) Biogeochemistry of forested catchments in a changing environment. A German case study. Ecological studies, vol 172. Springer, Berlin, pp 69–98

Köstner BMM, Schulze E-D, Kelliher FM, Hollinger DY, Byers JN, Hunt JE, McSeveny TM, Meserth R, Weir PL (1992) Transpiration and canopy conductance in a pristine broad-leaved forest of *Nothofagus*: an analysis of xylem sap flow and eddy correlation measurements. Oecologia 91:350–359

Köstner B, Tenhunen JD, Alsheimer M, Wedler M, Scharfenberg H-J, Zimmermann R, Falge E, Joss U (2001) Controls on evapotranspiration in a spruce forest catchment of the Fichtelgebirge. In: Tenhunen JD, Lenz R, Hantschel R (eds) Ecosystem approaches to landscape management in Central Europe. Ecological studies, vol 147. Springer, Berlin, pp 379–415

Kucera J, Cermák J, Penka M (1977) Improved thermal method of continual recording the transpiration flow rate dynamics. Biol Plant 19(6):413–420

Mauder M, Liebethal C, Gockede M, Leps J-P, Beyrich F, Foken T (2006) Processing and quality control of flux data during LITFASS-2003. Bound Lay Meteorol 121:67–88

McDowell N, Barnard H, Bond BJ, Hinckley T, Hubbard R, Ishii H, Köstner B, Meinzer FC, Marshall JD, Magnani F, Phillips N, Ryan MG, Whitehead D (2002) The relationship between tree height and leaf area: sapwood area ratio. Oecologia 132:12–20

Mund M, Kummetz E, Hein M, Bauer GA, Schulze E-D (2002) Growth and carbon stocks of a spruce forest chronosequence in central Europe. For Ecol Manag 171:275–296

Ryan MG, Phillips N, Bond BJ (2006) The hydraulic limitation hypothesis revisited. Plant Cell Environ 29:367–381

Schulze E-D, Cermák J, Matyssek R, Penka M, Zimmermann R, Vasicek F, Gries W, Kucera J (1985) Canopy transpiration and water fluxes in the xylem of the trunk of Larix and Picea trees—a comparison of xylem flow, porometer and cuvette measurements. Oecologia 66:475–483

Schulze E-D, Hantschel R, Werk KS, Horn R (1989) Wate relations of two Norway spruce stands at different stages of decline. In: Schulze E-D, Lange OL, Oren R (eds) Forest decline and air pollution. Ecological studies, vol 77. Springer, Berlin, pp 341–351

Schwärzel K, Menzer A, Clausnitzer F, Spank U, Häntzschel J, Grünwald T, Köstner B, Bernhofer C, Feger KH (2009) Soil water measurements deliver reliable estimates of water fluxes: a comparative study in a beech and a spruce stand in the Tharandt forest (Saxony Germany). Agric For Meteorol 149:1994–2006

Smith DM, Allen SJ (1996) Measurement of sap flow in plant stems. J Exp Bot 47:1833–1844

Staudt K, Serafimovich A, Siebicke L, Pyles RD, Falge E (2011) Vertical structure of evapotranspiration at a forest site (a case study). Agric For Meteorol 151:709–729

Tenhunen JD, Falge E, Ryel R, Manderscheid B, Peters K, Ostendorf B, Joss U, Lischeid G (2001a) Modelling of fluxes in a spruce forest catchment in the Fichtelgebirge. In: Tenhunen JD, Lenz R, Hantschel R (eds) Ecosystem approaches to landscape management in Central Europe. Ecological Studies, vol 147. Springer, Berlin, pp 417–503

Tenhunen JD, Matzner E, Heindl B, Chiba Y, Manderscheid B (2001b) Assessing environmental influences on ecological function of a spruce forest catchment in the Fichtelgebirge. In: Tenhunen JD, Lenz R, Hantschel R (eds) Ecosystem approaches to landscape management in Central Europe. Ecological Studies, vol 147. Springer, Berlin, pp 357–375

Tenhunen JD, Valentini R, Köstner B, Zimmermann R, Granier A (1998) Variation in forest gas exchange at landscape to continental scales. Ann Sci For 55:1–11

Thomas C, Martin JG, Göckede M, Siqueira MB, Foken T, Law BE, Loescher HW, Katul G (2008) Estimating daytime subcanopy respiration from conditional sampling methods applied to multi-scalar high frequency turbulence time series. Agric For Meteorol 148:1210–1229

Wullschleger SD, Meinzer FC, Vertessy RA (1998) A review of whole-plant water use studies in tree. Tree Physiol 18:499–512

Chapter 6
Coherent Structures and Flux Coupling

Christoph K. Thomas, Andrei Serafimovich, Lukas Siebicke, Tobias Gerken, and Thomas Foken

6.1 Introduction

Coherent structures in the atmosphere are one important canopy flow mode in the roughness sublayer of forests of any architecture as they have the ability to transport energy and matter over long distances in a spatially coherent fashion (Gao et al. 1989; Shaw et al. 1989; Paw U et al. 1992; Thomas and Foken 2007a). Their importance for the horizontal and vertical transport and exchange in forest canopies

C.K. Thomas (✉)
University of Bayreuth, Micrometeorology Group, 95440 Bayreuth, Germany

Bayreuth Center of Ecology and Environmental Research, University of Bayreuth, Bayreuth, Germany
e-mail: christoph.thomas@uni-bayreuth.de

A. Serafimovich
Helmholtz-Zentrum Potsdam, Deutsches GeoForschungsZentrum GFZ, Telegrafenberg, Haus A 6, 14473 Potsdam, Germany

L. Siebicke
Department of Bioclimatology, Georg-August University of Göttingen, Büsgenweg 2, 37077 Göttingen, Germany

T. Gerken
Department of Land Resources and Environmental Sciences, Montana State University, 334 Leon Johnson Hall, Bozeman, MT 59717, USA

T. Foken
Am Herrgottsbaum 28, 96120 Bischberg, Germany

Bayreuth Center of Ecology and Environmental Research, University of Bayreuth, Bayreuth, Germany

C. K. Thomas, L. Siebicke, A. Serafimovich, T. Gerken, and T. Foken: Affiliation during the work at the Waldstein sites – University of Bayreuth, Department of Micrometeorology, Germany

T. Foken (ed.), *Energy and Matter Fluxes of a Spruce Forest Ecosystem*,
Ecological Studies 229, DOI 10.1007/978-3-319-49389-3_6

arises from the fact that the associated velocity perturbations are substantially stronger compared to the other common flow modes including the ubiquitous stochastic "background" turbulence, von Kármán vortices shed by canopy elements such as tree trunks and branches, the submeso-scale modes (Thomas 2011), canopy waves (Cava et al. 2004), and boundary-layer scale convective eddies (Poggi et al. 2004; Thomas et al. 2006). Coherent structures are commonly referred to as "organized motions," which expresses that individual motions have distinct and predictable temporal and spatial scales including a quasi-stationary arrival frequency, as opposed to the random stochastic motions, which can only be described in terms of their ensemble probability density function. The terminology of "coherent structures" in atmospheric flows is ambiguous in the literature and has been used to describe a variety of flow phenomena resulting from a variety of generating mechanisms (see overview in Kallistratova and Kouznetsov 2004).

For the purpose of this chapter focusing on flow phenomena and flux coupling in plant canopies, we define a coherent structure as a spatially coherent motion whose length and vertical dimensions scale with the density and depth of the vegetated canopy. In vector time series, they occur as a fairly symmetric triangle-like pattern, whereas in scalar time series, they have an asymmetric ramp-like shape (Thomas and Foken 2007b). The physical process connected with one event can be separated into an initial upward motion (ejection, burst) followed by a rapid downward motion (sweep, gust). The temporal scale varies from several seconds up to a few minutes.

Based on the similarity of structural characteristics of coherent structures in the atmosphere under varying stability conditions, Gao et al. (1989) identified the vertical wind shear as the main generating mechanism of coherent structures. The results of Paw et al. (1992) supported this finding by demonstrating a functional relationship between the occurrence frequency of coherent structures and the canopy shear scale $U_{hc}h_c^{-1}$, where U_{hc} is the mean horizontal wind speed at the canopy height, h_c. Raupach et al. (1996) continued to investigate coherent structures in the forest air layer and proposed a theory for their generation in neutral stratification called the mixing-layer analogy. This theory states that if the above-canopy and canopy air layers are allowed to mix, a mixing layer develops in which coherent structures form in the atmosphere as a result of flow instabilities created at the height of the maximum vertical shear, i.e., the inflection point of the horizontal velocity profile. The initial phase of their evolution can be described as a hairpin vortex that may organize into larger-scale structures (Zhou et al. 1999; Hommema and Adrian 2003; Adrian 2007).

While coherent structures have been investigated by a large number of authors across a wide spectrum of forest and agricultural canopies, the coherent structures' research conducted at the Waldstein site contributed three important aspects to this field of research: firstly, the development of a refined automated and largely objective detection algorithm based upon pattern recognition algorithms using the wavelet transformation; secondly, the definition of a set of distinct exchange regimes, which allows for a categorization of the varying degrees of vertical and horizontal coupling between the sub-canopy, canopy, and above-canopy air layers by coherent structures; and thirdly, an alternative explanation for the occurrence

of systematic spatial CO_2 concentration gradients and thus sub-canopy horizontal advection by linking the horizontal and vertical exchange regimes with the spatial distribution of plant area density.

In this chapter, we will focus on these abovementioned aspects rather than providing a comprehensive review of coherent structures in forest canopies. Our goal is to provide a synthesis of the novel aspects in research on coherent structures connected to the Waldstein experimental site from peer-reviewed publications and unpublished academic theses. The overarching objectives of analyzing coherent structures at this site are to improve our understanding of the dynamic turbulent exchange process at the plant-air interface, to reduce uncertainty in flux estimates of energy and matter, and to utilize the specific information about the exchange process to partition the net carbon exchange and gauge their impact on horizontal gradients and advection. The reader is referred to Appendix A to find information about the dates and experimental setups of field experiments and campaigns references in this chapter.

6.2 Materials and Methods

6.2.1 Detection Algorithm and Conditional Flux Computation

Here, we will briefly review the analytical method presented by Thomas and Foken (2005) to extract individual coherent structures from the time series of vector components and scalars by means of conditional sampling with the goal of computing their ensemble averaged statistics including duration and arrival frequency [Figs. 6.1 and 6.2 from Thomas and Foken (2005) and Zeeman et al. (2013), respectively]. In a subsequent step, the flux contribution of the ejection and sweep phases and that of the total coherent structure can be computed by applying a triple decomposition to the conditionally sampled time series (Antonia et al. 1987; Bergström and Högström 1989; Thomas and Foken 2007a).

As a first step, outliers in high-frequency time series are removed using a despiking method (Vickers and Mahrt 1997) with a window length of 300 s and an initial threshold criterion of 6.5 standard deviations (σ) repeated iteratively a maximum number of ten times to prepare the observed signals for analysis. This test detects and removes spikes while preserving the sharply localized instationarities commonly associated with coherent structures. Vector components are rotated using a sector-wise planar fit rotation (Wilczak et al. 2001) or double-rotation method (Thomas et al. 2013). Scalar time series are corrected for time lags compared to the vertical wind trace by shifting the time series until the vector-scalar covariance is maximized. To reduce the computation time needed for the subsequent wavelet analysis, signals are linearly block-averaged to a 2 Hz sampling resolution. This step does not significantly alter the statistical properties of the contained coherent structures as their time scales typically exceed tens of seconds. Any times series of quantity x is then normalized by subtracting the mean X and dividing by the

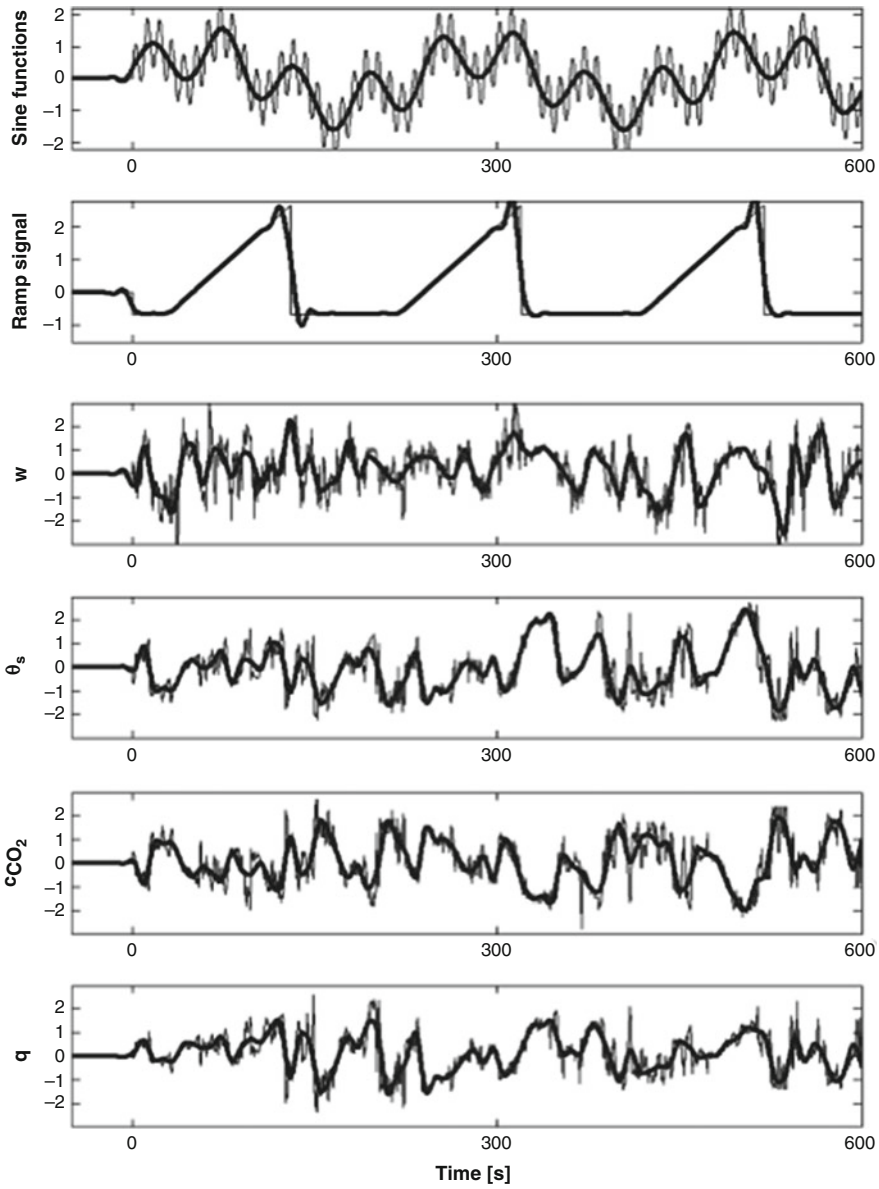

Fig. 6.1 Zero-padded extended and normalized original (*thin*) and low-pass filtered (*bold*) time series, which was block-averaged data to a resolution of 2 Hz for an artificial sinusoidal and ramp signals (*upper two panels*), and for observed time series of the vertical wind w, potential sonic temperature θ_s, carbon dioxide concentration c_{CO_2}, and specific humidity q (Adapted from Thomas and Foken (2005), with kind permission © Springer 2005, All rights reserved)

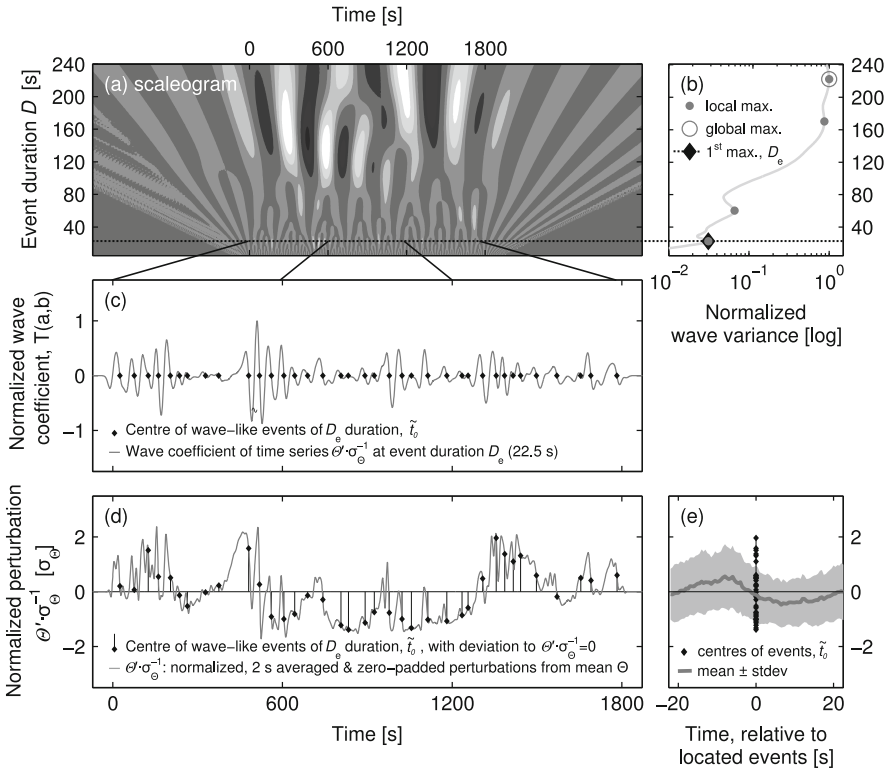

Fig. 6.2 An example of the application of the coherent structure detection methodology (Adapted from Zeeman et al. (2013), with kind permission © Springer 2013, All rights reserved) showing (**a**) the scalogram of wavelet coefficients expressed in brightness for the normalized air temperature perturbations (θ'), the (**b**) normalized wavelet variance and occurring variance maxima, the (**c**) normalized wavelet coefficients and the localization of events in time, the (**d**) time series of normalized air temperature perturbations θ' with indication of the localized events, and (**e**) the ensemble mean and standard deviation of the normalized θ' for these localized events within a $2D_e$ time window. The event duration D_e is determined from the first occurring variance maximum as shown in (**b**), which in this case is 22.5 s

standard deviation σ_x, except for the vertical wind w, which is normalized by $w_\sigma w^{-1}$ only. In a last step, time series are passed through a low-pass wavelet filter using the biorthogonal set of wavelets BIOR5.5 to filter out all small-scale high-frequency turbulence with event durations $D < D_c = 6.2$ s, where D_c is the critical event duration. D_c is determined from the turbulence spectrum and is thought to spectrally separate the small-scale stochastic turbulence from the longer-scale coherent structures. For practical purposes, it is assumed to be constant over time. The chosen value is in close agreement with that of other studies [$D_c = 5$ s in Lykossov and Wamser (1995), $D_c = 7$ s in Brunet and Collineau (1994), and $D_c = 5.7$ s in Chen and Hu (2003)]. We prefer this set of wavelet functions since its localization in frequency is better than, e.g., that of the HAAR wavelet (Kumar

and Foufoula-Georgiou 1994). The purpose of low-pass filtering the times series is to facilitate the detection of the spectral peak associated with coherent structures in the wavelet variance spectra.

After zero-padding the time series to avoid sharp instationarities at both ends, a continuous wavelet transformation is applied to the signal $f(t)$ using the complex Morlet wavelet as the analyzing mother wavelet (Fig. 6.2):

$$T_p(a,b) = \frac{1}{a^p}\int_{-\infty}^{+\infty} f(t)\Psi\left(\frac{t-b}{a}\right)dt \tag{6.1}$$

where $T_p(a,b)$ are the wavelet coefficients, a the dilation scale, and b the translation parameter and the normalization factor $p = 1$ in our case. The complex Morlet wavelet function is best localized in the frequency domain and well suited to determine the spectral peak associated with coherent structures. The duration scales D used for the wavelet transform ranges between 6 s and 240 s with a step width of 1 s. The event duration D can be linked to the dilation scale a of the wavelet transform (e.g., Collineau and Brunet 1993) by

$$D = \left(\frac{1}{2}\right)f^{-1} = \frac{a\pi}{f_s\omega^0_{\Psi_{1,1,0}}}, \tag{6.2}$$

where f is the natural frequency corresponding to the event duration, f the sampling frequency of the time series, and ω^0_ψ the center frequency of the mother wavelet function. For illustration purposes, the event duration D corresponds to half the period length of a sine function. The wavelet variance spectrum $W_p(a)$ is then computed as

$$W_p(a,b) = \int_{-\infty}^{+\infty} \left|T_p(a,b)\right|^2 db. \tag{6.3}$$

The characteristic event duration or temporal scale of coherent structures D_e was determined from scale *ae* at which *Wp*(*a*) exhibits its first spectral peak where the subscript "e" stands for event. Due to the local character of the wavelet transform, D_e corresponds to the characteristic event duration of coherent structures and not to their arrival frequency or periodicity (Howell and Mahrt 1997).

Applying another wavelet transformation at the previously determined event duration D_e using the Mexican-hat wavelet function allows for detection and extraction of individual coherent structures. Its wavelet coefficients $T_p(a_e, b)$ exhibit a zero-crossing along with a defined change in sign at the moment of occurrence (see Table 2 in Thomas and Foken 2005). Zero-crossings offer the advantage of being easily detected and avoid the need to define thresholds. The last step yields the individual moments of occurrence as well as the total number of detected coherent structures in a given time interval.

Expanding upon the classical Reynold's decomposition of any instantaneous variable into its temporal mean and perturbation thereof, $x = X + x'$, the pertur-

bations can be subdivided into a portion contributed by the coherent structures and small-scale stochastic background turbulence, $x' = x_{cs} + x_t$, arriving at a triple decomposition (Antonia et al. 1987; Bergström and Högström 1989). If one samples a signal $x(t)$ using the detected moments of occurrence of coherent structures as the sampling condition and subsequently applies a conditional averaging operator $\langle\rangle$overall subsamples, one obtains

$$\langle x' \rangle = \langle x_l \rangle \,, \tag{6.4}$$

where the right-hand term is the contribution of coherent structures to the fluctuation and $\langle x_t \rangle = 0$ under the assumption that coherent structures and small-scale turbulence are uncorrelated. Invoking Reynold's second postulate on the product of two arbitrary variables x and y and applying an averaging operator over the conditional sample given by

$$\widetilde{\langle x \rangle} = \frac{1}{2D_e} \int_{-D_e}^{+D} \langle x'(t) \rangle \, \delta t. \tag{6.5}$$

one can compute the total flux as

$$\widetilde{\langle x'y' \rangle} = \widetilde{\langle x' \rangle \langle y' \rangle} + \widetilde{\langle x_t y_t \rangle}, \tag{6.6}$$

where the left-hand term represents the total flux of the conditionally sampled region of the turbulent flow, the first term on the right-hand side is the flux contribution of coherent structures, and the second term is that of the small-scale stochastic turbulence. It is convenient to write Eq. 6.6 as

$$F(x,y)_{\text{tot}} = F(x,y)_{\text{cs}} + F(x,y)_t. \tag{6.7}$$

The flux contributions of the ejection phase F_{ej} and of the sweep phase F_{sw} are determined by applying the averaging operator in Eq. 6.5 within $[-D_{\text{e}}, 0]$ and $[0, +D_{\text{e}}]$, respectively, whereas $F_{\text{cs}} = F_{\text{ej}} + F_{\text{sw}}$. Assuming scalar similarity, all signals are sampled according to the events contained in the sonic temperature traces. This choice seems justified as (i) coherent structures were found to be well pronounced in T_s time series during day and night, and its use facilitates the comparison with other studies.

6.2.2 *Adapted Experimental Setup*

Diagnosing the vertical and horizontal flux of energy and matter and the degree of coupling in a forest canopy requires spatially explicit observations. These locations are expected to represent the flow dynamics in the main vertical canopy layers,

i.e., the sub-canopy layer or clear bole space, the tree crown layer, and the above-canopy layer, or to represent the horizontal canopy architecture for the main flow directions. The first will result in simultaneous measurements from sonic anemometers and trace gas analyzers in a vertical profile with at least three to five observational levels within the forest canopy (Thomas and Foken 2007a), with the latter adding horizontal transects of sub-canopy observations for the main wind directions (Serafimovich et al. 2011). Chapter 2 and Appendix A in this volume give an exhaustive description of the experimental setups used to investigate coherent structures at the Waldstein-Weidenbrunnen site, while here we mention only some key elements. Fast-response data from all sensors are collected at a sampling frequency f_s of at least 10 Hz to adequately capture the high-frequency stochastic turbulence. The time stamps of the data acquisition systems recording the fast-response data of the individual sensors need to be synchronized to be within $1/f_s$ to eliminate artifacts due to time lags. Only accurately recorded time stamps allow for tracking of individual coherent structures to determine their penetration depth with the goal of diagnosing vertical coupling and determination of their effective transporting velocities (Zeeman et al. 2013). For the WALDATEM 2003 and EGER IOP1 (2007) and IOP2 (2008) field campaigns (Chap. 1) at the Waldstein site, the wavelet detection algorithm described in Sect. 6.2.1 was run in the field in a quasi-online fashion to facilitate interpretation of the vertical and horizontal exchange.

6.3 Results and Discussions

6.3.1 Exchange Regimes for Vertical Coupling

It is conceivable to use two alternative approaches for the definition of exchange regimes from coherent structures analysis to indicate a coupling or decoupling between individual levels: the first approach is based upon the comparison of time-averaged flow statistics such as variances and covariances across levels in combination with the assumption that a coupled state requires coherent structures to contribute equally to the total flux at all levels (Thomas and Foken 2007a). Alternatively, one could track single coherent structures in signal traces across the vertical and horizontal to determine their penetration depth from their lagged moment of occurrence to infer mass and energy transport and thus coupling (Zeeman et al. 2013). Here, we will focus on the former since it was originally developed from observations at the Waldstein experimental site and has been used extensively to interpret the transport of passive and chemically reactive trace gases in the canopy layer.

A comparison of the flux contribution of the sweep and ejection phases across several observational levels in the canopy layer can be used to determine coupling or exchange regimes across the vertical (Thomas and Foken 2007a) or horizontal dimension (Serafimovich et al. 2011). Defining exchange regimes following the

statistical approach for conditionally sampled coherent structures requires the assumption that the flux contributed by coherent structures F_{cs} should be equal or similar throughout the portion of the canopy controlled by the coherent exchange. Furthermore, one may invert this argument and define levels as being decoupled if they show a significantly different flux contribution F_{cs}. In a strict sense, this assumption is valid solely for the momentum transfer as its only source is located above the canopy. For scalars, the canonical distribution of sinks and sources may alter the local height-dependent flux (Katul et al. 1995; Ruppert et al. 2006). However, one can argue that a single coherent structure can be interpreted as one spatially cohesive motion transporting momentum and scalars across the depth of the canopy. It may thus transport against local gradients arising from local sinks and sources and force the communication of air across the vertical and horizontal dimension. This may be particularly true for the strong sweep phase, which dominates the transport within the canopy (Thomas and Foken 2007b). Therefore, the coherent exchange F_{cs} is expected be less prone to modification of local sinks and sources than the total flux.

Based upon the turbulence observations from five levels in a vertical profile during the WALDATEM-2003 experiment, Thomas and Foken (2007a) proposed five distinctly different exchange regimes, which are listed below in order of increasing vertical coupling (see Fig. 6.3).

Wave Motion (Wa) The flow above the canopy is dominated by linear wave motion rather than by turbulence. These periods can be determined from the angle in the phase spectrum between the velocity component and scalar (Cava et al. 2004; Thomas and Foken 2007b). As linear waves usually produce very low to zero scalar flux, the vertical mass flux is assumed to be negligible and thus the above-canopy level to be decoupled from levels below.

Fig. 6.3 Conceptual depiction of the vertical exchange regimes in order of increasing degree of vertical coupling (*left to right*, adapted from Göckede et al. 2007) with kind permission © Authors 2007, CC License 4.0, All rights reserved: Wave motion, Decoupled canopy, Decoupled sub-canopy, Coupled sub-canopy by sweeps, Fully coupled canopy

Decoupled Canopy (Dc) The mass and energy transfer above the canopy is decoupled from that in the crown and sub-canopy. The flux contribution of the sweep and ejection phases between the above-canopy and within-canopy levels are opposite in sign. In general, there is no coherent transport of energy and matter into or out of the canopy.

Decoupled Sub-canopy (Ds) The above-canopy air communicates with the air in the crown layer, but the flux is decoupled from that in the sub-canopy. The region of coherent exchange is limited to the canopy, as the flux contribution of sweeps and ejections at the lower portion of the canopy and the sub-canopy is either opposite in sign or negligible.

Coupled Sub-canopy by Sweeps (Cs) Only the strong sweep motions force the mass and energy exchange between the above-canopy and sub-canopy layers. The flux contributions during the ejection phase between these two levels are either negligible or opposite in sign. This regime is a typical transition regime between Ds and C.

Fully Coupled Canopy (C) Coherent structures communicate across the entire depth of the roughness sublayer including the above-canopy, canopy, and the sub-canopy layers. Both ejection and sweep phases of coherent structures substantially contribute to the vertical mass and energy exchange.

As an example for the temporal pattern of exchange regimes, a case study over 4 days is presented in more detail (Fig. 6.4). Characteristic for this period is the consistent nocturnal linear wave regime (Wa). The generation was facilitated by (i) the strong radiative cooling leading to large negative buoyancy fluxes and (ii) a direction of the flow approaching over some hills southeast of the Waldstein (Thomas and Foken 2007b). The assigned exchange regime suggests a vertical decoupling between within-canopy and above-canopy air (Wa, Dc). Note that the relative flux contribution for scalars seems to increase during these regimes while it remains constant for momentum. However, large pseudo fluxes can be created by linear waves passing through a sensor fixed in space since the vector and scalar time series are phase-shifted but tightly correlated without actually inducing energy and mass transfer. During the day, the strong solar radiation in concert with moderate longitudinal winds (<3.5 ms^{-1} above the canopy) results in unstable stratification and vigorous thermally driven turbulence. During the first half of the day, the buoyancy flux at the lower portion of the canopy was weaker compared to the levels above supporting the determined regimes Ds and Dc. Only for the second half of the day, the canopy and sub-canopy were temporarily or fully coupled as indicated by the Cs and C regimes. The increase of the relative flux contribution of coherent structures of up to a ratio of 0.5 coincided with the transition of exchange regimes

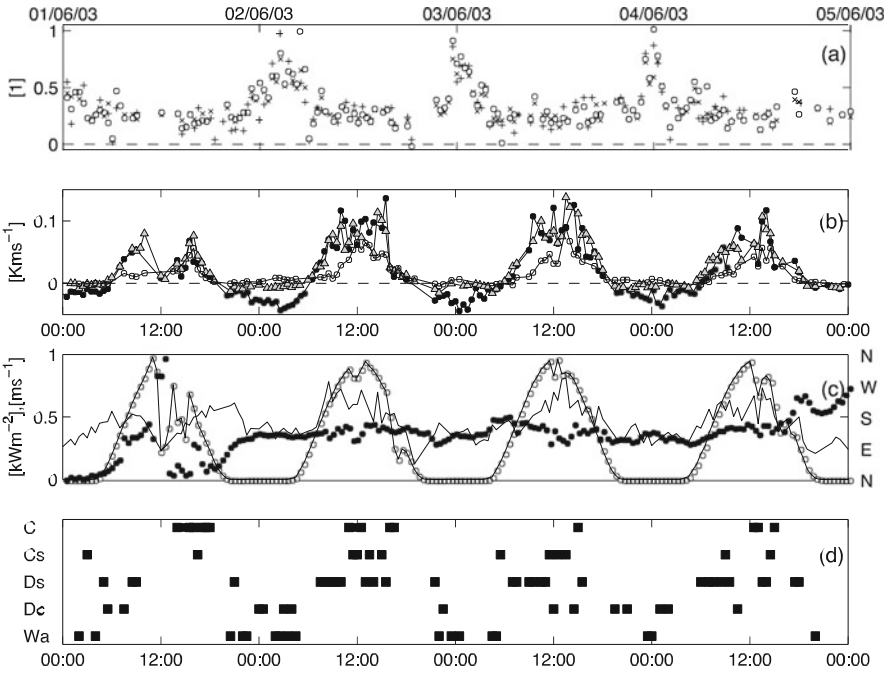

Fig. 6.4 Observations and exchange regimes for the period June 1–3 2003 during the WALDATEM-2003 conducted at the Waldstein experimental site (adapted from Thomas and Foken 2007a, with kind permission © Springer 2007, All rights reserved) (**a**) Relative flux contribution of coherent structures $F_{cs}F_{tot}{}^{-1}$ for carbon dioxide (*open circles*), buoyancy (*crosses*), and latent heat (*pluses*) above the canopy. (**b**) Kinematic buoyancy flux of coherent structures H_{cs} above the canopy (*filled circles*), the canopy top (*gray triangles*), and within the crown layer (*open circles*). (**c**) Friction velocity (*solid line*), incoming shortwave radiation (*open circles*), and wind direction (*filled circles*) above the canopy. (**d**) Characterization of the exchange regimes

from Dc to Ds. We presume that this moment may also coincide with the flushing of carbon dioxide-enriched air accumulated over the night. These flushing events were consistently preceded by a low net total flux contribution of coherent structures $F_{cs} = F_{sw} + F_{ej}$ with the sweep and ejection phases having flux contributions of similar magnitude but opposite sign. Sweeps transporting carbon dioxide-enriched air down into the canopy and ejections transporting carbon dioxide-enriched air accumulated during the night out of the sub-canopy lead to a vanishing net flux, while the mass transport and thus coupling are significant. The determination of exchange regimes therefore requires distinguishing between the sweep and ejection phases, while exchange regimes solely based upon the total net coherent flux may be misleading and unphysical.

6.3.2 Exchange Regimes for Horizontal Coupling

Serafimovich et al. (2011) extended the concept of vertical exchange regimes to the horizontal by analyzing observations from a horizontal transect of stations during the EGER experiment. Instead of evaluating the statistical contribution of the sweep and ejection phases to the vertical buoyancy flux across different levels, these horizontal exchange regimes utilize the horizontal flux contribution of the sweep and ejection phases to the buoyancy flux separated into an along-slope and cross-slope component. A linear model with slope α fitted to the flux contribution across an along- and cross-slope transects of stations is used as a reference.

Horizontally Coupled State (C_h) The flux contribution of both sweep and ejection phases is equal to or larger than the slope α. The mass and energy exchange between the transect station is considered to be coupled and air to communicate horizontally.

Horizontally Decoupled State (Dc_h) The flux contribution of both the sweep and ejection phases is either smaller than the reference α or opposite in sign. This state indicates a decoupled coherent mass and energy transport along the transect.

Figure 6.5 gives an example of analyzing both the vertical and horizontal exchange regimes for a 5-day period during the EGER experiment. At night, the airflow in the canopy and above-canopy layers is dominated by wave motions, which suggests a consistent decoupling. During the daylight hours, a full coupling or temporary coupling by sweeps was observed, with the transition periods indicating a partial coupling only. In contrast to the pronounced diurnal cycle of the vertical coupling, the horizontal coupling in the sub-canopy does not show any diurnal pattern but a distinct directional dependence. Cross-slope coupling was more often observed than along-slope coupling, which may be related to the fact that the cross-slope transect was aligned with the mean wind direction.

In a next step, Serafimovich et al. (2011) combined the information about both the horizontal and vertical exchange regimes into defining three general categories describing the bulk two-dimensional coupling:

Horizontal and Vertical Decoupling The sub-canopy is decoupled horizontally (Dc_h) indicating significantly different contribution of coherent structures to the horizontal turbulent fluxes across the transect. The sub-canopy flux is decoupled from the canopy and above-canopy layers (Dc, Ds). Coherent structures do not communicate momentum and mass across the canopy.

Horizontal Decoupling with Vertical Coupling Coherent structures penetrate deeply into the canopy causing a vertical communication of air, while they do not contribute to horizontal transport.

Full Horizontal and Vertical Coupling The sub-canopy air is coupled with that in the canopy and above-canopy air while coherent structures also force the horizontal communication of air. Coherent structures penetrate deeply into the canopy while they also propagate longitudinally.

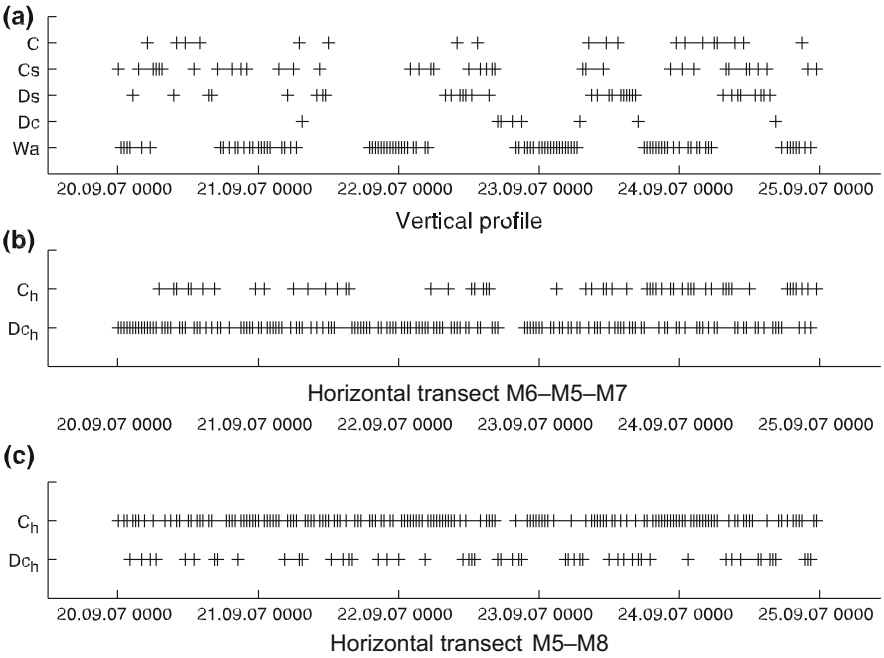

Fig. 6.5 Exchange regimes during a 5-day period during the EGER experiment at the Waldstein-Weidenbrunnen site (Adapted from Serafimovich et al. (2011) with kind permission © Springer 2011, All right reserved) across (**a**) the vertical profile covering the above-canopy, canopy, and sub-canopy layers, (**b**) the horizontal along-slope transect, and (**c**) the horizontal cross-slope transect. The ordinates denote the following exchange regimes: C, full coupling; Cs, coupling by sweeps; Ds, decoupled sub-canopy; Dc, decoupled canopy; Wa, wave motion; C_h, horizontally coupled sub-canopy layer; and Dc_h, horizontally decoupled sub-canopy layer

Applying this bulk 2-D classification system of the exchange to the observations yielded that the full horizontal and vertical coupling was observed more often for the along-wind than the cross-wind component of the horizontal coupling regime (See Fig. 8 and Table 3 in Serafimovich et al. 2011). This observation matches well with the notion that the mixing-layer coherent structures are vertically deep motions with a scale of approximately twice the canopy height and evolve and penetrate into the canopy as they propagate with the mean wind. As a result, these coherent structures appear as streaks in large eddy simulations when viewed from above (Kanani-Suhring and Raasch 2015). If the station spacing in the cross-wind direction exceeds that of the cross-wind length scale of the coherent structure, then these structures may not contribute spatially equal to the mass and energy transfer in the sub-canopy layer. In fact, when viewed in a coordinate system moving with the mean convective velocity at the canopy top, the pressure field may create quiescent buffer zones of low-velocity or stagnant air between the higher-velocity fluid pockets of the sweeps, which separate individual coherent structures from each other.

6.3.3 Implementation for Quantifying Daytime Sub-canopy Respiration

Thomas et al. (2008) developed a mathematical formulation for the calculation of the daytime respiration flux from high-frequency eddy-covariance data building upon a conceptual framework proposed by Scanlon and Albertson (2001). It is based upon conditionally sampling data organized into quadrants (e.g., Shaw et al. 1983). This method uses a modified relaxed eddy accumulation approach originally proposed by Businger and Oncley (1990) in combination with a hyperbolic threshold. The main assumption of the Thomas et al. (2008) method is that respiration signals originating in the sub-canopy carry a unique identifiable signature in the scalar-scalar cross-correlation between CO_2 and water vapor, which is maintained as they are transported through the canopy. This signature is distinguishable from other sinks and sources and allows for conditional sampling of the respiration signal and the calculation of a sub-canopy respiration CO_2 flux during daytime conditions. These respiration signals appear as excursions from the similarity-theory predictions for an actively photosynthesizing and transpiring plant canopy. Coherent structures play a key role in preserving this unique sub-canopy scalar-scalar fingerprint as only this flow mode can transport air vertically through the canopy in a coherent fashion on time scales short enough to avoid significant mixing with the air carrying the different scalar-scalar fingerprint of the main tree crown.

Combining the vertical coherent exchange regimes with the daytime respiration analysis yielded that the correlation coefficient between CO_2 and water vapor was found to be strongly negative with $r_{c,q} \approx -0.60$ for the fully coupled exchange regime (C) during daytime conditions. The signals progressively decorrelated with decreasing vertical coupling from exchange regime Cs to Dc and eventually arrived at a positive correlation of $r_{c,q} \approx 0.35$ for the Wa regime. A strongly negative correlation indicates that the scalar-scalar fingerprint of the tree crown dominates and that mixing is sufficiently strong to integrate overall sinks and sources in agreement with the definition of the C regime. In contrast, a positive correlation indicates that vertical mixing is negligible, which agrees with the definition of the Dc and Wa regimes.

Thomas et al. (2008) concluded that the method produces meaningful daytime estimates of sub-canopy respiration in stands of low and moderate density with little understory and negligible sub-canopy photosynthesis and fails in dense and multi-layered canopies such as the Waldstein-Weidenbrunnen site. To evaluate this conclusion, the method was applied to the EGER IOP1 (2007) data set collected at the turbulence tower in whose vicinity the forest is less dense (Chap. 2). The key difference between this and the original study for the Waldstein-Weidenbrunnen site (Thomas et al. 2008) was the application of a smaller $r_{c,q}$ threshold for the selection of respiration events as the decorrelation between CO_2 and water vapor was generally low.

An example of the quadrant analysis is shown in Fig. 6.6 separated for day- and nighttime conditions. For the 23 m observational level, the diurnal pattern in

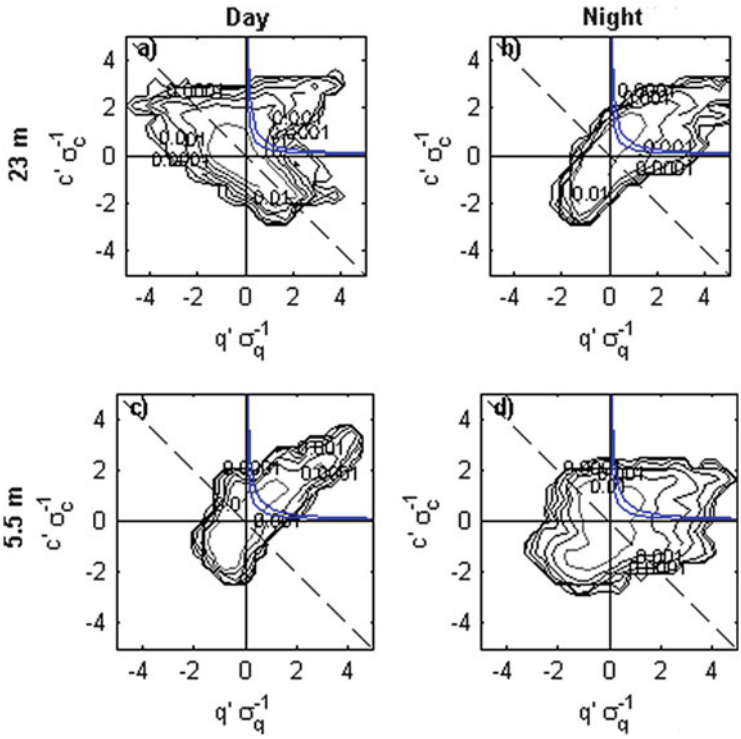

Fig. 6.6 Scalar probability density contour plots of normalized *c'* and *q'* fluctuations for daytime and nighttime conditions. (**a**), (**c**): September 21, 2007—13:30 to 14:00 h at 23 m and 5.5 m, respectively. (**b**), (**d**): September 21, 2007—22:00–22:30 h at 23 m and 5.5 m, respectively. The dashed line indicates a −1:1 relationship. Hyperbolic thresholds of $H = 0.25$ (*inner*) and $H = 0.5$ (*outer*) for the first quadrant are also shown

the scalar-scalar correlation agrees with that originally proposed by Thomas et al. (2008) switching signs during transition from the light to dark regime. In contrast, the data observed at 5.5 m show no diurnal change, which indicates that respiration is the dominant process in the sub-canopy. A good agreement between respiration estimates from the modified REA method and an independent Arrhenius-type model parameterized using nighttime data was found for the above-canopy observations (Fig. 6.7). In spite of the agreement, several limitations were found. During daytime conditions and especially around noon, the respiration signal becomes very weak and difficult to detect most likely because of the increased mixing during intense convective forcing of the turbulence. The vanishing respiration signals lead to gaps in the time series, which will need to be addressed. Other shortcomings include the model used to compute the proportionality factor in the REA formulation and the lack of an objective criterion to determine the hyperbolic threshold criterion (H). The method will fail for conditions when the $r_{c,q}$ is positive as found for the sub-canopy observations. Therefore, the method is restricted to systems close to the

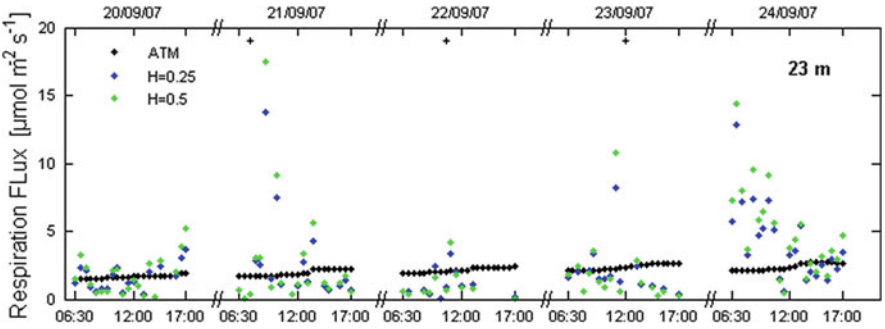

Fig. 6.7 Daytime respiration flux estimated at 23 m height. Fluxes are calculated by a conditional hyperbolic REA sampling with $H = 0.25$ (*blue*) and 0.5 (*green*). Each data point represents a 30-minute interval. The *black line* indicates the flux estimates derived by an Arrhenius-type model (ATM—Subke et al. 2004). *Black crosses* mark at the top indicate low data quality (Quality flag of 7–8 according to Foken et al. 2004)

canopy height. Nonetheless, this method provides a viable alternative to compute independent estimates of daytime respiration not available from the classical eddy-covariance method that can be utilized for comparison with extrapolating the nighttime fluxes using a simple temperature model. Thomas et al. (2013) showed that applying this method to compute the sub-canopy respiration as an indirect method to account for advective respiration losses under conditions of a decoupled sub-canopy significantly improves the annual net exchange estimate (NEE) for carbon by enhancing ecosystem respiration by up to 63 % (from 1233 to 2009 gC m^{-2} yr^{-1}).

6.3.4 *Implications for Spatial Heterogeneity of Sub-canopy Carbon Dioxide Concentrations, Gradients, and Horizontal Advection*

The previous sections demonstrated that coherent structures are a major flow mode controlling the transport of air across the canopy volume. If one assumes that the penetration depth and strength of coherent structures depend on the local density of plant biomass, i.e., the architecture of the forest, acting as an efficient sink for momentum, then it is conceivable that the spatial variation of biomass creates a similarly variable pattern in coherent air exchange. Since the vertical gradient of CO_2 in forests is steep with differences between the forest floor and above the canopy amounting to several hundred parts per million, we hypothesize that the horizontal variability of the vertical coherent air exchange may create systematic pockets of lower and higher CO_2 concentration in the sub-canopy as a result of the varying degrees of mixing. These pockets then define stationary, i.e., temporally,

invariant gradients that may lead to significant and systematic horizontal advection when multiplied with a nonzero mean advective sub-canopy velocity. Hence, the forest canopy architecture itself may be an important driver for the spatial variability of the contribution of the individual terms of the canopy mass balance. To our knowledge, this phenomenon has not been included in the discussion of sub-canopy scalar and particularly CO_2 exchange, which is traditionally thought to be controlled by soil respiration rates and soil composition, temperature, and moisture (Staebler and Fitzjarrald 2004) or by gravitationally driven density currents on sloped surfaces (Aubinet et al. 2003). Similar investigations were done during The EGER field campaigns in 2007 and 2008 (Siebicke et al. 2012).

To test this hypothesis, the plant area index (PAI) as a relative measure of vertically integrated canopy density (Fig. 6.8) and its spatial gradient (Fig. 6.9) were mapped and compared against the sub-canopy CO_2 concentrations sampled in ten discrete locations indicated by the black dots (Fig. 6.10). It is evident that air sampled at one higher PAI location was relatively enriched (M5, Fig. 6.10b, for location numbers see Fig. 6.8) compared against that at a lower PAI site (M13, Fig. 6.10a) for dynamically stable stratification evaluated above the canopy. Here CO_2 concentrations were relatively depleted throughout the diurnal period. A possible explanation for the stationary high-CO_2 pockets is the limited turbulent diffusion which includes the coherent transport that may enhance the canopy density effects. A consistent relationship between PAI and mean CO_2 concentration perturbation for all ten sampling locations in the sub-canopy could not be established though; however, it was found that sampling locations with large PAI gradient (Fig. 6.7) – like M13 – had the longest duration and strongest amplitude of coherent structures similar to those found at the forest edge (Eder et al. 2013). Note, however, that the results for the two selected locations shown in Fig. 6.10 represent a large number of samples and thus lend some preliminary support to our initial hypothesis. Even though canopy density may be important in defining stationary scalar gradients and coherent transport, other drivers such as orientation of the local slope in relation to the direction of the approaching flow, variations in the above-canopy wind velocity, and the distribution of shortwave radiation, nutrients, and understory vegetation may exert additional control on the sub-canopy CO_2 transport. These results prompt future research at this site to include spatially explicit information about all potential drivers to establish causality and gain a mechanistic understanding.

6.4 Conclusions

The field experiments conducted at the Waldstein experimental site made a significant contribution to our understanding of the transport at the forest canopy air interface. Synthesizing the results from several intensive field campaigns conducted over a period of more than two decades prompts us to draw a set of general conclusions:

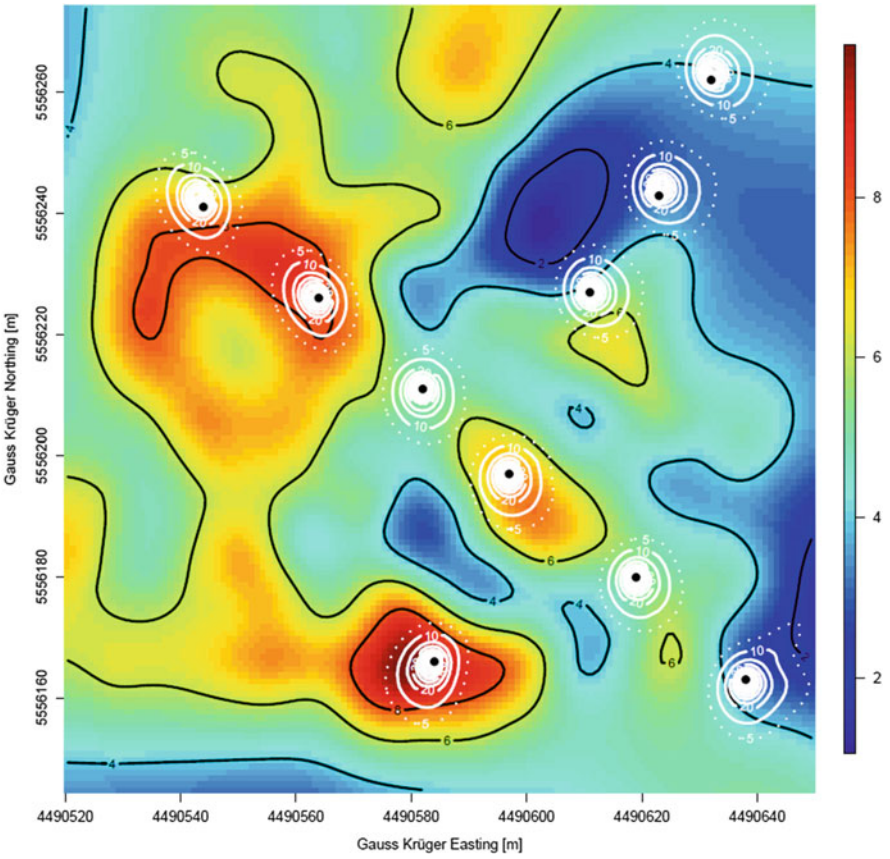

Fig. 6.8 Map of the plant area index (PAI) given as colors with *black* contour lines in a Gauss-Krueger coordinate system. *Black dots* indicate the positions of the sub-canopy air inlets (from NW to SE: M10, M11, M12, M5, M9, M8; from NE to SW: M14, M13, M6, M5, M7). *White isolines* are the relative contribution to the local footprint for stable stratification with a contour spacing of 10 %. The outermost area encloses the area from which 95 % of the flux originates. Raw PAI from E. Falge (pers.com.). Measurements were conducted during the EGER IOP1 experiment in 2007 (Siebicke 2011, published with kind permission of © Author 2011, All rights reserved)

- The vertical exchange regimes determined based upon the mean flux contribution of the sweep and ejection phases of the coherent structures (Thomas and Foken 2007a), which were observed across several vertical layers in the forest canopy, are physically and biologically meaningful. They offer means to diagnosing the degree and depth of the vertical coupling, which is crucial for the quality control and interpretation of trace gas and energy fluxes from tall vegetation (see also Chap. 12).
- The analysis of the coherent forest air exchange is key to understanding the fluxes of reactive trace gases and particulate matter (Foken et al. 2012; Chaps. 8 and 9)

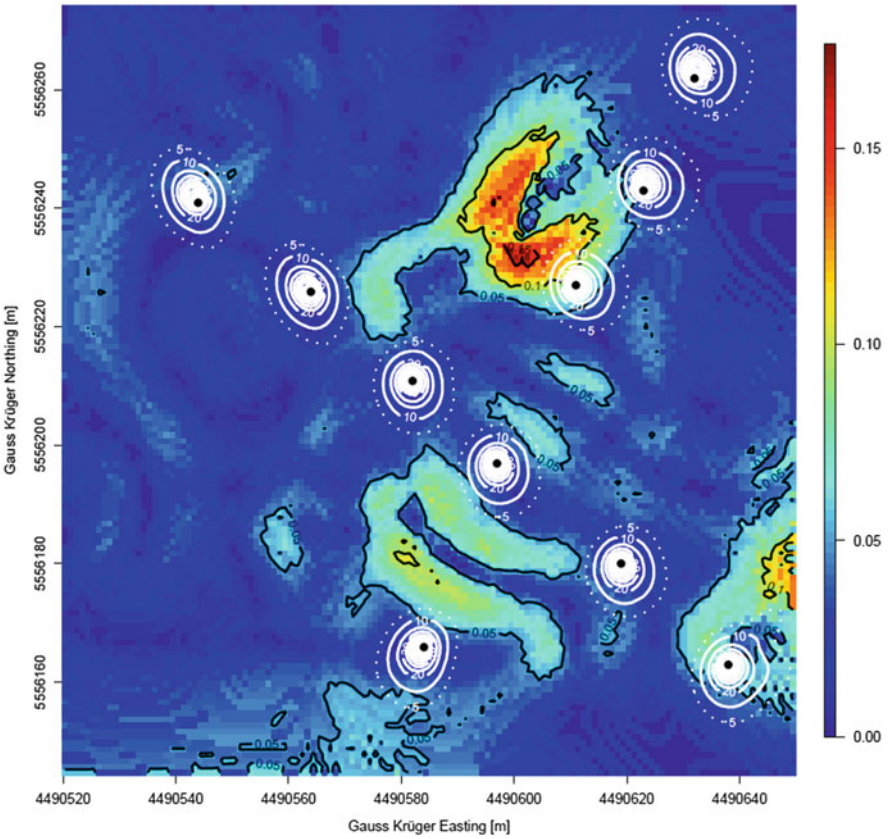

Fig. 6.9 Spatial gradients of PAI [$m^2\ m^{-2}\ m^{-1}$] of the data displayed in Fig. 6.6

as they exert an important control on the Damköhler number, which is defined as the ratio of the transporting time scale to that of the chemical reaction.

- Evaluating the full three-dimensional carbon and energy balance for a forest volume, which includes the vertical and horizontal flux divergences and advective component, requires a careful investigation of the degree of horizontal coupling along the direction of the mean mass flow (Serafimovich et al. 2011).
- The spatial distribution of plant biomass including leaf area may create stationary sub-canopy scalar gradients by exerting a systematic control on the penetration depth and horizontal movement of coherent structures. There is some support that transition areas from low to high PAI may be prone to strong vertical coherent transport and mixing of CO_2-depleted above-canopy air into the sub-canopy. However, these gradients lead to horizontal advection only if the horizontal mass flow is aligned with their spatial orientation.
- The analysis of advective mass transport without a detailed investigation of the coherent transport across the horizontal and the vertical may lead to a

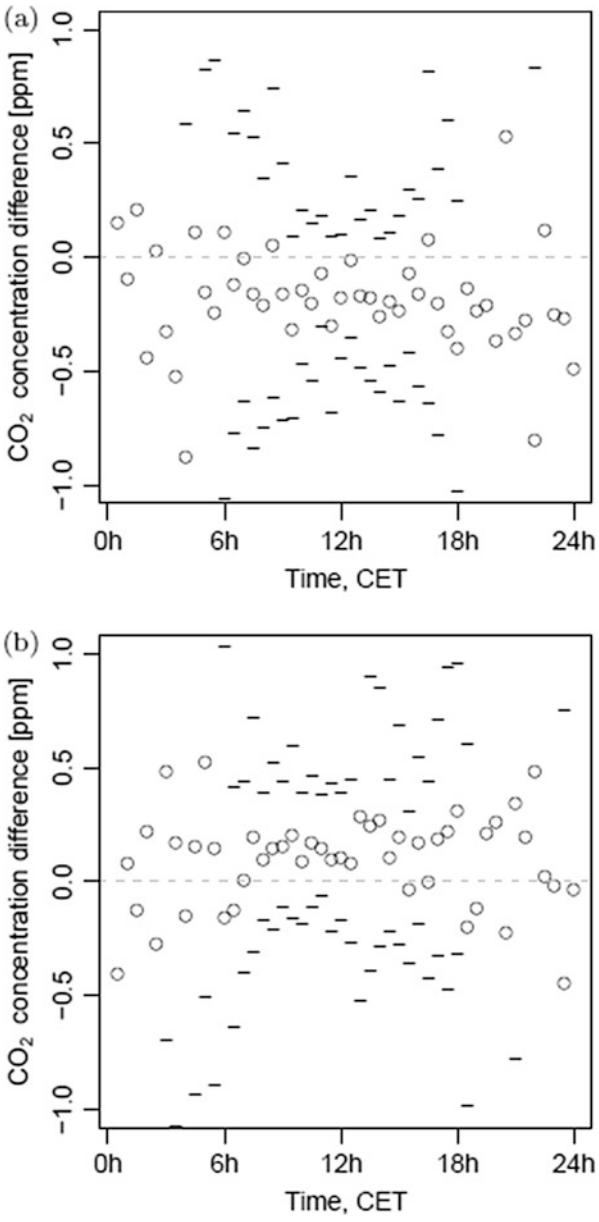

Fig. 6.10 Mean diurnal cycle of local CO_2 concentration perturbations for (**a**) a sample location with a low representative PAI (M13) and (**b**) a high representative PAI (M5) (**b**). *Circles* depict the mean, dashes the standard deviation of the individual 30-minute intervals. Number of observations: 1181 spanning the period 11th of June to 13th of July, 2008. For locations of stations M13 and M5, see caption of Fig. 6.6. (Siebicke 2011, published with kind permission of © Author 2011, All rights reserved)

misinterpretation of the observations (Aubinet et al. 2010), since horizontal decoupling and limited vertical mixing frequently coincide, particularly in higher PAI stands.

In spite of the significant progress in detecting, extracting, and quantifying coherent structures and understanding their role for vertical and horizontal exchange and coupling regimes, many questions remain open. From our perspective, the most pressing questions are connected to elucidating the links between spatial heterogeneity of the surface architecture and the spatiotemporal variability of the forest flow modes and forest mass and scalar transport. Explicit spatial information over several orders of magnitude from decimeter to hundreds of meters is required here to advance this field of research. To this end, the recently developed spatially continuous quasi three-dimensional sensing technology of fiber-optic distributed temperatures sensing (DTS) may offer novel experimental insights at the field scale (Thomas et al. 2012; Sayde et al. 2015). This technology is capable of sensing air temperature and wind speed at submeter resolution over a distance of hundreds of meters with a temporal resolution of seconds. It has the potential to yield the observations necessary to better diagnose energy and mass transport in the roughness-sublayer transport. An advantage of the spatially resolving information from DTS is that it eliminates the need for strong assumptions such as ergodicity, Taylor's hypothesis of frozen turbulence, and scaling laws such as the convective velocity scale (Finnigan 1979; Shaw et al. 1995).

References

Adrian RJ (2007) Hairpin vortex organization in wall turbulence. Phys Fluids. doi:10.1063/1.2717527

Antonia RA, Browne LWB, Bisset DK, Fulachier L (1987) A description of the organized motion in the turbulent far wake of a cylinder at low Reynolds numbers. J Fluid Mech 184:423–444

Aubinet M, Feigenwinter C, Heinesch B et al (2010) Direct advection measurements do not help to solve the night-time CO_2 closure problem: evidence from three different forests. Agric For Meteorol 150:655–664

Aubinet M, Heinesch B, Yernaux M (2003) Horizontal and vertical CO_2 advection in a sloping forest. Bound Lay Meteorol 108:397–417

Bergström H, Högström U (1989) Turbulent exchange above a pine forest. II. Organized structures. Bound Lay Meteorol 49:231–263

Brunet Y, Collineau S (1994) Wavelet analysis of diurnal and nocturnal turbulence above a maize canopy. In: Foufoula-Georgiou E, Kumar P (eds) Wavelets in geophysics. Academic Press, San Diego, pp 129–150

Businger JA, Oncley SP (1990) Flux measurement with conditional sampling. J Atmos Ocean Technol 7:349–352

Cava D, Giostra U, Siqueira M, Katul G (2004) Organised motion and radiative perturbations in the nocturnal canopy sublayer above an even-aged pine forest. Bound Lay Meteorol 112:129–157

Chen J, Hu F (2003) Coherent structures detected in atmospheric boundary-layer turbulence using wavelet transforms at Huaihe River Basin, China. Bound Lay Meteorol 107:429–444

Collineau S, Brunet Y (1993) Detection of turbulent coherent motions in a forest canopy. Part I: wavelet analysis. Bound Lay Meteorol 65:357–379

Eder F, Serafimovich A, Foken T (2013) Coherent structures at a forest edge: properties, coupling and impact of secondary circulations. Bound Lay Meteorol 148:285–308
Finnigan JJ (1979) Turbulence in waving wheat. II. Structure of momentum transfer. Bound Lay Meteorol 16:213–236
Foken T, Göckede M, Mauder M, Mahrt L, Amiro BD, Munger JW (2004) Post-field data quality control. In: Lee X et al (eds) Handbook of micrometeorology: a guide for surface flux measurement and analysis. Kluwer, Dordrecht, pp 181–208
Foken T, Meixner FX, Falge E et al (2012) Coupling processes and exchange of energy and reactive and non-reactive trace gases at a forest site—results of the EGER experiment. Atmos Chem Phys 12:1923–1950. doi:10.5194/acp-12-1923-2012
Gao W, Shaw RH, Paw U KT (1989) Observation of organized structures in turbulent flow within and above a forest canopy. Bound Lay Meteorol 47:349–377
Göckede M, Thomas C, Markkanen T et al (2007) Sensitivity of Lagrangian Stochastic footprints to turbulence statistics. Tellus B 59:577–586. doi:10.1111/j.1600-0889.2007.00275.x
Hommema SE, Adrian RJ (2003) Packet structure of surface eddies in the atmospheric boundary layer. Bound Lay Meteorol 106:147–170
Howell JF, Mahrt L (1997) Multiresolution flux decomposition. Bound Lay Meteorol 83:117–137
Kallistratova MA, Kouznetsov RD (2004) Systematization of experimental data on forms and scales of coherent structures in the atmosphere. In: 12th international symposium on acoustic remote sensing, Cambridge
Kanani-Suhring F, Raasch S (2015) Spatial variability of scalar concentrations and fluxes downstream of a clearing-to-forest transition: a large-eddy simulation study. Bound Lay Meteorol 155:1–27. doi:10.1007/s10546-014-9986-3
Katul G, Goltz SM, Hsieh CI et al (1995) Estimation of surface heat and momentum fluxes using the flux-variance method above uniform and non-uniform terrain. Bound Lay Meteorol 80:249–282
Kumar P, Foufoula-Georgiou E (1994) Wavelet analysis in geophysics: an Introduction. In: Foufoula-Georgiou E, Kumar P (eds) Wavelets in geophysics. Academic Press, San Diego, pp 1–43
Lykossov VN, Wamser C (1995) Turbulence intermittency in the atmospheric surface layer over snow-covered sites. Bound Lay Meteorol 72:393–409
Paw U KT, Brunet Y, Collineau S et al (1992) Evidence of turbulent coherent structures in and above agricultural plant canopies. Agric For Meteorol 61:55–68
Poggi D, Porporato A, Ridolfi L et al (2004) The effect of vegetation density on canopy sub-layer turbulence. Bound Lay Meteorol 111:565–587
Raupach MR, Finnigan JJ, Brunet Y (1996) Coherent eddies and turbulence in vegetation canopies: the mixing-layer analogy. Bound Lay Meteorol 78:351–382
Ruppert J, Thomas C, Foken T (2006) Scalar similarity for relaxed eddy accumulation methods. Bound Lay Meteorol: 39–63. doi:10.1007/s10546-005-9043-3
Sayde C, Thomas CK, Wagner J, Selker JS (2015) High-resolution wind speed measurements using actively heated fiber optics. Geophys Res Lett 42:10,064–10,073. doi:10.1002/2015GL066729
Scanlon TM, Albertson JD (2001) Turbulent transport of carbon dioxide and water vapor within a vegetation canopy during unstable conditions: identification of episodes using wavelet analysis. J Geophys Res D 106:7251–7262
Serafimovich A, Thomas CK, Foken T (2011) Vertical and horizontal transport of energy and matter by coherent motions in a tall spruce canopy. Bound Lay Meteorol 140:429–451. doi:10.1007/s10546-011-9619-z
Shaw RH, Brunet Y, Finnigan JJ, Raupach MR (1995) A wind tunnel study of air flow in waving wheat: two-point velocity statistics. Bound Lay Meteorol 76:349–376
Shaw RH, Paw U KT, Gao W (1989) Detection of temperature ramps and flow structures at a deciduous forest site. Agric For Meteorol 47:123–138
Shaw RH, Tavangar J, Ward DP (1983) Structure of the reynolds stress in a canopy layer. J Clim Appl Meteorol 22:1922–1931

Siebicke L (2011) Advection at a forest site—an updated approach. PhD Thesis, University of Bayreuth, Bayreuth, 113 pp

Siebicke L, Hunner M, Foken T (2012) Aspects of CO_2-advection measurements. Theor Appl Climatol 109:109–131

Staebler RM, Fitzjarrald DR (2004) Observing subcanopy CO_2 advection. Agric For Meteorol 122:139–156. doi:10.1016/j.agrformet.2003.09.011

Subke J-A, Buchmann N, Tenhunen JD (2004) Soil CO_2 fluxes in spruce forests—temporal and spacial variation, and environmental controls. In: Matzner E (ed) Biogeochemistry of forested catchments in a changing enivironment, a German case study. Ecological studies, vol 172. Springer, Berlin, pp 127–141

Thomas CK (2011) Variability of subcanopy flow, temperature, and horizontal advection in moderately complex terrain. Bound Lay Meteorol 139:61–81. doi:10.1007/s10546-010-9578-9

Thomas C, Foken T (2005) Detection of long-term coherent exchange over spruce forest using wavelet analysis. Theor Appl Climatol 80:91–104. doi:10.1007/s00704-004-0093-0

Thomas C, Foken T (2007a) Flux contribution of coherent structures and its implications for the exchange of energy and matter in a tall spruce canopy. Bound Lay Meteorol 123:317–337. doi:10.1007/s10546-006-9144-7

Thomas C, Foken T (2007b) Organised motion in a tall spruce canopy: temporal scales, structure spacing and terrain effects. Bound Lay Meteorol 122:123–147. doi:10.1007/s10546-006-9087-z

Thomas CK, Kennedy AM, Selker JS et al (2012) High-resolution fibre-optic temperature sensing: a new tool to study the two-dimensional structure of atmospheric surface layer flow. Bound Lay Meteorol 142:177–192. doi:10.1007/s10546-011-9672-7

Thomas C, Martin JG, Goeckede M et al (2008) Estimating daytime subcanopy respiration from conditional sampling methods applied to multi-scalar high frequency turbulence time series. Agric For Meteorol 148:1210–1229. doi:10.1016/J.Agrformet.2008.03.002

Thomas CK, Martin JG, Law BE, Davis K (2013) Toward biologically meaningful net carbon exchange estimates for tall, dense canopies: multi-level eddy covariance observations and canopy coupling regimes in a mature Douglas-fir forest in Oregon. Agric For Meteorol 173:14–27. doi:10.1016/j.agrformet.2013.01.001

Thomas C, Mayer J-C, Meixner FX, Foken T (2006) Analysis of low-frequency turbulence above tall vegetation using a Doppler sodar. Bound Lay Meteorol 119:563–587. doi:10.1007/s10546-005-9038-0

Vickers D, Mahrt L (1997) Quality control and flux sampling problems for tower and aircraft data. J Atmos Ocean Technol 14:512–526

Wilczak JM, Oncley SP, Stage SA (2001) Sonic anemometer tilt correction algorithms. Bound Lay Meteorol 99:127–150

Zeeman MJ, Eugster W, Thomas CK (2013) Concurrency of coherent structures and conditionally sampled daytime sub-canopy respiration. Bound Lay Meteorol 146:1–15. doi:10.1007/s10546-012-9745-2

Zhou J, Adrian RJ, Balachandar S, Kendall TM (1999) Mechanisms for generating coherent packets of hairpin vortices in channel flow. J Fluid Mech 387:353–396. doi:10.1017/S002211209900467X

Chapter 7
Dynamics of Water Flow in a Forest Soil: Visualization and Modelling

Christina Bogner, Britta Aufgebauer, Oliver Archner, and Bernd Huwe

7.1 Introduction

Soil water constitutes an important part of the water and energy cycles (e.g. Seneviratne et al. 2010). It influences the climate by affecting evaporation and surface energy fluxes and is coupled to precipitation patterns (e.g. Koster et al. 2004). Taylor et al. (2012), for example, analysed a global-scale data set and concluded that afternoon rainfall was more likely over soils that are drier than their surroundings. Soil moisture also plays an important role in the occurrence of droughts (Hirschi et al. 2011; Miralles et al. 2014), is considered a key factor in the context of climate change (Jung et al. 2010; Sheffield and Wood 2008) and is related to carbon fluxes (Suseela et al. 2012; Granier et al. 2007). Furthermore, the dynamics of soil water content and soil surface properties control the partitioning of precipitation into infiltration and runoff and thus affect groundwater recharge.

C. Bogner (✉) • B. Aufgebauer
Chair of Ecological Modelling, University of Bayreuth, 95440 Bayreuth, Germany

Bayreuth Center of Ecology and Environmental Research, University of Bayreuth, Bayreuth, Germany
e-mail: christina.bogner@uni-bayreuth.de

O. Archner
University of Bayreuth, BayCEER IT and Database Systems Group, 95440 Bayreuth, Germany

B. Huwe
University of Bayreuth, Soil Physics Group, 95440 Bayreuth, Germany

Bayreuth Center of Ecology and Environmental Research, University of Bayreuth, Bayreuth, Germany

T. Foken (ed.), *Energy and Matter Fluxes of a Spruce Forest Ecosystem*,
Ecological Studies 229, DOI 10.1007/978-3-319-49389-3_7

In the soil, water moves along the gradient of the soil water potential (Ψ_s, in general the sum of gravitational, pressure and osmotic potentials) that describes its energy state. In unsaturated soils the pressure potential is negative and is called matric potential. Models for water movement in the unsaturated (i.e. vadose) zone are most frequently based on the Richards equation—a combination of conservation of mass and Darcy's law for saturated flow. It relates changes of soil water content to changes in gradients of gravitational and pressure potentials. However, the flow description via the Richards equation does not account for every kind of water movement in soils. Actually, it fails to describe many types of preferential flow, in particular macropore flow. Preferential flow encompasses all phenomena where water moves faster than predicted by the Richards equation and bypasses a portion of the soil matrix (Hendrickx and Flury 2001). Although preferential flow is a common phenomenon, we still lack an adequate theory for its description (Beven and Germann 2013).

In this work we use the Richards equation to model the water flow in the vadose zone at the Coulissenhieb II site. We are aware of the critique of this approach and use it in the pragmatic sense of Beven and Germann (2013) not as a "physically based, but a convenient conceptual approximation". Richards equation is applicable to infiltration as well as moisture redistribution and sink terms like root water uptake can be readily incorporated. We assess the usefulness of the model by comparing its output with measurements, in our case matric potentials. While several methods of comparisons between a model and data exist (e.g. Mahecha et al. 2010), we choose here the (weighted) permutation entropy (Bandt and Pompe 2002; Fadlallah et al. 2013). It describes the complexity of a time series and can distinguish between regular (e.g. periodic) and random behaviour, for example. In contrast to many other measures of complexity, permutation entropy can be easily calculated for any arbitrary series of observations (Bandt and Pompe 2002). Our goal is to assess whether the model can reproduce the temporal structure of measured matric potentials in different depths.

The site Coulissenhieb II has been studied for several years. Our research is part of the DFG Research Unit 562 "Dynamics of soil processes under extreme meteorological boundary conditions" that analysed the effects of freeze/thaw and drying/rewetting events on soil processes (e.g. Matzner and Borken 2008; Borken and Matzner 2009). In this chapter, we focus on water fluxes in the vadose zone and (1) characterize the temporal dynamics of soil matric potentials, (2) compare the complexity of measured and modelled matric potentials and (3) estimate soil water fluxes by modelling and summarize our findings on preferential flow from previous studies.

7.2 Material and Methods

7.2.1 Measurements of Matric Potentials

The study site Coulissenhieb II (former Weidenbrunnen II) is part of the Lehstenbach catchment and is described in Chaps. 2 and 15. The acidic soils developed from a granitic parent material, have a sandy to loamy texture and an up to 15-cm thick mor-type organic layer. They vary gradually from Cambisols in the southern part of the study area to Podzols in the northern part (soil classification according to IUSS Working Group WRB 2015). The stone content fluctuates strongly within the site and with soil depth and ranges between a few percent in the topsoil and up to 75% in the subsoil (Gerstberger et al. 2004).

Several plots have been established by the DFG Research Unit 562 to study soil processes under extreme meteorological conditions (Fig. 7.1). Some of the plots were used for manipulation experiments like induced drought or freezing (e.g. Borken and Matzner 2009; Hentschel et al. 2009). In this chapter we concentrate on the control plots (denoted by C1, C2 and C3) that were run under environmental conditions without any manipulation. The control plots were instrumented with two (C1 and C3) or four (C2) replicates of tensiometers in 20, 40 and 90 cm depth, separated by a distance of approximately one meter. These devices measure the matric potential Ψ_m which results from the interaction (capillary forces and adsorption) between the soil matrix and water (e.g. Hillel 1998). The negative gradient of the matric potential is one of the important driving forces for soil water flow in an unsaturated soil. The data were recorded hourly.

On January 18, 2007 the storm Kyrill damaged the study site severely. At C1, for example, all trees had to be removed and the tensiometers at C2 were reinstalled further south. Due to the subsequent bark beetle attacks in 2008 further trees were felled. Accordingly, the density of trees decreased during the analysed period from January 1, 2006 to December 31, 2010 (Fig. 7.1). Since the trees were removed from Coulissenhieb II, the understory grasses and bushes dominate the vegetation cover.

7.2.2 Modelling Matric Potentials and Soil Water Fluxes

We modelled the soil water fluxes and the matric potentials with WHNSIM (Water Heat and Nitrogen Simulation Model, Huwe and Totsche 1995). This model has been used before to assess water fluxes in forest soils. Zirlewagen and von Wilpert (2001), for example, used WHNSIM to model water fluxes in a mixed-species stand of European beech (*Fagus sylvatica L.*), silver fir (*Abies alba Mill.*) and Norway spruce (*Picea abies (L.) Karst.*). Kaiser and Guggenberger (2005) studied the leaching of dissolved organic matter during storm flow in a 90-year-old European beech forest (*F. sylvatica L.*).

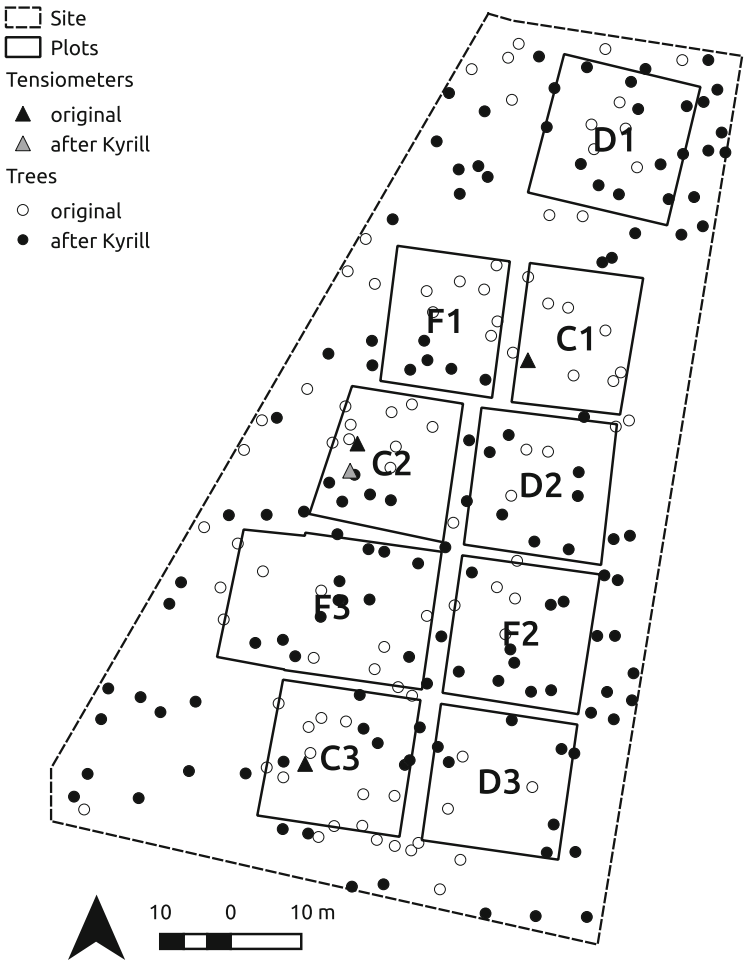

Fig. 7.1 Location of different plots and the tensiometers at the Coulissenhieb II site. C: control plots, D: drying/wetting and F: freezing/thawing. After the storm Kyrill in January 2007 and the subsequent bark beetle attacks, several trees were removed. The tensiometers at C2 were moved because the original location has been destroyed during the storm

WHNSIM solves the one-dimensional Richards equation for water flow in variably saturated soils numerically. The model is driven by atmospheric conditions at the upper boundary, namely precipitation, potential evapotranspiration and air temperature. These data were measured either at the Weidenbrunnen or the Pflanzgarten sites (see Chap. 2, Appendices A and B). The precipitation data were thoroughly corrected and the exact procedure is outlined in Chap. 3. The potential evapotranspiration was estimated from the Eddy-covariance data. We multiplied the measured values by the inverse of the correction factor used for gapfilling, which was made with a Priestley–Taylor approach (see Chap. 4). In 2007 some missing

values occurred and were filled by averages of corresponding time periods in 2008 and 2009. In WHNSIM, snow cover and snow melt were calculated with a simple day-degree approach. The control parameter for snow melt was adjusted based on field observations. In the study area, a snow cover usually develops in January and persists until March (Lischeid et al. 2002).

Inside the model, the soil profile is represented as a one-dimensional soil column with different compartments. They may or may not correspond to soil horizons and serve to discretize the soil column. To solve the Richards equation the model needs the soil-water retention curve and the hydraulic conductivity characteristics $K(\theta)$ as a product of the saturated hydraulic conductivity K_{sat} and the relative conductivity K_{rel} for every compartment. Zuber (2007) measured K_{sat} and the soil-water retention curve in the laboratory on undisturbed soil cores (100 cm^3, height 4 cm) sampled in 2005 at C2. The measurements of K_{sat} were done on a permeameter (Eijkelkamp Agrisearch Equipments, 2003) using the constant-head method. However, laboratory measurements are seldom representative for K_{sat} in the field. Therefore, we adjusted them manually in accordance with literature values to optimally fit the measured matric potentials, leaving the relative conductivities unchanged. The soil-water retention curves were determined with a pressure plate in a desiccation experiment and ignore possible hysteresis effects. We calculated the unsaturated hydraulic conductivity with the Millington–Quirk capillary bundle model that determines K_{rel} (Millington and Quirk 1961). WHNSIM was run in the forward mode without any inverse parameter estimation.

The lower boundary condition was set to free drainage. We estimated the initial values of matric potential in each compartment from the matric potentials in 20, 40 and 90 cm soil depth recorded by the first set of tensiometers at C1. WHNSIM allows for root water uptake and evaporation at the soil surface. The vertical root distribution was calculated from the data by Gaul et al. (2008). Actual root water uptake was determined based on potential transpiration rates in different depths and reduction functions that depend on the binding energy of soil water (i.e. matric potential).

7.2.3 Comparison Between Measured and Modelled Matric Potentials

Natural time series can exhibit behaviours of different degrees of complexity ranging from regular to random. The complexity of a natural time series results from the nonlinearity of underlying processes, their different interactions and possibly measurement noise. In our case, the measured matric potential is the result of the signal propagation from precipitation to throughfall to infiltration and reflects the influence of the soil hydraulic properties, evapotranspiration and possible measurement errors. In general, regular structure like periodic signals (e.g.

yearly cycle such as in evapotranspiration) is easier to model than irregular signals. Garland et al. (2014) even proposed to use complexity as a measure of predictability of a signal. We use complexity to compare the behaviour of the model output with measured matric potentials.

Different measures of complexity can be calculated, however, most of them are not defined for an arbitrary series or observations. To quantify the complexity of real-world time series Bandt and Pompe (2002) proposed to use the permutation entropy (PE). It works on the ranks (order of values) and not on the actual measured values.

We briefly introduce the permutation entropy. For more details the reader is referred to the original publication. We take an example time series $x = (3.1, 5.2, 7.9, -3.1, 4.0, 11.9, 0.3)$ and compare the direct neighbours by counting pairs for which $x_t < x_{t+1}$ and pairs for which $x_t > x_{t+1}$, t being the time index. In our example four pairs are of the first kind (we call them permutation 01) and two pairs are of the second kind (we call them permutation 10). With this information we calculate the permutation entropy of order $n = 2$ using the definition by Shannon (Shannon 1948)

$$H(n) = -\sum p(\pi) \log p(\pi) \tag{7.1}$$

where $p(\pi)$ are the probabilities of the permutations and summation runs over all permutations of order n. Thus in our case, using the relative frequencies of permutations 01 and 10 determined above, we get

$$H(2) = -(4/6)\log(4/6) - (2/6)\log(2/6) \approx 0.92 \tag{7.2}$$

This definition can be extended to higher orders n by comparing several consecutive values (i.e. for $n = 3$ we consider three consecutive values, for $n = 4$ four and so on). There are $n!$ permutations of order n and PE will vary between 0 and $\log(n!)$. By dividing it by $\log(n!)$ we obtain a normalized measure in the range $[0, 1]$. Obviously, the number of samples (consecutive values) that we can use to determine the permutations decreases for increasing n. Bandt and Pompe (2002) suggested that the length of the time series should be larger than $n!$ and recommend "for practical purposes [...] $n = 3, \ldots, 7$".

PE does not take the amplitude of the measured values into account. Fadlallah et al. (2013) argued in their work, however, that for tracking abrupt changes like peaks in time series amplitude information was important. They proposed a modification of the original PE by weighting the frequencies of permutations by the variance of the considered values. The weighted permutation entropy (WPE) is better suited for time series with large amplitudes in the signal compared to noise. WPE values close to zero indicate that a time series is regular (or monotonic) and contains only few different patterns. In contrast, very large values near one result from a high number of different patterns and are typical for noise.

In order to judge whether WHNSIM can adequately represent the complexity of the matrix potentials at the study site, we calculated the WPE of the measured and modelled time series. Comparable complexities would suggest that the model captures the relevant processes that generate the measured matric potentials. We used a window of 90 days that was slid by 1 day through the time series. This allows us to consider the temporal dynamics of the WPE and to identify time slots of agreement and disagreement between the model and the measurements. We set the order n of the entropy to four. This combination of window length and the order n is in-line with the guidelines in Bandt and Pompe (2002).

WHNSIM runs on a daily basis. In order to compare the model output with tensiometer data we calculated the daily median for every measured time series and cleaned the data manually where necessary (to remove obviously erroneous values). Furthermore, the data contained gaps that we closed before calculating the WPE. The longest time series with the smallest amount of gaps were recorded at C1 by the first set of tensiometers and we used these measurements for further analysis. To close the gaps we applied the Singular System Analysis (SSA) (Golyandina and Osipov 2007). SSA is a model-free technique to decompose a signal in a (small) number of interpretable components like trend, periodicities and noise (Broomhead and King 1986; Golyandina et al. 2001). Additionally, it can be used to infer missing values from the information contained in the time series. In this case, SSA has two adjustable parameters, the window length L that we sat to 100 and the maximum proportion of missing values τ that we fixed at 0.2. The calculations were done using the `R` package `simsalabim` (L. Gudmundsson, http://simsalabim.r-forge.r-project.org/).

7.2.4 Visualizing Soil Water Fluxes

Tensiometers provide local measurements over a small integration volume. Consequently, single devices cannot address the spatial variability of the unsaturated water flow in soils. In particular, tensiometers fail to capture preferential flow if their measurement volume does not contain preferential flow paths. Preferential flow in forest soils has been described by several authors (e.g. Moore et al. 1986; Sidle et al. 2001; Bundt et al. 2001). It is particularly pronounced along root macropores that might persist as preferential pathways for a long time. Hagedorn and Bundt (2002), for example, used isotope analysis to show that preferential flow paths in a structured forest soil were stable for decades. At a larger scale, Lin (2006) demonstrated the stability of soil moisture patterns and preferential flow pathways.

Because we lack adequate modelling tools, preferential flow is often assessed empirically in tracer experiments. A dye tracer solution is applied evenly onto the soil surface. After the tracer infiltration, horizontal or vertical soil profiles are excavated and photographed. The images of stained soils are then analysed to infer the dominant flow regime or the occurrence of preferential flow based on the morphology of flow patterns (e.g. Bogner et al. 2013).

To analyse the flow regime at Coulissenhieb II, Bogner et al. (2008, 2010, 2012, 2013) did several tracer experiments with Brilliant Blue FCF. They visualized and identified the main flow types using images of stained vertical soil profiles. Additionally, they sampled the soil in stained parts of the profile (preferential flow paths) and unstained parts (soil matrix) and analysed it for fine root distribution, bulk density, soil texture, exchangeable cations, total C, total N and pH. A detailed description of the sampling procedure, laboratory work and methods of data analysis can be found in the original publications.

7.3 Results and Discussion

7.3.1 Matric Potential

7.3.1.1 Temporal Variability

We measured matric potentials in the range of −534 and 21 hPa (20 cm depth), −419 and 42 hPa (40 cm depth) and −301 and 82 hPa (90 cm depth). Figure 7.2 shows the time series after data cleaning (i.e. median values with measurement errors removed manually). The tensiometers reacted quickly to rainfall and the dynamics between the different control plots was comparable. Over extended periods of time, the soil was remarkably wet and saturated regularly even in 20 cm depth, particularly after snow melt. Actually, during the installation of the tensiometers in 2005, groundwater entered the soil pits in approximately 90 cm depth (U. Hell, personal communication). This is in agreement with Weyer et al. (2014) who reported shallow groundwater at Coulissenhieb II.

The smallest matric potentials were recorded during dryer periods in summer. However, these values do not indicate any water stress, at least for the trees. The matric potentials in the forest floor were probably lower. In 90 cm depth, the tensiometers reacted less to the summer drying than in the upper soil. We attribute this to the distribution of roots at the study site. According to Gaul et al. (2008) the distribution of fine roots attained its maximum in the upper soil in the first 30 cm and decreased rapidly with depth. Therefore, soil drying due to root water uptake is more pronounced in the upper soil.

WHNSIM reproduced the overall level of the measured matric potentials in different depths (Fig. 7.3). Also large signals like snow melt or drying during summer were synchronous to measurements. In 90 cm depth, however, the modelled values appeared smoother (for example, December 2007–January 2008). Because the model was not specifically designed for the plot C1, we compared the distribution of the modelled matric potentials with all available data on the control plots. While the distributions were similar in 20 and 40 cm depths (Fig. 7.4), in 90 cm depth the model failed to reproduce the lowest matric potentials. However, in this depth, the variability between the tensiometers was large compared to the upper soil (Fig. 7.2).

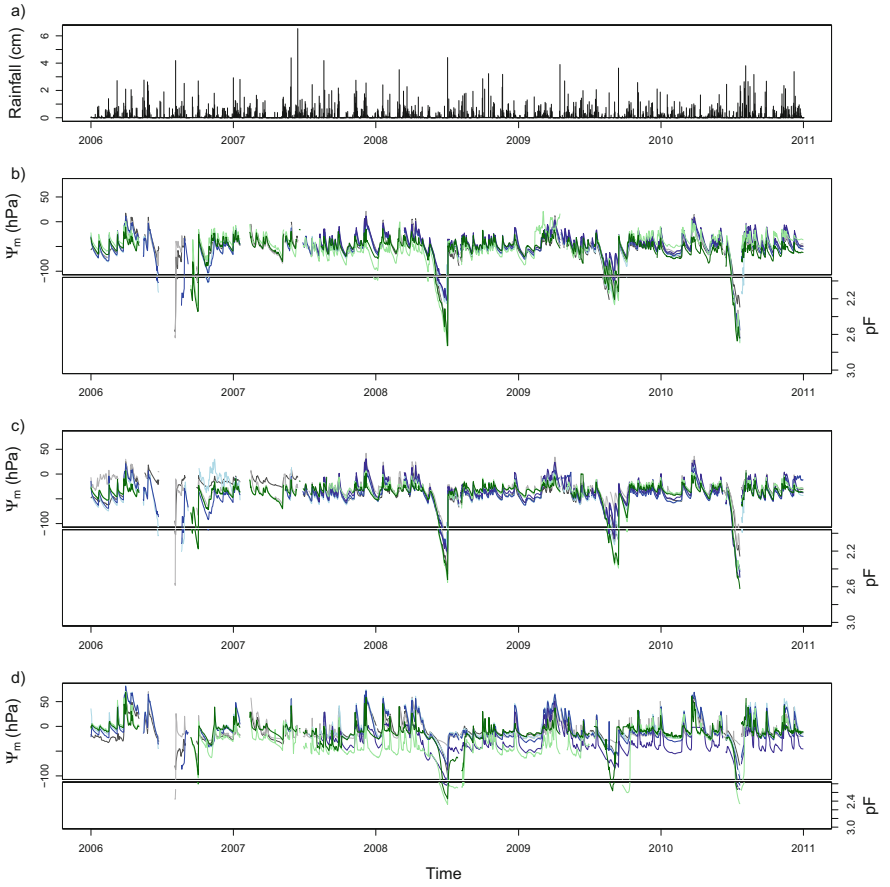

Fig. 7.2 Rainfall (**a**) and measured matric potentials in (**b**) 20 cm, (**c**) 40 cm and (**d**) 90 cm depth at different control plots. The *y*-axis of the matric potentials is split and very small values are shown as pF values (logarithm of the absolute value of the matric potential). *Colours* indicate different sets of tensiometers on different plots: *greys* on C1, *blues* on C2 and *greens* on C3

Therefore, the predicted values were still in the range of natural variability at the study site.

The storm Kyrill on 18 January 2007 was an extremely destructive event for the study site. The measured time series of 1 year before the storm were too short to infer any systematic changes in the matric potentials between the pre- and after-storm periods. However, shortly after the storm, the response of the tensiometers changed. Although the period from March to April 2007 was very dry, the matric potentials remained high. In contrast, WHNSIM predicted a drying of the soil comparable to similar environmental conditions in summer 2008, for example. This difference between the predicted soil drying and the measured matric potentials might be due

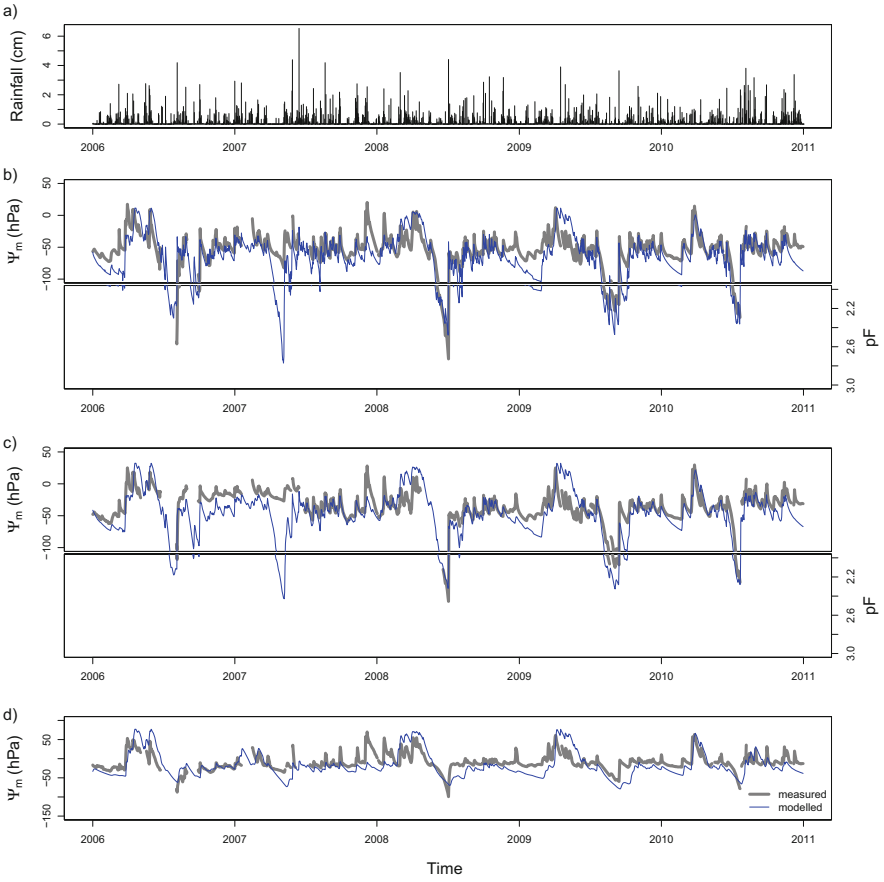

Fig. 7.3 Rainfall (**a**), measured and modelled matric potentials Ψ_m in (**b**) 20 cm, (**c**) 40 cm and (**d**) 90 cm depth. The *y*-axis of the matric potentials is split and very small values are shown as pF values (logarithm of the absolute value of the matric potential). The *grey line* shows the measured matric potentials at the control plot C1

to destroyed roots and therefore diminished root water uptake in the soil shortly after the storm.

After Kyrill and the felling of trees, the understory developed rapidly and dominates now the vegetation cover. Several studies indicate that evapotranspiration from the understory becomes important or even larger than the contribution of the overstory in old and thin stands (e.g. Black et al. 1989; Phillips and Oren 2001; Roberts 1983). Köstner et al. (2001) showed that under clear weather and good soil water availability up to 44% of evapotranspiration at Coulissenhieb could originate from the understory. We suppose that this contribution increased after the storm damages. Accordingly, after the root system of the understory developed the root water uptake could be comparable to the amounts before the storm.

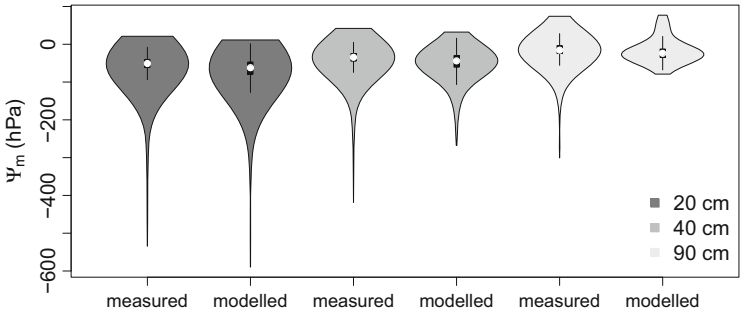

Fig. 7.4 Violinplots of measured and modelled matric potentials in different soil depths. Violinplots combine box plots with density plots. The *small black boxes* are standard box plots and the *white dot* indicates the median. The symmetrical areas around the box plots show smoothed density plots

7.3.1.2 Hydraulic Redistribution

WHNSIM runs on a daily basis. While it considers root water uptake in general, it cannot simulate any daily dynamics of the soil–root system like hydraulic redistribution, for example. Hydraulic redistribution is a passive process where water moves through plant roots from moist to dry soil according to the water potential gradient at the soil–root interface (e.g. Nadezhdina et al. 2010; Prieto et al. 2012). The movement of water between the soil and plant roots is controlled by the gradient between the soil water potential (Ψ_s) and the leaf water potential (Ψ_ℓ) in the plant. This gradient determines how roots take up water from soil during transpiration, for example, when Ψ_ℓ is lower than Ψ_s. However, when Ψ_s drops below Ψ_ℓ water can move in any direction in the soil–plant continuum from moist to dry soil through roots (e.g. Nadezhdina et al. 2010; Prieto et al. 2012).

Hydraulic redistribution results in daily cycles of Ψ_s. During the day it decreases because water moves from the soil to the atmosphere driven by a low Ψ_ℓ (transpiration). In contrast, during the night when Ψ_ℓ is larger than Ψ_s, this upwards movement can stop and water can move from moister soil parts to dryer soil parts thus increasing Ψ_s. If the osmotic potential is negligible and the measurements are taken at the same elevation, this signal is visible in the matric potential.

Figure 7.5 shows the daily variation of the matric potential at C1 and C2 from August 12 to August 19, 2009 in 20 cm depth. While the matric potential at C1 shows a typical pattern of hydraulic redistribution, there is no daily cycle at C2. This might be due to moister conditions (larger matric potential) and different distributions of roots in the vicinity of the tensiometers. This is in agreement with previously published results. Although hydraulic redistribution was found in different ecosystems, it is a temporally and spatially discontinuous process (e.g. Nadezhdina et al. 2006; Caldwell et al. 1998; Warren et al. 2007). Its occurrence depends on the spatial distribution of roots and temporal variation of soil moisture (it is more pronounced when the soil is dry). Spatial heterogeneity of root water

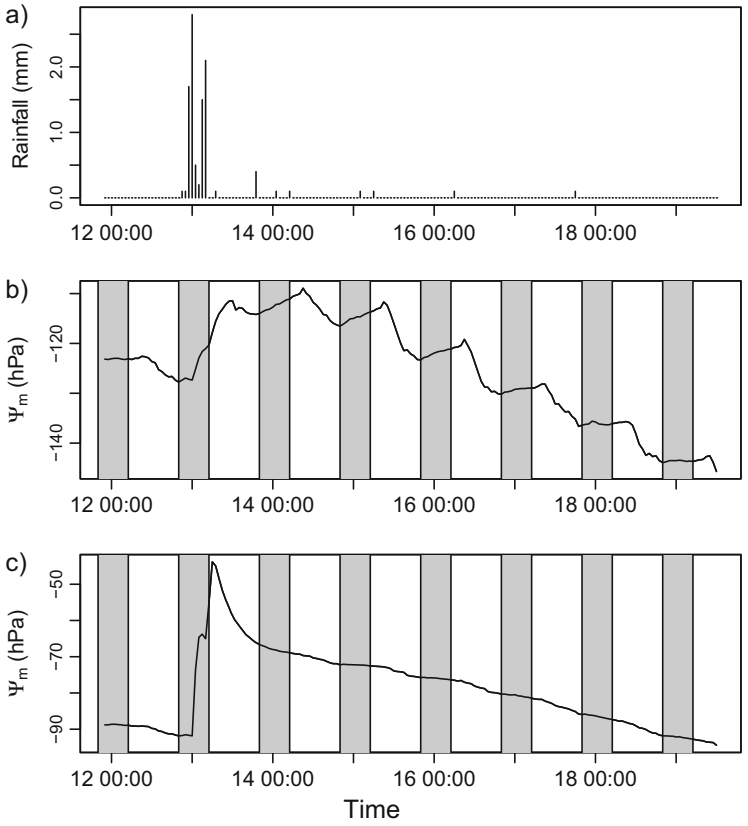

Fig. 7.5 Rainfall (**a**) and measured matric potentials in 20 cm depth at (**b**) C1 and (**c**) C2 from August 12 to August 19, 2009. *Grey stripes* show night time (20:00–05:00 CET). At C1 matric potential decreased during the day and increased during the night indicating hydraulic redistribution. Note the different ranges on the *y*-axis

uptake at Coulisenhieb II is also discussed in Chap. 15. The authors calculated principal components of the same tensiometer data studied here and related them to the evapotranspiration flux. They argue that the root water uptake at C1 might be larger than at C2.

7.3.1.3 Complexity of Measured and Modelled Matric Potentials

The WPE quantifies the complexity of a time series. Figure 7.6 compares the WPE of matric potentials measured at C1 with modelled values. In general, the drying of the soil (for example, during summer 2008) is characterized by a minimum of the matric potential and a drop of the WPE. This is in accordance with its definition and desired because these parts of the signal contain many monotonic (i.e. only

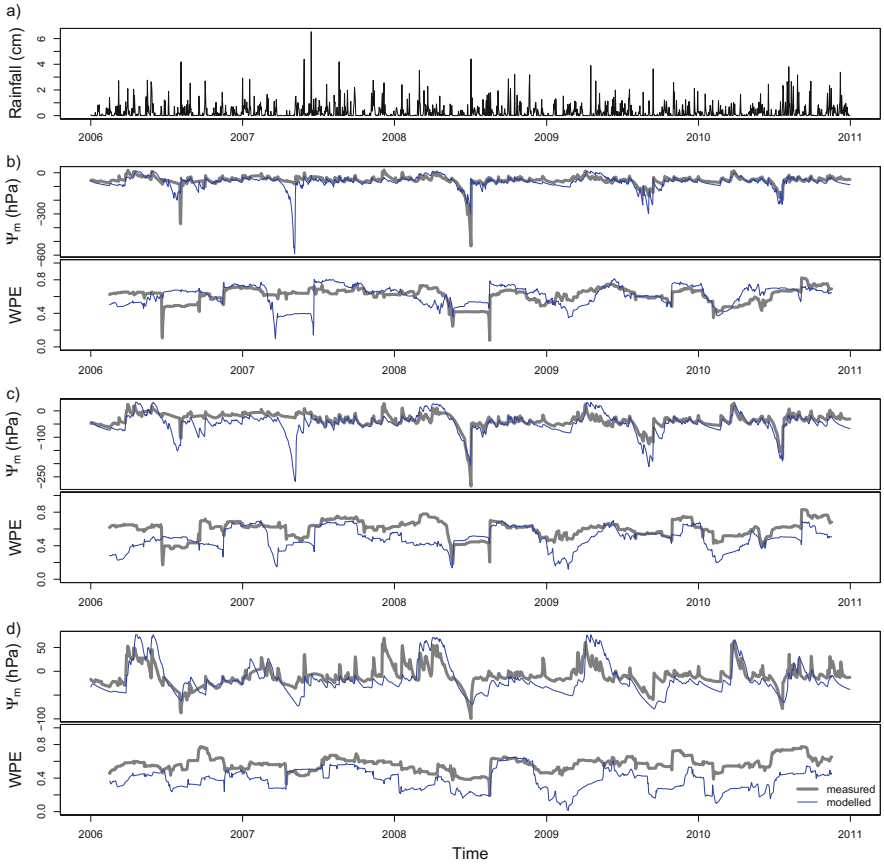

Fig. 7.6 Rainfall (**a**), measured and modelled matric potentials and their weighted permutation entropies in (**b**) 20 cm, (**c**) 40 cm and (**d**) 90 cm depth

descending and only ascending) patterns and thus exhibit low complexity (Fadlallah et al. 2013).

In 20 cm depth, the WPE of measured and modelled matric potentials are comparable, except the obvious disagreements in summer 2006 and 2007. The former is due to missing values that were filled by SSA. Because in 2006 the gap was particularly large and occurred during soil drying (a minimum in the signal), filling it was challenging. The disagreement in 2007 is probably due to diminished root water uptake after the storm Kyrill as discussed in Sect. 7.3.1. With increasing depth the WPEs of measured and modelled time series become more dissimilar. In particular, in 90 cm depth, the measured time series is more complex than predicted by WHNSIM which agrees with the general impression of a more damped modelled signal.

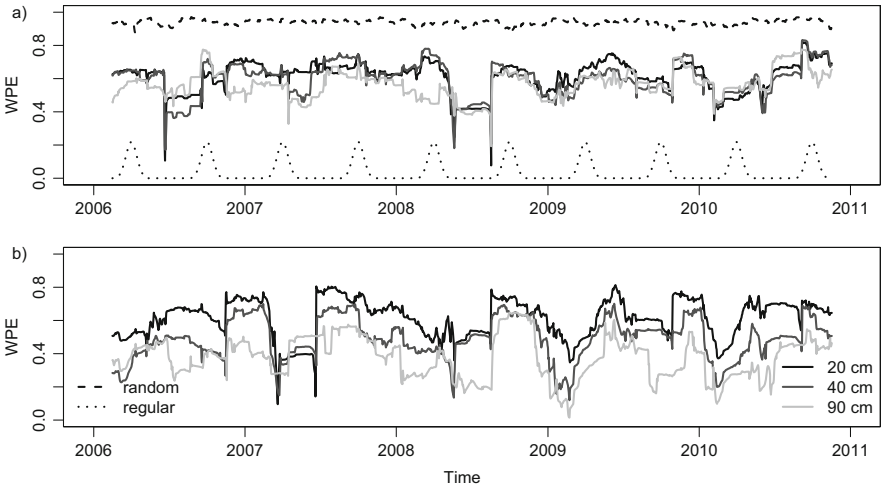

Fig. 7.7 Weighted permutation entropy of (**a**) measured and (**b**) modelled matric potentials in different soil depths. For comparison, the WPEs of a completely random signal (Gaussian white noise with standard deviation of 0.01) and a completely regular signal (sine wave with a period of 1 year) are included

While in the measured time series, the overall levels of the WPE are comparable between depths, they differ substantially in WNHSIM (Fig. 7.7). This indicates that the model cannot adequately represent the complexity of the matric potential in the deep soil and probably misses some important processes. However, WHNSIM captures the synchronicity between the tensiometers in different depths (albeit at different mean levels of complexity). Actually, the WPEs of the measured and the modelled time series vary in parallel.

7.3.2 Soil Water Fluxes

7.3.2.1 Flow Patterns at Profile Scale and Their Influence on Soil Chemistry

Figure 7.8 shows typical Brilliant Blue stained flow patterns in a soil profile at C1. Preferential flow is evident at this scale. According to Bogner et al. (2010) root macropores build the main preferential flow paths, particularly in the densely rooted upper soil (Fig. 7.8, 0–30 cm). Indeed, in the whole soil profile the fine root density is approximately 40–70% larger in the preferential flow paths than in the surrounding matrix (Bogner et al. 2010). A subsequent cluster analysis confirmed that the root density could best explain the morphology of flow patterns at Coulissenhieb II (Bogner et al. 2013).

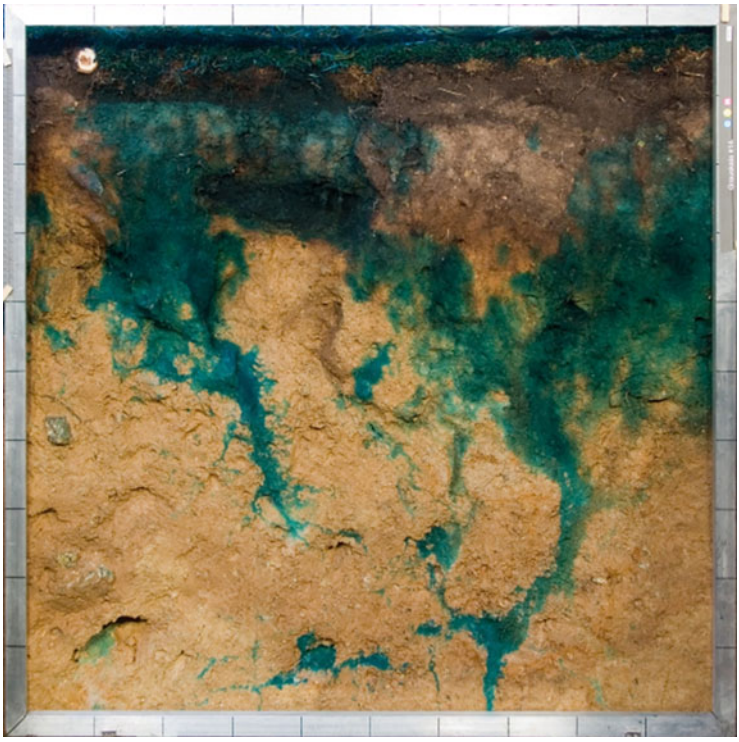

Fig. 7.8 Flow paths visualized in a tracer experiment with Brilliant Blue FCF at C1. The ticks on the frame are spaced by 10 cm

The dominant flow regime at Coulissenhieb II changes with depth. In the organic horizons, water infiltrates locally, probably through zones of small water repellency (Greiffenhagen 2005). Flühler et al. (1996) named this flow zone "attractor zone". Subsequently, water moves along root macropores through the "transmission zone" where preferential flow dominates. Below approximately 30 cm depth the root density decreases and the macropores end. Accordingly, water is forced to enter the soil matrix and the flow in this "dispersion zone" is dominated by heterogeneous matrix flow with large patterns (Bogner et al. 2010).

Preferential flow directly affects the soil chemistry. Bogner et al. (2012) found more total C and N in preferential flow paths compared to soil matrix, probably due to root exudates and transport of DOC from organic horizons. Similarly, the contents of Ca and Mg that originated from an accidental liming of the study area were larger due to transport via preferential paths. Additionally, the authors found more Fe and smaller pH values that they interpreted as hints at an enhanced podzolization.

7.3.2.2 Modelling Results and Preferential Flow at Catchment Scale

In the studied period, the modelled yearly soil water fluxes ranged between 66–88 cm, 56–81 cm and 55–74 cm in 20 cm, 40 cm and 90 cm depth, respectively. The smallest fluxes were calculated in 2006 and 2009, the largest in 2007. This is in accordance with the respective variation in precipitation and evapotranspiration (see Appendix B and Chap. 15). Because of the large hydraulic conductivity of the forest floor, WHNSIM produced very little surface runoff which is plausible for this flat area and consistent with field observations (Lischeid et al. 2002). Therefore, the deep drainage in 90 cm depth was approximately equal to precipitation minus evapotranspiration. Figure 7.9 depicts the seasonal dynamics of soil water fluxes. While the snow melt around April produced the largest fluxes, the smallest values were calculated in January–February due to snow cover and in June–July because of low precipitation. The median fluxes were comparable between depths, whereas the variability decreased with depth.

We lack independent flux measurements in the soil to evaluate the correctness of the calculated fluxes. While the overall balance seems plausible, we cannot evaluate the dynamics of the soil water fluxes or quantify the contribution of preferential flow. According to a previous study by Lischeid et al. (2002), the matric potentials at Coulissenhieb were representative for upslope sites in the Lehstenbach catchment, although different from wetlands. The authors stated that the shape of the matrix potential curves and the soil moisture curves were similar and resembled the catchment runoff, at least for a wetting-up period and large matric potentials (i.e. wet soils) in autumn. Thus, according to their findings, for wet periods where most of groundwater recharge and soil water flow occurs the flow regime at the catchment scale could be quantified as translatory (i.e. by displacement of old water) with little evidence for preferential flow.

These results seem in disagreement with the occurrence of preferential flow at the profile scale as described above. However, this can be explained with the connectivity of preferential flow paths at catchment scale. In their paper, Beven and Germann (2013) state that "we should not expect preferential flow lines to be continuous links between rainfall inputs and stream channels or rills". Water in preferential flow paths can therefore originate from locally saturated soil matrix. In other words, the displacement of old water into preferential flow paths can occur and contribute to runoff. This shows that the quantification of the importance of preferential flow at catchment scale remains a challenge.

7.4 Conclusions

Soil water is an essential climate variable and at heart of many ecosystem processes. The most frequently used approach to model soil water fluxes is based on the Richards equation as a convenient conceptual approximation that incorporates root water uptake. According to this concept, soil water moves along the gradient of

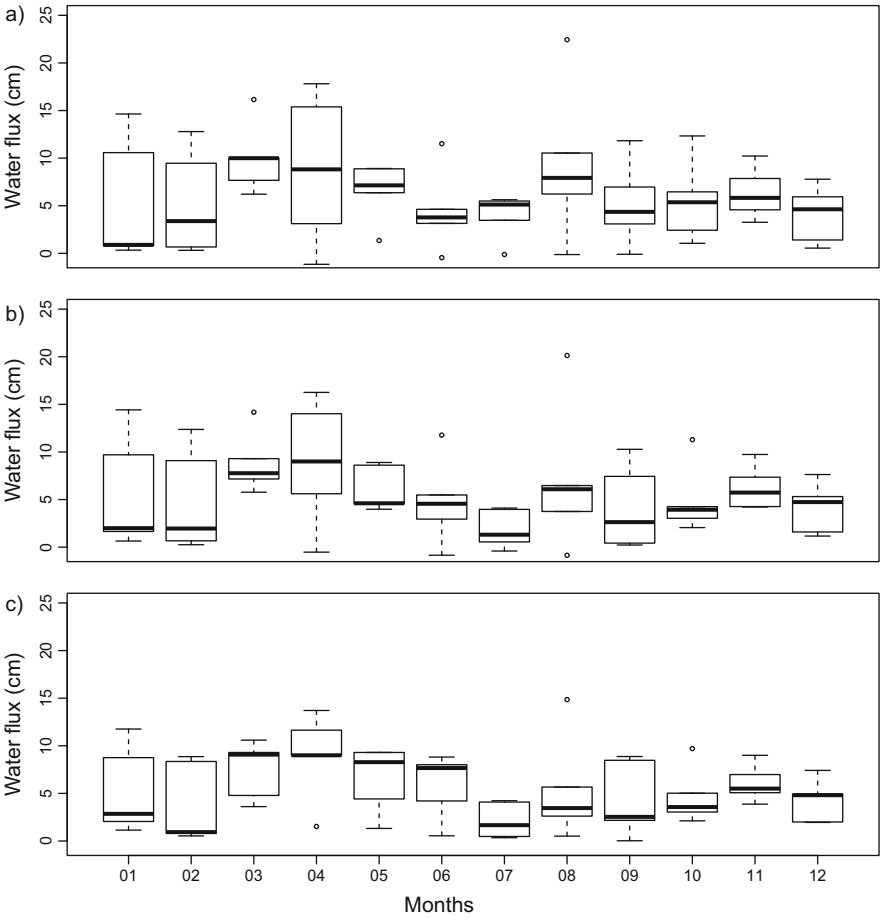

Fig. 7.9 Variability of modelled monthly soil water fluxes in (**a**) 20 cm, (**b**) 40 cm, (**c**) 90 cm depth in the period from January 1, 2006 to December 31, 2010

the matrix potential that can be measured with tensiometers. We have compared measured and modelled time series of matric potential using weighted permutation entropy. The model WHNSIM reproduced the overall level of matric potentials in all depths. However, while it captured the complexity of the measurements in the upper soil, the matrix potentials in 90 cm depth were less complex indicating a more regular and damped signal. This result suggests that WHNSIM misses some important processes at least in the deeper soil. However, the model reproduced the synchronicity of the matric potentials in different depths that was also observed in the measurements. Finally, the comparison of measured and modelled matric potential revealed reduced root water uptake after the storm Kyrill. We attribute this reduction to root destruction after the storm.

The soil water fluxes at Coulissenhieb II have a clear seasonal pattern. Large fluxes occur in spring during snow melt and small ones during dryer periods in summer. We could identify preferential flow in dye tracer experiments and attribute it mainly to macropore flow along root channels. It has a direct influence on soil chemistry and might enhance podzolization in preferential flow paths. While preferential flow can be visualized at profile scale at least by destructive experiments, its identification and quantification at the catchment scale remains challenging.

Acknowledgements We thank Uwe Hell, Andreas Kolb and Gerhard Müller for assistance in the field. Dr. Tobias Zuber contributed to the initial model setup. This research was supported by the German Science Foundation (DFG Research Unit 561, mainly Hu 636/11-2,3).

References

Bandt C, Pompe B (2002) Permutation entropy: a natural complexity measure for time series. Phys Rev Lett 88(17):174102

Beven K, Germann P (2013) Macropores and water flow in soils revisited. Water Resour Res 49(6):3071–3092

Black T, Kelliher F, Wallace J, Stewart J, Monteith J, Jarvis P (1989) Processes controlling understorey evapotranspiration [and discussion]. Philos Trans R Soc Lond B Biol Sci 324(1223):207–231

Bogner C, Wolf B, Schlather M, Huwe B (2008) Analysing flow patterns from dye tracer experiments in a forest soil using extreme value statistics. Eur J Soil Sci 59(1):103–113

Bogner C, Gaul D, Kolb A, Schmiedinger I, Huwe B (2010) Investigating flow mechanisms in a forest soil by mixed-effects modelling. Eur J Soil Sci 61:1079–1090

Bogner C, Borken W, Huwe B (2012) Impact of preferential flow on soil chemistry of a podzol. Geoderma 175–176:37–46

Bogner C, y Widemann BT, Lange H (2013) Characterising flow patterns in soils by feature extraction and multiple consensus clustering. Ecol Inform 15:44–52

Borken W, Matzner E (2009) Reappraisal of drying and wetting effects on c and n mineralization and fluxes in soils. Glob Chang Biol 15(4):808–824

Broomhead D, King GP (1986) Extracting qualitative dynamics from experimental data. Physica D 20(2-3):217–236

Bundt M, Widmer F, Pesaro M, Zeyer J, Blaser P (2001) Preferential flow paths: biological 'hot spots' in soils. Soil Biol Biochem 33(6):729–738

Caldwell MM, Dawson TE, Richards JH (1998) Hydraulic lift: consequences of water efflux from the roots of plants. Oecologia 113(2):151–161

Fadlallah B, Chen B, Keil A, Príncipe J (2013) Weighted-permutation entropy: a complexity measure for time series incorporating amplitude information. Phys Rev E 87(2):022911

Flühler H, Durner W, Flury M (1996) Lateral solute mixing processes - a key for understanding field-scale transport of water and solutes. Geoderma 70(2-4):165–183

Garland J, James R, Bradley E (2014) Model-free quantification of time-series predictability. Phys Rev E 90(5):052910

Gaul D, Hertel D, Borken W, Matzner E, Leuschner C (2008) Effects of experimental drought on the fine root system of mature Norway spruce. For Ecol Manag 256(5):1151–1159

Gerstberger P, Foken T, Kalbitz K (2004) The Lehstenbach and Steinkreuz catchments in ne Bavaria, Germany. In: Matzner E (ed) Biogeochemistry of forested catchments in a changing environment. Ecological studies, vol 172. Springer, Berlin, Heidelberg, pp 15–44

Golyandina N, Osipov E (2007) The "Caterpillar"-SSA method for analysis of time series with missing values. J Stat Plan Inference 137(8):2642–2653

Golyandina N, Nekrutkin V, Zhigljavsky AA (2001) Analysis of time series structure: SSA and related techniques. CRC, Boca Raton, FL

Granier A, Reichstein M, Bréda N, Janssens I, Falge E, Ciais P, Grünwald T, Aubinet M, Berbigier P, Bernhofer C et al (2007) Evidence for soil water control on carbon and water dynamics in European forests during the extremely dry year: 2003. Agric For Meteorol 143(1):123–145

Greiffenhagen A (2005) Einfluss der Humusauflage auf das Benetzungsverhalten und den Wasserhaushalt von Kiefernstandorten. PhD thesis, Institut für Ökologie, Technische Universität Berlin, Germany

Hagedorn F, Bundt M (2002) The age of preferential flow paths. Geoderma 108(1-2):119–132

Hendrickx JMH, Flury M (2001) Uniform and preferential flow mechanisms in the vadose zone. In: Council NR (ed) Conceptual models of flow and transport in the fractured vadose zone. National Academy Press, Washington, DC, pp 149–187

Hentschel K, Borken W, Zuber T, Bogner C, Huwe B, Matzner E (2009) Effects of soil frost on nitrogen net mineralization, soil solution chemistry and seepage losses in a temperate forest soil. Glob Chang Biol 15(4):825–836

Hillel D (1998) Environmental soil physics. Academic, New York

Hirschi M, Seneviratne SI, Alexandrov V, Boberg F, Boroneant C, Christensen OB, Formayer H, Orlowsky B, Stepanek P (2011) Observational evidence for soil-moisture impact on hot extremes in southeastern Europe. Nat Geosci 4(1):17–21

Huwe B, Totsche K (1995) Deterministic and stochastic modelling of water, heat and nitrogen dynamics on different scales with whnsim. J Contam Hydrol 20(3):265–284

IUSS Working Group WRB (2015) World Reference Base for Soil Resources 2014, update 2015. International soil classification system for naming soils and creating legends for soil maps. World Soil Resources Reports No. 106. FAO, Rome

Jung M, Reichstein M, Ciais P, Seneviratne SI, Sheffield J, Goulden ML, Bonan G, Cescatti A, Chen J, De Jeu R et al (2010) Recent decline in the global land evapotranspiration trend due to limited moisture supply. Nature 467(7318):951–954

Kaiser K, Guggenberger G (2005) Storm flow flushing in a structured soil changes the composition of dissolved organic matter leached into the subsoil. Geoderma 127(3):177–187

Koster RD, Dirmeyer PA, Guo Z, Bonan G, Chan E, Cox P, Gordon C, Kanae S, Kowalczyk E, Lawrence D et al (2004) Regions of strong coupling between soil moisture and precipitation. Science 305(5687):1138–1140

Köstner B, Tenhunen J, Alsheimer M, Wedler M (2001) Controls on evapotranspiration in a spruce forest catchment of the Fichtelgebirge. In: Tenhunen J, Lenz R, Hantschel R (eds) Ecosystem approaches to landscape management in Central Europe. Ecological Studies, vol 147. Springer, Berlin, Heidelberg, pp 377–415

Lin H (2006) Temporal stability of soil moisture spatial pattern and subsurface preferential flow pathways in the shale hills catchment. Vadose Zone J 5(1):317–340

Lischeid G, Kolb A, Alewell C (2002) Apparent translatory flow in groundwater recharge and runoff generation. J Hydrol 265(1):195–211

Mahecha MD, Reichstein M, Jung M, Seneviratne SI, Zaehle S, Beer C, Braakhekke MC, Carvalhais N, Lange H, Le Maire G, Moors E (2010) Comparing observations and process-based simulations of biosphere-atmosphere exchanges on multiple timescales. J Geophys Res 115(G2):G02003

Matzner E, Borken W (2008) Do freeze-thaw events enhance c and n losses from soils of different ecosystems? A review. Eur J Soil Sci 59(2):274–284

Millington RJ, Quirk JP (1961) Permeability of porous solids. Trans Faraday Soc 57:1200–1207

Miralles DG, Teuling AJ, van Heerwaarden CC, de Arellano JVG (2014) Mega-heatwave temperatures due to combined soil desiccation and atmospheric heat accumulation. Nat Geosci 7(5):345–349

Moore I, Burch G, Wallbrink P (1986) Preferential flow and hydraulic conductivity of forest soils. Soil Sci Soc Am J 50(4):876–881

Nadezhdina N, Čermák J, Gašpárek J, Nadezhdin V, Prax A (2006) Vertical and horizontal water redistribution in norway spruce (*Picea abies*) roots in the Moravian upland. Tree Physiol 26(10):1277–1288

Nadezhdina N, David TS, David JS, Ferreira MI, Dohnal M, Tesař M, Gartner K, Leitgeb E, Nadezhdin V, Cermak J et al (2010) Trees never rest: the multiple facets of hydraulic redistribution. Ecohydrology 3(4):431–444

Phillips N, Oren R (2001) Intra and inter-annual variation in transpiration of a pine forest. Ecol Appl 11(2):385–396

Prieto I, Armas C, Pugnaire FI (2012) Water release through plant roots: new insights into its consequences at the plant and ecosystem level. New Phytol 193(4):830–841

Roberts J (1983) Forest transpiration: a conservative hydrological process? J Hydrol 66(1):133–141

Seneviratne SI, Corti T, Davin EL, Hirschi M, Jaeger EB, Lehner I, Orlowsky B, Teuling AJ (2010) Investigating soil moisture–climate interactions in a changing climate: a review. Earth Sci Rev 99(3):125–161

Shannon CE (1948) A mathematical theory of communication. Bell Syst Tech J 27:379–423

Sheffield J, Wood EF (2008) Global trends and variability in soil moisture and drought characteristics, 1950-2000, from observation-driven simulations of the terrestrial hydrologic cycle. J Climate 21(3):432–458

Sidle RC, Noguchi S, Tsuboyama Y, Laursen K (2001) A conceptual model of preferential flow systems in forested hillslopes: evidence of self-organization. Hydrol Process 15(10):1675–1692

Suseela V, Conant RT, Wallenstein MD, Dukes JS (2012) Effects of soil moisture on the temperature sensitivity of heterotrophic respiration vary seasonally in an old-field climate change experiment. Glob Chang Biol 18(1):336–348

Taylor CM, de Jeu RA, Guichard F, Harris PP, Dorigo WA (2012) Afternoon rain more likely over drier soils. Nature 489(7416):423–426

Warren JM, Meinzer FC, Brooks JR, Domec JC, Coulombe R (2007) Hydraulic redistribution of soil water in two old-growth coniferous forests: quantifying patterns and controls. New Phytol 173(4):753–765

Weyer C, Peiffer S, Schulze K, Borken W, Lischeid G (2014) Catchments as heterogeneous and multi-species reactors: an integral approach for identifying biogeochemical hot-spots at the catchment scale. J Hydrol 519:1560–1571

Zirlewagen D, von Wilpert K (2001) Modeling water and ion fluxes in a highly structured, mixed-species stand. For Ecol Manag 143(1):27–37

Zuber T (2007) Untersuchungen zum Wasserhaushalt eines Fichtenwaldstandorts unter Berücksichtigung der Humusauflage. PhD thesis, University of Bayreuth, Germany

Chapter 8
Trace Gas Exchange at the Forest Floor

Matthias Sörgel, Michael Riederer, Andreas Held, Daniel Plake, Zhilin Zhu, Thomas Foken, and Franz X. Meixner

8.1 Introduction

The fluxes measured above an ecosystem are the net fluxes that integrate over all processes (see Chaps. 4 and 6). To quantify the different contributions from, for example, soil respiration and leaf gas exchange, they have to be measured separately, which classically has been achieved by applying enclosures. Recently, conditional sampling methods have also been applied to eddy-covariance (EC) measurements above canopy (Thomas et al. 2008; Zeeman et al. 2013, Chap. 6) to infer below canopy respiration fluxes. The study of Zeeman et al. (2013) utilizes the detection of coherent structures (Chap. 6) that are important drivers of the exchange throughout the canopy and can be used to qualitatively describe the coupling of the different layers of the forest (e.g., Thomas and Foken 2007). Normally, EC measurement systems have not been applied below 2 m (Thomas and Foken 2007; Serafimovich et al. 2011; Zeeman et al. 2013), and therefore decoupling of the forest floor from the layers above cannot be excluded. Furthermore, the influence of subcanopy advection (Chap. 6) on these measurements still needs to be clarified. Several studies

M. Sörgel (✉) • F.X. Meixner
Max Planck Institute for Chemistry, Biogeochemistry Department, Hahn-Meitner-Weg 1, 55128 Mainz, Germany
e-mail: m.soergel@mpic.de

M. Riederer
Ostbayerische Technische Hochschule Regensburg, Regensburg Center of Energy and Resources, 93049 Regensburg, Germany

A. Held
Atmospheric Chemistry, University of Bayreuth, 95440 Bayreuth, Germany

Bayreuth Center of Ecology and Environmental Research, University of Bayreuth, Bayreuth, Germany

T. Foken (ed.), *Energy and Matter Fluxes of a Spruce Forest Ecosystem*,
Ecological Studies 229, DOI 10.1007/978-3-319-49389-3_8

(e.g., Baldocchi and Meyers 1991; Subke and Tenhunen 2004) successfully applied EC measurements below canopy to infer respiration fluxes. Application of data quality control for EC flux data (see Chap. 12) yielded a rejection rate of >60 % in the study of Subke and Tenhunen (2004), owing to the prerequisites of EC (like stationary conditions and well-developed turbulence) that are not always fulfilled below canopy. Furthermore, vegetation at the forest floor will influence respiration fluxes measured by EC (e.g., Misson et al. 2007). As they are cheap and relatively easy to handle, different designs of enclosures have been applied for decades to determine soil respiration fluxes, but without careful application, errors in fluxes can be large. Furthermore, chambers alter the natural layering above the surface and thus the diffusion gradient out of the soil, which alters the flux, although this effect has been reported to change the flux by less than 15 % (Davidson et al. 2002). The largest effect seems to be from altering pressure perturbations that are important for mass transport (e.g., Lund et al. 1999; Davidson et al. 2002) and from the exclusion of coherent structures and a longwave cooling (Riederer et al. 2014).

Another approach to the measurement of fluxes is the use of inert passive tracers like the radioactive noble gas radon. The decay of radioactive elements like uranium and thorium in soils leads to the exhalation of the radioactive noble gases such as ^{222}Rn and ^{220}Rn that have lifetimes of 3.5 days and 55.6 s, respectively. As radon is a noble gas, neither chemical reactions nor uptake by the biosphere change its concentration in air. Therefore, it is a perfect tracer for soil emissions. CO_2, for example, is taken up by the understory vegetation and by the canopy when photosynthesis is active. Otherwise, the plants become a source as well due

D. Plake
UCL Umwelt Control Labor GmbH, Josef-Rethmann-Straße 5, 44536 Lünen, Germany

Z. Zhu
Key Laboratory of Ecosystem Network Observation and Modeling, Institute of Geographic Sciences and Natural Resources Research, Chinese Academy of Sciences, Beijing, 100101, China

T. Foken
Am Herrgottsbaum 28, 96120 Bischberg, Germany

Bayreuth Center of Ecology and Environmental Research, University of Bayreuth, Bayreuth, Germany

M. Riederer, T. Foken: Affiliation during the work at the Waldstein sites—University of Bayreuth, Department of Micrometeorology, Bayreuth, Germany

M. Sörgel: Affiliation during the work at the Waldstein sites—University of Bayreuth, Atmospheric Chemistry, 95440 Bayreuth, Germany

D. Plake, Z. Zhu: Affiliation during the work at the Waldstein sites—Max Planck Institute for Chemistry, Biogeochemistry Department, Hahn-Meitner-Weg 1, 55128 Mainz, Germany

to respiration at night. ^{222}Rn can be used to infer bulk diffusion coefficients by combining soil fluxes with profile measurements (Lehmann et al. 2001). A method for the direct determination of the transport time between two heights of a profile of ^{220}Rn has been proposed by Lehmann and coworkers (1999).

Alternatively, fluxes close to the surface can be calculated from profile measurements by using models. For the turbulent layer fluxes can be calculated in an iterative way from two heights according to the approach of Richter and Skeib (1984, 1991), henceforth named RS. As the transition from turbulent to laminar flow occurs close to the surface, there are also models available that explicitly calculate the fluxes for the different layers. These are referred to as hydrodynamic multilayer models (e.g., Foken 1979, 1984), as they were derived from hydrodynamic investigations.

In this chapter we present results from the EGER IOP 2 campaign (Chap. 1) at the Waldstein site, which examined the trace gas exchange at the forest floor. The central issue to be addressed is how coupling/decoupling of the near forest floor layer (below the height at which sonic anemometers can be applied) can be detected and the consequences of decoupling for flux measurements higher above (see Chap. 6). We use a multilayer model together with profiles with high vertical resolution close to the forest floor in order to compare modelled and measured surface concentrations of ^{222}Rn, CO_2, H_2O, and O_3. The model is first validated against sensible heat flux measurements by eddy covariance, and then calculated effective surface concentrations and measured surface concentrations of these different compounds (inert => very reactive) are compared. The influence of driving forces of trace gas exchange (radiation, turbulence, stability, and coupling) below canopy on the measurement of (reactive) trace gases profiles will be discussed.

8.2 Materials and Methods

8.2.1 Site Description

All investigations described in this chapter were done at the Waldstein-Weidenbrunnen site near the "Main Tower" (M1), which is described in detail in Chap. 2. The measurements were conducted during the intensive measuring period IOP 2 (June–July 2008) of the EGER project (Chap. 1). For the measurements near the ground, an additional, 2 m high, structure was installed at the forest floor. The forest floor measurements during IOP 2 were made around 25 m west-south-west of the main tower (see Fig. A1.2; Appendix A). Chamber measurements were also installed nearby. For further details see Appendix A.

8.2.1.1 Wind, Temperature, and Radiation Measurements

The wind profiles at the forest floor were measured by two-dimensional sonic anemometers (WS425, Vaisala, Helsinki, Finland) at 0.03 m, 0.30 m, 1.0 m, and 2.00 m above the ground. For measurements at the two lower heights, the anemometers were placed upside down and the wind direction was corrected afterwards. Temperature profiles were obtained by placing unshielded thermocouples (type E—chromel/constantan) at 0.01 m, 0.02 m, 0.04 m, 0.08 m, 0.3 m, 0.16 m, and 0.32 m and custom-built psychrometers (with active ventilation and radiation shielding) with thermocouples at 0.09 m, 0.26 m, 1.00 m, and 2.05 m.

Global radiation was measured by a pyranometer (type Li-200SZ, Licor, USA), net radiation by a net radiometer (type NR-lite, Kipp and Zonen, The Netherlands), and the photolysis frequency of NO_2 by a filter radiometer (Meteorologie Consult, Germany).

8.2.1.2 Trace Gas Measurements

Carbon dioxide soil flux was measured with a static chamber setup (Department of Environmental Geosciences, University of Basel, Basel, Switzerland; see Lehmann et al. 2004) and a commercial nondispersive infrared CO_2 analyzer (GMP343, Vaisala, Helsinki, Finland). ^{222}Rn fluxes were measured at the same chamber system by an alpha spectrometer (Alpha Guard, Genitron, Frankfurt, Germany). Soil fluxes of CO_2 and radon were derived from a linear rise of the trace gas concentration in the chamber during closure time according to Lehmann et al. (2004). The chamber had a diameter of 22.5 cm and the chamber system had a total volume of 10.2 L. The total volume consists of tubings, drying cartridges, 7.5 L chamber volume, and a 2.0 L delay volume to remove the ^{220}Rn. The chamber was closed every 3 h (IOP 1) or 2 h (IOP 2) for 50 min, which was long enough for a significant concentration rise and provided enough measurement points for radon (time resolution 10 min). Inside the chamber a ventilator mixed the enclosed volume. Additionally, profiles of ^{222}Rn and ^{220}Rn were measured at 0.00 m, 0.03 m, 0.1 m, and 0.3 m above ground. Two controlled valves were introduced to enable switching between two measurement heights measured by one analyzer. To improve the performance of the alpha guards, a Nafion drying system was introduced to dry the sample air. The sensitivity was 1 count per 20 Bq m^{-3} and the detection limit about 12 Bq m^{-3}. The alpha guards are not capable of distinguishing between the two measured radon isotopes. Therefore, the setup consists of two sets of two alpha guards. Each pair of analyzers had a delay volume of 0.0032 m^3 between the analyzer units. The flow through the system was kept constant to assure a mean residence time of the sample air in the delay volume of about 10 half-life times of ^{220}Rn, to solely (98 %) detect ^{222}Rn in the second instrument.

Reactive trace gases (NO, NO_2, and O_3) and profiles of CO_2 and water vapor have been measured by a profile system by switching between inlets at different heights (close to the forest floor, 0.005 m, 0.03 m, 0.1 m, 0.3 m, and 0.9 m; within

the canopy, 3 m, 10 m, 16.5 m, and 20.5 m; as well as above canopy at 25 m and 31.5 m above ground level). We focus here on the measurement heights close to the forest floor (up to 1 m). The inlet tubes for the sample air were all 55 m long and protected by a Teflon filter (PTFE; pore size 5 μm), a funnel to prevent raindrops from entering and an insect-proof net at the inlet. The lines were isolated, heated, and radiation shielded. Furthermore, opaque Teflon tubes (blue pigments, 1/4″) were used. The inlet for the lowest height was split into four inlets to reduce flow for each inlet from 7–9 L min^{-1} total to about 2 L min^{-1} for each inlet in order to reduce the effect of the local disturbance of the gradient by high airflows near the ground.

Nitrogen oxides (NO and NO_2) were measured by chemiluminescence analyzers (CLD 780 TR, Ecophysics, Dürnten, Switzerland). NO_2 was converted to NO by diode-based blue light converters (Droplet Measurement Technologies, Boulder, CO, USA). Ozone was measured by UV absorption (model 49c, Thermo Fischer Scientific, Franklin, MA, USA) and CO_2 and H_2O by nondispersive IR absorption (model 840, Licor, Lincoln, Nebraska, USA).

Ozone fluxes were measured by fast chemiluminescence O_3 sondes (GEFAS GmbH, Germany) and a Gill R2 3D ultrasonic anemometer (Gill, UK). The setup was placed at about 3 m distance from the forest floor station. Therefore, the O_3 signal of the fast instrument could not be used as an absolute signal and was only used for the fluctuations, with the mean signal being measured by a slow analyzer (in this case model 49c, see above). For more details regarding ozone fluxes see Chap. 9.

8.2.2 Modelling of Fluxes Near the Forest Floor

In contrast to the modelling approaches for the whole canopy (Chap. 16), simple parameterizations were used for the exchange at the forest floor. Instead of the simple bulk approach, which is usually applied to two fixed levels (surface and 10 m height), an approach with the profile coefficient Γ (Foken 2008) that integrates over the lowest layers was applied:

$$Q_H = \Gamma\,(T_1 - T_2) \tag{8.1}$$

Eq. (8.1) and the following equations were written for the sensible heat flux (in kinematic units), but they are similar for trace gas fluxes. This approach was used in two different ways:

1. The measuring heights z_1 and z_2 are in the upper part of the profile in the trunk space but at a distance that is large enough to measure a significant gradient. In contrast to simple two-point parameterizations, the applied method according to Richter and Skeib (1984, 1991), hereafter named RS, is also applicable in a stratified layer. From temperature and wind profile measurements, the calculation of the Obukhov length and of the Richardson numbers is possible.

2. For measuring heights $z_1 = 0$ and z_2 an aerodynamic approach according to Foken (1979, 1984) was applied. This approach is parameterized for the molecular or laminar layer (thickness 0.001 m), the molecular-turbulent buffer layer (thickness 0.01 m) and the neutral or stratified turbulent layer. As some of the parameterizations are derived from hydrodynamical arguments, the parameterization is called the hydrodynamic multilayer model (hereafter simply called multilayer model). It was applied to calculate the conditions at the surface for a given flux, for example, surface temperature for a given sensible heat flux. This calculated surface temperature is often not identical with the true surface temperature (Sodemann and Foken 2005; Lüers and Bareiss 2010), which indicates a decoupling near the surface, and therefore the turbulent conditions in the trunk space cannot be applied in the vicinity of the surface.

For the calculation of the effective surface concentrations, both methods have been combined. The RS approach was used to calculate fluxes from two heights in the turbulent layer and the multilayer model to calculate the effective surface concentration from this given flux and the profile. The congruence of these modelled effective surface concentrations with measured surface concentrations is used as a criterion to define coupled and decoupled situations of the near forest floor layer (<1 m). This coupling mechanism has to be distinguished from the coupling of the canopy to the above air layers by coherent structures (Thomas and Foken 2007; Chap. 6).

8.2.2.1 Parameterization According to Richter and Skeib (1984, 1991)

The RS parameterization is based on the calculation of critical height z_c, which is the height of the dynamical sublayer. For $z > z_c$ the atmosphere is stratified. In this approach the universal function by Skeib (1980) is applied. For the calculation of the friction velocity u_* and the $u_{(z)}$ obtained from wind measurements at two levels follows:

$$u(z_2) - u(z_1) = \frac{u_*}{\kappa} \cdot \left\{ \begin{array}{ll} \ln\left(\frac{z_2}{z_1}\right) & z_1 < z_2 < z_c \\ \ln\left(\frac{z_c}{z_1}\right) + \frac{1}{n_u}\left[1 - \left(\frac{z_2}{z_c}\right)^{-n_u}\right] & z_1 \le z_c \le z_2 \\ \frac{1}{n_u}\left[\left(\frac{z_1}{z_c}\right)^{-n_u} - \left(\frac{z_2}{z_c}\right)^{-n_u}\right] & z_c < z_1 < z_2 \end{array} \right\} \tag{8.2}$$

The part in the curly brackets divided by the von-Kármán-constant κ is the reciprocal profile coefficient. The sensible heat flux can be calculated in an

analogous manner

$$T(z_2) - T(z_1) = \mathrm{Pr}_t \frac{Q_H}{\kappa u_*} \begin{cases} 1\mathrm{n}\left(\frac{z_2}{z_1}\right) & z_1 < z_2 < z_c \\ 1\mathrm{n}\left(\frac{z_c}{z_1}\right) + \frac{1}{n_T}\left[1 - \left(\frac{z_2}{z_c}\right)^{-n_T}\right] & z_1 \le z_c \le z_2 \\ \frac{1}{n_T}\left[\left(\frac{z_1}{z_c}\right)^{-n_T} - \left(\frac{z_2}{z_c}\right)^{-n_T}\right] & z_c < z_1 < z_2 \end{cases} \quad (8.3)$$

with the turbulent Prandtl number Pr_t. The solution of the model can be done in an iterative way. The necessary calculation of the critical height and coefficients n_u and n_T are given in the original literature or by Foken (2008).

8.2.2.2 Parameterization According to Foken (1979, 1984)

This approach uses an integration of the profile coefficient from the surface up to a level in the neutral or stratified turbulent layer

$$\Gamma = \left(\int_0^z \frac{dz}{K_T + \nu_{Tt} + \nu_T} \right)^{-1}, \quad (8.4)$$

where K_T is the turbulent diffusion coefficient, ν_{Tt} the molecular-turbulent diffusion coefficient in the buffer layer, and ν_T the molecular diffusion coefficient. The following setting of the parameters is based on experimental work over the ocean (Foken et al. 1978); for details see the original literature or Foken (2008):

$$\Gamma = \frac{\kappa \cdot u_*}{\kappa \cdot \mathrm{Pr} \cdot \frac{\delta_T \cdot u_*}{\nu} + \kappa \cdot \delta_T^+ + 1\mathrm{n}\frac{u_* \cdot z}{30\,\nu}} \quad (8.5)$$

Here Pr is the Prandtl number, $\delta_T^+ \approx 4$ the dimensionless temperature difference in the buffer layer, $\delta_T \approx 6$ the dimensionless thickness of the molecular layer, and υ the kinematic viscosity. In the case of a stratified atmosphere, a fourth summand that reflects the stability dependency must be included in the denominator.

8.3 Results and Discussion

8.3.1 Driving Forces of Subcanopy Exchange

8.3.1.1 Radiation

On average, about 10 % of the shortwave radiation is able to penetrate the canopy and reach the forest floor as observed from measurements about 10 m south of the

forest floor measurements (see Appendix A). Generally, the radiation distribution at the forest floor is very variable in space and time (Chap. 14) due to different PAI (Chap. 2) and changing solar zenith angle over the day. The amount of attenuated radiation at the Waldstein site changes over the course of the day between 5 % and 40 % due to the canopy structures (Sörgel et al. 2011). Generally, the radiation balance below canopy was found to be dominated by longwave radiation in contrast to daytime conditions above the forest canopy. The incoming and outgoing longwave radiation fluxes were both about 400 W m^{-2}. As incoming and outgoing radiations were more or less balanced, there was no net contribution to the energy exchange. The direct influence of the radiation to the exchange conditions seems to be limited to spots of direct radiation, the so-called sunflecks. Passing sunflecks cause changes in the temperature profile and—due to heating of the ground surface—to stability as well (see Fig. 8.1). During IOP 2 global radiation was therefore below 25 W m^{-2} during most of the day (before 8:00 and after 14:30). Maximum values of 350 W m^{-2} to 600 W m^{-2} were reached at 10:00, and a second maximum with about 70 W m^{-2} was reached at 13:00. Net radiation followed the global radiation closely except for the peak in the afternoon. A small negative peak in net radiation during that period might be explained by the heterogeneity as well. It seems that the sensor itself was in the shadow but the ground below was heated by sunlight and was therefore increasing the outgoing radiation. Even larger differences

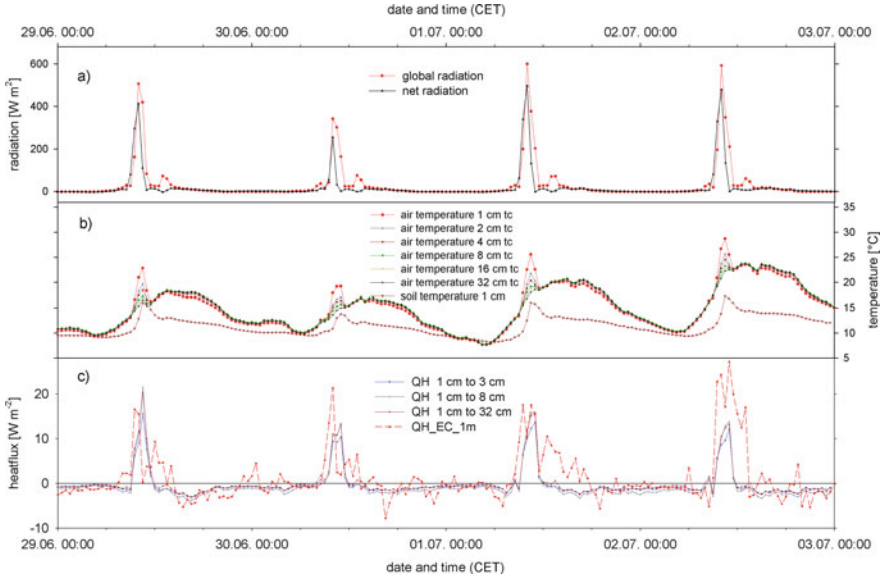

Fig. 8.1 Frame (**a**) shows global and net radiation measured at the forest floor site. A logarithmic profile of air temperature measured close to the ground surface with unshielded thermocouples and the soil temperature measured in 1 cm depth is shown in frame (**b**). Frame (**c**) shows sensible heat fluxes calculated from the temperature profiles by the multilayer model and for comparison the measured sensible heat flux from a nearby eddy covariance measurement at 1 m height

in magnitude and timing were found to radiation measurements of the four radiation components (longwave and shortwave in and out) at about 10 m horizontal distance (not shown here).

8.3.1.2 Temperature Profiles

During the golden days of IOP 2, the temperatures were between 7.7 °C and 28.7 °C at the forest floor (0.01 m) and between 7.6 °C and 23.7 °C at 1 m height. Temperature profiles showed consistently lowest temperatures at the forest floor, except for the time of day when sunflecks hit the ground below the sensors (Fig. 8.1). During those periods (8:00 to 12:00), positive temperature differences between 0.01 and 0.32 m of up to 7.5 K were observed. After those peaks the differences dropped to about zero and then became slowly negative, with the maximum negative values of about −1 K occurring in the evening (16:30 to 19:00). Thereafter, the temperature differences diminished, reaching values around zero in the early night.

8.3.1.3 Wind Profiles

Wind profiles in the lowermost 2 m show strong attenuation toward the ground and are log-linear between 1 m and 0.03 m except for very low wind speeds in the evening. Wind speeds at 2 m were higher than extrapolated from the profile between 0.03 and 1 m due to the more open trunk space in that height. Wind speeds at 2 m were on average 0.8 m s^{-1} with maximum values of about 1.4 m s^{-1}. Wind speeds at 0.03 m hardly exceed 0.5 m s^{-1} and are, on average, about 0.3 m s^{-1}. The average value for the same period at 1 m was 0.7 m s^{-1}, and the maxima were around 1 m s^{-1}. For comparison, the average wind speed above canopy at 32 m was 2.9 m s^{-1} with a maximum of 4.7 m s^{-1}. Minima in wind speed at the forest floor occurred in the evening or in the early night during IOP 2. Coinciding with the minima in wind speed, wind direction changes (see Fig. 8.1). During daytime, winds at 1 m and 2 m were predominantly from the south, whereas at night the wind direction changed to east. A change in wind direction was consistently observed between the upper (1 m and 2 m) and the lower (0.03 m and 0.3 m) levels. This might be due to local channeling of the flow close to the ground. During daytime this difference was less obvious as wind speeds and wind direction were very variable.

8.3.2 Comparison of Measured and Modelled Fluxes

8.3.2.1 Friction Velocity

Wind speeds close to the forest floor were generally low due to the strong attenuation of the wind by the canopy although in the more open trunk space a secondary wind

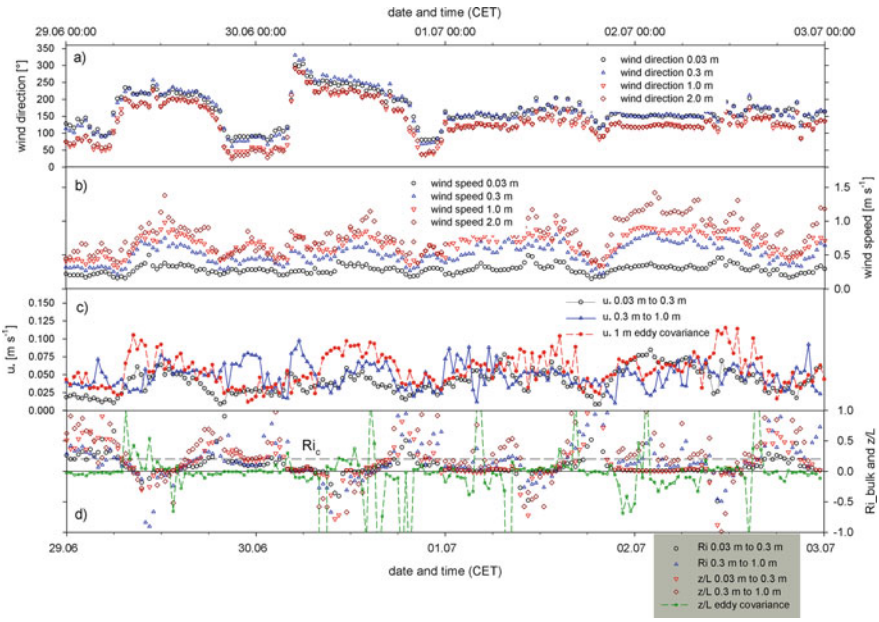

Fig. 8.2 Wind speed (frame **a**) and wind direction (frame **b**) in the lowest 2 m above the forest floor. Frame (**c**) shows the friction velocity calculated from the wind profile and for comparison the friction velocity determined by a nearby eddy covariance measurement. Additionally, the bulk Richardson number calculated from two different profile heights (0.03 m to 0.3 m and 0.3 m to 1 m) is shown in comparison to $\varsigma = z/L$ determined from the same profile heights and as calculated from the eddy covariance measurements (frame **d**)

maximum occurs (see above). Nevertheless, close to the forest floor, the influence of the ground surface causes a strong attenuation as per definition the wind speed is zero at the surface. During IOP 2, wind speeds at 1 m height therefore hardly exceed 1 m s^{-1}. Consequently, values of the friction velocity are comparatively low as well. The diurnal cycle of u_* follows that of wind speed although due to higher scatter the diurnal course is less obvious (Fig. 8.2). Values are higher during daytime and lower during nighttime and show minima around sunset and in the early night coinciding with minima in wind speed and changes in wind direction. The u_* values derived from eddy covariance measurements, and those from the wind profiles agree within the variation, but differences can be up to a factor of two. Nevertheless, both methods show comparably small friction velocities (on average about 0.04 m s^{-1}) and therefore comparably (above-canopy average $u_* = 0.6$ m s^{-1}) low turbulence. In addition to the locally produced turbulence from the shear of the horizontal wind, coherent structures that are generated above canopy play an important role in the exchange of canopy air with the above air layers (Thomas and Foken 2007; Serafimovich et al. 2011; Sörgel et al. 2011 and Chap. 6). These structures were found to occasionally reach down to 2 m (lowest measurement level), but it remains unknown if the mixing prevails down to the forest floor. From the results of Sörgel

et al. (2011), it was indicated that these structures provide mixing down to 0.5 m, as eddy covariance measurements are limited to some level above the forest floor and decoupling of the layers close to the surface can still occur below that measurement height.

8.3.2.2 Sensible Heat Flux

The multilayer model was developed for the determination of the energy exchange and was therefore compared to the sensible heat fluxes measured by eddy covariance at 1 m height. Sensible heat fluxes were calculated for several layers according to Eq. (8.1), with the profile parameters derived from the multilayer model according to Eq. (8.5). Temperature differences for the lower layers were derived from a profile (0.01 m to 0.32 m) of unshielded thermocouples. Although these temperature measurements might be influenced by radiation, there was no other available technique that could be used in the proximity of the surface. Furthermore, radiation was low for most of the day (see above). The shielded and actively ventilated thermocouples had a minimum installation height of about 0.1 m. Due to the active ventilation they also disturb the layering near the surface and thus the natural gradient. Therefore, they were just used for the upper part of the profile (0.1 m to 1 m). A shielding without active ventilation would result in a temperature measurement that is not equilibrated with the surrounding air due to the low wind speeds at the ground. Therefore, the unshielded thermocouples were used. Having these difficulties in mind, the agreement between the heat fluxes derived from the multilayer model and those from the eddy covariance is surprisingly good (see Fig. 8.1). At night all fluxes are nearly zero (detection limit of sensible heat flux >5 W m^{-2}; e.g., Nordbo et al. 2012) except for short turbulent events or coherent structures that touch down into the trunk space (Chap. 11). Daytime fluxes coincide with direct radiation (see above) and reach up to 25 W m^{-2}. The agreement of the daytime fluxes is good as well and differences can be attributed to different footprints as the profile measurements are always fixed to the temperature level 0.03 m and on a very small spatial scale, whereas the flux measurements have a footprint size of about 10 m. This might be indicated by the fact that the agreement in timing of the peaks of profile-derived fluxes and eddy covariance fluxes shifts from day to day. Furthermore, fluxes derived from the upper measurement heights that have a larger footprint agree better. The horizontal inhomogeneity of the ground cover (Chap. 2) and the sunflecks might be responsible for the deviations in the afternoon as well, where modelled sensible heat fluxes drop to about zero right after the peak, whereas the eddy fluxes are still positive. Other reasons for this discrepancy in the afternoon might be the well-mixed conditions that cause temperature differences between the heights to be in the uncertainty range of the temperature sensors (0.1 K). Furthermore, in the afternoon the cooling starts first at the forest floor, while the sensible heat flux at 1 m is still positive and larger.

8.3.2.3 Stability

From the wind and temperature profiles, the stability of the air column close to the forest floor can be determined by the bulk Richardson number (Ri_B) and the stability parameter $\varsigma = z/L$, with L being the Obukhov length and z the reference height. The calculations have been done for different heights within the profile. Figure 8.2 shows the results for the layers 0.03 m to 0.3 m and from 0.3 m to 0.9 m. The values of both methods generally agree well for ς derived from local measurements (wind and temperature gradients). The agreement between the different heights is good as well. But in general, the agreement between both methods is better than between the different layers. For some periods, nighttime values of the upper layer exceed the critical Richardson number (0.2), whereas at the lower levels values are close to zero and therefore in better agreement with the eddy covariance measurements. Only for some unstable episodes is the agreement between the upper levels and the eddy covariance derived stability better than for the lower level. Some of the deviations (e.g., timing of unstable conditions) between the values derived from profiles and those from eddy covariance might be caused by different radiation regimes (horizontal separation of systems) as discussed above, as the unstable conditions are clearly linked to heating of the surface by direct sunlight in the sunflecks. Depending on stability, the footprint of the eddy covariance measurement is about 10 m. Therefore, the profile should be within the footprint of the sonic (3 m horizontal separation) most of the time, but the footprint of the profile is much smaller, especially for the lower levels. Nevertheless, at low wind speeds, due to nearby obstacles (stems) and under stable conditions without well-developed turbulence, the eddy covariance measurements are prone to difficulties as well (e.g., for forest floor measurements Baldocchi and Meyers 1991; Subke and Tenhunen 2004; Launiainen et al. 2005). As can already be seen from the temperature profiles, predominantly neutral conditions prevail and unstable and stable episodes occur in the morning and evening, respectively (see Figs. 8.1 and 8.2). Neutral conditions occur mainly from midnight to the early morning and in the afternoon. Eddy covariance measurements show predominately neutral conditions for the whole day with some more randomly distributed stable and unstable episodes. In the morning, unstable conditions occurred simultaneously with the increased radiation, but eddy covariance measurements showed either neutral conditions or shorter stable episodes before and after the values from the local profile. As these episodes are driven by the thermal (static) stability of the air, all three methods applied based on the dynamic stability are not valid during these events. The sunflecks cause local heating of the surface that induces local free convection. In the evening and in the early night, u_* drops to very low values (see Fig. 8.1), and therefore stable stratification develops due to cooling of the surface. These stable episodes coincide with minima in wind speed between 0.3 m and 2 m and changes in wind direction (Fig. 8.1). Another effect that limits the comparability of profile-derived values and eddy covariance measurements is the decoupling of the near forest floor layer. During the decoupling, gradients increase and dynamic stability at 1 m might not be affected.

8.3.3 Comparison of Modelled and Chamber Fluxes

8.3.3.1 Radon Fluxes

The multilayer model was applied to calculate trace gas fluxes as well. As fluxes of ^{222}Rn and CO_2 have been additionally measured at the forest floor by a static chamber, another possibility for intercomparison exists. For the further analysis, only ^{222}Rn was used. Fluxes from the chamber are much lower and less variable. They vary around 0.025 Bq m^{-2} s^{-1}, whereas the modelled fluxes are around 0.125 Bq m^{-2} s^{-1} with maxima reaching up to 0.35 Bq m^{-2} s^{-1}. Therefore, modelled fluxes are sometimes more than a factor of 10 higher. As radon is a noble gas, it undergoes no chemical reactions and, unlike CO_2, is not actively taken up by plants. The half-life time (τ) of 3.8 days is sufficiently long to allow radon to be viewed as stable during the closure time of the chamber (50 min; $<1/100\tau$). Therefore, the differences in the flux should be caused by physical processes such as different pressure within and outside the chamber or a different diffusion gradient. As a third independent approach (like eddy covariance) is missing for radon fluxes, deciding which approach failed is not straightforward. The model has been shown to reproduce the sensible heat flux very well (esp. given the difficulties of the inhomogeneous radiation field at the forest floor). The enclosures are known to suffer from different problems that can lead to either overestimation or underestimation of the flux. In our study the flux was calculated by using a linear fit of the concentration rise. Recent publications suggest that linear fits tend to underestimate the flux (e.g., Davidson et al. 2002; Kutzbach et al. 2007). According to Davidson and coworkers (2002), underestimation was in the range of 5–15 %, but due to the higher uncertainty of the nonlinear fit, they preferred a linear fit. Kutzbach et al. (2007) found 70 % underestimation due to the use of linear fits instead of an exponential model. Nevertheless, they report as well that the curvatures often deviate from the theoretical model, pointing to disturbances of the soil flux by the chamber. An overpressure of just 0.5 Pa was reported to reduce the flux by 70 % (Lund et al. 1999). As the chamber flux is fairly constant, the deviation to the modelled flux varies a lot: from 0 % to 85 % lower fluxes. In principle, the chamber design was intended to deal with the above-discussed problems. The chamber had a height of about 20 cm (depending on the depth it was buried into the ground) and was equipped with a capillary as a vent to equilibrate the pressure. Nevertheless, the differential pressure between the chamber and ambient has not been measured and therefore pressure effects cannot be excluded. Furthermore, (wind-induced) pressure differences might even be unmeasurable as they are compensated by mass flows in/out of the soil (Bain et al. 2005), which are the reason for the altered CO_2 flux as well. Also the larger volume (20 cm height) used to avoid fast accumulation was overcome by the comparably long closure time (50 min) that was necessary for measuring radon in parallel (maximum time resolution for one data point is 10 min). The chamber was additionally equipped with a fan to provide complete mixing. The fan destroys the natural gradient above the soil and was thought to

increase the flux by increasing the gradient between the soil air and the chamber air. Nevertheless, it seems that due to the long closure time, the opposite effect dominates: the rising concentration in the chamber reduces the flux. Furthermore, pressure fluctuations have been proposed to be an important driver of mass transport across the soil-air interface (Kimball and Lemon 1971). Depending on the pressure fluctuations induced by the fan, this effect can be larger or lower that in outside air. But even technically advanced systems still suffer from the enclosure technique itself by changing the exchange conditions and the preventing cooling of the surface by outgoing longwave radiation (Riederer et al. 2014). An alternative method of determining near-surface fluxes might be provided by the "thoron clock" (Lehmann et al. 1999; Plake and Trebs 2013), which just needs a measured thoron (^{220}Rn) gradient and no enclosures.

8.3.3.2 Carbon Dioxide Fluxes

Similar results as for ^{222}Rn were obtained for CO_2. As can be seen in Fig. 8.3, the CO_2 flux determined from the chamber is much less variable and somehow marks a lower limit for the modelled flux. With regard to the mean modelled flux, the chamber flux is lower by about a factor of 2.5. Besides this difference, the modelled and the chamber fluxes are both always positive, which is related to the same ground cover for both measurements (measurements co-located on moss) without substantial assimilation. Therefore, only respiration fluxes were

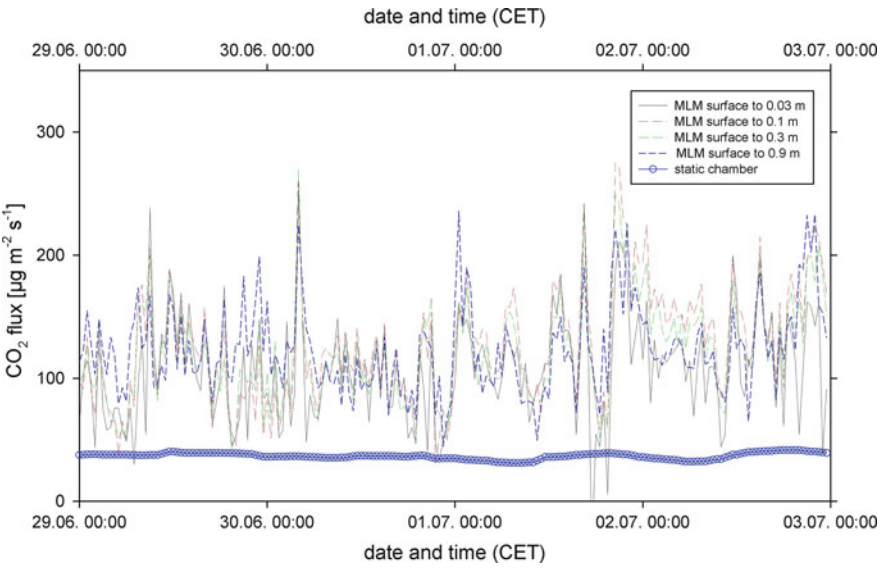

Fig. 8.3 CO_2 fluxes as modelled by the multilayer model (MLM) for different layers compared to those measured by a collocated static chamber system

measured. Unfortunately, no co-located CO_2 eddy covariance measurements were available, but the magnitude and dynamics of the modelled values agree much better with respiration fluxes from the Waldstein site derived from conditional sampling (Thomas et al. 2008) than the chamber fluxes. This therefore supports the argumentation derived for ^{222}Rn that the chamber measurements most probably failed to produce reasonable fluxes.

8.3.4 Determination of the Coupling Situation at the Forest Floor

As discussed above, the multilayer model was shown to reproduce sensible heat fluxes very well and has therefore been used to calculate trace gas fluxes from profiles, while static chamber measurements failed to produce reasonable fluxes and were therefore excluded from further analysis. In the case of CO_2, the only available eddy covariance measurements (not shown here) in the trunk space were about 80 m away, over a different ground cover. Therefore, the values were not comparable. The measured (eddy covariance) and modelled O_3 fluxes will be discussed below. Another possibility for comparison, but more importantly for the detection of coupling and decoupling in the lowest meter, was to use the multilayer model for calculation of an effective surface concentration that was compared to measured surface concentrations. The agreement of those two concentrations was then used as a measure of whether the near forest floor layer was coupled or decoupled from the layers above. The RS approach was thereby used to calculate a flux from the profile, and subsequently the multilayer model was used to calculate an effective surface concentration from that flux.

Radon is best suited for this kind of investigation as it does not react or change its phase (as does water) nor is it influenced by plants (fixation, evapotranspiration, etc.). It is therefore not influenced by chemical or physical processes other than transport, at least in a reasonably short time compared to the decay time (3.8 d). As can be seen in Fig. 8.4, periods with large discrepancies (with even peaks in opposite directions) alternate with periods with good agreement between modelled and measured surface concentration. They are marked C_x for coupled situations and D_x for decoupled situations ($x = 1, 2, 3, \ldots$). For decoupled situations we can distinguish two different cases with respect to the model. Either the decoupling takes place between 0.1 m and 0.3 m (the profile heights used for modelling) or decoupling occurs below 0.1 m. In the first case, the gradient increases, and the model therefore overestimates the effective surface concentration because the flux given by the RS parameterization is overestimated. In the latter case, the decoupling takes place below the lower profile height used to calculate the flux. The ^{222}Rn accumulation below the heights used for the calculation of the effective surface concentration leads to an underestimation. Significantly higher ^{222}Rn concentrations were observed at 0.3 m than at 0.03 m for some periods. Therefore, the gradient is

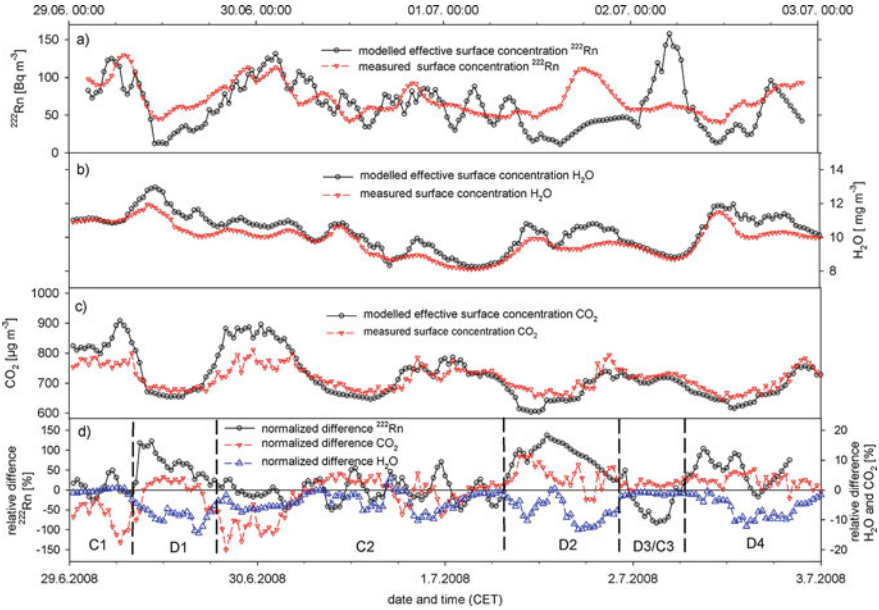

Fig. 8.4 Modelled effective surface concentrations and measured surface concentrations for (**a**) ^{222}Rn, (**b**) water vapor, and (**c**) CO_2. The ^{222}Rn data have been smoothed by a moving average (window size 5). Frame (**d**) shows the relative difference (difference normalized to the mean) between measured and modelled values

reversed. This might be due to the advection of ^{222}Rn, as its lifetime is sufficiently long and its emanation from the ground is very heterogeneously distributed. A drawback of the use of ^{222}Rn is its low activity relatively to the sensors' sensitivity and the low time resolution of the measurements. In combination with the heterogeneous distribution of the ^{222}Rn emanation, the signals are very variable, and therefore relative differences between measured and modelled surface concentration reach up to a factor of two. Without smoothing the signal with a moving average (window size 5), the relations between the signals would be hardly visible. Nevertheless, during some periods agreement is comparably good and the periods are therefore labeled as coupled. As the relative error of the ^{222}Rn measurement is 40 %, the relative difference of $\pm$50 % between measured and modelled surface concentrations is still regarded as good agreement. In principle, coupling derived from water vapor and CO_2 (see below) confirms these periods, although these measurements are associated with other problems as discussed below.

8.3.4.1 Water Vapor

Water vapor does not react in significant amounts in the troposphere and can therefore be regarded as chemically inert as well. Unlike radon, it undergoes phase

changes (condensation/evaporation) and its cycling is altered by vegetation due to transpiration. Also unlike radon, the effective surface concentration tends to be higher than the measured concentration for all situations (Fig. 8.4). The tendency for overestimation of the effective surface concentration for water vapor might be due to the different footprints for the different heights. The surrounding ground cover vegetation is thought to increase water vapor levels in the upper heights of the profile due to transpiration, whereas the very local measurements at 0.03 m are on a much dryer surface. Nevertheless, the covariation of both curves (measured and modelled) is higher than for ^{222}Rn and the relative deviation is much smaller (mostly <10 %). This is probably due to the higher sensitivity of the analyzer compared to the ^{222}Rn measurements. Nevertheless, deviation of the values is largest during decoupled situations as well. Only for the decoupled case (D3) that had opposite peaks in the case of ^{222}Rn does water vapor show an almost perfect agreement between modelled and measured concentration (relative difference <5 %). During this period the site was influenced by a strong low-level jet (not explicitly shown in Chap. 11). But as shown in another example in Chap. 11, the low-level jets can enhance mixing from air layers above the canopy down to the forest floor during nighttime.

8.3.4.2 Carbon Dioxide

Modelled and measured CO_2 concentrations agree generally well (within 10 %). Similar to ^{222}Rn and water vapor, periods with good agreement alternate with those having larger deviations of measured and modelled concentrations. These periods agree, in principle, with those also found for ^{222}Rn and water vapor. Other than for water vapor, which was consistently overestimated, CO_2 shows overestimation during nighttime and slight underestimation during daytime, which is clearly visible from Fig. 8.4 for at least the first 2 days. As already discussed for H_2O, this might be caused by the surrounding vegetation that is within the footprint of the upper heights of the profile. The higher nighttime values are due to additional respiration by the plants and the lower daytime values due to assimilation.

Therefore, all three trace gases show a consistent picture. Periods of good vertical coupling and decoupling alternate, but detection of local coupling/decoupling is hampered by the different footprints of the profile heights and the high variability of forest floor fluxes.

8.3.5 Reactive Trace Gases

The reactive trace gases NO, NO_2, and O_3 form a so-called triad by forming a set of chemical reactions where NO and O_3 combine to NO_2 and are reformed by photolysis of NO_2. They form a photo stationary state that can be expressed by the Leighton ration (Leighton 1961). As the photolysis frequency of NO_2 is

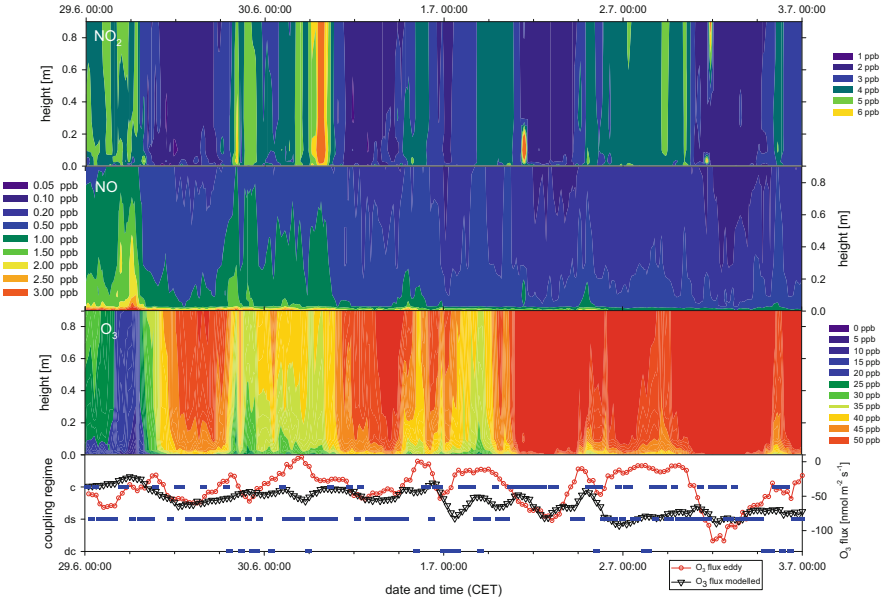

Fig. 8.5 Contour plot of the mixing ratios of the reactive trace gases NO_2, NO, and O_3 in the lowest meter above ground. For comparison the measured and modelled (from the gradients) O_3 fluxes are shown together with the coupling regimes of the 2 m eddy measurement with the above layers. Dc (decoupled canopy whole canopy decoupled from the air layer above), Ds (decoupled subcanopy only subcanopy decoupled), and C (fully coupled canopy)

comparably low at the forest floor (10 % from above canopy) and NO values are comparably high due to the well-known microbial soil emissions, consumption of NO and O_3 and therefore production of NO_2 dominate. This is shown in Fig. 8.5 by the anti-correlation of NO and O_3 values. In addition to the direct chemically induced anti-correlation, during the course of the week NO emissions decline and O_3 formation (above canopy) increases. This is due to the dry conditions after a rain event on the 25th of June. Ozone mixing ratios are well known to increase in warm dry weather (e.g., US-EPA 2006; Bloomer et al. 2010), and NO emissions have been found to peak after rain events (e.g., Davidson 1992; Scholes et al. 1997). As the background of NO_2 is quite variable, the formation of NO_2 is less obvious, but NO_2 values often showed maximum values at around 1 m. Furthermore, higher NO_2 values often coincide with high values of NO and low O_3 values (Fig. 8.5). The NO_2 background is mainly influenced by transport of anthropogenic and biogenic emissions. Although during daytime NO is formed by photolysis of NO_2 above canopy and is transported downward (e.g., Horii et al. 2004; Foken et al. 2012; Chap. 9), clear profiles with largest values at the soil surface were observed for NO, pointing to the dominance of NO soil emissions close to the ground. The accumulation of NO that follows the depletion of O_3 seems to be more related to the decoupling of the trunk space from above air layers (see Fig. 8.5), as steep NO and

O_3 gradients in the first meter are not linked to the decoupling and coupling of the near forest floor layer as determined in the previous section from comparison of the effective surface concentrations of ^{222}Rn, H_2O, and CO_2 (see above and Fig. 8.4).

8.3.5.1 Ozone Fluxes

In the case of O_3, nearby eddy covariance measurements (1 m height, see Chap. 9) could be compared to the modelled flux of the multilayer model. Reactive trace gases, such as O_3, entail difficulties for such intercomparison, as due to chemical reactions, they have sources or sinks within the measured profile. Therefore, the flux is not constant with height, which is one of the general assumptions for the application of profile methods. Next to the reactions of O_3 directly at the soil surface or uptake to ground vegetation, the gas phase reaction with (soil emitted) nitrogen oxide (NO) is the main sink at the forest floor. The eddy covariance flux represents the total (deposition and chemical reactions) flux at 1 m height, while the modelled fluxes integrate the profile from the surface or 0.3 m up to 0.9 m. All fluxes are negative as the soil is solely a sink for O_3, and O_3 sources are located above canopy. Both fluxes vary within the same range but the eddy covariance fluxes are predominately lower. The modelled fluxes generally overestimate the flux compared to the eddy covariance measurements predominantly at times when large gradients of O_3 are observed in the lowest meter. The large gradients are presumably caused by the titration of O_3 by NO during times of low mixing (see Fig. 8.5). In such cases, chemical reactions act faster than the transport, causing a so-called chemical flux. A measure for the dominance of transport over chemistry or vice versa is the Damköhler number (Damköhler 1940). Therefore, modelling based on gradient methods overestimates the flux if Damköhler numbers are in the critical range $0.1 < Da < 10$. The periods of good agreement of modelled and measured fluxes are characterized by high O_3 and low NO values (longer chemical timescale). Furthermore, high O_3 values and low gradients are observed down to the lowest measurement level during these periods. It seems, by comparison of the fluxes, that these are more influenced by the coupling of the trunk space to the air layers above (Chaps. 6 and 11) than by decoupling of the surface as discussed above. Regarding the coupling of the canopy by coherent exchange, mixing ratio differences down to 0.9 m were lower during coupled situations (Foken et al. 2012). Effective coupling at least down to 0.5 m from about 10:00 to 13:00 local time was determined for the measurements of nitrous acid (HONO) during IOP 1 (Sörgel et al. 2011; Chap. 1), serving as a hint that decoupling might be related to a small layer very close to the surface during times of a well-coupled canopy. As the ground surface is an irreversible sink for O_3, the O_3 concentration must approach zero at the surface. As O_3 values at the lowest measurement level (0.005 m) are, on average, 26 ppb with a minimum of 4.5 ppb and a maximum of 55 ppb, the gradients in the lowest layer or in the laminar layer must be very steep. Therefore, the canopy coupling just seems to influence the height of the layer in the proximity of the surface, where O_3 depletion is strongest.

8.4 Conclusions

Some of the challenges for flux measurements at the forest floor are the heterogeneity of sources, the presence of local obstacles, the inhomogeneous radiation and the intermittent turbulence with occasionally decoupling of the different layers. Thereby, two different mechanisms of decoupling: (a) the coupling of the forest canopy by coherent structures (see Chaps. 6 and 11) and (b) the decoupling of the near forest floor layer. To identify coupling or decoupling, the magnitude and the sign of fluxes are compared. We successfully tested a new approach to the detection of decoupling of the near forest floor layer by calculating an effective surface concentration from a given flux with a multilayer model and comparing this to measured concentrations. Measured eddy covariance and modelled sensible heat fluxes from the multilayer model showed surprisingly good agreement, which was not expected based on the heterogeneity of available energy at the forest floor and the generally low fluxes (max. 25 W m^{-2}) that were often close to the detection limit of the eddy covariance method. As the multilayer model was shown to reproduce the sensible heat flux very well, it is assumed to be a suitable tool for deriving fluxes of (reactive) trace gases as well. When compared to CO_2 and ^{222}Rn flux measurements obtained by a static chamber system, no good agreement was found. This was probably caused by one of the well-known technical problems of enclosures that can alter the soil flux. Therefore, chamber measurements should always be validated against an independent measurement at the best co-located eddy covariance measurements. But even the best technical solutions will still suffer from the disturbed exchange conditions caused by enclosing the above soil air. Therefore, other methods of inferring soil fluxes should be favored.

Another advantage of using the model was that it allowed the calculation of effective surface concentrations that could be compared to measured surface concentrations for several tracers (including ^{222}Rn, H_2O, CO_2, and O_3) and subsequently be used to infer the decoupling of the near forest floor layer. Radon is, in principle, perfectly suited for such a task as it is chemically inert and is emitted solely from the ground. It turned out, however, that the precision and time resolution of the ^{222}Rn measurements put limits on this method. Furthermore, ^{222}Rn has a lifetime sufficient for it to be advected, which disturbs the local gradients. In addition, due to heterogeneous sources and sinks at the forest floor, the different footprints of the heights of the profile represent averages of different fluxes, which interfere with the comparison of a very local surface condition. Nevertheless, periods of good agreement of measured and modelled effective surface concentration were similar for ^{222}Rn, H_2O, and CO_2. The agreements (and disagreement) of modelled and measured surface concentration was used to infer coupling or decoupling of the ground surface form the air layers above. So far, the decoupling of the near forest floor layer has not been reported, although it has important implications on how soil-chamber and in-soil measurements can be linked to measurements in or above the trunk space. As a consequence, respiration fluxes derived from conditional sampling of eddy covariance fluxes above canopy

(Chap. 6) have to be revisited as well. Nevertheless, the gradients of reactive trace gases and also the fluxes of O_3 seemed to be predominantly influenced by the coupling with the above layers by coherent structures and to a lesser extent by the decoupling of the soil layer, but the canopy coupling only influenced the height of the layer where most of O_3 depletion is strongest. Assessment of the influence of the decoupling of the near forest floor layer on the magnitude of trace gas fluxes is not straightforward and needs longer time series of collocated eddy covariance fluxes and highly resolved profiles in the lowest meter above ground. Nevertheless, the results show that profile measurements close to the ground are important for validating the link between fluxes in and out of the soil determined by laboratory or chamber measurements and fluxes measured in the trunk space. As sensible heat fluxes showed good agreement, one might further focus on the temperature by (a) using fiber-optic distributed temperatures sensing (Thomas et al. 2012) which will overcome the problem of measured gradients becoming more local with decreasing height and (b) by using infrared surface temperature sensors or cameras to compare the "real" surface temperature to those modelled from the gradients and fluxes. Furthermore, the use of ^{220}Rn instead of ^{222}Rn will lead to more counts and almost no advection due to the low radioactive decay time (56 s).

Acknowledgment The authors gratefully acknowledge financial support by the German Science Foundation (DFG projects EGER, FO 226/16-1, ME 2100/4-1 and ZE 792/4-1) and by the Max Planck Society. For borrowing a static chamber and two radon monitors, we would like to thank Franz Conen from the Department of Environmental Sciences of the University of Basel. We would like to thank Johannes Lüers and Korbinian Hens for sharing their experience with radon measurements at the Waldstein site.

References

Bain WG, Hutyra L, Patterson DC, Bright AV, Daube BC, Munger JW, Wofsy SC (2005) Wind-induced error in the measurement of soil respiration using closed dynamic chambers. Agric For Meteorol 131:225–232

Baldocchi DD, Meyers TP (1991) Trace gas exchange above the floor of a deciduous forest: 1. Evaporation and CO_2 efflux. J Geophys Res 96(D4):7271–7728

Bloomer BJ, Vinnikov KY, Dickerson RR (2010) Changes in seasonal and diurnal cycles of ozone and temperature in the eastern U.S. Atmos Environ 44:2543–2551

Damköhler G (1940) Der Einfluss der Turbulenz auf die Flammengeschwindigkeit in Gasgemischen. Z Elektrochem 46:601–652

Davidson EA (1992) Pulses of nitric oxide and nitrous oxide flux following wetting of dry soil: an assessment of probable sources and importance relative to annual fluxes. Ecol Bull 42:149–155

Davidson EA, Savage K, Verchot LV, Navarro R (2002) Minimizing artifacts and biases in chamber-based measurements of soil respiration. Agric For Meteorol 113:21–37

Foken T (1979) Vorschlag eines verbesserten Energieaustauschmodells mit Berücksichtigung der molekularen Grenzschicht der Atmosphäre. Z Meteorol 29:32–39

Foken T (1984) The parametrisation of the energy exchange across the air-sea interface. Dyn Atmos Oceans 8:297–305

Foken T (2008) Micrometeorology. Springer, Berlin, Heidelberg, 308 pp, (2nd edition 2017)

Foken T, Kitajgorodskij SA, Kuznecov OA (1978) On the dynamics of the molecular temperature boundary layer above the sea. Bound-Lay Meteorol 15:289–300

Foken T, Meixner FX, Falge E, Zetzsch C, Serafimovich A, Bargsten A, Behrendt T, Biermann T, Breuninger C, Dix S, Gerken T, Hunner M, Lehmann-Pape L, Hens K, Jocher G, Kesselmeier J, Lüers J, Mayer JC, Moravek A, Plake D, Riederer M, Rütz F, Scheibe M, Siebicke L, Sörgel M, Staudt K, Trebs I, Tsokankunku A, Welling M, Wolff V, Zhu Z (2012) Coupling processes and exchange of energy and reactive and non-reactive trace gases at a forest site—results of the EGER experiment. Atmos Chem Phys 12:1923–1950

Horii CP, Munger JW, Wofsy S, Zahniser M, Nelson D, McManus JB (2004) Fluxes of nitrogen oxides over a temperate deciduous forest. J Geophys Res 109:D08305

Hübner J, Siebicke L, Lüers J, Foken T (2016) Forest climate in vertical and horizontal scales. In: Foken T (ed) Energy and Matter Fluxes of a Spruce Forest Ecosystem. Springer, Berlin, Heidelberg

Kimball BA, Lemon ER (1971) Air turbulence effects upon soil gas exchange. Soil Sci Soc Am J 35:16–21

Kutzbach L, Schneider J, Sachs T, Giebels M, Nykänen H, Shurpali NJ, Martikainen PJ, Alm J, Wilmking M (2007) CO_2 flux determination by closed-chamber methods can be seriously biased by inappropriate application of linear regression. Biogiosciences 4:1005–1025

Launiainen S, Rinne J, Pumpanen J, Kulmala L, Kolari P, Keronen P, Siivola E, Pohja T, Hari P, Vesala T (2005) Eddy covariance measurements of CO_2 and sensible and latent heat fluxes during a full year in a boreal pine forest trunk-space. Boreal Environ Res 10:569–588

Lehmann BE, Lehmann M, Neftel A, Gut A, Tarakanov SV (1999) 220 Radon calibration of near-surface turbulent gas transport. Geophys Res Lett 5:607–610

Lehmann BE, Neftel A, Tarakanov SV (2001) Continuous on-line calibration of diffusive soil-atmosphere trace gas transport using vertical ^{220}Rn- and ^{222}Rn activity profiles. Radiochim Acta 11–12:839–843

Lehmann BE, Ihlya B, Salzmann S, Conen F, Simon E (2004) An automatic static chamber for continuous ^{220}Rn and ^{222}Rn flux measurements from soil. Radiat Meas 38:43–50

Leighton PA (1961) Photochemistry of air pollution. Academic Press, New York

Lüers J, Bareiss J (2010) The effect of misleading surface temperature estimations on the sensible heat fluxes at a high Arctic site—the Arctic Turbulence Experiment 2006 on Svalbard (ARCTEX-2006). Atmos Chem Phys 10:157–168

Lund CP, Riley WJ, Pierce LL, Field B (1999) The effects of chamber pressurization on soil-surface CO_2 flux and the implications for NEE measurements under elevated CO_2. Glob Chang Biol 5:269–281

Misson L, Baldocchi DD, Black TA, Blanken PD, Brunet Y, Curiel Yuste J, Dorsey JR, Falk M, Granier A, Irvine MR, Jarosz N, Lamaud E, Launiainen S, Law BE, Longdoz B, Loustau D, McKay M, Paw U KT, Vesala T, Vickers D, Wilson KB, Goldstein AH (2007) Partitioning forest carbon fluxes with overstory and understory eddy-covariance measurements: a synthesis based on FLUXNET data. Agric For Meteorol 144:14–31

Nordbo A, Järvi L, Vesala T (2012) Revised eddy covariance flux calculation methodologies—effect on urban energy balance. Tellus Ser B 64:18184. doi:10.3402/tellusb.v64i0.18184

Plake D, Trebs I (2013) An automated system for selective and continuous measurements of vertical thoron profiles for the determination of transport times near the ground. Atmos Meas Tech 6:1017–1030

Richter SH, Skeib G (1984) Anwendung eines Verfahrens zur Parametrisierung des turbulenten Energieaustausches in der atmosphärischen Bodenschicht. Geod Geophys Veröff, R II 26:80–85

Richter SH, Skeib G (1991) Ein Verfahren zur Parametrisierung von Austauschprozessen in der bodennahen Luftschicht. Abh Meteorol Dienstes DDR 146:15–22

Riederer M, Serafimovich A, Foken T (2014) Eddy covariance—chamber flux differences and its dependence on atmospheric conditions. Atmos Meas Tech 7:1057–1064

Scholes MC, Martin R, Scholes RJ, Parsons D, Winstead E (1997) NO and N_2O emissions from savanna soils following the first simulated rains of the season. Nutr Cycl Agroecosyst 48:115–122

Serafimovich A, Thomas C, Foken T (2011) Vertical and horizontal transport of energy and matter by coherent motions in a tall spruce canopy. Bound-Lay Meteorol 140:429–451

Skeib G (1980) Zur Definition universeller Funktionen für die Gradienten von Windgeschwindigkeit und Temperatur in der bodennahen Luftschicht. Z Meteorol 30:23–32

Sodemann H, Foken T (2005) Special characteristics of the temperature structure near the surface. Theor Appl Climatol 80:81–89

Sörgel M, Trebs I, Serafimovich A, Moravek A, Held A, Zetzsch C (2011) Simultaneous HONO measurements in and above a forest canopy: influence of turbulent exchange on mixing ratio differences. Atmos Chem Phys 11:841–855

Subke JA, Tenhunen JD (2004) Direct measurements of CO_2 flux below a spruce forest canopy. Agric For Meteorol 126:157–168

Thomas C, Foken T (2007) Flux contribution of coherent structures and its implications for the exchange of energy and matter in a tall spruce canopy. Bound-Lay Meteorol 123:317–337

Thomas C, Martin J, Goeckede M, Siqueira M, Foken T, Law B, Loescher H, Katul G (2008) Estimating daytime subcanopy respiration from conditional sampling methods applied to multi-scalar high frequency turbulence time series. Agric For Meteorol 148:1210–1229

Thomas CK, Kennedy AM, Selker JS et al (2012) High-resolution fibre-optic temperature sensing: a new tool to study the two-dimensional structure of atmospheric surface layer flow. Bound-Lay Meteorol 142:177–192. doi:10.1007/s10546-011-9672-7

U.S. EPA (2006) Air quality criteria for ozone and related photochemical oxidants. EPA/600/R-05/004aF-cF. U.S. Environmental Protection Agency, Washington, DC

Zeeman MJ, Eugster W, Thomas CK (2013) Concurrency of coherent structures and conditionally sampled daytime sub-canopy respiration. Bound-Lay Meteorol 146:1–15

Chapter 9
Reactive Trace Gas and Aerosol Fluxes

Andreas Held, Malte Julian Deventer, Franz X. Meixner, Sebastian Schmitt, Matthias Sörgel, Linda Voß, and Veronika Wolff

9.1 Introduction

In addition to studying long-term carbon and water vapor fluxes (see Chap. 4), quantifying the surface-atmosphere exchange of reactive trace gases and aerosols is extremely important for a full understanding of biogeochemical cycles and

A. Held (✉)
Atmospheric Chemistry, University of Bayreuth, 95440, Bayreuth, Germany

Bayreuth Center of Ecology and Environmental Research, University of Bayreuth, Bayreuth, Germany
e-mail: andreas.held@uni-bayreuth.de

M.J. Deventer
Department of Geography, University of California, Berkeley, CA, 94720, USA

F.X. Meixner • M. Sörgel
Max Planck Institute for Chemistry, Hahn-Meitner-Weg 1, 55128 Mainz, Germany

S. Schmitt
Forschungszentrum Jülich, IEK-8, 52425 Jülich, Germany

L. Voß
GEO-NET Umweltconsulting GmbH, Große Pfahlstraße 5a, 30161 Hannover, Germany

V. Wolff
Agroscope, Reckenholzstrasse 191, 8046 Zürich, Switzerland

M. J. Deventer: Affiliation during the work at the Waldstein sites—University of Münster, Institut für Landschaftsökologie, Heisenbergstr. 2, 48149 Münster, Germany.

L. Voß, V. Wolff: Affiliation during the work at the Waldstein sites—Max Planck Institute for Chemistry, Hahn-Meitner-Weg 1, 55128 Mainz, Germany.

M. Sörgel, S. Schmitt: Affiliation during the work at the Waldstein sites—Atmospheric Chemistry, University of Bayreuth, 95440 Bayreuth, Germany.

A. Held: Affiliation during the work at the Waldstein sites before 2003—Department of Climatology, Bayreuth Institute of Terrestrial Ecosystem Research (BITÖK), University of Bayreuth, Germany.

T. Foken (ed.), *Energy and Matter Fluxes of a Spruce Forest Ecosystem*,
Ecological Studies 229, DOI 10.1007/978-3-319-49389-3_9

their implications for air quality and climate. For example, turbulent fluxes of nitric oxide (NO), nitrogen dioxide (NO_2), and ozone (O_3) as well as chemical reactions of the $NO/NO_2/O_3$ triad influence atmospheric ozone concentrations and thus oxidant budgets and the self-cleansing capacity of the atmosphere (see also Chap. 3). Atmospheric aerosol particles exhibit a direct climate effect due to scattering and absorption of radiation, and an indirect climate effect through aerosol-cloud interactions, which is currently considered the largest individual source of uncertainties in estimating the anthropogenic radiative forcing (Boucher et al. 2013).

Direct quantification of the turbulent exchange of reactive trace gases and aerosols by micrometeorological techniques is challenging for various reasons (see also Chap. 19): Firstly, both turbulence and chemistry contribute to changes in trace gas or aerosol concentrations. In particular, when the characteristic time scales of chemical reactions and turbulent transport are similar, it is difficult to separate chemical production or loss processes from turbulent transport. Secondly, for many trace gas and for aerosol measurements, fundamental assumptions required for valid flux measurements may be violated. For example, the aerosol number concentration cannot be considered a conservative scalar, and thus, the assumption of steady-state conditions required for direct eddy covariance measurements is violated under certain conditions. Thirdly, technical limitations of the available instrumentation for some trace gases and for size-resolved or chemically speciated aerosol measurements restrict their application in micrometeorological flux measurement techniques.

In this chapter, we will present flux measurements of reactive trace gases and aerosols carried out at the Waldstein-Weidenbrunnen site over the last 20 years. We will focus on ozone deposition and its implications for the $NO/NO_2/O_3$ triad, biogenic emissions of volatile organic compounds (VOC) from Norway spruce and their subsequent oxidation reactions, and, finally, the turbulent exchange of aerosol particles between a spruce canopy and the atmosphere.

In forest ecosystems such as the Waldstein site, dry deposition to the vegetation canopy is an important sink for tropospheric ozone (cf. Figure 9.1). The presence of tall vegetation significantly modifies the properties of the surface and thus the turbulent exchange conditions. Typically, the transport within the canopy is much slower than above the canopy, which provides additional time for chemical reactions in the canopy. In particular, ozone concentrations are closely linked to NO and NO_2, which play an important role in tropospheric chemistry. NO may be emitted from the forest soil and react with peroxy radicals to produce ozone. Depending on the ambient NO_2 concentrations, NO_2 may be taken up by the canopy (cf. Lerdau et al. 2000). Therefore, ozone exchange fluxes in a spruce forest such as the Waldstein site have to be evaluated in light of the chemical reactions of ozone with NO, NO_2, and other reactive nitrogen compounds such as nitrous acid (HONO; cf. Chap. 8).

Additional reaction partners for ozone at the Waldstein site include volatile organic compounds (VOC), in particular monoterpenes such as alpha-pinene. Emission strengths of biogenic VOC from Norway spruce are mainly dependent on temperature; however, emission patterns and strengths may change considerably depending on other factors such as plant age or environmental stress. Due to fast

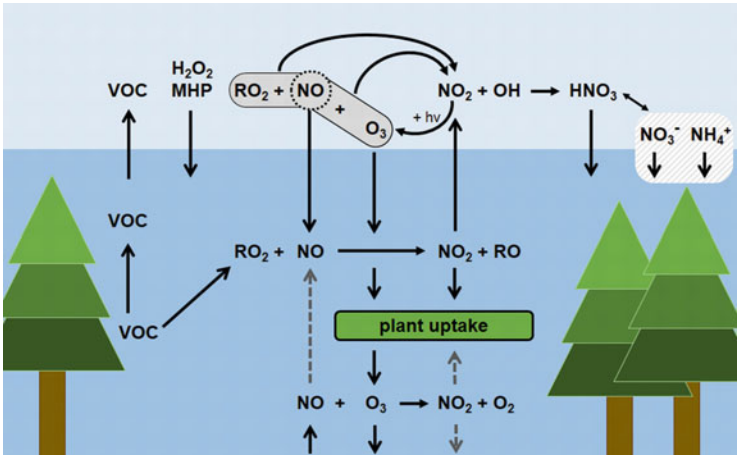

Fig. 9.1 Schematic representation of the trace gas fluxes above, within, and below the Waldstein spruce canopy

chemical reactions, branch emissions of volatile organic compounds may differ substantially from VOC exchange fluxes above the canopy. Both turbulent transport and chemical reactions of VOC have to be taken into account when quantifying the VOC budget in a forest ecosystem. Oxidation products of biogenic VOCs may partition into the particle phase, and thus, be an important source of new aerosol particles by gas-to-particle conversion.

The contribution of biogenic VOC oxidation products to new particle formation links the budgets of ozone, volatile organic compounds, and atmospheric aerosol particles at the Waldstein site. Turbulent transport may quickly remove freshly formed particles from the atmosphere. However, aerosol emission bursts and bidirectional aerosol fluxes, i.e., simultaneous emission of small particles and deposition of larger particles, have been observed at the Waldstein site. Climate and health effects of atmospheric aerosol particles depend strongly on aerosol concentration, size, chemical composition, and their spatial distribution in the atmosphere.

Close to the ground, number and mass concentrations and the spatial distribution of the atmospheric aerosol are determined to a large extent by surface-atmosphere exchange. Dry deposition can account for a large fraction of particle removal from the atmosphere. Directly measuring vertical aerosol fluxes, and thus quantifying dry deposition, is a prerequisite for a full understanding of the aerosol spatial distribution and associated environmental effects. While the contribution of vertical aerosol fluxes to the CO_2-dominated atmospheric carbon cycle can be considered insignificant, the net mass exchange of aerosol compounds such as sulfate and nitrate is important for the atmospheric sulfur and nitrogen cycles. Considering cloud formation and the number of cloud condensation nuclei, it is also important to evaluate whether forest canopies typically act as net sinks or net sources with respect to particle number. Therefore, improved and more comprehensive parameterizations

of vertical transport and exchange of aerosol particles in air quality and climate models are research priorities.

9.2 Materials and Methods

Direct micrometeorological flux measurements require fast-response sensors for the scalar of interest. For several trace gases such as ozone and nitrogen oxides, instrumentation has become available that is sufficiently fast for application in eddy covariance (EC) setups. However, for other trace gases such as nitric acid or organic peroxides, and for most aerosol properties, the measurement capabilities are limited with respect to time response. Therefore, if direct flux measurements are not possible due to technical limitations, indirect methods such as the aerodynamic gradient method (GRAD) or relaxed eddy accumulation (REA) are applied. In these methods, fluxes are derived from concentration differences measured at different heights or in updraft and downdraft samples collected by conditional sampling. Thus, GRAD and REA techniques require highly accurate and precise trace gas or aerosol instrumentation.

Most trace gas and aerosol flux measurements at the Waldstein-Weidenbrunnen site were carried out above the spruce canopy on top of the main tower at 32 m above ground level (agl). In dedicated field studies, additional flux measurements were made within and below the canopy. Many of the reactive trace gas and aerosol flux measurements presented in this chapter were carried out as part of large coordinated field experiments, either within the BEWA project or within the EGER project. The BEWA field experiments (Steinbrecher et al. 2004; Klemm et al. 2006) were conducted at the Waldstein site in the summers of 2001 and 2002, focusing on regional biogenic emissions of reactive volatile organic compounds (BVOC) from forests. The EGER project (Foken et al. 2012) studied exchange processes in mountainous regions in three intensive observation periods (IOP1/2/3) in the years 2007, 2008, and 2011.

For micrometeorological flux measurements of reactive trace gases and aerosols, combined measurements of the vertical wind speed (with a sonic anemometer) and the trace gas or aerosol concentration (with an appropriate analyzer) are required. In the following, the basic working principles of trace gas and aerosol analyzers, which have been applied in flux measurements at the Waldstein-Weidenbrunnen site, will be briefly summarized. For details about the full technical setup and data evaluation, the reader is referred to the literature.

9.2.1 Trace Gas Flux Instrumentation

Reactive trace gas flux measurements of ozone, nitrogen oxides, nitric acid, organic peroxides, and volatile organic compounds have been performed at the Waldstein-

Table 9.1 Instrumentation for reactive trace gas flux measurements at the Waldstein site

Trace gas	Principle of analyzer	Flux method	Reference
O_3	Solid-phase chemiluminescence	EC	Güsten and Heinrich (1996)
O_3	UV absorption	GRAD	Tsokankunku (2014)
NO/NO_2	Chemiluminescence	EC	Tsokankunku (2014)
NO/NO_2	Chemiluminescence	GRAD	Tsokankunku (2014)
HNO_3	NaCl denuder/ion chromatography (IC)	REA	Pryor et al. (2002)
Peroxides	Liquid chromatography with fluorescence detection (HPLC-FLD)	REA	Valverde-Canossa (2004)
VOC	Proton-transfer-reaction mass spectrometry (PTR-MS)	REA	Graus et al. (2006)
VOC	Gas chromatography with flame ionization detection (GC-FID)	REA	Steinbrecher et al. (2000)
VOC	Gas chromatography with mass spectrometry and flame ionization detection (GC-MS/FID)	REA	Schmitt (2013)

EC eddy covariance, *GRAD* aerodynamic gradient method, *REA* relaxed eddy accumulation

Weidenbrunnen site. Table 9.1 summarizes the applied trace gas analyzers and flux methods, which will be briefly explained in the following.

Fast-response ozone sensors based on solid-phase chemiluminescence (Güsten and Heinrich 1996) have been widely used in EC flux measurements of ozone. Ozone reacts with a dry chemiluminescent dye, and the resulting light intensity is proportional to the ozone concentration. There are various manufacturers of fast ozone sensors based on this principle, e.g., GFAS GmbH (Germany) or Enviscope GmbH (Germany). These sensors provide high-frequency (20 Hz) data of ozone fluctuations, however, no absolute ozone concentration measurements because of rapid degradation of the chemiluminescent dye, which changes the absolute sensitivity of the sensor for ozone. In order to derive ozone fluxes, ozone concentrations are measured side-by-side with slow-response ozone analyzers based on UV absorption.

For direct EC flux measurements of NO and NO_2, a fast two-channel NO/NO_2 analyzer (CLD 790SR-2, Eco Physics, Switzerland) was employed with a measuring frequency of 5 Hz. NO concentrations were quantified by the chemiluminescence reaction of NO with excess ozone: A certain fraction of the reaction product NO_2 will be in an excited state NO_2^*. NO_2^* returns to the ground state by photon emission, and these photons are then detected and counted. For NO_2 concentration measurements, NO_2 is converted to NO before the chemiluminescence measurement, which then yields the total concentration of NO and converted NO_2, i.e., NO_x. The concentration of NO_2 is calculated as the difference of the NO_x and the NO measurement, taking into account the efficiency of the NO_2 converter. For the flux measurements presented in Sect. 9.3.1, NO_2 was converted to NO with two blue light converters (AQD, MetCon GmbH, Germany) in series with a high

conversion efficiency. For calibration of the fast-response NO/NO_2 measurements, the concentrations were compared to a slow-response NO/NO_2 chemiluminescence analyzer (CLD TR-780, Eco Physics, Switzerland) measuring side-by-side.

For nitric acid (HNO_3) REA flux measurements (cf. Pryor et al. 2002), HNO_3 was sampled in one of three NaCl-coated denuders depending on the vertical wind speed: one for updrafts, one for downdrafts, and a third for constant sampling. The concentration difference of the updraft and downdraft sample was used for the REA approach, while the third denuder sample provided the average HNO_3 concentration for the entire measurement period. In order to increase the updraft/downdraft concentration differences, a dynamic dead band was applied. After HNO_3 sampling in the field, the denuders were extracted in deionized water and analyzed for NO_3^- by ion chromatography in the laboratory.

REA flux measurements of hydrogen peroxide and organic peroxides were conducted by collecting peroxides on two helix-shaped sampling coils depending on the vertical wind speed. The sampling coils were kept at a constant temperature of 5 °C, and deionized water acidified with H_3PO_4 was used as the scrubbing solution. Immediately after collection, the samples were analyzed by liquid chromatography (HPLC) with a fluorescence detector using post-column derivatization with horseradish peroxidase (Valverde-Canossa 2004).

Canopy-scale flux measurements of volatile organic compounds (VOC) require both sensitive and specific analyzers. Proton-transfer-reaction mass spectrometry (PTR-MS) is an extremely sensitive technique for the quantification of volatile organic compounds. The chemical ionization technique is based on proton transfer reactions from H_3O^+ reagent ions to volatile organic compounds (e.g., Lindinger et al. 1998). In the VOC flux measurements conducted during the BEWA field experiments, PTR-MS was applied in a REA setup. Meanwhile, the PTR-MS technique is sufficiently fast for application in direct EC flux measurements of VOC (e.g., Karl et al. 2001; Müller et al. 2010). In REA flux measurements, VOC analysis may also be performed by gas chromatography with flame ionization detection (GC-FID) or mass spectrometry (GC-MS). During the BEWA field experiments, VOC updraft and downdraft samples were collected depending on the vertical wind speed and separately directed to an online GC-FID system (HC1010, Airmotec, Germany). Details about the Airmotec VOC analysis including pre-concentration and cryo-focusing can be found in Steinbrecher et al. (2000). Schmitt (2013) utilized the GLOBOENET (Global Biogenic Organic Emissions Network) VOC REA sampler of the National Center for Atmospheric Research (NCAR, Boulder, CO, USA) to collect updraft and downdraft VOC samples on Tenax/Carbograph two-stage adsorbent tubes. Subsequently, the samples were sent to NCAR for offline analysis by thermal desorption GC-MS/FID for identification and quantification of isoprene and the five dominant monoterpene species.

9.2.2 Aerosol Flux Instrumentation

At the Waldstein-Weidenbrunnen site, measurements of net aerosol number fluxes, of size-resolved aerosol number fluxes, and of chemically speciated aerosol mass fluxes have been performed. The applied instruments and flux methods are summarized in Table 9.2. Further details about the aerosol instrumentation will be given in the following.

Aerosol number fluxes are frequently measured by eddy covariance with condensation particle counters (CPC), even though most commercially available CPCs are too slow for 10 Hz measurements due to the instrumental design with recirculation zones and laminar flow inside. In general, the aerosol sample enters a heated saturation chamber, which is typically saturated with butanol vapor. In a second step, both the particles and the butanol vapor enter a cooled condensation chamber, where the mixture becomes oversaturated with respect to butanol. This leads to condensation of butanol on particles with diameters as small as 3 nm (cf. Table 9.2) and rapid growth of these particles. Finally, the grown particles are individually detected and counted by light scattering.

In order to increase the time response of the CPC measurement, Wehner et al. (2011) built a fast mixing-type CPC (Fast CPC), where butanol-saturated air is mixed with the aerosol sample in a small mixing volume. Similar to laminar flow CPCs, the lower cutoff diameter depends on the temperature difference between the saturator temperature and the condenser temperature. In the Fast CPC used at the Waldstein site, this diameter varied between 6.4 nm and 9.9 nm. In a characterization experiment, Wehner et al. (2011) report an e-folding response time of 5 ms for their Fast CPC.

For size-resolved aerosol number flux measurements, an electrical low pressure impactor (ELPI+, Dekati Ltd., Finland) was applied. In the ELPI+ aerosol spectrometer, particles are electrically charged by corona discharge and separated according to their aerodynamic diameter in a 13-stage cascade impactor (17 nm to 10 μm) and a backup filter stage (6–17 nm). When the charged particles are collected on the impaction plates, they produce a current, which is proportional to the total particle concentration of the respective size fraction. The currents are measured individually using 14 electrometers with a measuring frequency of 10 Hz.

Total ammonium and nitrate fluxes (including both gas and particle phases) were derived from concentration measurements at two heights (30.9 m and 24.4 m agl) above the canopy with a wet chemical instrument, the gradient of aerosol and gases online registrator (GRAEGOR, ECN Petten, Netherlands). Gas and particle samples are collected simultaneously at two heights with a pair of wet annular denuders and steam-jet aerosol collectors, respectively. In the denuders, water-soluble gases diffuse into the sample solution.

Table 9.2 Instrumentation for aerosol flux measurements at the Waldstein site

Flux target	Instrument	Manufacturer	Diameter range	Flux method	Reference
Net aerosol number	CPC 3760A	TSI Inc. (USA)	>11 nm	EC	Held and Klemm (2006)
Net aerosol number	UCPC 3025	TSI Inc. (USA)	>3 nm	EC	Held and Klemm (2006)
Net aerosol number	Fast CPC	Custom-built (Wehner et al. 2011)	>6.4 nm	EC	Kittler F., personal communication
Size-resolved aerosol number	ELPI+	Dekati Ltd. (Finland)	6 nm to 10 μm	EC	Deventer et al. (2015)
Chemically speciated aerosol mass	GRAEGOR	ECN Petten (Netherlands)	Not specified	GRAD	Wolff et al. (2010a, 2010b)
Chemically speciated aerosol mass	LAMPAS2	Custom-built (Trimborn et al. 2000)	200 nm to 10 μm	IDES	Held et al. (2003)

CPC condensation particle counter, *UCPC* ultrafine condensation particle counter, *ELPI* electrical low pressure impactor, *GRAEGOR* gradient of aerosol and gases online registrator, *LAMPAS* laser mass analyzer for particles in the airborne state, *EC* eddy covariance, *GRAD* aerodynamic gradient method, *IDES* irregular disjunct eddy sampling

Subsequently, the sample air is mixed with a supersaturated flow of deionized water vapor in the steam-jet aerosol collector. Due to water vapor condensation, the particles rapidly grow to droplets, which are collected in a cyclone. Finally, the denuder sample solution (containing the dissolved gas-phase species) and the cyclone solution (containing the dissolved particulate species) are sequentially analyzed for anions using ion chromatography (IC) and for NH_3/NH_4^+ using flow injection analysis (FIA).

Held et al. (2003) presented the first approach to combine aerosol mass spectrometry and a micrometeorological technique to derive chemically speciated aerosol fluxes. The aerosol mass spectrometer LAMPAS2 (Laser Mass Analyzer for Particles in the Airborne State; Trimborn et al. 2000) ionizes individual aerosol particles by laser desorption ionization. Individual particles are hit by a pulsed ionization laser, which leads to (partial) vaporization and ionization. The resulting positive and negative ions are analyzed with a bipolar time-of-flight mass spectrometer, which yields information about the chemical composition of this individual particle. Because the exact sampling time of each analyzed particle is known, the corresponding vertical wind speed can be attributed to each individual particle composition in a post-processing step, and virtual conditional sampling is possible. Due to the fact that the timing of the aerosol analysis is irregular, this approach was called irregular disjunct eddy sampling (IDES).

9.3 Results and Discussion

A large number of reactive trace gas and aerosol flux measurements have been carried out at the Waldstein-Weidenbrunnen site over the last 20 years. Firstly, flux measurements of the $NO/NO_2/O_3$ triad and related flux measurements of HNO_3, organic peroxides, and volatile organic compounds will be summarized. Then, total and size-resolved aerosol number fluxes and chemically speciated aerosol mass fluxes will be presented and discussed. Finally, the observed fluxes will be compared with various parameterizations of turbulent transport and coupled chemistry-transport models.

9.3.1 Reactive Trace Gas Flux Measurements

In forest ecosystems such as the Waldstein site, dry deposition to the vegetation canopy is an important sink for trace gases such as ozone.

9.3.1.1 Ozone Fluxes

Turbulent deposition fluxes of ozone have been measured by eddy covariance since the late 1990s at the Waldstein-Weidenbrunnen site. Klemm and Mangold (2001) report ozone deposition fluxes varying from roughly −3 to −14 nmol m^{-2} s^{-1} on a daily average basis. In a more detailed analysis of the diurnal cycle of ozone deposition fluxes, the median flux values range from −0.5 to −8.6 nmol m^{-2} s^{-1} (Klemm et al. 2004). Klemm et al. (2004) also compared ozone fluxes measured above and below the canopy (at 32 m and 3 m agl) during the BEWA field campaign. The ozone flux ratio above/below the canopy ranged from 3.3 to 8.9.

This is consistent with Tsokankunku (2014), who obtained ozone deposition fluxes up to −25 nmol m^{-2} s^{-1} above the canopy and up to −2.5 nmol m^{-2} s^{-1} below the canopy, from eddy covariance measurements during EGER IOP2. However, ozone fluxes derived from a gradient approach for the same period ranged from −10 nmol m^{-2} s^{-1} to +10 nmol m^{-2} s^{-1} above the canopy and up to −2.5 nmol m^{-2} s^{-1} below the canopy. Obviously, the discrepancy between the eddy covariance and gradient methods above the canopy indicates a nonuniform distribution of ozone sources and sinks across the canopy.

Zhu et al. (2009) compared ozone fluxes measured at three different levels, above, within, and below the canopy (32 m, 17 m, 1 m agl) during EGER IOP2. During the day, the mean ozone flux was −11.0 nmol m^{-2} s^{-1} above the canopy, −7.0 nmol m^{-2} s^{-1} within the canopy, and −0.8 nmol m^{-2} s^{-1} below the canopy. At night, the mean ozone flux was −5.2 nmol m^{-2} s^{-1} above the canopy, −3.2 nmol m^{-2} s^{-1} within the canopy, and −0.5 nmol m^{-2} s^{-1} below the canopy. This indicates that ozone deposition in the layer from 1 m to 17 m agl contributes most to the total deposition (about 54 %), while the layer below 1 m agl contributes about 8 %, and the layer from 17 m to 32 m agl contributes roughly 38 % to the total deposition flux on a daily mean basis.

During EGER IOP3, Voß (2015) analyzed ozone fluxes measured at the Waldstein-Weidenbrunnen site above the undisturbed canopy (32 m agl) and at 5.5 m agl about 280 m south of the main tower at the Köhlerloh clearing, representing a disturbed part of the ecosystem. They calculated median ozone deposition fluxes of −13 nmol m^{-2} s^{-1} above the canopy and −7.5 nmol m^{-2} s^{-1} at the clearing, with distinct diurnal patterns and the highest absolute values during daytime. This diurnal variation indicates stomatal activity as an important controlling factor. However, the observed nighttime deposition suggests that additional ozone sinks exist. A comparison of the ozone deposition fluxes in the undisturbed and disturbed parts of the ecosystem shows that a reduction of the vegetation, e.g., by wind disturbances, is also reflected in reduced ozone deposition fluxes equivalent to the ratio of the leaf area indices of the canopies before and after the disturbance.

Evidently, during advection and vertical transport within the canopy, there is time for chemical reactions. Ozone concentrations are closely linked to concentrations of NO and NO_2 through reactions R9.1–R9.3:

$$O_3 + NO \rightarrow NO_2 + O_2 \quad \text{(R9.1)}$$

$$NO_2 + h\nu \rightarrow NO + O \quad \text{(R9.2)}$$

$$O + O_2 + M \rightarrow O_3 + M \quad \text{(R9.3)}$$

The effectiveness of R9.1 as a sink for ozone depends on the spatial distribution of O_3 and NO sources and the transport of these compounds. If NO is emitted from the soil and ozone mixed into the canopy from aloft, R9.1 may be limited when turbulent mixing is not active or when the sub-canopy is vertically decoupled from above-canopy layers (cf. Chap. 6). The production of ozone by R9.2 and R9.3 mainly depends on the photolysis rate of NO_2, which is considerably reduced below the canopy. Therefore, the chemical reactions of ozone with NO, NO_2, and other reactive compounds have to be taken into account when evaluating ozone exchange fluxes within and above the canopy.

9.3.1.2 NO_x Fluxes

NO and NO_2 fluxes were measured by eddy covariance and compared with a gradient approach during EGER IOP2 (Tsokankunku 2014). NO fluxes above the canopy were directed toward the surface and ranged up to -1.75 nmol m^{-2} s^{-1} both in the eddy covariance and the gradient flux measurements. In contrast, NO_2 eddy covariance fluxes were positive from 0 to $+2$ nmol m^{-2} s^{-1}, whereas NO_2 fluxes obtained from the gradient method ranged from -2 to $+2$ nmol m^{-2} s^{-1}. With the gradient method, NO/NO_2 fluxes were also calculated below the canopy close to the ground. Here, NO fluxes were positive from $+0.1$ to $+0.45$ nmol m^{-2} s^{-1}, which reflects NO soil emissions. NO_2 fluxes ranged from -0.2 to $+0.3$ nmol m^{-2} s^{-1}.

Breuninger et al. (2012, 2013) obtained exchange fluxes of NO and NO_2 between the spruce canopy and the atmosphere from dynamic chamber measurements at the branch level. During daytime, nitrogen oxide exchange fluxes were mostly directed toward the vegetation surface (NO, -0.110 to $+0.090$ nmol m^{-2} s^{-1}; NO_2, -0.341 to $+0.058$ nmol m^{-2} s^{-1}). At night, NO exchange fluxes were exclusively positive ($+0.002$ to $+0.023$ nmol m^{-2} s^{-1}), while NO_2 exchange fluxes were still mostly negative (-0.414 to $+0.155$ nmol m^{-2} s^{-1}). At the same time, ozone exchange fluxes were almost exclusively directed toward the vegetation surface (-1.167 to $+0.293$ nmol m^{-2} s^{-1}). Interestingly, the NO_2 compensation point concentrations,

i.e., the NO_2 concentration above which the canopy acts as a net NO_2 sink and below which the canopy acts as a net NO_2 source, calculated from these data were not significantly different from zero, thus challenging the existence of a NO_2 compensation point concentration for spruce.

Table 9.3 summarizes trace gas fluxes of ozone and nitrogen oxides observed at the Waldstein site. Ozone fluxes are mostly negative, i.e., directed toward the surface. Ozone deposition is typically higher during the day and reduced to about 50 % at night, which is consistent with reduced stomatal uptake when stomata are closed (Foken et al. 2012).

The chemical reaction of ozone with NO (R9.1) also contributes to an apparent uptake of ozone within the canopy. For the Waldstein site, both NO emissions from the soil and anthropogenic NO sources are quite small, and NO mixing ratios are typically well below 1 ppb. Nevertheless, the conversion of NO to NO_2 might contribute to apparent ozone deposition, in particular when the photolysis reaction of NO_2 (R9.2) is efficiently suppressed in the dark canopy. In fact, during dark periods without solar radiation, only ozone deposition was derived from a gradient approach, while also positive ozone fluxes (apparent emission) were observed when high NO concentrations and sunlight created an ozone sink above the canopy (Tsokankunku 2014).

Above the canopy, observed NO fluxes are mostly negative indicating efficient uptake within the canopy. Below the canopy, most of the NO emitted from the soil (e.g., Bargsten et al. 2010) is oxidized by O_3 in the first meter above the forest floor. This reaction acts as a below-canopy or in-canopy source of NO_2, which results in above-canopy emission fluxes of NO_2. NO_2 can be released from the canopy because NO_2 photolysis is strongly reduced in the dark canopy and because uptake by the spruce needles is quite low (Breuninger et al. 2012, 2013). Obviously, the distribution and magnitudes of the biological and chemical sources and sinks of NO and NO_2 have to be taken into account when comparing measurements of fluxes and concentration differences of these reactive trace gases.

9.3.1.3 Fluxes of Additional Reactive Trace Gases

Additional chemical reactions, e.g., the oxidation of NO_2 with OH, the reaction of NO with organic peroxy radicals, or the reaction of ozone with volatile organic compounds, expand the reactions of the chemical triad NO-NO_2-O_3 and can act as alternative sinks (or sources) of nitrogen oxides and ozone. Table 9.4 provides an overview of exchange fluxes of additional trace gases observed at the Waldstein site.

During daytime, photolysis of NO_2 competes with the reaction of NO_2 with the OH radical, which produces nitric acid (HNO_3). At the Waldstein-Weidenbrunnen site, mean HNO_3 concentrations of 32 nmol m^{-3} were reported for measurements in May 2002 (Pryor and Klemm 2004) and mean concentrations of 14 nmol m^{-3} as well as maximum concentrations of 69 nmol m^{-3} during EGER IOP1 (Wolff et al. 2010b). Pryor and Klemm (2004) calculated mean HNO_3 deposition fluxes of -1.5 nmol m^{-2} s^{-1} during daytime, ranging from roughly -7 to $+1$ nmol m^{-2} s^{-1}.

Table 9.3 Overview of observed trace gas fluxes at the Waldstein site: ozone and nitrogen oxides

Trace gas	Method	Height (m)	Specification	Flux (nmol m^{-2} s^{-1})	Reference
O_3	EC	32	Daily mean	−3 … −14	Klemm and Mangold (2001)
O_3	EC	32	Median	−0.5 … −8.6	Klemm et al. (2004)
O_3	EC	32		−25 … 0	Tsokankunku (2014)
O_3	GRAD	32/25		−10 … +10	Tsokankunku (2014)
O_3	EC	32	Daytime mean	−11.0	Zhu et al. (2009)
O_3	EC	32	Nighttime mean	−5.2	Zhu et al. (2009)
O_3	EC	32 (forest)	Median	−11.0	Voß (2015)
O_3	EC	17	Daytime mean	−7.0	Zhu et al. (2009)
O_3	EC	17	Nighttime mean	−3.0	Zhu et al. (2009)
O_3	EC	5.5 (clearing)	Median	−7.5	Voß (2015)
O_3	EC	1		−2.5 … 0	Tsokankunku (2014)
O_3	GRAD	1/0.005		−2.5 … 0	Tsokankunku (2014)
O_3	EC	1	Daytime mean	−0.8	Zhu et al. (2009)
O_3	EC	1	Nighttime mean	−0.5	Zhu et al. (2009)
NO	EC	32		−1.75 … 0	Tsokankunku (2014)
NO	GRAD	32/25		−1.75 … 0	Tsokankunku (2014)
NO	GRAD	1/0.005		+0.1 … +0.45	Tsokankunku (2014)
NO_2	EC	32		0 … +2	Tsokankunku (2014)
NO_2	GRAD	32/25		−2 … +2	Tsokankunku (2014)
NO_2	GRAD	1/0.005		−0.2 … +0.3	Tsokankunku (2014)

Table 9.4 Overview of observed trace gas fluxes at the Waldstein site: reactive nitrogen compounds, peroxides, and volatile organic compounds. Total NO_3^- and total NH_4^+ represent sum of trace gas and aerosol fluxes

Trace gas	Method	Height (m)	Specification	Flux (nmol m^{-2} s^{-1})	Reference
HNO_3	REA	32	Daytime mean	−1.5	Pryor et al. (2003), Pryor and Klemm (2004)
Total NO_3^-	GRAD	30.9/24.4	Monthly mean (September 2007)	−4.7	Wolff et al. (2010a, 2010b)
Total NH_4^+	GRAD	30.9/24.4	Monthly mean	−2.9	Wolff et al. (2010a, 2010b)
H_2O_2	REA	32	Daily mean	−0.8 ± 0.3	Valverde-Canossa et al. (2006)
MHP	REA	32	Daily mean	−0.03 ± 0.03	Valverde-Canossa et al. (2006)
HMHP	REA	32	Daily mean	−0.7 ± 0.5	Valverde-Canossa et al. (2006)
Isoprene	REA	32	Daytime max	up to +7	Steinbrecher et al. (2004)
Isoprene	REA	32	Daytime max	+1 to +1.5	Graus et al. (2006)
Isoprene	REA	32	Daytime max	+4.1 ± 0.8	Schmitt (2013)
Monoterpenes	REA	32	Daytime max	up to +5	Steinbrecher et al. (2004)
Monoterpenes	REA	32	Daytime max	+2	Graus et al. (2006)
Monoterpenes	REA	32	Daytime max	+5.5 ± 1.4	Schmitt (2013)

Cases of positive HNO_3 fluxes were observed in the morning hours and occurred together with positive ozone fluxes. This was interpreted as an indication of chemically induced flux divergence involving the NO-NO_2-O_3 triad. Apart from HNO_3 production by the reaction of NO_2 and OH, HNO_3 may be formed by repartitioning of ammonium nitrate or by hydrolysis of N_2O_5 in wet surface films on needles (Finlayson-Pitts and Pitts 2000). This indicates a non-negligible influence of gas-particle partitioning and the coupling of gaseous and aqueous phase chemistry on the concentrations and fluxes of reactive nitrogen species.

Wolff et al. (2010b) used a gradient approach to quantify the total ammonium (NH_3/NH_4^+) and the total nitrate (HNO_3/NO_3^-) exchange fluxes at the canopy top. When considering the sum of the gas and particle phases, repartitioning between the phases does not affect the total concentrations and fluxes. The total concentrations are conserved, and thus, the gradient approach for total ammonium and nitrate fluxes is less prone to flux divergence due to chemical reactions than for the individual compounds. Both total ammonium and total nitrate concentrations were dominated by the particulate phase. The mean total ammonium flux was -4.7 nmol m^{-2} s^{-1} with maximum daytime deposition fluxes up to -36 nmol m^{-2} s^{-1}. For total nitrate, the mean flux was -2.9 nmol m^{-2} s^{-1} and maximum daytime deposition fluxes up to -19 nmol m^{-2} s^{-1}. Both the total ammonium and nitrate fluxes were generally larger during sunny periods and smaller during cooler and more humid conditions. The total ammonium fluxes even showed emission events from wet or drying surfaces, while the total nitrate fluxes were always negative. This indicates that even though the total concentrations are not influenced by phase partitioning, the different deposition behavior of gaseous and particulate species is obviously reflected in changes of the total exchange fluxes.

Wolff et al. (2010b) point out that the exchange of reactive species seems not to be limited by any surface resistance. This is supported by REA flux measurements of hydrogen peroxide (H_2O_2) during the BEWA campaign in July 2001 (Valverde-Canossa et al. 2006). With maximum H_2O_2 mixing ratios of 1 ppb and less than 200 ppt of individual organic peroxides, Valverde-Canossa et al. (2006) observed daily mean H_2O_2 deposition fluxes of -0.8 ± 0.3 nmol m^{-2} s^{-1}, daily mean fluxes of hydroxymethyl hydroperoxide (HMHP) of -0.7 ± 0.5 nmol m^{-2} s^{-1}, and daily mean fluxes of methyl hydroperoxide (MHP) of -0.03 ± 0.03 nmol m^{-2} s^{-1}. During daytime, high deposition velocities suggest a negligible surface uptake resistance for H_2O_2, such that turbulent transport controls its surface exchange. In contrast, significantly smaller deposition velocities were observed for MHP indicating a significant surface uptake resistance. For HMHP, the REA measurements showed mainly deposition fluxes, while concentration profiles suggested in-canopy chemical production by reaction of ozone with alkenes. Such ozonolysis reactions within the canopy are also expected to affect the surface exchange of H_2O_2 and other organic peroxides, especially at nighttime.

With typical time scales of hours to days, H_2O_2 production by recombination of HO_2 is not expected to affect its turbulent transport with typical time scales in the order of minutes. However, laboratory studies (e.g., Hasson et al. 2001) suggest that H_2O_2 production from ozonolysis of alkenes can considerably influence the surface

exchange of H_2O_2. For MHP, in contrast, the yield from ozonolysis of alkenes is generally low, and typical time scales for MHP production and loss reactions are several hours.

The spruce trees at the Waldstein site are an important biogenic source of volatile organic compounds (VOC) including monoterpenes, isoprene, and other alkenes. Steinbrecher et al. (2004) reported maximum daytime canopy fluxes of isoprene up to +7 nmol m^{-2} s^{-1} and up to +5 nmol m^{-2} s^{-1} for the sum of monoterpenes derived from relaxed eddy accumulation with proton transfer reaction mass spectrometry (PTR-MS) in a case study in July 2001 during the BEWA field campaign. For the same field campaign, Graus et al. (2006) compared VOC canopy fluxes derived from REA PTR-MS and from a combination of REA and gas chromatography (REA GC). Both techniques agreed well during daytime with maximum isoprene fluxes up to +1.5 nmol m^{-2} s^{-1} and maximum monoterpene fluxes of +2.5 to +3 nmol m^{-2} s^{-1}. At night, negative monoterpene fluxes up to −1.5 nmol m^{-2} s^{-1} were obtained from the REA GC technique, while REA PTR-MS fluxes were close to zero.

The observed daytime fluxes were found to be consistent with plant emission fluxes derived from enclosure measurements on the branch level. Grabmer et al. (2006) obtained a monoterpene standard emission rate of 0.50 μg C g^{-1} dwt h^{-1} (dwt, leaf dry weight) from their measurements, which result in maximum daytime fluxes of 2.3 nmol m^{-2} s^{-1} under the specific conditions during the observation period. The standard emission rate of isoprene was determined to be 0.32 μg C g^{-1} dwt h^{-1}, resulting in a maximum daytime isoprene flux of 2.1 nmol m^{-2} s^{-1}. It has to be kept in mind that some of the volatile organic compounds emitted from the spruce needles are removed from the atmosphere by chemical reaction within the canopy. Thus, only a fraction of the primarily emitted VOC is released from the canopy to the atmosphere above due to in-canopy oxidation during turbulent transport.

The VOC above-canopy fluxes observed during the BEWA field campaign are consistent with the canopy fluxes derived from REA sampling and offline GC analysis in July 2013 (Schmitt 2013). The daily maximum isoprene fluxes were +4.1 ± 0.8 nmol m^{-2} s^{-1}, and the daily maximum fluxes of the sum of five monoterpenes were +5.5 ± 1.4 nmol m^{-2} s^{-1}. By comparison with the VOC emission pattern expected for Norway spruce taken from the MEGAN model (Guenther et al. 2012), Schmitt (2013) concluded that the emissions of α-pinene, β-pinene, camphene, Δ3-carene, and limonene contribute about 80 % to the total monoterpene emissions at the Waldstein site. Typical concentrations of the sum of these five monoterpenes ranged from roughly 1 to 70 nmol m^{-3} in the measurement period from May to October 2013.

Figure 9.1 schematically summarizes the reactive trace gas fluxes observed at the Waldstein-Weidenbrunnen site. Obviously, the vegetation is an important biogenic source of volatile organic compounds, which may contribute to a chemical flux divergence of the $NO/NO_2/O_3$ triad (e.g., Vilà-Guerau de Arellano et al. 1993). A certain fraction of the primarily emitted VOCs will be transported across the canopy and contribute to the observed above-canopy emission flux. Another fraction will

be oxidized within the canopy and yield oxygenated VOC or peroxy radicals (RO_2). Peroxy radicals and the hydroperoxyl radical (HO_2) can form hydrogen peroxide (H_2O_2) and organic peroxides such as methyl hydroperoxide (MHP), which exhibit a deposition flux to the canopy. Above-canopy NO deposition and NO soil emissions indicate an efficient in-canopy sink for NO. Because NO surface uptake can be considered negligible, chemical reactions seem to be important sink processes. For example, the reaction of NO with OH may form nitrous acid (HONO). Within the dark canopy, the reaction of NO with ozone or with peroxy radicals is probably more important. In particular, even small mixing ratios of peroxy radicals in the ppt range may affect $NO/NO_2/O_3$ exchange fluxes because the reaction constant of NO with the hydroperoxyl and other peroxy radicals is about 500 times higher than the reaction constant of NO with ozone. Thus, the oxidation of NO to NO_2 by organic peroxy radicals may shift the concentration ratios of the $NO/NO_2/O_3$ triad and will contribute to ozone formation if NO_2 is subsequently photolyzed. NO_2 may be taken up by plants; however, above-canopy emission of NO_2 was typically observed. Also above the canopy, NO_2 may react with OH and form nitric acid (HNO_3), which exhibited deposition fluxes. Photochemical production is an important source of ozone above the canopy, which contributes to overall ozone deposition. In addition, ozone is an extremely important oxidant for many primarily emitted volatile organic compounds. For example, monoterpene ozonolysis yields a large variety of oxygenated volatile organic compounds, which may finally partition into the particle phase after several oxidation steps. Thus, organic compounds contribute to both sink and source processes of ozone, and differences in VOC concentrations within and above the canopy reflect a complex interplay of turbulent transport and chemical reactions.

9.3.2 Aerosol Flux Measurements

The Waldstein site is located in a semirural area, where local anthropogenic aerosol sources are marginal. A large fraction of secondary inorganic aerosol, i.e., aerosol compounds such as sulfate, nitrate, and ammonium that have partitioned into the particle phase by chemical reaction of precursor gases (e.g., SO_2, NO_x, NH_3, see Chap. 3), indicates aerosol aging during long-range transport and advection to the Fichtelgebirge mountains (Klemm 2004). Extended areas of forest stands with an increased surface roughness may enhance turbulent exchange and thus aerosol deposition to the forest. On the other hand, local and regional formation of secondary organic aerosol from oxidation products of biogenic volatile organic compounds can contribute substantially to aerosol number concentrations during new particle formation events (e.g., Held et al. 2004). Therefore, the forest may act as a net aerosol sink or source, and aerosol flux measurements are required to quantify the surface exchange of particulate matter.

9.3.2.1 Aerosol Number Fluxes

Eddy covariance measurements of aerosol number fluxes were carried out during the BEWA field campaign in 2001 and 2002 (Held and Klemm 2006). The combination of a sonic anemometer and a condensation particle counter yields the net exchange with respect to the aerosol number concentration across the measurement height 22 m agl. In July/August 2001, the median aerosol deposition flux was -6.4×10^6 m^{-2} s^{-1} for particles with diameters (D) larger than 11 nm and -13.9×10^6 m^{-2} s^{-1} for $D > 3$ nm. The 95 % quantile flux was -30.5×10^6 m^{-2} s^{-1} ($D > 11$ nm) and -69.2×10^6 m^{-2} s^{-1} ($D > 3$ nm). This is consistent with measurements in July/August 2002, when the median aerosol deposition flux was -9.4×10^6 m^{-2} s^{-1} ($D > 11$ nm) and -16.7×10^6 m^{-2} s^{-1} ($D > 3$ nm) and the 95 % quantile flux was -60.9×10^6 m^{-2} s^{-1} ($D > 11$ nm) and -92.4×10^6 m^{-2} s^{-1} ($D > 3$ nm). Obviously, the net aerosol exchange is typically directed toward the surface. Eighty-six percent of the measurements in 2001 showed net deposition versus 14 % net emission. Similarly, net deposition was observed in 92 % of the flux measurements in 2002 compared with only 8 % of net emission.

Interestingly, the strongest deposition fluxes of more than 300×10^6 particles m^{-2} s^{-1} occurred during new particle formation events. Held et al. (2004) found strong indications that oxidation products of biogenic volatile organic compounds contribute considerably to secondary aerosol formation at the Waldstein site. However, if particles had been formed within the canopy, they were either too small to be detected with the ultrafine condensation particle counter (i.e., $D < 3$ nm), or the emission of these particles was obscured by stronger particle deposition. Alternatively, the time scale of VOC emission from the canopy by turbulent transport may have been faster than the time scale of the multistep oxidation mechanism of primarily released VOCs, which finally yielded condensable organic vapors that partition into the particle phase. Thus, secondary aerosol formation can act as a particle source above the forest canopy, while efficient turbulent deposition of nm-scale particles quickly removes these particles from the atmosphere. In other words, the forest acts both as a source of organic precursor gases for secondary aerosol formation and as a sink for freshly formed particles through turbulent deposition.

In August 2011, additional aerosol number flux measurements were carried out on the Köhlerloh clearing at 2.25 m agl with a Fast CPC (Wehner et al. 2011) ranging from -15.6×10^6 m^{-2} s^{-1} to $+9.1 \times 10^6$ m^{-2} s^{-1} and a median deposition flux of -3.3×10^6 m^{-2} s^{-1} (Kittler F., personal communication). Again, net aerosol deposition was clearly predominant.

9.3.2.2 Size-Resolved Number Fluxes

When comparing particles with diameters larger than 3 nm vs. 11 nm, significantly larger deposition fluxes of the smallest particle fraction are evident. These differences can be attributed to the particles in the diameter range between 3 nm

and 11 nm. This particle fraction typically contributes less than 25 % to the total number concentration; however, the contribution to the total deposition flux is frequently more than 50 % (Held and Klemm 2006). In fact, the deposition velocity v_d, calculated by dividing the negative aerosol flux by the aerosol number concentration, is significantly larger for $D > 3$ nm than for $D > 11$ nm. This size dependence of aerosol deposition is expected from theoretical descriptions of particle motion in the atmosphere: Small particles ($D < 100$ nm) are efficiently removed by diffusional processes, whereas large particles ($D > 1$ μm) are removed by sedimentation. In the diameter range from 100 nm to 1 μm, the so-called accumulation mode, the efficiency of dry deposition exhibits a minimum.

Moreover, bidirectional aerosol number fluxes were observed at the Waldstein-Weidenbrunnen site, i.e., aerosol deposition fluxes in one size range and simultaneously aerosol emission fluxes in another size range. As an example, Fig. 9.2a shows the diurnal cycle of aerosol number fluxes for two different diameter ranges on 12 July 2002 measured during the BEWA field campaign. The corresponding temporal evolution of the aerosol size distribution (Fig. 9.2b) indicates a new particle formation event. The buoyancy flux (Fig. 9.2c) shows a typical diurnal cycle with slightly negative values during the night and well-developed turbulence during the day.

The aerosol fluxes in Fig. 9.2a represent the total number fluxes of all particles with a diameter larger than 11 nm ($D > 11$ nm) versus $D > 3$ nm. Obviously, at nighttime the aerosol fluxes are close to zero in both diameter ranges. However, in the morning hours around 09:00 AM, the net aerosol fluxes of the measurements including the smaller particle fraction ($D > 3$ nm) become negative, while the net aerosol fluxes for $D > 11$ nm become positive. This indicates strong aerosol deposition of very small particles and at the same time aerosol emission of larger particles. Indeed, the particle fraction in the diameter range from 3 nm to 11 nm contributes strongly to the flux measurement for $D > 3$ nm. Therefore, the net aerosol emission measured for $D > 11$ nm was obscured by strong deposition of particles from 3 nm to 11 nm. This also suggests different source and sink distributions for different aerosol size fractions.

Recently, Deventer et al. (2015) carried out size-resolved eddy covariance aerosol flux measurements in the diameter range from 6 nm to 1.4 μm at a height of 32 m agl. The overall net deposition flux was -41×10^6 m^{-2} s^{-1}. However, the size-resolved aerosol fluxes were highly variable with respect to magnitude and direction. About 30 % of the quality-assured net fluxes were positive, and bidirectional fluxes were observed on a regular basis. Typically, the smallest particle size fractions exhibited the largest fraction of emission periods. In contrast, the net fluxes of accumulation mode particles with diameters larger than 0.2 μm were mostly negative. These observations may be explained either by true bidirectional aerosol exchange due to different locations of the sources of different aerosol size fractions or by evaporation of ammonium nitrate aerosol, which may be misleadingly interpreted as an emission flux. Chemically speciated aerosol flux measurements may be helpful to support one or the other explanation.

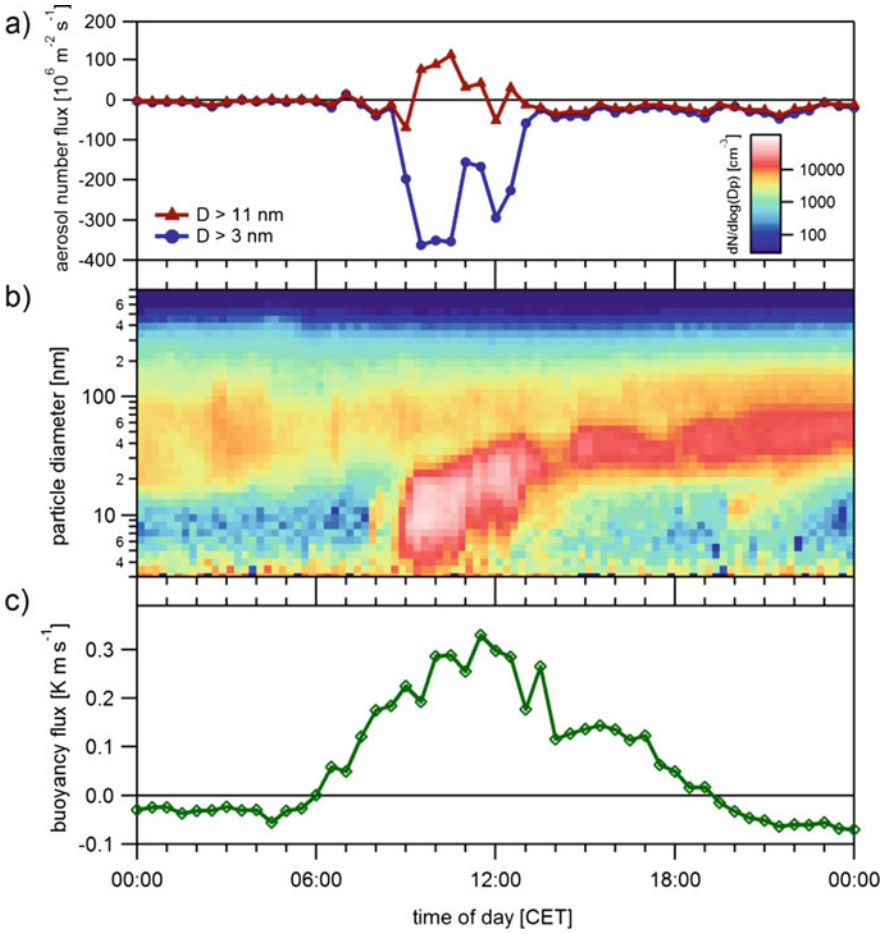

Fig. 9.2 An example of (**a**) bidirectional aerosol number fluxes, (**b**) the corresponding evolution of the aerosol size distribution, and (**c**) buoyancy fluxes observed on 12 July 2002

9.3.2.3 Chemically Speciated Aerosol Fluxes

The gradient measurements of total ammonium (NH_3/NH_4^+) and total nitrate (HNO_3/NO_3^-) exchange fluxes at the canopy top were already discussed in Sect. 9.3.1 (Wolff et al. 2010b). The mean total ammonium flux was -4.7 nmol m^{-2} s^{-1} and the mean total nitrate flux was -2.9 nmol m^{-2} s^{-1}. Since both total ammonium and total nitrate concentrations were dominated by the particulate phase, Wolff et al. (2010b) presumed that the particulate phase also dominates the observed deposition fluxes, at least for total nitrate. If this assumption holds, the total ammonium and nitrate deposition fluxes do not directly support (nor disprove) ammonium nitrate evaporation in the canopy. However, Held et al. (2003) used a combination

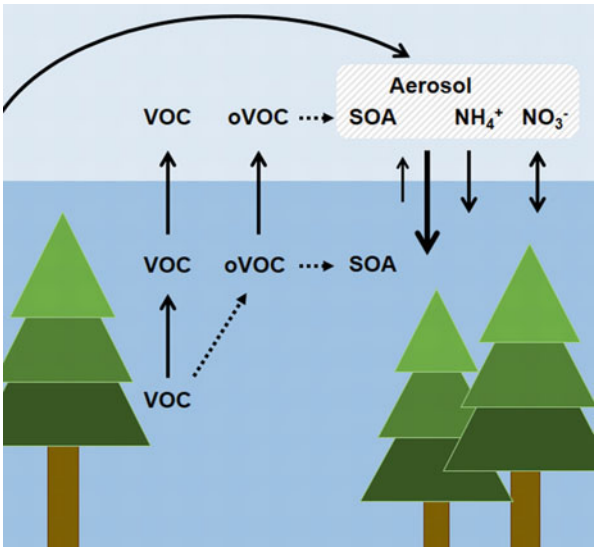

Fig. 9.3 Schematic representation of the interaction of aerosol fluxes and VOC chemistry at the Waldstein site (oVOC, oxygenated VOC; SOA, secondary organic aerosol); *solid arrows* indicate transport processes; *broken arrows* represent chemical reaction mechanisms

of irregular disjunct eddy sampling and single particle analysis by aerosol mass spectrometry and determined particulate nitrate emission with a confidence of 89 % in a case study at the Waldstein-Weidenbrunnen site.

Figure 9.3 summarizes the interactions of VOC emission and oxidation with secondary aerosol formation and aerosol transport at the Waldstein site. In most cases, aerosol deposition to the canopy is dominant, especially during periods of secondary aerosol formation, e.g., from oxidation products of biogenic VOC. In addition, aerosol that underwent aging during regional transport contributes to inorganic aerosol deposition. However, brief aerosol emission periods and bidirectional fluxes of different aerosol size fractions have been observed. It remains an open question whether these observations are true emission events or related to phase transitions of semi-volatile aerosol species such as ammonium nitrate or semi-volatile organic compounds.

9.3.3 Comparison of Flux Observations and Models

It is instructive to compare the observed trace gas and aerosol fluxes with flux parameterizations or flux models in order to evaluate the underlying process understanding.

For ozone deposition to tall vegetation, one-layer models with a simplified representation of the turbulent transport and the vegetation surfaces (big-leaf models) have been widely used. Klemm and Mangold (2001) compared ozone fluxes measured by eddy covariance at the Waldstein-Weidenbrunnen site with a simple big-leaf model. The measured daily average ozone deposition fluxes up to

−14 nmol m^{-2} s^{-1} were stronger than the modeled values, which ranged up to −6 nmol m^{-2} s^{-1}. Interestingly, both the modeled ozone mixing ratios and the modeled ozone deposition velocities, and thus, the modeled ozone fluxes, declined from May to October. In contrast, no clear seasonality was found for the measured fluxes, except for more frequent strong nocturnal fluxes toward the end of October. The discrepancy between the model and the measurements was explained by more efficient surface deposition compared to the model parameterization.

Schröter et al. (2002) emphasized the importance of ozone surface deposition by comparing ozone mixing ratios measured with UV absorption analyzers at the ground and with a LIDAR slightly above the ground. They found good agreement for ozone measurements 52 m agl at the top of the Schneeberg mountain, while the LIDAR measurements were systematically higher than the ground-based measurements at the Waldstein site and in the Weißenstadt basin. This difference was explained by ozone surface deposition and − in the case of the Weißenstadt basin − additional advection of ozone-depleted air.

A more detailed analysis of the diurnal cycles of measured and modeled ozone fluxes (Klemm et al. 2004) showed a general agreement of the magnitude of the median flux values (measured, up to −8.6 nmol m^{-2} s^{-1}; modeled, up to −9 nmol m^{-2} s^{-1}). However, large differences of the modeled fluxes during daytime and night, driven by a low stomatal resistance during the day versus closed stomata and a high cuticular resistance at night, do not reflect the measured diurnal cycles of the ozone flux. At night, the measured ozone deposition fluxes were unexpectedly large and not adequately parameterized in the ozone deposition model. Because stomata are closed and the stomatal uptake is strongly reduced at night, the large nighttime deposition fluxes suggest non-stomatal uptake. Both surface deposition and chemical reaction might contribute to this removal pathway. Deposition of ozone to vegetation surfaces has been studied extensively (e.g., Pilegaard et al. 1995; Fares et al. 2008). For example, ozone can react with plant waxes and with compounds deposited onto plant surfaces. In addition, the surface uptake of ozone is enhanced for wet leaves or needles (e.g., Fuentes et al. 1992; Zhang et al. 2002; Altimir et al. 2006), even though the water solubility of ozone is not large.

The surface wetness is often high at night, when humidity conditions within the canopy support the formation of liquid films on the spruce needles (e.g., Klemm et al. 2002). However, the parameterization of enhanced ozone surface deposition as a function of humidity or leaf surface wetness is not yet quantitative. This is corroborated by Voß (2015), who found a clear dependence of the deviation of measurements and model results on relative humidity when comparing ozone fluxes observed at the Waldstein site and modeled using the multilayer canopy-chemistry exchange model (MLC-CHEM).

Ganzeveld et al. (2006a) evaluated the H_2O_2 and organic peroxide exchange fluxes observed by Valverde-Canossa et al. (2006) with a single-column model (SCM) version of the coupled chemistry-climate model ECHAM4 adjusted to the Waldstein-Weidenbrunnen site (Ganzeveld et al. 2006b). From a comparison of the measured and simulated H_2O_2 fluxes, the observed H_2O_2 surface uptake resistance

was found to be much smaller than estimated by the model. However, even when using a very small surface uptake resistance in the model, the simulated H_2O_2 fluxes were still lower than the observed fluxes due to an underestimation of the turbulent transport. At night, when turbulent mixing was suppressed, non-stomatal uptake and chemical transformations, which are linked to the $NO/NO_2/O_3$ triad, were key controls of H_2O_2 mixing ratios. This intercomparison study of peroxide measurements and model simulations emphasizes the important role of turbulent transport, which controls the deposition of peroxides that are chemically produced above the canopy. At the same time, the production of peroxides depends on the emission flux of biogenically emitted organic precursor gases, e.g., a potential contribution to H_2O_2 production from terpene ozonolysis.

Forkel et al. (2006) applied the one-dimensional canopy-chemistry model CACHE to the Waldstein spruce canopy during the BEWA field experiments in order to compare measured and simulated VOC emission fluxes. The general levels of both the mixing ratios and the fluxes of isoprene and monoterpenes were in good agreement between the observations and the model simulations. However, the model could not reproduce the observed strong fluctuations, which have been attributed to the patchiness of the forest canopy. The model simulations suggested that the above-canopy VOC emission fluxes were about 10–15 % lower than the primary emission fluxes from the branches due to chemical reactions within the canopy. For individual species such as limonene, the above-canopy emission fluxes were reduced by up to 30 % due to the higher reactivity of these species. Furthermore, the simulations indicated that daytime VOC oxidation was not only due to ozone and OH radicals but also due to nitrate radicals in the lower part of the canopy.

The VOC emission fluxes measured during the BEWA field experiments at the Waldstein-Weidenbrunnen site were also used to validate a regional-scale semi-empirical BVOC (seBVOC) emission model (Smiatek and Steinbrecher 2006). For validation, the seBVOC model was run in point mode. The simulated diurnal cycles of isoprene and monoterpene fluxes resembled the observations. Taking into account the reduction of primary emission fluxes due to chemical reactions, the measured and simulated fluxes agreed within a factor of less than two for isoprene, and a factor of three for monoterpenes, which is considered to be well within the range of other upscaling studies. Further, it was noted that the emission potentials observed at the Waldstein site were at the lower end of values reported for Norway spruce.

With respect to aerosol deposition, Peters and Eiden (1992) introduced a size-dependent parameterization of the dry deposition velocity of aerosol particles to a spruce forest, which was applied to a spruce stand in Wülfersreuth, close to the Waldstein site. Later, Peters and Bruckner-Schatt (1995) extended this model in order to calculate dry deposition velocities of both gases and particles. Held et al. (2006) evaluated net aerosol number flux measurements together with a size-resolved particle deposition model by Zhang et al. (2001) based on the Slinn (1982) approach. In most cases, the model simulations were in fair agreement with the eddy covariance measurements. The size-resolved aerosol deposition flux was derived from a combination of the particle deposition model and size distribution measurements. The results indicated that the aerosol number flux was controlled by

ultrafine particles with diameters smaller than 50 nm, whereas the estimated aerosol mass flux was dominated by accumulation mode particles.

A more sophisticated simulation of aerosol deposition fluxes was carried out with the one-dimensional SOLVEG model (Katata et al. 2011). The net aerosol number fluxes calculated with SOLVEG agreed well with the observed fluxes. Size-resolved deposition velocities agreed well with measurements for diameters larger than 1 μm and for diameters smaller than 100 nm. However, for the accumulation mode, the calculated deposition velocities were significantly smaller than the measured ones. This discrepancy may be (partly) explained by flux divergence induced by a phase transition of semi-volatile aerosol species.

9.4 Conclusions

Over the last 20 years, reactive trace gas fluxes including ozone, nitrogen oxides, and volatile organic compounds as well as aerosol number and mass fluxes have been measured at the Waldstein-Weidenbrunnen site. The atmosphere-surface exchange of reactive trace gases and aerosols is influenced by turbulent transport, chemical reactions, and phase transitions. When interpreting turbulent flux measurements of reactive species, one should always evaluate the potential of chemical reactions to act as source and sink processes. For example, ozone formed outside of the canopy by photochemistry is removed from the atmosphere by turbulent deposition to surfaces, by stomatal and non-stomatal uptake, and by reaction with NO, which is also a sink for nitric oxide and a source for nitrogen dioxide. This in-canopy NO sink explains the observed flux convergence, with NO deposition above the canopy and at the same time NO soil emission close to the ground (see also Chap. 8). The same chemical reaction R9.1 acts as an in-canopy source of NO_2. In fact, NO_2 emission fluxes are observed above the canopy because NO_2 photolysis is strongly reduced within the canopy due to shading, and plant uptake of NO_2 has been shown to be quite small at the Waldstein site. At the same time, plant surfaces are important for ozone removal, which is corroborated by the observation of reduced ozone deposition fluxes in a clearing compared to the undisturbed forest canopy. One might speculate that a future increase in disturbance events such as wind storms will reduce the areas of undisturbed canopy and thus reduce ozone deposition to plant surfaces.

In order to assess the interaction of turbulent transport and chemistry, the characteristic turbulent and chemical time scales must be compared. For example, the Damköhler number, i.e., the ratio of the turbulent transport time and the chemical reaction time, has been evaluated for the $NO/NO_2/O_3$ triad (e.g., Lenschow 1982; Tsokankunku 2014; Plake et al. 2015) or VOC exchange fluxes (e.g., Rinne et al. 2012). However, canopy coupling regimes (see Chaps. 6 and 19) add an additional constraint on the potential for chemical reactions of compounds from different sources. For example, canopy decoupling may efficiently suppress the transport of ozone into the lower canopy and as a result shut down NO_2 production due to reaction of ozone with NO from soil emissions. Therefore, vertical profiles of con-

centration and flux measurements are required to help identify and quantify multiple sources and sinks of reactive species and chemically induced flux divergence.

Considering the turbulent aerosol exchange, it can be concluded that the Waldstein forest canopy typically acts as a net sink with respect to particle number but may also act as a net source of particle mass. Both an increased surface roughness and the presence of needle surfaces promote turbulent deposition of nm-scale particles to the canopy. At the same time, VOCs are emitted from the canopy that potentially contribute to new particle formation. If particle formation by multiple oxidation reactions of primarily emitted VOCs is faster than the vertical turbulent transport of VOCs to the canopy top, above-canopy particle emission fluxes are expected. Freshly formed particles exhibit diameters of less than 10 nm, and indeed, the smallest particle size fractions show the largest fraction of emission periods. Overall, however, net deposition number fluxes prevail at the Waldstein site, i.e., new particles are typically formed by secondary aerosol formation above the canopy and efficiently removed by deposition to the canopy. While it is still difficult to directly quantify the turbulent mass exchange of particle-borne nutrients or pollutants, dry deposition of compounds such as sulfate and nitrate must be assessed and contrasted with wet deposition (see Chap. 3). The presented chemically speciated aerosol flux measurements help to constrain atmospheric budgets and cycles of nitrogen. Nevertheless, there are still technical limitations and conceptual challenges that need to be tackled in order to address yet unresolved questions with respect to reactive trace gas and aerosol fluxes within and above tall vegetation.

Acknowledgments The research summarized in this chapter was funded by the Federal Ministry of Education, Science, Research and Technology (BMBF, PT BEO 51-0339476 C, and PT UKF 07ATF25) and the German Science Foundation (DFG) in the first EGER period (IOP1/2: ME 4100/4-1) and in the second EGER period (IOP3: PAK 446), as well as HE 5214/4-1. The authors acknowledge support by all participants of the BEWA 2000 and EGER field experiments and by the technical staff of the University of Bayreuth. Scientific contributions and instrumental support by Otto Klemm (WWU Münster, Germany) are gratefully acknowledged. The 2013 VOC REA flux measurements were supported by A. A. Turnipseed and A. B. Guenther, then at the National Center for Atmospheric Research (Boulder, Colorado, USA).

References

Altimir N, Kolari P, Tuovinen J-P, Vesala T, Bäck J, Suni T, Kulmala M, Hari P (2006) Foliage surface ozone deposition: a role for surface moisture? Biogeoscience 3:209–228

Bargsten A, Falge E, Pritsch K, Huwe B, Meixner FX (2010) Laboratory measurements of nitric oxide release from forest soil with a thick organic layer under different understory types. Biogeoscience 7:1425–1441

Boucher O, Randall D, Artaxo P, Bretherton C, Feingold G, Forster P, Kerminen V-M, Kondo Y, Liao H, Lohmann U, Rasch P, Satheesh SK, Sherwood S, Stevens B, Zhang XY (2013) Clouds and aerosols. In: Stocker TF, Qin D, Plattner G-K, Tignor M, Allen SK, Boschung J, Nauels A, Xia Y, Bex V, Midgley PM (eds) Climate change 2013: the physical science basis. Contribution of working group I to the fifth assessment report of the Intergovernmental Panel on Climate Change. Cambridge University Press, Cambridge, pp 571–657

Breuninger C, Oswald R, Kesselmeier J, Meixner FX (2012) The dynamic chamber method: trace gas exchange fluxes (NO, NO_2, O_3) between plants and the atmosphere in the laboratory and in the field. Atmos Meas Tech 5:955–989

Breuninger C, Meixner FX, Kesselmeier J (2013) Field investigations of nitrogen dioxide (NO_2) exchange between plants and the atmosphere. Atmos Chem Phys 13:773–790

Deventer MJ, Held A, El-Madany TS, Klemm O (2015) Size-resolved eddy covariance fluxes of nucleation to accumulation mode aerosol particles over a coniferous forest. Agric Forest Meteorol 214–215:328–340

Fares S, Loreto F, Kleist E, Wildt J (2008) Stomatal uptake and stomatal deposition of ozone in isoprene and monoterpene emitting plants. Plant Biol 10:44–54

Finlayson-Pitts BJ, Pitts JN (2000) Chemistry of the upper and lower troposphere. Academic Press, San Diego, CA, p. 969

Foken T, Meixner FX et al (2012) Coupling processes and exchange of energy and reactive and non-reactive trace gases at a forest site – results of the EGER experiment. Atmos Chem Phys 12:1923–1950

Forkel R, Rappenglück B, Steinbrecher R, Klemm O, Held A, Graus M, Grabmer W, Hansel A (2006) Trace gas exchange and gas phase chemistry in a Norway spruce forest: a study with a coupled 1-dimensional canopy atmospheric chemistry emission model. Atmos Environ 40:S28–S42

Fuentes JD, Gillespie TJ, Den Hartog G, Neumann HH (1992) Ozone deposition onto a deciduous forest during dry and wet conditions. Agric Forest Meteorol 62:1–18

Ganzeveld L, Valverde-Canossa J, Moortgat GK, Steinbrecher R (2006a) Evaluation of peroxide exchanges over a coniferous forest in a single-column chemistry-climate model. Atmos Environ 40:S68–S80

Ganzeveld L, Klemm O, Rappenglück B, Valverde-Canossa J (2006b) Evaluation of meteorological parameters over a coniferous forest in a single-column chemistry-climate model. Atmos Environ 40:S21–S27

Grabmer W, Kreuzwieser J, Wisthaler A, Cojocariu C, Graus M, Rennenberg H, Steigner D, Steinbrecher R, Hansel A (2006) VOC emissions from Norway spruce (*Picea abies* L. [Karst]) twigs in the field—Results of a dynamic enclosure study. Atmos Environ 40:S128–S137

Graus M, Hansel A, Wisthaler A, Lindinger C, Forkel R, Hauff K, Klauer M, Pfichner A, Rappenglück B, Steigner D, Steinbrecher R (2006) A relaxed-eddy-accumulation method for the measurement of isoprenoid canopy-fluxes using an online gas-chromatographic technique and PTR-MS simultaneously. Atmos Environ 40:S43–S54

Guenther AB, Jiang X, Heald CL, Sakulyanontvittaya T, Duhl T, Emmons LK, Wang X (2012) The Model of Emissions of Gases and Aerosols from Nature version 2.1 (MEGAN2.1): an extended and updated framework for modeling biogenic emissions. Geosci Model Dev 5:1471–1492

Güsten H, Heinrich G (1996) On-line measurements of ozone surface fluxes: Part I. Methodology and instrumentation. Atmos Environ 30:897–909

Hasson AS, Ho AW, Kuwata KT, Paulson SE (2001) Production of stabilized Criegee intermediates and peroxides in the gas phase ozonolysis of alkenes. 2. Asymmetric and biogenic alkenes. J Geophys Res 106:34143–34153

Held A, Klemm O (2006) Direct measurement of turbulent particle exchange with a twin CPC eddy covariance system. Atmos Environ 40:S92–102

Held A, Hinz K-P, Trimborn A, Spengler B, Klemm O (2003) Towards direct measurement of turbulent vertical fluxes of compounds in atmospheric aerosol particles. Geophys Res Lett 30:2016. doi:10.1029/2003GL017854

Held A, Nowak A, Birmili W, Wiedensohler A, Forkel R, Klemm O (2004) Observations of particle formation and growth in a mountainous forest region in central Europe. J Geophys Res 109:D23204. doi:10.1029/2004JD005346

Held A, Nowak A, Wiedensohler A, Klemm O (2006) Field measurements and size-resolved model simulations of turbulent particle transport to a forest canopy. J Aerosol Sci 37:786–798

Karl T, Guenther A, Jordan A, Fall R, Lindinger W (2001) Eddy covariance measurement of biogenic oxygenated VOC emissions from hay harvesting. Atmos Environ 35:491–495

Katata G, Nagai H, Zhang L, Held A, Sera D, Klemm O (2011) Development of an atmosphere-soil-vegetation model for investigation of radioactive materials transport in the terrestrial biosphere. Prog Nuclear Sci Technol 2:530–537

Klemm O (2004) Trace gases and particles in the atmospheric boundary layer at the Waldstein site: present state and his historic trends. In: Matzner E (ed) Biogeochemistry of forested catchments in a changing environment, A German case study, Ecological studies, vol 172. Springer, Heidelberg, pp 45–58

Klemm O, Mangold A (2001) Ozone deposition at a forest site in NE Bavaria. Water Air Soil Poll: Focus 1:223–232

Klemm O, Milford C, Sutton MA, Spindler G, van Putten E (2002) A climatology of leaf surface wetness. Theor Appl Climatol 71:107–117

Klemm O, Mangold A, Held A (2004) Turbulent deposition of ozone to a mountainous forest ecosystem. In: Matzner E (ed) Biogeochemistry of forested catchments in a changing environment, A German case study, Ecological studies, vol 172. Springer, Heidelberg, pp 203–213

Klemm O, Held A, Forkel R, Gasche R, Kanter H-J, Rappenglück B, Steinbrecher R, Müller K, Plewka A, Cojocariu C, Kreuzwieser J, Valverde-Canossa J, Schuster G, Moortgat GK, Graus M, Hansel A (2006) Experiments on forest/atmosphere exchange: climatology and fluxes during two summer campaigns in NE Bavaria. Atmos Environ 40:S3–20

Lenschow DH (1982) Reactive trace species in the boundary layer from a micrometeorological perspective. J Meteor Soc Japan 60:472–480

Lerdau MT, Munger JW, Jacob DJ (2000) The NO_2 flux conundrum. Science 289:2291–2293

Lindinger W, Hansel A, Jordan A (1998) Proton-transfer reaction mass spectrometry (PTR-MS): on-line monitoring of volatile organic compounds at pptv levels. Chem Soc Rev 27:347–354

Müller M, Graus M, Ruuskanen TM, Schnitzhofer R, Bamberger I, Kaser L, Titzmann T, Hörtnagl L, Wohlfahrt G, Karl T, Hansel A (2010) First eddy covariance flux measurements by PTR-TOF. Atmos Meas Tech 3:387–395

Peters K, Bruckner-Schatt G (1995) The dry deposition of gaseous and particulate nitrogen compounds to a spruce stand. Water Air Soil Poll 85:2217–2222

Peters K, Eiden R (1992) Modelling the dry deposition velocity of aerosol particles to a spruce forest. Atmos Environ 26A:2555–2564

Pilegaard K, Jensen NO, Hummelshoj P (1995) Seasonal and diurnal variation in the deposition velocity of ozone over a spruce forest in Denmark. Water Air Soil Poll 85:2223–2228

Plake D, Sörgel M, Stella P, Held A, Trebs I (2015) Influence of meteorology and anthropogenic pollution on chemical flux divergence of the NO–NO_2–O_3 triad above and within a natural grassland canopy. Biogeoscience 12:945–959

Pryor SC, Klemm O (2004) Experimentally derived estimates of nitric acid dry deposition velocity and viscous sub-layer resistance at a conifer forest. Atmos Environ 38:2769–2777

Pryor SC, Barthelmie RJ, Jensen B, Jensen NO, Sörensen LL (2002) HNO_3 fluxes to a deciduous forest derived using gradient and REA methods. Atmos Environ 36:5993–5999

Pryor SC, Klemm O, Barthelmie R (2003) An investigation of the magnitude of resistance terms in dry deposition fluxes to a conifer forest. In: BACCI workshop on surface flux, micrometeorology and chemistry, Risø, 11–12 November 2003

Rinne J, Markkanen T, Ruuskanen TM, Petäjä T, Keronen P, Tang MJ, Crowley JN, Rannik U, Vesala T (2012) Effect of chemical degradation on fluxes of reactive compounds – a study with a stochastic Lagrangian transport model. Atmos Chem Phys 12:4843–4854

Schmitt SH (2013) Fluxes of monoterpenes from a spruce forest: establishing sampling and analytical procedures. MSc Thesis, University of Bayreuth, Germany

Schröter M, Obermeier A, Brüggemann D, Klemm O (2002) Application of a ground-based Lidar for studies of the dynamics of ozone in a mountainous basin. Environ Sci Pollut Res 9:381–384

Slinn WGN (1982) Predictions for particle deposition to vegetative surfaces. Atmos Environ 16:1785–1794

Smiatek G, Steinbrecher R (2006) Temporal and spatial variation of forest VOC emissions in Germany in the decade 1994–2003. Atmos Environ 40:S166–S177

Steinbrecher R, Klauer M, Hauff K, Stockwell R, Jaeschke W, Dietrich W, Herbert F (2000) Biogenic and anthropogenic fluxes of non-methane hydrocarbons over an urban-impacted forest, Frankfurter Stadtwald, Germany. Atmos Environ 34:3779–3788

Steinbrecher R, Rappenglück B, Hansel A, Graus M, Klemm O, Held A, Wiedensohler A, Nowak A (2004) Vegetation-atmospheric interactions: the emissions of biogenic volatile organic compounds (BVOC) and their relevance to atmospheric particle dynamics. In: Matzner E (ed) Biogeochemistry of forested catchments in a changing environment, A German case study, Ecological studies, vol 172. Springer, Heidelberg, pp 215–235

Trimborn A, Hinz K-P, Spengler B (2000) Online analysis of atmospheric particles with a transportable laser mass spectrometer. Aerosol Sci Technol 33:191–201

Tsokankunku A (2014) Fluxes of the NO-O_3-NO_2 triad above a spruce forest canopy in south-eastern Germany. PhD Thesis, University of Bayreuth, Germany

Valverde-Canossa J (2004) Sources and sinks of organic peroxides in the planetary boundary layer. PhD Thesis, Johannes Gutenberg Universität Mainz, Germany

Valverde-Canossa J, Ganzeveld L, Rappenglück B, Steinbrecher R, Klemm O, Schuster G, Moortgat GK (2006) First measurements of H2O2 and organic peroxides surface fluxes by the relaxed eddy-accumulation technique. Atmos Environ 40:S55–S67

Vilà-Guerau de Arellano J, Duynkerke PG, Builtjes PJH (1993) The divergence of the turbulent diffusion flux in the surface layer due to chemical reactions: the NO-O_3-NO_2 system. Tellus 45B:23–33

Voß L (2015) Measurements and modeling of ozone fluxes in and above Norway spruce canopies. PhD Thesis, Johannes Gutenberg University Mainz, Germany

Wehner B, Siebert H, Hermann M, Ditas F, Wiedensohler A (2011) Characterisation of a new Fast CPC and its application for atmospheric particle measurements. Atmos Meas Tech 4:823–833

Wolff V, Trebs I, Ammann C, Meixner FX (2010a) Aerodynamic gradient measurements of the NH_3-HNO_3-NH_4NO_3 triad using a wet chemical instrument: an analysis of precision requirements and flux errors. Atmos Meas Tech 3:187–208

Wolff V, Trebs I, Foken T, Meixner FX (2010b) Exchange of reactive nitrogen compounds: concentrations and fluxes of total ammonium and total nitrate above a spruce canopy. Biogeoscience 7:1729–1744

Zhang L, Gong S, Padro J, Barrie L (2001) A size-segregated particle dry deposition scheme for an atmospheric aerosol module. Atmos Environ 35:549–560

Zhang L, Brook JR, Vet R (2002) On ozone dry deposition – with emphasis on non-stomatal uptake and wet canopies. Atmos Environ 36:4787–4799

Zhu Z, Tsokankunku A, Plake D, Falge E, Foken T, Meixner FX (2009) Multi-level eddy covariance measurements for ozone fluxes above, within and below spruce forest canopy. In: Luers J, Foken T (eds) Proceedings of the international conference of atmospheric transport and chemistry in forest ecosystems. Arbeitsergebn, Univ Bayreuth, Abt Mikrometeorol. ISSN 1614–8916. 40:32

Chapter 10
Isotope Fluxes

Bodo Wichura, Johannes Ruppert, Michael Riederer, and Thomas Foken

10.1 Introduction

The examination of the major source and sink processes of the atmospheric CO_2 budget, their variability in space and time, as well as their trends is a prerequisite for the understanding of the perturbations of the global carbon cycle caused by direct human impacts, the past and present climate changes, as well as future projections of climate change (IPCC 2013). An important sink for atmospheric CO_2 is the terrestrial biosphere. The determination of net ecosystem exchange (NEE) of CO_2 has therefore become a fundamental tool for the investigation of the carbon balance of terrestrial ecosystems.

B. Wichura (✉)
Deutscher Wetterdienst, Climate and Environment Consultancy, Regional Office Potsdam, Postfach 600552, 14405 Potsdam, Germany
e-mail: bodo.wichura@dwd.de

J. Ruppert
Research Institute of the Cement Industry, Tannenstr. 2, 40476 Düsseldorf, Germany

M. Riederer
Ostbayerische Technische Hochschule Regensburg, Postfach 120327, 93025 Regensburg, Germany

T. Foken
Am Herrgottsbaum 28, 96120 Bischberg, Germany

Bayreuth Center of Ecology and Environmental Research, University of Bayreuth, Bayreuth, Germany

B. Wichura, J. Ruppert, M. Riederer, T. Foken: Affiliation during the work at the Waldstein sites: Department of Micrometeorology, University of Bayreuth.

T. Foken (ed.), *Energy and Matter Fluxes of a Spruce Forest Ecosystem*,
Ecological Studies 229, DOI 10.1007/978-3-319-49389-3_10

The NEE is the result of the two relatively large flux components—assimilation as a sink (CO_2 uptake during photosynthesis) and respiration as a source (CO_2 release during respiration from above- and belowground) of CO_2. Photosynthesis and respiration processes are sensitive to multiple environmental factors, e.g., temperature, soil moisture availability, and changes in global radiation. Therefore, changes in climate forcing may result in different ecosystem responses (Baldocchi et al. 2001; Ehleringer et al. 2002; Baldocchi and Bowling 2003; Baldocchi and Valentini 2004; Helliker et al. 2005; Reichstein et al. 2007).

Furthermore, consequential changes in ecosystem carbon balances may form significant positive and negative feedbacks to the greenhouse warming effect (Flanagan and Ehleringer 1998). Therefore, the analysis of NEE flux components (assimilation and respiration), as well as the corresponding processes, is critical for obtaining insights into ecosystem responses to climate forcing and their feedbacks to the greenhouse warming effect (Ciais et al. 1995; Lloyd et al. 1996; Buchmann 2000; Field and Raupach 2004; Reichstein et al. 2007).

The eddy covariance (EC) method has become a fundamental tool for the investigation of the carbon balance of terrestrial ecosystems. This method is commonly applied to measure the atmospheric CO_2 exchange of different ecosystems around the globe (Aubinet et al. 2000, 2012; Baldocchi et al. 2001; Baldocchi 2014). The derivation of the annual sum of NEE is complicated by characteristic diurnal and seasonal variation in the governing gross flux components of assimilation and respiration. Consequently, a high potential for systematic errors exists (Goulden et al. 1996; Moncrieff et al. 1996), and studies on the determination of the flux components are essential for the understanding of ecosystem responses to climate forcing and their feedbacks to the greenhouse warming effect (Grace and Rayment 2000).

Additional information is required to achieve both the partitioning of NEE measured by the eddy covariance method into its component fluxes and an understanding of the corresponding processes. This might be provided by a tracer, which can identify the individual contributions to the net flux at ecosystem scale. A method that assesses typical scalar correlations for taking conditional samples of the turbulent gas exchange is suggested by Thomas et al. (2008). The isotopic signature of CO_2 – that is, the CO_2 isotope ratios with respect to $^{13}CO_2$ – can serve as a tracer because photosynthetic uptake discriminates against the heavier isotope (Farquhar et al. 1989; Yakir and Sternberg 2000). Based on specific and different isotopic signatures of the assimilation flux and the respiration flux, the combination of the bulk CO_2 and the isotope mass balances can facilitate flux partitioning at local ecosystem scale (Yakir and Wang 1996; Bowling et al. 1999a, b, 2001; Wichura et al. 2000, 2004; Ogée et al. 2004; Knohl and Buchmann 2005; Ruppert 2008; Wichura 2009; Riederer et al. 2014).

Due to discrimination against the heavier isotope ^{13}C during stomatal uptake of CO_2 and photosynthesis in C3 vegetation, the biomass and all following compartments within the dynamic C cycle are ^{13}C depleted with respect to the atmosphere. The ^{13}C isotopic ratio therefore increases in the air during the assimilation period. Both effects account for a distinct diurnal cycle of the $^{13}CO_2/^{12}CO_2$ mixing ratio in ecosystem air (Flanagan et al. 1996; Lloyd et al. 1996).

Isotope mass balances may be determined by measurements of $^{13}CO_2$ iso-fluxes. They can be determined by means of the flux-gradient method (Flanagan et al. 1996), modeling approaches (Lloyd et al. 1996; Ogée et al. 2003), hyperbolic relaxed eddy accumulation (HREA; Bowling et al. 2001, 2003; Wichura et al. 2004; Ruppert 2008; Wichura 2009; Riederer et al. 2014), the hybrid eddy covariance–flask-gradient method (Bowling et al. 1999a; Griffis et al. 2004), and direct isotopic eddy covariance (Griffis et al. 2008; Sturm et al. 2012; Wehr et al. 2013).

The HREA method allows for maximized differences of the isotopic signatures in samples for IRMS laboratory analysis. This principle is able to yield an improved signal-to-noise ratio for the isotopic parameters, which is essential for the determination of iso-fluxes. HREA measurements of $^{13}CO_2$ iso-fluxes were conducted at FLUXNET station DE-Bay (Waldstein-Weidenbrunnen) during three intensive measuring campaigns in 1999, 2000, and 2003. Furthermore, HREA $^{13}CO_2$ iso-fluxes were measured at the extensively managed submontane grassland site "Voitsumra," near the Waldstein-Weidenbrunnen site, during an intensive measuring campaign in 2010. HREA isotope samples were collected using cryogenic traps during campaigns 1999 and 2000. During campaigns 2003 and 2010, whole-air samples of CO_2, $^{13}CO_2$, and $CO^{18}O$ isotopes were sampled. Eddy covariance measurements of CO_2 fluxes were carried out simultaneously during all campaigns.

The chapter is organized as follows. The approach used to separate the flux components (assimilation and respiration) of NEE on the basis of combined measurements of turbulent fluxes of $^{13}CO_2$ isotope and of carbon dioxide CO_2 is described. The HREA measuring method and the different implementations of $^{13}CO_2$ iso-flux HREA measurement systems are outlined. CO_2 EC as well as $^{13}CO_2$ HREA measurement results for all campaigns are summarized and discussed. The capabilities of $^{13}CO_2$ iso-flux measurements for NEE flux partitioning as well as for the examination of CO_2 exchange mechanisms over forests are highlighted.

10.2 Materials and Methods

10.2.1 Balances of CO_2 and $^{13}CO_2$

The balance of CO_2 density ρ_c at a point in the transition region between an ecosystem and the atmosphere might be described by

$$\frac{\partial \rho_c}{\partial t} + \frac{\partial \left(u_i \rho_c\right)}{\partial x_i} = Q_c. \tag{10.1}$$

In Eq. (10.1), u_i are the components of wind velocity in direction i, and Q_c denotes sources or sinks for CO_2 in the volume of air under consideration. Molecular diffusion of ρ_c is neglected in Eq. (10.1). Applying the rules of Reynolds decomposition and averaging (overbar), considering the densities of dry air ρ_a and of carbon dioxide ρ_c by introduction of the mixing ratio $s = \rho_c/\rho_a$, assuming horizontal homogeneity of Q_c as well as of horizontal wind velocities (i.e., vertical wind velocity w and vertical coordinate z are remaining), expressing fluctuations of ρ_c' by means of fluctuations of s' and of those of dry air ρ_a' (Webb et al. 1980; Lee 1998; Paw U et al. 2000), and supposing that both the mean vertical flux and the mean vertical gradient of dry air vanish, Eq. (10.1) can be transformed to (for a detailed summary, see Wichura (2009),

$$\overline{\rho}_a \frac{\partial \overline{s}}{\partial t} + \overline{\rho}_a \frac{\partial \overline{w's'}}{\partial z} = \overline{Q_c}. \tag{10.2}$$

According to Eq. (10.1), the balance of $^{13}CO_2$ isotope density is

$$\frac{\partial (\Re \rho_c)}{\partial t} + \frac{\partial (u_i \Re \rho_c)}{\partial x_i} = \Re_P Q_c. \tag{10.3}$$

where $\Re$ is the isotope ratio $^{13}CO_2/^{12}CO_2$ and $\Re_P$ is the isotope ratio, belonging to Q_c, the sources and sinks for CO_2 in the considered volume of air, respectively. Note that Eq. (10.3) represents the "iso-density" $\Re\rho_c$, a linear combination of $\Re$ and ρ_c, instead of the balance of $\Re$ itself (see Raupach (2001) for detailed discussion). Analogous to the transformation of Eq. (10.1), Eq. (10.3) can be transformed to (for a detailed summary, see Wichura 2009)

$$\overline{\rho_a} \frac{\partial \left(\overline{\Re}\,\overline{s}\right)}{\partial t} + \overline{\rho_a} \frac{\partial \left(\overline{\Re}\,\overline{w's'}\right)}{\partial z} = \overline{\Re_P}\,\overline{Q_c}. \tag{10.4}$$

All products of $\Re'$ with other fluctuating quantities are neglected in Eq. (10.4) (see Raupach 2001).

10.2.2 NEE Partitioning and $^{13}CO_2$ Iso-fluxes

Processes of assimilation and of respiration in an ecosystem result in sources and sinks of CO_2 (Q_A and Q_R). They are subsumed in Eqs. (10.1) and (10.2) in Q_c. The net ecosystem exchange (NEE) of CO_2 can be expressed by the balance of CO_2 using Eq. (10.2), by integration from the bottom to the top (height z_m) of a column

between the ecosystem and the atmosphere

$$\begin{aligned} \mathrm{NEE} &= \overline{\rho}_\mathrm{a} \int_0^{z_\mathrm{m}} \frac{\partial \overline{s}}{\partial t}\ dz' + \overline{\rho}_\mathrm{a} \int_0^{z_\mathrm{m}} \frac{\partial \overline{w's'}}{\partial z}\ dz' = \int_0^{z_\mathrm{m}} \left(\overline{Q_\mathrm{A}} + \overline{Q_\mathrm{R}}\right)\ dz' \\ \mathrm{NEE} &= S_\mathrm{c} + \ F_\mathrm{c} = A \ + R. \end{aligned} \tag{10.5}$$

S_C and F_C are the storage and the turbulent flux of CO_2 within the column. They are balanced by the total fluxes of assimilation A and respiration R (autotrophic as well as heterotrophic, Lloyd et al. 1996; Bowling et al. 2001; Ehleringer et al. 2002). Note that NEE partitioning can be based on the application of common flux partitioning models (FPM). In FPM, R is generally estimated on the basis of a Lloyd–Taylor function (Lloyd and Taylor 1994) that specifies the temperature dependence of respiration by a simple exponential temperature regression model. Nighttime NEE is often used for parameterization of ecosystem respiration due to the absence of assimilation during this time period (Lloyd and Taylor 1994; Falge et al. 2001; Reichstein et al. 2005; Ruppert et al. 2006a; Ammann et al. 2007). Estimation of A in FPM can be based, in general, on the parameterization of daytime solar radiation-dependent gross primary production (Falge et al. 2001; Ruppert et al. 2006a) by implementation of a Michaelis–Menten function (Michaelis and Menten 1913).

Analogous to Eq. (10.5), the Iso-Net Ecosystem Exchange $\mathrm{NEE_{ISO}}$ of $^{13}CO_2$ can be derived from Eq. (10.4) by integration

$$\begin{aligned} \mathrm{NEE_{ISO}} &= \overline{\rho}_\mathrm{a} \int_0^{z_\mathrm{m}} \frac{\partial \left(\overline{\Re \overline{s}}\right)}{\partial t}\ dz' + \overline{\rho}_\mathrm{a} \int_0^{z_\mathrm{m}} \frac{\partial \left(\overline{\Re}\ \overline{w's'}\right)}{\partial z}\ dz' = \int_0^{z_\mathrm{m}} \left(\overline{\Re_\mathrm{A}}\ \overline{Q_\mathrm{A}} + \overline{\Re_\mathrm{R}}\ \overline{Q_\mathrm{R}}\right)\ dz' \\ \mathrm{NEE_{ISO}} &= S_{\Re\mathrm{c}} \ + F_{\Re\mathrm{c}} \ = \ \overline{\Re_\mathrm{A} A} + \ \overline{\Re_\mathrm{R} R}\ . \end{aligned} \tag{10.6}$$

$S_{\Re\mathrm{c}}$ and $F_{\Re\mathrm{c}}$ are the storage and the turbulent iso-flux of $^{13}CO_2$ within the column. They are balanced by the iso-fluxes of assimilation $\overline{\Re_\mathrm{A} A}$ and respiration $\overline{\Re_\mathrm{R} R}$, where $\Re_\mathrm{A}$ and $\Re_\mathrm{R}$ are the isotope ratios of CO_2 as the result of assimilation and respiration.

Applying the sign convention that all fluxes from (to) the ecosystem to the atmosphere have a positive (negative) sign, Eq. (10.5) may be rearranged to (cf. Lloyd et al. 1996)

$$\overline{\rho}_\mathrm{a} \int_0^{z_\mathrm{m}} \frac{\partial \overline{s_\mathrm{i}}}{\partial t}\ dz = F_\mathrm{oi} - F_\mathrm{io} + R - A. \tag{10.7}$$

F_{oi} and F_{io} are the turbulent fluxes of CO_2 from (to) the atmosphere to (from) the ecosystem, respectively. Likewise, Eq. (10.6) reads

$$\overline{\rho}_a \int_0^{z_m} \frac{\partial \left(\overline{\Re_i s_i}\right)}{\partial t}\, dz = \overline{\Re_{oi}} F_{oi} - \overline{\Re_{io}} F_{io} + \overline{\Re_R} R - \overline{\Re_A} A. \tag{10.8}$$

After replacement and rearrangement of Eqs. (10.7) and (10.8), introducing δ-notation for the isotope ratio $\delta^{13}C = (\Re_{sample}/\Re_{standard} - 1) \cdot 1000$ ‰ where $\Re_{sample}$ and $\Re_{standard}$ are the isotope ratios $^{13}C/^{12}C$ of the sample and of a standard (Vienna Pee Dee Belemnite (VDPD) for carbon), respectively, the isotope balance can be written as

$$\overline{\rho}_a \int_0^{z_m} \left[\overline{s_i} \frac{\partial \delta_i}{\partial t}\right] dz = F_{oi} (\delta_{oi} - \delta_i) - F_{io} (\delta_{io} - \delta_i) + R (\delta_R - \delta_i) - A (\delta_A - \delta_i). \tag{10.9}$$

where $\delta_{oi} = \delta_o$ and $\delta_{io} = \delta_i$ (i.e., the second term on the right-hand side of Eq. (10.9) vanishes) are the isotope ratios of CO_2, entering and leaving the column from and to the atmosphere above, respectively, assuming a well-mixed canopy layer. δ_R and δ_A are the isotope ratios of respired and assimilated CO_2 within the column. If the changes in the CO_2 mixing ratio $\overline{s_i}$ and in the isotope ratio δ_i are small compared to the fluxes of CO_2 and $^{13}CO_2$ (steady state), the left-hand sides of Eqs. (10.7) and (10.9) vanish, and, after rearrangement, separate equations for R and A can be formulated (Wichura et al. 2004):

$$\begin{aligned} R &= (F_{oi} - F_{io}) \tfrac{\delta_A}{\delta_R - \delta_A} - (F_{oi}\delta_o - F_{io}\delta_i) \tfrac{1}{\delta_R - \delta_A} \\ A &= (F_{oi} - F_{io}) \tfrac{\delta_R}{\delta_R - \delta_A} - (F_{oi}\delta_o - F_{io}\delta_i) \tfrac{1}{\delta_R - \delta_A}. \end{aligned} \tag{10.10}$$

The first bracket terms of R and A in Eq. (10.10) represent the turbulent flux of CO_2 and can be measured by an eddy covariance system. The second bracket terms in Eq. (10.10) represent the $\delta^{13}C$ iso-flux and can be measured by a hyperbolic relaxed eddy accumulation system. Equation (10.10) shows that besides the turbulent fluxes of $^{13}CO_2$, information about the isotopic ratios of assimilated and respired CO_2, δ_A, and δ_R, respectively, is necessary for CO_2 flux partitioning. Note that estimation of R and A by Eq. (10.10) is made valid by the assumption of adequate turbulent mixing and stationary conditions, only. In any other case, additional terms from Eq. (10.10) have to be considered.

The derivation of δ_A from measurements is based on the general definition of isotopic discrimination Δ (Farquhar et al. 1989; O'Leary et al. 1992; Farquhar and Lloyd 1993; O'Leary 1993). In Buchmann et al. (1997, 1998), the definition was utilized to derive the ecosystem discrimination Δ_e.

$$\Delta_e = \frac{\delta_o - \delta_i}{1 + \delta_i} \tag{10.11}$$

δ_A can be estimated with measurements of $\delta_o = \delta_{oi}$ and $\delta_i = \delta_{io}$ by rearrangement of Eq. (10.11) if Δ_e is known (see Bowling et al. 2001, 2003):

$$\delta_A = \delta_i - \Delta_e \tag{10.12}$$

Ruppert (2008) found that, on small timescales, Δ_e can be defined as the ecosystem discrimination of the atmospheric exchange at measurement height against isotopes in the lower boundary layer air.

$$\Delta_e = \frac{\delta_o - \delta_c}{1 + \delta_c} \tag{10.13}$$

δ_C is the flux-weighted isotopic signature of the turbulent exchange $^{13}CO_2$ which can be measured directly (Ruppert 2008):

$$\delta_c = \frac{F_{oi}\delta_o - F_{io}\delta_i}{F_{oi} - F_{io}}. \tag{10.14}$$

Note that Ruppert (2008) discussed other definitions of isotopic discrimination Δ in more detail. Generally, these definitions are different depending on the measuring height and therefore on the scale, for which they are valid. It is important to keep in mind—and analyze in detail—which term of isotopic discrimination and of corresponding isotopic signature is utilized for any specific application of the isotopic partition approach (see Ruppert (2008) for a detailed discussion).

δ_R, the isotopic ratio of respired CO_2, can be determined by the Keeling plot method (intercept of a plot of 13C vs. inverse carbon concentration of respiration samples; Keeling 1958, 1961). It has been used in several studies for NEE partitioning purposes (see, e.g., Yakir and Wang 1996; Bowling et al. 2001; Pataki et al. 2003).

10.2.3 Hyperbolic Relaxed Eddy Accumulation Method

In the conditional sampling or relaxed eddy accumulation method (REA method; Businger and Oncley 1990), the turbulent flux is determined from the concentration difference measured in updraft and downdraft air samples. This concentration difference is scaled with the intensity of turbulent vertical mixing measured by the standard deviation of the vertical wind speed σ_w, based on the assumption of flux-variance similarity. Because air sampling is not proportional to the vertical wind speed, it is referred to as relaxed sampling. Consequently, REA is an indirect method for flux measurements. It relies on a parameterization in which the so-called *b*-factor is determined from a second scalar quantity (proxy scalar) that shows similarity in its atmospheric transport (scalar similarity; Wyngaard and Moeng 1992; Ruppert et al. 2006b) and for which the fluctuations of concentration can be measured in the

field with high temporal resolution:

$$F_C = \overline{\rho_a}\ b\,(\zeta)\ \ \sigma_w\ \ \left(\overline{s_\uparrow} - \ \overline{s_\downarrow}\right). \tag{10.15}$$

$\overline{s_\uparrow}$ and $\overline{s_\downarrow}$ are the average mixing ratios of CO_2 in updraft and downdraft air samples, respectively. The proportionality factor $b(\zeta)$ is a coefficient, which is a function of stability, characterized by $z = z/L$, where z is the height above the surface and L is the Obukhov length. $b(\zeta)$ can then be determined for the proxy scalar by rearranging (Eq. 10.15) on the basis of either (1) simulation of REA sampling on high-frequency scalar time series and its resulting concentration difference $\left(\overline{s_\uparrow} - \ \overline{s_\downarrow}\right)$ or (2) measured concentration difference from a real REA air sampling for the proxy scalar ρ_x:

$$b\,(\zeta) = \frac{\overline{w'\rho_x'}}{\sigma_w\left(\overline{\rho_{x\uparrow}} - \overline{\rho_{x\downarrow}}\right)} \approx \frac{\overline{w's'}}{\sigma_w\left(\overline{s_\uparrow} - \overline{s_\downarrow}\right)} \tag{10.16}$$

For the proxy scalar, $F_{\rho C}$ is normally determined by eddy covariance (EC) measurements $F_{\rho C} = \overline{w'\rho_x'}$.

The proportionality factor $b(\zeta)$ is well defined, with a value of 0.627 for an ideal Gaussian joint frequency distribution (JFD) of the vertical wind velocity and a scalar (Wyngaard and Moeng 1992). Many studies demonstrate the relative stability of average factors $b(\zeta)$ in unstable and moderately stable conditions (Businger and Oncley 1990; Baker et al. 1992; Oncley et al. 1993; Pattey et al. 1993; Katul et al. 1994, 1996; Foken et al. 1995; Gao 1995; Nie et al. 1995; Beverland et al. 1996; Ammann 1999; Milne et al. 1999; Baker 2000; Ammann and Meixner 2002). Nevertheless, significant variability of factors $b(\zeta)$ for individual 30 min periods is observed, and different factors are discussed (Oncley et al. 1993; Pattey et al. 1993; Gao 1995; Guenther et al. 1996; Ruppert et al. 2006b). Several studies point out that skewness in the JFD of w' and c' and structures in the turbulent exchange cause changes in factors $b(\zeta)$ (Katul et al. 1996; Milne et al. 2001; Fotiadi et al. 2005; Ruppert et al. 2006b). The study by Ruppert et al. (2006b) attributes observed variation in the scalar exchange to events at time scales >60 s. This limits the use of a unique factor $b(\zeta)$ for all time scales and suggests the determination of individual factors for each sampling period (Ruppert 2008; Ruppert et al. 2012).

Application of a wind deadband for small vertical wind speeds, in which no samples are taken, increases the concentration difference between the updraft and downdraft air accumulation reservoirs and thereby the certainty of the flux measurement, especially if chemical sensor resolution is a limiting factor (Businger and Delany 1990; Businger and Oncley 1990; Delany et al. 1991; Pattey et al. 1993).

In hyperbolic relaxed eddy accumulation (HREA), the concept of a threshold value is continued in order to measure isotope fluxes with an REA system. In HREA the deadband rejects not only samples with small fluctuations of the vertical wind speed w' but also samples with small deviations from the mean scalar concentration

ρ'_X, which further increases the concentration difference $\overline{\rho_{x\uparrow}} - \overline{\rho_{x\downarrow}}$ (Bowling et al. 1998, 1999b, 2003):

$$\left| \frac{w'}{\sigma_w} \frac{\rho'_X}{\sigma_{\rho X}} \right| \leq H \tag{10.17}$$

The threshold for HREA sampling is defined by Eq. (10.17), where $\sigma_{\rho X}$ is the standard deviation of the proxy scalar ρ_X. The hyperbolic deadband with the size H must be determined online from a proxy scalar measured with high temporal resolution, which again assumes scalar similarity. A deadband reduces the frequency of valve switching during sampling and, at the same time, the number of samples used for flux calculation. It also reduces the sensitivity of REA methods to uncertain definition of the mean vertical wind speed needed for segregating samples in the up and down reservoirs (see, for instance, Businger and Oncley 1990; Pattey et al. 1993). A comparison of general characteristics of eddy sampling methods like REA and HREA and different sources of error for flux determination are presented in a paper by Ruppert et al. (2002). Methodological problems regarding the application of HREA are addressed in more detail in Wichura et al. (2004). Riederer et al. (2014) showed for measurements on managed grasslands that scalar similarity between proxy scalars and scalars of interest can be affected by management events in ecosystems. They conclude that the REA and HREA technique cannot be applied shortly after meadow management without the risk of huge HREA flux errors.

The $\delta^{13}C$ iso-flux can be measured by a hyperbolic relaxed eddy accumulation system with adequate resolution of CO_2 and of ^{13}C isotope mixing ratio differences in up- and downdrafts, $\overline{s_\uparrow} - \overline{s_\downarrow}$ and $\overline{\delta^{13}C_\uparrow} - \overline{\delta^{13}C_\downarrow}$, respectively,

$$F_{\delta^{13}C} = \overline{\rho_a}\ b(\zeta)\ \sigma_w\ \left(\overline{\delta^{13}C_\uparrow s_\uparrow} - \overline{\delta^{13}C_\downarrow}\ \overline{s_\downarrow} \right) \tag{10.18}$$

(see Eq. (10.15)). The relationship between ^{13}C isotope ratios and CO_2 concentrations found in Keeling plots (e.g., Buchmann et al. 1998) suggests that CO_2 may show the highest degree of scalar similarity to ^{13}C isotopes. The assumption is that the use of CO_2 mixing ratios shows sufficient scalar similarity with the unknown fast fluctuations of the CO_2 isotopic composition. A detailed discussion of the effects of scalar similarity in HREA flux measurements is presented by Ruppert et al. (2006b).

10.2.4 HREA Measuring Systems

Based on the experiences of the first HREA $^{13}CO_2$ flux measurements (Bowling et al. 1999a, b), a similar HREA measurement system was used for measurements in the years 1999 and 2000 (Wichura et al. 2000, 2004; Wichura 2009). Figure 10.1 schematically illustrates the HREA system layout and shows details of the valve control box of the HREA system.

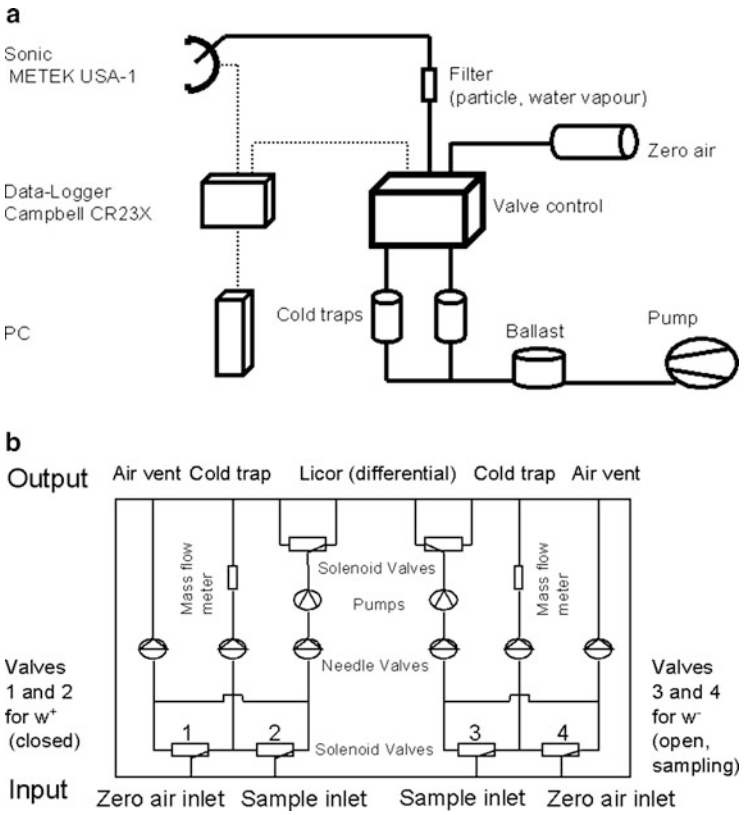

Fig. 10.1 Schematic diagram of the system layout (**a**) and of the valve control box (**b**) for the HREA measurement system that was used for measurements in years 1999 and 2000 (Wichura et al. 2004; Wichura 2009), published with kind permission of © Springer 2004 and Author 2009, All rights reserved

In addition to the system that was used for the first HREA $^{13}CO_2$ flux measurements (Bowling et al. 1999a, b), an additional third line ("Licor (differential)" in Fig. 10.1a) in both sampling paths (up- and downdraft) was added to the new HREA system in order to solve the problem of the need for simultaneous mixing ratio measurements for CO_2 (see Eq. 10.18), which is a precondition for calculating a consistent $^{13}CO_2$ flux. For this purpose, an additional infrared gas analyzer (IRGA) in differential mode was used to measure the mean CO_2 mixing ratio of either the updraft or the downdraft air. A filter protected the intake line of the HREA system and was installed close to the measurement path of the sonic anemometer. A flow rate of 0.4 l min^{-1} (laminar flow) was chosen as a trade-off between the limited volume of cryogenic traps for HREA $^{13}CO_2$ samples and the requirements of turbulence measurements.

HREA measurements require high-frequency data of vertical wind velocity and of a proxy scalar in order to calculate the HREA deadband in accordance with Eq. (10.17). High-frequency vertical wind velocity as well as proxy scalar data

(acoustic temperature) were provided by an ultrasonic anemometer in the years 1999 and 2000. A recursive low-pass filter was applied during data acquisition in order to calculate running mean values of the vertical wind velocity and the acoustic temperature and to determine their current fluctuations (Bowling et al. 1999a; Aubinet et al. 2000). A threshold value of $H = 1.1$ was chosen, in accordance with earlier measurements of $^{13}CO_2$ fluxes (Bowling et al. 1999b) and with HREA simulation runs that were performed using eddy covariance measurements available for the measurement site from previous field campaigns. HREA $^{13}CO_2$ samples for up- and downdraft air were collected in cold traps. A detailed description of the HREA system is given in Wichura (2009).

The HREA system was modified for HREA measurements in the years 2003 and 2010. A whole-air HREA sampling system and sampling procedure was implemented in order to overcome the difficulties with cryogenic purification of CO_2 encountered during sample collection by the preceding system. The whole-air sampling allowed subsequent high-precision isotope analysis in a laboratory directly from the accumulated updraft and downdraft air samples (Bowling et al. 2003). The aim of the construction of a new sampling system was the further improvement of the accuracy of isotope sampling (Ruppert 2008; Ruppert et al. 2012). Sample volumes were increased in order to also allow direct and precise analysis of the corresponding bulk CO_2 mixing ratios.

Figure 10.2 schematically illustrates the whole-air HREA system layout and shows details of the foil balloon bags that served—instead of cryogenic traps—as intermediate reservoirs for samples of $^{13}CO_2$. The high-frequency vertical wind velocity and CO_2 mixing ratio values, required for HREA measurements, were provided by an ultrasonic anemometer and an infrared gas analyzer. According to the hyperbolic deadband (Eq. 10.17), these data control the mechanical valve system for taking up- and downdraft air samples.

The filter-protected intake line of the system, tested and optimized for time lag and turbulent flow, was installed close to the measurement path of the sonic anemometer. The time lag between the air sample in the tube and the signal of the sonic anemometer was determined beforehand via cross-correlation analysis and provided in the HREA controlling software for online correction (Ruppert 2005).

For the online definition of the hyperbolic deadband during REA sampling according to Eq. (10.17), the vertical wind speed fluctuations w' were determined from the 3D wind vector after application of the planar-fit correction (Wilczak et al. 2001). The standard deviation of the vertical wind speed as well as the average and standard deviations of the CO_2 density were continuously recalculated from the most recent 6 min of data by the application of a linear-weighting function, by which the newest data was rated three times more important than the oldest data. A threshold value of $H = 1.0$ was chosen in accordance with results of studies regarding the scalar similarity for REA methods (Ruppert et al. 2006b). HREA $^{13}CO_2$ samples for up- and downdraft air were collected in two 45 cm diameter Mylar® foil balloons, which were equipped with stainless steel filling tubes, partially perforated, inserted through the foil valve of the balloons (Fig. 10.2). An airtight seal was achieved by wrapping a strong rubber band around the filling tube and foil

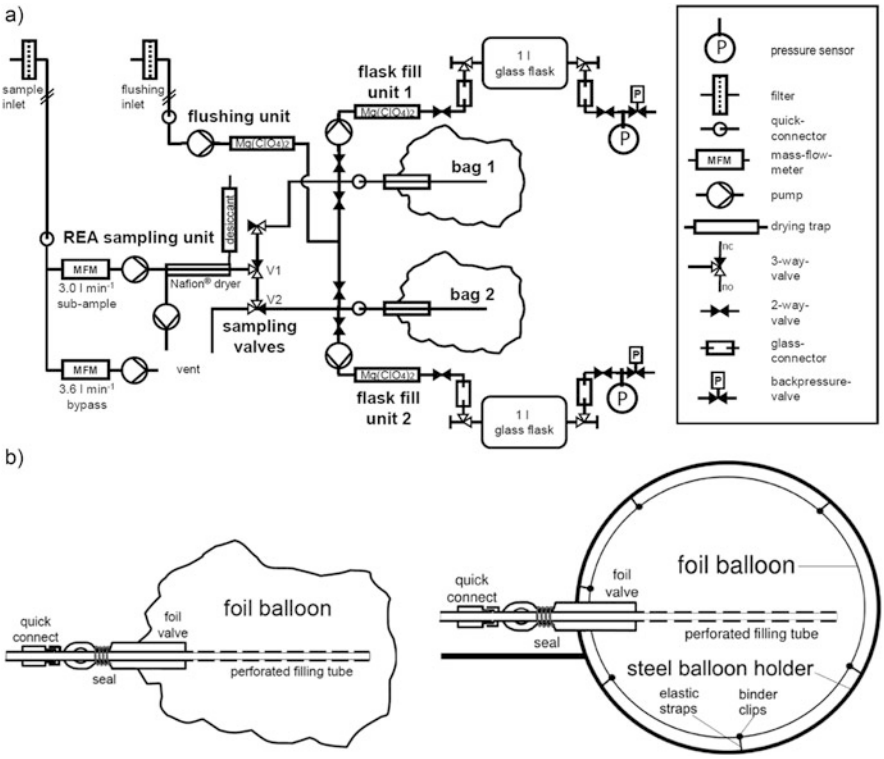

Fig. 10.2 Design of the whole-air HREA system (**a**) that was used for measurements in years 2003 and 2010 with foil balloon bags as intermediate reservoirs (**b**) (Ruppert 2008; Ruppert et al. 2012), published with kind permission of the © Authors 2008, 2012, All rights reserved

valve. A detailed description of the HREA system is given in Ruppert (2008) and Ruppert et al. (2012).

10.2.5 Measurement Sites and Campaigns

All HREA measurements were carried out at the spruce forest site Waldstein-Weidenbrunnen (FLUXNET station DE-Bay) on its main tower (see Chap. 2) during intensive measurement campaigns in the years 1999, 2000, and 2003. The general instrumentation of the tower and some additional instrumentation in 2003 are given in Appendix A. In addition, HREA measurements were carried out at the submontane grassland site "Voitsumra," about 5.8 km south of the Waldstein-Weidenbrunnen site at 624 m a.s.l. (50°05′25″ N, 11°51′25″ E) in 2010 (see Riederer et al. 2014), in order to apply the method over low vegetation. The specific instrumentation for the HREA measurement campaigns is compiled in Table 10.1.

Table 10.1 Instrumentation of HREA measurements during campaigns at site Waldstein-Weidenbrunnen in years 1999, 2000, and 2003 and at site Voitsumra in 2010

Period measuring complexes	Wind components	CO_2 concentration	$^{13}C/^{12}C$ isotope ratio	HREA system reference
1999				
EC CO_2 flux	Solent 1012 R2	Li-Cor 6262		See Fig. 10.1 Wichura (2009)
HREA ^{13}C flux	METEK USA-1	Li-Cor 6262 (differential mode)	Cryo-trap samples, mass spectrometer	
2000				
EC CO_2 flux	METEK USA-1	Li-Cor 7500		See Fig. 10.1 Wichura (2009)
HREA ^{13}C flux	METEK USA-1	Li-Cor 6262 (differential mode)	Cryo-trap samples, mass spectrometer	
2003				
EC CO_2 flux	METEK USA-1	Li-Cor 7500		See Fig. 10.2 Ruppert (2008)
HREA ^{13}C flux	METEK USA-1	Li-Cor 7500 (whole-air samples)	Whole-air samples, mass spectrometer	
2010				
EC CO_2 flux	METEK USA-1	Li-Cor 7500		See Fig. 10.2 Riederer et al. (2014)
HREA ^{13}C flux	METEK USA-1	Li-Cor 7500 (whole-air samples)	Whole-air samples, mass spectrometer	

10.3 Results and Discussion

10.3.1 Differences in HREA Samples of CO_2 and $\delta^{13}C$ Up- and Downdrafts

Results of CO_2 mixing ratios as well as of isotope ratios in $\delta^{13}C$ up- and downdrafts measured by HREA systems during campaigns in the years 1999, 2000, 2003, and 2010 are shown in Figs. 10.3, 10.4, 10.5, and 10.6. HREA CO_2 up- and downdraft results show differences that are large enough to resolve measurable differences in $\delta^{13}C$ (Bowling et al. 1999b). The results for $\delta^{13}C$ up- and downdrafts show significant differences for most of the HREA measurements in Figs. 10.3–10.6, taking into account the accuracy of the mass spectrometer analysis. The isotopic analysis was performed in the trace gas laboratory of the Max Planck Institute in Jena, Germany, with a high level of overall precision for $\delta^{13}C$ of about 0.013 ‰ vs. VPDB (valid for sample analysis for both HREA systems, Vienna Pee Dee Belemnite (VPDB), Ghosh et al. 2005). For further details of the IRMS high-precision analysis system and procedures, see Werner et al. (2001).

The results for control samples, for which the same air was sampled simultaneously in the up- and downdraft line of the HREA system in 1999 and 2000, showed maximum differences of 0.040 ‰ vs. VPDB (Wichura et al. 2000; Wichura 2009). Several tests with components and with the complete whole-air HREA system

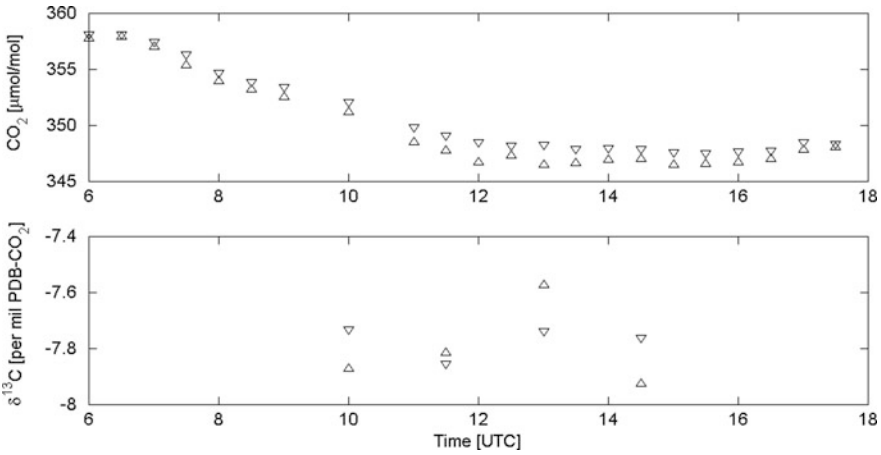

Fig. 10.3 HREA CO_2 mixing ratios (*upper graph*) and HREA $\delta^{13}C$ (*lower graph*) isotope ratios of updraft and downdraft air samples taken above a spruce forest at 33 m above ground (FLUXNET station Waldstein-Weidenbrunnen, DE-Bay) during the experiment 1999 by the application of a hyperbolic deadband of $H = 1.1$ (HREA). *Upward triangles* = updraft air samples, *downward triangles* = downdraft air samples (Wichura et al. 2004; Wichura 2009), published with kind permission of © Springer 2004 and Author 2009, All rights reserved

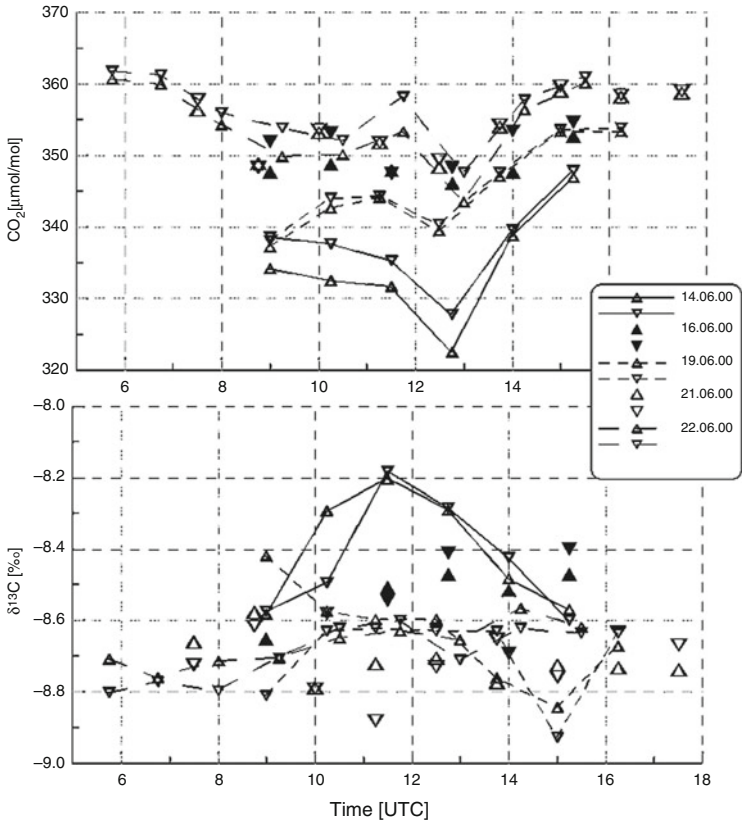

Fig. 10.4 HREA CO_2 mixing ratios (*upper graph*) and HREA $\delta^{13}C$ (*lower graph*) isotope ratios of updraft and downdraft air samples taken above a spruce forest at 33 m above ground (FLUXNET station Waldstein-Weidenbrunnen, DE-Bay) during the experiment 2000 by the application of a hyperbolic deadband of $H = 1.1$ (HREA). *Upward triangles* = updraft air samples, *downward triangles* = downdraft air samples (Wichura 2009), published with kind permission of the © Authors 2009, All rights reserved

(campaigns in 2003 and 2010) showed small standard deviations of 0.022 ‰ and 0.014 ‰ vs. VPDB, respectively (Ruppert 2008; Ruppert et al. 2012).

The $\delta^{13}C$ up- and downdraft values ranged between −8.29 and −7.51 ‰ (vs. VPDB) and between −8.93 and −8.18 ‰ (vs. VPDB) in the years 1999 (Fig. 10.3) and 2000 (Fig. 10.4), respectively. Comparing the results of $\delta^{13}C$ up- and downdraft values in 1999 and 2000, it is obvious that isotope ratios were generally less negative during campaign 1999 than during campaign 2000. The result suggests that processes of assimilation (respiration) were more (less) important for the metabolism of the forest canopy in 1999 than in 2000 (see next chapter for discussion).

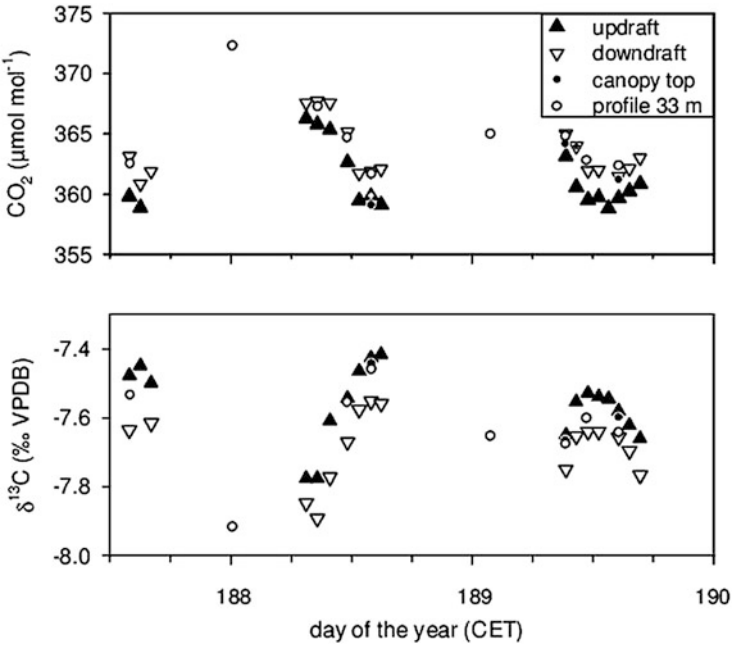

Fig. 10.5 CO_2 mixing ratios (*upper graph*) and $\delta^{13}C$ (*lower graph*) isotope ratios of updraft and downdraft air samples taken above a spruce forest at 33 m above ground (FLUXNET station Waldstein-Weidenbrunnen, DE-Bay) during the WALDATEM-2003 experiment by the application of a hyperbolic deadband of $H = 1.0$ (HREA). *Solid upward triangles* = updraft air samples, *unfilled downward triangles* = downdraft air samples. *Unfilled circles* represent air samples taken simultaneously with an isotope and trace gas profile system also at 33 m. *Solid circles* represent profile samples from the canopy top at 15 m or 22 m (Ruppert 2008), published with kind permission of the © Authors 2008, All rights reserved

The $\delta^{13}C$ up- and downdraft values ranged between −7.95 and −7.41 ‰ (vs. VPDB) for measurement campaign 2003 (Fig. 10.5). The $\delta^{13}C$ up- and downdraft values ranged between −8.10 and −7.45 ‰ (vs. VPDB) for the measurements made in 2010 (Fig. 10.6). The results from both campaigns support the outcomes from years 1999 and 2000. The magnitudes of $\delta^{13}C$ up- and downdraft results for campaign 2003 (Fig. 10.5) and for campaign 2010 (Fig. 10.6) are similar to those of year 1999 (Fig. 10.3).

This finding is understandable for the campaigns in 1999 and 2003, as they were carried out at the same spruce forest site. It is not an intuitive result for the comparison of $\delta^{13}C$ signatures for a spruce forest site and an extensively managed grassland site. Similar $\delta^{13}C$ isotopic signatures imply similar magnitudes of pools and/or similar processes of CO_2 exchange between an ecosystem and the atmosphere (see next chapter for discussion).

The diurnal trends of $\delta^{13}C$ in up- and downdrafts showed $^{13}CO_2$-depleted air (i.e., $\delta^{13}C$ is more negative) during morning hours until about noon for all measuring

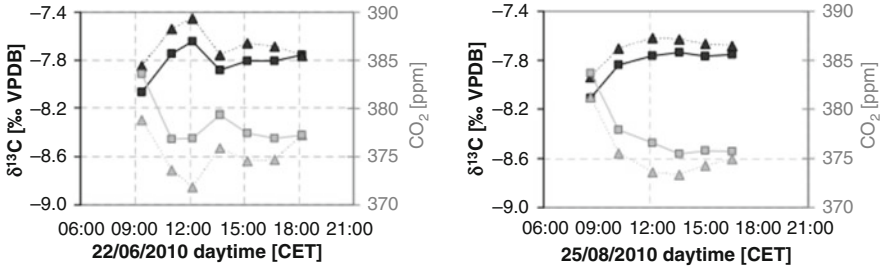

Fig. 10.6 CO_2 mixing ratios (bright symbols) and $\delta^{13}C$ (dark symbols) isotope ratios of updraft and downdraft air samples taken at the extensively managed submontane grassland site "Voitsumra" at the edge of the low mountain range "Fichtelgebirge" prior to (*left graph*), and 5 weeks after (*right graph*), summer mowing during the experiment 2010 by the application of a hyperbolic deadband of $H = 1.0$ (HREA). *Upward triangles* = updraft air samples, *squares* = downdraft air samples (Riederer et al. 2014), published with kind permission from the © Authors 2014, CC 3.0 License, All rights reserved

campaigns (Figs. 10.3–10.6), whereas afterward the air is more enriched in $^{13}CO_2$ ($\delta^{13}C$ is less negative). This result is consistent with our understanding of ecosystem processes. In the morning, the canopy air (updrafts) is less enriched in $^{13}CO_2$ ($\delta^{13}C$ is more negative) because of respiratory processes in the canopy during the night.

At noon and in the afternoon, the updraft air is more enriched in $^{13}CO_2$ because of discrimination against $^{13}CO_2$ during photosynthetic processes in the ecosystem. Note the reverse in $\delta^{13}C$ diurnal trends in the afternoon, indicating an increase of respiration in the canopy. The magnitudes in differences in CO_2 as well as in $\delta^{13}C$ up- and downdrafts indicate morning (afternoon) exchange processes of CO_2 that are already (still) directed to the canopy, whereas the $^{13}CO_2$ differences indicate processes that are still (already) directed out of the canopy in the morning (afternoon) for measurements in 1999, 2000, and 2003 (Figs. 10.3–10.5). A similar result was also found for measurements above a deciduous forest (Bowling et al. 1999a).

Those results most likely stem from a complex interaction of turbulent exchange processes with processes of ecosystem activity (assimilation, respiration, see Sect. 10.3.4 for more details). The findings indicate a time shift between both processes, a result that was found by other measurements as well (Foken et al. 2001).

Magnitudes of differences in $\delta^{13}C$ up- and downdrafts for measurements in 1999 and 2000 (Figs. 10.3 and 10.4, respectively) as well as their sign partially deviate from those in 2003 and 2010 (Figs. 10.5 and 10.6, respectively). To our best understanding, this is due to different HREA measuring systems (see Sect. 10.2.4) as well as due to the different hyperbolic deadbands ($H = 1.1$ in 1999 and 2000; $H = 1.0$ in 2003 and 2010) that were employed in the different campaigns.

Note that a similar enrichment of $^{13}CO_2$ in the atmosphere can be observed in the daily course of $\delta^{13}C$ in up- and downdrafts for an extensively managed grassland site as well (Fig. 10.6, left graph). The influence of the grassland management (Fig. 10.6, right graph) is also clearly reflected by the daily course of $\delta^{13}C$ in up-

and downdrafts. The air is less enriched in $^{13}CO_2$ ($\delta^{13}C$ is less negative) due to less photosynthetic activity in the ecosystem than before summer mowing of the grassland site.

10.3.2 CO_2 Fluxes and $^{13}CO_2$ Iso-fluxes

The turbulent fluxes of CO_2 and the turbulent iso-fluxes of $^{13}CO_2$ determined by EC and HREA, respectively, are shown for measurement campaigns 1999, 2000, 2003, and 2010 in Figs. 10.7, 10.8, and 10.9. The flux data quality was evaluated and confirmed according to test criteria described by Foken and Wichura (1996), Ruppert et al. (2006a), and Foken et al. (2012); see Ruppert (2008), Wichura (2009), and Riederer et al. (2014) for details. $^{13}CO_2$ turbulent isotope flux densities, measured by HREA (Fig. 10.7) and by whole-air HREA (Figs. 10.8 and 10.9), were determined from the measured CO_2 mixing ratios as well as from isotope ratios in $\delta^{13}C$ up- and downdrafts and measured effective b_{co_2}-factors, according to Eqs. (10.16) and (10.18); again, see Ruppert (2008), Wichura (2009), and Riederer et al. (2014) for details.

The turbulent CO_2 fluxes from measurement campaigns 1999 and 2000 are shown in Fig. 10.7. The daily courses of CO_2 fluxes show a remarkable variation. These intraday—as well as the day-to-day—deviations originate from different meteorological boundary conditions (in particular radiation balance) and subsequent changes of photosynthetic activity of the forest ecosystem; see Wichura (2009) for a detailed discussion.

The results of $\delta^{13}C$ up- and downdraft values in 1999 and 2000 suggest that in 1999, the processes of assimilation (and respiration) were more (and less) important for the metabolism of the forest canopy than in 2000 (see Sect. 10.3.1).

At first glance, this interpretation seems to be contradicted by the results of CO_2 up- and downdraft measurements (Figs. 10.3 and 10.4) as well as of CO_2 fluxes (Fig. 10.7). However, the result is consistent if the concept of the iso-density, as a linear combination of $\Re$ and ρ_c (see Eq. 10.3), and the corresponding iso-fluxes of $^{13}CO_2$ are taken into account. Even for similar magnitudes of CO_2 fluxes, the $\delta^{13}C$ up- and downdraft values may differ from each other due to different pools of assimilated or respirated CO_2 reservoirs and different processes of assimilation or respiration of CO_2 fluxes that were incorporated in the turbulent exchange processes between ecosystem and atmosphere (see Wichura (2009) for a more detailed discussion).

The abovementioned results support the hypothesis that the proportion of CO_2, which was already modified by assimilation (or respiration) processes of the forest ecosystem and which was incorporated in the exchange processes between ecosystem and atmosphere, was greater (or smaller) during the measurement period 1999 than during the period 2000. The hypothesis is supported by the meteorological boundary conditions: due to higher temperatures and lower humidity conditions during campaign 2000, the proportion of CO_2, which was incorporated

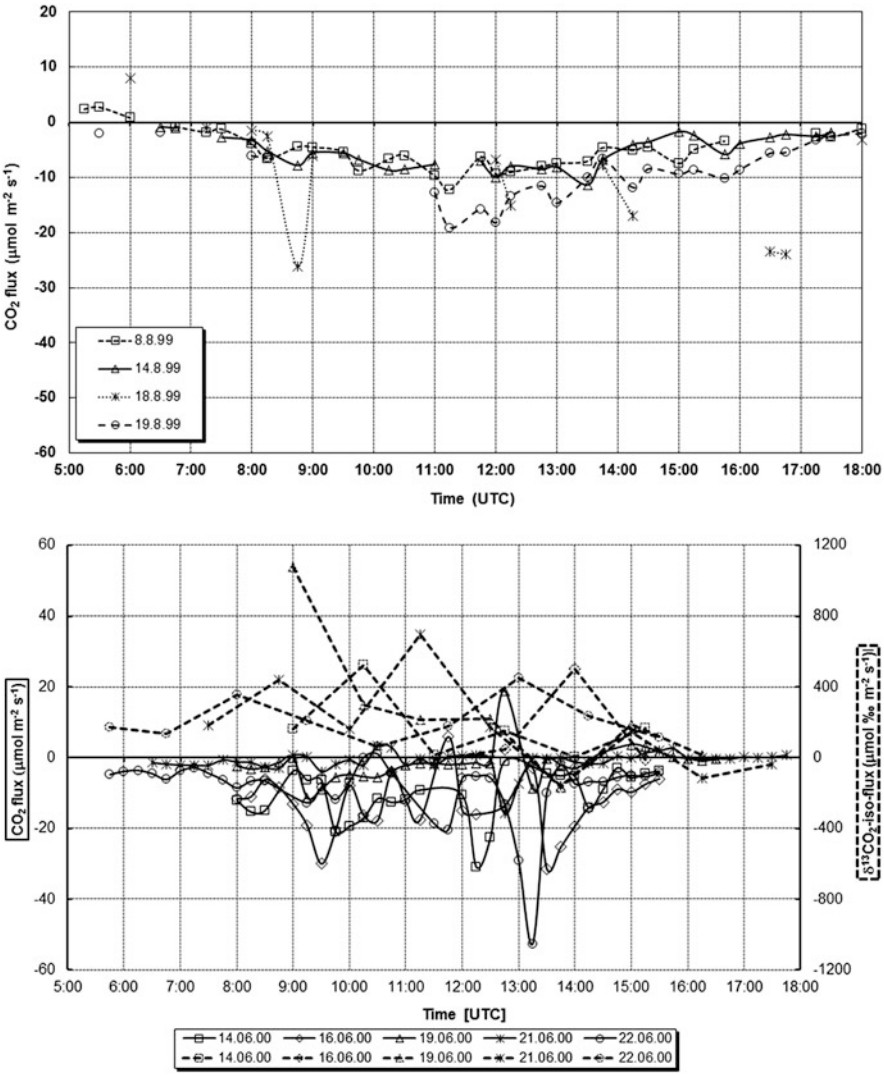

Fig. 10.7 EC CO_2 fluxes (*solid lines*) and HREA $\delta^{13}C$ iso-fluxes (*broken lines*) above a spruce forest at 33 m above ground (FLUXNET station Waldstein-Weidenbrunnen, DE-Bay) during the experiment 1999 (*upper graph*) and 2000 (*lower graph*, both from Wichura 2009), published with kind permission of the © Author 2009, All rights reserved

in the exchange processes between ecosystem and atmosphere, was most likely more enriched by respired CO_2 than in 1999 (see Wichura (2009) for a detailed documentation and discussion). Unfortunately, the hypothesis cannot be confirmed by a comparison of $\delta^{13}C$ iso-flux results, because of measurement errors of mean CO_2 mixing ratio values of up- and downdraft air in the HREA system (additional

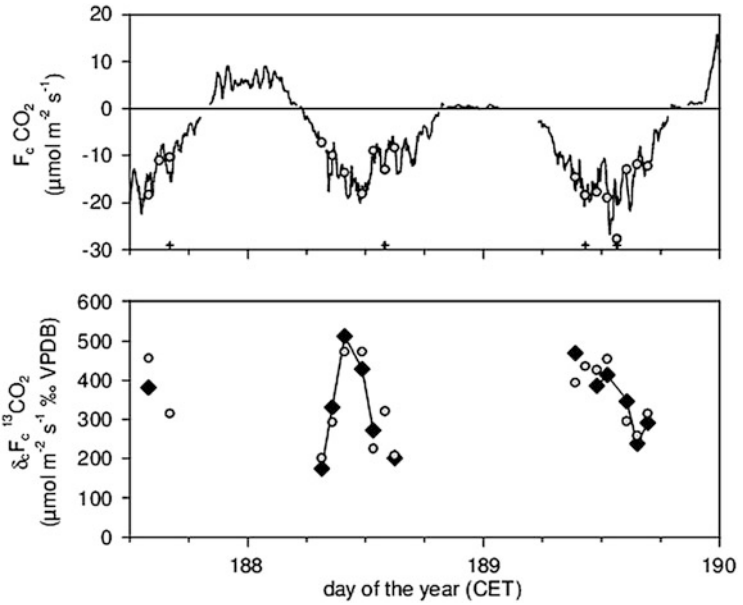

Fig. 10.8 Whole-air HREA CO_2 fluxes (*upper graph*) and $\delta^{13}C$ iso-fluxes (*lower graph*) above a spruce forest at 33 m above ground (FLUXNET station Waldstein-Weidenbrunnen, DE-Bay) during the WALDATEM-2003. The *solid line* in (*the upper graph*) indicates the turbulent CO_2 fluxes continuously measured with the EC system as reference. Measured b_{co_2}-factors (see Eq. (10.16)) were used for the estimation of iso-fluxes determined by HREA (diamonds in lower graph). *Gray circles* represent HREA fluxes calculated from measured concentration and isotopic differences and simulated b_{co_2}-factors. Either updraft or downdraft CO_2 mixing ratios of four samples marked with "+" at the bottom of (*upper graph*) showed insufficient accuracy and were therefore replaced by simulated values. Consequently, for these samples, turbulent iso-fluxes in (*lower graph*) could only be determined based on simulated b_{co_2}-factors (*gray circles*) (see Ruppert (2008) for more detailed information), published with kind permission from the © Author 2008, All rights reserved

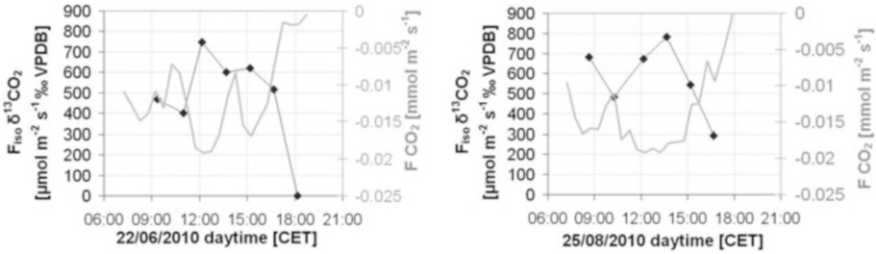

Fig. 10.9 EC CO_2 fluxes (*bright lines*) and whole-air HREA $\delta^{13}C$ iso-fluxes (*dark symbols*) at the extensively managed submontane grassland site "Voitsumra" at the edge of the low mountain range "Fichtelgebirge" prior to (*left graph*), and 5 weeks after (*right graph*), summer mowing during the experiment 2010 (Riederer et al. 2014), published with kind permission from the © Authors 2014, CC 3.0 License, All rights reserved

infrared gas analyzer (IRGA) in differential mode, see Sect. 10.2.4). Therefore, $\delta^{13}C$ iso-fluxes (see Eq. 10.18) are not available for measurement period 1999 as they are for the measurements in 2000 (Fig. 10.7).

Turbulent iso-fluxes of $^{13}CO_2$ for measurements in 2000 are shown in Fig. 10.7. During most time periods, (positive) $\delta^{13}C$ iso-fluxes correspond to (negative) CO_2 fluxes, as expected for the turbulent exchange of CO_2 between ecosystem and atmosphere during assimilation. However, some of the results do not show this negative correlation, likely due to inhomogeneity of boundary conditions (spatial inhomogeneity of the forest ecosystem or spatiotemporal inhomogeneity of micrometeorological conditions), their interaction, and their influence on exchange mechanisms between ecosystem and atmosphere (again, see Sect. 10.3.4 for more details).

The turbulent CO_2 fluxes determined during the campaign 2003 are shown in Fig. 10.8. They reflect the photosynthetic activity and CO_2 uptake during daytime after a rainy period. CO_2 release into the atmosphere during nighttime is inhibited during the second night (day of year (doy) 189) and at the beginning of the third night by very stable stratification of the air in the forest canopy in combination with low horizontal wind velocities, which results in minimal CO_2 fluxes and rejection of some data (gaps in the solid line) due to poor flux data quality.

Variation in the EC CO_2 fluxes during daytime is caused by variable radiation balance due to changing cloud cover (see Ruppert (2008) for more details). Downward turbulent transport of CO_2 (negative CO_2 fluxes by convention) correlates with isotopic enrichment of the canopy air (see Figs. 10.5 and 10.8) due to assimilation of CO_2 and linked discrimination of the heavier isotopes and corresponding positive turbulent iso-fluxes of $^{13}CO_2$ (Fig. 10.8).

The maximum $\delta^{13}C$ iso-fluxes were observed shortly before noon. The influence of isotopic enrichment is reflected in the positive trend of isotope ratios observed in HREA on day 188 and in the morning of day 189 in Fig. 10.5. In the $\delta^{13}C$ up- and downdraft data, this trend reverses after noon on day 189. Nevertheless, the maintained positive isotopic differences in Fig. 10.5 and consequently positive turbulent $\delta^{13}C$ iso-fluxes in Fig. 10.8 indicate that turbulent air exchange between the boundary layer and the canopy air continues to enrich boundary layer air with heavier isotopes. This finding again supports the hypothesis that inhomogeneity of boundary conditions and resulting exchange mechanisms (advective processes) are dominating the air composition change during this period (see Ruppert (2008) for a detailed discussion).

Results of EC CO_2 fluxes and whole-air HREA $\delta^{13}C$ iso-fluxes measured at the extensively managed grassland site during experiment 2010 are shown in Fig. 10.9. The daily courses of CO_2 fluxes show variations due to different meteorological boundary conditions (in particular radiation balance) and subsequent changes of photosynthetic activity.

The enrichment of $^{13}CO_2$ in the atmosphere can be observed in Fig. 10.6 as well as in Fig. 10.9. Sufficient water availability after mowing, due to a high groundwater level and moderate air temperature, excludes reduced stomatal conductance and

therefore the noon depression (Fig. 10.9, right graph). High enrichment of $^{13}CO_2$ at noon on 22 June relies on increased assimilation (Fig. 10.9, left graph). This assumption is supported by the development of the NEE, which shows the largest CO_2 uptake during that time (cf. next chapter). The pattern of $\delta^{13}C$ iso-fluxes acts to a certain extent in accordance with the $\delta^{13}C$ differences of the $^{13}CO_2$ values of up- and downdrafts (cf. Fig. 10.6) (see Riederer et al. (2014) for more details).

In general, the $\delta^{13}C$ iso-fluxes for all measurement campaigns (Figs. 10.7–10.9) match the results of other studies (Bowling et al. 1999a, 2001). They differ in magnitude from those studies, a result that may be most likely explained by the different ecosystems where the measurements took place [spruce forest and grassland ecosystem for the studies presented here versus deciduous forest in Bowling et al. (1999a, 2001)].

10.3.3 $^{13}CO_2$ Signatures and NEE Partitioning

The ensemble averages of the flux-weighted isotopic signature of the turbulent exchange $^{13}CO_2$ (δ_c; c.f. Eq. 10.10) show (Fig. 10.10) that processes of assimilation were predominant during morning hours (more negative values of δ_c due to higher amounts of $\delta^{13}C$ iso-fluxes compared to the corresponding CO_2 fluxes; c.f.

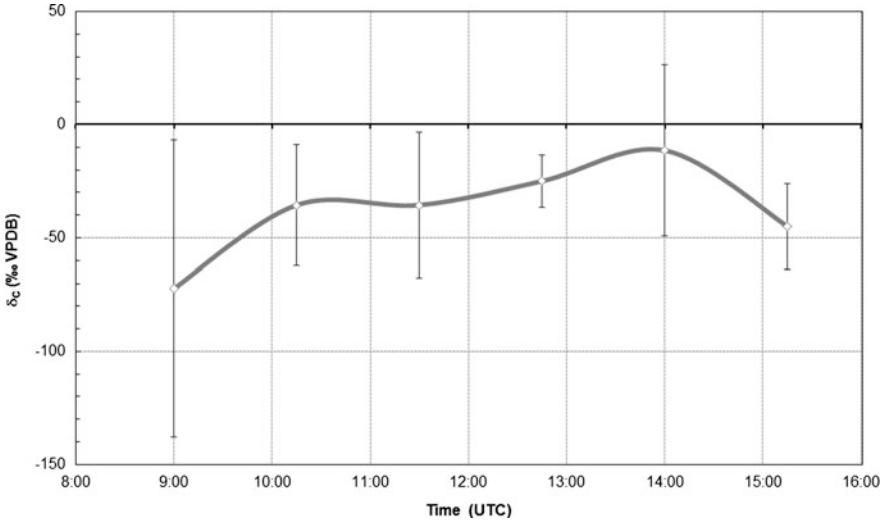

Fig. 10.10 Ensemble averages of flux-weighted isotopic signature of the turbulent exchange $^{13}CO_2$ (δ_c) above a spruce forest at 33 m above ground (FLUXNET station Waldstein-Weidenbrunnen, DE-Bay) during the experiment 2000. Values are consecutive ensemble averages calculated from of all days with results of HREA $^{13}CO_2$ iso-flux measurements. Error bars indicate the standard deviation for ensemble averages; see Wichura (2009) for more detailed information.

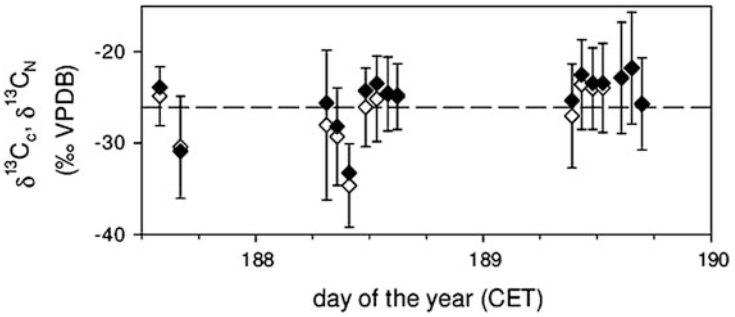

Fig. 10.11 Flux-weighted isotopic signature of the turbulent exchange of $^{13}CO_2$ ($\delta^{13}C_c$, *white diamonds*) and of net ecosystem exchange (NEE) of CO_2 ($\delta^{13}C_N$, *black diamonds*) above a spruce forest at 33 m above ground (FLUXNET station Waldstein-Weidenbrunnen, DE-Bay) during the WALDATEM-2003 experiment. Error bars indicate the estimated standard deviation for a single measurement. *Dashed lines* indicate the average of the isotopic signature of the atmospheric turbulent exchange. See Ruppert (2008) for more detailed information, published with kind permission of the © Author 2008, All rights reserved

Fig. 10.7) during the campaign 2000. Note the higher variability of δ_c during morning hours that stems mostly from higher variability of corresponding $\delta^{13}C$ iso-fluxes as a result of different meteorological boundary conditions (see Wichura (2009) for more details). The mean of all values of flux-weighted isotopic signature of the turbulent exchange $^{13}CO_2$ for campaign 2000 is -37.4 (± 32.1) ‰ VPDB or -30.5 (± 25.4) ‰ VPDB including or excluding the highly variable values of δ_c around 9:00 UTC, respectively. These values are plausible compared with the results of other authors, who found isotopic signatures of -16 ‰ to -35 ‰ VPDB (Vogel 1993) or -20 ‰ to -35 ‰ VPDB (Dawson et al. 2002). Values are close to the average δ_c of 16 samples of -26.0 (± 3.2) ‰ VPDB that were estimated during the WALDATEM-2003 experiment (see Fig. 10.11). Note that the standard deviation of flux-weighted isotopic signature of the turbulent exchange $^{13}CO_2$ is much smaller for the whole-air HREA system, indicating a higher quality of HREA $\delta^{13}C$ iso-flux measurements.

Time courses of δ_c in Figs. 10.10 and 10.11 do not reflect the diurnal and seasonal variability due to their limited number of HREA $\delta^{13}C$ iso-flux measurements. Nevertheless, values are close with those predicted for 50° N latitude by a global-scale model presented by Suits et al. (2005).

In order to compare the partitioning methodologies of NEE into assimilation (A) and respiration (R), two different approaches were applied to results of experiments in 2003 and 2010: the common FPM (see Eq. (10.5) and comments thereafter) and the isotopic flux partitioning method (see Eqs. (10.6) and (10.10) and comments thereafter).

An overview of the CO_2 flux components in the NEE mass balance for campaign 2003 is presented in Fig. 10.12. NEE was determined from the sum of the EC CO_2 flux and the storage flux determined from HREA updraft air CO_2 mixing ratios. The

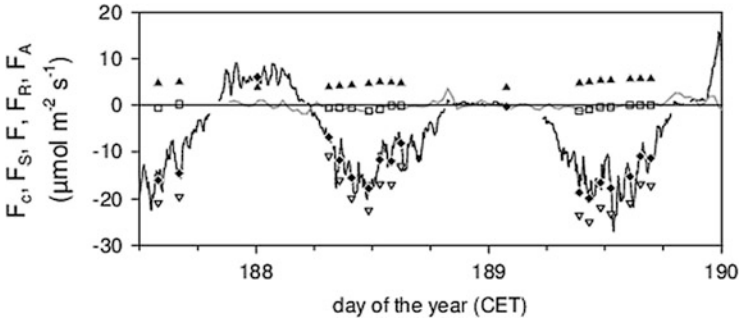

Fig. 10.12 Net ecosystem exchange of CO_2 (NEE = F, *black diamonds*) and individual flux components above a spruce forest at 33 m above ground (FLUXNET station Waldstein-Weidenbrunnen, DE-Bay) during the WALDATEM-2003. NEE is determined from the sum of the EC CO_2 flux (F_c, *black line*) and the storage flux determined from HREA updraft air CO_2 mixing ratios ($S_c = F_S$, *unfilled squares*). The net assimilation flux ($A = F_A$, *gray triangles*) results from the difference of NEE and the estimated respiration flux ($R = F_R$, *black triangles*) (Ruppert 2008), published with kind permission from the © Author 2008, All rights reserved

net assimilation flux A was calculated as the difference of NEE and the estimated respiration flux R (see Ruppert (2008) for more detailed information).

As discussed before, in the second night, the atmospheric turbulent exchange F_c was inhibited by a very strong temperature inversion within the forest canopy resulting in stable stratification. Consequently, hardly any of the respired CO_2 left the forest by vertical exchange. Instead, wavelike motions were detected in the turbulent time series of the sonic anemometer profile; see next chapter for discussion. The stable stratification persisted and was observed well into the morning hours. The inhibited turbulent exchange caused poor data quality of the eddy covariance flux measurements (missing data of F_c in Fig. 10.12). Observed storage fluxes were relatively small. However, small peaks of storage increase in air below measurement height are visible at sunset.

During the first night, the respiration model for F_R seems to slightly underestimate the nighttime total ecosystem respiration (TER, at nighttime equal to NEE, i.e., $R = F_R = F =$ NEE). On the other hand, the estimation of daytime respiration flux F_R from the temperature regression of nighttime TER involves an overestimation because of the partial inhibition of dark respiration by light (Sharp et al. 1984). Furthermore, by definition, daytime foliar respiration shall be excluded from R for the isotopic flux partitioning method according to Eq. (10.6). Foliar respiration is instead assigned to the net assimilation flux $A = F_A$ during daytime for this method.

An example of the isotopic flux partitioning for 1 day during experiment 2003 is displayed in Fig. 10.13. The results were obtained assuming a constant canopy isotope discrimination Δ_{canopy} (17.8 ‰). δ_A was determined by an equation corresponding to (10.12) for canopy isotope discrimination instead of ecosystem discrimination of the atmospheric exchange against isotopes in the lower boundary layer air Δ_e (see Ruppert (2008) for a more detailed discussion). δ_R was estimated

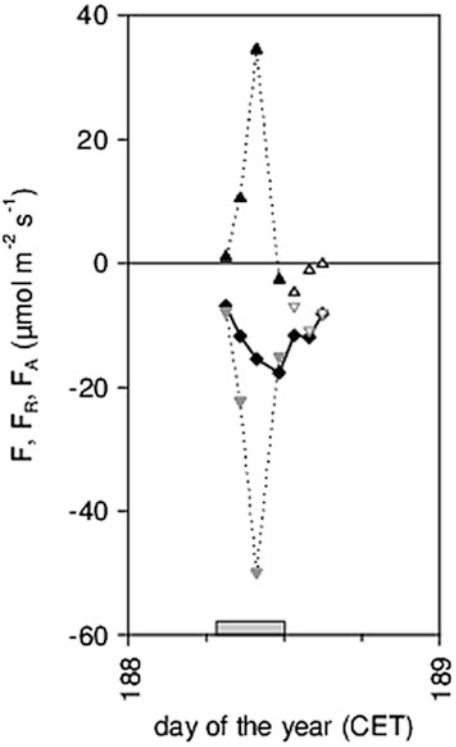

Fig. 10.13 Isotopic flux partitioning of the NEE = F (*black diamonds* connected by *solid line*) into the assimilation flux F_A (*gray triangles*) and respiration flux (*black triangles*) based on whole-air HREA $\delta^{13}C$ isotopic signatures measured on day 188 above a spruce forest at 33 m above ground (FLUXNET station Waldstein-Weidenbrunnen, DE-Bay) during the WALDATEM-2003. The isotopic signature δ_A of the assimilation flux was determined based on the assumption of a constant canopy isotope discrimination $\Delta_{canopy} = 17.8$ ‰. The isotopic signature δ_R of the respiration flux was determined from Keeling plot intercepts of sub-canopy air samples, (Ruppert 2008). Published with kind permission of the © Author 2008, All rights reserved

by the Keeling plot method (Keeling 1958, 1961, see Sect. 10.2.3). The gross flux components $A = F_A$ and $R = F_R$ of the NEE $= F$ were calculated by Eq. (10.10) from HREA whole-air samples of $\delta^{13}C$ up- and downdrafts as well as from $\delta^{13}C$ iso-fluxes.

In the example (Fig. 10.13), the diurnal variability of the isotope discrimination is explicitly ignored (constant value of Δ_{canopy}). Consequently, $A = F_A$ values show unrealistically high assimilation rates.

During the measuring periods with prevailing isotopic disequilibrium (difference of $\delta_A - \delta_R$, gray bar in Fig. 10.13), in one case $A = F_A$ is smaller than the NEE $= F$ so that $R = F_R$ becomes negative. Although $A = F_A$ includes the daytime foliar respiration, it should exhibit more negative values than the NEE $= F$, and $R = F_R$ should always have positive values. Results from periods with a lack of isotopic

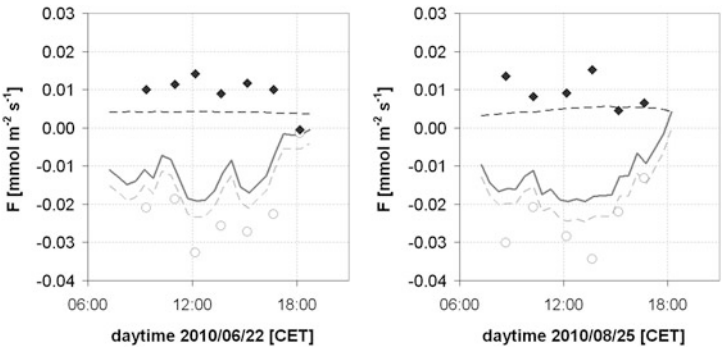

Fig. 10.14 Comparison of NEE flux partitioning with isotopic background (respiration flux R, *black diamonds*; assimilation flux A, *light-gray circles*) and a common flux partition method (*dashed lines* in same colors) at the extensively managed submontane grassland site "Voitsumra" at the edge of the low mountain range "Fichtelgebirge" prior to (*left graph*), and 5 weeks after (*right graph*), summer mowing during the experiment 2010. The NEE measured via eddy covariance is illustrated as a *dark-gray solid line* (Riederer et al. 2014), published with kind permission from the

disequilibrium (unfilled symbols in Fig. 10.13) should be discarded, because the isotopic flux partitioning methods must fail under such conditions. The comparison of the estimated respiration fluxes $R = F_R$ presented in Fig. 10.13 and in Fig. 10.12 indicates that isotopic flux partitioning might yield highly variable and unrealistic respiration fluxes when the isotopic disequilibrium and the isotopic signature δ_A of the assimilation flux $A = F_A$ are determined from constant canopy isotope discrimination Δ_{canopy}.

The assumption of a constant value of Δ_{canopy} stems from the lack of a clearly defined value of isotope discrimination at ecosystem level (as it would be Δ_e, see Eq. 10.11) due to its dependence on measurement height (see discussion in Ruppert (2008) for more details). Furthermore, inhomogeneity of boundary conditions (spatial inhomogeneity of forest ecosystems and spatiotemporal inhomogeneity of micrometeorological conditions) and their influence on exchange mechanisms between ecosystem and atmosphere may violate the assumptions of turbulent mixing and stationarity (see Eq. 10.10) and may lead to unrealistic results of HREA $^{13}CO_2$ isotope measurements above tall canopies.

In order to show the capability of the isotopic flux partitioning method, both partition methodologies of NEE were also tested at the extensively managed submontane grassland site. Results of the comparison of NEE flux partitioning by a common FPM (see Eq. 10.5) and the isotopic flux partitioning method (see Eqs. 10.6 and 10.10) for the campaign 2010 are displayed in Fig. 10.14.

On both days, NEE (Fig. 10.14) shows variations according to incoming shortwave radiation (see Riederer et al. (2014) for more details). While the morning rise of photosynthetic activity was not sampled, evening breakdown to a respiration-dominated system was captured. The last values in Fig. 10.14 (left graph) in the

evening show a special case. There is no longer any difference between up- and downdraft isotope ratios, and so $\delta^{13}C$ iso-flux, and consequently assimilation and respiration fluxes (A and R, respectively), becomes zero. This comes along with a lack of photosynthesis and discrimination, but above all with turbulent fluxes that come to a standstill, as confirmed by a very small NEE (Fig. 10.14, left graph). This pattern is not shown by the common FPM. Apart from that, the isotopic flux partitioning shows a much greater variability, whereas the FPM insufficiently reproduces natural respiration changes, causing assimilation fluxes A to exactly follow the NEE. Sometimes both approaches provide partially similar fluxes, but the isotopic model is able to describe various underlying fluxes of the NEE; that is, more intense reactions to environmental conditions are attributed to the ecosystem (Ruppert 2008). The quite constant respiration provided by the temperature-based FPM results from relatively small temperature variations during both measurement periods (see Riederer et al. (2014) for more details).

However, temperature is only one of the driving mechanisms of respiration. Photosynthetic activity, for example, supplies root exudates to soil life and accounts for a large portion of root-derived respiration (Kuzyakov and Gavrichkova 2010). Discrimination of $^{13}CO_2$ is an input factor in the isotopic model. It is directly coupled to all assimilation-based processes, which become apparent in the assimilation flux closely connected to the incoming shortwave radiation. The same applies to wind velocity, essential for atmospheric fluxes and considered only in the isotopic model as an input parameter of the $\delta^{13}C$ iso-flux. The diurnal cycle of the assimilation flux A (see Fig. 10.14), determined from HREA measurements of $\delta^{13}C$ iso-fluxes, can be explained clearly by the diurnal cycles of incoming shortwave radiation and wind velocity (see Riederer et al. (2014) for more details).

Almost all values of the isotopic model show these dependences to some extent. This representation of the environmental influences, in combination with the agreement with the established common flux partitioning model, suggests the good performance of the isotopic model, and there is no evidence for restrictions comparable to those found for complicated coupling regimes in high-vegetation ecosystems (Ruppert 2008; Wichura 2009) as discussed in the next chapter.

10.3.4 Structure of CO_2 Exchange Mechanisms over Forests

The discussion of the HREA $^{13}CO_2$ measurements, taking into account the results of EC CO_2 fluxes, showed that the exchange of carbon dioxide above a spruce forest stems from a superposition of different processes and mechanisms. The change in the atmospheric and/or metabolic conditions influences both the turbulent exchange between the forest canopy and atmosphere (coupling/decoupling of the turbulent exchange of CO_2 between canopy and atmosphere, in-canopy CO_2 storage) and the metabolism of the ecosystem (assimilation, respiration). It results in different consequences for CO_2 and $^{13}CO_2$ exchange processes, depending on the boundary conditions.

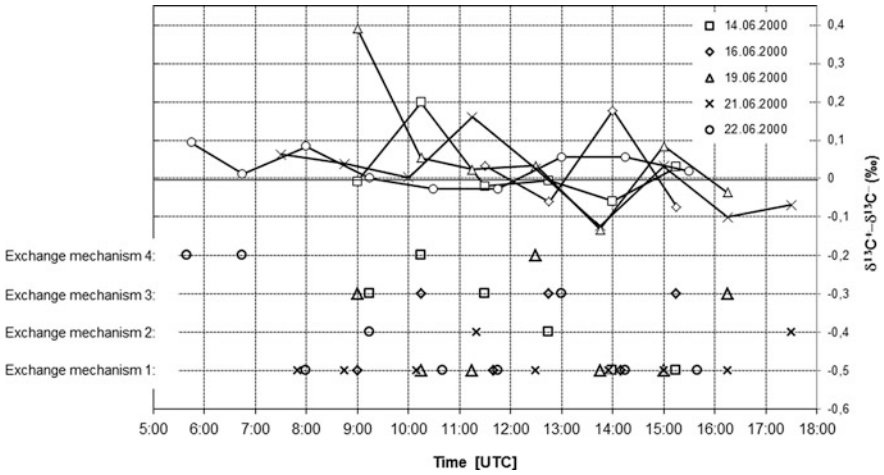

Fig. 10.15 HREA $\delta^{13}C$ differences for isotope ratios of up- and downdraft air samples (*upper part* of graph) and corresponding turbulent exchange mechanisms (1–4, *lower part* of graph) for the experiment 2000 (FLUXNET station Waldstein-Weidenbrunnen, DE-Bay), (Wichura 2009). Published with kind permission of the © Author 2009, All rights reserved

In order to evaluate exchange mechanisms between the forest ecosystem and atmosphere, the structure of turbulence was investigated using the mixing layer analogy for exchange processes above a forest canopy according to Raupach et al. (1996) for the measurement campaign 2000. The shear scale and the wavelength of coherent structures are characteristic scales of a mixing layer above tall canopies. The shear scale depends on the horizontal wind velocity and on the wind gradient near the canopy height. The wavelength of coherent structures corresponds to the wavelength of the initial Kelvin–Helmholtz instability of a mixing layer (Finnigan 2000), which can be estimated by analyzing a time series with wavelet technique (Brunet and Irvine 2000). According to Raupach et al. (1996), both length scales are related linearly by a constant factor, even for different stratification conditions (Brunet and Irvine 2000).

Comparing the characteristic length scales (shear scale and wavelength of coherent structures) for the vertical wind velocity and for CO_2, different turbulent exchange mechanisms were found from results of the 2000 campaign (Fig. 10.15).

The analyses of exchange mechanisms (see Fig. 10.15) showed that the turbulent exchange of momentum and of CO_2 between the spruce forest and the atmosphere were temporarily decoupled from each other (Wichura et al. 2004; Wichura 2009). Furthermore, results demonstrate that the turbulent CO_2 exchange between the forest ecosystem and the atmosphere only temporarily show properties of a mixing layer. The results of wavelet analyses provided information for a consistent interpretation of EC CO_2 and HREA $^{13}CO_2$ iso-flux measurements (see Wichura (2009) for a more detailed discussion).

Four mechanisms of CO_2 exchange between the ecosystem and the atmosphere were identified: CO_2 is exchanged outside (mechanisms 1, 3, and 4) or within (mechanism 2) a mixing layer. Momentum and CO_2 are exchanged in different (mechanisms 1 and 3) or in comparable (mechanisms 2, 4) length scales (see Fig. 10.15). These mechanisms of CO_2 partly correspond to coupling regimes that were studied in more detail by Thomas and Foken (2007); see Chap. 6 for a detailed discussion.

Ruppert (2008) used results of Thomas and Foken (2007) (see Chap. 6) in order to determine the status of coupling of the turbulent exchange between the sub-canopy, canopy, and above-canopy space. They indicated complete decoupling and the existence of wavelike patterns in the time series of the second night (see Figs. 10.8 and 10.11). The complex process of stepwise-enhanced coupling in the morning is generally reflected well, including the prolonged decoupling of the sub-canopy space in the morning of day 189. In the early morning hours, the temporal resolution of the exchange and coupling status could be enhanced by the identification of maxima and minima in the CO_2 mixing ratio time series (c.f. Fig. 10.5). For the HREA measurement periods during daytime, generally well-coupled conditions were indicated for the canopy space. Only for the first sampling periods in the morning of day 188 and 189 and the last sampling period in the late afternoon of day 189 should partial decoupling of the sub-canopy space be assumed (see Ruppert (2008) for more details).

10.4 Conclusions

The quantification of net ecosystem exchange (NEE) of CO_2 using the eddy covariance method has become an important tool for investigating the carbon balance of terrestrial ecosystems. As the analysis of NEE flux components (assimilation and respiration) is critical for obtaining insights into ecosystem responses to climate forcing and their feedbacks to the greenhouse warming effect, flux partitioning methods are applied. Whereas common methods for the partitioning of the NEE are based on models describing the dependency of the flux components on temperature and light response, the alternative approach directly assesses the specific and different isotopic signatures of assimilation and respiration fluxes, respectively.

The methodological background for the combined use of $^{13}CO_2$ and CO_2 fluxes and the technique for measuring $^{13}CO_2$ fluxes is summarized in this chapter. The basic principle for isotopic flux partitioning on the basis of simultaneous $^{13}CO_2$ iso-flux and CO_2 flux measurements is derived from an analysis of mass balance equations for $^{13}CO_2$ and CO_2 (see Sects. 10.2.1 and 10.2.2). As pointed out, a straightforward isotopic flux partitioning is made feasible only where an adequate turbulent mixing of the atmospheric surface layer as well as the stationarity of exchange processes between ecosystem and atmosphere are assumed. These requirements are not necessarily fulfilled at complex measurement sites as, for instance, above forest ecosystems. On the other hand, the first attempts to apply

isotopic flux partitioning were carried out for forest measurement sites where robust signals in isotopic signatures due to higher rates of assimilation and respiration in those ecosystems were anticipated (Bowling et al. 1999a; Ehleringer et al. 2002; Wichura et al. 2004).

When $^{13}CO_2$ iso-flux measurements were first carried out (Bowling et al. 1998, 1999b; Wichura et al. 2004; Ruppert 2008; Wichura 2009), no fast sensors for EC $^{13}CO_2$ iso-flux measurements were available that would be able to sufficiently resolve the isotopic signatures observed even above forest ecosystems. Alternatively, conditional sampling methods provided the basis for isotopic flux measurements, as accumulated air samples can be analyzed with high precision by isotope ratio mass spectrometry (IRMS) in the laboratory. Combination of this method with the hyperbolic relaxed eddy accumulation method (HREA) and with cryo-trap and whole-air sampling allows the $^{13}CO_2$ iso-fluxes to be quantified (Sect. 10.2.4). HREA samples for CO_2 and of $\delta^{13}C$ in up- and downdrafts showed significant differences for most of the HREA measurements, taking into account the accuracy of the IRMS analysis. Results from HREA $^{13}CO_2$ measurements at FLUXNET station DE-Bay (Waldstein-Weidenbrunnen) above a spruce forest during three intensive measuring campaigns in 1999, 2000, and 2003, as well as at the submontane grassland site "Voitsumra" near Waldstein-Weidenbrunnen during an intensive measuring campaign in 2010, showed the feasibility of these methods.

However, the application of HREA $^{13}CO_2$ measurements in general is expensive and time-consuming and is therefore only applicable for short-term and special investigations. Moreover, the use of HREA systems for $^{13}CO_2$ measurements does not only require the availability of highly accurate IRMS analyses, it also demands detailed micrometeorological analyses. Application of conditional sampling methods requires the similarity in the turbulent exchange of measured and of proxy scalars (Sect. 10.2.3). While there is some evidence for good scalar similarity between CO_2 and its isotopic signatures in the turbulent exchange, its relation may change temporarily, for example during morning transition periods (Ruppert 2008).

Uncertainties in HREA $^{13}CO_2$ iso-flux measurements may furthermore result from the fact that the CO_2 exchange above tall and complex ecosystems (as the spruce forest at FLUXNET station Waldstein-Weidenbrunnen) stems from a superposition of different processes and mechanisms. The change in the atmospheric and/or metabolic conditions influences both the turbulent exchange between the forest canopy and atmosphere (coupling/decoupling of the turbulent exchange of CO_2 between canopy and atmosphere, in-canopy CO_2 storage) and the metabolism of the ecosystem (assimilation, respiration). It results in different consequences for CO_2 and $^{13}CO_2$ exchange processes, depending on the boundary conditions (Sect. 10.3.4).

As atmospheric and/or metabolic conditions may result in exchange mechanisms with coupling or decoupling of the canopy and the atmospheric surface layer, the preconditions for isotopic flux partitioning of NEE (adequate turbulent mixing, stationarity) of EC CO_2 flux and HREA $^{13}CO_2$ iso-flux measurements may be violated. This results in problems for the adequate estimation of isotopic signatures (e.g., δ_C) and of isotopic discrimination (e.g., Δ_e). Consequently, information about

the isotopic ratios of assimilated and respired CO_2, δ_A and δ_R, as a prerequisite for CO_2 flux partitioning becomes imprecise. These problems prevented the full success of NEE partitioning on the basis of simultaneous $^{13}CO_2$ iso-flux and CO_2 flux measurements above a spruce forest at FLUXNET station DE-Bay Waldstein-Weidenbrunnen (Sect. 10.3.3).

On the other hand, it turned out that the isotopic approach works well when the results of HREA $^{13}CO_2$ iso-flux and EC CO_2 flux measurements at the submontane grassland site "Voitsumra" nearby Waldstein-Weidenbrunnen are used. Moreover, it can enhance results of a common flux partitioning method based on Lloyd–Taylor and Michaelis–Menten functions. An advantage is a better reproduction of environmental conditions, due to the direct inclusion of ecosystem discrimination of ^{13}C and wind velocity in the model. However, the method is very sensitive and is even more requiring of an exact determination of the isotopic signatures, and uncertainties regarding the determination of isotopic ratios δ_A and δ_R need to be further investigated (Sect. 10.3.3, Riederer et al. 2014).

In summary, the great hope of obtaining an independent NEE flux partitioning method on the basis of different isotopic signatures of assimilation and respiration fluxes in order to verify and enhance common flux partitioning methods (see Chap. 4) has only been partly fulfilled. HREA measurements for $^{13}CO_2$ enabled the first quasi-direct iso-flux estimates for $^{13}CO_2$ compared to indirect gradient methods. The measured $^{13}CO_2$ iso-fluxes established the first data sets for a coniferous forest.

Modern laser techniques (Wehr et al. 2013) might be a direct EC alternative to measure $^{13}CO_2$ iso-fluxes in the future, and they may also be adapted for long-term experiments. However, their accuracy of 0.020–0.030 ‰ VPDB is lower than the high level of overall precision for $\delta^{13}C$ of about 0.013 ‰ VPDB of the Max Planck Institute for Biogeochemistry in Jena.

Although the results of this chapter only partly fulfill the expectations that were associated with the HREA measurements of $^{13}CO_2$ iso-fluxes and their application for NEE flux partitioning, the group gained and shared expert knowledge about the implementation of different HREA systems (cryo-trap and whole-air sampling), their application for isotope flux measurements, and their field operation. The studies contributed input to the scientific community with respect to examination of scalar similarity as a prerequisite for HREA application (Ruppert et al. 2006b). They enabled a contribution to the investigation of the structure of turbulence above forest ecosystems, including the examination of the coupling processes (Thomas and Foken 2007). Furthermore, they influenced the construction of other relaxed eddy accumulation systems (Moravek et al. 2014).

Acknowledgments This research was funded by the Federal Ministry of Education, Science, Research and Technology (PT BEO-0339476 C, D) and the joint research project "FORKAST" by the Bavarian State Ministry of Sciences, Research and the Arts.

References

Ammann C (1999) On the applicability of relaxed eddy accumulation and common methods for measuring trace gas fluxes, vol 73. Zürcher Geographische Schriften, Zürich

Ammann C, Meixner FX (2002) Stability dependence of the relaxed eddy accumulation coefficient for various scalar quantities. J Geophys Res 107(D8):ACL7-1–ACL7-9

Ammann C, Flechard CR, Leifeld J, Neftel A, Fuhrer J (2007) The carbon budget of newly established temperate grassland depends on management intensity. Agr Ecosyst Environ 121(1–2):5–20

Aubinet M, Grelle A, Ibrom A, Rannik Ü, Moncrieff J, Foken T, Kowalski AS, Martin PH, Berbigier P, Bernhofer C, Clement R, Elbers J, Granier A, Grünwald T, Morgenstern K, Pilegaard K, Rebmann C, Snijders W, Valentini R, Vesala T (2000) Estimates of the annual net carbon and water exchange of forests: the EUROFLUX methodology. Adv Ecol Res 30:113–175

Aubinet M, Vesala T, Papale D (eds) (2012) Eddy covariance. A practical guide to measurement and data analysis, Springer atmospheric sciences. Springer Netherlands, Dordrecht

Baker JM (2000) Conditional sampling revisited. Agric For Meteorol 104:59–65

Baker JM, Norman JM, Bland WL (1992) Field-scale application of flux measurement by conditional sampling. Agric For Meteorol 62:31–52

Baldocchi D (2014) Measuring fluxes of trace gases and energy between ecosystems and the atmosphere – the state and future of the eddy covariance method. Glob Chang Biol 20(12):3600–3609

Baldocchi DD, Bowling DR (2003) Modelling the discrimination of $^{13}CO_2$ above and within a temperate broad-leaved forest canopy on hourly to seasonal time scales. Plant Cell Environ 26(2):231–244

Baldocchi D, Valentini R (2004) Geographic and temporal variation of carbon exchange by ecosystems and their sensitivity to environmental perturbations. In: The global carbon cycle: integrating humans, climate and the natural world. Island Press, Washington, DC, pp 479–491

Baldocchi D, Falge E, Gu L, Olson R, Hollinger D, Running S, Anthoni P, Bernhofer C, Davis K, Evans R, Fuentes R, Goldstein A, Katul G, Law B, Lee X, Malhi Y, Meyers T, Munger W, Oechel W, Paw U KT, Pilegaard K, Schmid HP, Valentini R, Verma S, Vesala T, Wilson K, Wofsy S (2001) FLUXNET: a new tool to study the temporal and spatial variability of ecosystem–scale carbon dioxide, water vapor, and energy flux densities. Bull Am Meteorol Soc 82(11):2415–2434

Beverland IJ, Milne R, Boissard C, ONeill DH, Moncrieff JB (1996) Measurements of carbon dioxide and hydrocarbon fluxes from a sitka spruce forest using micrometeorological techniques. J Geophys Res 101(D17):22807–22815

Bowling DR, Turnipseed AA, Delany AC, Baldocchi DD, Greeoberg JP, Monson RK (1998) The use of relaxed eddy accumulation to measure biosphere-atmosphere exchange of isoprene and other biological trace gases. Oecologia 116(3):306–315

Bowling DR, Baldocchi DD, Monson RK (1999a) Dynamics of isotopic exchange of carbon dioxide in a Tennessee deciduous forest. Global Biogeochem Cycles 13(4):903–922

Bowling DR, Delany AC, Turnispseed AA, Baldocchi DD, Monson RK (1999b) Modification of the relaxed eddy accumulation technique to maximize measured scalar mixing ratio differences in updrafts and downdrafts. J Geophys Res 104(D8):9121–9133

Bowling DR, Tans PP, Monson RK (2001) Partitioning net ecosystem carbon exchange with isotopic fluxes of CO_2. Glob Chang Biol 7:127–145

Bowling DR, Pataki DE, Ehleringer JR (2003) Critical evaluation of micrometeorological methods for measuring ecosystem-atmosphere isotopic exchange of CO_2. Agric For Meteorol 116(3-4):159–179

Brunet Y, Irvine MR (2000) The control of coherent eddies in vegetation canopies: streamwise structure spacing, canopy shear scale and atmospheric stability. Bound-Lay Meteorol 94(1):139–163

Buchmann N (2000) Biotic and abiotic factors controlling soil respiration rates in Picea abies stands. Soil Biol Biochem 32:1625–1635

Buchmann N, Kao W-Y, Ehleringer J (1997) Influence of stand structure on carbon C-13 of vegetation, soils, and canopy air within deciduous and evergreen forests in Utah, United States. Oecologia 110:109–119

Buchmann N, Brooks JR, Flanagan LB, Ehleringer JR (1998) Carbon isotope discrimination of terrestrial ecosystems. In: Griffiths H, Robinson D, Van Gardingen P (eds) Stable isotopes and the integration of biological, ecological and geochemical processes. BIOS Scientific Publishers Ltd., Oxford

Businger JA, Delany AC (1990) Chemical sensor resolution required for measuring surface fluxes by three common micrometeorological techniques. J Atmos Chem 10:399–410

Businger JA, Oncley SP (1990) Flux measurement with conditionial sampling. J Atmos Oceanic Tech 7:349–352

Ciais P, Tans PP, Trolier M, White JWC, Francey RJ (1995) A large northern hemisphere terrestrial CO_2 sink indicated by the $^{13}C/^{12}C$ ratio of atmospheric CO_2. Science 269:1098–1101

Dawson TE, Mambelli S, Plamboeck AH, Templer PH, Tu KP (2002) Stable isotopes in plant ecology. Annu Rev Ecol Syst 33:507–559

Delany AC, Oncley SP, Businger JA, Sievering E (1991) Adapting the conditional sampling concept for a range of different chemical species. In: Seventh symposium on meteorological observations and instruments, New Orleans, LA, 14–18 January 1991. American Meteorological Society, pp 22–25

Ehleringer JR, Bowling DR, Flanagan LB, Fessenden J, Helliker B, Martinelli LA, Ometto JP (2002) Stable isotopes and carbon cycle processes in forests and grasslands. Plant Biol 4:181–189

Falge E, Baldocchi D, Olson R, Anthoni P, Aubinet M, Bernhofer C, Burba G, Ceulemans R, Clement R, Dolman H, Granier A, Gross P, Grunwald T, Hollinger D, Jensen NO, Katul G, Keronen P, Kowalski A, Lai CT, Law BE, Meyers T, Moncrieff H, Moors E, Munger JW, Pilegaard K, Rannik U, Rebmann C, Suyker A, Tenhunen J, Tu K, Verma S, Vesala T, Wilson K, Wofsy S (2001) Gap filling strategies for defensible annual sums of net ecosystem exchange. Agric For Meteorol 107:43–69

Farquhar GD, Lloyd J (1993) Carbon and oxygen isotope effects in the exchange of carbon dioxide between terrestrial plants and the atmosphere. In: Ehleringer JR, Hall AE, Farquhar GD (eds) Stable isotopes and plant-water relations. Physiological ecology. Academic Press, San Diego, CA, pp 47–70

Farquhar GD, Ehleringer JR, Hubick KT (1989) Carbon isotope discrimination and photosynthesis. Annu Rev Plant Physiol Plant Mol Biol 40:503–537

Field CB, Raupach MR (2004) the global carbon cycle: integrating humans, climate, and the natural world. Island Press, Washington, DC

Finnigan J (2000) Turbulence in plant canopies. Annu Rev Fluid Mech 32:519–571

Flanagan LB, Ehleringer JR (1998) Ecosystem-atmosphere CO_2 exchange: interpreting signals of change using stable isotope ratios. Trends Ecol Evol 13(1):10–14

Flanagan LB, Brooks JR, Varney GT, Berry SC, Ehleringer JR (1996) Carbon isotope discrimination during photosynthesis and the isotope ratio of respired CO_2 in boreal forest ecosystems. Global Biogeochem Cycles 10(4):629–640

Foken T, Wichura B (1996) Tools for quality assessment of surface-based flux measurements. Agric For Meteorol 78:83–105

Foken T, Dlugi R, Kramm G (1995) On the determination of dry deposition and emission of gaseous compounds at the biosphere-atmosphere interface. Meteorol Z 4:91–118

Foken T, Wichura B, Klemm O, Gerchau J, Winterhalter M, Weidinger T (2001) Micrometeorological conditions during the total solar eclipse of August 11, 1999. Meteorol Z 10:171–178

Foken T, Leuning R, Oncley SR, Mauder M, Aubinet M (2012) Corrections and data quality control. In: Aubinet M, Vesala T, Papale D (eds) Eddy covariance: a practical guide to measurement and data analysis. Springer Netherlands, Dordrecht, pp 85–131

Fotiadi AK, Lohou F, Druilhet A, Serça D, Brunet Y, Delmas R (2005) Methodological development of the conditional sampling method. Part I: Sensitivity to statistical and technical characteristics. Bound-Lay Meteorol 114(3):615–640

Gao W (1995) The vertical change of coefficient b, used in the relaxed eddy accumulation method for flux measurement above and within a forest canopy. Atmos Environ 29(17):2339–2347

Ghosh P, Patecki M, Rothe M, Brand WA (2005) Calcite-CO_2 mixed into CO_2-free air: a new CO_2-in-air stable isotope reference material for the VPDB scale. Rapid Commun Mass Spectrom 19(8):1097–1119

Goulden ML, Munger JW, Song-Miao F, Daube BC, Wofsy SC (1996) Measurements of carbon sequestration by long-term eddy covariance: methods and a critical evaluation of accuracy. Glob Chang Biol 2(3):169–182

Grace J, Rayment M (2000) Respiration in the balance. Nature 404:819–820

Griffis TJ, Baker JM, Sargent SD, Tanner BD, Zhang J (2004) Measuring field-scale isotopic CO_2 fluxes with tunable diode laser absorption spectroscopy and micrometeorological techniques. Agric For Meteorol 124(1–2):15–29

Griffis TJ, Sargent SD, Baker JM, Lee X, Tanner BD, Greene J, Swiatek E, Billmark K (2008) Direct measurement of biosphere-atmosphere isotopic CO_2 exchange using the eddy covariance technique. J Geophys Res Atmos 113(D8):20

Guenther A, Baugh W, Davis K, Hampton G, Harley P, Klinger L, Vierling L, Zimmerman P, Allwine E, Dilts S, Lamb B, Westberg H, Baldocchi D, Geron C, Pierce T (1996) Isoprene fluxes measured by enclosure, relaxed eddy accumulation, surface layer gradient, mixed layer gradient, and mixed layer mass balance techniques. J Geophys Res 101(D13):18555–18567

Helliker BR, Berry JA, Betts AK, Bakwin PS, Davis KJ, Ehleringer JR, Butler MP, Ricciuto DM (2005) Regional-scale estimates of forest CO_2 and isotope flux based on monthly CO_2 budgets of the atmospheric boundary layer. In: Griffiths H, PG J (eds) The carbon balance of forest biomes. Taylor & Francis Group, New York, pp 77–92

IPCC (2013) Climate change 2013: the physical science basis. In: Stocker TF, Qin D, Plattner G-K, Tignor M, Allen SK, Boschung J, Nauels A, Xia Y, Bex V, Midgley PM (eds) Contribution of working group I to the fifth assessment report of the intergovernmental panel on climate change. Cambridge University Press, Cambridge

Katul G, Albertson J, Chu C-R, Parlange M, Stricker H, Tylor S (1994) Sensible and latent heat flux predictions using conditional sampling methods. Water Resour Res 30(11):3053–3059

Katul GG, Finkelstein PL, Clarke JF, Ellestad TG (1996) An investigation of the conditional sampling method used to estimate fluxes of active, reactive, and passive scalars. J Appl Meteorol 35(10):1835–1845

Keeling CD (1958) The concentration and isotopic abundances of atmospheric carbon dioxide in rural areas. Geochim Cosmochim Acta 13:322–334

Keeling CD (1961) The concentration and isotopic abundance of carbon dioxide in rural and marine air. Geochim Cosmochim Acta 24:277–298

Knohl A, Buchmann N (2005) Partitioning the net CO_2 flux of a deciduous forest into respiration and assimilation using stable carbon isotopes. Glob Biogeochem Cycles 19:4 (GB4008)

Kuzyakov Y, Gavrichkova O (2010) REVIEW: Time lag between photosynthesis and carbon dioxide efflux from soil: a review of mechanisms and controls. Glob Chang Biol 16(12): 3386–3406

Lee X (1998) On micrometeorological observations of surface-air exchange over tall vegetation. Agric For Meteorol 91:39–49

Lloyd J, Taylor JA (1994) On the temperature dependence of soil respiration. Func Ecol 8:315–323

Lloyd J, Kruijt B, Hollinger DY, Grace J, Francey RJ, Wong S-C, Kelliher FM, Miranda AC, Farquhar GD, Gash JHC, Vygodskaya NN, Wright IR, Miranda HS, Schulze E-D (1996) Vegetation effects on the isotopic composition of atmospheric CO_2 at local and regional scales: theoretical aspects and a comparison between rain forest in Amazonia and a boreal forest in Siberia. Austral J Plant Physiol 23:371–399

Michaelis L, Menten ML (1913) Die Kinetik der Invertinwirkung, Kinetics of the invertin reaction. Biochem Z 49:333–369

Milne R, Beverland IJ, Hargraeves K, Moncrieff JB (1999) Variation of the b coefficient in the relaxed eddy accumulation method. Bound-Lay Meteorol 93:211–225

Milne R, Mennim A, Hargreaves K (2001) The value of the β coefficient in the relaxed eddy accumulation method in terms of fourth-order moments. Bound-Lay Meteorol 101(3):359–373

Moncrieff JB, Malhi Y, Leuning R (1996) The propagation of errors in long-term measurements of land-atmosphere fluxes of carbon and water. Glob Chang Biol 2(3):231–240

Moravek A, Foken T, Trebs I (2014) Application of a GC-ECD for measurements of biosphere-atmosphere exchange fluxes of peroxyacetyl nitrate using the relaxed eddy accumulation and gradient method. Atmos Meas Tech 7(7):2097–2119

Nie D, Kleindienst TE, Arnts RR, Sickles JE (1995) The design and testing of a relaxed eddy accumulation system. J Geophys Res 100(D6):11415–11423

O'Leary MH (1993) Biochemical basis of carbon isotope fractionation. In: Ehleringer JR, Hall AE, Farquhar GD (eds) Stable isotopes and plant-water relations. Physiological ecology. Academic Press, San Diego, CA, pp 19–28

O'Leary MH, Madhavan S, Paneth P (1992) Physical and chemical basis of carbon isotope fractionation in plants. Plant Cell Environ 15:1099–1104

Ogée J, Peylin P, Ciais P, Bariac T, Brunet Y, Berbigier P, Roche C, Richard P, Bardoux G, Bonnefond JM (2003) Partitioning net ecosystem carbon exchange into net assimilation and respiration using $^{13}CO_2$ measurements: a cost-effective sampling strategy. Global Biogeochem Cycles 17(2):1070

Ogée J, Peylin P, Cuntz M, Bariac T, Brunet Y, Berbigier P, Richard P, Ciais P (2004) Partitioning net ecosystem carbon exchange into net assimilation and respiration with canopy-scale isotopic measurements: an error propagation analysis with $^{13}CO_2$ and $CO^{18}O$ data. Global Biogeochem Cycles 18(2):GB2019

Oncley SP, Delany AC, Horst TW, Tans PP (1993) Verification of flux measurement using relaxed eddy accumulation. Atmos Environ 27A(15):2417–2426

Pataki DE, Ehleringer JR, Flanagan LB, Yakir D, Bowling DR, Still CJ, Buchmann N, Kaplan JO, Berry JA (2003) The application and interpretation of Keeling plots in terrestrial carbon cycle research. Global Biogeochem Cycles 17(1):22-1–22-14

Pattey E, Desjardins RL, Rochette P (1993) Accuracy of the relaxed eddy-accumulation technique, evaluated using CO_2 flux measurements. Bound-Lay Meteorol 66(4):341–355

Paw U KT, Baldocchi DD, Meyers TP, Wilson KB (2000) Correction of eddy-covariance mesurements incorporating both advective effects and density fluxes. Bound-Lay Meteorol 97:487–511

Raupach MR (2001) Inferring biogeochemical sources and sinks from atmospheric concentrations: general considerations and applications in vegetation canopies. In: Schulze E-D, Heimann M, Harrison S et al (eds) Global biogeochemical cycles in the climate system. Academic Press, San Diego, CA, pp 416, 441–459

Raupach MR, Finnigan JJ, Brunet Y (1996) Coherent eddies and turbulence in vegetation canopies: the mixing-layer analogy. Bound-Lay Meteorol 78:351–382

Reichstein M, Falge E, Baldocchi D, Papale D, Aubinet M, Berbigier P, Bernhofer C, Buchmann N, Gilmanov T, Granier A, Grünwald T, Havránková K, Ilvesniemi H, Janous D, Knohl A, Laurila T, Lohila A, Loustau D, Matteucci G, Meyers T, Miglietta F, Ourcival J-M, Pumpanen J, Rambal S, Rotenberg E, Sanz M, Tenhunen J, Seufert G, Vaccari F, Vesala T, Yakir D, Valentini R (2005) On the separation of net ecosystem exchange into assimilation and ecosystem respiration: review and improved algorithm. Glob Chang Biol 11(9):1424–1439

Reichstein M, Papale D, Valentini R, Aubinet M, Bernhofer C, Knohl A, Laurila T, Lindroth A, Moors E, Pilegaard K, Seufert G (2007) Determinants of terrestrial ecosystem carbon balance inferred from European eddy covariance flux sites. Geophys Res Lett 34(L01402):1–5

Riederer M, Hübner J, Ruppert J, Brand WA, Foken T (2014) Prerequisites for application of hyperbolic relaxed eddy accumulation on managed grasslands and alternative net ecosystem exchange flux partitioning. Atmos Meas Tech 7(12):4237–4250

Ruppert J (2005) ATEM software for atmospheric turbulent echange measurements using eddy covariance and relaxed eddy accumulation systems and Bayreuth whole-air REA system setup. Abt Mikrometeorologie, Arbeitsergebnisse 28:Print: ISSN 1614-8916, 1627 pp

Ruppert J (2008) CO_2 and isotope flux measurements above a spruce forest. PhD-Thesis, online publication: urn:nbn:de:bvb:703-opus-5419. University of Bayreuth, Bayreuth

Ruppert J, Wichura B, Delany AC, Foken T (2002) Eddy sampling methods. A comparison using simulation results. In: 15th symposium on boundary layer and turbulence, Wageningen, 15–19 July 2002. Am Meteorol Soc, pp 27–30

Ruppert J, Mauder M, Thomas C, Lüers J (2006a) Innovative gap-filling strategy for annual sums of CO_2 net ecosystem exchange. Agric For Meteorol 138(1–4):5–18

Ruppert J, Thomas C, Foken T (2006b) Scalar similarity for relaxed eddy accumulation methods. Bound-Lay Meteorol 120:39–63

Ruppert J, Riederer M, Brand WA, Foken T (2012) Whole-air relaxed eddy accumulation for the measurement of isotope and trace-gas fluxes. Arbeitsergebnisse, Universität Bayreuth, Abt. Mikrometeorologie, vol 51. University of Bayreuth, Bayreuth

Sharp RE, Matthews MA, Boyer JS (1984) Kok effect and the quantum yield of photosynthesis light partially inhibits dark respiration. Plant Physiol 75(1):95–101

Sturm P, Eugster W, Knohl A (2012) Eddy covariance measurements of CO_2 isotopologues with a quantum cascade laser absorption spectrometer. Agric For Meteorol 152:73–82

Suits NS, Denning AS, Berry JA, Still CJ, Kaduk J, Miller JB, Baker IT (2005) Simulation of carbon isotope discrimination of the terrestrial biosphere. Global Biogeochem Cycles 19(1):n/a–n/a

Thomas CK, Foken T (2007) Flux contribution of coherent structures and its implications for the exchange of energy and matter in a tall spruce canopy. Bound-Lay Meteorol 123(2):317–337

Thomas C, Martin JG, Goeckede M, Siqueira MB, Foken T, Law BE, Loescher HW, Katul G (2008) Estimating daytime subcanopy respiration from conditional sampling methods applied to multi-scalar high frequency turbulence time series. Agric For Meteorol 148(8–9):1210–1229

Vogel JC (1993) Variability of carbon isotope fractionation during photosynthesis. In: Ehleringer JR, Hall AE, Farquhar GD (eds) Stable isotopes and plant carbon-water relations. Physiological ecology. Academic Press, San Diego, CA, pp 29–38

Webb EK, Pearman GI, Leuning R (1980) Correction of flux measurements for density effects due to heat and water vapour transfer. Q J Roy Meteorol Soc 106(447):85–100

Wehr R, Munger JW, Nelson DD, McManus JB, Zahniser MS, Wofsy SC, Saleska SR (2013) Long-term eddy covariance measurements of the isotopic composition of the ecosystem–atmosphere exchange of CO_2 in a temperate forest. Agric For Meteorol 181:69–84

Werner RA, Rothe M, Brand WA (2001) Extraction of CO_2 from air samples for isotopic analysis and limits to ultra high precision delta^{18}O determination in CO_2 gas. Rapid Commun Mass Spectrom 15(22):2152–2167

Wichura B (2009) Untersuchungen zum Kohlendioxid-Austausch über einem Fichtenwaldbestand. Hyperbolic-Relaxed-Eddy-Accumulation Messungen für das stabile Kohlenstoffisotop ^{13}C und Waveletanalysen des turbulenten Kohlendioxid-Austauschs. PhD, Bayreuther Forum Ökologie 114, Universität Bayreuth

Wichura B, Buchmann N, Foken T (2000) Fluxes of the stable carbon isotope ^{13}C above a spruce forest measured by hyperbolic relaxed eddy accumulation method. In: 14th symposium on boundary layers and turbulence, Aspen, Colorado, 7–11 August 2000. Boundary layer and turbulence conference series. American Meteorological Society, pp 559–562

Wichura B, Ruppert J, Delany AC, Buchmann N, Foken T (2004) Structure of carbon dioxide exchange processes above a spruce forest. In: Matzner E (ed) Biogeochemistry of forested catchments in a changing environment: A German case study, Ecological studies, vol 172. Springer, Berlin, pp 161–176

Wilczak JM, Oncley SP, Stage SA (2001) Sonic anemometer tilt correction algorithms. Bound-Lay Meteorol 99:127–150

Wyngaard JC, Moeng C-H (1992) Parameterizing turbulent diffusion through the joint probability density. Bound-Lay Meteorol 60(1-2):1–13

Yakir D, Sternberg LSL (2000) The use of stable isotopes to study ecosystem gas exchange. Oecologia 123(3):297–311

Yakir D, Wang X-F (1996) Fluxes of CO_2 and water between terrestrial vegetation and the atmosphere estimated from isotope measurements. Nature 380:515–517

Chapter 11
Influence of Low-Level Jets and Gravity Waves on Turbulent Fluxes

Andrei Serafimovich, Jörg Hübner, Monique Y. Leclerc, Henrique F. Duarte, and Thomas Foken

11.1 Introduction

The vertical wind distribution within the atmospheric boundary layer is an important weather phenomenon and has a significant impact on ecological processes. Numerous experiments carried out at the FLUXNET (Baldocchi et al. 2001) station DE-Bay near the Weidenbrunnen in the Fichtelgebirge observe a secondary wind

A. Serafimovich (✉)
Helmholtz Centre Potsdam, GFZ German Research Centre for Geosciences, Telegrafenberg, 14473 Potsdam, Germany
e-mail: andrei.serafimovich@gfz-potsdam.de

J. Hübner
Uhl Windkraft Projektierung GmbH & Co. KG, Max-Eyth-Str. 40, 73479 Ellwangen, Germany

M.Y. Leclerc
Atmospheric Biogeosciences Lab, The University of Georgia, Griffin, GA 30223, USA

H.F. Duarte
Department of Atmospheric Sciences, College of Mines and Earth Sciences, University of Utah, Salt Lake City, UT 84112-0102, USA

T. Foken
Am Herrgottsbaum 28, 96120 Bischberg, Germany

Bayreuth Center of Ecology and Environmental Research, University of Bayreuth, Bayreuth, Germany

A. Serafimovich, J. Hübner, T. Foken: Affiliation during the work at the Waldstein sites: Department of Micrometeorology, University of Bayreuth, Bayreuth, Germany

H.F. Duarte: Affiliation during the work at the Waldstein sites: Atmospheric Biogeosciences Lab, The University of Georgia, Griffin, GA 30223, USA

T. Foken (ed.), *Energy and Matter Fluxes of a Spruce Forest Ecosystem*,
Ecological Studies 229, DOI 10.1007/978-3-319-49389-3_11

maximum around the first decameters above the ground (Thomas et al. 2006; Thomas and Foken 2007b). It is well known that in the case of stable stratification of the atmospheric boundary layer, the topography has a strong influence on the wind field up to several hundred meters above the ground. Therefore, the nocturnal phenomena in the atmospheric boundary layer such as the low-level jet (LLJ) responsible for shear processes and resulting in high turbulence near the ground surface (Banta et al. 2002; Karipot et al. 2006) should not be neglected in the analysis of wind profiles. It is important to investigate the occurrence of LLJs and to examine the relationships between the jet properties, generated turbulence, and the related transport of energy and matter.

Wind shear is one of the main sources of gravity waves. Gravity waves are an essential part of the dynamics of the atmosphere over a wide band of meteorological scales. Their importance as a source of energy and momentum transport is widely accepted. Due to their wide range of wavelengths and periods, phase and group speeds, the propagation of gravity waves affects a wide range of atmospheric phenomena on large synoptic to micrometeorological scales. The energy and momentum transported by gravity waves is transferred to the mean flow (Nappo 2012) or dissipated in the form of turbulence (Einaudi and Finnigan 1993; Smedman et al. 1995), enhancing turbulent transport when the wave becomes unstable and breaks. Most gravity wave studies are carried out using the linear wave theory (Gossard and Hooke 1975; Lindzen and Tung 1976) providing, under linearization of the primitive set of equations for an inviscid, non-rotating fluid, relationships between wind components, temperature, pressure, and air density.

In recent studies, investigation of gravity waves and their effects on atmospheric phenomena is carried out on different scales. For example, large scale gravity waves having horizontal periods on the order of hundreds and thousands of kilometers are studied using synoptic or mesoscale approaches. The large scale gravity waves interact with breaking Rossby waves (Zülicke and Peters 2006), clouds and precipitation (Koch and O'Handley 1997), damaging winds (Pecnick and Young 1984), and multiple layers of polar mesosphere summer echoes (Hoffmann et al. 2005). The small scale gravity waves have been studied from the micrometeorological point of view. These waves occur mostly in stably stratified atmospheric layers close to the surface during the nighttime in the nocturnal boundary layer or in the long-lived stable boundary layer in polar regions (King et al. 1987; Rees et al. 2001; Sun et al. 2003).

Another important phenomenon in the atmospheric boundary layer is that of coherent structures. Over the past few decades, coherent structures have become a key point of many studies in the turbulence research of flow dynamics in laboratory flows and the atmospheric boundary layer (Raupach and Thom 1981; Bergström and Högström 1989; Gao et al. 1989; Shaw et al. 1989; Paw U et al. 1992; Raupach et al. 1996; Brunet and Irvine 2000; Thomas and Foken 2007b). Coherent structures appear in measurements of wind, temperature, or scalar concentration

as approximate periodic ramps connected with the ejection-sweep cycles (Katul et al. 1997; Finnigan 2000; Foster et al. 2006) and contribute significantly to the turbulent transport above and within the canopy (Maitani and Shaw 1990; Katul et al. 1997; Thomas and Foken 2007a). As was shown by Raupach et al. (1996) and Finnigan (2000), in the simplest cases of planar homogeneous and stationary flows, the sources of coherent structures above plant canopies are Kelvin-Helmholtz instabilities observed in plane mixing layers. Brunet and Irvine (2000) then demonstrated that the mixing layer analogy applies in a variety of plant canopies for an expanded range of atmospheric stabilities.

The interactions between the mean flow, waves, and turbulence, and coherent structure generation in the presence of gravity waves are the key points of many recent studies. Einaudi and Finnigan (1993) investigated wave-turbulence coupling. Nappo et al. (2008) studied the influence on plume dispersion of an internal gravity wave following a pressure jump. The impact of wave breaking or Kelvin-Helmholtz shear instability on wave-induced turbulent diffusion was examined in the works of Sun et al. (2003) and Cheng et al. (2005). A number of studies reported simultaneous occurrence of gravity waves in the vicinity of the canopy (canopy waves) and ramps near the canopy top (Paw U et al. 1992; Lee et al. 1997), suggesting that canopy waves are produced by Kelvin-Helmholtz instabilities induced by the strong wind shear.

However, interactions between coherent structures and waves are still poorly understood, and a generalized theory regarding turbulent mixing and turbulent flux exchange in the presence of periodic atmospheric wave motions is missing. On the other hand, there is a relative lack of studies dealing with the local effects produced by gravity waves propagating along a specific measuring site. The main objective of this work is to study a gravity wave in conjunction with a strong wind shear event and to develop a comprehensive analysis of the wave characteristics using linear theory. The effects of the wave propagation close to the surface and their impact on coherent structures and turbulent exchange in the vicinity of a tall canopy will be examined.

11.2 Material and Methods

11.2.1 Experimental Setup

The results presented here were obtained in the frame of the EGER project (ExchanGE processes in mountainous Regions). This project is focused on the detailed investigation of interaction processes at different scales and their role in the budgets of energy and matter within the soil-vegetation-atmosphere system. The overview of the project can be found in Foken et al. (2012) and Chap. 1.

Data were obtained in the period of June–July 2008 and 2011 during the second and third intensive measuring campaigns (IOP 2 and IOP 3) of the project. The experiment was carried out at the FLUXNET site Waldstein-Weidenbrunnen (DE-Bay, 50°08′N, 11°52′E). The site is located at an altitude 775 m a.s.l. in the Fichtelgebirge Mountains in North-Eastern Bavaria, Germany. The coniferous canopy mainly consists of spruce trees with mean canopy height $h_c = 25$ m. A detailed description of the site is given in Gerstberger et al. (2004), and the reference data can be found in Staudt and Foken (2007) and Chap. 2.

The experimental design of the second intensive observation period IOP 2 almost repeats the design of the first campaign IOP 1. More details about instrumentation can be found in Serafimovich et al. (2011) and Appendix A. High-frequency measurements (20 Hz) of wind components (u, v, w), sound temperature T_s, density of carbon dioxide CO_2 and water vapor H_2O were performed. Six ultrasonic anemometers (USA-1 Metek GmbH, CSAT3 Campbell Scientific, Inc., Solent R2 Gill Instruments Ltd.) and six fast-response gas analyzers (LI-7000 and LI-7500, LI-COR Biosciences) were installed on the 36 m tall tower (Turbulence Tower, TT) at 0.09, 0.22, 0.52, 0.72, 0.92, 1.44 h_c levels, and an ultrasonic anemometer and a fast-response gas analyzer were installed at 1.28 h_c level on the second 32 m tall tower (Main Tower, MT) standing 60 m away from the above tower.

The atmospheric boundary layer was profiled with an acoustic and radioacoustic radar remote sensing system SODAR-RASS. The measurements were performed with a system consisting of a phase array Doppler SODAR DSDPA.90–64 with a 1290-MHz-RASS extension by Metek GmbH. The acoustic sounding system was located at a distance of approximately 250 m from the towers in a forest clearing. Two operating modes were used. Vertical wind speed and temperature were measured using the first mode for 25 min. The vertical range of measurements was from 20 to 200 m a.g.l. In the second mode the atmospheric boundary layer was profiled for a period of 5 min up to an observational level of 900 m, using a vertical resolution of 30 m. This gave a mean profile of the wind vector. A second SODAR (referred to as miniSODAR, Scintec AG) without a RASS extension was installed 500 m away and provided 5-min mean profiles up to 200 m a.g.l. These measurements were extended by the data from the 482 MHz windprofiler of the German Weather Service at Bayreuth (Northern Bavaria, Germany), located 22 km to the South–West of the Waldstein measuring site. The windprofiler measured vertical profiles of the horizontal wind vector and virtual temperature in the atmosphere. The technical data of the radar system are given in Lehmann et al. (2003). During the IOP 3 the miniSODAR system (Scintec AG) was installed at the forest edge 250 m to the south-east from the MT.

In addition, the measurements at MT provide meteorological data of wind, temperature, humidity, and radiative fluxes within and above the canopy.

11.2.2 Instruments: Principles of Operation

Radar Wind Profiler (RWP) and SODAR (SOund Detecting And Ranging) are active remote sensing systems for ground-based observations of wind in the atmosphere. Both systems can be extended by the Radio Acoustic Sounding System (RASS) to measure virtual temperature profiles.

11.2.2.1 Windprofiler/SODAR

The principles of measurements of atmospheric turbulence by means of either electromagnetic or acoustic waves do not differ fundamentally. RWP systems transmit electromagnetic waves with known frequencies in the VHF (30–300 MHz) and UHF (300–3000 MHz) ranges in the atmosphere. The corresponding wavelengths are on the order of 1.0–10.0 m in the VHF and 0.1–1.0 m in the UHF ranges (Clifford et al. 1994). These waves will be affected by atmospheric processes such as reflection, scattering, refraction, and absorption, and their properties such as propagation direction, phase, and signal strength will be changed. In this case, the RWP primarily uses the backscattering of electromagnetic waves due to natural fluctuations in the refractive index, which in the frequency band of the RWP is a function of temperature and water vapor pressure. The influence of the atmospheric pressure p is negligible (Sauvageot 1992).

The DBS method uses three to five beams emitted in series in different directions. One of the beams is always in the vertical direction and the other beams are tilted from the vertical at a predetermined angle α. Depending on the transmitted frequency, the frequency of backscattered echo will be shifted due to the Doppler effect, and this can be used for direct measurements of the radial wind speed v_r:

$$v_r = \frac{\Delta f \lambda}{2}, \tag{11.1}$$

where Δf is the Doppler shift between the transmitted and received frequency and the wavelength λ results from the ratio between the propagation speed c of the wave and transmission frequency f:

$$\lambda = \frac{c}{f}. \tag{11.2}$$

Successive measurements carried out under the assumption of homogeneous conditions in three non-coplanar directions in space allow the calculation of the 3D wind vector. However, the assumption of homogeneity is usually valid for averaging over long time periods. Varying of the beam direction is controlled by a phase-shifted signal generated by a phased array antenna composed of numerous transmitting elements and a phase shifter.

The three wind components u, v, and w can be obtained from the radial wind velocities v_{rx} calculated as follows (index x characterizes the different beam directions, 1 and 2 are tilted antennas, 3 is vertical antenna):

$$u(z) = \frac{v_{r1}(z) - v_{r3}(z)\cos\alpha}{\sin\alpha}, \tag{11.3}$$

$$v(z) = \frac{v_{r2}(z) - v_{r3}(z)\cos\alpha}{\sin\alpha}, \tag{11.4}$$

$$w(z) = v_{r3}(z). \tag{11.5}$$

The measuring principle of the SODAR system is very similar to the RWP. Instead of electromagnetic waves, acoustic waves with much lower transmission frequencies (1–4 kHz) are emitted. The corresponding wavelengths are in the order of 0.09 to 0.35 m (Clifford et al. 1994). While electromagnetic waves are propagated at light speed, the speed of acoustic waves is significantly lower: approximately 343 ms^{-1} for air with normal humidity and a temperature of 20 °C. Due to this massive difference in the propagation velocity and the resulting longer detection time, acoustic waves provide better spatial resolution. However, due to the smaller wavelength and stronger attenuation in the atmosphere, the range of the acoustic waves is significantly lower.

11.2.2.2 RASS

The RASS principle is based on the measurement of temperature-dependent sound speed using backscattering of radio waves from an acoustic wave front. The RASS system consists of an acoustic wave and electromagnetic wave transmitters. The acoustic wave transmitted in the atmosphere modulates the refractive index. If the acoustic wavelength matches the Bragg wavelength of the radar (half of the radar wavelength), an enhanced backscattered echo will be observed. Due to the Doppler effect, the frequency of the backscattered echo will be shifted by the velocity of the acoustic wave front. The Bragg condition is fulfilled in different heights by different wavelengths of acoustic waves. Therefore, varying the frequency of the acoustic wave, detecting the heights of the enhanced backscattered signal, and using the known relationship between the speed of sound and the virtual temperature T_v, the profiles of T_v can be derived.

11.2.3 Data Calculation

To detect wave motions and coherent structures from observed time series, the spectral analysis using wavelet transform has been used. A detailed discussion about data preparation and wavelet analysis can be found in Thomas and Foken (2005). Here the main steps will be summarized.

Using a despiking test (Vickers and Mahrt 1997) with a window length 300 s and initial criteria of 6.5 standard deviations, outliers in 20 Hz high-frequency series were removed. Wind vector components were rotated sector-wise on a monthly basis according to planar fit rotation methods (Wilczak et al. 2001). To account for delays in sensor response and data recording, time series of scalar components were corrected for time lags. Comparing time series of carbon dioxide and water vapor concentrations s with vertical wind component w and finding the maximum of $\overline{w'(t)s'(t+\Delta t)}$, where the prime denotes the oscillation part of the signal and the overbar denotes time averaging, time lags were estimated.

Nowadays the wavelet technique has become a standard tool for the detection of wave motions and coherent structures in measurements. Due to the ability of the wavelet spectrum to be resolved in time and height, this technique gives additional information about wave structure and location. A more detailed review of the wavelet applications in geophysics can be found in Kumar and Foufoula-Georgiou (1997) or Torrence and Compo (1998). Wavelet transform is successfully applied to detect gravity waves in the atmosphere (Zink and Vincent 2001) and coherent structures in the vicinity of a tall canopy (Thomas and Foken 2005).

The wavelet transform itself denotes the correlation between measured function $f(t)$ observed at fixed location and the version of the mother wavelet, which is scaled with a factor a and translated by a dilation b:

$$T_p(a,b) = \frac{1}{a^p} \int_{-\infty}^{+\infty} f(t) \Psi \left(\frac{t-b}{a} \right) dt, \tag{11.6}$$

where $T_p(a,b)$ are the wavelet coefficients, a the dilation scale, b the translation parameter, p the normalization factor ($p = 1$ in our case), and Ψ the Morlet wavelet function. As in many other geophysical studies, the Morlet wavelet was used in this analysis due to a good localization in the frequency domain, with it exhibiting only one distinct peak (Pike 1994). The wavelet variance spectrum $W_p(a)$ is then determined by

$$W_p(a) = \int_{-\infty}^{+\infty} \left| T_p(a,b) \right|^2 db. \tag{11.7}$$

Both wavelet coefficients and wavelet variance spectrum give the information about predominant frequencies and wavelengths in the background wind flow.

To reduce computation time for the wavelet analysis, all time series were block averaged to a 2 Hz resolution. Finally, all time series were passed through a low-

pass wavelet filter to remove small-scale high-frequency turbulence. According to the spectral gap between high-frequency turbulence and low-frequency coherent structures, the critical event duration D_c was chosen to be 6.2 s, which is in close agreement with values used in other studies (Brunet and Collineau 1994; Chen and Hu 2003). To detect coherent structures, the time series $f(t)$ were zero-padded and a continuous wavelet transform (Grossmann and Morlet 1984; Kronland-Martinet et al. 1987) using the Morlet wavelet was performed (Eq. (11.6)). For the following estimation of coherent structures, the wavelet variance spectrum $W_p(a)$ (Eq. (11.7)) was determined. The characteristic duration of coherent structures for each 30 min time interval was obtained by the location of the maximum of the wavelet variance spectrum. Finally, according to Thomas and Foken (2007a), Reynolds-averaged flux and flux contribution of coherent structures were derived using a conditional sampling analysis and averaging method (Antonia 1981).

Following Thomas and Foken (2007a), the exchange regimes between air above the canopy, the canopy, and the trunk space were investigated. This method is based on the analysis of the portion of the sensible heat exchange by coherent structures between three levels: subcanopy level, canopy level, and air above the canopy. One can define the following exchange regimes:

- Wa – wave motion. There is no turbulence above the canopy, the linear gravity waves dominate in the flow.
- Dc – decoupled canopy. Turbulent motions are present above the canopy, but there is no coherent transport between the canopy and the atmosphere.
- Ds – decoupled subcanopy. The coherent exchange takes place only between the canopy and the atmosphere, the trunk space is decoupled.
- Cs – coupled by sweeps. The sweep phases of coherent structures are responsible for the exchange of energy and matter between atmosphere, canopy, and subcanopy. The role of ejection phases is insignificant.
- C – fully coupled canopy. The atmosphere, canopy, and the trunk space of the forest are fully coupled by coherent structures.

For more details see Chap. 6.

11.2.4 Meteorological Situation

As shown by the wind rose (Fig. 11.1), over the canopy at the Waldstein site prevail west and south-east winds with wind speeds on the order of 2–5 ms^{-1}. Such a west wind was observed during the daytime from 9:00 to 20:00 on 30 June, 2008 (Fig. 11.2). The wind speed increased to reach the maximum 4 ms^{-1} at noon and then fell to 1.2 ms^{-1}. At 20:00 the wind started to change its direction and increase in amplitude. This effect lasted for 4 h till 24:00. During this period the wind speed increased to 3.7 ms^{-1} with wind gusts up to 6.8 ms^{-1} and then decreased to 2.1 ms^{-1}, and the wind changed direction from west to south-east.

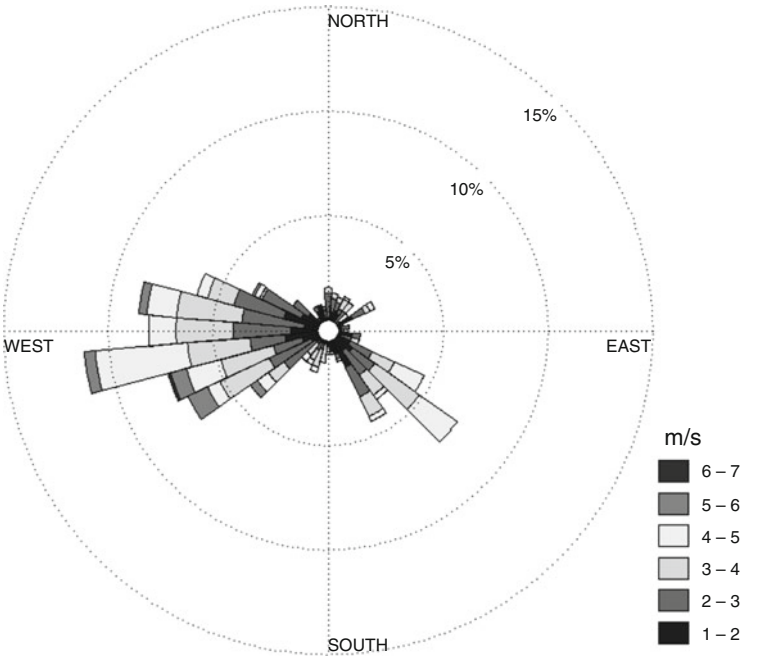

Fig. 11.1 Wind rose derived from the measurements at TT at 36 m height for the period June 17–July 02, 2008 during IOP 2

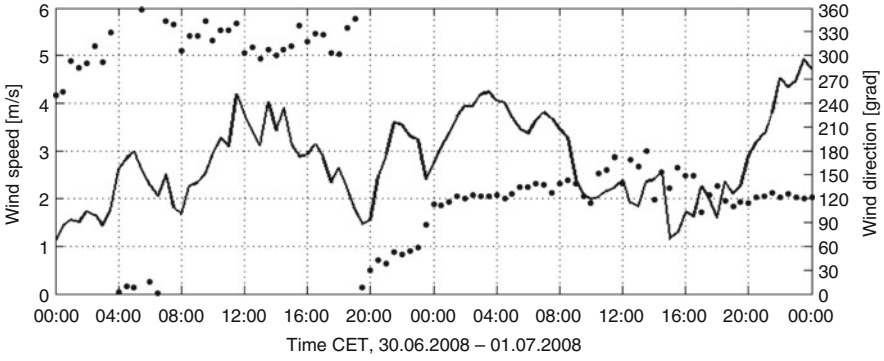

Fig. 11.2 Mean wind speed (*line*) and wind direction (*dots*) averaged for 30 min at MT at 32 m height for the period June 30–July 01, 2008 during IOP 2

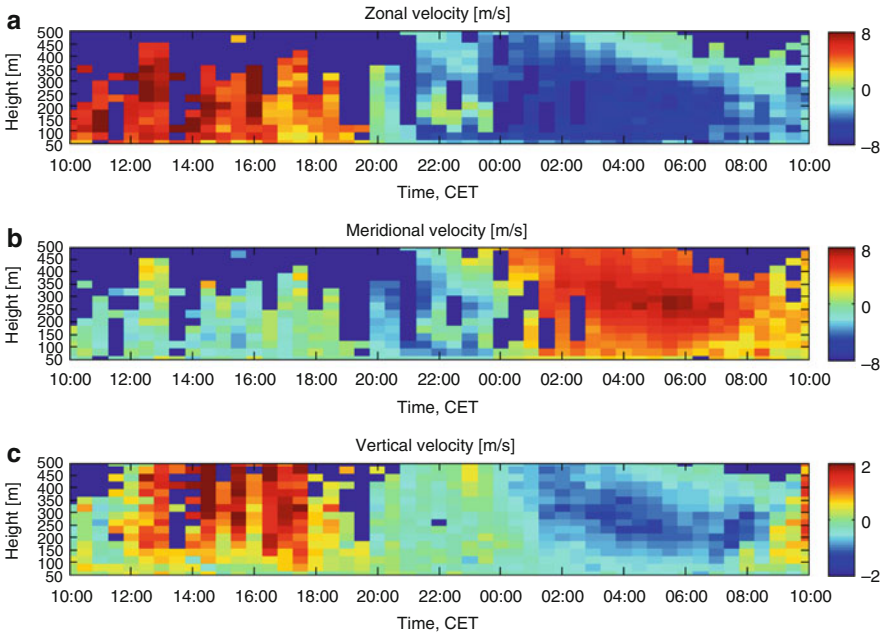

Fig. 11.3 Zonal (**a**), meridional (**b**), vertical (**c**) velocities measured with SODAR/RASS for the period 10:00 June 30–10:00 July 01, 2008 during IOP 2. Dark blue color corresponds to gaps

Figure 11.3 shows height-time cross-sections of the zonal, meridional, and vertical wind components observed by the SODAR/RASS system over Waldstein site. During the daytime on June 30 in the atmospheric boundary layer the meridional wind was weak, whereas a strong zonal wind component on the order of 8 ms^{-1} indicates a westerly wind. As mentioned above, the situation changes at 20:00 CET. The zonal wind component decreases until 01:00 CET and reaches $-8\,ms^{-1}$, and the meridional wind component increases until 01:00 CET and reaches a clear maximum on the order of 8 ms^{-1} between 250 and 350 m at 05:00 CET. The vertical wind component is mostly positive during the daytime on June 30, then falls to small values around zero at 24:00 and reaches the negative maximum at 04:00 CET. The situation observed describes the evaluation of an LLJ with a strong shear effect.

Due to the effect of environmental noise, the SODAR/RASS data unfortunately contain a lot of gaps during the period of the wind rotation (dark blue area in Fig. 11.3). Therefore, for the following analysis the wind measurements observed with the miniSODAR system will be used. As shown in Fig. 11.4, smoothed zonal, meridional, and vertical winds derived from these data confirm a wind rotation effect and wind maxima detected by the SODAR/RASS system and described above.

Figure 11.5 shows the exchange regimes observed at the Waldstein site for the period June 30–July 2, 2008. The principle of the method is described in Thomas and Foken (2007a) and Chap. 6. When wind begins to rotate at 20:00 on June 30 the

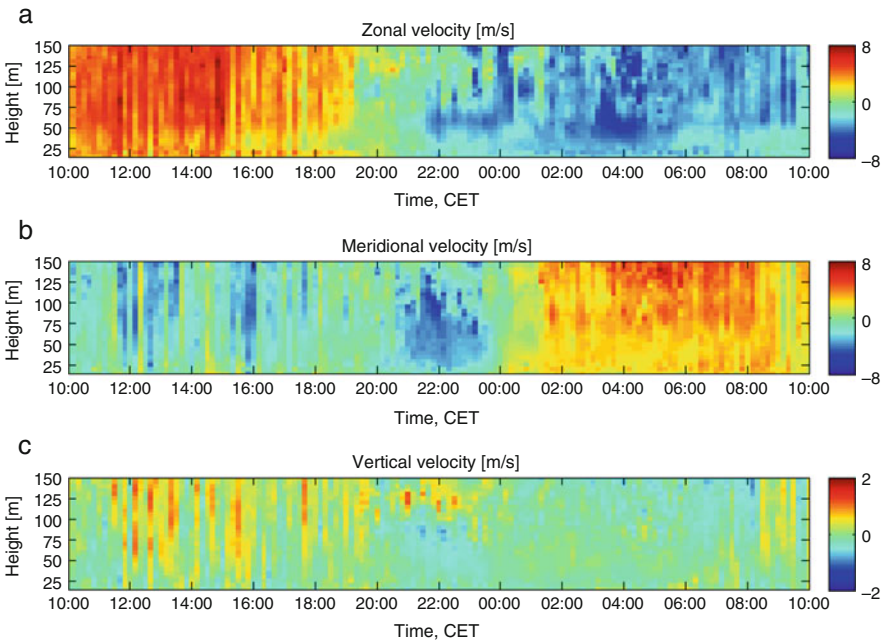

Fig. 11.4 Zonal (**a**), meridional (**b**), vertical (**c**) velocities averaged for 10 min measured with miniSODAR for the period 10:00 June 30–10:00 July 01, 2008 during IOP 2

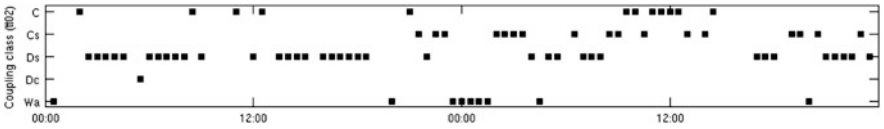

Fig. 11.5 Characterization of the turbulent exchange regimes for the period June 30–July 02, 2008 during IOP 2. Wa, Dc, Ds, Cs, C indicate wave motion, decoupled canopy, decoupled subcanopy, coupled subcanopy by sweeps, and fully coupled states

"fully coupled C" state changes to the "coupled by sweeps Cs" with the following "decoupled subcanopy Ds" state, and finally coming to the state "wave motion Wa" around midnight, suggesting that the atmospheric wave motion occurs above the measuring site.

As demonstrated by Baas and Driedonks (1985), Paw U et al. (1992), and Cava et al. (2004), waves are an important phenomena near the canopy level. In the following sections evidence of the wave motion above the Waldstein forest site and the impact of waves on the turbulent transport will be discussed.

11.3 Results and Discussion

11.3.1 Low-Level Jets

An LLJ is a strong wind whose maximum speed may be in the order of 10–20 ms^{-1}. This maximum can be found mostly at an altitude of 100–300 m above ground (Stull 1988). Various criteria for the identification of LLJs can be found in the scientific literature. Bonner (1968) categorized LLJs based on speed and height occurrence of jets. The pragmatic definition of LLJ can be specified as follows: the LLJ exists if the observed maximum of the wind speed is 2 ms^{-1} larger than the wind speed in the remaining overlying atmospheric boundary layer (Stull 1988). Other definitions of LLJ, based on physical aspects of the wind in the boundary layer, can be found in Blackadar (1957) and Holton (1967).

The LLJ at the Waldstein site usually originates from south-east and south-west (Fig. 11.6), coming along with negative vertical winds (downward), a well-coupled system and good mixing. Only during weakened LLJ events and/or the formation of gravity waves above the forest canopy is an accumulation of CO_2 within the trunk space observable.

An example of an LLJ observed from 30 June to 1 July 2008 is shown in Fig. 11.7. The wind velocity of the jet was found to be above 10 ms^{-1} for about 6 h at a height of 300 m, temporally descending to 200 m. The wind direction of the LLJ was SE, while above the LLJ the wind direction moved from SE over S to W. In the LLJ the vertical wind was negative (downward).

In Fig. 11.8, vertical distributions of NO and O_3 concentrations are shown during the LLJ event shown in Fig. 11.7. Due to the increased shear, a better mixing was found during the period with the LLJ between 02:00 and 08:00, with a maximum at 04:00. The better mixing resulted in a reduction of concentrations accumulated near the surface (Fig. 11.8). In the early morning, at approximately 04:00, when

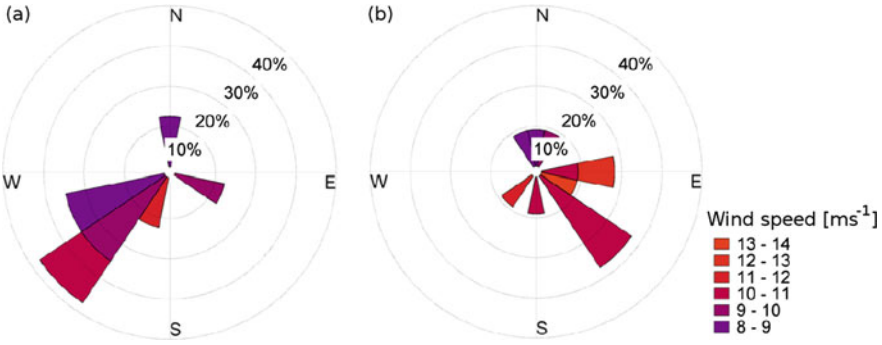

Fig. 11.6 Wind roses for all LLJ events (**a**) during the IOP 1 period ($n = 8$) and (**b**) during the IOP 2 period ($n = 11$). Maximum achieved wind speed and the wind direction measured at the same height are used

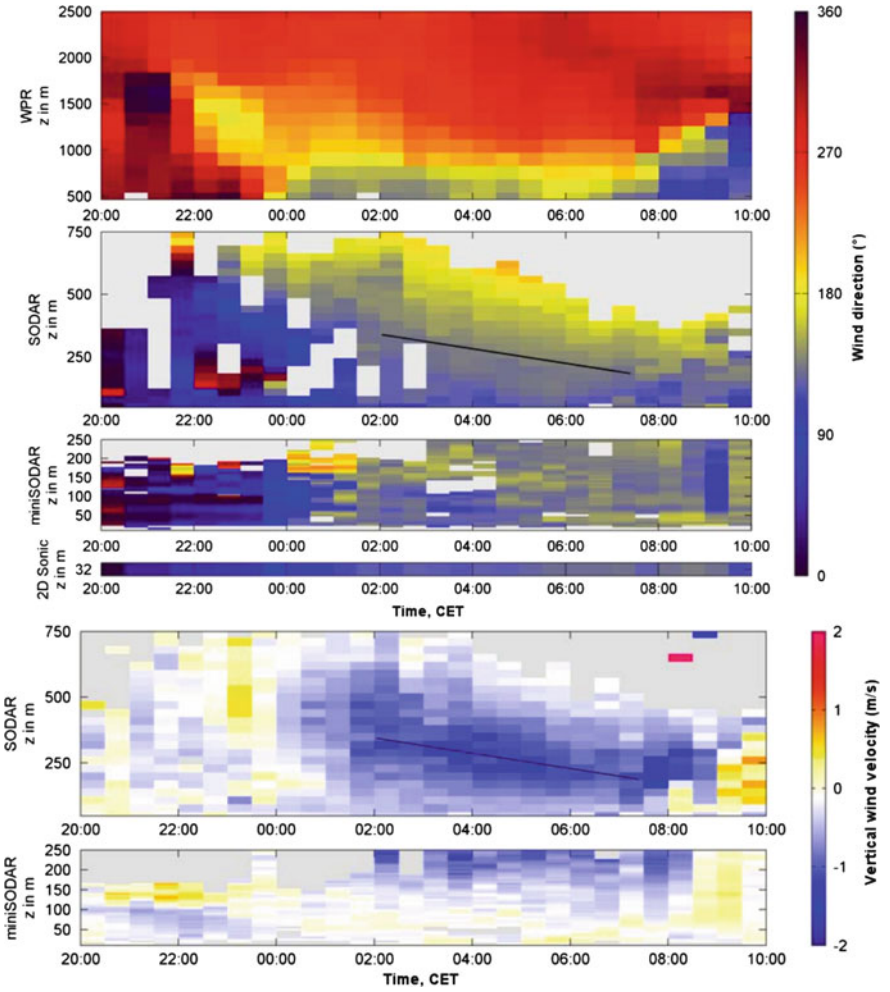

Fig. 11.7 Time-height profile from windprofiler, sodar, mini-sodar and sonic data of the wind direction (*above*), and vertical wind velocity (*below*) in the night from 30 June to 1 July 2008. The axis of the low-level jet is highlighted (Foken et al. 2012), published with kind permission, ©Authors 2012, CC Attribution 3.0 License, All rights permitted

the LLJ occupied lower heights, the atmosphere close to the surface is suddenly mixed resulting in high NO concentrations, probably representing an outflow of the upper Eger river valley during easterly winds. The most impressive is the inflow of fresh air with high O_3 concentrations between 22:00 and 24:00, connected with the occurrence of gravity waves.

During IOP 3 an LLJ event occurred in the night from 27 June 22:00 CET to 28 June 08:00 CET. These days were hot and dry (see Chap. 14), which facilitated the formation of LLJ events (Fig. 11.9). Maximum wind velocities up to 10 ms^{-1}

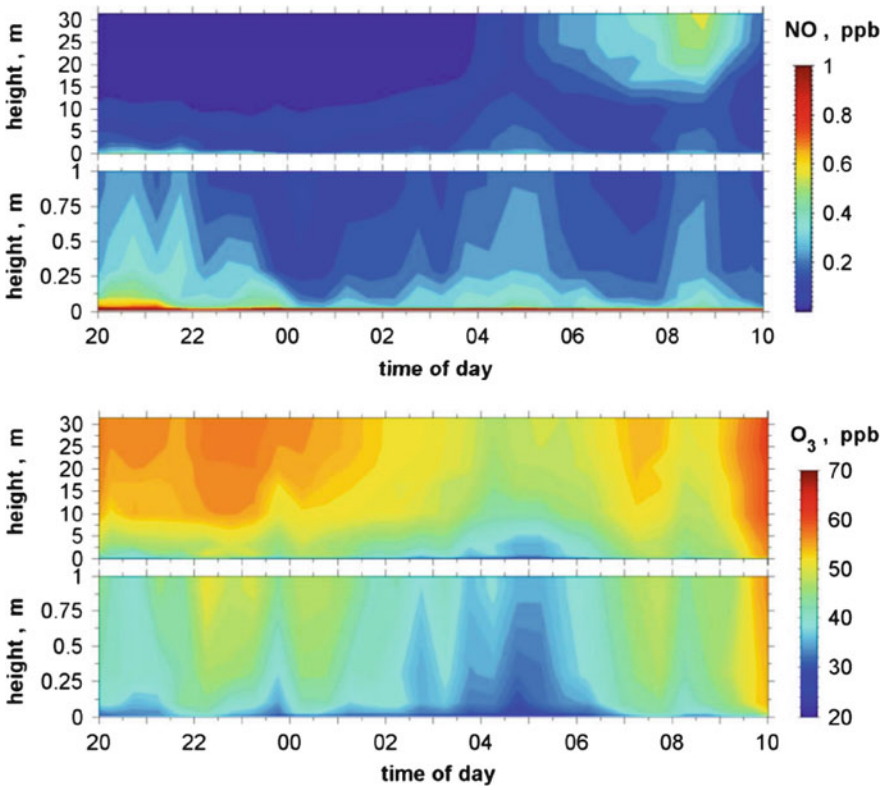

Fig. 11.8 Averaged vertical profiles in the night from 30 June to 1 July 2008 (CET time) for NO and O3 (Foken et al. 2012), published with kind permission, ©Authors 2012, CC Attribution 3.0 License, All rights permitted

occurred between the heights of 180–220 m from 22:00 to 00:30 CET. After 00:30 CET, a weakened LLJ event could be observed around the height of 100 m with wind velocities up to 7 ms^{-1}. The vertical winds were negative (downward) over the total time of the LLJ, with a maximum of -1 ms^{-1}, and the typical south to south-easterly winds were prevailing. CO_2 fluxes were up to 7–12 μ mol m^{-2} s^{-1}.

Figure 11.10 presents the horizontal profiles measured with the horizontal mobile measuring system (HMMS) during this LLJ event. The HMMS is described in Hübner et al. (2014) and Chap. 14. During 20:00–22:00 CET (northerly winds), there is a CO_2 concentration maximum (Fig. 11.10b) near the forest edge, which confirmed the assumption of changed turbulent structures caused by the forest edge. Also temperature (Fig. 11.10a) was lower near the edge. At the clearing the CO_2 concentration was equal to the atmospheric concentration of around 380 ppm. Between 22:00 and 00:30 CET, the conditions at the site changed significantly, and the LLJ with southerly winds and higher wind velocities prevailed. First the lower CO_2 concentration was blown into the forest and the horizontal profile was nearly

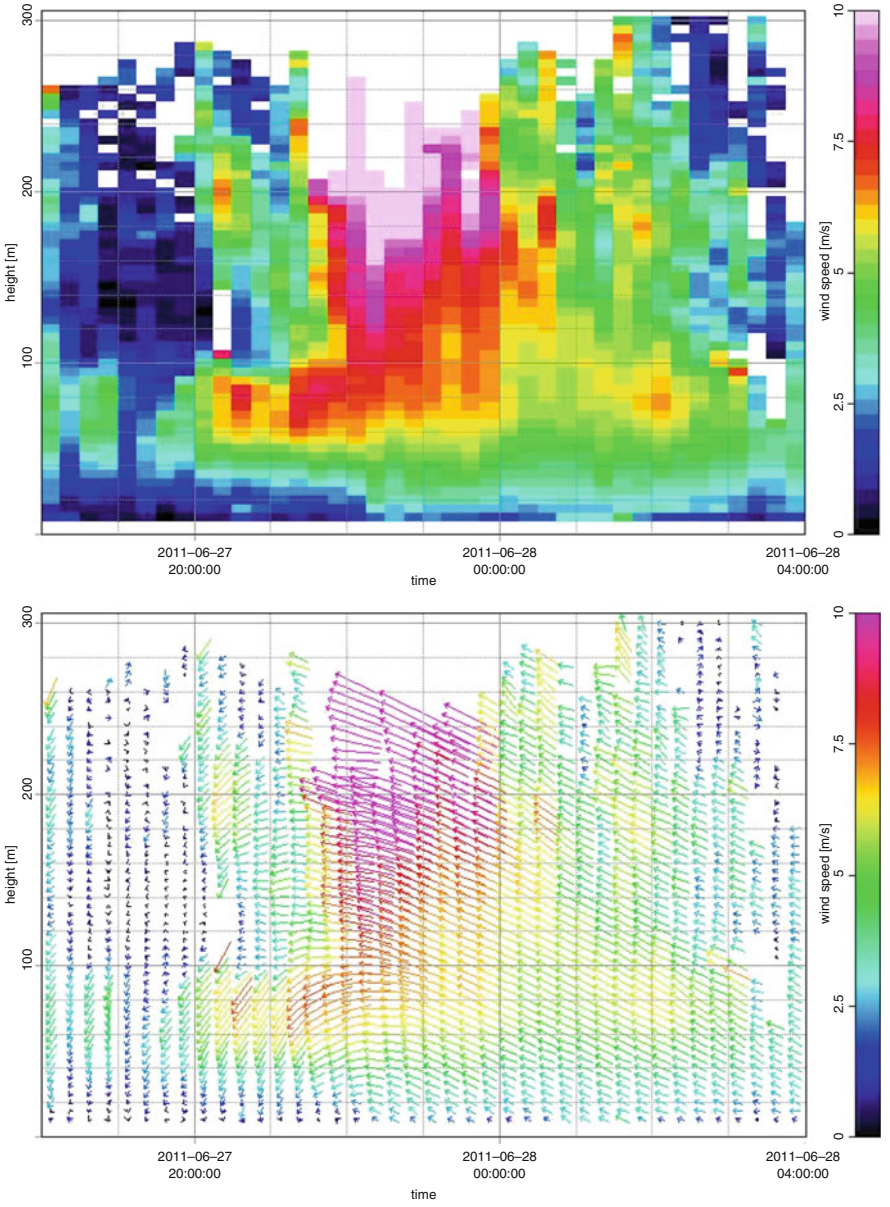

Fig. 11.9 Wind speed and wind vector measured with miniSODAR operated by the University of Georgia at the Köhlerloh Clearing for the period 18:00 June 26–04:00 June 27, with an LLJ on June 28 between 0:00 (height 180 m) and 2:30 (80 m)

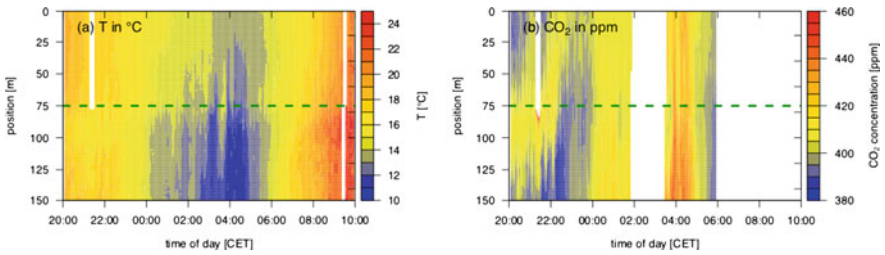

Fig. 11.10 Horizontal profiles measured with the HMMS from 27 June 20:00 CET to 28 June 2011 10:00 CET for temperature T (**a**) and CO_2 concentration (**b**). Position shows distance in meters, with starting point in the forest (0 m), forest edge (75 m), horizontal *green dotted line* and endpoint at the clearing (150 m). Remark: The color scaling is different in all graphs

mixed, and after 00:30 CET with the weakened LLJ event and lower wind velocities, there was an accumulation of CO_2 again over the total transect. Around 01:30 CET wind velocities up to 8 ms^{-1} led to an inflow of colder, CO_2-depleted air at the forest edge.

During 03:00–04:30 CET the wind direction changed in the height of 200–250 m to north, while above and below the wind direction was still south. The wind velocity was very low (less than 2 ms^{-1}). The temperature decreased and the humidity increased during this situation. Unfortunately, CO_2 concentration measurements were not available up to that time due to connection failures. But at 03:30 CET there was another concentration minimum near the forest edge. After 04:00 CET the wind velocity increased to 4–6 ms^{-1} at 100 m and the wind direction was again south. But because of the still weakened LLJ at this time, an accumulation of CO_2 could be observed. After 05:00 CET, the wind velocity increased at a height of 200 m to 10 ms^{-1} and the system was well mixed again.

11.3.2 Gravity Waves

Three main types of gravity waves are defined: high-frequency gravity waves, midrange gravity waves, and gravity waves with low frequencies. An overview of all types of gravity waves can be found in Nappo (2012). The work discussed here is related to gravity waves with low frequencies, so-called inertia-gravity waves.

The main characteristics of gravity waves are intrinsic frequency $\hat{\omega}$, zonal k, meridional l, and vertical m wavenumbers, phase $\hat{v}_p$ and group $\hat{c}_g$ velocities. Intrinsic frequency describes wave period in time domain $\hat{T}$ in the coordinate system moving with a wave, whereas horizontal and vertical wavenumbers represent horizontal (L_x, L_y) and vertical (L_z) wavelengths in spatial domain. Phase velocity is the speed at which a point of constant phase moves in the direction of the wave propagation. Gravity waves are dispersive waves. Therefore, the individual wave

components (and hence the energy) may move through the wave group with a group velocity as the group propagates along.

Almost all investigations of gravity waves have been done using the linear theory, which provides dependencies between wave characteristics under linearized solutions of fluid-dynamical equations. Following works of Cho (1995), Kunze (1985), and Sato (1994), the vertical shear effect in the background wind field was considered. To investigate inertia-gravity waves three relations were applied. The dispersion relation is given by

$$\hat{\omega}^2 = f_c^2 + \frac{N^2 k_h^2}{m^2} - \frac{2fk_h}{m}\frac{\partial \overline{v}}{\partial z}, \tag{11.8}$$

where f_c is the Coriolis parameter, N is the Brunt-Väisälä frequency, and $\partial\overline{v}/\partial z$ is the vertical wind shear component in direction perpendicular to gravity wave propagation, $k_h = \sqrt{k^2 + l^2}$ is horizontal wavenumber. The polarization relation is given by

$$R = \left| \frac{f_c}{\hat{\omega}} - \frac{k}{m\hat{\omega}}\frac{\partial \overline{v}}{\partial z} \right|, \tag{11.9}$$

where R is the axial ratio of the minor to the major axis of the polarization ellipse. The intrinsic frequency, i.e. the frequency in a coordinate system moving with the gravity wave, differs from the observed frequency which is relative to the fixed position at the ground. Therefore, the Doppler relation connects both frequencies:

$$\omega_{ob} = \hat{\omega} + \overline{u}k_h, \tag{11.10}$$

where ω_{ob} is the observed frequency and $\overline{u}$ is the mean background horizontal wind component in the same direction as the horizontal wavenumber k_h.

To examine background wind fields and localize wave motions in time and height, a wavelet transform has been applied to miniSODAR wind measurements. Figure 11.11 shows wavelet power spectra of zonal and meridional winds. The bold cyan line outlines the region with 95% significance level. The area above the green line (Fig. 11.11a, c) and on the right-hand side of the green line (Fig. 11.11b, d) indicates the cone of influence. The wavelet power spectra of time series (Fig. 11.11a, c) show significant wave periods between 0.6 and 1.1 h. The remarkable feature is that initially the wave motion is observed in the meridional wind between 20:00 and 22:00 CET on July 30 and then in the zonal wind between 22:00 and 24:00 CET on July 30. Furthermore, the significant vertical wavelength on the order of 30–70 m at the altitudes between 40 and 140 m was found in the wavelet power spectra of zonal and meridional wind profiles (Fig. 11.11b, d). In evaluating the results of the wavelet transform for the frequency content, bandpass filter parameters can be defined to filter out a gravity wave from the background wind fields. In this study the bandpass filter was constructed with a bandwidth of 0.6–1.6 h in the time and 20–90 m in the height. Fast Fourier transform (FFT) was

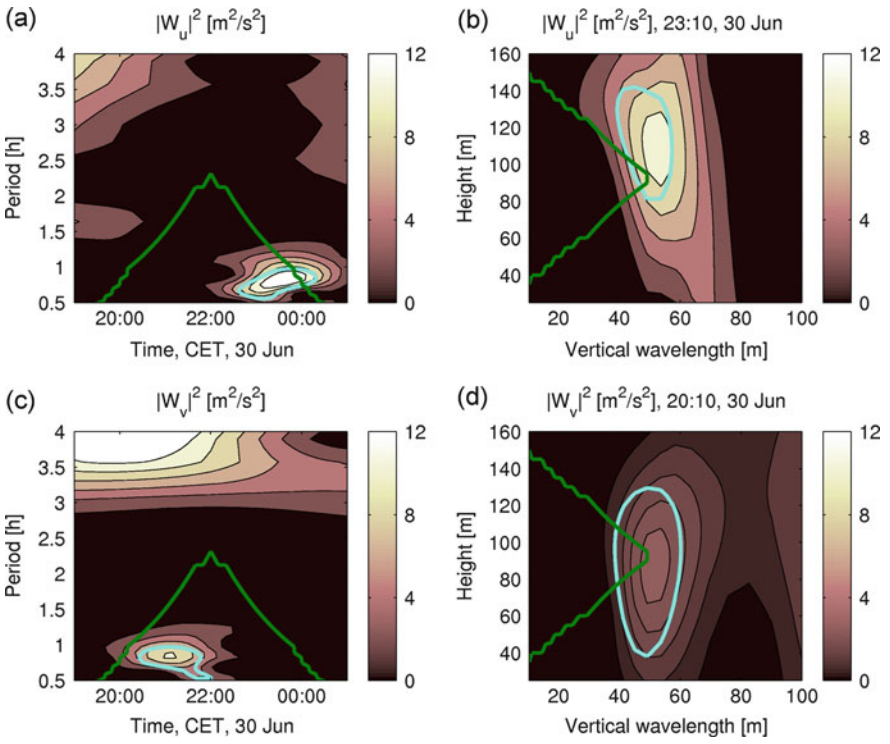

Fig. 11.11 Wavelet spectra of zonal (**a**, **b**) and meridional (**c**, **d**) winds. The *left panel* (**a**, **c**) shows wavelet spectra of the time series, the *right panel* (**b**, **d**) shows wavelet spectra of the height profiles

used to filter out the gravity wave with dominant observed frequency 64 min and wavelength 53 m. To avoid the sidelob effects and unwanted responses the signal was multiplied by the Hanning window. First, the FFT was applied to the time series and a mean contribution of each frequency was derived. By the removal of unwanted harmonics the range of interest (0.6–1.60 h) was selected and wind perturbations were obtained through a reconstruction using the inverse FFT and division by the Hanning window. The same principle was applied to vertical profiles of horizontal winds to derive wind perturbations in the range of interest of 20–90 m. The resulting wind perturbations are shown in Fig. 11.12. The dashed lines indicate lines of constant phase with preferred downward phase propagation. The vertical and temporal distances between the phase lines correspond to vertical wavelength and observed period detected with the wavelet transform (Fig. 11.11), respectively.

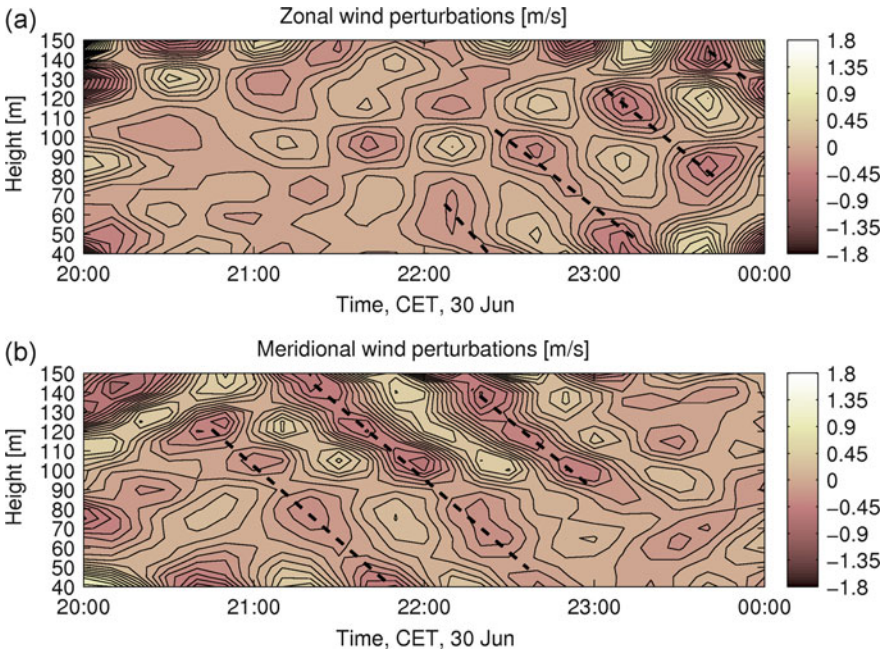

Fig. 11.12 Zonal (**a**) and meridional (**b**) wind perturbations on 30 June 2008 from 20:00 to 24:00 after band pass filtering with bandwidth of 0.6–16 h in time and 20–90 m in height

11.3.2.1 Rotary Spectrum

The rotary spectrum technique determines how energy is divided between upward and downward propagating gravity waves (Thompson 1978; Guest et al. 2000). The rotary spectrum is an asymmetric function represented by the fast Fourier transform of complex velocity vector profiles $u'(z) + iv'(z)$. The peaks in the spectrum indicate the presence of the gravity wave and the difference between amplitudes of the positive and negative parts of the spectrum allows the detection of the rotation direction of the horizontal wind perturbations with height. In the rotary spectrum, counterclockwise rotating waves are associated with positive frequencies, while clockwise rotating waves are associated with negative frequencies. It should be noted that in the northern hemisphere, counterclockwise rotation of horizontal wind perturbations with height indicates downward vertical energy propagation of a gravity wave, and clockwise rotation indicates upward vertical energy propagation of a gravity wave.

The analysis of the rotary spectrum reveals the presence of an inertia-gravity wave and its dominant vertical energy propagation. Figure 11.13 shows the rotary spectrum applied to wind perturbation after bandpass filtering with a bandwidth of 0.6–1.6 h in time and 20–90 m in height. The spectra were averaged for the period of wind rotation effect from 20:00 CET to 24:00 CET on June 30. The

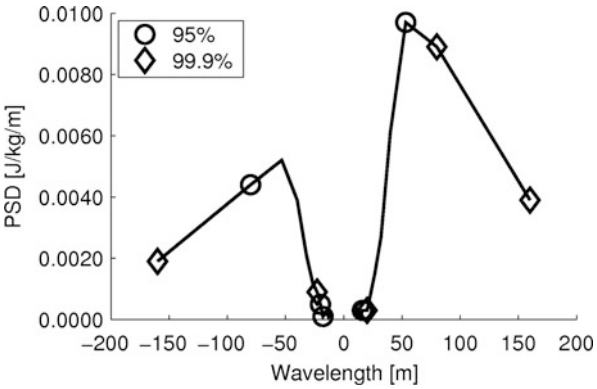

Fig. 11.13 Rotary spectrum averaged for 4 h from 20:00 CET to 24:00 CET on 30 June 2008. Open circle, open diamond correspond to 95 and 99.9% significance levels, respectively

spectrum maximum indicates the presence of the gravity wave with the vertical period of 53 m. The rotary spectrum shows in its negative part the weaker clockwise rotational power corresponding to upward energy propagation and in its positive part the stronger counterclockwise rotational power corresponding to a dominant downward energy propagation, respectively. The spectrum is significant, except at the peak in the negative part due to the variability for the averaged period.

11.3.2.2 Hodograph Analysis

Hodograph analysis is used to estimate the intrinsic frequency of gravity wave $\hat{\omega}$, vertical wavelength L_z, and direction of the horizontal and vertical wave propagation. The hodograph is presented by a trace of the end of a wind perturbation vector with a height. If enough points are taken into account, then one vertical wavelength of gravity wave can be spawned, and an ellipse can be fitted.

Following linear theory without wind shear effect (Gill 1982), horizontal wind perturbations u' and v' depend on the intrinsic gravity wave $\hat{\omega}$ and Coriolis parameter f_c:

$$v' = -i \cdot u' \cdot \frac{f_c}{\hat{\omega}}. \tag{11.11}$$

Using Eq. (11.11) and the ratio of the minor and the major axis of the fitted ellipse, the intrinsic frequency $\hat{\omega}$ can be derived. The major axis of the hodograph is parallel to the direction of horizontal wave propagation undefined by 180°. A clockwise rotational sense of the hodograph in the northern hemisphere indicates upward energy propagation, whereas a counterclockwise rotational sense indicates downward energy propagation. The main disadvantage of the hodograph analysis is a high sensitivity to the applied filter used for the separation of a gravity wave from a mean flow (Zhang et al. 2004). This method is valid only for monochromatic waves and shows variable results in the case of the superposition of different waves.

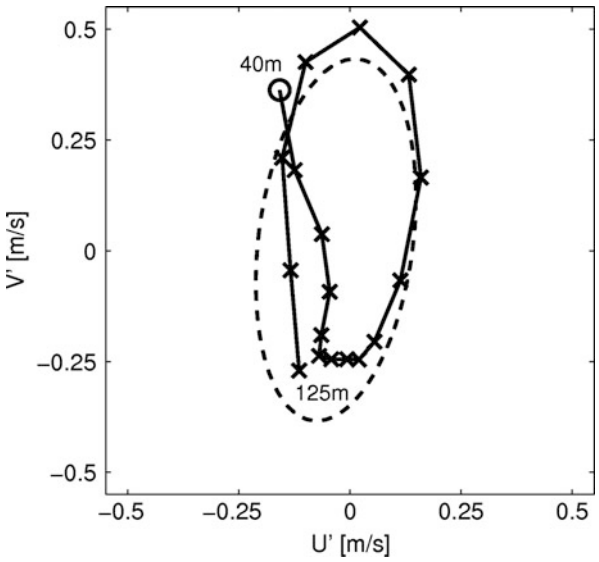

Fig. 11.14 Hodograph of the wind perturbations measured at 22:30 CET on 30 June 2008 (solid line – measured profile, dashed line – fitted ellipse, open circle – starting point of the hodograph, labels correspond to height above the ground)

The hodograph analysis applied to the horizontal wind profile measured at 22:30 CET on June 30 (Fig. 11.14) reveals downward energy propagation from the counterclockwise rotational sense. The ratio of the fitted ellipse is 0.42 and the major axis is directed to 7° from the north. The full turn of the hodograph corresponds to the vertical wavelength on the order of 70 m, and the intrinsic period $2\pi/\hat{\omega}$ derived from the axes ratio of the fitted ellipse was found to be on the order of 6.6 h.

11.3.2.3 Stokes Parameter Spectra

To provide a more statistical description of the wave field, averaging over wavenumber band and over time duration of the gravity wave is required. These two factors are implemented in the Stokes parameter technique. The so-called Stokes parameters of gravity wave field I, D, P, Q were introduced by Vincent and Fritts (1987) and improved by Eckermann and Vincent (1989). This technique represents the vertical profile of horizontal wind perturbations as a partially polarized wave field. The four Stokes parameters I, D, P, Q then correspond to the total variance of gravity wave, axial anisotropy, "in-phase" covariance associated with linear polarization, and "in quadrature" covariance associated with circular wave polarization, respectively. The Stokes parameters can be defined in time or frequency spaces. In this work, Stokes parameters were derived in the frequency domain using fast

Fourier transform (Eckermann and Vincent 1989):

$$I_{m_1,m_2} = K \int_{m_1}^{m_2} \left(\overline{U_R^2(m)} + \overline{U_I^2(m)} + \overline{V_R^2(m)} + \overline{V_I^2(m)} \right) dm, \tag{11.12}$$

$$D_{m_1,m_2} = K \int_{m_1}^{m_2} \left(\overline{U_R^2(m)} + \overline{U_I^2(m)} - \overline{V_R^2(m)} - \overline{V_I^2(m)} \right) dm, \tag{11.13}$$

$$P_{m_1,m_2} = 2K \int_{m_1}^{m_2} \left(\overline{U_R(m) V_R(m)} + \overline{U_I(m) V_I(m)} \right) dm, \tag{11.14}$$

$$Q_{m_1,m_2} = 2K \int_{m_1}^{m_2} \left(\overline{U_I(m) V_R(m)} + \overline{U_R(m) V_I(m)} \right) dm, \tag{11.15}$$

where m is the vertical wavenumber, U_R, V_R are the real parts of the spectra and U_I, V_I are the imaginary parts of the spectra of wind perturbation profiles $u'(z)$ and $v'(z)$, overbars denote averages over a number of independent spectral realizations to remove the effects of incoherent motions, and K is a constant which scales the squared Fourier terms to power spectral densities. Using the derived Stokes parameters, the degree of the gravity wave polarization d_{m_1,m_2}, phase difference δ_{m_1,m_2} between zonal and meridional wind perturbations, the major axis orientation Θ_{m_1,m_2}, and the averaged ellipse axial ratio R_{m_1,m_2} are estimated:

$$d_{m_1,m_2} = \frac{(D_{m_1,m_2}^2 + P_{m_1,m_2}^2 + Q_{m_1,m_2}^2)^{\frac{1}{2}}}{I_{m_1,m_2}} \tag{11.16}$$

$$\delta_{m_1,m_2} = \arctan\left(\frac{Q_{m_1,m_2}}{P_{m_1,m_2}} \right) \tag{11.17}$$

$$\Theta_{m_1,m_2} = \frac{1}{2} \arctan\left(\frac{P_{m_1,m_2}}{D_{m_1,m_2}} \right) \tag{11.18}$$

$$R_{m_1,m_2} = \tan\alpha \tag{11.19}$$

where

$$\alpha = \frac{1}{2} \arcsin\left(\frac{Q_{m_1,m_2}}{d_{m_1,m_2} \cdot I_{m_1,m_2}} \right) \tag{11.20}$$

The most attractive feature of this analysis is that the wave motion is well described due to the averaging in time and wave number bands, which can be selected on the basis of the times and wavelengths of the maxima located in the wavelet spectra.

To achieve a more statistical description of the gravity wave field, the Stokes parameter technique was applied. The Stokes parameters derived from miniSODAR measurements and averaged over the period 20:00–24:00 June 30 are presented in Table 11.1. The ratio of the polarization ellipse was found to be on the order of 0.65 and the major axis is directed to 31.2° from the north.

Table 11.1 Stokes parameters derived from miniSODAR measurements on 30 June 2008

Filter band (time, height)	0.6–1.6 h, 20–90 m
Averaged time (CET)	20:00–24:00 30 June, 2008
Degree of polarization, d_{m_1,m_2}	0.28
Major axis orientation, Θ_{m_1,m_2}	31.2°
Phase difference, δ_{m_1,m_2}	−68.8°
Ellipse axial ratio,	0.65

Table 11.2 Gravity wave parameters derived from analysis of Stokes parameter spectra

Mean horizontal wind, $\overline{U}$, ms^{-1} (in the wave propagation direction)	−1.8
Wind shear component, $\partial\overline{V}/\partial z$, s^{-1}	$2.9 \cdot 10^{-3}$
Brunt-Väisälä frequency, N, s^{-1}	$11.9 \cdot 10^{-3}$
Coriolis parameter, f, rad s^{-1}	$11.2 \cdot 10^{-5}$
Intrinsic period, $2\pi/\hat{\omega}$, h	7.3
Observed period, $2\pi/\omega_{ob}$, h	1.06
Horizontal wavelength, $2\pi/k_h$, km	−3.4
Vertical wavelength, $2\pi/m$, m	53.3
Horizontal phase velocity, $\hat{\upsilon}_{ph}$, ms^{-1}	$-13.0 \cdot 10^{-2}$
Vertical phase velocity, $\hat{\upsilon}_{pz}$, ms^{-1}	$0.2 \cdot 10^{-2}$
Horizontal group velocity, $\hat{c}_{gh}$, ms^{-1}	$-9.0 \cdot 10^{-2}$
Vertical group velocity, $\hat{c}_{gz}$, ms^{-1}	$-0.14 \cdot 10^{-2}$

11.3.2.4 Gravity Wave Characteristics

To derive the gravity wave characteristics, a solution of three equations was used: the dispersion relation (Eq. (11.8)), the polarization relation (Eq. (11.9)), and the Doppler equation (Eq. (11.10)). The ellipse ratio R_{m_1,m_2} was obtained by the Stokes parameter analysis, and the vertical wavenumber m is given by the evaluation of the wavelet or fast Fourier transforms (Figs. 11.11b, d and 11.13). The coordinate system was rotated to the direction of the wave propagation Θ_{m_1,m_2} obtained by the Stokes parameter technique. In this system the mean horizontal wind component U is oriented in the wave propagation direction and the mean horizontal wind component V is oriented perpendicular to the direction of the wave propagation Θ_{m_1,m_2}. The Brunt-Väisälä frequency N was derived from temperature measurements with the SODAR/RASS system and the Coriolis parameter f is a constant for a given location (the value over the Waldstein site is $11.2 \cdot 10^{-5}$ rad s^{-1}). Then Eqs. (11.8) and (11.9) were then solved to obtain the intrinsic frequency $\hat{\omega}$ and the horizontal wavenumber k. The derived gravity wave characteristics are presented in Table 11.2.

The results indicate that a gravity wave with horizontal wavelength on the order of 3.4 km, intrinsic period 7.6 h, and vertical wavelength ∼53 m occurred over the measuring site. Due to the Doppler effect the observed period of the wave relative to the fixed position was found to be on the order of 1.06 h. As was mentioned above the wave propagation direction obtained with hodograph analysis and Stokes

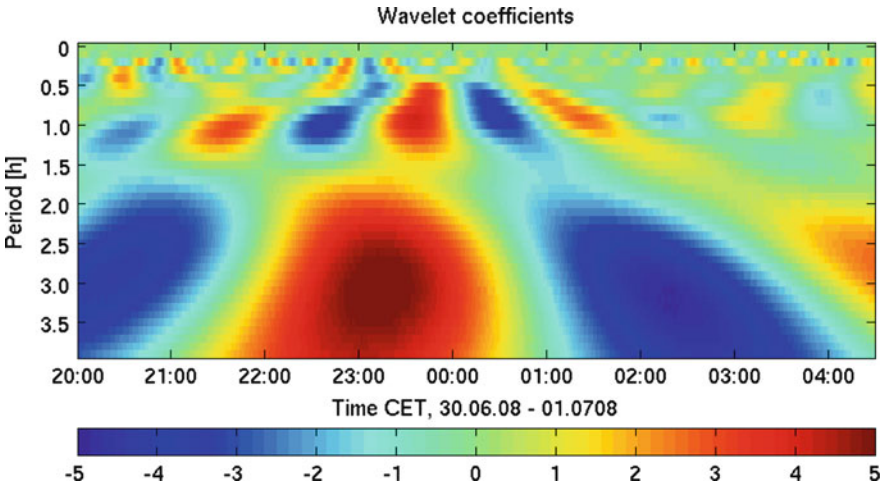

Fig. 11.15 Wavelet coefficients derived from the vertical wind measurements at 36 m height for the period June 30–July 01, 2008 during IOP 2

parameter spectra is undefined by 180°. It should be noted that the Doppler relation between intrinsic and observed periods of the detected gravity wave (Eq. (11.10)) is sensitive to the background wind speed, but the equation is fulfilled only if the propagation from south-west to north-east is selected, resulting in the negative horizontal wavenumber.

These results were confirmed by wind measurements with an ultrasonic anemometer installed at the top of TT. To detect wave frequencies over the canopy during the wind rotation event, 2 Hz wind measurements for the period 20:00 June 30–04:00 July 01, 2008 have been used. Fig. 11.15 shows the coefficients of the wavelet transform derived using Eq. (11.6). Besides the vertical wind oscillation with a period of 3.2 h lasting through the entire time, one can see the wave event with a period ∼1 h which arises shortly after 20:00 and vanishes around 02:00.

Using the method described in Chap. 6, coherent structures were extracted from turbulent time series, and Reynolds fluxes and fluxes transported by these structures were estimated. Figure 11.16 shows the number of coherent structures detected and their frequencies for the period of 4 h before the detected gravity wave event (crosses) and during the gravity wave appearance (circles). Each point indicates a mean duration of coherent structures for a 30 min interval detected as a peak in the wavelet variance spectrum. The dashed and solid lines represent the linear regression model fitted for both periods, respectively. As shown in Fig. 11.16, the number of detected coherent structures slightly increases and higher frequencies or short structures are observed during the gravity wave occurrence in contrast to the preceding period.

A clear impact of gravity wave propagation over a measuring site was found in the turbulent momentum exchange. As shown in Fig. 11.17 (black line) the

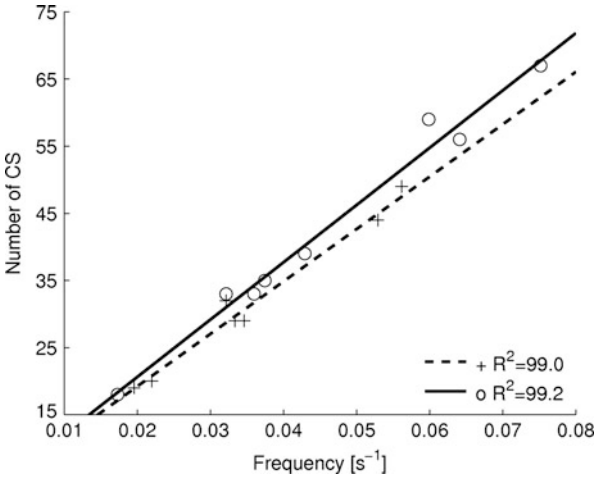

Fig. 11.16 Number of coherent structures and their frequencies detected for the period 16:00–20:00 (*crosses*) and 20:00–24:00 (*circles*) June 30, 2008. *Dashed and solid lines* represent the linear regression model for both periods, respectively

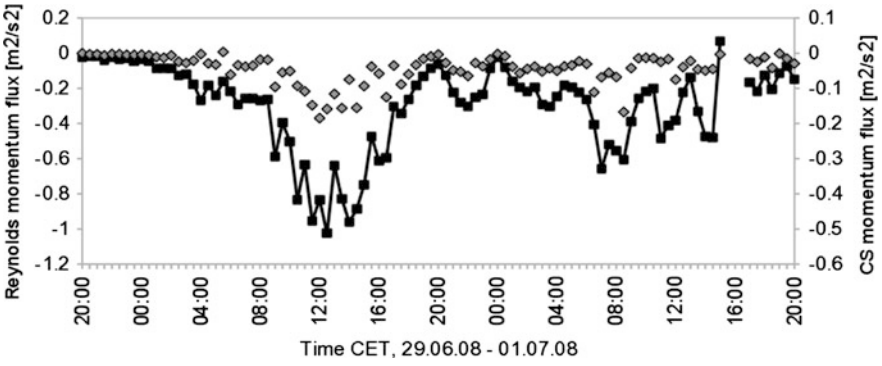

Fig. 11.17 Reynolds momentum flux (black line), momentum flux transported by coherent structures (gray dots) measured at the height 36 m for the period June 29–July 01, 2008 during IOP 2

estimated Reynolds-averaged momentum flux reaches the first maximum on the order of 1.1 $m^2\,s^{-2}$ around noon and the second maximum is observed between 20:00 and 24:00 when the gravity wave occurs. During this period the momentum transport by coherent structures is higher as well (Fig. 11.17 grey points) and reaches 20% of the Reynolds flux. The sensible heat, latent heat and carbon dioxide fluxes are not affected by the gravity wave (not shown here).

Partitioning the momentum flux transported by coherent structures during ejection and sweep phases (Fig. 11.18 black line and grey points, respectively), one can see that before the gravity wave appears momentum above the canopy is transported

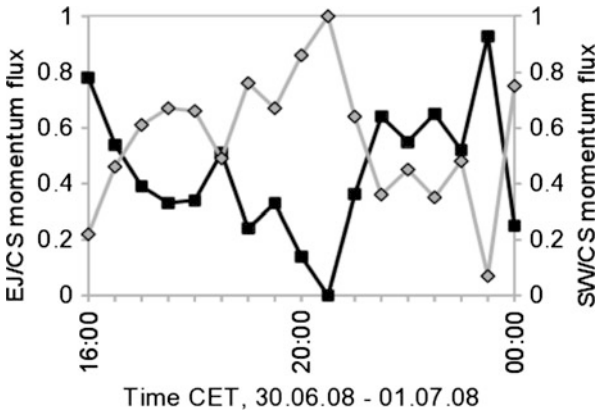

Fig. 11.18 Ratio of the flux transported during the ejection phase to the total flux transported by coherent structures (*black line*) and ratio of the flux transported during the sweep phase to the total momentum flux transported by coherent structures (*gray line*) for the momentum coherent exchange measured at the height 36 m for the period June 29–July 01, 2008 during IOP 2

mostly by "sweeps" events reaching almost 100% at 20:00, whereas after that the contribution of the "ejection" phases is higher to the momentum transport. This suggests that turbulent exchange by sweep motions is suppressed by downward propagated gravity waves, whereas the ejections are compensating for this effect.

11.4 Conclusions

Nocturnal carbon dioxide fluxes measured using eddy-covariance technique are influenced by non-stationary atmospheric processes. The boundary-layer phenomena such as low-level jets are able to generate wind shear and turbulence close to the surface. Low-level jets influence transport processes at the spatial scale of the measuring site and may re-distribute vertical concentration profiles and increase surface fluxes due to strong vertical shear. Changes of CO_2 concentration perpendicular to the forest edge indicate that the contribution of coherent structures and their scale plays an important role in transport processes in heterogeneous areas. These phenomena have to be taken into account when analyzing long term carbon flux measurements, especially for the sites located over flat terrain, because they are highly susceptible to the occurrence of low-level jets. The increased shear caused by low-level jets also leads to a better mixing of trace gases such as NO and O_3 at the forest floor and in the canopy.

Moreover, wind shear is one of the main sources of gravity waves. A complete study of the gravity wave characteristics and wave effects on the coherent momentum exchange above the canopy level has been presented. The gravity wave, detected during the second intensive observation period IOP 2 of the EGER project, was connected to the wind rotation and wind shear event in the ascending LLJ observed in the Fichtelgebirge mountains, North-Eastern Bavaria, Germany.

To filter out the wind perturbations associated with the gravity wave, the wavelet transform of the mean wind measurements was used. The wave characteristics were analyzed using the rotary spectrum, hodograph, and Stokes-parameter spectral analysis. Evaluation of the equations of the linear theory showed that the wave propagates from south-west to north-east and has the intrinsic period 7.3 h, which due to the Doppler shift corresponds to the observed period of about 64 min. The derived horizontal and vertical wavelengths were on the order of −3.4 km and 53 m, respectively. During the wave event the analysis revealed stronger counterclockwise rotational power corresponding to the downward energy at the height range of 40–120 m.

The impact of the downward wave energy propagation on the turbulent momentum exchange above the forest measuring site was found. It was shown that coherent structures have smaller time scales when the gravity wave is observed. Finally, the occurrence of a gravity wave in the vicinity of the canopy leads to a higher transport of the momentum and an increase of the turbulent exchange by coherent structures. The partitioning of the momentum transport between the sweep and ejection phases of coherent structures shows a higher activity of sweeps in the turbulent momentum exchange before the gravity wave event and higher momentum transport by the ejection phases when the gravity wave is observed.

This study has shown that the ecosystem fluxes are affected by different atmospheric phenomena occurring up to several hundred meters above the ground, and such processes as wind shear, low-level jets, and gravity waves should not be neglected in the analysis of turbulent fluxes, and the effects of these have to be investigated along with other surface processes.

Acknowledgements The project was funded by the German Science Foundation (FO 226/16-1, ME2100/4-1 and FO 226/21-1). The authors wish to acknowledge the technical support given by the staff of the Bayreuth Center for Ecology and Environmental Research (BayCEER) of the University of Bayreuth, and the German Weather Service for providing the windprofiler data. The authors also wish to gratefully acknowledge Stephanie Schier (now Dix) for her support during work on her Master's Thesis and all those who supported the field measurements, especially Lukas Siebicke, Katharina Staudt, Johannes Lüers, and Johannes Olesch for advice, comments, and technical assistance.

References

Antonia RA (1981) Conditional sampling in turbulence measurements. Ann Rev Fluid Mech 13:131–156. doi:10.1146/annurev.fl.13.010181.001023

Baas AFD, Driedonks AGM (1985) Internal gravity waves in a stably stratified boundary layer. Bound-Layer Meteorol 31:303–323

Baldocchi D, Falge E, Lianhong G, Olson R, Hollinger D, Running S, Anthoni P, Bernhofer C, Davis K, Evans R, Fuentes J, Goldstein A, Katul G, Law B, Lee X, Malhi Y, Meyers T, Munger W, Oechel W, Paw U KT, Pilegaard K, Schmid HP, Valentini R, Verma S, Vesala T, Wilson K, Wofsy S (2001) FLUXNET: a new tool to study the temporal and spatial variability of ecosystem-scale carbon dioxide, water vapor, and energy flux densities. Bull Am Meteorol Soc 82:2415–2434

Banta RM, Newsom RK, Lundquist JK, Pichugina YL, Coulter RL, Mahrt L (2002) Nocturnal low-level jet characteristics over Kansas during cases-99. Bound-Layer Meteorol 105:221–252

Bergström H, Högström U (1989) Turbulent exchange above a pine forest II. Organized structures. Bound-Layer Meteorol 49:231–263. doi:10.1007/BF00120972

Blackadar AK (1957) Boundary layer wind maxima and their significance for the growth of nocturnal inversions. Bull Am Meteorol Soc 38:283–290

Bonner WD (1968) Climatology of the low level jet. Mon Weather Rev 96:833–850

Brunet Y, Collineau S (1994) Wavelet analysis of diurnal and nocturnal turbulence above a maize canopy. In: Foufoula-Georgiou E, Kumar P (eds) Wavelets in geophysics, wavelet analysis and its applications, vol 4. Academic Press, San Diego, pp 129–150

Brunet Y, Irvine MR (2000) The control of coherent eddies in vegetation canopies: streamwise structure spacing, canopy shear scale and atmospheric stability. Bound-Layer Meteorol 94:139–163. doi:10.1023/A:1002406616227

Cava D, Giostra U, Siqueira M, Katul G (2004) Organised motion and radiative perturbations in the nocturnal canopy sublayer above an even-aged pine forest. Bound-Layer Meteorol 112:129–157. doi:10.1023/B:BOUN.0000020160.28184.a0

Chen J, Hu F (2003) Coherent structures detected in atmospheric boundary-layer turbulence using wavelet transforms at Huaihe River Basin, China. Bound.-Layer Meteorol 107:429–444. doi:10.1023/A:1022162030155

Cheng Y, Parlange MB, Brutsaert W (2005) Pathology of Monin-Obukhov similarity in the stable boundary layer. J Geophys Res 110:D06,101. doi:10.1029/2004JD004923

Cho J (1995) Inertio-gravity wave parameter estimation from cross-spectral analysis. J Geophys Res 100:18,727–18,737

Clifford SF, Kaimal JC, Lataitis RJ, Strauch RG (1994) Ground-based remote profiling in atmospheric studies - an overview. In: Proceedings of the IEEE, vol 82, pp 313–355

Eckermann S, Vincent R (1989) Falling sphere observations gravity waves motions in the upper stratosphere over Australia. Pageoph 130:509–532

Einaudi F, Finnigan JJ (1993) Wave-turbulence dynamics in the stably stratified boundary layer. J Atmos Sci 50:1841–1864. doi:10.1175/1520–0469(1993)050<1841:WTDITS>2.0.CO;2

Finnigan J (2000) Turbulence in plant canopies. Ann Rev Fluid Mech 32:519–571. doi:10.1146/annurev.fluid.32.1.519

Foken T, Meixner F, Falge E, Zetzsch C, Serafimovich A, Bargsten A, Behrendt T, Biermann T, Breuninger C, Dix S, Gerken T, Hunner M, Lehmann-Pape L, Hens K, Jocher G, Kesselmeier J, Lüers J, Mayer JC, Moravek A, Plake D, Riederer M, Rütz F, Scheibe M, Siebicke L, Sörgel M, Staudt K, Trebs I, Tsokankunku A, Welling M, Wolff V, Zhu Z (2012) Coupling processes and exchange of energy and reactive and non-reactive trace gases at a forest site results of the EGER experiment. Atmos Chem Phys 12:1923–1950. doi:10.5194/acp-12-1923-2012

Foster RC, Vianey F, Drobinski P, Carlotti P (2006) Near-surface coherent structures and the vertical momentum flux in a large-eddy simulation of the neutrally-stratified boundary layer. Bound-Layer Meteorol 120:229–255. doi:10.1007/s10546-006-9054-8

Gao W, Shaw RH, Paw U KT (1989) Observation of organized structure in turbulent flow within and above a forest canopy. Bound-Layer Meteorol 47:349–377. doi:10.1007/BF00122339

Gerstberger P, Foken T, Kalbitz K (2004) The Lehstenbach and Steinkreuz chatchments in NE Bavaria, Germany. In: Matzner E (ed) Biogeochemistry of forested catchments in a changing environment: ecological Studies, vol 172. Springer, Heidelberg, pp 15–41

Gill AE (1982) Atmosphere-Ocean dynamics. Academic, San Diego

Gossard EE, Hooke WH (1975) Waves in the atmosphere. Elsevier, New York

Grossmann A, Morlet J (1984) Decomposition of hardy functions into square integrable wavelets of constant shape. J Math Anal 15:723–736

Guest FM, Reeder MJ, Marks CJ, Karoly DJ (2000) Inertia-gravity waves observed in the lower stratosphere over Macquarie Island. J Atmos Sci 57:737–752

Hoffmann P, Rapp M, Serafimovich A, Latteck R (2005) On the occurrence and formation of multiple layers of polar mesosphere summer echoes. Geophys Res Lett 32, L05812. doi:10.1029/2004GL021409

Holton J (1967) The diurnal boundary layer wind oscillation above sloping terrain. Tellus 19:199–205

Hübner J, Olesch J, Falke H, Meixner FX, Foken T (2014) A horizontal mobile measuring system for atmospheric quantities. Atmos Meas Tech 7:2967–2980

Karipot A, Leclerc MY, Zhang G, Martin T, Starr G, Hollinger D, McCaughey JH, Hendrey GR (2006) Nocturnal CO2 exchange over a tall forest canopy associated with intermittent low-level jet activity. Theor Appl Climatol 85:243–248

Katul G, Kuhn G, Schieldge J, Hsieh CI (1997) The ejection-sweep character of scalar fluxes in the unstable surface layer. Bound-Layer Meteorol 83:1–26. doi:10.1023/A:1000293516830

King JC, Mobbs SD, Darby MS, Rees JM (1987) Observations of an internal gravity wave in the lower troposphere at Halley, Antarctica. Bound-Layer Meteorol 39:1–13. doi:10.1007/BF00121862

Koch SE, O'Handley C (1997) Operational forecasting and detection of mesoscale gravity waves. Wea Forecast 12:253–281. doi:10.1175/1520-0434(1997)012<0253:OFADOM>2.0.CO;2

Kronland-Martinet R, Morlet J, Grossmann A (1987) Analysis of sound patterns through wavelet transforms. Int J Pattern Recognit Artif Intell 1:273–302

Kumar P, Foufoula-Georgiou E (1997) Wavelet analysis for geophysical applications. Rev Geophys 35:385–412

Kunze E (1985) Near-inertial wave propagation in geostrophic shear. J Phys Oceanogr 15:544–565

Lee X, Neumann H, Hartog G, Mickle R, Fuentes J, Black T, Yang P, Blanken P (1997) Observation of gravity waves in a boreal forest. Bound-Layer Meteorol 84:383–398. doi:10.1023/A:1000454030493

Lehmann V, Dibbern J, Görsdorf U, Neuschaefer J, Steinhagen H (2003) The new operational UHF wind profiler radars of the deutscher wetterdienst. In: Wandinger U, Engelmann R, Schmieder K (eds) 6th International Symposium on Tropospheric Proling (ISTP) - extended abstracts. Institute for Tropospheric Research, pp 489–491

Lindzen RS, Tung KK (1976) Banded convective activity and ducted gravity waves. Mon Weather Rev 104:1602–1617. doi:10.1175/1520-0493(1976)1048<1602:BCAADG>2.0.CO;2

Maitani T, Shaw RH (1990) Joint probability analysis of momentum and heat fluxes at a deciduous forest. Bound-Layer Meteorol 52:283–300. doi:10.1007/BF00122091

Nappo CJ (2012) An introduction to atmospheric gravity waves. International geophysics series, vol 102. Academic, San Diego

Nappo CJ, Miller DR, Hiscox AL (2008) Wave-modified flux and plume dispersion in the stable boundary layer. Bound-Layer Meteorol 129:211–223. doi:10.1007/s10546-008-9315-9

Paw U KT, Brunet Y, Collineau S, Shaw RH, Maitani T, Qiu J, Hipps L (1992) On coherent structures in turbulence above and within agricultural plant canopies. Agric For Meteorol 61:55–68

Pecnick MJ, Young JA (1984) Mechanics of a strong subsynoptic gravity wave deduced from satellite and surface observations. J Atmos Sci 41:1850–1862. doi:10.1175/1520-0469(1984)041<1850:MOASSG>2.0.CO;2

Pike CJ (1994) Analysis of high resolution marine seismic data using wavelet transform. In: Foufoula-Georgiou E, Kumar P (eds) Wavelets in geophysics. Wavelet analysis and its applications, vol 4. Academic, San Diego, pp 183–211

Raupach MR, Thom AS (1981) Turbulence in and above plant canopies. Ann Rev Fluid Mech 13:97–129

Raupach MR, Finnigan JJ, Brunet Y (1996) Coherent eddies and turbulence in vegetation canopies: the mixing-layer analogy. Bound-Layer Meteorol 78:351–382. doi:10.1007/BF00120941

Rees JM, Staszewskib WJ, Winklerc JR (2001) Case study of a wave event in the stable atmospheric boundary layer overlying an Antarctic Ice Shelf using the orthogonal wavelet transform. Dyn Atmos Oceans 34:245–261. doi:10.1016/S0377-0265(01)00070-7

Sato K (1994) A statistical study of the structure, saturation and sources of inertia-gravity waves in the lower stratosphere observed with the MU radar. J Atmos Terr Phys 56:755–774

Sauvageot H (1992) Radar meteorology. Artech House, Boston

Serafimovich A, Thomas C, Foken T (2011) Vertical and horizontal transport of energy and matter by coherent motions in a tall spruce canopy. Bound-Layer Meteorol 140:429–451. doi:10.1007/s10546-011-9619-z

Shaw RH, Paw U KT, Gao W (1989) Detection of temperature ramps and flow structures at a deciduous forest site. Agric For Meteorol 47:123–138

Smedman AS, Bergström H, Högström U (1995) Spectra, variances and length scales in a marine stable boundary layer dominated by a low level jet. Bound-Layer Meteorol 76:211–232. doi:10.1007/BF00709352

Staudt K, Foken T (2007) Documentation of reference data for the experimental areas of the Bayreuth Centre for Ecology and Environmental Research (BayCEER) at the Waldstein site. Arbeitsergebnisse, Universität Bayreuth, Abt Mikrometeorologie. Print, ISSN:1614-8916 35:37

Stull RB (1988) An introduction to boundary layer meteorology. Kluwer Academic Publishers, Dordrecht/Boston/London

Sun J, Lenschow DH, Burns SP, Banta RM, Newsom RK, Coulter R, Frasier S, Ince T, Nappo C, Balsley BB, Jensen M, Mahrt L, Miller D, Skelly B (2003) Atmospheric disturbances that generate intermittent turbulence in nocturnal boundary layers. Bound-Layer Meteorol 110:255–279. doi:10.1023/A:1026097926169

Thomas C, Foken T (2005) Detection of long-term coherent exchange over spruce forest using wavelet analysis. Theor Appl Climatol 80:91–104. doi:10.1007/s00704-004-0093-0

Thomas C, Foken T (2007a) Flux contribution of coherent structures and its implications for the exchange of energy and matter in a tall spruce canopy. Bound-Layer Meteorol 123:317–337. doi:10.1007/s10546-006-9144-7

Thomas C, Foken T (2007b) Organised motion in a tall spruce canopy: temporal scales, structure spacing and terrain effects. Bound-Layer Meteorol 122:123–147. doi:10.1007/s10546-006-9087-z

Thomas C, Mayer JC, Meixner FX, Foken T (2006) Analysis of low-frequency turbulence above tall vegetation using a doppler sodar. Bound-Layer Meteorol 119:563–587

Thompson R (1978) Observation of inertial waves in the stratosphere. Q J R Meteorol Soc 104:691–698

Torrence C, Compo GP (1998) A practical guide to wavelet analysis. Bull Am Meteorol Soc 79(1):61–78

Vickers D, Mahrt L (1997) Quality control and flux sampling problems for tower and aircraft data. J Atmos Ocean Tech 14:512–526. doi:10.1175/1520-0426(1997)014<0512:QCAFSP>2.0.CO;2

Vincent R, Fritts D (1987) A climatology of gravity wave motions in the mesopause region at Adelaide, Australia. J Atmos Sci 44:748–760

Wilczak JM, Oncley SP, Stage SA (2001) Sonic anemometer tilt correction algorithms. Bound-Layer Meteorol 99:127–150. doi:10.1023/A:1018966204465

Zhang F, Wang S, Plougonven R (2004) Uncertainties in using the hodograph method to retrieve gravity wave characteristics from individual soundings. Geophys Res Lett 31:L11110. doi:10.1029/2004GL019841

Zink F, Vincent R (2001) Wavelet analysis of stratospheric gravity wave packets over Macquarie Island. J Geophys Res 106:10275–10288

Zülicke C, Peters D (2006) Simulation of inertiagravity waves in a poleward-breaking Rossby wave. J Atmos Sci. doi:10.1175/JAS3805.1

Chapter 12
Development of Flux Data Quality Tools

Thomas Foken, Mathias Göckede, Johannes Lüers, Lukas Siebicke, Corinna Rebmann, Johannes Ruppert, and Christoph K. Thomas

12.1 Introduction

In the 1990s, the eddy covariance technique became more popular due to commercially available devices, not only sonic anemometers but also gas analyzers. This was the start of larger flux networks like EUROFLUX and AMERIFLUX. In

T. Foken (✉)
Am Herrgottsbaum 28, 96120 Bischberg, Germany

Bayreuth Center of Ecology and Environmental Research, University of Bayreuth, Bayreuth, Germany
e-mail: foken@micrometeorology.de

M. Göckede
Max-Planck-Institute for Biogeochemistry, Hans Knöll Str. 10, 07745 Jena, Germany

J. Lüers
Bayreuth Center of Ecology and Environmental ResearchUniversity of Bayreuth 95440, Bayreuth, Germany

L. Siebicke
Bioclimatology, Georg-August-University Göttingen, Büsgenweg 2, 37077 Göttingen, Germany

C. Rebmann
Helmholtz-Centre for Environmental Research – UFZ, Permoserstr. 15, 04318 Leipzig, Germany

J. Ruppert
Research Institute of the Cement Industry, Tannenstr. 2, 40476 Düsseldorf, Germany

C.K. Thomas
Group of Micrometeorology, University of Bayreuth, 95440 Bayreuth, Germany

Bayreuth Center of Ecology and Environmental Research, University of Bayreuth, 95440 Bayreuth, Germany

T. Foken, M. Göckede, J. Lüers, L. Siebicke, C. Rebmann, J. Ruppert, C.K. Thomas: Affiliation during the work at the Waldstein sites: Department of Micrometeorology, University of Bayreuth, Bayreuth, Germany

T. Foken (ed.), *Energy and Matter Fluxes of a Spruce Forest Ecosystem*,
Ecological Studies 229, DOI 10.1007/978-3-319-49389-3_12

parallel, two important issues were addressed by development of the data quality analysis of flux data (Foken and Wichura 1996; Vickers and Mahrt 1997) and the footprint (Leclerc and Foken 2014) with the first applicable footprint models (Schuepp et al. 1990; Schmid 1997). Both flux data quality tools were combined (Foken et al. 2004) and applied to European FLUXNET sites (Rebmann et al. 2005; Göckede et al. 2008). This offers the possibility of replacing the gap filling tool for fluxes (Falge et al. 2001), which uses the friction velocity as a cutoff criterion (Goulden et al. 1996), with a tool that uses the data quality as a cutoff criterion (Ruppert et al. 2006). The application of all these developments on forest sites was tested and developed at the Waldstein-Weidenbrunnen site before further application to other sites. These studies were completed by investigations of energy balance closure (Foken 2008a), the investigation of integral turbulence characteristics (Foken et al. 2012a), and coordinate rotation methods and advection (Siebicke et al. 2012). This chapter gives an overview of all these methods and their application to the Waldstein-Weidenbrunnen site as a guide to the description of the data quality of long-term flux sites. This chapter also has a significant historical component describing the development of different methods for flux data quality tools.

12.2 Materials and Methods

12.2.1 Data for This Investigation

All investigations described in this chapter were done using the turbulence data measured at the top of the "Main Tower" at a height of 31 m above ground. The details of these measurements are given in Chap. 2. The relevant periods of investigation are given in Table 12.1.

12.2.2 Integral Turbulence Characteristics

Integral turbulence characteristics – normalized standard deviations of the three wind components, the temperature, the moisture, etc. – are constant or are a function of stratification and characterize the development of the atmospheric turbulence very well (Lumley and Panofsky 1964; Tillman 1972). These characteristics were therefore used by Foken and Wichura (1996) as a tool for characterizing the data quality of eddy covariance data. They showed that these characteristics have significant deviations from the theoretical model equations in the case of large heterogeneities on the upwind side, intermittent turbulence, internal boundary layers, etc.

In the classical textbooks, the integral turbulence characteristics are often only given for neutral stratification as a constant value (Lumley and Panofsky 1964; Panofsky and Dutton 1984). For the investigations of this chapter, similarity

Table 12.1 Data sets used in these investigations

Year	Period	Scientific problem	Reference
1997–1999		Energy balance closure	Aubinet et al. (2000)
1998	May–August	Footprint	Rebmann (2003)
1998	06.07.–10.08.	Integral characteristics, footprint	Foken et al. (1999, 2000), Foken and Leclerc (2004)
2003		Gap filling	Ruppert et al. (2006)
2003	21.05.–01.08.	Footprint and data quality	Göckede et al. (2005a, 2008)
2003	24.06.–17.07.	Turbulence profile	Göckede et al. (2007)
2003–2006	21.05.2003–14.08.2006	Advection	Siebicke et al. (2012)
2007	06.09–07.10. (EGER-IOP1)	Turbulence profile Footprint climatology Roughness sublayer Advection Energy balance closure	Foken et al. (2012a) Siebicke (2008) Foken et al. (2012a, Suppl.) Siebicke et al. (2012) Foken et al. (2012a, Suppl.)
2008	01.06.–15.07. (EGER-IOP2)	Advection Energy balance closure	Siebicke et al. (2012) Foken et al. (2012a, Suppl.)

relations for diabatic conditions are applied (Foken et al. 1991) for the wind components (u, v horizontal wind components, w vertical wind component, u_* friction velocity)

$$\sigma_{u,v,w} \Big/ u_* = c_1 \left(z \Big/ L \right)^{c_2}, \tag{12.1}$$

and for temperature and other scalars (T temperature, T_* temperature scale)

$$\sigma_T \Big/ T_* = c_1 \left(z \Big/ L \right)^{c_2}. \tag{12.2}$$

At least for the vertical wind, there are no significant differences between the parameterizations that are available, such as those by Panofsky et al. (1977). The integral turbulence characteristics for temperature and other scalars in the case of neutral stratification are not exact because $T_* \to 0$. Not considered were influences of the mixed layer height (Johansson et al. 2001) in the case of free convection (Thomas and Foken 2002). The relevant coefficients c_1 and c_2 are given in Table 12.2. For stable stratification, the same functions with $|z/L|$ can be used as a first guess.

Based on the Rossby similarity, some authors (Tennekes 1982; Högström 1990) assumed, at least in the neutral case, a visible dependency on the Coriolis parameter. Such a parameterization is given according to Thomas and Foken (2002) in Table 12.3.

Table 12.2 Integral turbulence characteristics for diabatic stratification (Foken et al. 1991, 1997; Thomas and Foken 2002)

Parameter	z/L	c_1	c_2
σ_w/u_*	$0 > z/L > -0.032$ $-0.032 > z/L$	1.3 2.0	0 1/8
σ_u/u_*	$0 > z/L > -0.032$ $-0.032 > z/L$	2.7 4.15	0 1/8
σ_T/T_*	$0.02 < z/L < 1$ $0.02 > z/L > -0.062$ $-0.062 > z/L > -1$ $-1 > z/L$	1.4 0.5 1.0 1.0	$-1/4$ $-1/2$ $-1/4$ $-1/3$

Table 12.3 Parameterization of the integral turbulence characteristics for neutral and slightly unstable and stable stratification (Thomas and Foken 2002)

Parameter	$-0.2 < z/L < 0.4$
σ_w/u_*	$0.21 \ln\left(\frac{z_+ f}{u_*}\right) + 3.1 \qquad z_+ = 1$ m
σ_u/u_*	$0.44 \ln\left(\frac{z_+ f}{u_*}\right) + 6.3 \qquad z_+ = 1$ m

First investigations of the integral turbulence characteristics at the Waldstein-Weidenbrunnen site already showed significant influences of the surface characteristics on the upwind side (Foken et al. 1999). These findings were used by Foken and Leclerc (2004) to develop a method of footprint validation with natural tracers, which was successfully applied by Göckede et al. (2005b) on flat terrain.

12.2.3 Footprint Models

Footprint models are nowadays a widely used tool for characterizing the source area as well as the data quality of flux measurements (Leclerc and Foken 2014). The first models for practical application were analytical models based on the equations of turbulent diffusion (Schuepp et al. 1990; Schmid 1994, 1997). The Schuepp et al. (1990) model was already used in 1997–1999 for net ecosystem exchange (NEE) measurements by Rebmann (2003), and the FSAM model by Schmid (1997) was used in 1998 for footprint studies of the Waldstein-Weidenbrunnen site (Foken et al. 2000). With this model, a method of linking the quality of turbulence data with footprint information was developed (Göckede et al. 2004) and applied to 18 CARBOEUROFLUX stations (Rebmann et al. 2005). This research was possible due to the application of the Waldstein-Weidenbrunnen data as a test data set for the development of the methods (for results, see Sect. 12.3.3) and a close European cooperation to analyze the basics and benefits of footprints, presented in a special issue of the journal *Agricultural and Forest Meteorology* (Vesala et al. 2004) and further overview papers (Vesala et al. 2008, 2010; Rannik et al. 2012).

Table 12.4 Coefficients for Eq. (12.3)

Reference	i	a_i	α_i	β_i	γ_i
Rannik et al. (2003), neutral, for *Hyytiälä* site	u	2.30	1.0	1.0	−0.3
	v	1.75	1.0	0.85	−0.2
	w	1.25	0.9	1.2	−0.63
Waldstein-Weidenbrunnen site, 2007	u	2.01	8.97	1.37	0.29
	v	1.60	5.18	1.11	0.34
	w	1.13	0.9	1.2	−0.63

Due to the shortcomings of the FSAM model, including limitations in the range of stratification, and the success of the Finnish colleagues in building a practical and applicable Lagrangian footprint model (Rannik et al. 2000, 2003), the method developed to combine data quality and footprint was updated with the Lagrangian model. The new model (Göckede et al. 2006) was completed by performing a flux averaging of the surface characteristics (roughness length) according to Hasager and Jensen (1999) using a spectral method. This new method was applied to 25 CARBOEROPE-IP stations for a general data quality classification (Göckede et al. 2008). In this approach, the turbulence characteristics within the forest of the Finish Hyytiälä site (Rannik et al. 2003) were used. It was later shown that these characteristics are nearly identical for the Waldstein-Weidenbrunnen site (Foken et al. 2012a), as is shown in Sect. 12.3.1 and Table 12.4 (Göckede et al. 2007). The sensitivity of the Lagrangian footprint model to the turbulence statistics was tested by Göckede et al. (2007). This was also the first paper to take into account the turbulence coupling at a forest site (Thomas and Foken 2007a) and bring this into the data analysis as a third influence parameter. For more details, see Chap. 6.

The Department of Micrometeorology was involved in the development and validation of backward Lagrangian and LES models (Steinfeld et al. 2008), but these models were not applied to the Waldstein-Weidenbrunnen site. These studies were used for quality classification of footprint models, which is also relevant for this chapter (Markkanen et al. 2009).

12.2.4 Energy Balance Closure

According to the law of conservation of energy, the incoming and outgoing energy fluxes at the Earth surface should balance each other

$$R_\mathrm{n} = Q_H + Q_E + Q_G, \tag{12.3}$$

with the net radiation R_n, the sensible heat flux Q_H, the latent heat flux Q_E, and the ground heat flux Q_G. But most of the experiments, and also a first study of FLUXNET sites (Wilson et al. 2002), have shown that the net radiation is always

larger than the sum of the right side of Eq. (12.3). In the first guide for carbon flux measurements (Aubinet et al. 2000), the degree of energy balance closure was indicated as a measure of the quality of the eddy covariance data. It was assumed that this method has systematic errors. But it could be shown, for example, by an experiment realized in 2000 in California (Oncley et al. 2007), that not the measuring technique but mesoscale influences are responsible for this problem. The guide for flux measurements was therefore corrected in this point (Aubinet et al. 2003). Recently the heterogeneity of the landscape surrounding a measuring station was identified as the main reason for the problem (Foken 2008a; Stoy et al. 2012). Therefore, the location of the flux station, and not the data quality, is more or less a reason for the degree of energy balance closure. Of course, if the non-closure shows unrealistic values, then the data quality should also be checked.

There are many papers of the Department of Micrometeorology available concerning the energy balance closure, including proposals for correction methods (Charuchittipan et al. 2014), but the Waldstein-Weidenbrunnen site was only one example of this research. The available results are given in this chapter at Sect. 12.3.3 and for the forest edge in Chap. 13.

12.3 Results and Discussions

12.3.1 Integral Turbulence Characteristics

The aim of the first research on integral turbulence characteristics was a test of the application of the proposed data quality control for eddy covariance measurements by Foken and Wichura (1996) on heterogeneous and forested surfaces, because De Bruin et al. (1991) classified sites according to the type of heterogeneities. Besides a data set from the Waldstein-Weidenbrunnen site from 1998 (Table 12.1), a similar data set from a very heterogeneous area in Northern Bohemia (Czech Republic) was investigated. For all wind directions from homogeneous areas, it was found that the integral turbulence characteristics are in good agreement with the theory (Foken et al. 1999). In an analysis of the Weidenbrunnen data, a special distribution of the differences between the integral characteristics and the model (Eqs. 12.1 and 12.2; Tables 12.2 and 12.3) was found. Figure 12.1 shows a distribution of differences larger than 30 %, which is a moderate or low data quality (Foken et al. 2004), according to the wind direction as represented by wind roses. For the integral turbulence characteristic of the horizontal wind speed (σ_u/u_*), most of the cases are in the westerly sector, which has the highest frequency of wind directions. Interestingly, σ_w/u_* does not follow this distribution. The vertical wind velocity indicates the lowest data quality in sectors with low wind velocities or in sectors that are affected by significant heterogeneities. Therefore, a more specific data analysis was done (Foken et al. 2000). Figure 12.2 illustrates the standard deviation of wind direction in unstable and stable conditions as a function of wind direction. This variable is used in several models to determine atmospheric stratification (Hicks et al. 1987) or classify diffusion in air pollution studies (Blackadar 1997). The

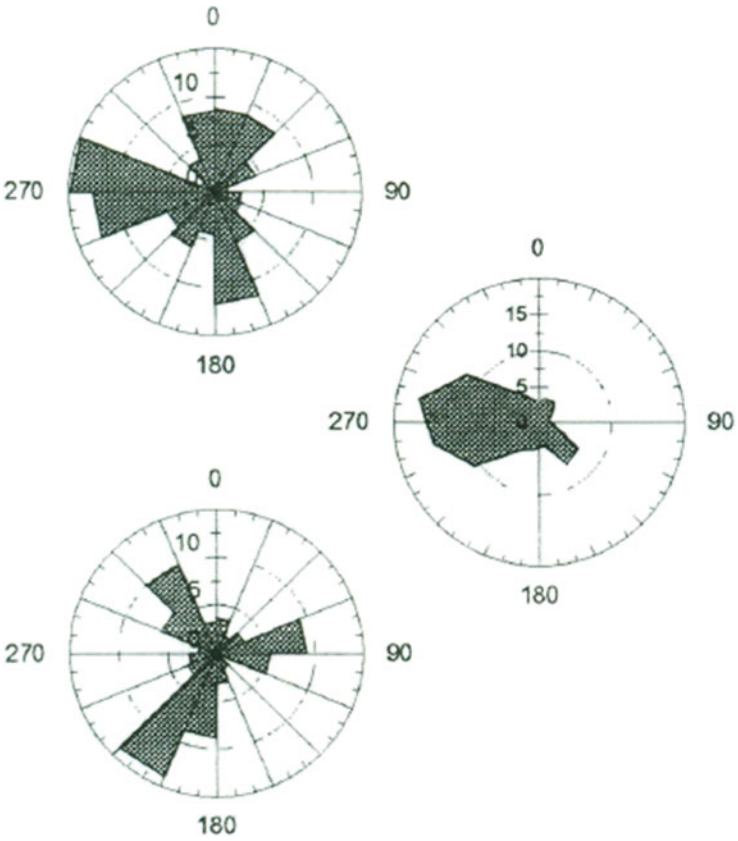

Fig. 12.1 Frequency in % of cases with differences greater than 30 % between measurements and the model according to the equation of integral characteristics. *Left side* (*above*), σ_u/u_*; *left side* (*below*), σ_w/u_*; *right side*, frequency distribution of the wind direction (Foken et al. 1999, Published with kind permission of © Authors 1999, All rights reserved)

observations show that the standard deviation of the wind direction is significantly higher for winds for the sector 225° to 270° than for other wind directions. This is a result of the step change between the forest height and the clear-cut (Waldstein-Pflanzgarten site) at a distance of about 250 m, which occurs within the main source region of the measured flux. The dependence of the normalized standard deviation of the vertical wind velocity on wind direction is shown in Fig. 12.3. For unstable stratification, a good agreement was found between data and the parameterized values (Fig. 12.3a). In contrast, in stable conditions with large footprint areas (Fig. 12.3b), a significant difference was found in the wind sector 180° to 225°. For this situation, the source area of the flux includes the peaks of "Großer Waldstein" (see Chap. 2), which produce significant mechanical turbulence. This was a first

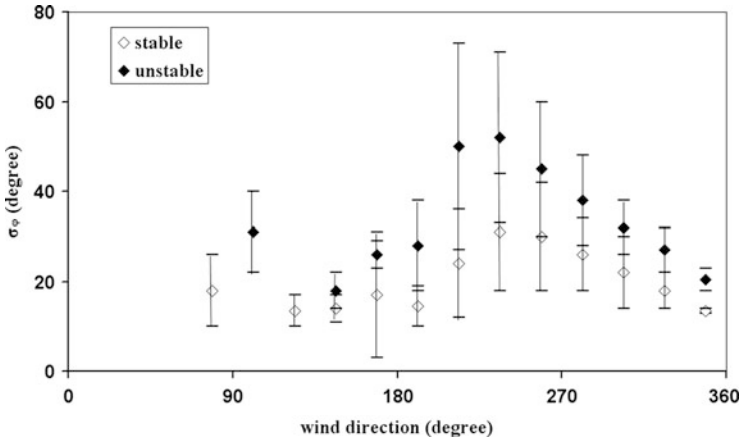

Fig. 12.2 Standard deviation of the wind direction for the Waldstein-Weidenbrunnen site for unstable and stable stratification (Foken et al. 2000, Published with kind permission of © Authors 2000, All rights reserved), also published later in Foken and Leclerc (2004) and Foken (2008b)

indication that data quality and footprint must be considered together (see this chapter at Sect. 12.3.2).

With the use of footprint models for forested areas, the vertical profile of the integral turbulence characteristics became highly important. For their sensitivity analysis of footprint models (see Sect. 12.3.2) on vertical turbulence profiles, Göckede et al. (2007) also investigated these profiles with a data set from 2003 (Table 12.1, Fig. 12.4). They separated the profiles for different stages of coupling between the atmosphere and the canopy (Thomas and Foken 2007b), which is discussed in more detail in Chap. 6. These stages of coupling are very closely connected to the stratification. Therefore, the differences in the profiles are also the result of stability.

While the profiles of the mean wind speed above a canopy are strongly affected by the existence of the roughness sublayer (see Sect. 12.3.2), the effect on integral characteristics is not well investigated, and only a few such investigations are available (Raupach et al. 1996; Finnigan 2000). The turbulence characteristics within a forest are spatially heterogeneous and distinct from those associated with the surface boundary layer (Baldocchi and Meyers 1998). For measurements inside the canopy ($z < h_c$, z height; h_c canopy height), a parameterization was proposed by Rannik et al. (2003)

$$\begin{aligned} \frac{\sigma_i}{u_*} &= a_i \left\{ \exp\left[-\alpha_i \left(1 - \frac{z}{h_c} \right)^{\beta_i} \right] (1 - \gamma_i) + \gamma_i \right\} \\ i &= u, v, w; \quad z < h_c \end{aligned} \tag{12.4}$$

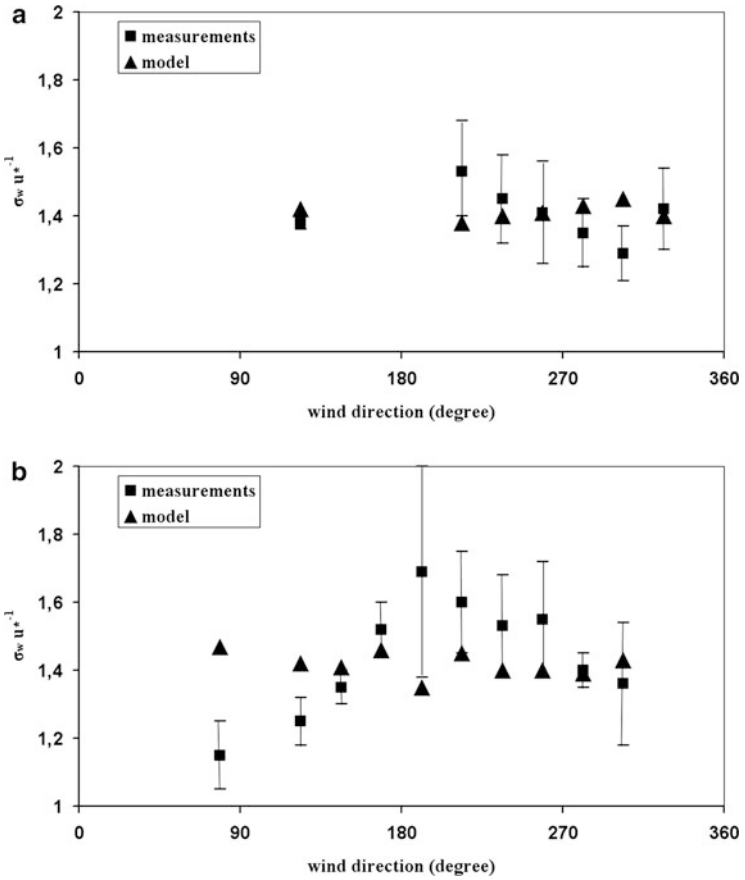

Fig. 12.3 Normalized integral turbulence characteristics of the vertical wind velocity at Waldstein-Weidenbrunnen site for unstable (*above*) and stable (*below*) stratification compared with the parameterization given in Table 12.2 (Foken et al. 2000, Published with kind permission of © Authors 2000, All rights reserved), also published later in Foken and Leclerc (2004) and Foken (2008b)

and above the canopy constant values were assumed

$$\begin{aligned} \frac{\sigma_i}{u_*} &= a_i \\ i &= u, v, w; \quad z > h_c \end{aligned} \tag{12.5}$$

The values of the parameters α, β, and γ are given in Table 12.4. With the measurements made in 2007 at the Waldstein-Weidenbrunnen site, new coefficients for the u and v components of the parameterization according to Eq. (12.4) were determined, while for w the original coefficients were used (Foken et al. 2012a).

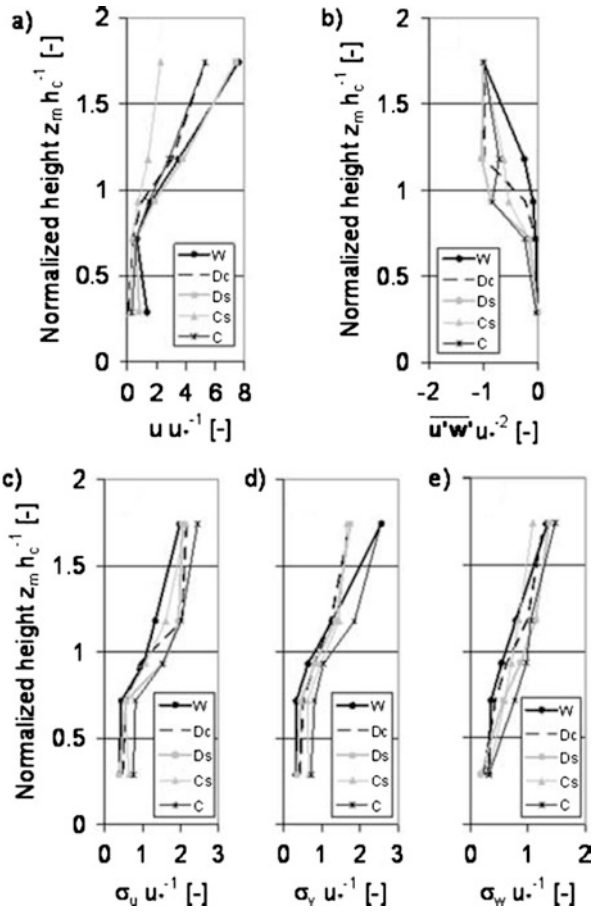

Fig. 12.4 Representative profiles of measured turbulence statistics for Waldstein-Weidenbrunnen site of five exchange regimes: wind speed (**a**), vertical momentum flux (**b**), standard deviation of alongwind (**c**), crosswind (**d**), and vertical wind (**e**). Values normalized with friction velocity. The measurement period was June 24–July 17, 2003. The stability parameter $\zeta = z/L$ at the uppermost profile level ranges from very stable (W, $\zeta = 0.534$) over stable (Ds, $\zeta = 0.101$) and near-neutral (Dc, $\zeta = 0.015$) to unstable (Cs, C, $\zeta = -0.286$). W, Dc, Ds, Cs, and C are coupling classes according to Thomas and Foken (2007b) (Göckede et al. 2007, Published with kind permission of © Authors 2007, All rights reserved)

The results are shown in Fig. 12.5. Göckede et al. (2007) have also shown that the parameterization by Rannik et al. (2003) is in good agreement with the model by Massman and Weil (1999) for the Waldstein-Weidenbrunnen site, where the plant-area index profile is given by Thomas and Foken (2007b, see also Chap. 2). Especially the w component is nearly identical. From these findings, it can be concluded that the integral turbulence characteristics of the vertical wind field are nearly independent of the site and only the horizontal components are site specific, however, without a significant bias.

The success of the extension of the application of integral turbulence characteristics to forested areas offered the possibility of also using the quality tests for eddy covariance data (Foken and Wichura 1996; Foken et al. 2004) as an indicator for data selection. The standard procedure of the FLUXNET community is a filtering with the u_* criterion (Goulden et al. 1996; Falge et al. 2001; Reichstein et al. 2005), i.e., all data with u_* below a threshold value are classified as erroneous and will be replaced by a gap-filling procedure. Therefore, also data with low friction velocities

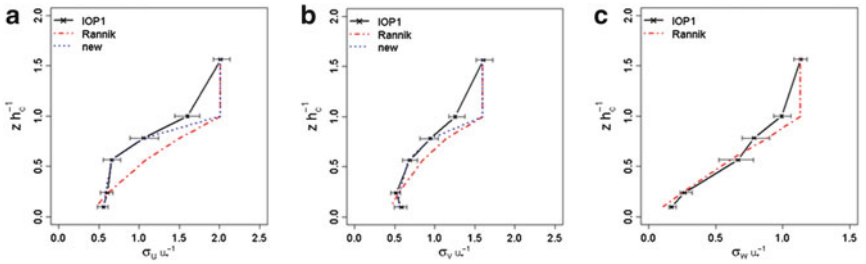

Fig. 12.5 Measurements (*crossed black line*) and model parameterizations (*red dot-dashed line*) for profiles of the integral turbulence characteristics of wind velocity components u, v, and w within the Waldstein-Weidenbrunnen forest stand and inside the lower roughness sublayer (near-neutral stratification). For u and v, the parameterization of Rannik et al. (2003) was modified to fit the measurements during EGER IOP-1 (2007), for w the original coefficients were used (Foken et al. 2012a, Published with kind permission of © Authors 2012, CCA 3.0 License, All rights reserved)

are not available for the development of the gap-filling procedure for NEE or for the flux partitioning into assimilation and respiration, and the parameterization for low wind velocities is only an extrapolation. A possible consequence is an overestimation of gap-filled fluxes (Wohlfahrt et al. 2005). Ruppert et al. (2006) proposed a data selection with sensor-specific quality flags and the flagging system for steady-state conditions and the development of the turbulence using the integral turbulence characteristics (Foken and Wichura 1996; Foken et al. 2004). Only data with the highest quality were used for the development of the parameterizations. The additional benefit of the method is the availability of high-quality data for low wind conditions for the development of the parameterizations. Therefore, the bias of parameterized values may be reduced. But the methods need the availability of raw data, which were generally not available where preprocessing occurred at the sites and a final processing, including gap filling, at a central data center. Figure 12.6 shows the comparison of the proposed method and the application of the u_* criterion on the annual cycle of NEE for 2003. It is easy to see that the u_* criterion simply deletes all low-wind periods. The proposed method has the largest gaps during the nonsteady-state period during sunrise and sunset. However, the number of available nighttime data is much larger than that obtained using the u_* criterion. On the other hand, there are also some gaps at daytime, probably related to nonsteady-state periods. The non-sensitivity of the u_* criterion to erroneous daytime data was also criticized by Acevedo et al. (2009), who proposed a σ_w criterion, which partly follows our proposal. The method by Ruppert et al. (2006) was applied to all flux data of the Waldstein-Weidenbrunnen site, including those presented in Chap. 4.

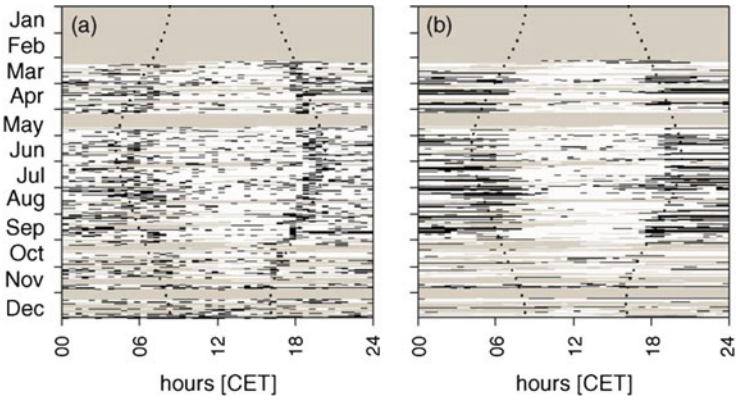

Fig. 12.6 Distribution of quality data by day and hour through 2003 obtained at the Waldstein-Weidenbrunnen site using criteria based on (**a**) stationarity and integral turbulence characteristic tests and (**b**) friction velocity criterion, $u_* < 0.3$ m s^{-1}. *White* areas indicate accepted and *black* areas rejected data with *gray* areas indicating missing data due to rain, fog, ice, or instrumental failures. The *dotted lines* indicate astronomical sunrise and sunset (Ruppert et al. 2006, published with kind permission of © Elsevier 2006, All rights reserved)

12.3.2 Footprints and Data Quality

12.3.2.1 Zero-Plane Displacement

For the application of footprint models, the height above the ground – or height above the zero-plane displacement height in the case of high vegetation – is essential. This is connected to the existence of the roughness sublayer (Garratt 1978). The usual procedure used to characterize the roughness sublayer could not be realized for the Waldstein-Weidenbrunnen site, simply because none of the towers (see Chap. 2) was tall enough for the installation of a sufficient number of measurement levels between the top of the canopy (25–27 m a.gr.) and the roughness sublayer height z_* (presumably > 50 m a.gr.). Therefore, Foken et al. (2012a, Suppl.) preferred the use of the following alternative to derive the desired correction function $\varphi_*(z/z_*)$, which must be used in addition to the universal stability function in the denominator of the profile functions. The function φ_* has been determined from data obtained during the recent field experiment COPS (Wulfmeyer et al. 2011), performed over a growing maize field (for details, see Eigenmann et al. 2009).

In Fig. 12.7, the results of the COPS experiment over maize are shown in comparison with the data from the Waldstein-Weidenbrunnen site (only in the range $z/z_* = 0.41$–0.45) following the equations

$$\phi_* (z/z_*) = \exp\left[-0.7\ (1 - z/z_*)\right] \tag{12.6}$$

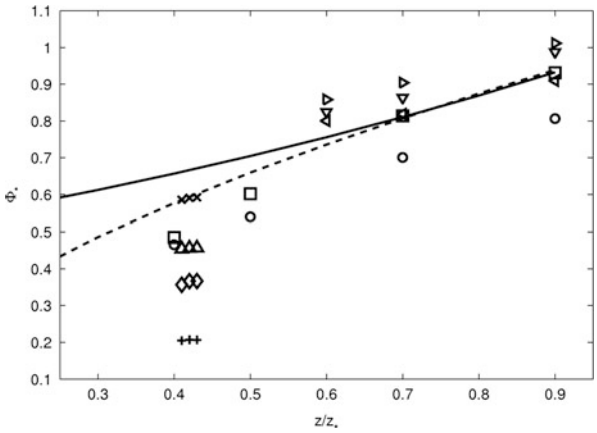

Fig. 12.7 The calculated φ_* values of the EGER data are presented by *crosses*, *upward-pointing triangles*, *diamonds*, and *plus signs* (Foken et al. 2012a, Suppl., Published with kind permission of © Authors 2012, CCA 3.0 License, All rights reserved). The *crosses* represent u_* values (dimension m s^{-1}) smaller than 0.4 and larger than 0.2. The *upward-pointing triangles* represent $0.4 < u_* < 0.6$, the *diamonds* $0.6 < u_* < 0.8$, and the *plus signs* $0.8 < u_* < 1.2$. The calculated φ_* values of the COPS data for a canopy height of 1.2 m are represented by *squares* and *circles*. The *squares* represent $0.2 < u_* < 0.3$ and the *circles* represent $0.3 < u_* < 0.6$. The calculated φ_* values of the COPS data for a canopy height of 2.9 m are represented by *downward-pointing*, *right-pointing*, and *left-pointing triangles*. The *downward-pointing triangles* represent $0.2 < u_* < 0.3$, the *right-pointing triangles* display $0.3 < u_* < 0.4$, and *left-pointing triangles* display $0.4 < u_* < 0.5$. Furthermore, the *solid line* represents the equation developed by Garratt (1992), and the *dashed line* represents the equation developed by Mölder et al. (1999)

(Garratt 1992) and

$$\phi_{*u} = \left(\frac{z}{z_*}\right)^{\eta} \tag{12.7}$$

(Cellier and Brunet 1992). A strong dependence on the friction velocity was found. For moderate friction velocities up to 0.6 m s^{-1}, Eq. (12.7) gives the best approximation with $\eta = 0.6$, which was also found by Mölder et al. (1999). A slight but not significant dependence on stability was also recognized. The enhancement factor for the momentum exchange at 31 m height is therefore approximately 1.6.

Similar to other authors (Mölder et al. 1999), the number of measuring points and the accuracy of the data were not adequate for the calculation of the universal function of the roughness sublayer for scalars. For the temperature profile over the maize field, the linear relationship with $\eta = 1.0$ was in agreement with Mölder et al. (1999). At the forest site the scalars at a height of 23–25 m, at the top of the canopy, already showed an increased gradient to the top of the tower and no reduced gradient according to the roughness sublayer assumption. Therefore, for scalars no additional enhancement factor should be used.

12.3.2.2 Characteristics of the Underlying Surface

For a correct calculation of footprints in relation to different land use classes, high-quality land cover maps are important (Leclerc and Foken 2014). Land cover maps can be derived from topographic maps or by the conversion of remote-sensing spectral bands into land cover types with standard classifiers such as the maximum likelihood classifier (Richards 1993). In both cases, an in situ comparison over a test area (ground truthing) is necessary. Reithmaier et al. (2006) tested the influence of map resolution on the frequency of different land use types in the Waldstein area. They found that, at their test site, the resolution of the images had no impact on the frequency of the land use type (see Table 12.5), and the contribution of certain land cover classes did not shift significantly between map versions. However, in the same study, Reithmaier et al. (2006) also showed that the higher level of details present in the land cover structure of a remote-sensing map can significantly shift footprint results as compared to the use of a very low-resolution map (e.g., a 100×100 m^2 map excerpt from topographical maps). As shown in Fig. 12.8, the flux contribution from the target area (here, conifer forest) obtained using the land use classification of a topographic map is much larger than that obtained by the use of remote-sensing data. This shift is caused by the removal of small-scale heterogeneities, such as clearings, through the application of a majority filter to coarser maps. Though these areas may appear small and insignificant, their cumulative effect can be important in the average land use classification. Remote sensing identifies these areas and thus can provide a more realistic picture of the flux contributions.

In conclusion, the resolution of land use classification should be high, especially when landscapes are characterized by small-scale heterogeneities. This can be most effectively realized with the help of remote-sensing data. Over more homogeneous land covers and for footprint calculations for stable stratification with associated larger footprint areas, low-resolution maps are acceptable.

Table 12.5 Contribution of different land use types in percentage in the area of the FLUXNET site Waldstein-Weidenbrunnen (DE-Bay, 36.18 km^2) for different resolutions of remote-sensing images (Reithmaier et al. 2006)

Resolution	15 m	30 m	50 m	75 m	100 m
Conifer	61.1	61.1	61.0	61.2	61.1
Clearings	12.3	12.2	12.1	12.0	11.9
Grassland	5.6	5.6	5.5	5.7	5.6
Summer crops	6.5	6.5	6.6	6.6	6.7
Winter crops	6.2	6.2	6.4	6.3	6.6
Settlements	4.8	4.9	4.9	5.0	5.0
Quarry	0.3	0.3	0.3	0.4	0.4
Unclassified	3.2	3.2	3.1	3.0	2.7

Note: Due to a storm event in 2007, the area of clearings is now much larger than given in this table (see Chap. 2)

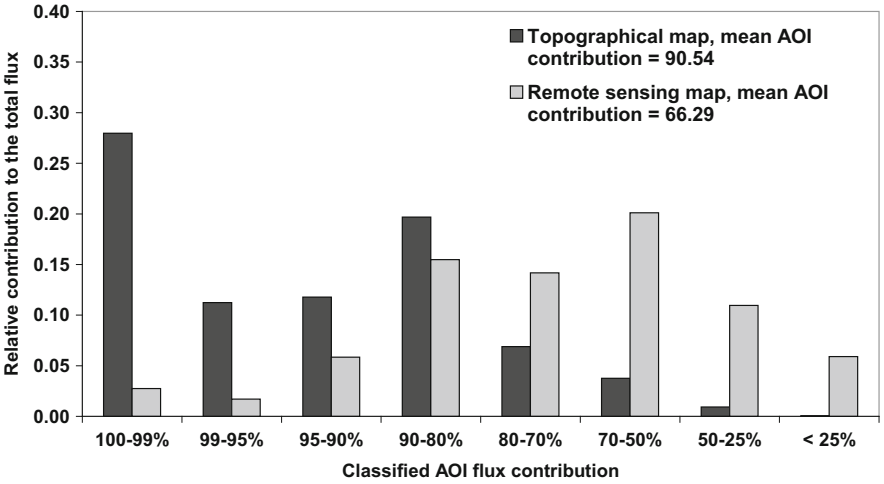

Fig. 12.8 Relative flux contribution of the area of interest (AOI, conifer forest) to the measured flux at the FLUXNET site Waldstein-Weidenbrunnen (DE-Bay) of both the remote-sensing data set (resolution 15 × 15 m^2) and the topographical map (resolution 100 × 100 m^2) according to Reithmaier et al. (2006), published with kind permission of © Springer, Vienna 2006, All rights reserved

12.3.2.3 Footprint Climatology

For a classification of measuring sites, Amiro (1998) proposed the application of a footprint climatology, through a superposition of all individual footprints over a certain time period. For the data set from July and August 1998 (Table 12.1), the first footprint climatology of the Waldstein-Weidenbrunnen site was calculated for the three different wind directions (Foken et al. 2000) that are dominant at the site (Fig. 12.9). Results from the footprint model by Schmid (1997) are shown in Göckede et al. (2004). This underlines the finding (see Sect. 12.3.1 and Fig. 12.3) that only for stable stratification can the hill of "Großer Waldstein" influence the measurements at the Waldstein-Weidenbrunnen site.

The footprint climatology is very important for the site because of the increasing number of clear-cuts due to beetle attacks and wind throw (see Chap. 2). For comparison, Fig. 12.10 shows the footprint climatologies from 2003 and 2007, both calculated with the method by Göckede et al. (2006). The sizes of the footprints are nearly identical in both cases. The small individual differences are related to the different data sets with different wind directions and stability distributions. However, of importance is the larger frequency of clearing in the footprint of the site after the "Kyrill" storm event in January 2003 (see Chaps. 2 and 19).

The different footprint climatologies in different heights were used by Rebmann (2003). For the gap-filling procedure in the case of stable stratification, she applied not the data obtained in 32 m height but in 22 m height in order to realize nearly the

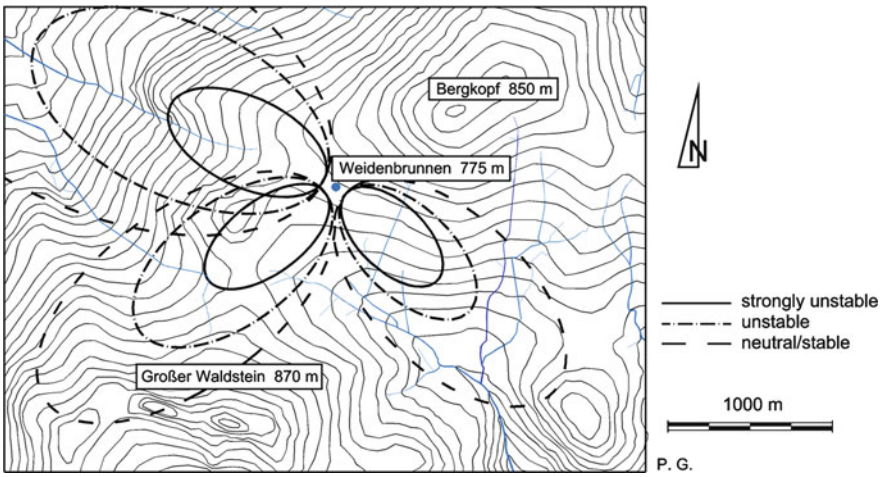

Fig. 12.9 Footprint climatology of the Waldstein-Weidenbrunnen site (06.07.–10.08.1998) for three dominant wind sectors and three stability classes (Foken et al. 2000, Published with kind permission of © Authors 2000, All rights reserved), also published later in Foken and Leclerc (2004) and Foken (2008b)

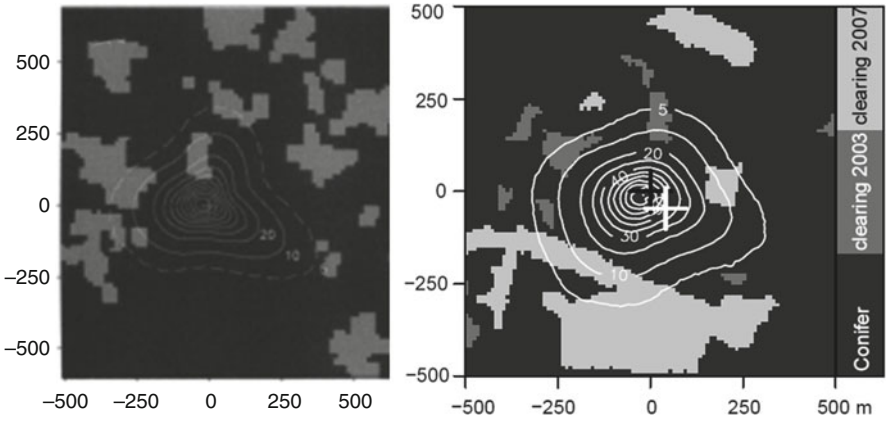

Fig. 12.10 Footprint climatologies of the Waldstein-Weidenbrunnen site for 2003 (*left*), calculation according to Göckede et al. (2008, Published with kind permission of © Authors 2008, CCA 3.0 License, All rights reserved) and 2007 (right, Siebicke 2008, Published with kind permission of © Authors 2008, All rights reserved) after the "Kyrill" storm event

same target area at day and night. Finally, the measured and calculated NEE values agreed better with this procedure.

According to the CARBOEUROPE-IP (see Chap. 1) investigation of 25 European FLUXNET stations (Göckede et al. 2005a, 2008) for a nearly 2.5-month data set in summer 2003 (Table 12.1), about 84 % of the flux is related to conifer forest and 14 % to clearings. This would indicate the Waldstein-Weidenbrunnen site to be

not one of the best stations, but if the target area were to be classified as mixed forest with clearings, as was done for other stations, then nearly 100 % of the fluxes would be related to this target area.

12.3.2.4 Linking Footprint and Flux Data Quality

This part is based on the papers by Göckede et al. (2004, 2006), who combined the footprint climatology first calculated with the model by Schmid (1997) and in the second paper with the model by Rannik et al. (2000, 2003), with the quality test for eddy covariance data (Foken and Wichura 1996) comprising a steady-state test and a test on developed turbulence using integral turbulence characteristics (see Sect. 12.3.1). The test results are given as quality flags (Foken et al. 2004, 2012b), which are linked with the footprint climatology.

For the footprint model, an average roughness length value for a heterogeneous grid element can be easily approximated as the arithmetic mean of the individual roughness length values of the patches composing the area. However, this so-called parameter aggregation is physically incorrect (Claussen 1990; Mölders et al. 1996; Foken 2008b). To account for this nonlinearity, several approaches to a flux aggregation method have been developed, with varying degrees of sophistication. Discussing different flux aggregation methods, Göckede et al. (2006) found that a more practicable approach to aggregate roughness lengths under consideration of local advection effects was developed by Hasager and Jensen (1999). This microscale aggregation model takes into account the response of the atmospheric flow for every roughness step change in arbitrary surface conditions. The physics consist of a linearized version of the atmospheric momentum equation in which only the advective term and the vertical flux divergence are assumed to be of importance (Hasager et al. 2003). The algorithms are solved by fast Fourier transform, which allows the time-efficient computation of the effective roughness parameter consistent with the average stress for a given background flow. To reduce computer time, the results were stored as look-up tables. In the case of the Waldstein-Weidenbrunnen site, these tables contain results for 12 wind direction sectors, 14 different settings for the stability of atmospheric stratification, and 5 temperature regimes in the range $-10\ °C < T_{air} < 30\ °C$. In the model, atmospheric stratification is induced by a temperature difference between the surface temperature T_{surf} and the temperature at measurement height, T_{air}, in the range $-4\ K < (T_{air} - T_{surf}) < 3\ K$, which corresponds to a stability range of about $-0.25 < z/L < 0.8$, the exact values depending on the temperature regime and the wind direction, with L being the Obukhov length. As the roughness length for more unstable cases was almost constant, model runs for values of z/L below -0.25 were not required.

The data quality of the turbulent fluxes measured at Waldstein-Weidenbrunnen site was twice linked with a footprint analysis, the first time using an analytical model by Schmid (1997) and the second time using a Lagrangian footprint model by Rannik et al. (2000, 2003). Here we will not report about the results obtained with the analytical model by Schmid (1997) and the application of a five-class

data quality-flagging schema (Mauder and Foken 2015) published by Rebmann et al. (2005). The results presented here are based on a Lagrangian footprint model (Rannik et al. 2000; Göckede et al. 2006) and on a nine-class data-flagging schema (Foken et al. 2004, 2012b). In this scheme, classes 1–3 are highest quality, 4–6 can be used for long-term investigations, 7 and 8 are low quality, and 9 should not be used. Furthermore, the Lagrangian footprint model is more precise in the footprint climatology, with 86 % of the fluxes from the target area instead of 79 % (Göckede et al. 2006). Some results of the Waldstein-Weidenbrunnen site were published by Göckede et al. (2008); this report follows the complete CARBOEUROPE-IP documentation (Göckede et al. 2005a).

The results of the momentum flux evaluation for the Weidenbrunnen site are presented in Fig. 12.11. The average data quality for the momentum flux at the Waldstein-Weidenbrunnen site is very high, and there are no disturbed wind sectors for any stratification regimes. The slightly reduced data quality during unstable stratification is a result of buoyancy effects disturbing the development of the turbulent flow field, which reduces the quality ratings of the integral turbulence characteristics. A similar result was found for the sensible heat flux (Fig. 12.12). Such findings are frequently obtained at sites with a nonhomogeneous land use structure with varying heat forcings in the area surrounding the tower; however, for all sectors the data quality is still very high. Influences of the Großer Waldstein hill for stable stratification, shown in Figs. 12.2 and 12.3, have a low frequency and have no influence on this long-term study. Another reason for the nearly symmetric distribution of the lower data quality may be flow distortion or self-correlation (crosstalk) problems due to the structure of the sonic anemometer (Wyngaard 1985, Göckede et al. 2008), here the Gill R3.

The average data quality for the sensible heat flux (Fig. 12.12) is rather low at the Waldstein-Weidenbrunnen site. However, this result is a consequence of the parameterization of the integral turbulence characteristics for the sensible heat flux, used to evaluate whether the turbulent flow field is fully developed in order to derive the quality flags of the Foken and Wichura (1996) approach. So far, the parameterization of this value is only reliable for unstable stratification, so that the bad quality results for neutral and stable stratification are more an effect of parameterization than an indication of measurement problems or disturbing site characteristics. Recent data quality studies exclude the integral turbulence characteristics for temperature in the case of neutral and stable stratification (Mauder and Foken 2015). The pattern of low data quality during periods with unstable stratification is nearly identical with that for the friction velocity (Fig. 12.11).

Because there are no valid parameterizations for the integral turbulence characteristics of the latent heat flux, even for unstable stratification, only the stationarity of the flow and the integral turbulence characteristics of the vertical wind component were considered, as was done for the quality evaluation of the sensible heat flux. The results consequently look much better than for the sensible heat flux. Figure 12.13 demonstrates that the footprint-based quality evaluation procedure applied in the context of this study did not reveal any wind sectors with significantly disturbed measurements of the latent heat flux at the Weidenbrunnen site. However,

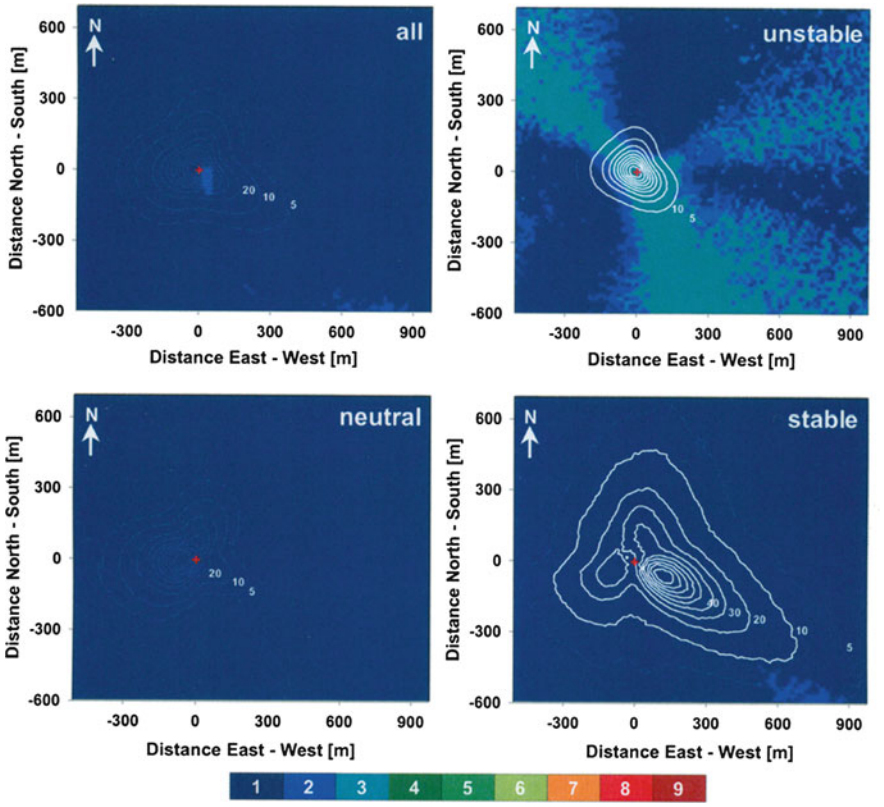

Fig. 12.11 Quality evaluation of the momentum flux determined for the Waldstein-Weidenbrunnen site for three different regimes of atmospheric stratification and their combination (*top left panel*). The tower position is marked by the *red cross*, and the *white isolines* indicate form and position of the footprint climatologies. The colors in the background show the average data quality of each matrix element (Göckede et al. 2005a, Published with kind permission of © Authors 2005, All rights reserved)

there seems to be an influence of frequent fog events coming from westerly and southwesterly directions, which slightly reduces the overall data quality in these sectors, mainly for neutral and stable stratification. For neutral stratification, the lower data quality from the southwest sector may be caused by those rain events which were not filtered out with other methods like precipitation measurements.

The CO_2 flux was treated the same way as the latent heat flux in the context of this study, so again no integral turbulence characteristics were considered for the CO_2 measurements. The results presented in Fig. 12.14 show no significant influence of the surrounding terrain on the data quality of this parameter at the Weidenbrunnen site. Similar to the latent heat flux, the data quality is slightly reduced for westerly and southwesterly wind directions, which can again be attributed to frequent fog or rain events coming from these directions.

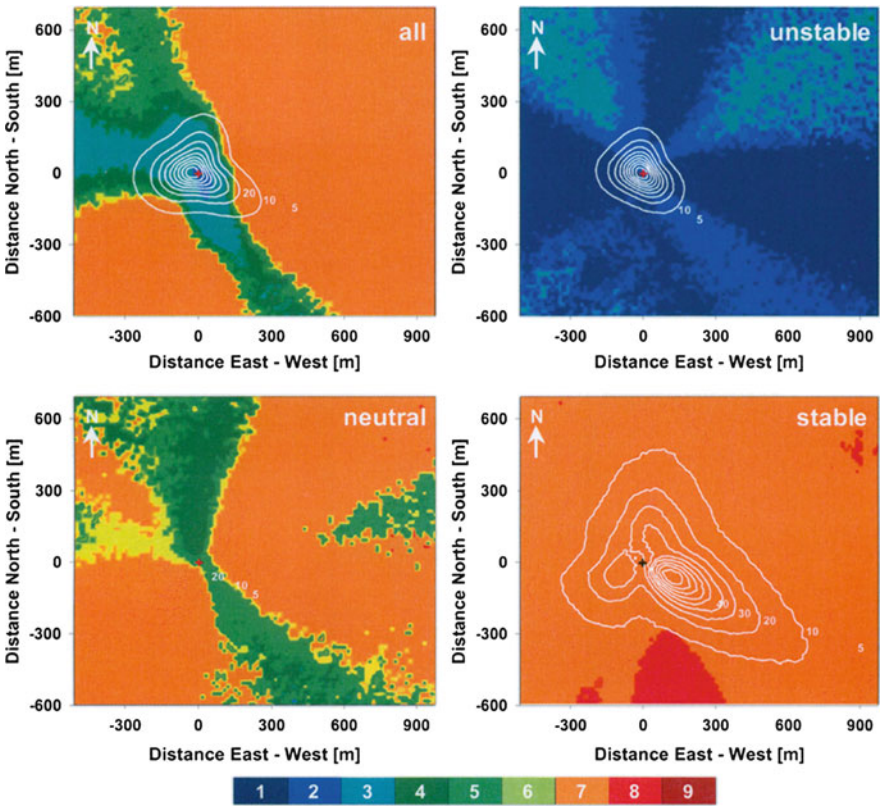

Fig. 12.12 Similar to Fig. 12.11 but for the sensible heat flux

The Waldstein-Weidenbrunnen site was classified as one of six CARBOEUROPE-IP stations having no significant problems of the data quality (Göckede et al. 2008).

12.3.2.5 Coordinate Rotation

The application of the coordinate rotation is essential for the eddy covariance method, because the mean vertical wind velocity should be zero over the averaging length of typically 30 min (double rotation, Kaimal and Finnigan 1994) or over a longer period (planar-fit rotation, Wilczak et al. 2001). The benefit of the latter method is that nonsteady-state time series do not generate unrealistic rotation angles, and the method can also be applied with different rotation matrixes for different wind sectors (Paw U et al. 2000; Siebicke et al. 2012). For nearly automatic and permanent measuring programs, the double rotation method is easier to handle (Rebmann et al. 2012), but for the Waldstein-Weidenbrunnen site, the planar-fit

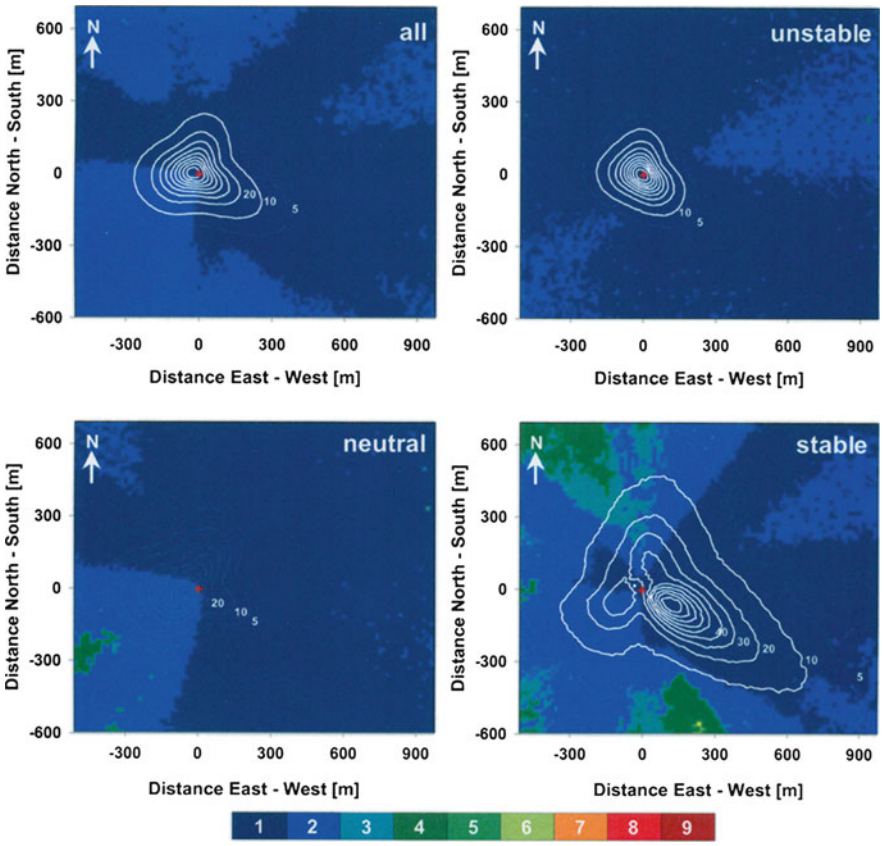

Fig. 12.13 Similar to Fig. 12.11 but for the latent heat flux

method has always been applied since 2002 (see Chap. 4) with a different plane for each month and without a sector-wise rotation. Göckede et al. (2006) proposed the application of the footprint approach to find the best coordinate rotations. They linked the mean vertical wind velocity with the footprint climatology.

The performance of the planar-fit coordinate rotation method was evaluated by the analysis of the vertical wind field. To do so, mean values of the vertical wind component before and after applying the coordinate rotation were computed for each grid cell. The visualization of these results may reveal structures in the vertical wind field, and finding these before the application of the coordinate rotation helps the evaluation of the influence of topography and/or sensor misalignment on the measurements. The visualization of the vertical wind component after applying the planar-fit method indicates whether or not the coordinate rotation was performed successfully, i.e., if there are still significant deviations from the ideal value of zero in certain wind sectors. In this case, the method can be repeated for single wind direction sectors. The results of the evaluation of the vertical wind field for the

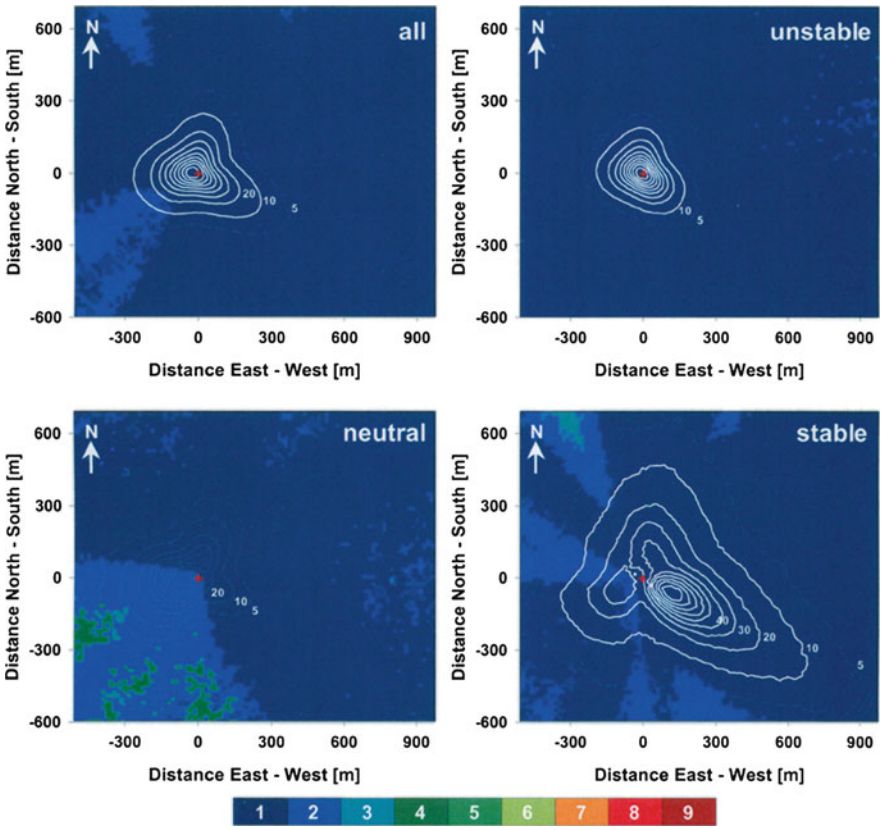

Fig. 12.14 Similar to Fig. 12.11 but for the carbon dioxide flux

Waldstein-Weidenbrunnen site are presented in Fig. 12.15. The application of the planar-fit coordinate rotation method was definitely necessary at the site, and it was performed successfully. The unrotated vertical wind field is generally tilted, with negative values of up to -0.15 m s^{-1} in the northeast and positive values of up to $+0.20$ m s^{-1} in the southwest of the tower position. After rotation of the vertical wind field, there are still certain horizontal structures to be seen, indicating that for some sectors the ideal mean value of zero for the mean vertical wind component could not be obtained. However, the remaining mean values do not exceed absolute mean values of 0.04 m s^{-1} and thus do not have a significant effect on the quality of the eddy covariance fluxes.

The rotation into the mean streamlines is essential for the determination of possible advection (Finnigan et al. 2003). Siebicke et al. (2012) analyzed the effect of different lengths of the planar-fit rotation period on the mean vertical wind velocity and a hypothetical vertical advection. The results of this systematic analysis are given in Fig. 12.16. Figure 12.16a shows the mean vertical wind velocity after

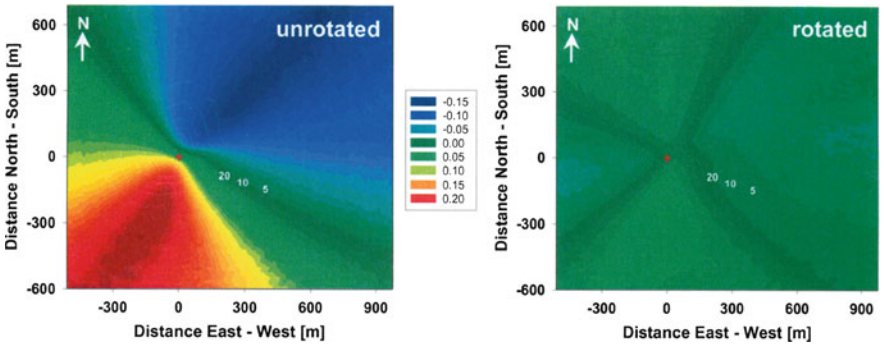

Fig. 12.15 Vertical wind component at the Waldstein-Weidenbrunnen site in the unrotated local (*left*) and rotated (*right*) coordinate system. The tower position is marked by the *red cross*, and the *white isolines* indicate form and position of the footprint climatology for all stratification cases. The colors in the background show the average value of the vertical wind component of each matrix element before (*left graph*) and after (*right graph*) performing the planar-fit coordinate rotation method (Göckede et al. 2005a, Published with kind permission of © Authors 20,105, All rights reserved)

sequential planar fit with window lengths from 2.3 to 400 days. Since planar fit acts as a high-pass filter tuned by the window length, the difference of the mean vertical wind velocity between a 2.3-day window length and a 400-day window length is due to the energy contained in the low-frequency part (periods between 2.3 and 400 days) of the spectrum. This difference is significant on the basis of the mean daily cycle of vertical wind velocity, particularly at night when the vertical wind velocity from a 400-day window length is about 200 % of the values from a 2.3-day window length (Fig. 12.16a). The impact of sequential planar-fit window length on the vertical advection is estimated by calculating the mean daily cycle of the vertical advection (Fig. 12.16c) from vertical wind velocity (Fig. 12.16a) and the vertical CO_2 concentration distribution (Fig. 12.16b). Differences in vertical wind velocity transfer to differences in vertical advection, with the largest differences at night when advection itself is the largest due to large vertical concentration gradients (Fig. 12.16b). The average impact of sequential planar-fit window length of 400 versus 2.3 days on vertical advection is expressed in Fig. 12.16d. The slope of a linear regression shows that vertical advection from a sequential planar fit with a window length of 400 days is about 50 % larger than vertical advection from a 2.3-day window length. Essentially the same results are obtained using data from EGER-IOP2-periode in June–July 2008 (see Chap. 1). Therefore, it was recommended that an intentional choice of the coordinate rotation window length be made and a sequence of rotation windows be applied if necessary rather than letting the window length be determined by an arbitrary length of the data set. A sequential coordinate rotation with adjustable window length as well as sector-wise coordinate rotation according to individually selectable sector borders should be made available as a user selectable option of major flux processing software packages, as realized by Mauder and Foken (2015).

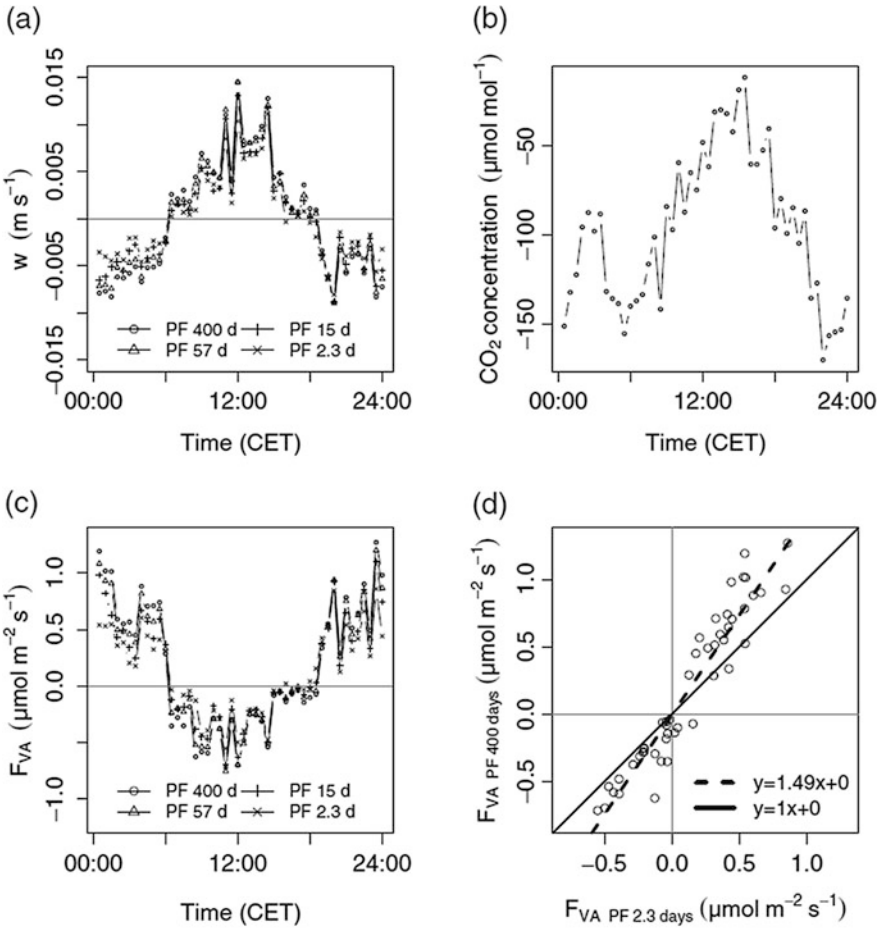

Fig. 12.16 (**a**) Mean daily cycle (30-min resolution) of vertical wind velocity on top of the main tower (long-term data set, see Table 12.1) for planar-fit window lengths from 2.3 to 400 days; (**b**) mean daily cycle (30-min resolution) of vertical CO_2 concentration distribution (difference between the concentration at 32 m height and the mean concentration of the profile from 0 to 32 m during EGER-IOP1 (Table 12.1)); (**c**) hypothetical mean daily cycle of vertical advection, computed as a product of data in (**a**) and (**b**), for planar-fit window lengths from 2.3 to 400 days; (**d**) regression of vertical advection (as in **c**) with a planar-fit window length of 400 days versus vertical advection with a planar-fit window length of 2.3 days and linear model fit (*dashed line*) after Siebicke et al. (2012, published with kind permission of © Springer, Vienna 2012, All rights reserved)

12.3.3 Energy Balance Closure

The Waldstein-Weidenbrunnen site was one of the first sites for which data of the unclosed energy balance were published (Aubinet et al. 2000). Unfortunately, the

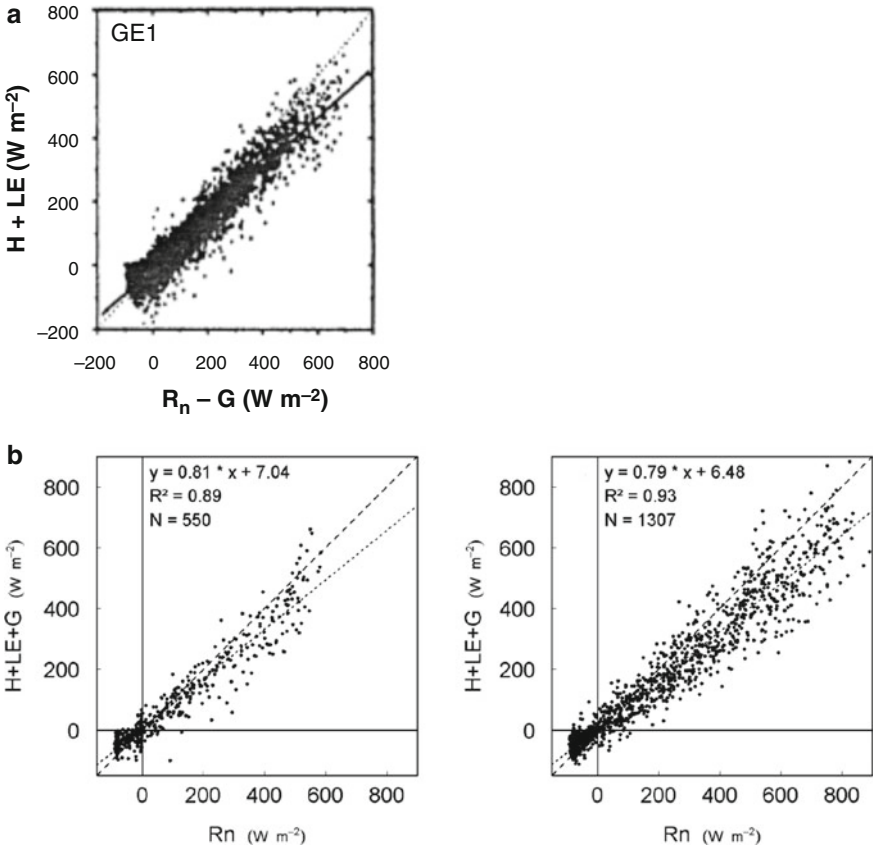

Fig. 12.17 (**a**) Comparison of the turbulent fluxes and the available energy for the period 1997–1999; the slope of the regression line is 0.80 (Aubinet et al. 2000, published with kind permission of © Academic Press, New York 2000, All rights reserved). (**b**) Comparison of the turbulent and the ground heat fluxes with the net radiation for the periods (see Table 12.1) EGER-IOP1 (2007, *left*) and EGER-IOP2 (2008, *right*) according to Foken et al. (2012a, Suppl., Published with kind permission of © Authors 2012, All rights reserved)

figures were reversed. The results for Waldstein-Weidenbrunnen (GE-1) are shown in the figure for GE-3. The corrected figure was published again by Foken (2008a) and shows an 80 % closure for the period 1997–1999 (Fig. 12.17a). The energy balance closure was also investigated for short periods during the EGER-IOP1/IOP2 research periods in 2007 and 2008 and was found to be 81 % and 79 %, respectively (Fig. 12.17b; Foken et al. 2012a, Suppl.). The results indicate that the large clearing south of the site resulting from the Kyrill storm event in January 2007 (see Chap. 2) had no visible influence on the energy balance closure – or that the reason for the unclosed energy balance are heterogeneities of the area (mountains, valleys, forest, and agricultural fields) and not the heterogeneity of typically 100–300 m

scale between forest and clearing. For further investigations of the whole data set, see Chap. 4.

12.4 Conclusions

Not all principal investigators of FLUXNET sites make raw data available to the larger community. Therefore, it was a good choice by the European carbon flux programs (see Chap. 1) to use the Waldstein-Weidenbrunnen site as a test site for data quality investigations and software intercomparisons (Mauder et al. 2008). The available raw data and the presented results for the site convinced the principal investigators to take part in an analysis of most of the European FLUXNET sites – 18 stations during CARBOEUROFLUX (Rebmann et al. 2005) and 25 stations during CARBOEUROP-IP (Göckede et al. 2008). Recent data quality analyses (Foken et al. 2012b; Mauder et al. 2013) and footprint investigations (Rannik et al. 2012) are an integral part of all flux measuring programs.

For the Waldstein-Weidenbrunnen site itself, it follows (Göckede et al. 2008) that no problems were found with the data quality and turbulent fluxes. About 86 % of the target area "spruce forest" is part of the footprint. If clearings are also included in the target area, the footprint covers nearly 100 %. The large clearing south of the site does not obviously affect the data quality. More details of the data quality analysis of the site are given in Chap. 4.

According to the investigations made at the Waldstein-Weidenbrunnen site, the following schema for data quality analysis is proposed:

- Generation of a land cover map of the site with a resolution lower than 100 m; if possible this should be on the basis of remote-sensing data.
- Calculation of a footprint climatology for turbulent fluxes over a time period of some months to a year, preferably with a Lagrangian model and a flux aggregation schema for the determination of the effective roughness length (Göckede et al. 2006).
- Linking of the footprint climatology with the data quality flags of the turbulent fluxes (Foken et al. 2004), which are available in most of the software packages (Foken et al. 2012b), for selection of possible areas and situations with a bad data quality rating.
- Linking the footprint climatology (about 1-month period) with the mean vertical wind (unrotated) to find wind direction sectors for the rotation. Control of the effect of rotation with this method. Application of the "sequential planar-fit rotation" method (Siebicke et al. 2012), which applies a sequence of individual rotations, where the optimal rotation length can be chosen depending on the site and application.
- Test of the energy balance closure. If the closure is lower than 100 % but larger than about 70 %, the site may be affected by mesoscale heterogeneities. In such cases, the sensible and latent heat flux should be corrected, probably according

to the buoyancy flux (Charuchittipan et al. 2014), but – according to the present state of knowledge—the trace gas fluxes should either not be corrected (Foken et al. 2012b) or corrected by a similar percentage as the latent heat flux (Gatzsche 2015, personal communication), but this needs further tests. If the closure is larger than 100 % or lower than 70 %, the data should be checked for possible errors.

For further recommendations for FLUXNET sites, see Chap. 19.

Acknowledgment This work was supported by the EU projects CARBOEUROFLUX (ENVK2-1999-00229), CARBOEUROPE-IP (GOCE-CT-2003-505572), and INTAS 1501, projects of the German Federal Ministry of Education and Research (VERTIKO project, afo-2000, 07 ATF37; fourth project of BITÖK, PT BEO 51-0339476 D), and the German Science Foundation, project FO 226/16-1. Furthermore, we thank Tobias Biermann, Martina Hunner, Alexander Mangold, Lucia Reithmaier (now Seebach), and Friederike Rütz for the calculation of selected results within their master theses and Matthias Mauder and Tiina Markkanen for supporting the CARBOEUROPE-IP data quality analysis.

References

Acevedo OC, Moraes OLL, Degrazia GA, Fitzjarrald DR, Manzi AO, Campos JG (2009) Is friction velocity the most appropriate scale for correcting nocturnal carbon dioxide fluxes? Agric Forest Meteorol 149:1–10

Amiro BD (1998) Footprint climatologies for evapotranspiration in a boreal catchment. Agric Forest Meteorol 90:195–201

Aubinet M, Grelle A, Ibrom A, Rannik Ü, Moncrieff J, Foken T, Kowalski AS, Martin PH, Berbigier P, Bernhofer C, Clement R, Elbers J, Granier A, Grünwald T, Morgenstern K, Pilegaard K, Rebmann C, Snijders W, Valentini R, Vesala T (2000) Estimates of the annual net carbon and water exchange of forests: the EUROFLUX methodology. Adv Ecol Res 30:113–175

Aubinet M, Clement R, Elbers J, Foken T, Grelle A, Ibrom A, Moncrieff H, Pilegaard K, Rannik U, Rebmann C (2003) Methodology for data acquisition, storage and treatment. In: Valentini R (ed) Fluxes of carbon, water and energy of European forests, Ecological studies, vol 163. Springer, Berlin, pp 9–35

Baldocchi D, Meyers T (1998) On using eco-physiological, micrometeorological and biogeochemical theory to evaluate carbon dioxide, water vapor and trace gas fluxes over vegetation. Agric Forest Meteorol 90:1–25

Blackadar AK (1997) Turbulence and diffusion in the atmosphere. Springer, Berlin/Heidelberg, 185 pp

Cellier P, Brunet Y (1992) Flux-gradient relationships above tall plant canopies. Agric Forest Meteorol 58:93–117

Charuchittipan D, Babel W, Mauder M, Leps J-P and Foken T (2014) Extension of the averaging time of the eddy-covariance measurement and its effect on the energy balance closure. Bound-Layer Meteorol 152:303–327

Claussen M (1990) Area-averaging of surface fluxes in a neutrally stratified, horizontally inhomogeneous atmospheric boundary layer. Atmos Environ Part A 24:1349–1360

DeBruin HAR, Bink NJ, Kroon LJ (1991) Fluxes in the surface layer under advective conditions. In: Schmugge TJ, André JC (eds) Workshop on land surface evaporation, measurement and parameterization. Springer, New York, NY, pp 157–169

Eigenmann R, Metzger S, Foken T (2009) Generation of free convection due to changes of the local circulation system. Atmos Chem Phys 9:8587–8600

Falge E, Baldocchi D, Olson R, Anthoni P, Aubinet M, Bernhofer C, Burba G, Ceulemans R, Clement R, Dolman H, Granier A, Gross P, Grunwald T, Hollinger D, Jensen NO, Katul G, Keronen P, Kowalski A, Lai CT, Law BE, Meyers T, Moncrieff H, Moors E, Munger JW, Pilegaard K, Rannik U, Rebmann C, Suyker A, Tenhunen J, Tu K, Verma S, Vesala T, Wilson K, Wofsy S (2001) Gap filling strategies for long term energy flux data sets. Agric Forest Meteorol 107:71–77

Finnigan J (2000) Turbulence in plant canopies. Annu Rev Fluid Mech 32:519–571

Finnigan JJ, Clement R, Malhi Y, Leuning R, Cleugh HA (2003) A re-evaluation of long-term flux measurement techniques, Part I: Averaging and coordinate rotation. Bound-Layer Meteorol 107:1–48

Foken T (2008a) The energy balance closure problem – an overview. Ecol Appl 18:1351–1367

Foken T (2008b) Micrometeorology, Springer, Berlin, 308 pp (2nd edition 2017)

Foken T, Leclerc MY (2004) Methods and limitations in validation of footprint models. Agric Forest Meteorol 127:223–234

Foken T, Wichura B (1996) Tools for quality assessment of surface-based flux measurements. Agric Forest Meteorol 78:83–105

Foken T, Skeib G, Richter SH (1991) Dependence of the integral turbulence characteristics on the stability of stratification and their use for Doppler-Sodar measurements. Z Meteorol 41:311–315

Foken T, Jegede OO, Weisensee U, Richter SH, Handorf D, Görsdorf U, Vogel G, Schubert U, Kirzel H-J, Thiermann V (1997) Results of the LINEX-96/2 experiment. Dt Wetterdienst, Forsch. Entwicklung, Arbeitsergebnisse. 48:75 pp

Foken T, Mangold A, Hierteis M, Wichura B, Rebmann C (1999) Characterization of the heterogeneity of the terrain by normalized turbulence characteristics. 13th symposium on boundary layer and turbulence, Dallas, TX, 10–15 Jan 1999. Am Meteorol Soc, Boston, pp 26–27

Foken T, Mangold A, Rebmann C, Wichura B (2000) Characterization of a complex measuring site for flux measurements. 14th symposium on boundary layer and turbulence, Aspen, CO, 07–11 Aug 2000. Am Meteorol Soc, Boston, pp 388–389

Foken T, Göckede M, Mauder M, Mahrt L, Amiro BD, Munger JW (2004) Post-field data quality control. In: Lee X et al (eds) Handbook of micrometeorology: a guide for surface flux measurement and analysis. Kluwer, Dordrecht, pp 181–208

Foken T, Meixner FX, Falge E, Zetzsch C, Serafimovich A, Bargsten A, Behrendt T, Biermann T, Breuninger C, Dix S, Gerken T, Hunner M, Lehmann-Pape L, Hens K, Jocher G, Kesselmeier J, Lüers J, Mayer JC, Moravek A, Plake D, Riederer M, Rütz F, Scheibe M, Siebicke L, Sörgel M, Staudt K, Trebs I, Tsokankunku A, Welling M, Wolff V, Zhu Z (2012a) Coupling processes and exchange of energy and reactive and non-reactive trace gases at a forest site – results of the EGER experiment. Atmos Chem Phys 12:1923–1950

Foken T, Leuning R, Oncley SP, Mauder M, Aubinet M (2012b) Corrections and data quality. In: Aubinet M et al (eds) Eddy covariance: a practical guide to measurement and data analysis. Springer, Dordrecht, pp 85–131

Garratt JR (1978) Flux profile relations above tall vegetation. Quart J Roy Meteorol Soc 104:199–211

Garratt JR (1992) The atmospheric boundary layer. Cambridge University Press, Cambridge, 316 pp

Göckede M, Rebmann C, Foken T (2004) A combination of quality assessment tools for eddy covariance measurements with footprint modelling for the characterisation of complex sites. Agric Forest Meteorol 127:175–188

Göckede M, Mauder M, Foken T (2005a) Report on results for the site Weidenbrunnen (DE-Wei), CARBOEUROPE-IP, Task 1.2.1 Footprint and quality assessment of main flux sites (unpublished). University of Bayreuth, Department of Micrometeorology, Bayreuth, 16 pp

Göckede M, Markkanen T, Mauder M, Arnold K, Leps JP, Foken T (2005b) Validation of footprint models using natural tracer measurements from a field experiment. Agric Forest Meteorol 135:314–325

Göckede M, Markkanen T, Hasager CB, Foken T (2006) Update of a footprint-based approach for the characterisation of complex measuring sites. Bound-Layer Meteorol 118:635–655

Göckede M, Thomas C, Markkanen T, Mauder M, Ruppert J, Foken T (2007) Sensitivity of Lagrangian stochastic footprints to turbulence statistics. Tellus. 59B:577–586

Göckede M, Foken T, Aubinet M, Aurela M, Banza J, Bernhofer C, Bonnefond J-M, Brunet Y, Carrara A, Clement R, Dellwik E, Elbers JA, Eugster W, Fuhrer J, Granier A, Grünwald T, Heinesch B, Janssens IA, Knohl A, Koeble R, Laurila T, Longdoz B, Manca G, Marek M, Markkanen T, Mateus J, Matteucci G, Mauder M, Migliavacca M, Minerbi S, Moncrieff JB, Montagnani L, Moors E, Ourcival J-M, Papale D, Pereira J, Pilegaard K, Pita G, Rambal S, Rebmann C, Rodrigues A, Rotenberg E, Sanz MJ, Sedlak P, Seufert G, Siebicke L, Soussana JF, Valentini R, Vesala T, Verbeeck H, Yakir D (2008) Quality control of CarboEurope flux data – Part 1: Coupling footprint analyses with flux data quality assessment to evaluate sites in forest ecosystems. Biogeoscience 5:433–450

Goulden ML, Munger JW, Fan F-M, Daube BC, Wofsy SC (1996) Measurements of carbon sequestration by long-term eddy covariance: method and critical evaluation of accuracy. Glob Chang Biol 2:159–168

Hasager CB, Jensen NO (1999) Surface-flux aggregation in heterogeneous terrain. Quart J Roy Meteorol Soc 125:2075–2102

Hasager CB, Nielsen NW, Jensen NO, Boegh E, Christensen JH, Dellwik E, Soegaard H (2003) Effective roughness calculated from satellite-derived land cover maps and hedge-information used in a weather forecasting model. Bound-Layer Meteorol 109:227–254

Hicks BB, Baldocchi DD, Meyers TP, Hosker RP Jr, Matt DR (1987) A preliminary multiple resistance routine for deriving dry deposition velocities from measured quantities. Water Air Soil Pollut 36:311–330

Högström U (1990) Analysis of turbulence structure in the surface layer with a modified similarity formulation for near neutral conditions. J Atmos Sci 47:1949–1972

Johansson C, Smedman A, Högström U, Brasseur JG, Khanna S (2001) Critical test of Monin-Obukhov similarity during convective conditions. J Atmos Sci 58:1549–1566

Kaimal JC, Finnigan JJ (1994) Atmospheric boundary layer flows: their structure and measurement. Oxford University Press, New York, NY, 289 pp

Leclerc MY, Foken T (2014) Footprints in micrometeorology and ecology, Springer, Heidelberg, 239 pp

Lumley JL, Panofsky HA (1964) The structure of atmospheric turbulence. Interscience Publishers, New York, NY, 239 pp

Markkanen T, Steinfeld G, Kljun N, Raasch S, Foken T (2009) Comparison of conventional Lagrangian stochastic footprint models against LES driven footprint estimates. Atmos Chem Phys 9:5575–5586

Massman WJ, Weil JC (1999) An analytical one-dimensional second-order closure model of turbulence statistics and the Lagrangian time scale within and above plant canopies of arbitrary structure. Bound-Layer Meteorol 91:81–107

Mauder M, Foken T (2015) Documentation and Instruction Manual of the Eddy-Covariance Software Package TK3 (update). Arbeitsergebn, Univ Bayreuth, Abt Mikrometeorol, ISSN 1614–8916. 62:64

Mauder M, Foken T, Clement R, Elbers J, Eugster W, Grünwald T, Heusinkveld B, Kolle O (2008) Quality control of CarboEurope flux data – Part 2: Inter-comparison of eddy-covariance software. Biogeoscience 5:451–462

Mauder M, Cuntz M, Drüe C, Graf A, Rebmann C, Schmid HP, Schmidt M, Steinbrecher R (2013) A strategy for quality and uncertainty assessment of long-term eddy-covariance measurements. Agric Forest Meteorol 169:122–135

Mölder M, Grelle A, Lindroth A, Halldin S (1999) Flux-profile relationship over a boreal forest – roughness sublayer correction. Agric Forest Meteorol 98-99:645–648

Mölders N, Raabe A, Tetzlaff G (1996) A comparison of two strategies on land surface heterogeneity used in a mesoscale ß meteorological model. Tellus 48A:733–749

Oncley SP, Foken T, Vogt R, Kohsiek W, DeBruin HAR, Bernhofer C, Christen A, van Gorsel E, Grantz D, Feigenwinter C, Lehner I, Liebethal C, Liu H, Mauder M, Pitacco A, Ribeiro L, Weidinger T (2007) The energy balance experiment EBEX-2000, Part I: Overview and energy balance. Bound-Layer Meteorol 123:1–28

Panofsky HA, Dutton JA (1984) Atmospheric turbulence – models and methods for engineering applications. Wiley, New York, NY, 397 pp

Panofsky HA, Tennekes H, Lenschow DH, Wyngaard JC (1977) The characteristics of turbulent velocity components in the surface layer under convective conditions. Bound-Layer Meteorol 11:355–361

Paw U KT, Baldocchi D, Meyers TP, Wilson KB (2000) Correction of eddy covariance measurements incorporating both advective effects and density fluxes. Bound-Layer Meteorol 97:487–511

Rannik Ü, Aubinet M, Kurbanmuradov O, Sabelfeld KK, Markkanen T, Vesala T (2000) Footprint analysis for measurements over heterogeneous forest. Bound-Layer Meteorol 97:137–166

Rannik Ü, Markkanen T, Raittila T, Hari P, Vesala T (2003) Turbulence statistics inside and above forest: influence on footprint prediction. Bound-Layer Meteorol 109:163–189

Rannik Ü, Sogachev A, Foken T, Göckede M, Kljun N, Leclerc MY, Vesala T (2012) Footprint analysis. In: Aubinet M et al (eds) Eddy covariance: a practical guide to measurement and data analysis. Springer, Berlin, pp 211–261

Raupach MR, Finnigan JJ, Brunet Y (1996) Coherent eddies and turbulence in vegetation canopies: the mixing-layer analogy. Bound-Layer Meteorol 78:351–382

Rebmann C (2003) Kohlendioxid-, Wasserdampf- und Energieaustausch eines Fichtenwaldes in Mittelgebirgslage. Dissertation, Universität Bayreuth, Bayreuth, 149 pp

Rebmann C, Göckede M, Foken T, Aubinet M, Aurela M, Berbigier P, Bernhofer C, Buchmann N, Carrara A, Cescatti A, Ceulemans R, Clement R, Elbers J, Granier A, Grünwald T, Guyon D, Havránková K, Heinesch B, Knohl A, Laurila T, Longdoz B, Marcolla B, Markkanen T, Miglietta F, Moncrieff H, Montagnani L, Moors E, Nardino M, Ourcvial J-M, Rambal S, Rannik U, Rotenberg E, Sedlak P, Unterhuber G, Vesala T, Yakir D (2005) Quality analysis applied on eddy covariance measurements at complex forest sites using footprint modelling. Theor Appl Climat 80:121–141

Rebmann C, Kolle O, Heinesch B, Queck R, Ibrom A, Aubinet M (2012) Data acquisition and flux calculations. In: Aubinet M et al (eds) Eddy covariance: a practical guide to measurement and data analysis. Springer, Dordrecht, pp 59–83

Reichstein M, Falge E, Baldocchi D, Papale D, Aubinet M, Berbigier P, Bernhofer C, Buchmann N, Gilmanov T, Granier A, Grünwald T, Havránková K, Ilvesniemi H, Janous D, Knohl A, Laurila T, Lohila A, Loustau D, Matteucci G, Meyers T, Miglietta F, Ourcival J-M, Pumpanen J, Rambal S, Rotenberg E, Sanz M, Tenhunen J, Seufert G, Vaccari F, Vesala T, Yakir D, Valentini R (2005) On the separation of net ecosystem exchange into assimilation and ecosystem respiration: review and improved algorithm. Glob Chang Biol 11:1424–1439

Reithmaier LM, Göckede M, Markkanen T, Knohl A, Churkina G, Rebmann C, Buchmann N, Foken T (2006) Use of remotely sensed land use classification for a better evaluation of micrometeorological flux measurement sites. Theor Appl Climat 84:219–233

Richards JA (1993) Remote sensing digital image analyse – an introduction. Springer, Berlin, 340 pp

Ruppert J, Mauder M, Thomas C, Lüers J (2006) Innovative gap-filling strategy for annual sums of CO_2 net ecosystem exchange. Agric Forest Meteorol 138:5–18

Schmid HP (1994) Source areas for scalars and scalar fluxes. Bound-Layer Meteorol 67:293–318

Schmid HP (1997) Experimental design for flux measurements: matching scales of observations and fluxes. Agric Forest Meteorol 87:179–200

Schuepp PH, Leclerc MY, MacPherson JI, Desjardins RL (1990) Footprint prediction of scalar fluxes from analytical solutions of the diffusion equation. Bound-Layer Meteorol 50:355–373

Siebicke L (2008) Footprint synthesis for the FLUXNET site Waldstein/Weidenbrunnen (DE-Bay) during the EGER experiment. Arbeitsergebn, Univ Bayreuth, Abt Mikrometeorol, ISSN 1614–8916. 38:45 pp

Siebicke L, Hunner M, Foken T (2012) Aspects of CO_2-advection measurements. Theor Appl Climat 109:109–131

Steinfeld G, Raasch S, Markkanen T (2008) Footprints in homogeneously and heterogeneously driven boundary layers derived from a Lagrangian stochastic particle model embedded into large-eddy simulation. Bound-Layer Meteorol 129:225–248

Stoy PC, Mauder M, Foken T, Marcolla B, Boegh E, Ibrom A, Arain MA, Arneth A, Aurela M, Bernhofer C, Cescatti A, Dellwik E, Duce P, Gianelle D, van Gorsel E, Kiely G, Knohl A, Margolis H, McCaughey H, Merbold L, Montagnani L, Papale D, Reichstein M, Serrano-Ortiz P, Sottocornola M, Saunders M, Spano D, Vaccari F, Varlagin A (2012) A data-driven analysis of energy balance closure across FLUXNET research sites: the role of landscape-scale heterogeneity. Agric Forest Meteorol 171–172:137–152

Tennekes H (1982) Similarity relations, scaling laws and spectral dynamics. In: Nieuwstadt FTM, Van Dop H (eds) Atmospheric turbulence and air pollution modelling. D. Reidel Publishing Company, Dordrecht, pp 37–68

Thomas C, Foken T (2002) Re-evaluation of integral turbulence characteristics and their parameterisations. 15th conference on turbulence and boundary layers, Wageningen, NL, 15–19 July 2002. Am Meteorol Soc, Boston, pp 129–132

Thomas C, Foken T (2007a) Organised motion in a tall spruce canopy: temporal scales, structure spacing and terrain effects. Bound-Layer Meteorol 122:123–147

Thomas C, Foken T (2007b) Flux contribution of coherent structures and its implications for the exchange of energy and matter in a tall spruce canopy. Bound-Layer Meteorol 123:317–337

Tillman JE (1972) The indirect determination of stability, heat and momentum fluxes in the atmospheric boundary layer from simple scalar variables during dry unstable conditions. J Clim Appl Meteorol 11:783–792

Vesala T, Rannik U, Leclerc MY, Foken T, Sabelfeld KK (2004) Foreword: Flux and concentration footprints. Agric Forest Meteorol 127:111–116

Vesala T, Kljun N, Rannik U, Rinne J, Sogachev A, Markkanen T, Sabelfeld K, Foken T, Leclerc MY (2008) Flux and concentration footprint modelling: state of the art. Environ Pollut 152:653–666

Vesala T, Kljun N, Rannik Ü, Rinne J, Sogatchev A, Markkanen T, Sabelfeld K, Foken T, Leclerc MY (2010) Flux and concentration footprint modelling. In: Hanrahan G (ed) Modelling of pollutants in complex environmental systems, vol II. ILM Publications, St. Albans, Glendale, pp 339–355

Vickers D, Mahrt L (1997) Quality control and flux sampling problems for tower and aircraft data. J Atmos Oceanic Tech 14:512–526

Wilczak JM, Oncley SP, Stage SA (2001) Sonic anemometer tilt correction algorithms. Bound-Layer Meteorol 99:127–150

Wilson KB, Goldstein AH, Falge E, Aubinet M, Baldocchi D, Berbigier P, Bernhofer C, Ceulemans R, Dolman H, Field C, Grelle A, Law B, Meyers T, Moncrieff J, Monson R, Oechel W, Tenhunen J, Valentini R, Verma S (2002) Energy balance closure at FLUXNET sites. Agric Forest Meteorol 113:223–234

Wohlfahrt G, Anfang C, Bahn M, Haslwanter A, Newesely C, Schmitt M, Drösler M, Pfadenhauer J, Cernusca A (2005) Quantifying nighttime ecosystem respiration of a meadow using eddy covariance, chambers and modelling. Agric Forest Meteorol 128:141–162

Wulfmeyer V, Behrendt A, Kottmeier C, Corsmeier U, Barthlott C, Craig G, Hagen M, Althausen D, Aoshima F, Arpagaus M, Bauer HS, Bennett L, Blyth A, Brandau C, Champollion C, Crewell S, Dick G, Di Girolamo P, Dorninger M, Dufournet Y, Eigenmann R, Engelmann R, Flamant C, Foken T, Gorgas T, Grzeschik M, Handwerker J, Hauck C, Höller H, Junkermann W, Kalthoff N, Kiemle C, Klink S, König M, Krauß L, Long CN, Madonna F, Mobbs S, Neininger B, Pal S, Peters G, Pigeon G, Richard E, Rotach M, Russchenberg H, Schwitalla T, Smith V, Steinacker R, Trentmann J, Turner DD, van Baelen J, Vogt S, Volkert H, Weckwerth T,

Wernli H, Wieser A, Wirth M (2011) The convective and orographically induced precipitation study (COPS): the scientific strategy, the field phase, and research highlights. Quart J Roy Meteorol Soc 137:3–30

Wyngaard JC (1988) Flow-distortion effects on scalar flux measurements in the surface layer: implications for sensor design. In: Hicks BB (ed) Topics in micrometeorology. A Festschrift for Arch Dyer. Springer Netherlands, Dordrecht, pp 19–26

Chapter 13
Interaction Forest–Clearing

Thomas Foken, Andrei Serafimovich, Fabian Eder, Jörg Hübner, Zhongming Gao, and Heping Liu

13.1 Introduction

For around the last 50 years, most of the forests in the Central European hilly regions have been affected by acid rain, beetles, and windthrow. Therefore, we can no longer find any homogeneous forest sites, but rather very patchy structures with small areas of forest and clearing which are often on a scale of 1 ha or smaller. But 20–30 years ago, most of the FLUXNET sites were installed at mostly homogeneous sites. Most of the available papers are related only to the forest, and one footprint discussion

T. Foken (✉)
Am Herrgottsbaum 28, 96120 Bischberg, Germany

Bayreuth Center of Ecology and Environmental Research, University of Bayreuth, Bayreuth, Germany
e-mail: foken@micrometeorology.de

A. Serafimovich
Helmholtz Centre Potsdam, GFZ German Research Centre for Geosciences, Telegrafenberg, Haus A 6, 14473 Potsdam, Germany

F. Eder
Alexander Thamm GmbH, Wilhelm-Wagenfeld-Str. 20, 80807 München, Germany

J. Hübner
Uhl Windkraft Projektierung GmbH & Co. KG, Max-Eyth-Str. 40, 73479 Ellwangen, Germany

Z. Gao • H. Liu
Department of Civil & Environmental Engineering, Washington State University, 405 Spokane Street, Pullman, WA, 99164-2910, USA

T. Foken, A. Serafimovich, F. Eder, and J. Hübner: Affiliation during the work at the Waldstein sites – Department of Micrometeorology, University of Bayreuth, Bayreuth, Germany

T. Foken (ed.), *Energy and Matter Fluxes of a Spruce Forest Ecosystem*,
Ecological Studies 229, DOI 10.1007/978-3-319-49389-3_13

separates forest footprints from non-forest footprints (Göckede et al. 2008). As well, clearings were the focus of researchers (Knohl et al. 2002). But the interaction between the forest and the clearing became a special research topic with the paper by Klaassen et al. (2002), who found increased fluxes at the forest edge at daytime. This study was very interesting for the discussion of the energy balance closure problem (Foken 2008), because these larger fluxes in the vicinity of the abrupt change from forest to clearing might indicate that local circulation systems are a reason for the "unclosed" energy balance. The first experimental studies were also supported by modeling projects (Sogachev et al. 2005; Klaassen and Sogatchev 2006). This was also a topic of wind tunnel studies and modeling approaches (Morse et al. 2002; Belcher et al. 2008). In these studies, it was found for the first time that the maximal flux is not at the forest edge but at a downwind distance of 5–10 canopy heights. This was underlined by several large eddy simulation (LES) studies (Dupont and Brunet 2009; Finnigan et al. 2009; Kanani-Sühring and Raasch 2015). In contrast, Schlegel et al. (2015) found from LES studies and measurements that in the case of a small-scale heterogeneous structure of the forest, the largest discontinuity of turbulence characteristics is near the forest edge.

The Waldstein–Weidenbrunnen site, together with the Köhlerloh site (see Chap. 1), is, after the Kyrill storm in 2007, an excellent natural laboratory for studying the processes highlighted above. We combine horizontal field studies presented in Chap. 14 with studies of coherent structures (Eder et al. 2013 and Chap. 6) and include all available measurements at the forest edge to give a comprehensive picture of secondary circulations, decoupling processes, and turbulent structures to support the recent discussions. The investigations were made within the EGER project and its third intensive measuring period (IOP3) from June 13 to July 26, 2011 (see Chap. 1).

13.2 Materials and Methods

13.2.1 Special Installations at the Forest Edge

According to the aim of the special investigation at the forest edge, a network of towers (Fig. 13.1, Table 13.1, additional to the standard installation given in Chap. 2) was installed. There was a direct line of towers from the Turbulence Tower (TT = M2) to the tower M3 at the forest edge and the tower M4 in the clearing, with turbulence measurements made at a minimum of two levels. Two additional towers (M6 and M7) were installed close to the edge, and the tower M8 was installed in the trunk space at the starting point of the horizontal moving measuring system (HMMS, Hübner et al. 2014). This system was able to measure up- and downwelling short- and longwave radiation, temperature, moisture, and CO_2 and O_3

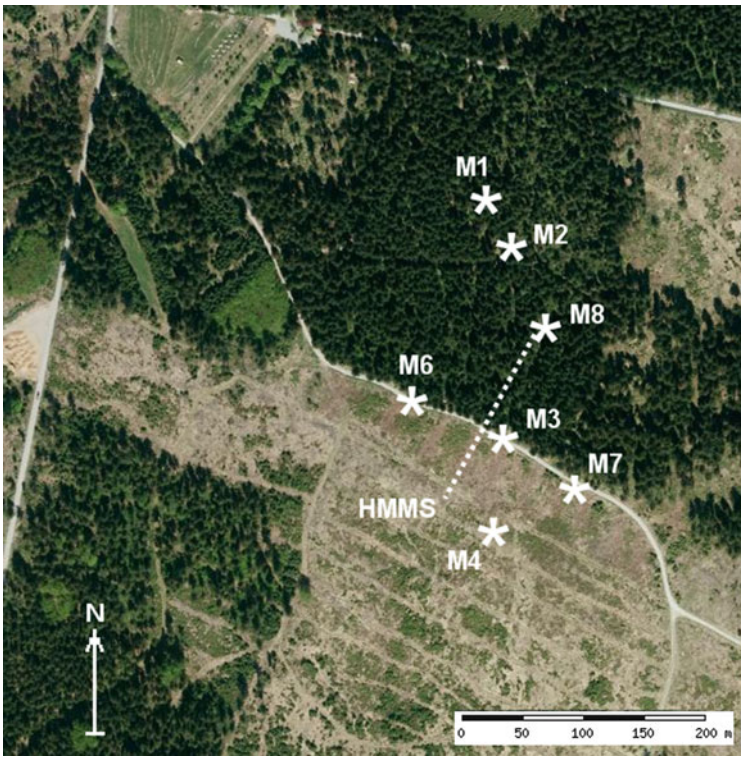

Fig. 13.1 Waldstein–Weidenbrunnen and Köhlerloh measuring sites and positions of the Main Tower (MT = M1), the Turbulence Tower (TT = M2), the forest edge tower M3, turbulence mast M4, towers M6–M8, and horizontal mobile measuring system (HMMS). For more detail, see Serafimovich et al. (2011b). Published with kind permission of © Authors and Bayerische Vermessungsverwaltung 2011, All rights reserved

concentrations along a 150 m path at 1 m height, with half of the path in the forest and half above the clearing (see also Chap. 14). The data were corrected for the dynamical error, dependent on the response time of the applied sensors (Brock and Richardson 2001; Hübner et al. 2014). Furthermore, a CO_2 profile was measured at seven levels on tower M3 (0.5, 2.25, 5, 8, 13, 26, and 36 m) with a LiCor gas analyzer LI-820 and a multiplexer system. The seven heights were measured within a time period of 8 min in parallel with a temperature profile with five heights (1, 5, 18, 25, and 39 m). The system was calibrated twice a day against a CO_2 standard gas and zero air (nitrogen). Unfortunately, the CO_2 profile data are only available for the second and third Golden Day periods (July 4–8 and 14–17), and the temperature data for the first (June 26 and 28–29). For the energy balance closure investigation, net radiation measurements at M1 (top) were used for M1 and M3 (for southerly

Table 13.1 Flux network during EGER-IOP3 (Serafimovich et al. 2011b; for tower positions, see Fig. 13.1), not all devices were used in this chapter (see also Appendix A)

Tower	Height	Sonic anemometer	Gas analyzer
M1 = MM	32 m	Metek USA-1	LiCor LI-7000
M2 = TT	36 m	Metek USA-1	LiCor LI-7500
	26 m	Metek USA-1	
	2 m	Metek USA-1	
M3	41 m	Campbell CSAT3	LiCor LI-7500
	27 m	Metek USA-1	LiCor LI-7500
	2 m	Gill HS	LiCor LI-7500
M4	5 m	Campbell CSAT3	LiCor LI-7500
	2 m	Campbell CSAT3	LiCor LI-7000
M6	5 m	Campbell CSAT3	LiCor LI-7540
	2 m	Metek USA-1	
M7	5 m	Campbell CSAT3	LiCor LI-7540
	2 m	Campbell CSAT3	
M8	2 m	Metek USA-1	

winds, the measurements at M3, 2 m height, were used). The soil heat flux in the forest was assumed to be 5 % of the net radiation. The heat storage in the biomass at noon is approximately 5 Wm^{-2} – on single days up to 10 Wm^{-2} for 2–3 h – and was included in the analysis for M1. For all other details, see Appendix A.

13.2.2 Methods Applied for This Investigation

13.2.2.1 Turbulence Data

The calculation of the turbulence data was done with the software package TK2/TK3 (Mauder and Foken 2004, 2015), which includes all relevant preprocessing and data correction tools (Foken et al. 2012b; Rebmann et al. 2012). Noteworthy are the rotation of the wind vector components by the application of a sector-wise planar fit (Wilczak et al. 2001) in order to remove the mean vertical wind within the 30-min files, the shift of the time series using the time lag of the maximum of the cross-correlation, and the application of a spike detection according to Vickers and Mahrt (1997). If the size of the data file deviated by more than 5 % from the expected file size due to data loss, the 30-min file was not processed.

For the analysis of coherent structure, the 20 Hz data were averaged to 2 Hz after collection in order to reduce computational time. This does not affect the results significantly because only high-frequency turbulence is removed. Furthermore, the time series are normalized by their mean value, and, to prevent border effects, they are extended by adding zero values at both ends. The high-frequency fluctuations

are removed by applying a low-pass filter. For this purpose, a discrete wavelet transformation with bio-orthogonal wavelets is run, which eliminates all fluctuations shorter than a critical event duration of 6.2 s (Thomas and Foken 2005).

13.2.2.2 Wavelet Analysis

After preparation of the 30-min files as described above, a continuous wavelet transform was performed using the Morlet wavelet, from which the wavelet power spectrum was calculated (Torrence and Compo 1998). It is possible to show the importance of different scales. For a location of individual structures in time and frequency, the Mexican Hat wavelet was used (Eder et al. 2013). If atmospheric transport is dominated by coherent structures of a certain scale, the power spectrum of the wavelet coefficients should exhibit a distinct peak at that scale. From this, it is possible to calculate the duration of coherent structures (Thomas and Foken 2005).

The first spectral peak corresponds to the coherent structures developing in the mixing layer above the forest canopy, while additional structures, e.g., which may arise from a heterogeneous canopy architecture, may cause additional peaks at larger scales in the wavelet variance spectrum (Zhang et al. 2007). In order to extract individual coherent events, the zero-crossing method serves as a detection criterion for coherent structures (Collineau and Brunet 1993a), and this proved to produce reliable results (Collineau and Brunet 1993b; Thomas and Foken 2005).

Coherent structures at high plant canopies can be divided into a sweep and an ejection. Thomas and Foken (2007a) assumed that the first half of the event is an ejection motion and the second half a sweep. Accordingly, the flux contribution of ejections (F_{ej}) and sweeps (F_{sw}) can be determined when the conditional averaging is applied over the relevant time intervals (Collineau and Brunet 1993a). Furthermore, Thomas and Foken (2007b) developed a method for determining the coupling of coherent structures in different levels of the canopy. For more details of this method, see Chap. 6.

For the purpose of investigation of the forest edge effect, the classification of the coupling regime after Thomas and Foken (2007b) is applied:

- Wave motion (Wa). The sub-canopy layer and forest canopy are decoupled from the layer above the canopy. Additionally, the flow above the canopy is dominated by linear gravity waves.
- Decoupled canopy (Dc). The above-canopy layer is decoupled from the canopy and the sub-canopy layers.
- Decoupled sub-canopy layer (Ds). The canopy layer is coupled to the air above the canopy, but the sub-canopy layer is still decoupled.
- Coupled sub-canopy layer by sweeps (Cs). The above-canopy and canopy layers are coupled, but the sub-canopy layer is coupled temporally only through the strong sweep motion, not through ejections.
- Fully coupled canopy (C). At all canopy levels, both ejections and sweeps contribute to the exchange of energy and matter: All canopy layers are coupled to the air above the canopy.

Because vertical and horizontal advection processes are closely connected (Aubinet et al. 2003), a similar approach for horizontal coupling was developed by Serafimovich et al. (2011a) with the coupling classes:

- Horizontal decoupled state (Dc_h) with no coupling from the reference site to the observation site.
- Horizontal coupled state (C_h). Coherent structures couple from the reference location to the observation location. The flux contribution of sweeps and ejections is larger at the observation site than at the reference site.

For more details about the data handling for the study of coherent structures, see Eder et al. (2013).

Furthermore, a continuous wavelet transformation was used to calculate local and global wavelet spectra, and an ensemble empirical mode decomposition was applied to extract dominant large-scale coherent structures (Zhang et al. 2010; Gao et al. 2016).

13.3 Results and Discussions

13.3.1 Horizontal and Vertical Fields at the Forest Edge

The horizontal distribution of meteorological elements measured with the HMMS was analyzed in Chap. 14. In the current chapter, only a few results from directly at the forest edge are presented. Because the largest gradients occur here, it is not easy to exactly correct the dynamical error of the response time of the sensors (Hübner et al. 2014), and the results look slightly "wavy" because the travel direction of the moving device changed from clearing–forest to forest–clearing for the next data set and so on. Figure 13.2 shows, for selected meteorological elements, a short time period in the afternoon for a sunny day. There is a very sharp change of the shortwave and longwave downwelling radiation at the forest edge. The high shortwave and the low longwave radiation measured at the clearing also influence the forest at the first few meters from the edge. Inside the forest, some sunny spots are visible. The availability of shortwave radiation is nearly unlimited in the first few meters into the forest. On the other hand, the longwave downwelling radiation is higher in the first few meters of the clearing in comparison to the data from the clearing, due to the longwave radiation of the trees. Highly interesting is the ozone distribution, which follows the distribution of the shortwave downwelling radiation in the forest but with higher ozone concentrations penetrating about 10 m further into the forest. The trunk space at a distance of about 15 m from the edge seems to be horizontally decoupled from the clearing due to low ozone concentration caused by the low radiation and possible reactions with nitrogen oxide (Foken et al. 2012a).

The most instructive vertical distribution of meteorological elements at the forest edge is the carbon dioxide concentration. Because it was measured with one

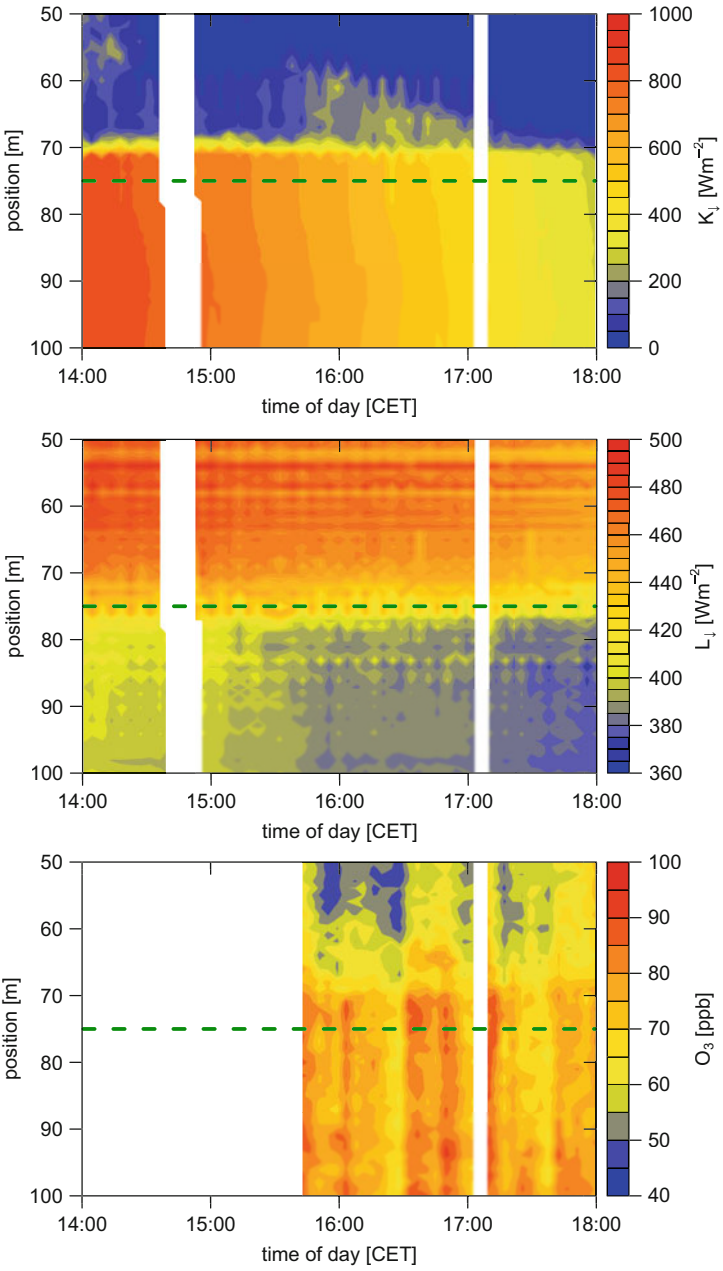

Fig. 13.2 Detailed horizontal profiles during daytime of June 28, 2011, at the forest edge (*horizontal green dotted line*), for shortwave downwelling radiation (*above*), longwave downwelling radiation (*middle*), and ozone (*below*), corrected for dynamical errors and measured with HMMS. Position shows distance from starting point in meters, starting in the forest (50 m) and ending at the clearing (100 m) (Hübner et al. 2014, published with kind permission of © Authors 2014, CC Attribution 3.0 License, All rights reserved)

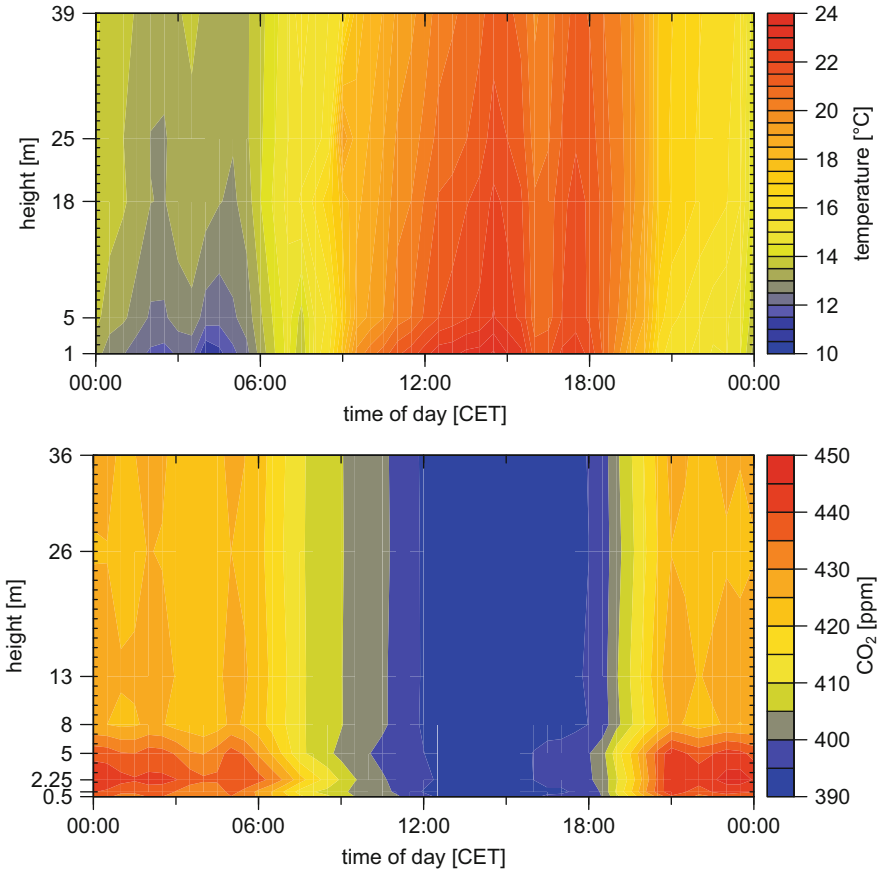

Fig. 13.3 Profile of averaged vertical temperature (*above*) and CO_2 (*below*), installed at M3 at the stated heights on the axis. Half-hour averaged data are presented as a contour plot for 3 days for temperature and 7 days for carbon dioxide (Golden Days, see text) of the EGER-IOP3 period

analyzer and a multiplexer, artifacts can be excluded. Figure 13.3 shows the mean daily cycle of 7 days (second and third Golden Day period of EGER-IOP3, see Chap. 1). Noteworthy are the significantly higher carbon dioxide concentrations of a layer below 5–8 m height during the night and the morning, but already beginning at 4 p.m., which corresponds to a possible oasis effect (see Sect. 13.3.4). The parallel temperature profile shown in Fig. 13.3 (3 days of the first Golden Day period of EGER-IOP3) indicates that at the forest edge, a very stable stratification is only available in the second half on the night – in contrast to the clearing. Because the periods with a uniform daily cycle of carbon dioxide and temperature are not identical, the stability parameter z/L (z, height; L, Obukhov length) was analyzed for both periods for the clearing (M4). The strongest stable stratification is always before midnight ($z/L \approx 0.3$), and the stable stratification is weaker after

midnight ($z/L \approx 0.2$). Therefore, it must be assumed that the high carbon dioxide concentrations are caused by a drainage flow from the trunk space with its higher carbon dioxide concentration (see Chap. 11) and the absence of stable temperature stratification at the edge, which is only present in the second half of the night as a result of strong decoupling above the clearing. It is interesting that directly above the surface in the lowest meter, the stratification is obviously not as stable as above this layer (only visible in the carbon dioxide concentration profile with an additional measuring point at 0.5 m), which could be a result of the roughness elements in this layer.

13.3.2 Coupling Regime

The coupling regime was found by Foken et al. (2012a) to be an excellent indicator for the exchange process in and above the forest and for the understanding of the transport and the reaction of trace gases. The authors could also show that there is a difference in the occurrence of the coupling classes in summer and autumn. While the daily cycle of the fully coupled canopy (C) does not differ, the frequency of the decoupled situations (Wa and Dc) is much higher in autumn, even with such situations at daytime. Similar differences in the coupling regime were found between the forest (Turbulence Tower M2) and the forest edge (tower M3) according to Eder et al. (2013). The data for a summer period show a similar frequency of the fully coupled canopy (C) for both sites (Fig. 13.4). In contrast, the frequency

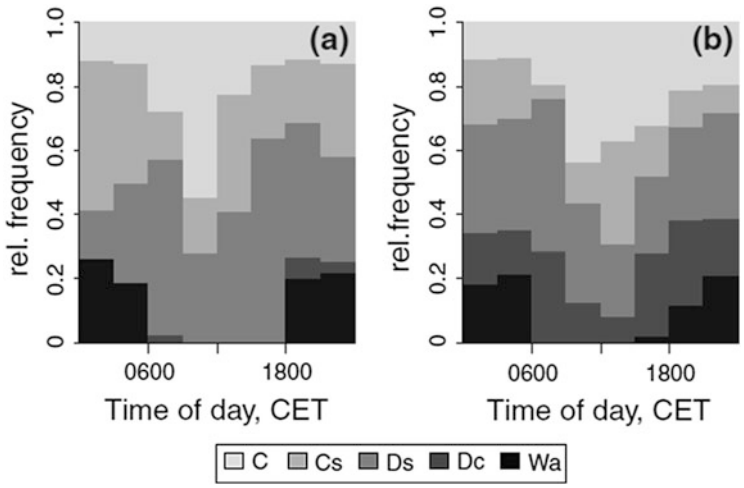

Fig. 13.4 Relative frequency of vertical coupling regimes as a function of time of day, both within the forest at the Turbulence Tower M2 (**a**) and at the forest edge tower M3 (**b**) for the period June 21, 2011, to July 02, 2011; abbreviations of coupling regimes are according to Sect. 13.2.2 (Eder et al. 2013, published with kind permission of © Springer, Berlin, Heidelberg, All rights reserved)

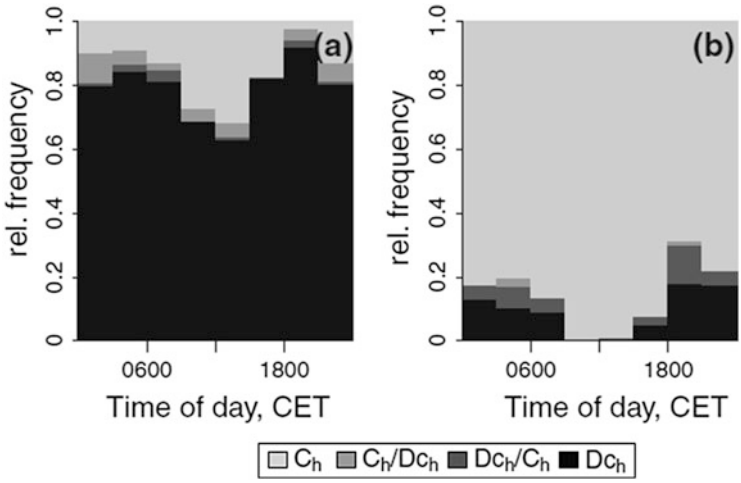

Fig. 13.5 Relative frequency of the horizontal coupling regimes (C_h, complete coupling; C_h/Dc_h, first two towers coupled but second and third tower decoupled; Dc_h/C_h, first two towers decoupled but second and third tower coupled; Dc_h, complete decoupling) as a function of time of day, both along the transect M8–M3–M4 perpendicular to the forest edge (**a**) and along the transect M6–M3–M7 (**b**) for the measurement height at 2.25 m above ground; data from the period June 13, 2011, to July 26, 2011, were used (Eder et al. 2013, published with kind permission of © Springer, Berlin, Heidelberg, All rights reserved)

of the decoupled situations (Wa and Dc) at the forest edge is much higher. This corresponds with the much more stable situation produced over the clearing by longwave radiation cooling, while over the forest – due to the generation of a mixing layer – mechanical turbulence is present much more often. This corresponds very well with Fig. 13.3, which shows a stable layer up to about 5 m height at the forest edge.

The frequency of the horizontal coupling perpendicular to the forest edge is comparable with the frequency of the vertically fully coupled canopy (Fig. 13.5). In all other situations, the clearing and the trunk space (75 m inside the forest at tower M8) are not coupled, and even the forest edge tower (M3) at 2.25 m height is not coupled with the clearing tower (M4). On the other hand, along the forest edge (towers M6–M3–M7), the coupling is, with the exception of some night situations, very good.

13.3.3 Coherent Structures

The size of coherent structures depends on the height of the canopy (Paw U et al. 1992; Finnigan 2000; Feigenwinter and Vogt 2005), and therefore, significant differences between the forest and the clearing should be found. Eder et al. (2013) investigated the event duration (D_e) and the mean temporal separation (T_x). In contrast, at the top of the canopy (M2 and M3) but also at the upper level (5.5 m) of the clearing tower M4, no significant differences could be found. However, the vertical profile (Fig. 13.6) shows significant differences in the trunk space at M2 and M3. The duration and the temporal separation of the structures inside the canopy are much longer than at the forest edge and above the canopy (Serafimovich et al. 2011a). Possible reasons are that only the largest structures can penetrate through the canopy (Thomas and Foken 2007b), and Dupont et al. (2012) stated that structures within the forest are linked to above-canopy coherent motions by pressure diffusion.

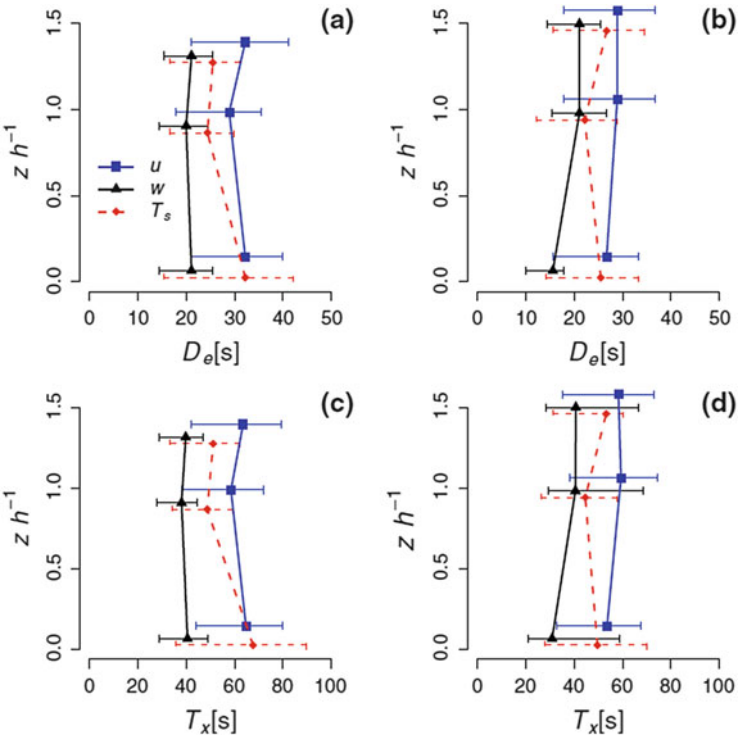

Fig. 13.6 Vertical profiles of event durations D_e (**a**, **b**) and streamwise distances T_x (**c**, **d**) of coherent structures within the forest at the Turbulence Tower M2 (**a**, **c**) and at the forest edge tower M3 (**b**, **d**) that were detected in the time series of the horizontal wind component u, vertical wind component w, and sonic temperature T_s; vertical axis shows measuring height z relative to canopy height h, symbols mark sample medians, and error bars represent interquartile ranges (Eder et al. 2013, published with kind permission of © Springer, Berlin, Heidelberg, All rights reserved)

Eder et al. (2013) found that the flux contribution of coherent structures is about 24–29 % above the forest for scalar fluxes and about 18 % for momentum flux. At the forest edge and the clearing, the contribution is significantly lower with 17–19 % and 12 %, respectively (Fig. 13.7a,d). This tendency is in agreement with the findings by Collineau and Brunet (1993b), who found 40 % for the sensible heat flux and 29 % for the momentum flux. The result also underlines the thesis by Dupont and Brunet (2009) that the structures need a distance of nine times the canopy height for a complete growth to occur. The highest flux contribution was found directly at the top of the canopy. In contrast, the flux contribution in the trunk space is relatively low, with 6 % for momentum flux and 15 % for buoyancy flux, which is also in agreement with literature results (Gao et al. 1989).

In the roughness sublayer above the forest, the ejection motion is stronger than at the canopy top (Fig. 13.7b,c), which is in accordance with previous studies and was reviewed in Chap. 6. When focusing on the contributions of sweeps and ejections at the forest edge (Fig. 13.7e, f), it can be stated that sweeps contribute more around the canopy top and even above the forest, but are not really significant. But at the level 2.25 m, sweeps dominate at the forest edge in contrast to the trunk space (Eder et al. 2013). It was found that in the daily cycle at the top of the towers M1 to M4, the contribution of the ejection is, for scalar and momentum fluxes, larger at daytime than at night. This effect is highly significant at the top of the forest edge tower, mainly for the momentum flux; therefore, upward convective structures at the forest edge at daytime can be postulated. The daily cycle at all towers at the lowest measuring height shows no significant differences between the towers, with more ejection at daytime than at night.

13.3.4 Penetration of Large-Scale Coherent Structures

The penetration of large coherent structures close to the surface was studied in more detail with the ensemble empirical mode decomposition (Gao et al. 2016). The analysis of single cases shows that in the wavelet structures, in the case of northerly winds and stable stratification, large coherent structures at M3 are visible only for the levels 26 and 41 m (Fig. 13.8a). In contrast, for southerly winds under stable stratification, no difference can be found in the coherent structures, including in the level 2.25 m (Fig. 13.8b). At daytime with unstable stratification, coherent structures are present at all levels and for all wavelengths, similar to Fig. 13.8b.

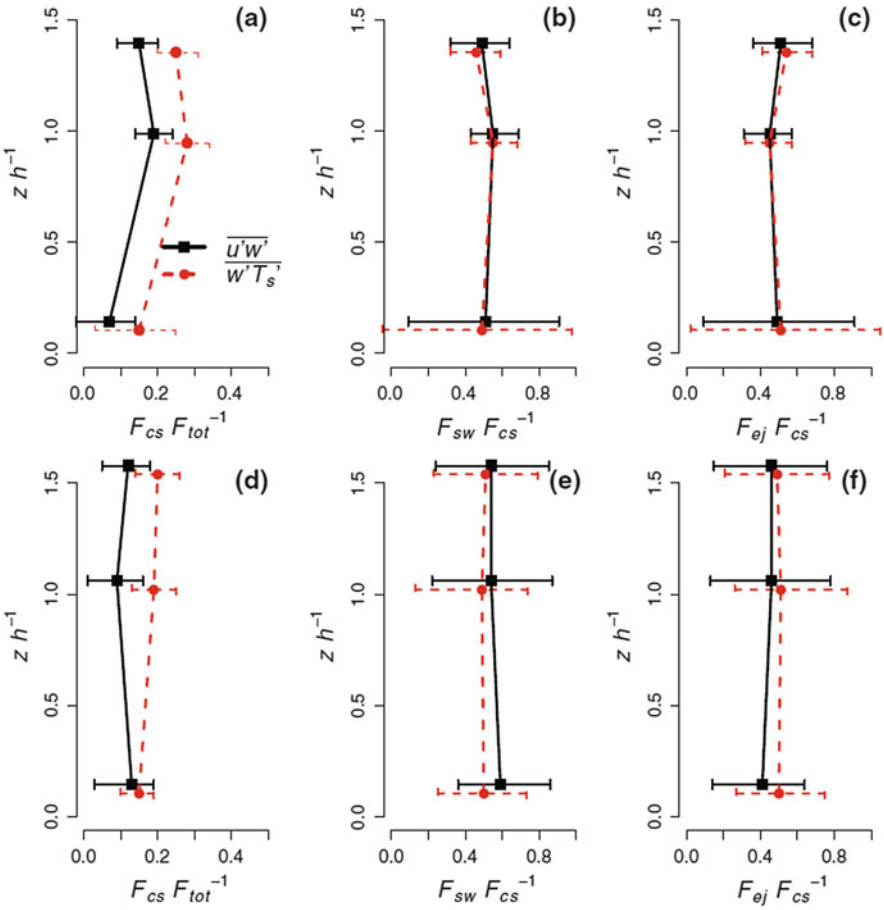

Fig. 13.7 Vertical profiles of the relative flux contribution of coherent structures $F_{cs}\ F_{tot}{}^{-1}$ (**a**, **d**), contributions of sweeps F_{sw} (**b**, **e**), and ejections F_{ej} (**c**, **f**) to coherent transport F_{cs} of momentum flux $\overline{u'w'}$ and buoyancy flux $\overline{w'T_s'}$ within the forest at M2 (**a**–**c**) and at the forest edge tower M3 (**d**–**f**); vertical axis shows measuring height z relative to canopy height h, symbols mark sample medians, and error bars represent interquartile ranges (Eder et al. 2013, published with kind permission of © Springer, Berlin, Heidelberg, All rights reserved)

This finding underlines the global spectra for the wind components (Fig. 13.9). For northerly wind, the energy is significantly lower at the 2.25 m level for all wind components. For southerly wind, the energy is nearly identical for the horizontal components. Only the vertical wind velocity has less energy – as usual – at the lower level for lower frequencies. The daytime measurements show a picture similar to the case of southerly winds.

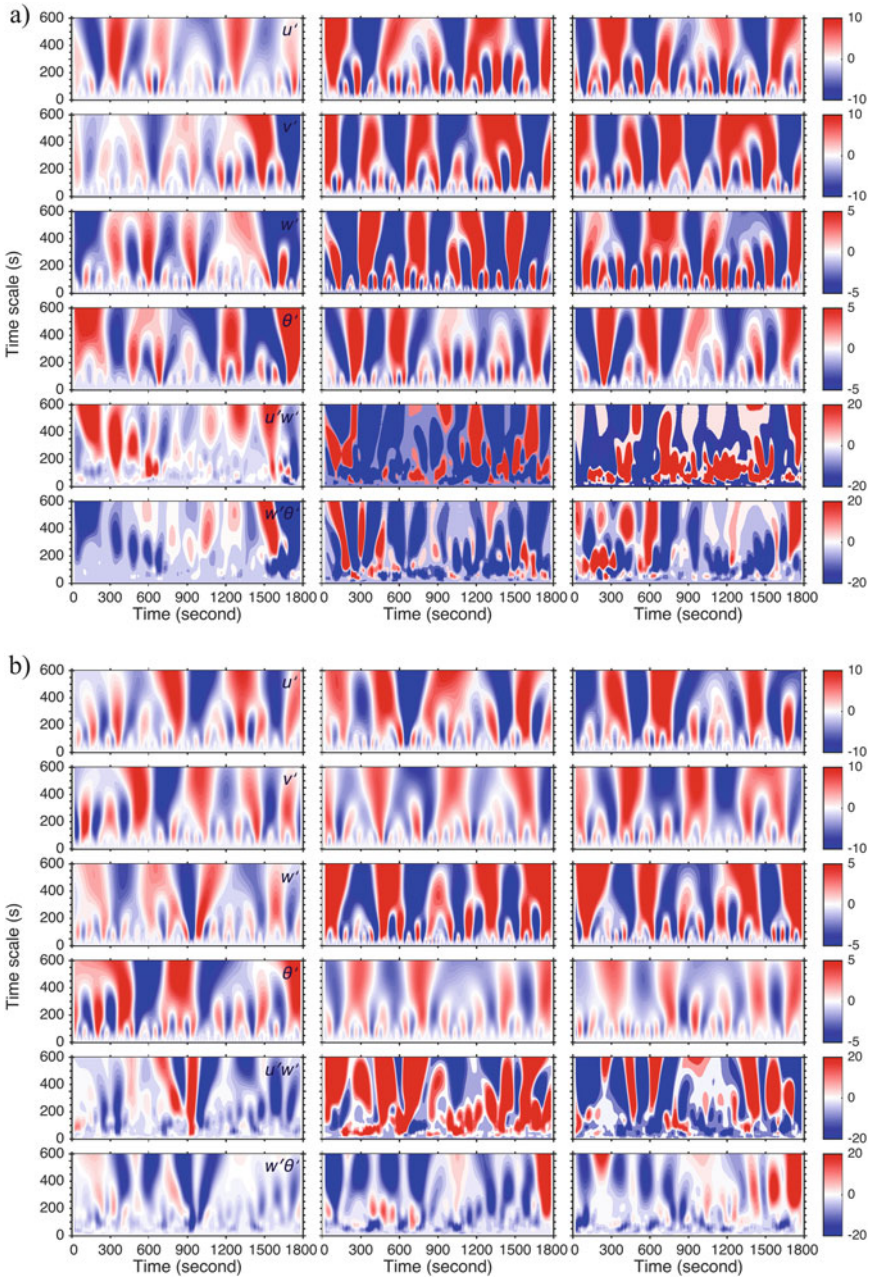

Fig. 13.8 Local wavelet spectra for northerly winds (**a** June 23, 2011, 19:30–20:00) and southerly winds (**b** June 22, 2011, 05:30–06:00). In the columns are shown from left to right the levels 2.25, 26, and 41 m, and in the lines from top to bottom the horizontal wind components along the mean wind direction and perpendicular to the mean wind direction, the vertical wind component, the temperature, the momentum flux, and the buoyancy flux

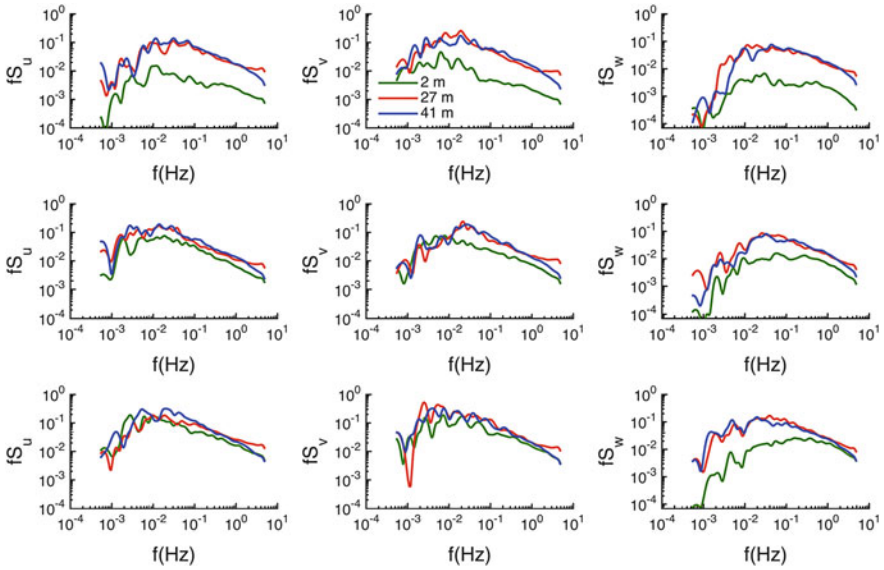

Fig. 13.9 Global wavelet spectra at three levels of tower M3 for the horizontal wind components in the mean wind direction (*u*, *left side*), perpendicular to the mean wind direction (*v*, *middle*), and for the vertical wind component (*w*, *right side*) with the frequency *f*. The upper panel shows the situation for stable stratification and northerly winds (June 23, 2011, 19:30–20:00, at 2.25 m: 0.32 ms^{-1}, 16°), the middle panel for stable stratification and southerly wind (June 22, 2011, 05:30–06:00, at 2.25 m: 0.88 ms^{-1}, 175°), and the lower panel for unstable stratification at daytime (June 21, 2011, 14:30–15:00, at 2.25 m: 1.4 ms^{-1}, 272°)

13.3.5 Energy Balance Closure Problem

Of special interest was the direct determination of the energy balance closure (Fig. 13.10), which was corrected for the heat storage in the canopy. The Bowen ratio is typically $Bo > 1$ for a spruce forest in summer. In contrast, at the forest edge (only cases with wind direction from the clearing were analyzed) and on the clearing, the Bowen ratio is $Bo < 1$, and it is lower in the late afternoon than during the day. This is an indicator for a small oasis effect. The net radiation at the Main Tower (M1) was also used for the forest edge tower M3 and was higher than in the clearing (M4). The residual at M1 was significantly higher, with up to about 200 Wm^{-2} at noon in comparison to both of the other towers with 100–150 Wm^{-2}. In approximate terms, in the afternoon from 3 p.m., the residual is nearly zero. This is an indicator of higher turbulent fluxes at the forest edge. More details about energy balance closure can be found in Chaps. 4 and 12.

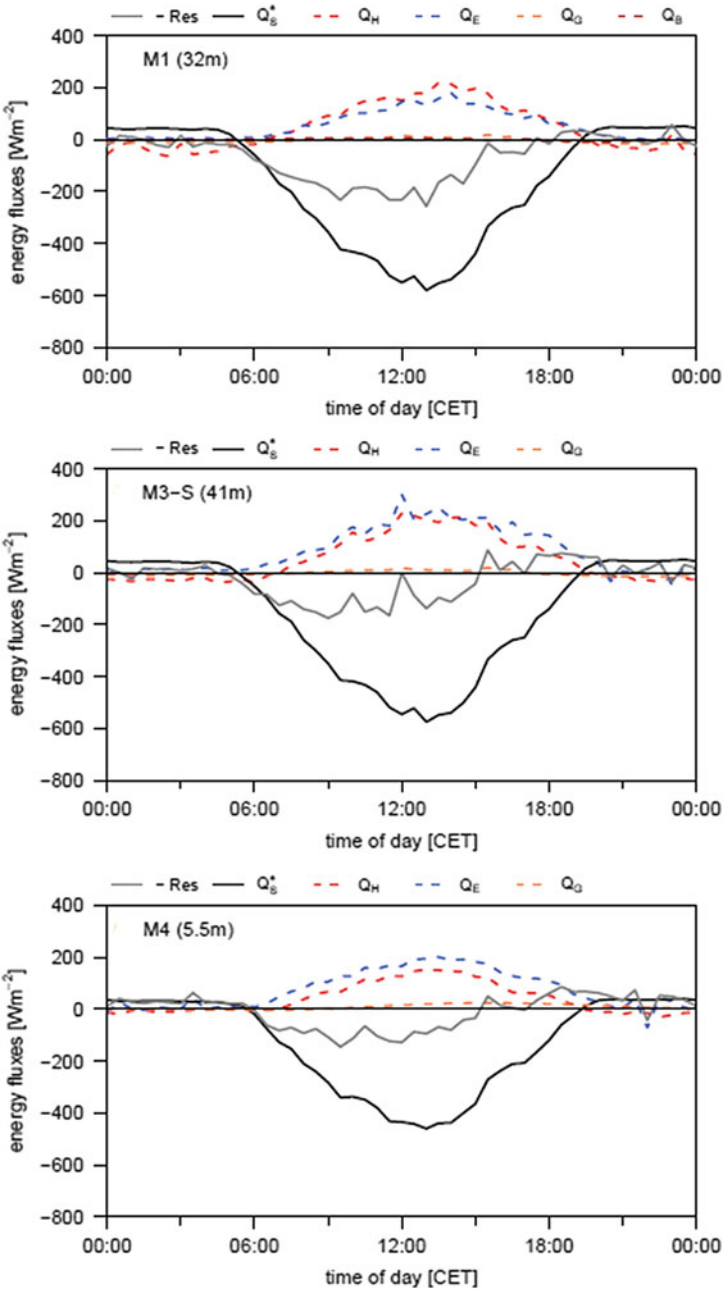

Fig. 13.10 Mean diurnal cycles of the observed energy fluxes along the transect perpendicular to the forest edge for 13 days (Golden Days) of the EGER-IOP3 period. Measurements were performed above the forest at M1 (*above*), at the forest edge at 41 m (M3, *middle*), and at the clearing (M4, *below*), with Q_H, sensible heat flux; Q_E, latent heat flux; Q_G, ground heat flux; Q_s^*, net radiation; *Res*, residual of the energy balance closure

13.4 Conclusions

The puzzle of the presented results invites an interesting discussion about the conditions at the forest edge: The conclusions are not final statements but form a request for further discussion or even research. For final conclusions, see Chap. 19.

Of surprise is the apparent low horizontal coupling. This may be a real effect according to the shown horizontal distribution of ozone but could also reflect a problem with the methodology. Because the horizontal structures are much longer in the forest sub-canopy than at the forest edge, but the analyzing methods look only for the first (shortest) significant structure (Thomas and Foken 2007a; Serafimovich et al. 2011a), it may be possible that the longer structures are also present at the clearing but that shorter structures are dominant. At daytime, the length of the first coherent structure is, due to the better vertical coupling, nearly identical at both sites, and therefore, the method indicates a horizontal coupling. This thesis can be underlined by the good horizontal coupling of the three towers along the forest edge, even under very stable stratification.

The strength of the horizontal coupling could also explain differences in the LES, with a flow maximum at a certain distance from the edge (Dupont and Brunet 2009; Finnigan et al. 2009; Kanani-Sühring and Raasch 2015) and no such maximum in other investigations (Schlegel et al. 2015). In nature, the sub-canopy vegetation is very dense at the forest edge, which can be responsible for the decoupling. If the LES model has a homogeneous tree structure up to the edge, the penetration of air can be large in the trunk space at the forest edge and can be a reason for the strong updrafts at a certain distance from the edge. This should be tested in further LES studies with a reduced airflow into the forest at the edge.

The different horizontal and vertical decoupling may also be affecting the interpretation of advection. The hypothesis of a closed mass balance by horizontal and vertical advection (Aubinet et al. 2003) is not realistic – even when the slope is about 3°, as at the Waldstein–Weidenbrunnen site – under such coupling situations. The alternative hypothesis that the horizontal CO_2 concentration differences are caused by the varying degree to which coherent structures affect the sub-canopy air exchange (see Chap. 6) may be more realistic. However, the two hypotheses may in fact be complementary: Spatially varying penetration depths of turbulent coherent structures may give rise to gradients that lead to horizontal advection by mean flow. Whether the two hypotheses are compatible mainly depends on the time scale at which coherent structures, horizontal concentration differences, and thus gradients occur. Near the forest edge, a drainage flow of carbon dioxide-rich air already starting at the late afternoon (oasis effect) was detected.

The lower turbulent fluxes and the large residual of the energy balance closure above the forest (M1) can also be interpreted in two ways: If the findings by LES (Dupont and Brunet 2009; Finnigan et al. 2009; Kanani-Sühring and Raasch 2015) that a maximal flux is at a distance from the forest edge of about ten times of the canopy height are true, then at the position of M1 (about five times the canopy height), the flux should be lower and not representative for the forest as a whole. On

the other hand, the larger turbulent fluxes at the forest edge in comparison to M1 and the clearing can also fulfill the energy balance closure concept (Foken 2008), with its large fluxes at heterogeneities, and it is in agreement with experimental findings by Klaassen et al. (2002).

Interesting is the decoupling at the forest edge occurring mainly in the second half of the night, while at the clearing (Fig. 13.10 for M4), the strongest stable stratification is – as usual – in the first half of the night. At the forest edge, the stabilization of the stratification due to longwave cooling is probably compensated by a warm drainage flow from the forest and a better vertical coupling. The large-scale coherent structures do not penetrate into this drainage flow (Figs. 13.8 and 13.9 for northerly winds). This may be a topic of further research, because the experimental design used was not adapted to investigate such processes. But such research could have a very practical aim, because the specific emissions of the variously sized clearings found in the increasingly heterogeneous forests are unknown and the few available studies cannot answer this question (Knohl et al. 2002).

No clear conclusion can be drawn about the existence of a secondary circulation. Eder et al. (2013) already concluded that the strong ejections at the forest edge can be an indication of a secondary circulation. In addition, the larger residual above the forest in comparison to the forest edge is a second criterion. Furthermore, the Köhlerloh clearing is large enough to generate convective processes (Shen and Leclerc 1997) and has unstable conditions with low wind speeds (Eigenmann et al. 2009). However, such situations are difficult to see with the sodar, although one situation was found by Foken et al. (2012a). Unfortunately, Doppler lidar measurements were not funded for this experiment. Such an experiment – combination of lidar measurements and LES modeling – was realized above the larger but isolated Yatir forest in Israel. Eder et al. (2015), using measurements and LES modeling, found secondary circulations which had a contribution to the turbulent fluxes of 19 %, slightly smaller than the typical closure gap at the Waldstein–Weidenbrunnen site (Chap. 12), with 17 % at the forest edge and about 25 % above the forest and the clearing. Therefore, it is not presumptuous to postulate the existence of secondary circulations for the Waldstein–Weidenbrunnen site as well, at least at daytime. Whether the size of the heterogeneities is related to forest–clearing or to forest areas–agricultural areas in the surroundings is still a question of further research (see also Chaps. 12 and 19).

Acknowledgment This research was funded by the German Science Foundation within the DFG PAK 446 project, mainly the subproject FO226/21-1. H. Liu acknowledges support by the National Science Foundation AGS under grant 1419614. The heat storage in the biomass was calculated by Kathrin Gatzsche in her master's thesis.

References

Aubinet M, Heinesch B, Yernaux M (2003) Horizontal and vertical CO_2 advection in a sloping forest. Bound-Lay Meteorol 108:397–417

Belcher SE, Finnigan JJ, Harman IN (2008) Flows through forest canopies in complex terrain. Ecol Appl 18:1436–1453

Brock FV, Richardson SJ (2001) Meteorological measurement systems. Oxford University Press, New York, 290 pp

Collineau S, Brunet Y (1993a) Detection of turbulent coherent motions in a forest canopy. Part I: Wavelet analysis. Bound-Lay Meteorol 65:357–379

Collineau S, Brunet Y (1993b) Detection of turbulent coherent motions in a forest canopy. Part II: Time-scales and conditional averages. Bound-Lay Meteorol 66:49–73

Dupont S, Brunet Y (2009) Coherent structures in canopy edge flow: a large-eddy simulation study. J Fluid Mech 630:93–128

Dupont S, Irvine M, Bonnefond J-M, Lamaud E, Brunet Y (2012) Turbulent structures in a pine forest with a deep and sparse trunk space: stand and edge regions. Bound-Lay Meteorol 143:309–336

Eder F, Serafimovich A, Foken T (2013) Coherent structures at a forest edge: properties, coupling and impact of secondary circulations. Bound-Lay Meteorol 148:285–308

Eder F, De Roo F, Rotenberg E, Yakir D, Schmid HP, Mauder M (2015) Secondary circulations at a solitary forest surrounded by semi-arid shrubland and their impact on eddy-covariance measurements. Agric For Meteorol 211–212:115–127

Eigenmann R, Metzger S, Foken T (2009) Generation of free convection due to changes of the local circulation system. Atmos Chem Phys 9:8587–8600

Feigenwinter C, Vogt R (2005) Detection and analysis of coherent structures in urban turbulence. Theor Appl Climatol 81:219–230

Finnigan J (2000) Turbulence in plant canopies. Annu Rev Fluid Mech 32:519–571

Finnigan JJ, Shaw RH, Patton EG (2009) Turbulence structure above a vegetation canopy. J Fluid Mech 637:687–424

Foken T (2008) The energy balance closure problem – an overview. Ecolog Appl 18:1351–1367

Foken T, Meixner FX, Falge E, Zetzsch C, Serafimovich A, Bargsten A, Behrendt T, Biermann T, Breuninger C, Dix S, Gerken T, Hunner M, Lehmann-Pape L, Hens K, Jocher G, Kesselmeier J, Lüers J, Mayer JC, Moravek A, Plake D, Riederer M, Rütz F, Scheibe M, Siebicke L, Sörgel M, Staudt K, Trebs I, Tsokankunku A, Welling M, Wolff V, Zhu Z (2012a) Coupling processes and exchange of energy and reactive and non-reactive trace gases at a forest site – results of the EGER experiment. Atmos Chem Phys 12:1923–1950

Foken T, Leuning R, Oncley SP, Mauder M, Aubinet M (2012b) Corrections and data quality. In: Aubinet M et al (eds) Eddy covariance: a practical guide to measurement and data analysis. Springer, Dordrecht, pp 85–131

Gao W, Shaw RH, Paw U KT (1989) Observation of organized structure in turbulent flow within and above a forest canopy. Bound-Lay Meteorol 47:349–377

Gao Z, Liu H, Russell ES, Huang J, Foken T, Oncley SP (2016) Large eddies modulating flux convergence and divergence in a disturbed unstable atmospheric surface layer. J Geophys Res: Atmos 121:1475–1492

Göckede M, Foken T, Aubinet M, Aurela M, Banza J, Bernhofer C, Bonnefond J-M, Brunet Y, Carrara A, Clement R, Dellwik E, Elbers JA, Eugster W, Fuhrer J, Granier A, Grünwald T, Heinesch B, Janssens IA, Knohl A, Koeble R, Laurila T, Longdoz B, Manca G, Marek M, Markkanen T, Mateus J, Matteucci G, Mauder M, Migliavacca M, Minerbi S, Moncrieff JB, Montagnani L, Moors E, Ourcival J-M, Papale D, Pereira J, Pilegaard K, Pita G, Rambal S, Rebmann C, Rodrigues A, Rotenberg E, Sanz MJ, Sedlak P, Seufert G, Siebicke L, Soussana JF, Valentini R, Vesala T, Verbeeck H, Yakir D (2008) Quality control of CarboEurope flux data – part 1: Coupling footprint analyses with flux data quality assessment to evaluate sites in forest ecosystems. Biogeosci 5:433–450

Hübner J, Olesch J, Falke H, Meixner FX, Foken T (2014) A horizontal mobile measuring system for atmospheric quantities. Atmos Meas Tech 7:2967–2980

Kanani-Sühring F, Raasch S (2015) Spatial variability of scalar concentrations and fluxes downstream of a clearing-to-forest transition: A Large-Eddy Simulation study. Bound-Lay Meteorol 155:1–27

Klaassen W, Sogatchev A (2006) Flux footprint simulation downwind of a forest edge. Bound-Lay Meteorol 121:459–473

Klaassen W, van Breugel PB, Moors EJ, Nieveen JP (2002) Increased heat fluxes near a forest edge. Theor Appl Climatol 72:231–243

Knohl A, Kolle O, Minayeva TY, Milyukova IM, Vygodskaya NN, Foken T, Schulze ED (2002) Carbon dioxide exchange of a Russian boreal forest after disturbance by wind throw. Glob Chang Biol 8:1–16

Mauder M and Foken T (2004) Documentation and instruction manual of the eddy covariance software package TK2. Arbeitsergebn, Univ Bayreuth, Abt Mikrometeorol 26:42 pp. ISSN 1614-8916

Mauder M and Foken T (2015) Documentation and Instruction Manual of the Eddy-Covariance Software Package TK3 (update). Arbeitsergebn, Univ Bayreuth, Abt Mikrometeorol 62:64. ISSN 1614-8916

Morse AP, Gardiner BA, Marshall BJ (2002) Mechanisms controlling turbulence development across a forest edge. Bound-Lay Meteorol 103:227–251

Paw U KT, Brunet Y, Collineau S, Shaw RH, Maitani T, Qiu J, Hipps L (1992) On coherent structures in turbulence above and within agricultural plant canopies. Agric For Meteorol 61:55–68

Rebmann C, Kolle O, Heinesch B, Queck R, Ibrom A, Aubinet M (2012) Data acquisition and flux calculations. In: Aubinet M et al (eds) Eddy covariance: a practical guide to measurement and data analysis. Springer, Dordrecht, pp 59–83

Schlegel F, Stiller J, Bienert A, Maas H-G, Queck R, Bernhofer C (2015) Large-eddy simulation study of the effects on flow of a heterogeneous forest at sub-tree resolution. Bound-Lay Meteorol 154:27–56

Serafimovich A, Thomas C, Foken T (2011a) Vertical and horizontal transport of energy and matter by coherent motions in a tall spruce canopy. Bound-Lay Meteorol 140:429–451

Serafimovich A, Eder F, Hübner J, Falge E, Voß L, Sörgel M, Held A, Liu Q, Eigenmann R, Huber K, Duarte HF, Werle P, Gast E, Cieslik S, Liu H and Foken T (2011b) ExchanGE processes in mountainous regions (EGER)- documentation of the intensive observation period (IOP3) June, 13th to July, 26th 2011. Arbeitsergebn, Univ Bayreuth, Abt Mikrometeorol 47:135. ISSN 1614-8916

Shen S, Leclerc MY (1997) Modelling the turbulence structure in the canopy layer. Agric For Meteorol 87:3–25

Sogachev A, Leclerc MJ, Karipot A, Zhang G, Vesala T (2005) Effect of clearcuts on footprints and flux measurements above a forest canopy. Agric For Meteorol 133:182–196

Thomas C, Foken T (2005) Detection of long-term coherent exchange over spruce forest. Theor Appl Climatol 80:91–104

Thomas C, Foken T (2007a) Organised motion in a tall spruce canopy: temporal scales, structure spacing and terrain effects. Bound-Lay Meteorol 122:123–147

Thomas C, Foken T (2007b) Flux contribution of coherent structures and its implications for the exchange of energy and matter in a tall spruce canopy. Bound-Lay Meteorol 123:317–337

Torrence C, Compo GP (1998) A practical guide to wavelet analysis. Bull Am Meteorol Soc 79:61–78

Vickers D, Mahrt L (1997) Quality control and flux sampling problems for tower and aircraft data. J Atmos Oceanic Tech 14:512–526

Wilczak JM, Oncley SP, Stage SA (2001) Sonic anemometer tilt correction algorithms. Bound-Lay Meteorol 99:127–150

Zhang G, Thomas C, Leclerc MY, Karipot A, Gholz HL, Foken T (2007) On the effect of clearcuts on turbulence structure above a forest canopy. Theor Appl Climatol 88:133–137

Zhang Y, Liu H, Foken T, Williams QL, Liu S, Mauder M, Liebethal C (2010) Turbulence spectra and cospectra under the influence of large eddies in the energy balance experiment (EBEX). Bound-Lay Meteorol 136:235–251

Chapter 14
Forest Climate in Vertical and Horizontal Scales

Jörg Hübner, Lukas Siebicke, Johannes Lüers, and Thomas Foken

14.1 Introduction

Microclimate – climate at small scales from 0.01 to 1000 m (Oke 1987) – is a main driver of forest ecosystem processes (e.g. Whittaker 1975; Breshears et al. 1997; Scharenbroch and Bockheim 2007; Chen et al. 1999; Vanwalleghem and Meentemeyer 2009; Closa et al. 2010). The five main variables of forest microclimate (Davies-Colley et al. 2000) are: sunlight, wind (velocity and direction), precipitation, (air and soil) temperature and (air and soil) moisture content.

J. Hübner (✉)
Uhl Windkraft Projektierung GmbH & Co. KG, Max-Eyth-Str. 40, 73479 Ellwangen, Germany
e-mail: joerg.huebner@uni-bayreuth.de

L. Siebicke
Faculty of Forest Sciences and Forest Ecology - Bioclimatology, University of Göttingen, Büsgenweg 2, 37077 Göttingen, Germany

J. Lüers
Bayreuth Center of Ecology and Environmental Research, University of Bayreuth, 95440 Bayreuth, Germany

T. Foken
Am Herrgottsbaum 28, 96120 Bischberg, Germany

Bayreuth Center of Ecology and Environmental Research, University of Bayreuth, Bayreuth, Germany

J. Hübner, L. Siebicke, J. Lüers, T. Foken: Affiliation during the work on the Waldstein sites: Department of Micrometeorology, University of Bayreuth, Bayreuth, Germany

T. Foken (ed.), *Energy and Matter Fluxes of a Spruce Forest Ecosystem*,
Ecological Studies 229, DOI 10.1007/978-3-319-49389-3_14

Microclimates of forest ecosystems show considerable differences at vertical and horizontal scales. In the vertical direction, the forest canopy acts like a barrier, which shields the below-canopy trunk space from solar radiation and reduces the (turbulent) exchange of air between the trunk space and the atmosphere above (e.g. Baumgartner 1956; Hutchison and Hicks 1985). Consequently, the microclimate in the trunk space can vary substantially from the microclimate above and within the forest canopy (Geiger et al. 2009; von Arx et al. 2013). The variation of the microclimate in the trunk space depends on the density of the forest canopy and the resulting amount of incident sunlight (Matlack 1993; Davies-Colley et al. 2000; Baker et al. 2014). Contrary to the microclimate of open areas, in forests, diurnal variations of air temperature and humidity in the trunk space are attenuated by the presence of the forest canopy (e.g. Aussenac 2000; Ma et al. 2010; von Arx et al. 2012, 2013), with distinct effects on understory plant growth (Aussenac 2000; Bonan 2008; Wicklein et al. 2012).

Horizontal heterogeneity of the forest canopy, particularly in patchy and more open forests with sunny spots and edge effects, causes considerable horizontal gradients of up- and downwelling radiation, temperature, moisture and the resulting wind regime (Murcia 1995; Matlack and Litvaitis 1999; Davies-Colley et al. 2000; Klaassen et al. 2002; Thomas 2011), with a strong impact on the microclimate (Chen et al. 1993, 1995; Davies-Colley et al. 2000). At forest edges, the different surfaces and the prevailing gradients of the aforesaid quantities can change the atmospheric-boundary layer (ABL) flow structure (Mahrt et al. 1994; Weaver and Avissar 2001), facilitating quasi-stationary secondary circulations near the forest edge. For forest-clearing interactions, see also Chap. 13.

Furthermore, advective (non-turbulent) transport, such as horizontal katabatic drainage within the trunk space and vertical advection, is common at night during stable stratification (Aubinet et al. 2003; Feigenwinter et al. 2008). During daytime, especially vertical advection is small due to turbulent mixing (Feigenwinter et al. 2008). However, advection can substantially contribute to the net ecosystem exchange (NEE) of forests, particularly at night when advective flux contributions can be significant and turbulent flux observations would underestimate total CO_2 fluxes under conditions of low turbulence (e.g. Lee 1998; Baldocchi et al. 2000; Paw U et al. 2000; Aubinet et al. 2003). Significant advection can develop under conditions with strong surface cooling due to radiative energy losses, subsequent formation of stable stratification and strong CO_2 concentration gradients (Aubinet et al. 2003). While there is general agreement that advective fluxes contribute to net ecosystem exchange, it remains challenging to quantify advection experimentally and accurately. A number of advection studies have been published; however, they are generally constrained by their ability to obtain representative measurements in heterogeneous ecosystems. Therefore, recent work at the heterogeneous spruce forest site Waldstein–Weidenbrunnen has focused on improving spatio-temporal representativity of advection estimates using new measurement techniques (Siebicke et al. 2011a,b).

This chapter focuses on the investigation of the microclimate and its variances at the Waldstein–Weidenbrunnen site. The aim has been to describe vertical differences between trunk space and above-canopy in a homogeneous part of the forest ecosystem, but also directly at a forest edge. Furthermore, horizontal differences in both parts of the forest (homogeneous and heterogeneous) were investigated. Therefore, coherent structures and different coupling regimes have been considered, since both affect microclimate (see Chap. 6). For the characterization of the microclimate, long-term measurements, but mainly data obtained during the Intense Observation Periods (IOPs) of the EGER project (ExchanGE processes in mountainous Regions; see Chap. 1), were used.

14.2 Material and Methods

Meteorological parameters, including temperature, wind velocity and radiation, have been measured at the Waldstein–Weidenbrunnen site in long-term experiments since 1997. In addition to a continuous monitoring program, a total of three Intense Observation Periods (IOPs) were conducted at the Waldstein–Weidenbrunnen site during the EGER project (ExchanGE processes in mountainous Regions). In IOP1 and IOP2 the measurements were realized in a relatively homogeneous part of the spruce forest in autumn 2007 (6 September–7 October 2007) and summer 2008 (1 June–15 July 2008; Foken et al. 2012), where footprint analyses have shown that the results are mainly unaffected by heterogeneity (Siebicke 2008). In IOP3 the investigations were carried out in a more heterogeneous part of the forest in summer 2011 (13 June–26 July 2011). Experiments during IOP3 focused on the impact of a forest edge on atmospheric flow and microclimate, studying the roughness change from the dense spruce forest to the open clearing 'Köhlerloh'. In the following text, the three IOPs are designated as EGER IOP1, EGER IOP2 and EGER IOP3.

The subsequent sections serve as a brief summary of the different measurements used for the characterization of the forest climate. Reference is made to the differences required for investigation and interpretation of vertical and horizontal scales.

14.2.1 Vertical Profile Measurements

14.2.1.1 Long-Term Measurements

The long-term measurements were carried out in vertical profiles at a 32 m high tower ('Main Tower') within the dense spruce forest. See Chap. 2 and Appendix A for more details of the measurement devices and the different measurement levels.

Furthermore, turbulent fluxes were measured above the canopy at three heights above ground (27 m in 2011 and 32 m at the 'Main Tower' and 36 m at the 'Turbulence Tower', 60 m south-east of the 'Main Tower'). See Chap. 4 for more details of flux measurements.

14.2.1.2 EGER Project

Apart from the continuously running program, measurements were conducted during the three IOPs of the EGER project at the Waldstein–Weidenbrunnen site. During all three IOPs, turbulent flux measurements were performed at three different levels at the 'Turbulent Tower', and an additional walk-up tower ('Forest-Edge Tower') with turbulent flux measurements and a total height of 42 m was installed directly at the forest edge during EGER IOP3. See Appendix A for location, equipping and all measurement levels.

In addition to the canopy protruding towers, in all three IOPs there were some small turbulence masts installed at various positions in the forest (IOP1 to IOP3), at the forest edge (IOP3) and at the clearing (IOP3). For more details of locations and equipping of the masts/towers see Chap. 2 as well as Serafimovich et al. (2008a,b, 2011a) and Foken et al. (2012).

14.2.1.3 Vertical Coupling Regimes

To detect the vertical coupling by coherent structures, turbulence tower measurements were performed at three different levels (sub-canopy, canopy and above-canopy). The relative occurrence of coherent structures at the different levels is used to classify vertical coupling between levels. Foken et al. (2012) describe this method as a good tool for the investigation of tall vegetation, where nighttime situations with sudden coupling/decoupling events are common. Five exchange regimes were proposed by Thomas and Foken (2007):

- **Wa – wave motion.** The flow above the canopy is dominated by linear wave motions (gravity waves), resulting in a greatly reduced scalar transport. The sub-canopy layer and forest canopy are decoupled from the layer above the canopy.
- **Dc – decoupled canopy.** The air above the canopy is decoupled from the sub-canopy layer and forest canopy (analogous to Wa regime).
- **Ds – decoupled sub-canopy.** The forest canopy layer is coupled with the air above the canopy, but the sub-canopy layer is still decoupled.
- **Cs – coupled sub-canopy by sweeps.** The canopy layer is coupled with the region above the canopy, but the sub-canopy layer is only coupled with the air above the canopy by strong sweep motions.
- **C – fully coupled canopy.** All layers are completely coupled and in all layers, both ejections and sweeps contribute to the exchange of energy and matter.

For more details see Chap. 6.

14.2.2 Horizontal Profile Measurements

Besides the vertical profile measurements named in Sect. 14.2.1, horizontal profile measurements were investigated at the Waldstein–Weidenbrunnen site as well. Therefore, two different approaches were used and are described here: an advection measuring program conducted during EGER IOP1 and IOP2 and a horizontal mobile measuring system (HMMS) installed during EGER IOP3.

14.2.2.1 Advection Measurements

The advection measurements were conducted during EGER IOP1 and IOP2 within the homogeneous part of the Waldstein–Weidenbrunnen site. Besides the above-mentioned turbulent CO_2 flux measurements made above-canopy at the 'Main Tower' and the 'Turbulence Tower', as well as CO_2 concentration profiles (Sect. 14.2.1 and Appendix A), CO_2 concentration was measured at multiple points along horizontal transects. During IOP1, a switching valve system coupled to a single LI-820 gas analyzer (LI-COR Biosciences Inc., Lincoln, Nebraska, USA) was used. For IOP2, an advanced system was developed, allowing for the parallel measurement of CO_2 concentrations at all the points along the transects at high frequency (Siebicke et al. 2011b). This was implemented using ten individual closed-path infrared gas analyzers, each one sampling one intake along the transects (five LI-6262, one LI-6251, LI-COR Biosciences Inc., Lincoln, Nebraska, USA; four BINOS, Leybold Heraeus GmbH). The new system provides substantial improvements in terms of spatio-temporal resolution. In addition to fully automatic multiple gas standard inter-calibration of the gas analyzers, a data-driven statistical procedure was developed for improved in-situ calibrations of the parallel analyzer array (Siebicke et al. 2011b). Horizontal wind velocity was measured at the same heights as CO_2 using 3D sonic anemometers (USA-1, METEK GmbH, Elmshorn, Germany; CSAT3, Campbell Scientific Inc., Logan, Utah, USA). Two horizontal transects were installed perpendicular to each other, one parallel to the up-slope direction and running from south-west (218.71°) to north-east (38.71°), and the other one perpendicular to the slope and running from northwest (308.71°) to south-east (128.71°). Vertical integration of horizontal advection is based on horizontal wind velocity measurements along a vertical profile at the 'Turbulence Tower' using 3D sonic anemometers at heights of 2.25, 5.5, 13, 18, 23 and 36 m, as well as on the above-mentioned vertical profile of CO_2 concentration. More details and additional instrumentation during EGER IOP1 and IOP2 are given in Serafimovich et al. (2008a,b), Foken et al. (2012), and more details of the CO_2 advection measuring program are given in Siebicke et al. (2011a,b).

14.2.2.2 Horizontal Mobile Measuring System

The fully automatic horizontal mobile measuring system (HMMS) was developed to investigate near-ground horizontal profiles of atmospheric quantities. It is based on the drive mechanism of a garden railway system (Hübner et al. 2014). The HMMS was installed for the first time in summer 2011 during the EGER IOP3 project at the Waldstein–Weidenbrunnen site. Installed at a constant height of 1 m above ground, the measuring track of the HMMS consisted of a straight line with a total length of 150 m - therefrom 75 m in the dense forest and 75 m at the clearing 'Köhlerloh' – perpendicular to the forest edge (see Chap. 2).

Speed and the driving direction of the HMMS were controlled by an analogue throttle (provided by Lehmann-Groß-Bahn, LGB, since 2007 part of Gebr. Märklin & Cie. GmbH, Göppingen, Germany), an expressly written HMMS software (installed on a Micro PC) and a data acquisition (DAQ) device with an analogue output. Position, speed and changes in direction were detected using a commercial raster bar code scanner (CLV412-1010, SICK Vertriebs GmbH, Düsseldorf, Germany) and the HMMS software. The DAQ device and the HMMS software were also used for data acquisition and storage.

In addition to meteorological quantities (temperature, humidity and short-/long-wave down/upwelling radiation), the HMMS also measured trace gas concentrations of carbon dioxide and ozone. In detail, the mounted sensors are (1) a modified HMP155 temperature and humidity (HUMICAP® 180R) probe (Vaisala Oyj, Vantaa, Finland), (2) a total of four radiation sensors (two pyranometers CMP3 and two pyrgeometers CGR3; Kipp & Zonen, Delft, The Netherlands), (3) a closed-path, single cell, non-dispersive infrared gas analyser for CO_2 concentration (OEM Gascard® NG CO_2, Edinburgh Instruments Ltd., Edinburgh, UK) and (4) a fast-response O_3 analyser (enviscope GmbH, Frankfurt, Germany). See Table 14.1 for sensor information and Hübner et al. (2014) for furthers details.

In order to measure meteorological variables across a forest edge using a moving system, sensor response times need to be sufficiently fast to capture gradients, particularly at the forest edge. However, some of the HMMS sensors' response times were too slow, introducing lags and averaging of the input signals. To correct for these lags, more precisely, the dynamic errors in the measurements of the HMMS sensors, two approaches were used:

1. A correction algorithm that considers a linear gradient along a defined distance was applied. The dynamic error could be corrected completely, but this algorithm required considerable effort and therefore only measurements which were used for detailed studies of the micrometeorological phenomena near the forest edge could be corrected (see Hübner et al. 2014)
2. An averaging over the preceding 15 s at selected locations along the HMMS transect was performed. This approach can be carried out for the whole data set, but is not as accurate as approach 1. Nevertheless, influences caused by small-scale fluctuations or the dynamic error could be reduced.

Table 14.1 Sensors mounted on the HMMS are a temperature (T) and a relative humidity sensor (RH), two pyranometers (down- and upwelling, $K_{\downarrow}$, $K_{\uparrow}$), two pyrgeometers (down- and upwelling, $L_{\downarrow}$, $L_{\uparrow}$), a CO_2 analyser and an O_3 analyser. The accuracies are taken from the manufacturers' information. Taken from Hübner et al. (2014)

Parameter	Sensor	Accuracy	Remark/Modification
T	Vaisala HMP155	$\pm$ 0.1 K	Radiation shield and ventilated with 4 m s^{-1}
RH	Vaisala HMP155	$\pm$ 1%	Radiation shield and ventilated with 4 m s^{-1}
$K_{\downarrow}$	Kipp & Zonen CMP3	$<$ 15 W m^{-2}	Amplifier used (factor: 50-fold)
$K_{\uparrow}$	Kipp & Zonen CMP3	$<$ 15 W m^{-2}	Amplifier used (factor: 100-fold)
$L_{\downarrow}$	Kipp & Zonen CGR3	$<$ 15 W m^{-2}	Amplifier used (factor: 500-fold); optional PT-100 temperature sensor
$L_{\uparrow}$	Kipp & Zonen CGR3	$<$ 15 W m^{-2}	Amplifier used (factor: 500-fold); optional PT-100 temperature sensor
CO_2	Edinburgh Instruments Gascard® NG CO_2 1000 ppm	$\pm$ 40 ppm	Vacuum pump DC24/16F (flow rate: 1.2 L min^{-1})
O_3	Enviscope O_3 analyser	$\sim$ 0.09 ppbv[a]	Vacuum pump DC24/80L(flow rate: 3.0 L min^{-1})

[a]Accuracy at a measuring frequency of 1 Hz and a mixing ratio of 50 ppbv (1 ppbv = mixing ratio of 10^{-9})

14.3 Results and Discussions

14.3.1 Microclimate Within and Above a Dense Forest

Microclimatological conditions within the homogeneous part of the forest were investigated at the Waldstein–Weidenbrunnen site during all EGER IOPs listed in Sect. 14.2.1.2. Particular attention was paid to the best possible determination of horizontal and vertical advective transport within the trunk space (Sect. 14.2.2.1; Siebicke et al. 2011a) since they are, in addition to turbulent and storage fluxes, recognized as important terms of the total net ecosystem exchange (NEE) budget. To investigate flux distribution and its sinks and sources, proper determination of the footprint is mandatory. At the Waldstein–Weidenbrunnen site, the footprint was located to the more homogeneous part of the Norway Spruce forest during neutral and unstable stratification (mainly during daytime; Siebicke 2008). During stable stratification the footprint was large and covered not only forest but also clearings, including parts of the open clearing 'Köhlerloh' (microclimate of the clearing 'Köhlerloh' will be investigated in Sect. 14.3.2). This is due to the complex terrain and the wind regime. During daytime, winds from south-west and anabatic flow above and below the canopy with coupled situations were the prevailing conditions. But during nighttime, decoupled conditions with above-canopy wind direction either south-westerly (synoptic) or south-easterly due to channeled flow from the Lehstenbach valley in the south-east and sub-canopy katabatic drainage from north-east were frequently observed. This implies different footprints for above-canopy

(turbulent flux) and below-canopy (horizontal advection) measurements during stable stratification.

14.3.1.1 Vertical (Turbulent) Exchange

The CO_2 gradient measurements using ten sub-canopy towers during EGER IOP1 and IOP2 suggest that gaps in the canopy (lower plant area index (PAI)) have an influence on vertical exchange. Gaps provide less resistance than dense canopy regions (high PAI), which have an impact on horizontal concentration gradients inside the canopy. The investigations showed a lower sub-canopy concentration due to mixing with air above the canopy (Fig. 14.1a). See Figs. 2.4 and 2.5 in Chap. 2 for the exact sample locations and Figs. 6.8 and 6.9 in Chap. 6 for more detailed spatial gradients of sub-canopy CO_2 concentration and its PAI dependency. Similar patterns were observed in the transect measurements of the HMMS during EGER IOP3 (Fig. 14.1b). Sub-canopy CO_2 concentration maxima during stable stratification correlated with the density of the canopy. Since no continuous PAI measurements were available along the transect, the difference of long-wave downwelling radiation $L_\downarrow$ at each measurement point (0 to 75 m) and the average field concentration along the forest section of the transect was taken, to interpret the density of the forest canopy. The difference is zero, where the point measurement was equal to the average field concentration. Where the difference was negative, the long-wave downwelling radiation $L_\downarrow$ was lower and thus the canopy less dense and where

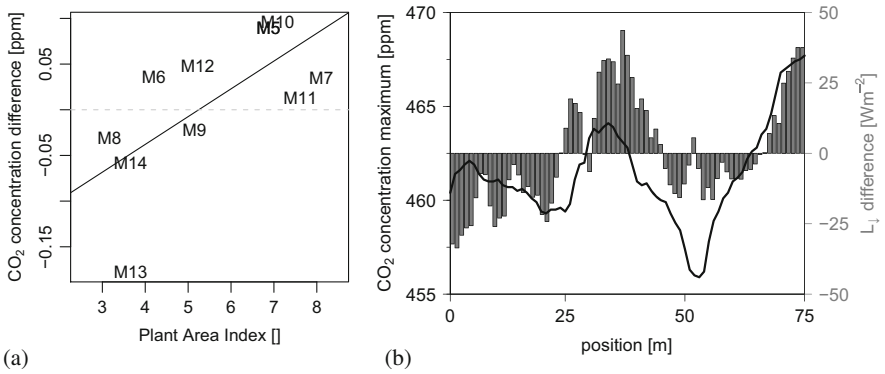

Fig. 14.1 (**a**) Mean local CO_2 concentration perturbations $c_i(t) - \tilde{c}(t)$ versus Plant Area Index, neutral stratification, all sample locations. Linear regressions shown as *solid line*. Number of values: 307 from 11th of June–13th of July, 2008 (IOP2). Sample locations according to Figs. 2.4 and 2.5 in Chap. 2. Taken from Siebicke (2010) with kind permission of © Author, 2010, All rights reserved. (**b**) Local CO_2 concentration maxima (*black solid line*) of the HMMS measurements during EGER IOP3 along the transect within the forest (Position 0–75 m) during stable stratification. *Bars* show the difference of long-wave downwelling radiation $L_\downarrow$ at each measurement point (0–75 m) and average field concentration along the total transect within the forest

the difference was positive, the canopy was more dense. In comparison, the CO_2 concentration maxima were up to 10 ppm lower beneath gaps in the canopy than beneath the dense canopy, which agrees with the findings during EGER IOP1 and IOP2.

Thus, sub-canopy gradients are affected by the density of the forest canopy and the extent of vertical exchange and vertical coupling. Both are mainly driven by coherent structures, which couple the trunk space, in-canopy and above-canopy air to varying degrees depending on atmospheric stratification. The investigations of Sörgel et al. (2011) indicated that coherent structures could propagate down to a height of 0.5 m (cf. also Chap. 8). There are currently five different coupling regimes defined, which are listed in Sect. 14.2.1.3. For detailed information of coherent structures and coupling regimes see Chap. 6. Vertical coupling has a typical diurnal variation which can be described as follows: During nighttime, with calm winds, low incoming radiation, lower temperatures, and the damped turbulent wind field due to the high roughness at the upper part of the canopy, there often occurs a stable stratification in- and above-canopy. Low wind shear and low friction velocity are prevailing, and consequently the vertical exchange is low and it is often the decoupled situations (Dc and Wa) which occur during this time of the day. But indeed, there are still some situations with a fully coupled vertical profile, mainly caused by coherent structures. During daytime, the vertical coupling changes completely and – due to the high turbulent mixing – there are often coupled situations prevailing with a full exchange between sub-canopy and above-canopy air. In the afternoon, the sub-canopy begins to decouple from the in-canopy and above-canopy, whereas the canopy remains coupled.

In the following, a typical diurnal variation of vertical coupling will be discussed, based on observations from 29 June 2008, the first of the 'golden days' during EGER IOP2. Vertical profiles of temperature (Fig. 14.2a) and of CO_2 concentration (Fig. 14.2b) at the 'Main Tower' for five selected 30-min intervals, corresponding to exchange regimes Cs (01:00 CET), Ds (07:00 CET), C (12:30 CET), Dc (19:00 CET), Wa (22:30 CET), are presented. Secondly, the wind- and CO_2 concentration fields are presented for two of the five cases: Fig. 14.3 (07:00 CET), corresponding to exchange regime Ds, and Fig. 14.4 (22:30 CET), corresponding to exchange regime Wa.

The exchange regime Cs, i.e. 'coupled sub-canopy by sweeps', as observed during the 01:00–01:30 CET 30-min example interval, was present with moderate vertical exchange in the middle of the night. The vertical temperature profile above 3 m was near neutral (Fig. 14.2a, 01:00 CET), allowing for vertical mixing. There was a clearly confined cold air layer below 3 m. Ejections with positive vertical wind velocities were observed to extend from the trunk space to the top level above the canopy at 36 m. During sweeps, characterized by a pronounced increase in above-canopy wind speed, a corresponding low CO_2 concentration was observed in the trunk space, including the 2 m level. In between sweeps, there was accumulation of high CO_2 concentrations close to the ground, affecting the 2 m concentration measurement level. Low concentration, associated with sweeps and high concentration between sweeps, were also observed in the corresponding

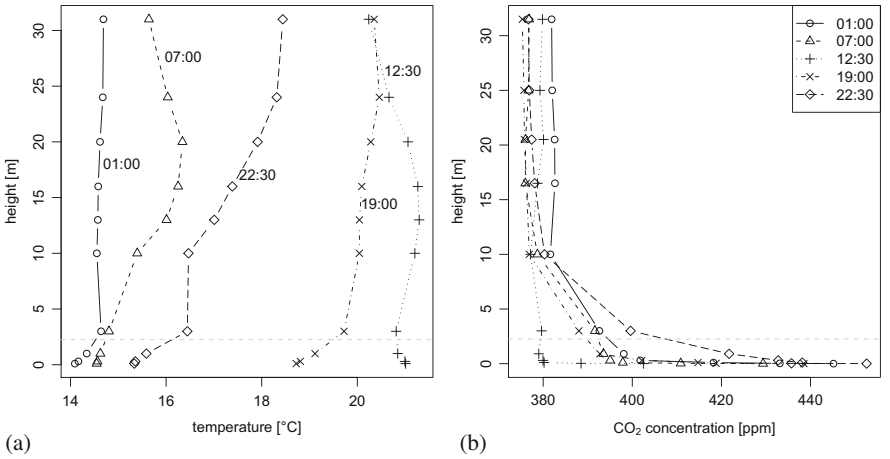

Fig. 14.2 Vertical profiles of temperature (**a**) and CO_2 concentration (**b**) on 29.06.2008 at the 'Main Tower' for five selected 30-min intervals, corresponding to exchange regimes Cs (01:00 CET), Ds (07:00 CET), C (12:30 CET), Dc (19:00 CET) and Wa (22:30 CET). Times indicate beginnings of 30-min intervals. *Dashed lines* mark height of horizontal sub-canopy CO_2 concentration measurements at 2.25 m above ground. Taken from Siebicke (2010) with kind permission of © Author, 2010, All rights reserved

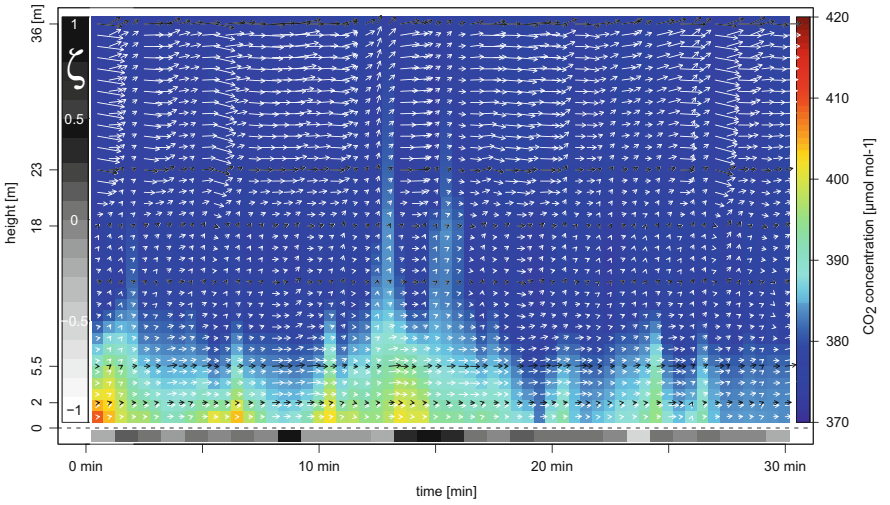

Fig. 14.3 Vertical profile of CO_2 concentration [µmol mol^{-1}] (*colours*) and wind velocity (*arrows*) versus time and stability parameter ζ (*grayscale bar*, *bottom*, legend: *left*). *Y*-axis: height above ground [m]. Wind vectors: resultant of absolute value of horizontal wind velocity and vertical wind velocity. *Black arrows*: measurements, *white arrows*: Akima interpolation (Akima 1970). Measurement heights and interpolation equivalent for CO_2. Exchange regime Ds (decoupled sub-canopy), 29.06.2008 07:00–07:30 CET. Taken from Siebicke (2010) with kind permission of © Author, 2010, All rights reserved

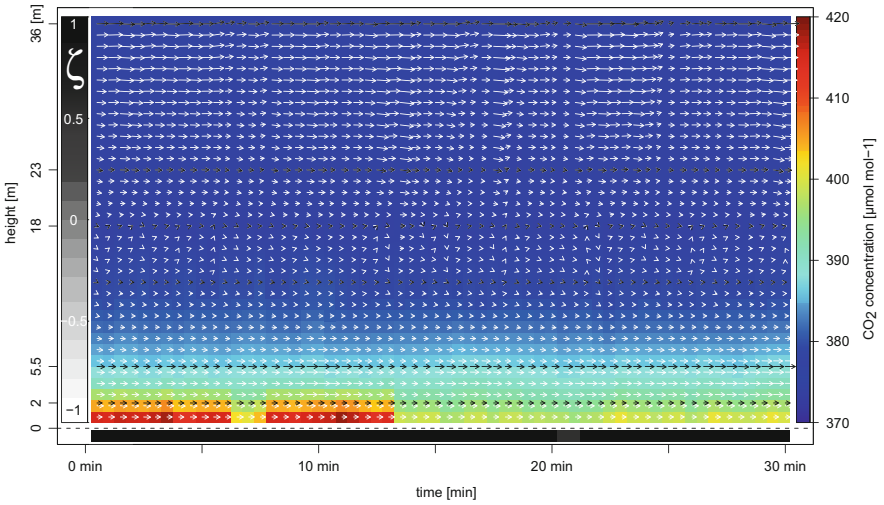

Fig. 14.4 Vertical profile of CO_2 concentration [µmol mol^{-1}] (*colours*) and wind velocity (*arrows*) versus time and stability parameter ζ (*grayscale bar*, *bottom*, legend: *left*). *Y*-axis: height above ground [m]. Wind vectors: resultant of absolute value of horizontal wind velocity and vertical wind velocity. *Black arrows*: measurements, *white arrows*: Akima interpolation (Akima 1970). Measurement heights and interpolation equivalent for CO_2. Exchange regime Wa (wave motion), 29.06.2008 22:30–23:00 CET. Taken from Siebicke (2010) with kind permission of © Author, 2010, All rights reserved

CO_2 concentration perturbation time series of M8. Comparing the concentration time series of locations M13, M5 and M8 (not shown), there was very little cross correlation, meaning each sample location had its own local condition, which was interpreted as vertical exchange dominating the concentration signal, given relatively minor horizontal coupling of sub-canopy sample points. See Chap. 6 for detailed investigations of these observations.

The exchange regime Ds, i.e. 'decoupled sub-canopy', was the most frequently observed regime. The selected 30-min interval shown in Fig. 14.2 marks the transition between night and day time conditions of trunk space CO_2 concentration. During the transition at around 06:00–07:00 CET, high trunk space CO_2 concentrations, which had gradually accumulated over night, were released during intermittent events. Despite the exchange classification Ds ('decoupled sub-canopy'), indicating moderate vertical exchange only, which is controlled by a temperature inversion at the canopy level (Fig. 14.2a, 07:00 CET) due to increasing radiation energy input in the upper canopy, a highly dynamic wind and concentration field and distinct events of vertical exchange were observed (Fig. 14.3). One major event of venting by vertical exchange started at minute 5 with increasing wind speed above the canopy and initially negative vertical wind velocity, followed by a secondary wind maximum in the trunk space at minutes 8 and 9 with low CO_2 concentration at the same time. Probably as a consequence of the wind maximum in the trunk space, two consecutive plumes with high CO_2 concentration were lifted

to the canopy level and subsequently vented to above-canopy layers by ejections, characterized by strong positive vertical wind velocities from minutes 11 to 13 and at minute 15. The second 15-min period of the interval was dominated by interwoven sweeps (e.g. minutes 18–19) and ejections (minutes 20.5, 24 and 26), with even lower trunk space CO_2 concentrations during sweeps and less dramatic ejections, due to the already diminished trunk space CO_2 resource.

The exchange regime C, i.e. 'fully coupled canopy', was typically observed during turbulent conditions around noon. Regarding the 30-min example at 12:30 CET, there still remained a weak temperature inversion that had moved to the lower canopy, but the nighttime cold air layer below 3 m had vanished (Fig. 14.2a, 12:30 CET) and there was no longer any increase of CO_2 concentration in the trunk space (Fig. 14.2b, 12:30 CET). Highly fluctuating and relatively high wind velocities were observed above-canopy, driving major sweeps into the canopy. During those sweeps, divergence of vertical wind velocities was frequently observed at the 23 m and 36 m measurement levels. Similarly, trunk space wind velocities were larger than before and after the sweeps and fluctuated, an indication of well-developed turbulence. Ejections and sweeps did not carry major CO_2 concentration differences, given the turbulent conditions, which effectively removed any accumulated CO_2, leaving the most notable concentration perturbations in the relatively sheltered canopy. Perturbations of local trunk space CO_2 concentrations were small, with little variation. However, as in the previous cases, there were differences in concentration perturbations between locations with low and high PAIs, i.e. small perturbations with little variance for the low PAI location M13 with some low amplitude coherent structures, M13 being closely tied to a relatively constant above-canopy concentration due to its sparse canopy versus higher variance and single positive structures in concentration perturbation at M5. The latter was interpreted as the sheltering effect of the canopy and the chance of accumulation of higher concentrations caused by soil and canopy respiration.

Later on that day, the exchange regime Dc, i.e. 'decoupled canopy', could be observed at 19:00 CET. That selected 30-min interval marks the transition between day time and nighttime conditions with a cooling canopy layer forced by a long-wave radiation loss and cold air accumulation below 3 m (Fig. 14.2a, 19:00 CET), as well as an accumulation of CO_2 in the trunk space (Fig. 14.2a, 19:00 CET). The transition period was characterized by an increase in mean trunk space CO_2 concentration, since canopy respiration overcompensated assimilation, with turbulent CO_2 fluxes above the canopy at 36 m being positive (not shown). Occasional sweeps still counteracted trunk space CO_2 accumulation, at the same time leading to a decrease in CO_2 concentration at the 2 m level. With regard to vegetation structure, the open canopy sample location M13 was the first to witness the increase in CO_2 concentration, whereas at more sheltered locations such as M5, CO_2 concentrations remained lower, before all locations entered a regime typical for nighttime conditions, showing large amplitude fluctuations with respect to local CO_2 concentration perturbations.

The final example describes the exchange regime Wa: 'wave motion' (Fig. 14.4), a common case of a hydrodynamically driven katabatic drainage flow, which has

been described before as a main driver for nighttime CO_2 advection in sloping terrain (Aubinet et al. 2003) and has been identified as one reason for the nighttime problem of eddy-covariance measurements (Aubinet 2008). The wind field from 22:30 to 23:00 CET was characterized by relatively constant velocities both above and below the canopy (Fig. 14.4). The presence of a sublayer drainage flow can be deduced from a strong temperature inversion from 0 m to 3 m above the ground surface (Fig. 14.2, 22:30 CET), the presence of a secondary wind maximum in the trunk space with a horizontal wind velocity of 0.6 m s^{-1} at the 2 m level and constant wind direction of 43° oriented downslope, flowing from north-east to south-west, which is a 180° turn relative to daytime wind direction with abrupt transitions (not shown). Given stable conditions for the whole 30-min interval shown (see grayscale bar at the bottom of Fig. 14.4), there were no signs of turbulence, but quasi-laminar flow conditions could be assumed. Regarding the CO_2 concentration field, all heights from 5 m level and above showed constant concentration over time (Fig. 14.4). At the 2 m level, high CO_2 concentration was observed during the first 12 min of the 30-min interval (see red colours at 2 m level in Fig. 14.4). Excluding high frequency fluctuations, the CO_2 concentration at M8 was constantly lower compared to the field average, and at M5 it was higher. In contrast, the concentration at the low PAI location M13 increased over the first 10 min, disturbed by coherent structures with low concentration (not shown). This was interpreted as an effect of entrainment of air from higher levels characterized by relatively low CO_2 concentration.

14.3.1.2 Horizontal and Vertical Advection

The investigations during the EGER project showed that advective transport was relatively small during the day and that daytime NEE of the spruce forest could be adequately described by the turbulent fluxes measured by eddy-covariance. On the other hand, advection played a major role in the budget during nighttime, since turbulent fluxes were small and therefore differences in thermal and roughness properties between clearings and forest could cause an advective flux. Clearings also represent possible drainage paths into or out of the otherwise closed forest trunk space that can be relevant for katabatic drainage flows and CO_2 advection.

Advection contributes significantly to NEE. The largest contribution from advection during the mean diurnal cycle was observed at night and during transition periods, particularly in the evening. During daytime, the turbulent flux was the dominant component. Figure 14.5 presents the impact of advection on the average daily cycle of NEE during IOP1 (Fig. 14.5a) and IOP2 (Fig. 14.5b). Major differences were observed when comparing total advection from IOP1 and IOP2, which are partly caused by the different sampling design (single gas analyzer during IOP1, multiple gas analyzers during IOP2) and the bias correction applied to sub-canopy CO_2 concentration measurements during IOP2 (Sect. 14.2.2.1). Daily sums for NEE with advection were less negative ($-2.6\,g\,C\,m^{-2}\,d^{-1}$) than without advection ($-5.0\,g\,C\,m^{-2}\,d^{-1}$) during EGER IOP2. This difference could

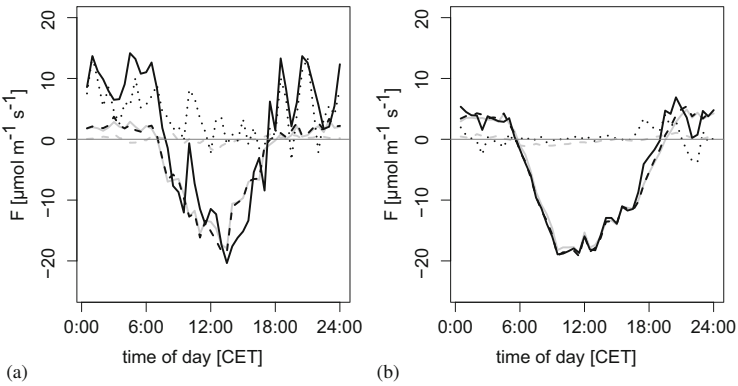

Fig. 14.5 Median daily cycle of NEE with a 30-min resolution for IOP1 (autumn) (**a**), and IOP2 (summer) (**b**), without advection (*black dashed line*), calculated as the sum of turbulent flux (*gray solid line*) and storage flux (*gray dashed line*) in comparison with NEE including advection (*black solid line*), calculated as the sum of turbulent flux, storage flux and the sum of vertical and horizontal advection (*dotted line*). Figure from Siebicke et al. (2011a) with kind permission of

be interpreted as an effect of the night flux error of the eddy-covariance measurements, i.e. an overestimation of carbon sequestration due to missing flux at night in the case without advection and a better representation of the true flux when including advection. This interpretation was supported by independent soil chamber measurements, which confirm the plausibility of the advection-corrected NEE estimate. However, daily sums of NEE during IOP1 were overcorrected by the inclusion of advection from discontinuous sampling (changing CO_2 flux from -6.0 to $1.3\,\mathrm{g\,C\,m^{-2}\,d^{-1}}$). Those findings imply that great caution has to be used when employing common discontinuous single analyzer multiplexed CO_2 gradient systems to estimate advection. Bias-corrected continuous multi-analyzer systems are preferable for more robust CO_2 gradient and advection estimates. Furthermore, Siebicke et al. (2011a) found that a planar fit coordinate rotation with a suitable window length was necessary for estimating vertical advection and NEE. In their particular study, they found a 50 % increase in vertical advection for planar fit window lengths of 400 days compared to 2.5-day window lengths. They introduced a continuously updating coordinate rotation approach, the 'sequential planar fit', which is less affected by long-term drifts in sensor installation or wind field.

14.3.2 Microclimate at a Forest Edge

Microclimate at a forest edge was investigated during EGER IOP3 along a 150 m long transect with the horizontal mobile measuring system (HMMS; Sect. 14.2.2.2). For detailed information see Hübner et al. (2014). The aim was to investigate the

prevailing near-ground horizontal gradients along the transect forest – forest edge – clearing and the impact of vertical exchange on horizontal gradients. Therefore, 14 days of measurements with the HMMS were taken from five different locations during the EGER IOP3 project (more than 250 h of operating time). One of the locations was situated in the forest (start of transect), one at the clearing (end of transect) and three were located in the transition areas of the forest edge, which were: forest (near edge), and forest edge and clearing (near edge). See Table 14.2 for exact positions of each location. Minima, maxima, median and interquartile ranges for all eight measured quantities are also presented in Table 14.2.

Although the lowest temperatures (16.5 °C) and highest humidities (9.5 g m^{-3}) occurred within the trunk space of the forest, by considering the median, the absolute minima/maxima and thus the highest variations were measured at the forest edge and at the clearing near the forest edge. Temperature fluctuations inside the forest show smaller amplitudes relative to observations at the forest edge and consequently microclimate has more stable conditions within the forest than at the clearing. This can be explained firstly by the role of the canopy in preventing the incident sunlight (short-wave downwelling radiation $K_{\downarrow}$) from reaching and warming the trunk space. Nevertheless, the amount of short-wave radiation penetrating through the canopy and reaching the trunk space is a function of canopy density and time (cf. 'sunny spots' in Fig. 14.6a), and causes small-scale heating within the forest floor with a distinct effect on stability, trace gas and sensible heat fluxes in the sub-canopy level (cf. Chap. 8). Secondly, the canopy – which was heated during daytime – emitted more thermal radiation during nighttime (long-wave downwelling radiation $L_{\downarrow}$) than the sky (even when it was cloudy) and thus the cooling effect was weakened within the trunk space compared to the clearing.

The emission of long-wave upwelling radiation ($L_{\uparrow}$) was less within the trunk space compared to the clearing and consequently $L_{\uparrow}$ had higher values within the forest. At and near the forest edge the highest temperatures were found during daytime, which can be explained by several factors: high incident sunlight ($K_{\downarrow}$) leading to (1) a heating at the clearing and thus a high long-wave upwelling radiation ($L_{\uparrow}$) there and (2) a heating of the canopy and thus the forest line at the forest edge, with high long-wave downwelling radiation ($L_{\downarrow}$), heats the adjacent area as well. Furthermore, (3) the location furthest from the forest edge at the clearing had – in spite of receiving the highest incident sunlight – lower maximum temperatures compared to the locations near the edge, since this location is the least wind sheltered, and in addition, most humid (from soil and ground water). Another indication of highest temperatures at the forest edge could be the presence of advective conditions acting mainly from the clearing towards the forest edge, with enlarged convective conditions directly at the forest edge, as observed by Eder et al. (2013) during EGER IOP3. They found a distinct daily pattern of coherent structures only at the forest edge, with strong ejections (upward movement) during daytime and strong sweeps (downward movement) during nighttime. This pattern was not found at the clearing and above the forest. They assumed the presence of a

Table 14.2 Temperatures, humidities, radiation components and gas concentrations measured with HMMS at five locations during EGER IOP3. IQR is the interquartile range from the first to the third quartile. Data based on all completed runs of the HMMS

Parameter		Forest	Forest (near FE)	Forest edge	Forest (near FE)	Clearing
Position		0–10 m	60–70 m	70–80 m	80–90 m	140–150 m
T [°C]	Min	9.0	9.0	8.7	8.7	8.8
	Max	28.2	30.3	30.4	30.5	30.1
	Median	16.5	16.8	16.9	16.9	16.9
	IQR	13.9–20.0	13.9–20.9	13.9–21.3	13.8–22.0	13.3–20.8
a [g m^{-3}]	Min	5.8	5.7	5.6	5.7	5.7
	Max	12.8	12.9	13.3	13.5	13.2
	Median	9.5	9.4	9.4	9.4	9.1
	IQR	2.2–8.1	2.3–8.0	2.3–8.0	2.3–8.1	2.4–7.8
$K_{\downarrow}$ [W m^{-2}]	Min	0	0	0	0	0
	Max	800.2	954.4	1148.2	1170.4	1181.2
	Median	19.0	29.1	78.5	131.6	184.5
	IQR	0–48.8	0–81.8	0–331.7	0–481.4	0–510.5
$K_{\uparrow}$ [W m^{-2}]	Min	0	0	0	0	0
	Max	105.9	129.8	199.9	195.9	175.3
	Median	0	0	4.6	15.6	28.5
	IQR	0–0	0–6.5	0–59.1	0–72.5	0–81.5
$L_{\downarrow}$[W m^{-2}]	Min	348.0	334.6	297.6	286.5	268.5
	Max	493.2	483.8	459.4	430.6	433.0
	Median	411.0	399.1	375.5	361.4	347.0
	IQR	395.4–438.1	382.3–423.1	349.7–397.5	333.2–388.0	318.1–377.0
$L_{\uparrow}$ [W m^{-2}]	Min	331.3	301.9	278.4	299.6	301.8
	Max	576.4	606.4	639.6	615.1	596.7
	Median	434.2	408.6	405.0	406.2	413.9
	IQR	414.9–457.2	385.7–441.6	374.6–457.1	372.4–462.1	372.0–465.5
CO_2 [a] [ppm]	Min	392.2	388.2	387.6	388.0	385.7
	Max	466.2	466.8	470.2	483.1	482.0
	Median	409.9	411.1	411.2	411.7	412.1
	IQR	402.4–430.9	401.4–423.1	401.8–422.7	402.0–423.1	401.4–422.5
O_3 [ppb]	Min	3.1	2.2	2.6	1.4	1.8
	Max	79.0	85.2	91.1	92.9	92.5
	Median	39	41	41.2	40.1	41.6
	IQR	23.8–48.9	27.8–50.8	28.6–51.3	27.6–50.5	30.9–50.9

[a]Only measurements before sunrise and after sunset could be used for the analyses of CO_2 concentrations due to radiation-induced errors in the CO_2 measurements (cf. Hübner et al. 2014)

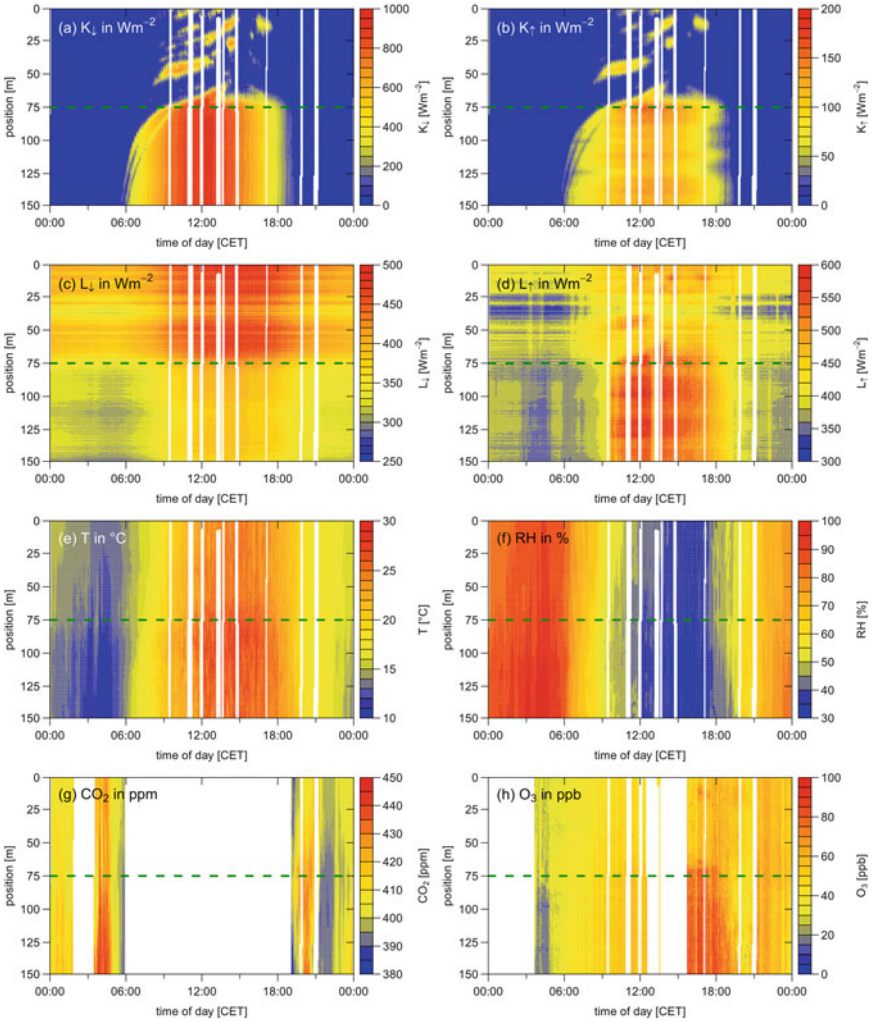

Fig. 14.6 Measured horizontal profiles for 28 June 2011 for all HMMS measurements. Short-wave down/upwelling radiation $K_{\downarrow}$, $K_{\uparrow}$ (**a**, **b**), Long-wave down/upwelling radiation $L_{\downarrow}$, $L_{\uparrow}$ (**c**, **d**), temperature T (**e**), relative humidity RH (**f**), CO_2 concentration (**g**) and O_3 concentration (**h**). Position shows distance from starting point in metres, with starting point in the forest (0 m), forest edge (75 m, *horizontal green dotted line*) and endpoint at the clearing (150 m). Remark: the colour scaling is different in all graphs. Taken from Hübner et al. (2014) with kind permission of © Authors, All rights reserved. Creative Commons Attribution 3.0 License

secondary circulation system since they were able to exclude flow distortion caused by the forest edge.

The lowest temperatures were observed at the forest edge during nighttime. This can be explained by (1) the stronger cooling at the clearing, (2) the different surfaces

and above all (3) the strong daily patterns of coherent structures, with strong sweeps (downward movement) during nighttime. These sweeps transported cold air near the forest edge towards the ground. See Chap. 13 for the interaction of the transect forest – clearing. Cold air drainage from the forest to the clearing can affect temperatures near the forest edge as well. Conditions with katabatic drainage and 'wave motions' were observed in the advection measurements during IOP1 and IOP2 (Sect. 14.3.1, Siebicke et al. 2011a).

Only nighttime values could be presented for CO_2 since there was a radiation-induced error in the CO_2 sensor. Therefore, the variability of CO_2 along the measurement transect was small with slightly higher values at the clearing. A comparable variation could be observed in the O_3 measurements, but the maxima for O_3 distinctly differs along the transect, with 14 ppb more at the clearing, which suggests a sun-induced photochemical production during daytime and a horizontal decoupling between the trunk space and the clearing as well as a possible reaction with nitrogen oxide.[1]

Figure 14.6 shows horizontal profiles along the complete HMMS measuring transect on 28 June 2011, a day with fair weather conditions during EGER IOP3 ('golden day'). A cloud-free sky, no morning fog, calm south-easterly winds during nighttime and northerly winds during daytime (typical for high pressure conditions at this site) were prevailing on this day. Both short-wave radiation components (Fig. 14.6a, b) and long-wave radiation components (Fig. 14.6c, d) showed a clear gradient at or close to the forest edge, as already presented in Table 14.2. Figure 14.6a, b illustrates the 'sunny spots' within the forest, which could also be discovered by lower values in the long-wave radiation at this position.

The increase of temperature (Fig. 14.6e) began significantly earlier at the clearing with the start of insolation (6:30 CET) than towards the forest edge (between 7:30 and 8:00 CET). This was caused by the orientation of the forest edge and the morning sun position (shadowing effect). Since insolation did not start at the forest edge before 9:00 CET it has to be suggested that the complete mixing along the transect was caused by the onset of turbulence. Humidity (Fig. 14.6f) showed a similar behaviour, with the earliest decrease occurring at the clearing and a delayed decrease at the forest edge. But it can be seen that the mixing occurred around 7:30 CET.

A CO_2 concentration maximum could be observed in the early morning and early evening under stable and uncoupled situations, with higher values at the clearing (Fig. 14.6g). This is in accordance with the findings of Foken et al. (2012), Serafimovich et al. (2011b) and the drainage flow discussed in Chap. 11 and Sect. 14.3.1 in this chapter. O_3 concentration (Fig. 14.6h) was highest in the

[1] Sun-induced photochemical reaction: $NO_2 + O_2 \xrightarrow{h\nu} NO + O_3$, but because ozone is a reactive gas, there also exists a back reaction: $NO + O_3 \longrightarrow NO_2 + O_2$ (Dlugi 1993; Foken et al. 1995). A precise statement of transport, gradients and reactions arising thereof can only be made when the Damköhler numbers *Da* are investigated (Molemaker and Vilà -Guerau de Arellano 1998). Because of this, the statement made above is only an assumption.

afternoon and lowest during nighttime at the clearing, with an obvious gradient near the forest edge, suggesting sun-induced O_3 production at the clearing and low transport into the forest. Trace gases are good indicators for coupling regimes (Foken et al. 2012), and if one looks at the O_3 concentrations in detail (especially from 16:00 to 18:00 CET), there is a variation along the total transect discernible, with a sudden decrease of approximately 20 ppb and afterwards an increase again. This decrease persisted each time for around 10 min (1 to 2 runs of the HMMS), and subsequently the O_3 concentration increased back to the initial value. This suggests a short exchange between near-ground air and air above, which is also typical for a secondary circulation system. See Chap. 13 about the interaction forest-clearing and Chap. 17 for large-eddy simulations at the Waldstein–Weidenbrunnen site.

14.4 Conclusions

The microclimate of a forest site is often as heterogeneous as the forest itself. This is also true for the Waldstein–Weidenbrunnen site, which was investigated over the past 10 to 20 years, especially during the EGER project in 2007, 2008 and 2011 (cf. history of the measuring site in Chap. 1 and description of the site in Chap. 2). The investigations have shown that the vertical exchange within forest ecosystems is related to coherent structures and dependent on atmospheric stratification and the coupling of different canopy layers (cf. Chaps. 6 and 8). Furthermore, vertical exchange was PAI-dependent, meaning that the lower the PAI (sparse canopy), the higher the vertical exchange and vice versa. In other words, vegetation structure influences the sub-canopy CO_2 concentration field locally, and furthermore, gradients are spatially inconsistent (cf. Chap. 6). But not only the vertical exchange was increased by gaps in the canopy, but also the heating of the near-surface trunk space caused by 'sunny spots' led to changes in stability and trace gases as well as sensible heat fluxes (cf. Chap. 8). Both aspects altered near-ground horizontal gradients and consequently the influence rose with increasing heterogeneity and reached an even higher value at large heterogeneities such as forest edges, for example. This could be shown by the investigations at a forest edge in 2011 (EGER IOP3) on the clearing 'Köhlerloh', very close to the Waldstein–Weidenbrunnen site. Only at the forest edge could a daily pattern in coherent structures be observed in the canopy height (Eder et al. 2013). During daytime, there were strong ejections (thermal updraft) measurable and strong sweeps (downdraft) during nighttime. In the lowest measuring height there was no significant daily pattern measurable from which it could be inferred that (especially large) coherent structures did not penetrate close to the surface (cf. Chap. 13 and Eder et al. 2013). Nevertheless, the highest variation in near-ground horizontal gradients of temperature, humidity and gas concentration (all are turbulence-influenced quantities) occurred directly at the forest edge. These observations and the temporarily finite changes in O_3 concentration, which is discussed in Sect. 14.3.2, may both indicate the presence of a secondary circulation system above the clearing. But secondary circulations

cannot be captured adequately by the eddy-covariance method near the surface and the wavelet analyses used for determination of coherent structures. Thus, the investigation of near-ground presence of secondary circulation systems should be strengthened in future research.

Boundary-layer events, like low-level jets and gravity waves, also had a distinct impact on vertical exchange and coherent structures (cf. Chap. 11). As a consequence, there was an enrichment of sub-canopy CO_2 concentration measurable, with a katabatic drainage following the slope of the Waldstein–Weidenbrunnen site from the forest towards the clearing.

Sub-canopy concentration is not only affected by large scale katabatic drainage and the distribution of sources and sinks in the canopy and in the soil, but also by vertical exchange across large vertical concentration gradients. Moreover, horizontal and vertical advection contributed significantly to the net ecosystem exchange (NEE), especially during nighttime and transition periods. Based on the knowledge gained, it is absolutely necessary to consider horizontal heterogeneities in order to properly determine the NEE of an ecosystem. A site-representative set-up would be required to determine fluxes correctly. However, in practice this is rarely feasible in forests with small-scale horizontal heterogeneity and that is why modelling or a combination of measuring and modelling should be encouraged.

Acknowledgements The full functionality and fast construction of the measurement devices would not have been possible without the support of our technician J. Olesch and the technical workshops of the University of Bayreuth. We want to thank the Max Planck Institute for Chemistry, Mainz, for the collaboration during the EGER project and for lending us measuring devices. Thanks must also go to J. Tenhunen and the company enviscope GmbH for lending us measuring devices and to the company Sick Vertriebs-GmbH for giving us a bar code scanner as a gift. Furthermore, we want to thank all PhD students of the Department of Micrometeorology, student assistants and G. Müller from BayCEER for helping us during the EGER project. This research was funded by the German Science Foundation (DFG) within the projects FO 226/16-1 and ME 2100/4-1 as well as the DFG PAK 446 project, mainly the subprojects FO226/21-1, ME 2100/5-1. The HMMS was funded by the Max-Planck-Institute for Chemistry, Mainz and the University of Bayreuth.

References

Akima H (1970) A new method of interpolation and smooth curve fitting based on local procedures. J Assoc Comput Mach 17:589–602

Aubinet M (2008) Eddy covariance CO_2 flux measurements in nocturnal conditions: an analysis of the problem. Ecol Appl 18:1368–1378

Aubinet M, Heinesch B, Yernaux M (2003) Horizontal and vertical CO_2 advection in a sloping forest. Bound-Layer Meteorol 108(3):397–417. doi:10.1023/A:1024168428135

Aussenac G (2000) Interactions between forest stands and microclimate: Ecophysiological aspects and consequences for silviculture. Ann For Sci 57(3):287–301. doi:10.1051/forest:2000119

Baker TP, Jordan GJ, Steel EA, Fountain-Jones NM, Wardlaw TJ, Baker SC (2014) Microclimate through space and time: microclimatic variation at the edge of regeneration forests over daily, yearly and decadal time scales. Forest Ecol Manag 334:174–184. doi:10.1016/j.foreco.2014.09.008

Baldocchi D, Finnigan JF, Wilson K, Paw U KT, Falge E (2000) On measuring net ecosystem carbon exchange over tall vegetation on complex terrain. Bound-Layer Meteorol 96(1–2):257–291. doi:10.1023/A:1002497616547

Baumgartner A (1956) Untersuchungen über den Wärme- und Wasserhaushalt eines jungen Waldes. Berichte des Deutschen Wetterdienstes 5, Nr. 28

Bonan GB (2008) Ecological climatology: concepts and applications, 2nd edn. Cambridge University Press, Cambridge

Breshears DD, Rich PM, Barnes FJ, Campbell K (1997) Overstory-imposed heterogeneity in solar radiation and soil moisture in a semiarid woodland. Ecol Appl 7(4):1201–1215. doi:10.1890/1051-0761(1997)007[1201:OIHISR]2.0.CO;2

Chen J, Franklin JF, Spies TA (1993) Contrasting microclimates among clearcut, edge, and interior of old-growth Douglas-fir forest. Agric For Meteorol 63(3–4):219–237. doi:10.1016/0168-1923(93)90061-L

Chen J, Franklin JF, Spies TA (1995) Growing-season microclimatic gradients from clearcut edges into old-growth Douglas-Fir forests. Ecol Appl 5(1):74–86. doi:10.2307/1942053

Chen J, Saunders SC, Crow TR, Naiman RJ, Brosofske K, Mroz GD, Brookshire BL, Franklin JF (1999) Microclimate in forest ecosystem and landscape ecology. BioScience 49(4):288–297. doi:10.2307/1313612

Closa I, Irigoyen JJ, Goicoechea N (2010) Microclimatic conditions determined by stem density influence leaf anatomy and leaf physiology of beech (Fagus sylvatica L.) growing within stands that naturally regenerate from clear-cutting. Trees 24(6):1029–1043. doi:10.1007/s00468-010-0472-3

Davies-Colley RJ, Payne GW, van Elswijk M (2000) Microclimate gradients across a forest edge. New Zeal J Ecol 24(2):111–121

Dlugi R (1993) Interaction of NO_x and VOC's within vegetation. In: Borrell PW (ed) Proceedings EUROTRAC symposium '92, SPB, Academic Publication, The Hague, pp 682–688

Eder F, Serafimovich A, Foken T (2013) Coherent structures at a forest edge: properties, coupling and impact of secondary circulations. Bound-Layer Meteorol 148(2):285–308. doi:10.1007/s10546-013-9815-0

Feigenwinter C, Bernhofer C, Eichelmann U, Heinesch B, Hertel M, Janous D, Kolle O, Lagergren F, Lindroth A, Minerbi S, Moderow U, Molder M, Montagnani L, Queck R, Rebmann C, Vestin P, Yernaux M, Zeri M, Ziegler W, Aubinet M (2008) Comparison of horizontal and vertical advective CO_2 fluxes at three forest sites. Agr For Meteorol 148(1):12–24. doi:10.1016/j.agrformet.2007.08.013

Foken T, Dlugi R, Kramm G (1995) On the determination of dry deposition and emission of gaseous compounds at the biosphere-atmosphere interface. Meteorol Z 4:91–118

Foken T, Meixner FX, Falge E, Zetzsch C, Serafimovich A, Bargsten A, Behrendt T, Biermann T, Breuninger C, Dix S, Gerken T, Hunner M, Lehmann-Pape L, Hens K, Jocher G, Kesselmeier J, Lüers J, Mayer JC, Moravek A, Plake D, Riederer M, Rütz F, Scheibe M, Siebicke L, Sörgel M, Staudt K, Trebs I, Tsokankunku A, Welling M, Wolff V, Zhu Z (2012) Coupling processes and exchange of energy and reactive and non-reactive trace gases at a forest site – results of the EGER experiment. Atmos Chem Phys 12(4):1923–1950. doi:10.5194/acp-12-1923-2012

Geiger R, Aron RH, Todhunter P (2009) The climate near the ground. Rowman & Littlefield, Lanham, MD

Hübner J, Olesch J, Falke H, Meixner FX, Foken T (2014) A horizontal mobile measuring system for atmospheric quantities. Atmos Meas Tech 7(9):2967–2980. doi:10.5194/amt-7-2967-2014

Hutchison BA, Hicks BB (eds) (1985) The forest-atmosphere interaction. In: Proceedings of the forest environmental measurements conference held at Oak Ridge, Tennessee, Oct 23–28, 1983, D. Reidel Publishing Company, Dordrecht

Klaassen W, van Breugel PB, Moors EJ, Nieveen JP (2002) Increased heat fluxes near a forest edge. Theor Appl Climatol 72(3–4):231–243. doi:10.1007/s00704-002-0682-8

Lee X (1998) On micrometeorological observations of surface-air exchange over tall vegetation. Agr For Meteorol 91(1–2):39–49. doi:10.1016/S0168-1923(98)00071-9

Ma S, Concilio A, Oakley B, North M, Chen J (2010) Spatial variability in microclimate in a mixed-conifer forest before and after thinning and burning treatments. Forest Ecol Manag 259(5):904–915. doi:10.1016/j.foreco.2009.11.030

Mahrt L, Sun J, Vickers D, MacPherson JI, Pederson JR, Desjardins RL (1994) Observations of fluxes and Inland breezes over a heterogeneous surface. J Atmos Sci 51(17):2484–2499. doi:10.1175/1520-0469(1994)051<2484:OOFAIB>2.0.CO;2

Matlack GR (1993) Microenvironment variation within and among forest edge sites in the eastern United States. Biol Conserv 66(3):185–194. doi:10.1016/0006-3207(93)90004-K

Matlack GR, Litvaitis JA (1999) Forest edges. In: Hunter ML Jr (ed) Maintaining biodiversity in forest ecosystems, Cambridge University Press, Cambridge, pp 210–233

Molemaker MJ, Vilà -Guerau de Arellano J (1998) Control of chemical reactions by convective turbulence in the boundary layer. J Atmos Sci 55(4):568–579. doi:10.1175/1520-0469(1998)055<0568:COCRBC>2.0.CO;2

Murcia C (1995) Edge effects in fragmented forests: implications for conservation. Trends Ecol Evol 10(2):58–62. doi:10.1016/S0169-5347(00)88977-6

Oke TR (1987) Boundary layer climates. Routledge Chapman & Hall, London

Paw U KT, Baldocchi DD, Meyers TP, Wilson KB (2000) Correction Of Eddy-covariance measurements incorporating both advective effects and density fluxes. Bound-Layer Meteorol 97(3):487–511. doi:10.1023/A:1002786702909

Scharenbroch BC, Bockheim JG (2007) Impacts of forest gaps on soil properties and processes in old growth northern hardwood-hemlock forests. Plant Soil 294(1–2):219–233. doi:10.1007/s11104-007-9248-y

Serafimovich A, Siebicke L, Staudt K, Lüers J, Biermann T, Schier S, Mayer JC (2008a) ExchanGE processes in mountainous Regions (EGER) - Documentation of the intensive observation period (IOP1) Sept, 6th to Oct, 7th 2007. Arbeitsergebn, University of Bayreuth, Abt Mikrometeorol. ISSN 1614-8916 36:147

Serafimovich A, Siebicke L, Staudt K, Lüers J, Biermann T, Schier S, Mayer JC (2008b) ExchanGE processes in mountainous Regions (EGER) - documentation of the intensive observation period (IOP2) June, 1st to July, 15th 2008. Arbeitsergebn, University of Bayreuth, Abt Mikrometeorol. ISSN 1614-8916 37:180

Serafimovich A, Eder F, Hübner J, Falge E, VoSS, Sörgel M, Held A, Liu Q, Eigenmann R, Huber K, Duarte HF, Werle P, Gast E, Cieslik S, Heping L, Foken T (2011a) ExchanGE processes in mountainous regions (EGER): documentation of the intensive observation period (IOP3) June, 13th to July, 26th 2011. Arbeitsergebn, University of Bayreuth, Abt Mikrometeorol. ISSN 1614-8916 47:137

Serafimovich A, Thomas C, Foken T (2011b) Vertical and horizontal transport of energy and matter by coherent motions in a tall spruce canopy. Bound-Layer Meteorol 140:429–451. doi:10.1007/s10546-011-9619-z

Siebicke L (2008) Footprint synthesis for the FLUXNET site Waldstein/Weidenbrunnen (DE-Bay) during the EGER experiment. Arbeitsergebn, University of Bayreuth, Abt Mikrometeorol, ISSN 1614-8916 38:49

Siebicke L (2010) Advection at a forest side - an updated approach. PhD thesis, University of Bayreuth, Bayreuth

Siebicke L, Hunner M, Foken T (2011a) Aspects of CO_2 advection measurements. Theor Appl Climatol 109(1–2):109–131. doi:10.1007/s00704-011-0552-3

Siebicke L, Steinfeld G, Foken T (2011b) CO_2-gradient measurements using a parallel multi-analyzer setup. Atmos Meas Tech 4(3):409–423. doi:10.5194/amt-4-409-2011

Sörgel M, Trebs I, Serafimovich A, Moravek A, Held A, Zetzsch C (2011) Simultaneous HONO measurements in and above a forest canopy: influence of turbulent exchange on mixing ratio differences. Atmos Chem Phys 11(2):841–855. doi:10.5194/acp-11-841-2011

Thomas CK (2011) Variability of Sub-Canopy flow, temperature, and horizontal advection in moderately complex terrain. Bound-Layer Meteorol 139(1):61–81. doi:10.1007/s10546-010-9578-9

Thomas C, Foken T (2007) Flux contribution of coherent structures and its implications for the exchange of energy and matter in a tall spruce canopy. Bound-Layer Meteorol 123(2):317–337. doi:10.1007/s10546-006-9144-7

Vanwalleghem T, Meentemeyer RK (2009) Predicting forest microclimate in heterogeneous landscapes. Ecosystems 12(7):1158–1172. doi:10.1007/s10021-009-9281-1

von Arx G, Dobbertin M, Rebetez M (2012) Spatio-temporal effects of forest canopy on understory microclimate in a long-term experiment in Switzerland. Agr For Meteorol 166–167:144–155. doi:10.1016/j.agrformet.2012.07.018

von Arx G, Graf Pannatier E, Thimonier A, Rebetez M (2013) Microclimate in forests with varying leaf area index and soil moisture: potential implications for seedling establishment in a changing climate. J Ecol 101(5):1201–1213. doi:10.1111/1365-2745.12121

Weaver CP, Avissar R (2001) Atmospheric disturbances caused by human modification of the landscape. Bull Am Meteorol Soc 82(2):269–281. doi:10.1175/1520-0477(2001)082<0269:ADCBHM>2.3.CO;2

Whittaker RH (1975) Communities and ecosystems. MacMillan, New York 2nd Revised edn.

Wicklein HF, Christopher D, Carter ME, Smith BH (2012) Edge effects on sapling characteristics and microclimate in a small temperate deciduous forest fragment. Nat Areas J 32(1):110–116. doi:10.3375/043.032.0113

Chapter 15
Catchment Evapotranspiration and Runoff

Gunnar Lischeid, Sven Frei, Bernd Huwe, Christina Bogner, Johannes Lüers, Wolfgang Babel, and Thomas Foken

15.1 Introduction

The Waldstein study site is part of the catchment of the Lehstenbach stream which has been subject to extensive hydrological monitoring programs and model studies. From a hydrologist's perspective, evapotranspiration is a major output flux, and is the second to largest hydrological flux rate, second to precipitation. Hydrologists prefer studying hydrological catchments because they allow to determine mass balances: Assuming long-term steady-state precipitation minus evapotranspiration should be equal to runoff via the catchment outlet. All three components have been

G. Lischeid (✉)
Leibniz Centre for Agricultural Landscape Research, Institute of Landscape Hydrology, Eberswalder Str. 84, 15374 Müncheberg, Germany

Institute of Earth and Environmental Sciences, University of Potsdam, Karl-Liebknecht-Strasse 24-25, 14476 Potsdam, Germany
e-mail: lischeid@zalf.de

S. Frei
Chair of Hydrology, University of Bayreuth, 95440 Bayreuth, Germany

Bayreuth Center of Ecology and Environmental Research, University of Bayreuth, Bayreuth, Germany

B. Huwe
Soil Physics Group, University of Bayreuth, 95440 Bayreuth, Germany

Bayreuth Center of Ecology and Environmental Research, University of Bayreuth, Bayreuth, Germany

C. Bogner
Chair of Ecological Modelling, University of Bayreuth, 95440 Bayreuth, Germany

Bayreuth Center of Ecology and Environmental Research, University of Bayreuth, Bayreuth, Germany

T. Foken (ed.), *Energy and Matter Fluxes of a Spruce Forest Ecosystem*,
Ecological Studies 229, DOI 10.1007/978-3-319-49389-3_15

measured in the Lehstenbach catchment. Thus, the mass balance approach allows for checking for reliability of the measurements or unknown losses.

Besides, merging the extensive data sets that are available from the Lehstenbach catchment is used to check and to deepen our understanding of both meteorological and hydrological processes. Plants and topsoil constitute the crucial zone of allocation of water provided by precipitation, either back to the atmosphere or down to the groundwater and subsequently to the streams. Coupling between atmosphere and hydrosphere in this zone has to be considered in both disciplines. However, different approaches are used for assessing processes at this interface, with different assumptions and simplifications with respect to the respective "other" system. In this chapter we will compare modeling approaches from both disciplines.

Besides, the short-term dynamics of observed state variables and fluxes are a valuable source of information. From a time series analysis perspective, the temporal dynamics of meteorological forcing via radiation and precipitation impose signals on state variables and flux rates. Here the term "signal" is used in a very broad sense as any change of an observed variable in time. These signals propagate either back to the atmosphere or through the soil down to the groundwater and streams which will be studied by various methods in this chapter.

Measuring temporal changes of state variable is much easier to perform compared to determining mass budgets or mass fluxes. This approach does not consider the respective mass fluxes or budgets. However, observed signals are closely related to the latter. Thus, a lot of information can be gained about the related processes. It has to be accounted for that the respective time scales might vary over some orders of magnitude, e.g., comparing dynamics in the lower atmosphere with those in the deeper groundwater. However, these systems are linked to each other and thus cannot be independent in a purely statistical sense.

J. Lüers
Bayreuth Center of Ecology and Environmental Research, University of Bayreuth, 95440 Bayreuth, Germany

W. Babel
Group of Micrometeorology, University of Bayreuth, 95440, Bayreuth, Germany

Bayreuth Center of Ecology and Environmental Research, University of Bayreuth, Bayreuth, Germany

T. Foken
Am Herrgottsbaum 28, 96120 Bischberg, Germany

Bayreuth Center of Ecology and Environmental Research, University of Bayreuth, Bayreuth, Germany

J. Lüers; W. Babel; T. Foken: Affiliation during the work at the Waldstein sites – Department of Micrometeorology, University of Bayreuth, Bayreuth, Germany

G. Lischeid: Affiliation during the work at the Waldstein sites – Department of Hydrogeology and Chair of Ecological Modelling, University of Bayreuth, Bayreuth, Germany

Consequently, this study aimed at assessing the effect size of precipitation and evapotranspiration on soil moisture, groundwater head, and discharge dynamics by combining mass budget and signal transformation approaches. Thus it could be tested whether and to what degree the two meteorological variables differed with respect to spatial patterns of the respective effects.

15.2 Materials and Methods

15.2.1 Hydrological Characterization of the Catchment

The Lehstenbach catchment (4.2 km^2) is located in the mountainous region "Fichtelgebirge" in South Germany, close to the border to the Czech Republic (Fig. 15.1). Here, numerous studies have been performed (e.g., Alewell et al. 2000; Matzner et al. 2004; Bogner et al. 2008; Lischeid and Bittersohl 2008). The altitude varies between 695 and 877 m above sea level. The mean annual temperature is 5.3 °C; the mean annual precipitation is 1162 mm (1971–2000, Foken 2003) on the basis

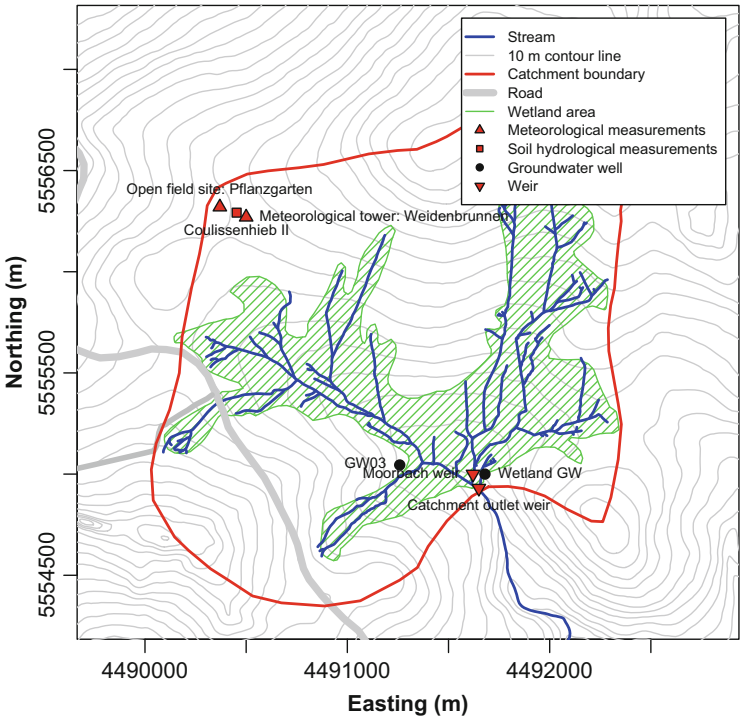

Fig. 15.1 Map of the Lehstenbach catchment with measurement sites

of a synthetic climate data set. For the years 2001–2010, we found a mean annual temperature of 6.5 °C and a mean annual precipitation of 1064 mm (Waldstein-Pflanzgarten). Snowpacks usually develop in January and persist until March, but with substantial interannual variance.

The geological parent material is Variscan granite, intensively weathered during tertiary, except for some outcrops at the mountain top. Thus coarse-grained unconsolidated sediments prevail down to larger depth. Mean thickness of the regolith is assumed to be about 30 m, based on geophysical surveys and drilling cores. However, no borehole reached down to the unweathered bedrock. There is some clear evidence from quarries close to the catchment area that the bedrock is fractured even at larger depth. In addition, one of the major tectonic faults in the area strikes parallel to the main stream in northwest–southeast direction. Thus it is expected that groundwater flow occurs within the bedrock, although presumably at negligible quantities. The catchment outlet is located between two minor topographic heights. Here the stream has incised in a bedrock ridge that blocks groundwater outflow of the catchment, forcing deep groundwater to well up before it discharges into the stream. In addition, a riparian wetland developed behind the bedrock ridge. Thus groundwater outflow out of the catchment is assumed to be negligible (Lischeid et al. 2002).

A rather dense network of mostly perennial small streams has developed in the catchment. Only the uppermost reaches of the stream fell dry occasionally during extended dry periods in the growing season. In some of the riparian wetlands, a semi-confining clayey layer has been found below the base of the peaty soil. Besides, there is clear evidence that the stream system is closely connected to the groundwater system.

Acidic soils like podzols or Dystric Arenosols and cambisols (according to IUSS/ISRIC/FAO, 2006) prevail in more than two thirds of the catchment area. Fens and bogs have developed in topographic depressions, especially close to the streams. Wetland soils cover about 30 % of the area (Gerstberger et al. 2004).

In total, 14 groundwater wells have been installed reaching down to between 10 and 26.3 m depth, with a maximum screening depth of 24.3 m below surface (Fig. 15.1; Lischeid and Bittersohl 2008). Mean groundwater level is more than 10 m below the surface in the upper parts of the watershed and close to the surface in the wetlands. Hydraulic conductivity has been assessed by pumping tests to be about 4×10^{-6} m s^{-1} in the uppermost 10 m of the aquifer (Lischeid et al. 2003). Mean transmissivity is about 7×10^{-5} m^2 s^{-1}, and the effective porosity about 0.1 (Lischeid et al. 2003).

15.2.1.1 Data

In this chapter, water fluxes and related state variables of the soil-atmosphere interface as well as of the vadose zone, the aquifer, and the streams were studied. Evapotranspiration was determined at the tower at the Waldstein-Weidenbrunnen site, additional meteorological data either at the tower or at the open-field site Waldstein-Pflanzgarten close by (Chap. 2; Fig. 2.1).

The precipitation data from Waldstein-Pflanzgarten are gap-corrected observations but not mass corrected (wind and evaporation error) after Richter (1995). That means only data gaps and measurement errors of the original Waldstein-Pflanzgarten observation were checked and if possible added or exchanged with precipitation data from several DWD stations nearby (e.g., DWD stations Weißenstadt, Fichtelberg-Oberfranken-Hüttstadl). A mass correction caused by wind- and snow-induced loss and wetting and evaporation effects inside the gauge (Foken 2003) was not applied. Evapotranspiration has been determined with the eddy-covariance method at the Waldstein-Weidenbrunnen site, from 2002 to 2006 at the "main tower" and on the "turbulence tower" from 2007 on. Inevitable gaps in the time series of half hourly latent heat fluxes had to be filled for estimation of long-term budgets, determined for the 2002–2009 period. Therefore, Priestley-Taylor potential evapotranspiration was calculated from 31 m air temperature and 28 m radiation balance measurements at the main tower and scaled to the eddy-covariance measurements by linear regression. For more details about instrumentation, eddy-covariance processing, quality control, and gap filling, see Chap. 4. Due to missing forcing, data gaps are still left, comprising between 3 and 34 days per year. These data gaps were filled with the mean values of the respective day of the year of the total 2002–2009 period, making use of the pronounced seasonal pattern of the evapotranspiration data.

Soil matrix potential had been continuously measured at 0.20, 0.40, and 0.90 m depth at different plots of the Coulissenhieb II site, located between the Pflanzgarten and the Weidenbrunnen site (Fig. 15.1) at 770 m a.s.l. Here, a series of field experiments had been performed in a mature Norway spruce stand, including artificially induced desiccation (Chen et al. 2011) and freezing (Schmitt and Glaser 2011) of the topsoil as part of the DFG Research Unit 562 "Dynamics of Soil Processes Under Extreme Meteorological Boundary Conditions" (Chap. 1). However, for this study, only data from the control plots C1, C2, and C3 have been considered. Soil matrix potential had been measured at hourly intervals.

In addition, groundwater data from the dormant season 2006–2007 were included in the analysis. Groundwater head had been measured at hourly intervals at two different sites in the downslope part of the catchment where depth to groundwater was not as large as in the upslope region. Groundwater observation well GW03 is located about 400 m northwest of the catchment outlet (Fig. 15.1). Depth to groundwater varied between 2.40 and 3.10 m below surface during the study period. The aquifer is not confined. The well was screened between 2 and 15.4 m below surface (Lischeid and Bittersohl 2008). Thus it did not reach down to the base layer of the aquifer, that is, the unweathered bedrock surface, which is presumably located 30–40 m below surface (Lischeid and Bittersohl 2008). Another shallow groundwater well was located in a wetland area close to the catchment outlet (Fig. 15.1; Weyer et al. 2014). It was screened between 0 and 1 m below surface. Here groundwater level varied between 0.15 m above and 0.45 m below surface during the study period.

This wetland was drained by a small stream without any tributaries from the upstream part of the catchment (Weyer et al. 2014). Discharge of that stream

had been monitored at a V-notch weir, about 60 m downstream of the shallow groundwater well and 75 m upstream of the catchment outlet. In addition, discharge had been monitored at the catchment outlet (Fig. 15.1).

Soil matrix potential, groundwater head, and discharge data of the wetland stream had been measured as part of the activities of the DFG Research Group 562 "Dynamics of Soil Processes Under Extreme Meteorological Boundary Conditions" at the University of Bayreuth. Discharge data of the catchment outlet were online provided by the Bavarian Environment Agency (http://www.gkd.bayern.de) which is highly appreciated.

15.2.1.2 Statistical Approaches

For statistical analyses and plotting of figures, the R software version 3.1.0 (R Core Team 2014) was used, including the packages "rgeos" (Bivand and Rundel 2014) and "maptools" (Bivand and Lewin-Koh 2014).

15.2.2 Principal Component Analysis of Time Series

Time series of hydrological state variables (e.g., soil matrix potential or groundwater head) or flux rates (e.g., stream discharge) usually differ substantially between different sites. The principal component analysis approach aims at using this as a source of information about the identity and the strength of the respective processes. It is based on the assumption that any observed time series can be regarded as a superposition of the effects of different processes.

In addition, the number of prevailing processes that make up the largest spatial and temporal fraction of the variance of the set of observed time series is assumed to be rather low. Differences between time series observed at different sites are then traced back to different strengths of the respective processes.

Principal component analysis (PCA), also known, e.g., as empirical orthogonal function (EOF) approach or Karhunen-Loève decomposition (KLD), is the best-known dimension reduction approach (Jolliffe 2002; Lee and Verleysen 2007). In mathematical terms, it performs an eigenvalue decomposition of a covariance matrix. Here, the latter is based on a set of time series of hydrological state variables and flux rates. These time series are synchronous (same measurement dates at all sites) and without gaps, but not necessarily equidistant. The resulting uncorrelated eigenvectors, that is, the time series of the scores of the principal components, are interpreted as "typical" result of a single process. Correlation of observed time series with any of the eigenvalues, called loading, can be used as a measure of the mean strength of the respective process at the respective site during the period covered by the observations. Usually the principal components are sorted by their eigenvalues, starting with the highest eigenvalue. Typically only the first principal components

are studied as they comprise a large fraction of the total variance, whereas the latter are supposed to be highly due to, beyond others, inaccuracies of the measurements.

Principal component analysis of a set of time series usually yields a first component that is close to a spatial average of all observed time series. Then subsequent principal components depict deviations from that mean behavior at different sites that are due to spatial variation of the respective processes or driving variables. Assigning these principal component results to processes usually is based on analysis of spatial patterns of the loadings or on correlation of the time series of component scores to that of supposed driving variables. Applications of principal component analysis or of the closely related isometric feature mapping to hydrological time series are described in more detail, e.g., by Lischeid et al. (2010), Böttcher et al. (2014), Lehr et al. (2015), and Hohenbrink et al. (2016). Principal component analysis considered only the shape of the time series rather than absolute numbers. In contrast to groundwater head and soil matrix potential data, discharge data were highly skewed and thus were logarithmized prior to analysis. Discharge data of one of the streams contained zero values; thus, a constant offset was added first here. All time series were then normalized to zero mean and unit variance to ensure equal weighting irrespective of the range or variance of observed values.

15.3 Results and Discussion

15.3.1 Long-Term Budgets

During the 2002–2009 period, annual mean values of precipitation, evapotranspiration, and runoff were 1033, 411, and 457 mm year^{-1}, respectively (Fig. 15.2). Catchment runoff of that period is nearly identical to the mean value of the 1988–2001 period of about 462 mm year^{-1} (Lischeid et al. 2004). Mean annual precipitation sum during the 2002–2009 period is about 89 % of the long-term mean of 1162 mm year^{-1} (Foken 2003). It has to be mentioned that the precipitation data used here have not been corrected with respect to wind-induced undercatch and evaporation losses, presumably resulting in an underestimation of the true precipitation. According to Richter (1995) mean error can amount to 10 % or more of the true precipitation. At the Lehstenbach site, wind-related undercatch especially during the winter period with snowfall is likely to be higher, whereas evaporation losses from the sampler likely are less compared to mean values in Germany (Foken 2003).

15.3.1.1 Reliability of Long-Term Budget Data

In the long run, when changes of the catchment groundwater store can be neglected, precipitation should equal the sum of evapotranspiration and runoff. However,

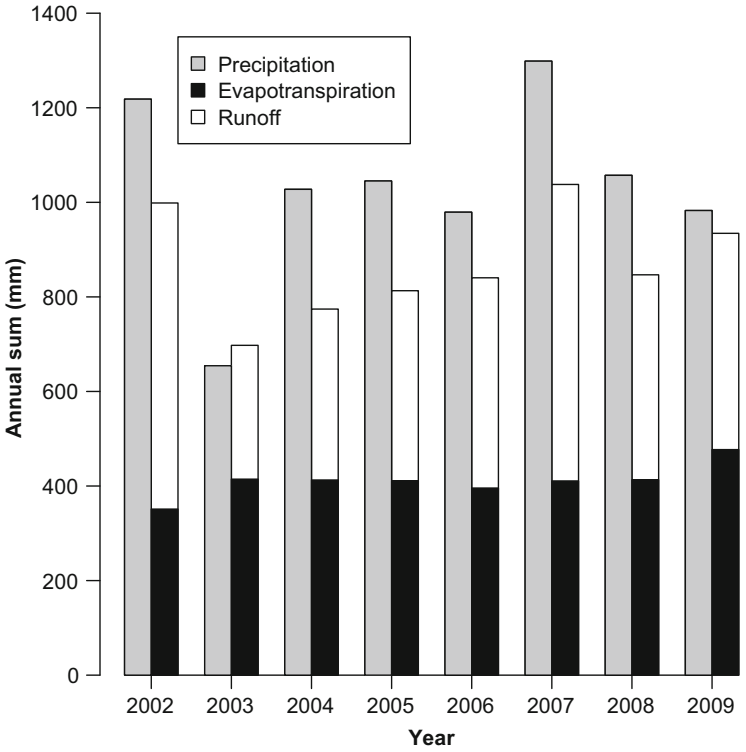

Fig. 15.2 Annual sum of precipitation (*gray bars* to the *left*), evapotranspiration, and runoff (*stacked bars* to the *right*) for the 2002–2009 period in the Lehstenbach catchment

the long-term data indicate a discrepancy of 165 mm year^{-1}. Given the fact that precipitation has even been underestimated, the "true" discrepancy presumably would be even higher. One possible reason might be a systematic overestimation of evapotranspiration. For this study the evaporation data of the footprint of the Waldstein-Weidenbrunnen site (Chap. 12) were transferred to the whole catchment, which is on the lee side of the ridge with lower wind speeds and therefore lower evapotranspiration. However, also the precipitation at the lee side should be lower. Another problem may be a systematic underestimation by the eddy-covariance method, as the average energy balance closure ratio for 2002–2009 is 79 %. However, evapotranspiration has not been corrected for the missing energy balance as the reasons for the non-closure are still unclear (Foken 2008), but the recently applied correction by Charuchittipan et al. (2014) would not increase the evapotranspiration significantly.

Secondly, catchment runoff might have been underrated. If that had been the only source of error in the long-term budgets, it would amount to 26 % at least [165 mm year^{-1}/(165 mm year^{-1} + 457 mm year^{-1})]. The runoff measurements have been calibrated at regular intervals. Thus it is very unlikely that an error of

that size would not have been detected. In addition, part of the catchment runoff might have occurred via groundwater flux underneath the stream and thus would not have been captured by the discharge measurements. However, it is not very likely that that would account for more than a few percent as discussed above. Measured discharge was divided by the catchment area to be compared to precipitation and evapotranspiration data. The catchment area was delineated based on topography data. The stream network as well as groundwater head data from 14 wells confirmed that delineation. However, none of the wells or springs were located close to the catchment boundary and thus could be used for a rigorous test. Nevertheless, an overrating of the catchment area by 26 % or more is very unlikely.

Annual discharge of the Lehstenbach stream in 2006 was compared to that of another 19 streams in the region. These data were provided by Bayerisches Landesamt für Umwelt (2006). Gauges of these streams were at maximum at 38 km distance from that of the Lehstenbach stream. Size of these catchments varied between 18.2 and 523 km^2 and elevation of the gauges between 313 and 519 m a.s.l., compared to 4.2 km^2 and 695 m a.s.l. of the Lehstenbach catchment. Annual specific discharge (i.e., discharge divided by catchment area) of these streams varied between 243 and 755 mm $year^{-1}$, where that of the Lehstenbach stream of about 444 mm $year^{-1}$ was very close both to the mean (478 mm $year^{-1}$) and to the median (471 mm $year^{-1}$). Specific discharge data were neither correlated with altitude of the gauge or catchment area nor were there any clear spatial patterns. Thus the comparison did not give any evidence for systematic underestimation of discharge at the Lehstenbach catchment.

Thirdly, precipitation and evapotranspiration have been measured at an uphill location, whereas the catchment runoff integrates over an area of about 4.2 km^2, where the elevation of the discharge weir is 180 m below that of the site of the meteorological measurements at the Weidenbrunnen site, and a large fraction of the catchment is shielded against westerly winds and is mainly exposed to the south. Thus it cannot be excluded that precipitation is substantially lower, and evapotranspiration is higher in large parts of the catchment compared to the Weidenbrunnen site. Throughfall underneath the canopies had been monitored at six sites in the catchment at biweekly intervals from February 1990 through November 1992 by Moritz et al. (1994). Throughfall varied systematically by up to 10 % between sites and was negatively correlated with tree age and tree height (Moritz et al. 1994). However, stand transpiration and evaporation from interception had not been measured here. However, a later study performed by Köstner et al. (2001) gave some evidence that stand transpiration at different sites in the catchment is fairly homogeneous in space (see below).

Reliability of the runoff data can be assessed by comparison with long-term data of stream runoff in larger catchments close by, provided by the Bayerisches Landesamt für Umwelt. Errors of the budgets are likely to decrease with increasing catchment size. On the other hand, elevation of the Lehstenbach catchment is considerably higher compared to the other sites. Thus it has to be expected that the Lehstenbach runoff stands out due to higher precipitation and lower evapotranspiration.

15.3.1.2 Role of Vegetation

Among the three observables, evapotranspiration was remarkably constant during the 8-year period. Standard deviation was only 34 mm year^{-1}, compared to 191 mm year^{-1} for precipitation and 124 mm year^{-1} for runoff. In 6 out of 8 years, annual evapotranspiration was nearly constant, varying by 5 % only (between 395 and 415 mm year^{-1}). Only in 2002 (351 mm year^{-1}) and 2009 (477 mm year^{-1}) major deviations were found.

These findings are consistent with those from other studies. For example, van Laanen et al. (2004) report on long-term time series of water budgets from the La Mancha Occidental catchment (Spain) 1941–1996 and the Noor catchment (Belgium) 1945–2001 that exhibited similar constant annual evapotranspiration (determined as the difference between precipitation and runoff). Annual evapotranspiration compensated only for 19 % or 25 %, respectively, of interannual differences of precipitation. This is presumably largely due to evaporation of intercepted rainfall. This interception fraction has been known to be roughly constant for decades (Calder and Newson 1979).

Obviously vegetation is very efficient in meeting its requirements of water. Only when a certain threshold is exceeded, surplus water can percolate to greater depth and eventually discharge to the streams. That threshold differs between different climate regions, vegetation types, and vegetation structures, but only to a surprisingly small degree. Transpiration of the understory vegetation has often been found to compensate for lower transpiration of less dense forest stands (Roberts 1983). This has, partly at least, been confirmed for the Lehstenbach catchment by Köstner et al. (2001). Correspondingly, long-term variability of water uptake by plants is very small compared to the usual interannual variability of precipitation or air temperature.

15.3.1.3 Relation to Residence Time and Size of the Groundwater Store

Long-term water budgets of the Lehstenbach catchment can be used to reveal some information about the groundwater store. Mean groundwater residence time in the catchment has been assessed by analysis of the seasonal patterns of ^{18}O data (Zahn 1995). It was 3.6 years at the catchment outlet and between 2.1 and >4 years at six different wells. Multiplying mean annual catchment runoff of about 457 mm year^{-1} by mean residence time results in a total groundwater store of about 1600 mm. These data match those of an alternative assessment, i.e., the ratio between mean transmissivity and mean hydraulic conductivity (=17 m), divided by the mean porosity as given above.

The large groundwater store ensured that stream discharge at the catchment outlet never was below 10 l s^{-1}, corresponding to 0.2 mm day^{-1}, since the start of the measurements in 1988. On the other hand, however, due to generation of very flashy runoff peaks in the extended riparian wetlands, stream runoff reacts with only 3–5

h of time delay compared to precipitation during major rain events (Lischeid et al. 2002). Maximum discharge was recorded in September 1998 with 775 l s^{-1}, corresponding to 15.9 mm day^{-1} (Lischeid et al. 2002). Steep discharge peaks came along with a substantial short-term variation of stream water quality, reflecting a mixture of acid shallow groundwater and rather well-buffered deep groundwater (Lischeid et al. 2002; Strohmeier et al. 2013; Frei et al. 2010, 2012). Short-term dynamics will be studied in more detail in the next section.

15.3.2 Short-Term Dynamics

Analysis of the short-term dynamics of hydrological state variables and fluxes is a common approach to learn more about the associated processes. Here the analysis focuses on two different aspects:

Firstly, processes at the atmosphere-soil interface are studied. From a hydrological perspective, the interplay between precipitation, snowmelt, and evapotranspiration is the driver both of the magnitude and of the short-term dynamics of the seepage flux underneath the rooting zone, comprising the input into the aquifer and subsequently to the stream network. A principal component analysis of time series of soil matrix potential close to the Waldstein-Weidenbrunnen site was performed to elucidate the role of evapotranspiration for generation of spatial and temporal patterns of soil hydrology.

Secondly, propagation of the hydrological input signal through the catchment was studied using time series of soil matrix potential, groundwater head, and stream runoff during the dormant season. Thus plant root water uptake can be neglected. This analysis addresses a key question of hydrological research: How does the water get to the stream, and what is the contribution of different flowpaths? The methodological approach is the same as before, that is, a principal component analysis of a set of time series.

15.3.2.1 Hydrological Signals Generated in the Topsoil

For this analysis, 16 time series of soil matrix potential from the Coulissenhieb II site were used from 20, 40, and 90 cm depth. They cover the year 2006 at hourly intervals. Only dates with a complete data set, that is, reliable values available for all tensiometers, were considered. Consequently there were some substantial lags, especially during the growing season, due to malfunction or to soil desiccation exceeding the measurement range of the tensiometers. However, the remaining data are sufficient to study different degrees of root water uptake during the growing season.

The first principal component explains 69.8 % of the total variance. The time series of the scores of the first principal component is very closely related to the time series of spatial mean of normalized observed values ($r = 99.8$). This is the

usual case when the principal component analysis is applied to a set of time series (Lischeid et al. 2010; Hohenbrink et al. 2016). Thus, about 70 % of the total variance of the data set can be ascribed to mean behavior.

The remaining principal components grasp the spatial variability, that is, deviation from the mean behavior at different sites. Different principal components are interpreted to reflect different effects, and the loadings of single sites, that is, correlation of the respective observed time series with that of the scores of the component, as a measure for the strength of the respective effect at that site.

Among the first ten principal components, correlation of the respective loadings with depth of the tensiometers is clearly the strongest for the fifth principal component ($r = 0.88$). Loadings are mostly negative for 20 cm depth and positive for 90 cm depth (Fig. 15.3).

Figure 15.4 illustrates the effect that is reflected by this principal component. It illustrates a case where half of the variance (equal to the squared Pearson correlation coefficient, i.e., the loading) is explained by the first component, that is, mean behavior, and the other half by the fifth component, assuming that spatial variance is exclusively due to this component. Different lines illustrate negative and positive loadings on the fifth component, respectively. The line with the negative loading, as was found for most of the topsoil tensiometers, exhibits sharp peaks, whereas the other line shows a very smooth and more damped dynamics. The latter is consistent with the expected behavior at greater depth compared to that in the uppermost soil layer. Thus it can be concluded that the fifth component reflects in the first place the effect of increasing damping of the input signal with depth.

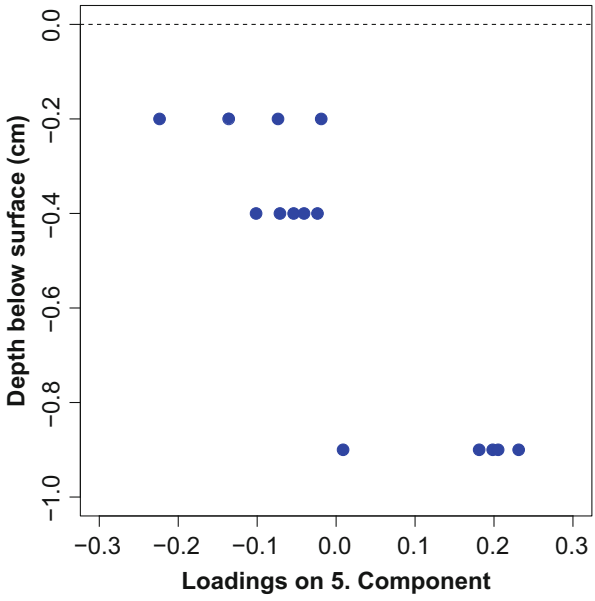

Fig. 15.3 Loadings of time series of matrix potential at different depths on the fifth principal component

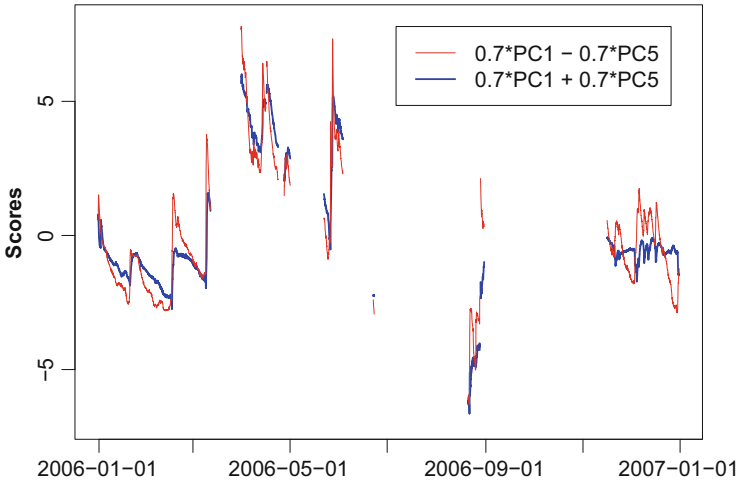

Fig. 15.4 Time series of scores of a combination of the first and fifth principal component

The strongest relationships between time series of the first ten principal components and that of measured evapotranspiration were found for the first and third principal component. As the scores of the first principal component are nearly identical with the spatial average of the dynamics at all tensiometers, the coefficient of correlation of about 4.8 % reflects the mean effect of evapotranspiration on the dynamics of soil matrix potential. In contrast, the third component can be interpreted as a measure to what degree the strength of the effect of evapotranspiration, or root water uptake, respectively, differs between different sites. According to Fig. 15.5, this effect accounts for 5.8 % of the total variance of the data set, that is, 19 % of the spatial variance.

Thus the loadings of time series of soil matrix potential at different sites and depth can be used to assess the strength of the effect of root water uptake on the dynamics of soil matrix potential. Remarkably all tensiometers at site C1 exhibit positive loadings, indicating a stronger than average effect of evapotranspiration (Fig. 15.6). In contrast, loadings are very close to zero or negative for all tensiometers at plot C2. This would suggest that plant water uptake at one site is systematically less compared to the other site which could be due to different physiological activity of the respective trees.

Loadings are close to zero at 90 cm depth, except for plot C1 (Fig. 15.6). In contrast, loadings differ much more at 20 and 40 cm depth. This would suggest that spatial heterogeneity of root water uptake is much more pronounced in the topsoil compared to greater depth. Please keep in mind that the third component grasps only deviations from the mean behavior in the stand and that the effect of soil depth on damping of the input signal is captured by the fifth component.

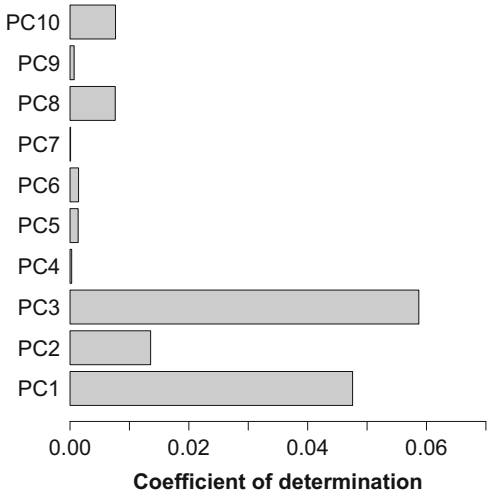

Fig. 15.5 Coefficient of determination (= squared Pearson correlation coefficient) between time series of measured evapotranspiration and time series of scores of the respective principal components

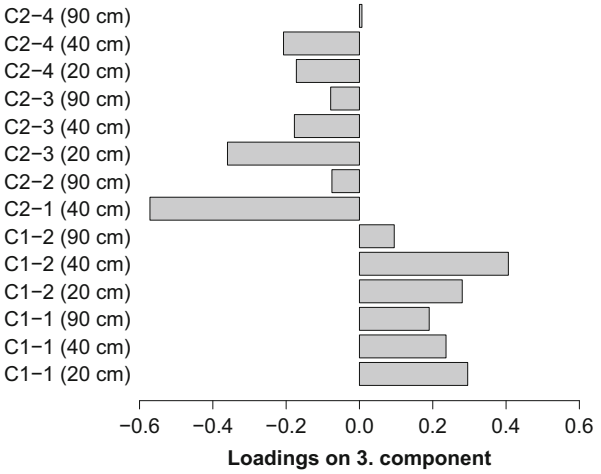

Fig. 15.6 Loadings of time series of soil matrix potential (at different sites and depths) on the third principal component

No data were available to test the hypothesis of different physiological activities at C1 compared to C2, e.g., sap flow measurements or assessments of spatial patterns of evapotranspiration via remote sensing. Nevertheless, the approach presented here would be worth to test to what degree spatial heterogeneity of plant physiology in a tree stand could be assessed by soil matrix data.

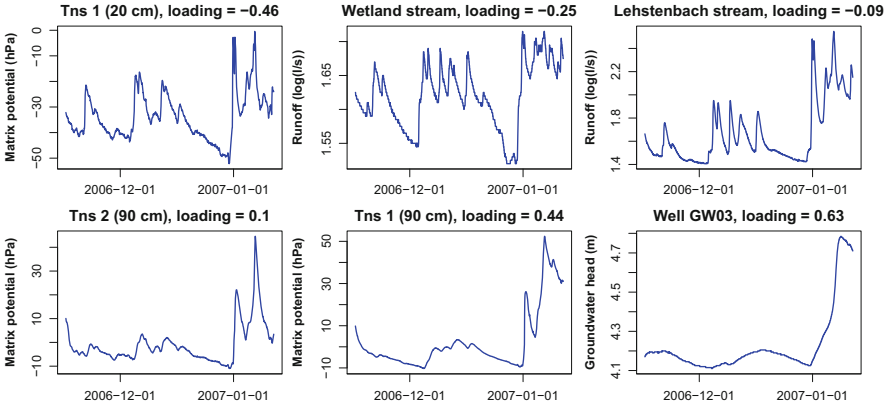

Fig. 15.7 Time series of selected sites, sorted by loadings on second principal component. *Tns* tensiometer site

15.3.2.2 Hydrological Signals Propagating Through the Subsoil

Propagation of hydrological signals through the catchment was studied performing a principal component analysis on time series of soil matrix potential, groundwater head, and stream runoff during the dormant season 16.11.2006–12.01.2007. Time resolution was 1 h.

Again the time series of scores of the first principal component are closely correlated with that of spatial means of z-normalized observed time series ($r^2 = 99.99$ %). The first component explains 77 % of the variance of the total data set, and the second another 12 %.

Loadings on the second principal component describe how the respective time series differ from mean behavior which is given by the time series of scores of the first principal component. This is illustrated in Fig. 15.7 where selected measured time series are shown, sorted by loadings on the second principal component. The higher the loadings, the more smoothed and damped the time series are. In addition, the higher the loadings, the more exceed the observed values in January 2007 those of the preceding months. Thus loadings on the second principal component can be used as a measure for the degree of smoothing or damping exhibited by the respective time series (cf. Lischeid et al. 2010; Hohenbrink et al. 2016).

Loadings on the second principal component are closely related to depth (Fig. 15.8). However, the data reveal substantial scatter. Some tensiometers at 20 cm depth exhibit similarly high loadings compared to some tensiometers at 90 cm depth. This is likely due to spatially differing soil texture and soil structure, as has been shown by Hohenbrink and Lischeid (2015), which is rarely depicted in soil hydrological models (Chap. 7).

Highest positive loading on the second component, that is, the most damped behavior, exhibited the time series of groundwater head at GW03, with depth to groundwater varying between 2.40 and 3.10 m below surface. In contrast, that of a

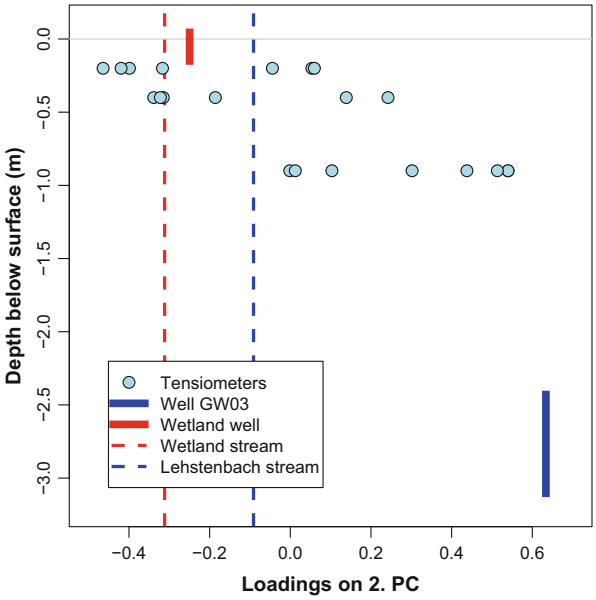

Fig. 15.8 Loadings on the second principal component versus depth of tensiometers or the range of depth to groundwater for the groundwater data, respectively. Loadings of the hydrographs of the two streams that cannot be related to a specific depth are given as vertical lines

shallow groundwater well in the wetland close to the catchment outlet is in the range of the uppermost tensiometers at the Coulissenhieb II site, about 1.8 km apart.

Damping of the hydrograph of the small stream that drains the wetland area is among the lowest found even in the uppermost tensiometers and even lower compared to shallow groundwater in the wetland. This corroborates the conclusion by Weyer et al. (2014) based on water quality data that runoff occurs mostly on or slightly below the surface of the wetland. Similar results were found in a model study based on data from the Lehstenbach catchment (Frei et al. 2010). In contrast, runoff at the catchment outlet is clearly more damped compared to the wetland stream, pointing to a stronger contribution of deeper groundwater. However, damping of the Lehstenbach catchment runoff is still less compared to that of soil matrix potential at 90 cm depth (Fig. 15.8). It can be concluded that near-surface runoff in the riparian wetlands plays a major role as well, which has been postulated based on solute concentration data before (Lischeid et al. 2002; Weyer et al. 2014).

A preceding study (Lischeid et al. 2002) had shown that time series of soil matrix potential did not differ systematically between different sites within the Lehstenbach catchment, except that upslope sites differed from the wetland sites. The same has been shown for solute concentration data (Schilli et al. 2010; Weyer et al. 2014). Thus, although only data from the Coulissenhieb II were available for this study, it can be concluded that these data were representative for the upslope parts of the catchment. In fact, the findings presented here confirm a coherent signal propagation

through the whole catchment over 1.7 km distance from the upslope Coulissenhieb II site to the catchment outlet.

Propagation of the precipitation signal from infiltration in the soil to the catchment outlet during stormflow occurs within 3–5 h (Lischeid et al. 2002). However, this comprises only 35 % of the total rainfall, that is, rain falling on the wetland areas. In contrast, propagation of the signal induced by evapotranspiration (which is close to zero during stormflow) is in the range of some years, that is, that of the mean residence time in the groundwater (see above). This difference in the respective travel time by at least 3 orders of magnitude results in substantial differences of solute concentration in the stream between baseflow and streamflow (Lischeid et al. 2002; Strohmeier et al. 2013; Weyer et al. 2014). However, the term "mean residence time" has to be used with outermost caution, as the residence time distribution of water passing through the subsoil is highly skewed, with a small fraction comprising very long residence time. Consequently, once contaminants have been released in the soil or groundwater, they will persist there for decades, at least in small quantities (Kirchner et al. 2000).

15.3.3 Evapotranspiration in Hydrological and Hydrogeological Model Approaches

Hydrological and hydrogeological models primarily focus on water (and solute) transport through soil and aquifer to the streams. Temporal variability of infiltrating precipitation and of plant root water uptake and bare soil evaporation generate spatial hydraulic gradients in the subsurface that are only slowly smoothed out due to very slow mass transport in the liquid phase. Thus the corresponding models in principle describe dissipation of external signals in the subsurface. The PCA analysis of soil matrix potential, groundwater heads, and stream discharge in this study nicely depicts the transformation of the input signal propagating through the catchment, resulting both in damping and delaying of the dynamics along the respective hydrological flowpaths.

Different models have been applied to the Lehstenbach catchment. Bogner et al. (Chap. 7) focus on soil water dynamics in the vadose zone. Lischeid et al. (2003) run a groundwater transport model to describe both the spatial patterns and temporal dynamics of groundwater head in the catchment. Frei et al. (2010, 2012) and Partington et al. (2013) focused on the interface between groundwater, vadose zone, and receiving streams to study effects of topography on stream discharge during storm events. Here stream discharge is described as the superposition of the contribution of various flowpaths that differ widely with respect to length, flow velocity, and impact on water quality (Lischeid et al. 2002, 2007). Thus, finally topography translates into apparently complex spatial and temporal patterns of soil moisture, groundwater head, stream discharge, and water quality (Partington et al. 2013; Frei et al. 2012).

Hydrological and hydrogeological models are powerful tools for assessing temporal and spatial patterns of hydrological state variables and fluxes. However, they are much less powerful with respect to determining absolute values and highly depend on high-quality precipitation and evapotranspiration data. Due to the inherent principle of mass conservation, incoming precipitation should be equal to the sum of evapotranspiration, runoff, and changes of the groundwater store. Models of the vadose zone and land surface schemes split precipitation between the latter three. Due to the complexity of the respective processes, substantial spatial variability, and shortage of respective data, this is often done in a very simplified way. In most cases, the respective parameters are determined by inverse modeling by fitting to the observed long-term budget. Although that approach might be adequate for spatially lumped models under approximately stationary conditions, it is highly questionable, e.g., for climate or land use change scenario studies (Beven 2001; Milly et al. 2008).

In contrast, most groundwater models require a quantification of groundwater recharge rather than precipitation (e.g., Lischeid et al. 2003), thus disregarding any evapotranspiration processes. But now, models are available that dynamically couple vadose zone, groundwater, and surface water systems. One example is the HydroGeoSphere model that has been applied to the Lehstenbach catchment recently (Partington et al. 2013).

15.4 Conclusions

Ecosystems split incoming precipitation into evaporation from soil and plant surface, transpiration of plants, and discharge of the residual fraction to receiving streams via deep seepage, groundwater flow, or surface runoff. Long-term data on precipitation, evapotranspiration, and catchment runoff in the Lehstenbach catchment confirmed findings from other sites in that forest transpiration was remarkably constant over the years in contrast to precipitation and catchment runoff. On the other hand, the data revealed substantial discrepancies between input via precipitation on the one hand side and the sum of evapotranspiration and runoff on the other side. The reason for that still is not clear.

Principal component analysis of time series of daily values was used to characterize both the generation of the hydrological input signal in the topsoil and its propagation through the catchment toward the catchment outlet. Substantial spatial heterogeneity was found. About 7 % of that heterogeneity in the topsoil could be traced back to the spatially differing degree of root water uptake within the apparently homogeneous spruce stand.

Following hydrological signals throughout the catchment revealed another effect of spatial heterogeneity. Groundwater flow in the Lehstenbach catchment occurs at the time scale of some years on average. However, a minor fraction bypasses the subsoil during heavy rainstorms and reaches the catchment outlet within a few hours. That fraction bypasses plant evapotranspiration as well because the latter is

close to zero during heavy rainstorms. During the last decades, hydrological studies in small headwater catchments mostly focused on stormflow generation processes during the rather short events and consequently did not consider evapotranspiration. However, increasing concern about climate change and the predicted future shortage of water resources in many parts of the world surely will shift hydrologists' focus toward droughts and the role of plant transpiration.

Acknowledgments The first author is indebted to Andreas Kolb and Christina Weyer who performed most of the hydrological installations, maintenance, and data processing in the Lehstenbach catchment even under harsh conditions. Funding for soil hydrological, groundwater head, and stream discharge measurements had been provided by the German Federal Ministry for Education, Science, Research, and Technology (BMBF, Grant No. PT BEO 51—0339476 A-D) and by the German Research Foundation (DFG) within the Research Group 562 (University of Bayreuth) "Dynamics of Soil Processes Under Extreme Meteorological Boundary Conditions" which is highly appreciated. Long-term measurements of evapotranspiration and precipitation were financed by the German Research Foundation (Fo 226/16-1, Fo 226/21-1) and the Oberfrankenstiftung (Grant. No. 01879).

References

Alewell C, Manderscheid B, Gerstberger P, Matzner E (2000) Effects of reduced atmospheric deposition on soil solution chemistry and elemental contents of spruce needles in NE—Bavaria, Germany. J Plant Nutr Soil Sci 163:509–516

Bayerisches Landesamt für Umwelt (2006) Deutsches Gewässerkundliches Jahrbuch. Rheingebiet, Teil II, Main. Mit einem Anhang: Bayer. Elbegebiet. 01.11.2005–31.12.2006. ISSN 2193-4851

Beven K (2001) On fire and rain (or predicting the effects of change). Hydrol Process 15:1397–1399. doi:10.1002/hyp.458

Bivand R, Lewin-Koh N (2014) maptools: Tools for reading and handling spatial objects. R package version 0.8-30. http://CRAN.R-project.org/package=maptools

Bivand R, Rundel C (2014) rgeos: Interface to Geometry Engine – Open Source (GEOS). R package version 0.3-8. http://CRAN.R-project.org/package=rgeos

Bogner C, Wolf B, Schlather M, Huwe B (2008) Analysing flow patterns from dye tracer experiments in a forest soil using extreme value statistics. Eur J Soil Sci 59:103–113. doi:10.1111/j.1365-2389.2007.00974.x

Böttcher S, Merz C, Lischeid G, Dannowski R (2014) Using Isomap to differentiate between anthropogenic and natural effects on groundwater dynamics in a complex geological setting. J Hydrol 519:1634–1641. doi:10.1016/j.jhydrol.2014.09.048

Calder IR, Newson MD (1979) Land use and upland water resources in Britain—A strategic look. J Am Water Resour Assoc 15:1628–1639

Charuchittipan D, Babel W, Mauder M, Leps JP, Foken T (2014) Extension of the averaging time in eddy-covariance measurements and its effect on the energy balance closure. Bound-Lay Meteorol 152(3):303–327. doi:10.1007/s10546-014-9922-6

Chen YT, Bogner C, Borken W, Stange CF, Matzner E (2011) Minor response of gross N turnover and N leaching to drying, rewetting and irrigation in the topsoil of a Norway spruce forest. Eur J Soil Sci 62:709–717. doi:10.1111/j.1365-2389.2011.01388.x

Foken T (2003) Lufthygienisch-Bioklimatische Kennzeichnung des oberen Egertales. Bayreuther Forum Ökologie. 100:69+XLVIII

Foken T (2008) The energy balance closure problem: an overview. Ecol Appl 18(6):1351–1367. http://www.jstor.org/stable/40062260

Frei S, Lischeid G, Fleckenstein J (2010) Effects of micro-topography on surface-subsurface exchange and runoff generation in a riparian wetland. Adv Water Res 33:1388–1401. doi:10.1016/j.advwatres.2010.07.006

Frei S, Knorr KH, Peiffer S, Fleckenstein JH (2012) Surface micro-topography causes hot spots of biogeochemical activity in wetland systems: a virtual modeling experiment. J Geophys Res 117:G00N12. doi:10.1029/2012JG002012

Gerstberger P, Foken T, Kalbitz K (2004) The Lehstenbach and Steinkreuz chatchments in NE Bavaria, Germany. In: Matzner E (ed) Biogeochemistry of forested catchments in a changing environment, a German case study, Ecological studies, vol 172. Springer, Heidelberg, pp 15–41

Hohenbrink T, Lischeid G (2015) Does textural heterogeneity matter? Quantifying transformation of hydrological signals in soils. J Hydrol 523:725–738. doi:10.1016/j.jhydrol.2015.02.009

Hohenbrink TL, Lischeid G, Schindler U, Hufnagel J (2016) Disentangling land management and soil heterogeneity effects on soil moisture dynamics. Vadose Zone J 15(1), DOI: 10.2136/vzj2015.07.0107

Jolliffe IT (2002) Principal component analysis. Springer series in statistics. Springer, New York, 489 pp

Kirchner JW, Feng X, Neal C (2000) Fractal stream chemistry and its implications for contaminant transport in catchments. Nature 43:524–527

Köstner B, Tenhunen JD, Alsheimer M, Wedler M, Scharfenberg H-J, Zimmermann R, Falge E, Joss U (2001) Controls on evapotranspiration in a spruce forest catchment of the Fichtelgebirge. In: Tenhunen JD, Lenz R, Hantschel R (eds) Ecosystem approaches to landscape management in Central Europe, Ecological studies, vol 147. Springer, Berlin, pp 379–415

Lee JA, Verleysen M (2007) Nonlinear dimensionality reduction, Information science and statistics. Springer, New York

Lehr C, Pöschke F, Lewandowski J, Lischeid G (2015) A novel method to evaluate the effect of a stream restoration on the spatial pattern of hydraulic connection of stream and groundwater. J Hydrol 527:394–401. doi:10.1016/j.jhydrol.2015.04.075

Lischeid G, Bittersohl J (2008) Tracing biogeochemical processes in stream water and groundwater using nonlinear statistics. J Hydrol 357:11–28. doi:10.1016/j.jhydrol.2008.03.013

Lischeid G, Kolb A, Alewell C (2002) Apparent translatory flow in groundwater recharge and runoff generation. J Hydrol 265:195–211

Lischeid G, Büttcher H, Hauck A (2003) Combining data-based and process-based approaches to minimize the complexity of a reactive sulfate transport model. Proceedings of the ModelCARE'2002 conference held at Prague, Czech Republic, June 2002. IAHS-Publications 277:402–408

Lischeid G, Alewell C, Moritz K, Bittersohl J (2004) Trends in the input-output relations: the catchment budgets. In: Matzner E (ed) Biogeochemistry of forested catchments in a changing environment. A German case study, Ecological studies, vol 172. Springer, Heidelberg, pp 437–456

Lischeid G, Kolb A, Alewell C, Paul S (2007) Impact of redox and transport processes in a riparian wetland on stream water quality in the Fichtelgebirge Region, Southern Germany. Hydrol Process 21:123–132. doi:10.1002/hyp.6227

Lischeid G, Natkhin M, Steidl J, Dietrich O, Dannowski R, Merz C (2010) Assessing coupling between lakes and layered aquifers in a complex Pleistocene landscape based on water level dynamics. Adv Water Res 33:1331–1339. doi:10.1016/j.advwatres.2010.08.002

Matzner E, Köstner B, Lischeid G (2004) Biogeochemistry of two forested catchments in a changing environment: a synthesis. In: Matzner E (ed) Biogeochemistry of forested catchments in a changing environment, A German case study, Ecological studies, vol 172. Springer, Heidelberg, pp 475–490

Milly PCD, Betancourt J, Falkenmark M, Hirsch RM, Kundzewicz ZW, Lettenmaier DP, Stouffer RJ (2008) Stationarity is dead: whither water management? Science 319:573–574. doi:10.1126/science.1151915

Moritz K, Bittersohl J, Müller FX, Krebs M (1994) Auswirkungen des Sauren Regens und des Waldsterbens auf das Grundwasser. Dokumentation der Methoden und Meßdaten des Entwicklungsvorhabens 1988–1992. Bayerisches Landesamt für Wasserwirtschaft, Materialien No. 40, München, 387 S

Partington D, Brunner P, Frei S, Simmons CT, Werner AD, Therrien R, Maier HR, Dandy GC, Fleckenstein JH (2013) Interpreting streamflow generation mechanisms from integrated surface-subsurface flow models of a riparian wetland and catchment. Water Resour Res 49:5501–5519. doi:10.1002/wrcr.20405

R Core Team 2014 R: A language and environment for statistical computing. R Foundation for Statistical Computing, Vienna, Austria. http://www.R-project.org/

Richter D (1995) Ergebnisse methodischer Untersuchungen zur Korrektur des systematischen Meßfehlers des Hellmann-Niederschlagmessers. Berichte des Deutschen Wetterdienstes 194, Offenbach, 93 pp

Roberts J (1983) Forest transpiration: a conservative hydrological process? J Hydrol 66:133–141

Schilli C, Lischeid G, Rinklebe J (2010) What processes prevail? Analyzing long-term soil-solution monitoring data using nonlinear statistics. Geoderma 158:412–420. doi:10.1016/j.geoderma.2010.06.014

Schmitt A, Glaser B (2011) Organic matter dynamics in a temperate forest as influenced by soil frost. J Plant Nutr Soil Sci 174:754–764. doi:10.1002/jpln.201100009

Strohmeier S, Knorr K-H, Reichert M, Frei S, Fleckenstein JH, Peiffer S, Matzner E (2013) Dynamics of dissolved organic carbon in runoff from a forested catchment: evidence from high frequency measurements. Biogeosci 10:905–916

Van Laanen HAJ, Fendeková M, Kupczyk E, Kasprzyk A, Pokojski W (2004) Flow generating processes. In: Tallaksen LM, van Lanen HAJ (eds) Hydrological drought. Processes and estimation methods for streamflow and groundwater, Developments in water science, vol 48. Elsevier, Amsterdam, pp 53–96

Weyer C, Peiffer S, Schulze K, Borken W, Lischeid G (2014) Catchments as heterogeneous, multi-species reactors: an integral approach for identifying biogeochemical hot-spots at the catchment's scale. J Hydrol 519:1560–1571. doi:10.1016/j.jhydrol.2014.09.005

Zahn MT (1995) Transport von Säurebildnern im Untergrund und Bedeutung für die Grundwasserversauerung. In: Proceedings des Internationalen Symposiums zur Grundwasserversauerung durch Atmosphärische Deposition. Ursachen–Auswirkungen– Sanierungsstrategien, 26–28 Oct 1994, Bayreuth. Informationsberichte des Bayerischen Landesamtes für Wasserwirtschaft 3/95: 143–151

Part IV
Modelling Studies of Energy and Matter Fluxes

Chapter 16
Modeling of Energy and Matter Exchange

Eva Falge, Katharina Köck, Kathrin Gatzsche, Linda Voß, Andreas Schäfer, Martina Berger, Ralph Dlugi, Armin Raabe, Rex David Pyles, Kyaw Tha Paw U, and Thomas Foken

16.1 Introduction

The modeling of energy and matter exchange above tall vegetation is one of the important challenges of micrometeorological modeling due to two exchange conditions that are different to those above low vegetation: First, within the canopy we can find counter-gradient fluxes (Deardorff 1966; Denmead and Bradley 1985, 1987). Therefore, the opposite sign of the gradient and the flux means that the classical model approach of the K-theory (a theory which assumes that turbulent eddies can be described analogous to molecular diffusion, that is that the flux is

E. Falge (✉)
Thünen-Institute, Institute of Climate-Smart Agriculture, Bundesallee 50, 38116 Braunschweig, Germany
e-mail: eva.falge@ti.bund.de

K. Köck
Schulstraße 14, 95032 Hof, Germany

K. Gatzsche
Leibniz Institute for Tropospheric Research, Permoserstraße 15, 04318 Leipzig, Germany

L. Voß
GEO-NET Umweltconsulting GmbH, Große Pfahlstraße 5a, 30161 Hannover, Germany

A. Schäfer
Thomann GmbH, Service Center, Hans-Thomann-Straße 9, 96138 Burgebrach, Germany

M. Berger • R. Dlugi
Arbeitsgruppe Atmosphärische Prozesse (AGAP), Gernotstraße 11, 80804 Munich, Germany

A. Raabe
Leipzig Institute for Meteorology, University of Leipzig, Stephanstraße 3, 04103 Leipzig, Germany

T. Foken (ed.), *Energy and Matter Fluxes of a Spruce Forest Ecosystem*,
Ecological Studies 229, DOI 10.1007/978-3-319-49389-3_16

proportional to local gradients) is not fulfilled. Secondly, there is a strong shear flow above the canopy, generating a so-called mixing layer (Raupach et al. 1996; Finnigan 2000; Harman and Finnigan 2007, 2008) or roughness sublayer (Garratt 1978), which influences the profiles of all meteorological parameters up to about two canopy heights above the top of the canopy.

Several different model approaches have been suggested to overcome the limitations of K-theory, with the two main types based on the Eulerian and Lagrangian approaches. Whereas in Lagrangian specification of the flow field the path line of individual parcels is followed in space and time, in Eulerian specification the flow velocity is defined as a function of location and time. The Lagrangian approach requires the input of the vertical velocity standard deviation, which must be obtained from other sources (Baldocchi et al. 2002), while the Eulerian approach can include the effects of plant canopies and vertically varying thermal stability effects in simulating turbulent moments as well as turbulent transport (Meyers and Paw U 1987; Inclán et al. 1996; Pyles et al. 2004). Other Eulerian approaches include large eddy simulation (LES, Shaw and Schumann 1992; see Chap. 17). Stull (1984) proposed a turbulent transilient theory. With a transilient matrix, different coupling stages between different layers in and above the canopy could be defined. Based on this theory, the model FLAME (Forest-Land-Atmosphere Model, Inclán et al. 1996) was developed for tall vegetation. With higher-order closure techniques, the effect of counter gradients can be modeled (Deardorff 1966). A first model approach by Meyers and Paw U (1986, 1987) was updated by Pyles et al. (2000) and was then known as the ACASA model (Advanced Canopy-Atmosphere-Soil Algorithm). Nevertheless, in the case of a fully coupled canopy (Thomas and Foken 2007), the K-approach should be also applicable.

Since different models follow different theories and serve different purposes and scopes, it is useful to apply different model types and compare their performances in describing complex system dynamics. In this respect, after a successful first test (Inclán et al. 1998), the FLAME was applied to the Waldstein-Weidenbrunnen site

R.D. Pyles • K.T. Paw U
Davis Atmospheric Science Section, University of California, One Shields Avenue, Davis, CA, 95616-8627, USA

T. Foken
Am Herrgottsbaum 28, 96120, Bischberg, Germany

Bayreuth Center of Ecology and Environmental Research, University of Bayreuth, Bayreuth, Germany

E. Falge, L. Voß: Affiliation during the work at the Waldstein sites—Max Planck Institute for Chemistry, Hahn-Meitner-Weg 1, 55128 Mainz, Germany

K. Gatzsche: Affiliation during the work at the Waldstein sites—Leipzig Institute for Meteorology, University of Leipzig, Stephanstr. 3, 04103 Leipzig, Germany

K. Köck (formerly Staudt), K. Gatzsche, A. Schäfer, T. Foken: Affiliation during the work at the Waldstein sites—Department of Micrometeorology, University of Bayreuth, Bayreuth, Germany

(Berger et al. 2004). In this chapter, we compare these results with an ACASA modeling. The ACASA model was already applied on this site (Staudt et al. 2011) and compared with the 3D model STANDFLUX (Falge et al. 1997, 2000; Tenhunen et al. 2001). This investigation will be extended to the clear-cut site Köhlerloh (see Chap. 2), and the ACASA model will also be applied to a full annual cycle of the year 2003 with its extreme, hot summer in Central Europe. Finally, results of a landscape version of SVAT-CN (Falge et al. 2005; Tenhunen et al. 2009) will be shown for this site on the basis of an analysis of the tree structure.

The FLAME was applied to a measuring period in summer 1998. All other model studies were carried out within the EGER project (ExchanGE processes in mountainous Regions, see Chap. 1) with intensive observation periods in 2007 (IOP1), 2008 (IOP2), and 2011 (IOP3). During IOP1 and IOP2, the ACASA model in the version from 05/2009 and the 3D model STANDFLUX were applied. This version of ACASA was also used for the calculation for the year 2003. For EGER IOP3, the ACASA version from 04/2013 was applied, which was also used for the comparison with the FLAME results from 1998.

Over time, a series of models was applied to the Waldstein site, addressing different research questions, ranging from testing appropriate model theory and model validation using different data sources, including accuracy and uncertainty, to upscaling options from plot to landscape. The underlying goals of these model applications were guided by questions regarding representation of relevant process, establishment of confidence in model output, or model consistency and robustness for multiple purposes. Obviously, not every model can and had been applied to every data set available at the Waldstein-Weidenbrunnen site. Nevertheless, the goal of this compendium is to summarize lessons learned from those model applications to provide a means to select appropriate models for future studies on energy and matter exchange above tall vegetation.

16.2 Materials and Methods

16.2.1 Model Descriptions

16.2.1.1 FLAME

The FLAME (Forest-Land-Atmosphere Model) according to Inclán et al. (1996) applied the transilient turbulence theory (Stull 1984) to study interactions in the system soil-vegetation-atmosphere, with special emphasis on forest canopies. The mean flow dynamic and thermodynamic conditions are determined from prognostic budget equations for horizontal wind components, potential temperature, and specific humidity and include the vertical divergences of the corresponding turbulent fluxes of momentum, sensible and latent heat, and Coriolis effect. Budget equations for trace substances are subsequently solved numerically (Inclán et al. 1999). The model considers sinks for momentum in the canopy and at the soil surface,

as well as sinks and sources of sensible and latent heat and trace substances at the surfaces of plant elements and in the soil. Within this framework, advection, for example, of sensible or latent heat, acts like a volume source or sink. This prognostic one-dimensional, first-order, nonlocal turbulence closure model is driven by the flow field and the radiation budget and therefore also solves the radiation and energy budget equations. The storage term includes all possible storages, such as the soil heat flux as well as the heat storage in the plant material and photosynthesis.

FLAME consists of three interactively coupled submodels describing the atmospheric boundary layer, the vegetation, and the soil. The vertical domain of FLAME reaches from the soil-saturated zone up to 3000 m height above the atmospheric boundary layer (ABL) and is normally divided into a maximum of 85 unequally spaced layers. In the case discussed in this study, the idealized tree is divided into five layers within the canopy crown and five in the trunk space. The layer height within the canopy is a function of leaf area index (LAI) increment as discussed by Inclán et al. (1996).

Above the canopy, the layers are unequally spaced up to 1000 m height in the atmosphere. Between 1000 m and the top of the atmospheric model, the layer heights are nearly constant, with steps of about 200 m. In the soil, 15 layers are used. They are also unequally spaced and are mounted between 0.001 m at the surface to a depth of 1.20 m.

FLAME has been applied in order to model exchange processes for different tall vegetation canopies like spruce and pine (Inclán et al. 1996, 1998; Constantin et al. 1998), as well as for a mixed forest mainly composed of oaks and pines (Inclán et al. 1999). In this study, we compare FLAME results with measured fluxes of sensible and latent heat and evaluate the effects of local advection, which may be of significant influence on budgets of water, carbon dioxide, and energy.

16.2.1.2 ACASA

The Advanced Canopy-Atmosphere-Soil Algorithm model (Pyles 2000; Pyles et al. 2000) is a one-dimensional, multilayer model. The most outstanding feature of ACASA is its third-order closure method for calculating the turbulent transfer within and above the canopy (Meyers and Paw U 1986, 1987). The model extends to twice the canopy height, with 20 equally spaced layers for the canopy and the air above. The 15 soil layers can be spaced irregularly. A fourth-order polynomial of Paw U and Gao (1988) calculates leaf, stem, and soil surface temperatures. The advantage of this method compared to simpler formulations is that temperatures of these components can also be calculated when these deviate significantly from ambient air temperatures. The shortwave radiative transfer through the canopy is calculated for near-infrared and visible radiation, which consist of both direct and diffuse radiation. Processes represented in these simulations are reflection, absorption, and transmittance (Meyers 1985). The approach for long-wave radiation

is similar. In the plant physiology and transmittance (Norman 1979; Meyers 1985) submodules, the Ball-Berry stomatal conductance (Leuning 1990; Collatz et al. 1991) and the Farquhar and von Caemmerer (1982) photosynthesis equation were combined following Su et al. (1996). Further processes within the canopy simulated in ACASA are canopy heat storage and canopy interception of precipitation. The ACASA model includes a multilayered soil module for the calculation of soil surface evaporation, soil moisture, and soil temperature, which was adapted from the MAPS (Mesoscale Analysis and Prediction System, Smirnova et al. 1997, 2000).

ACASA can be used to simulate the exchange of momentum, heat, water vapor, and CO_2 within and above the canopy. Half-hourly output data includes mean quantities, fluxes and third-order moments, as well as soil data. The layered nature of ACASA allows the identification of different local stabilities in each canopy air layer, with the simulation of the resulting effects of these sometimes completely different stabilities on interlayer turbulent transfer and vertical profiles of turbulent statistics. It should be noted that ACASA is currently linked to the Weather Research and Forecasting (WRF) regional model, and several types of carbon-nitrogen cycle models have been incorporated in addition to a dynamic vegetation model; however, these versions are not used in this paper (see, e.g., Falk et al. 2014; Xu et al. 2014). Also, a version of ACASA has been developed that includes the Coriolis effect and simulates turning of the wind direction inside plant canopies with reasonable accuracy (Pyles et al. 2004).

16.2.1.3 STANDFLUX and SVAT-CN

Canopy exchange of water and carbon dioxide was analyzed with the three-dimensional microclimate and gas exchange model, based on a 1D core module (SVAT-CN, Falge et al. 2005). The 1D core model is a combination of a multiple-layer soil water balance model and a multilayered canopy gas exchange model. It is derived from the Process-oriented Pixel model (PROXEL, Reichstein 2001) and predicts CO_2 and water vapor exchange by coupling controlling micrometeorological and ecophysiological processes. Canopy structure is represented in homogeneous layers allowing for multiple species or plant compartments and seasonal and species-specific variation in leaf area and physiological properties. Micrometeorological submodules calculate the leaf energy balance and radiation regime in each canopy layer and control gas exchange modules for photosynthesis, stomatal conductance, leaf, bole and soil respiration, and transpiration. Carbon exchange of C_3 species are simulated according to Farquhar et al. (1980). The soil modules comprise a flexible hybrid between a layered bucket model and classical basic liquid flow theory. Further soil processes include heat transport, distribution of transpiration demand proportional to soil resistance, and reduction of leaf physiological parameters with limiting soil moisture.

The STANDFLUX 3D landscape model is derived from the approach of Tenhunen et al. (2009) and describes canopy water vapor and carbon dioxide exchange based on rates calculated for individual pixels and as affected by local gradients

in photon flux density (PFD), atmospheric humidity, atmospheric carbon dioxide concentration, and air temperature. Direct, diffuse, and reflected PFD incident on foliage elements is calculated for a three-dimensional matrix of points superimposed over the stand or landscape. The model was used to calculate vertical exchange of radiation absorption, net photosynthesis, and evapotranspiration of the vegetation, soil evaporation, and CO_2 emission, but did not quantify lateral transport along topographic gradients except for runoff. The digital elevation model necessary for simulating lateral hydrological exchange was based on airborne LIDAR data described below.

16.2.2 Model Drivers and Input Parameters

16.2.2.1 FLAME

As stated in Berger et al. (2004), this prognostic version of the FLAME was initialized with DWD DM4 model data (grid box 78,111; 50.11°N, 11.93°E; elevation 637 m) or with radiosonde profiles from station Meiningen (50.57°N, 10.38°E; elevation 450 m) for the atmospheric boundary layer (ABL). Each variant was combined with measurements from the Waldstein-Weidenbrunnen site within the canopy (see Chap. 2 and Appendix A). Measurements were conducted at 31, 25, 21, 16, and 2 m height in the canopy. For July 14, 1998, FLAME was initialized at two different times: 7 CET and 13 CET. For the initialization at 7 CET, only the DWD DM4 model data were available for the ABL. At 13 CET, the initialization of the ABL was conducted with DWD DM4 model data as well as radiosonde data. For August 8, 1998, FLAME was initialized only at 13 CET with the radiosonde profile for the ABL conditions. All FLAME runs ended at 20 CET. The detailed description of the creation of the initialization profiles and differences in the vertical meteorological profiles at ABL height are included in Berger et al. (2004). For this purpose, the response to plant physiological processes is simply calculated by a "Jarvis-type" parameterization for average conditions from measurements at this site.

For the simulations with FLAME, at each time step, a transilient matrix (Stull 1984, 1993; Inclán et al. 1996) is calculated. An example at 15:30 CET of July 14, 1998, is given in Fig. 16.1. Therefore, both 13 CET initialization profiles were utilized. In Fig. 16.1 (left), the transilient matrix for the DWD DM4 initialized model run is shown. The matrix elements indicate the potential for mixing $Y_{i,j}$ between the grid box of destination i and the source grid box j. $Y_{i,j}$ is a measure of the instability of an air parcel, and therefore larger $Y_{j,i}$ elements represent greater turbulent mixing (Inclán et al. 1996). The matrix elements were multiplied by a factor of 1000, and contour lines were added to improve visualization. The elements near the main diagonal describe turbulence induced by smaller eddies, which stand for local transport. For the transilient matrix displayed in Fig. 16.1 (left), the small-scale mixing is characterized by an asymmetric distribution around

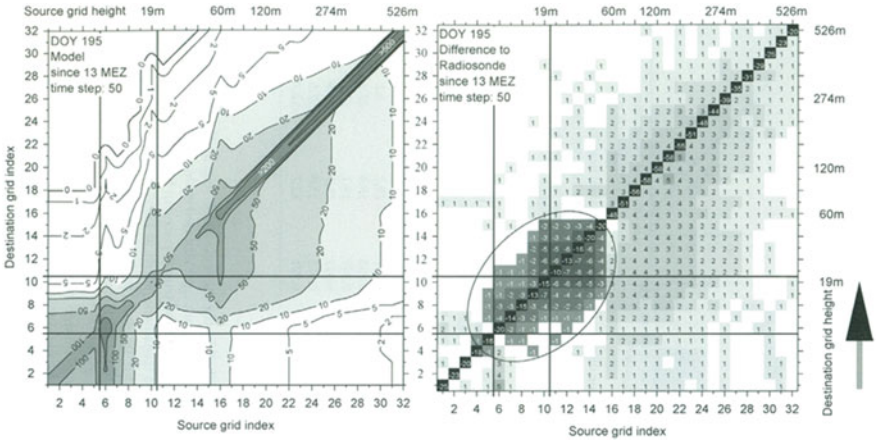

Fig. 16.1 *Left*: Transilient matrix for the 14 July 1998 at 15:30. *Right*: Difference from the transilient matrix. The abscissa indicates the source and the ordinate the destination of the air parcel for turbulent mixing. In the *right panel*, positive differences are highlighted by *light gray* and negative differences in *dark gray*, whereby the difference DWD model minus radiosonde was calculated. From Berger et al. (2004). Published with kind permission of © Springer, 2004. All Rights Reserved

the main diagonal. Small eddies propagate up to 530 m height. Turbulent mixing is enabled between the mixing layer above the canopy (reaches up to 120 m) and the trunk space of the forest. In the trunk space region of the forest, a main turbulent region is observed that originates from down mixing of air parcels from the lower canopy region. The elements with greater distance to the main diagonal represent nonlocal transport induced by larger eddies. There is, for instance, a moderate down mixing of turbulent energy from source region 15–17 (40–90 m height) toward the trunk space. The right panel of Fig. 16.1 shows the difference from the transilient matrix calculated with the radiosonde ABL profile for 15:30 CET. The small-scale turbulence, as well as the mixing in the upper canopy regions and above the crown, reaches higher values for the radiosonde initialization (DWD model minus radiosonde), but the general message is the same for both transilient matrices. The main reason for the differences in the transilient matrices may be the slightly different wind conditions in the initialization profiles.

16.2.2.2 ACASA, STANDFLUX, and SVAT-CN

To run the ACASA as well as the 3D model, half-hourly meteorological input data as well as initial soil conditions (soil temperature and soil moisture profiles) are needed. Required meteorological input data at the upper boundary of the model are precipitation rate, specific humidity, wind speed, downwelling shortwave radiation, downwelling long-wave radiation, air temperature, air pressure, and CO_2 concentration.

Model parameterization was obtained during the intensive campaigns of the EGER project (see Chap. 1), intensive measuring periods IOP1, IOP2, and IOP3, in fall 2007, early summer 2008, and 2011, respectively. Parameterization included information on vertical and horizontal leaf area distribution (plant area index, PAI), tree positions, sizes and tree density on the Waldstein-Weidenbrunnen site, and the target area of EGER IOP3 (see below). The parametrizations of ACASA for the measuring periods in 1998 and 2003 were similar to IOP1 and IOP2 (Staudt et al. 2011). For the applied parameters, see Table 16.1.

The response of net photosynthesis, stomatal conductance, and transpiration to temperature, radiation, relative humidity, and CO_2 concentration is important information for the parameterization of the Farquhar-type leaf modules in the 3D model and ACASA. For their parameterization, measurements of in situ CO_2 and H_2O leaf gas exchange were made using a portable gas exchange system (WALZ GFS3000, Walz, Effeltrich/Germany). Single factor dependencies of leaf gas exchange to light, temperature, CO_2 mixing ratio, and relative humidity were performed for *Picea abies* trees at the Waldstein-Weidenbrunnen in the canopy profile (10–11, 15–16, and 20–21 m above ground, during IOP1 and IOP2) and six representative species at the Köhlerloh clear-cut (during IOP3). The representativeness of the species selected for gas exchange measurements was determined by analyzing vegetation transects: three typical understory species of grown Norway spruce forests (*Deschampsia flexuosa*, *Picea abies*, and *Vaccinium myrtillus*), which together constitute ca. 60 % of the Köhlerloh clear-cut, *Calamagrostis villosa* for the Poaceae (ca. 9 %), and *Juncus effusus* for Juncaceae and Cyperaceae (ca. 3 %). In addition, *Alnus glutinosa* was selected for overstory deciduous tree saplings (approx. cover of 2 %). Vegetation heights and PAI of the different vegetation types were determined at three sites of the Köhlerloh area on four different dates. For more details on the measurements and setups, see Serafimovich et al. (2011) and Chap. 2.

The portable gas exchange system was operated using programs for radiation and CO_2 mixing ratio dependencies at five different temperatures (13, 18, 23, 28, and 33 °C) inside the cuvette and two different values of relative humidity in the inlet air, 50 and 65 %. The resulting response curves to temperature, radiation, CO_2 mixing ratio, and relative humidity were corrected for the leaf area within the chamber and analyzed with the physiologically based leaf gas exchange submodule to derive estimates for those parameters that describe carboxylase kinetics, electron transport, and stomatal function (Fig. 16.2). Sets of parameter values for representative species of the clear-cut canopy were obtained for use in calculating canopy flux rates at the clear-cut site. Analogous parameters were determined for old *Picea abies* trees in the canopy profile (10–11, 15–16, and 20–21 m above ground) at the Waldstein-Weidenbrunnen site.

During the intensive measuring campaigns of the EGER project, IOP1 and IOP2, surveys were performed with the objective of documenting the spatial distribution of the trees at the Waldstein-Weidenbrunnen site. In order to parameterize the models for even larger areas (e.g., 4 km^2 from Großer Waldstein up to Köhlerloh and Weidenbrunnen), in EGER IOP3, analyses of airborne LIDAR data in 1 m resolution (performed by the company Trimble/TopoSys) of elevation and vegetation surface

Table 16.1 Plant morphological parameter settings of the ACASA model

Parameter	Dimension	*Vaccinium*	*Deschampsia*	*Calamagrostis*	*Juncus*	*Picea abies*
Maximum rate of carboxylation at 25 °C	μmol $m^{-2}s^{-1}$	26.61	29.53	45.57	30.39	31.78
Activation energy[a]	J mol^{-1}	46,986	34,030	37,211	41,226	29,487
Deactivation energy[a]	J mol^{-1}	2×10^5	2×10^5	2×10^5	2×10^5	2×10^5
Entropy[a]	J mol^{-1} K^{-1}	238.8	254.4	243.2	240.1	245.0
Activation energy for RuBP[b] regeneration	J mol^{-1}	52,642	48,000	137,205	16,745	36,185
Entropy term for RuBP[b] regeneration	J mol^{-1}	488.2	511.4	468.7	492.4	486.2
Deactivation energy for RuBP[b] regeneration	J mol^{-1}	2×10^5	2×10^5	2×10^5	2×10^5	2×10^5
Potential rate of electron transport at 25 °C	μmol m^{-2} s^{-1}	86.12	157.46	198.32	128.92	123.98
Slope of the Ball-Berry formula	–	10.09	10.58	10.68	8.17	9.40
Minimal stomata conductance	mol m^{-2} s^{-1}	0.050	0.127	0.049	0.002	0.054
O_2 concentration within the cells	mol mol^{-1}	0.21	0.21	0.21	0.21	0.21
Quantum efficiency	–	0.0626	0.1223	0.0809	0.1215	0.0851
Leaf respiration rate at 0 °C	μmol m^{-2} s^{-1}	0.1154	0.9174	0.0817	0.6815	0.5413
Q_{10} temperature coefficient for leafs	–	2.7316	1.4226	2.7167	1.4632	1.8653
Mean leaf diameter	m	0.013	0.0004	0.005	0.005	0.001
Contribution to Köhlerloh clearing[c]	%	17.5	21.7	9.0	3.1	21.4

For further parameters, see Staudt et al. (2010)
[a]To calculate maximum rate of carboxylation at 25 °C
[b]Ribulose–1,5–biphosphate
[c]Furthermore 27.3 % dead wood

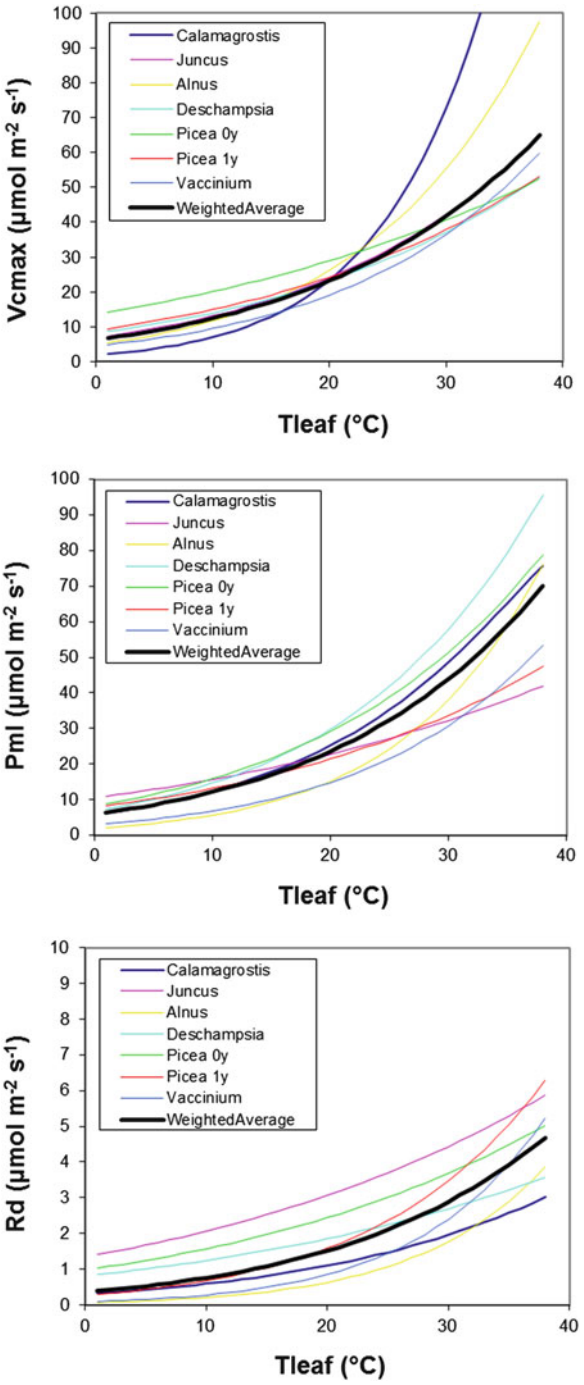

Fig. 16.2 Species-specific variability for key leaf gas exchange parameters in response to temperature: V_{cmax} for carboxylase kinetics, Pml for electron transport, and R_d for dark respiration

were used to ensure practicable representations of canopy structure for use in the models. We acquired a LIDAR scene with which to determine tree heights from the difference between the digital surface model and the digital elevation model. Measurements of PAI, as well as tree positions, trees per hectare (N: 50–900 trees ha^{-1}), tree circumferences (average CBH: 0.9–1.6 m), and tree heights (average H: 21–33 m), were made at 30 forest plots within the 4 km^2 area (see Chap. 2), being the domain of the 3D model applications. PAI of the sites was measured with two different optical approaches, the tall canopy analyzer LAI-2200 (LI-COR, Lincoln, USA) and hemispherical photographs from a digital camera (Nikon D3100) in combination with a circular fisheye lens, equipped with an external GPS sensor for exact positioning of each photograph taken. For more details on the measurements and setups, see Serafimovich et al. (2011). Regressions between ground-based measurements of PAI and tree heights were used together with the tree heights from the airborne LIDAR data to generate a PAI map for the forested area of the 4 km^2 model domain (see Fig. 16.3a).

For the parameterization of the 3D version of SVAT-CN, the difference between the digital surface and digital elevation models derived from the same LIDAR data was used to classify the land use into four different classes in the 4 km^2 target area: old forest stands (Norway spruce with tree heights above 4 m), young spruce forests, clearings, and roads. Input maps of plant area indices were generated using spatially resolved estimates of vegetation height in the target area and a ground-based regression equation between tree height and PAI for old forest stands and ground-based PAI measurements at *Köhlerloh* for young spruce forests and vegetated clearings. Instead of (unavailable) spatially resolved maps of soil types, a uniform soil type of loamy sand was assumed for the entire target area. This assumption seemed non-critical since precipitation input was high for the simulation period, and feedbacks of soil moisture on canopy gas exchange remained negligible. Due to small topographic gradients and the small size of the study area, no elevation dependent gradients in meteorological factors (e.g., temperature, humidity, precipitation, etc.) were considered. Measured meteorological data at the "Main Tower" (see Sect. 16.2.3) were assumed uniform over the area and used as model input on a half-hourly time step. Radiation input is dependent on aspect and topography as described by Wang et al. (2006). For each time step and each 25 m × 25 m pixel, SVAT-CN gas exchange results were obtained and stored in the form of target area maps.

From the airborne LIDAR data of elevation and vegetation surface (for 4 km^2, in 1 m resolution), tree heights, gap frequencies, and tree densities were derived to provide information for parameterization of the 3D model and the large eddy simulation (LES) model, which was developed at the University of Hannover LES to study the effect of horizontal variation in lower boundary conditions (see Chap. 17).

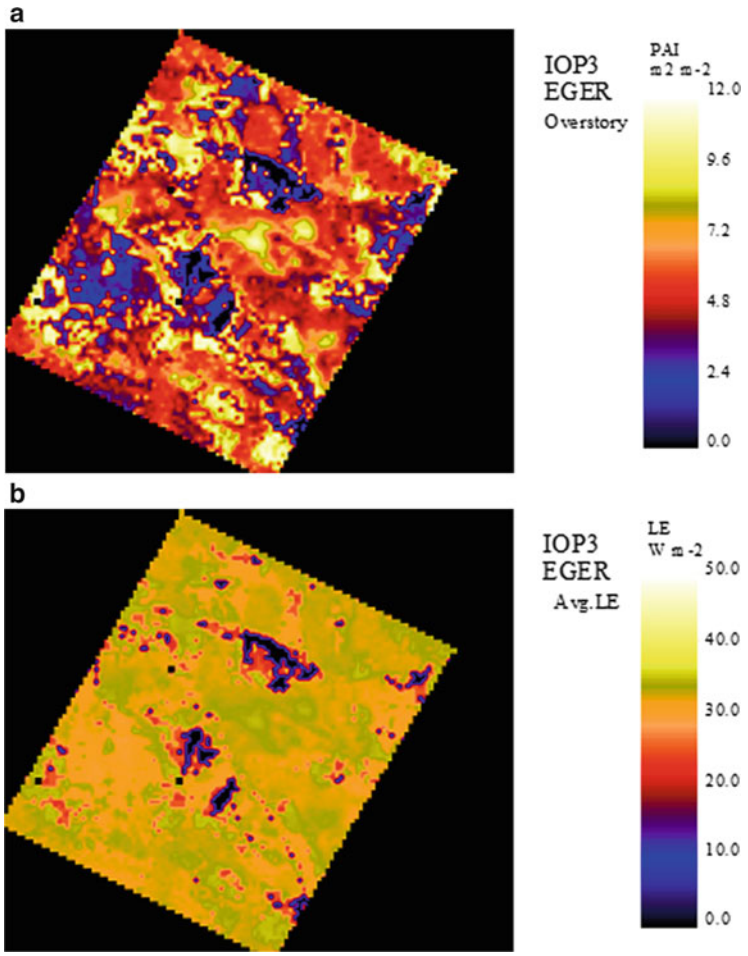

Fig. 16.3 (**a**) Map of the horizontal distribution of overstory PAI within the EGER II target area of 4 km^2. Note the clear-cut/windthrow areas with overstory PAI of 0 (*dark blue* to *black color*); the area in the upper middle of the target area is the *Köhlerloh* research area of IOP3. (**b**) 3D application for assessment of the horizontal variability in average latent heat exchange for IOP3 (average for May and June 2011)

16.2.3 Reference Eddy-Covariance Measurements

The eddy-covariance data of the sensible heat, latent heat, and carbon dioxide flux—which were used for the validation of the model results—were measured at the Waldstein-Weidenbrunnen site up to 2006 at the Main Tower (MT, 32 m height) and from 2007 at the Turbulence Tower (TT, 36 m height), see Chap. 2. For instrumentation and more information about the data set and flux partitioning, see Chap. 4. The eddy-covariance data for Köhlerloh clearing were measured at a

5.5 m tower in the middle of the clearing. The 1998 data set was described by Foken et al. (2000).

All data sets—except those for EGER IOP3 in 2011—were not corrected for energy balance closure (Foken 2008; and see Chap. 12). For IOP3 and the ACASA-FLAME intercomparison in 1998, two different methods for energy balance closure are applied. The first one is the correction presented by Twine et al. (2000), which preserves the Bowen ratio (EBC-Bo). This method is usually utilized for the correction of the heat fluxes with the assumption of measuring errors, but it assumes their scalar similarity. The second method accounts for the higher transport of sensible heat flux caused by secondary circulations. Thus, the buoyancy flux ratio is utilized by Charuchittipan et al. (2014) as an alternative correction method (EBC-HB). With the EBC-HB correction method, in most cases more energy of the residual is ascribed to the sensible heat flux. The difference to the EBC-Bo correction is especially marked for low Bowen ratios. At night, the applicability of the corrections is limited because of minor heat fluxes and negative Bowen ratios.

16.3 Results and Discussions

16.3.1 ACASA-FLAME Intercomparison

In order to effect an intercomparison between the two turbulence models ACASA and FLAME, the FLAME simulations described in Berger et al. (2004) in 1998 were utilized. That study applied the FLAME to a complex terrain for the first time. The aim of the investigation was to produce appropriate simulations with an adequate time resolution for the turbulent exchange at the Waldstein-Weidenbrunnen site. The ACASA model was successfully adapted for the Waldstein-Weidenbrunnen site by Staudt et al. (2010). To enable comparison, ACASA was retroactively applied to two single days (14 July and 8 August) in the summer of 1998.

For July 14, 1998, the ACASA simulations accord slightly better with the measured sensible heat fluxes (for both correction methods) than the FLAME simulations (Fig. 16.4a). For the 7 CET run, FLAME underestimates the maximal values of the sensible heat flux at noon. After 1 h initialization time, the two 13 CET runs of FLAME nearly equal the 7 CET model run (Fig. 16.4a). The time series of all three FLAME simulation runs progress to a local minimum of sensible heat flux between 15 and 16 CET, which is not observed in the measurements. In general, the simulated heat fluxes by ACASA follow the HB-corrected sensible heat fluxes, whereby the sensible heat fluxes simulated by FLAME are lower and thus agree better with the Bo-corrected sensible heat fluxes. At night, only simulations for ACASA exist, which are in good accordance with the measurements. To estimate the correlation between the measured and simulated fluxes for both correction methods and models, a linear regression was conducted. The results of the regression are depicted in Fig. 16.5a. ACASA simulations show a higher correlation

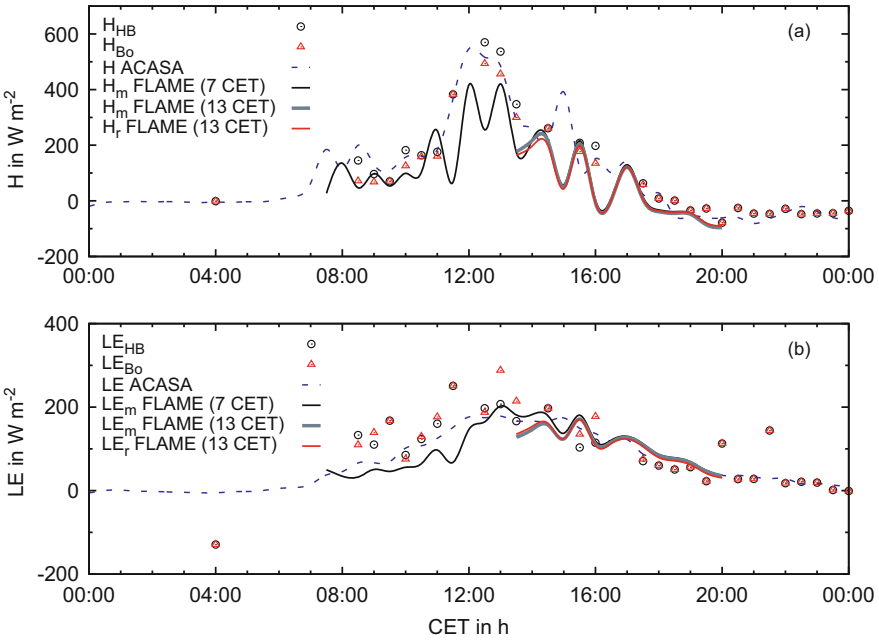

Fig. 16.4 Simulated and measured (**a**) sensible (H) and (**b**) latent heat (LE) fluxes for 14 July 1998 of the forest. Three FLAME simulations are shown, where the subscripts "m" and "r" indicate ABL initialization with DWD DM4 model or radiosonde data, respectively

coefficient as well as a slope nearly equal to unity according to the measured sensible heat fluxes, whereby slight underestimation for the HB-corrected fluxes and minor overestimation for the Bo-corrected fluxes occurs. The FLAME simulations consistently underestimate the measured sensible heat fluxes for both correction methods, independent of the initialization time and utilized initial ABL description. The correlation coefficient is lower than for the ACASA simulations, and the simulations fit better to the Bo-corrected fluxes. The intercepts are consistently negative, whereby the absolute value is lower for the ACASA simulations. In general, the number of compared data points is higher for the ACASA simulations because of the additional simulation of nighttime fluxes.

For both models, the simulation results for latent heat flux show nearly equal results. For the FLAME simulations initialized at 7 CET, a minimum occurs before noon that is not observed in the measurements (Fig. 16.4b). Both models underestimate the latent heat flux in the first half of the day, which changes over to a slight overestimation between 14 and 18 CET. Overall, the underestimation leads to slopes lower than one as well as positive intercepts for the linear regression (Fig. 16.5b). The correlation for the ACASA simulations is slightly higher than for the FLAME simulations initialized at 7 CET, because of the additional good match to the nighttime latent heat fluxes. The FLAME simulations for the 13 CET runs show

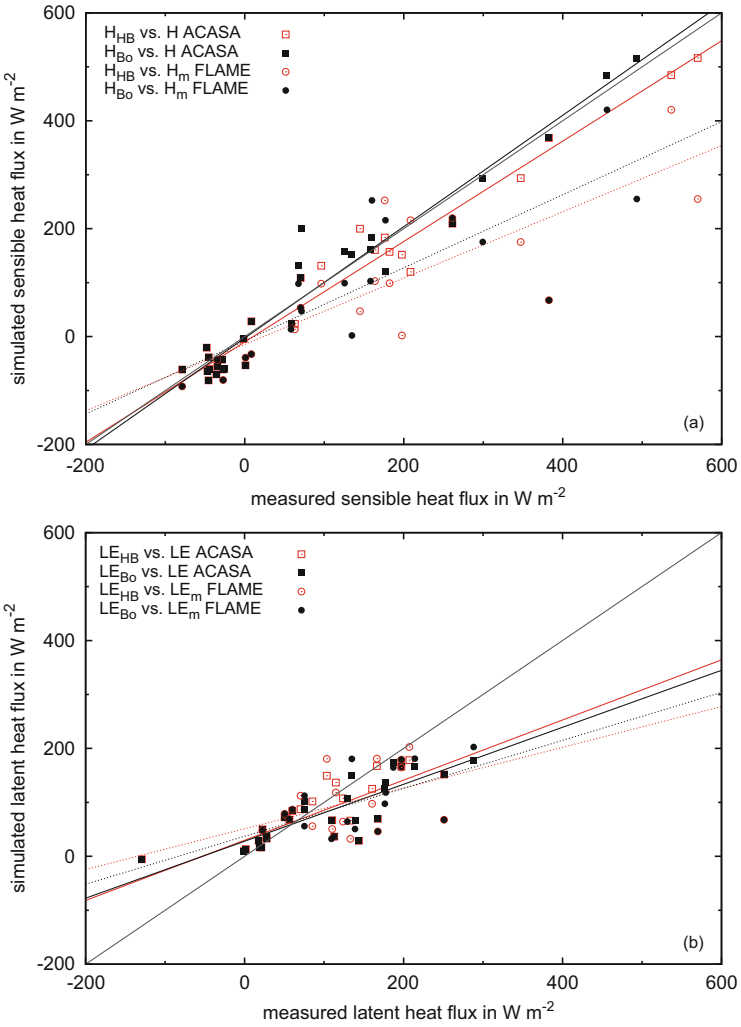

Fig. 16.5 Scatter plot of simulated versus measured (above) sensible (H) and (below) latent heat (LE) fluxes for July 14, 1998 of the forest. The FLAME simulation initialized at 7 CET was chosen, where the subscript "m" indicates ABL initialization with DWD DM4 model data

a higher correlation coefficient, since they do not contain an underestimation of the fluxes before noon.

For August 8, 1998, the FLAME simulations are only available between 13 CET and 20 CET. After the typical first hour of initialization, the sensible heat fluxes were underestimated for most of the time by FLAME. This underestimation results in a slope smaller than one for the linear regression, which is only based on 10 data points. ACASA simulations show overestimation of the amplitude for the

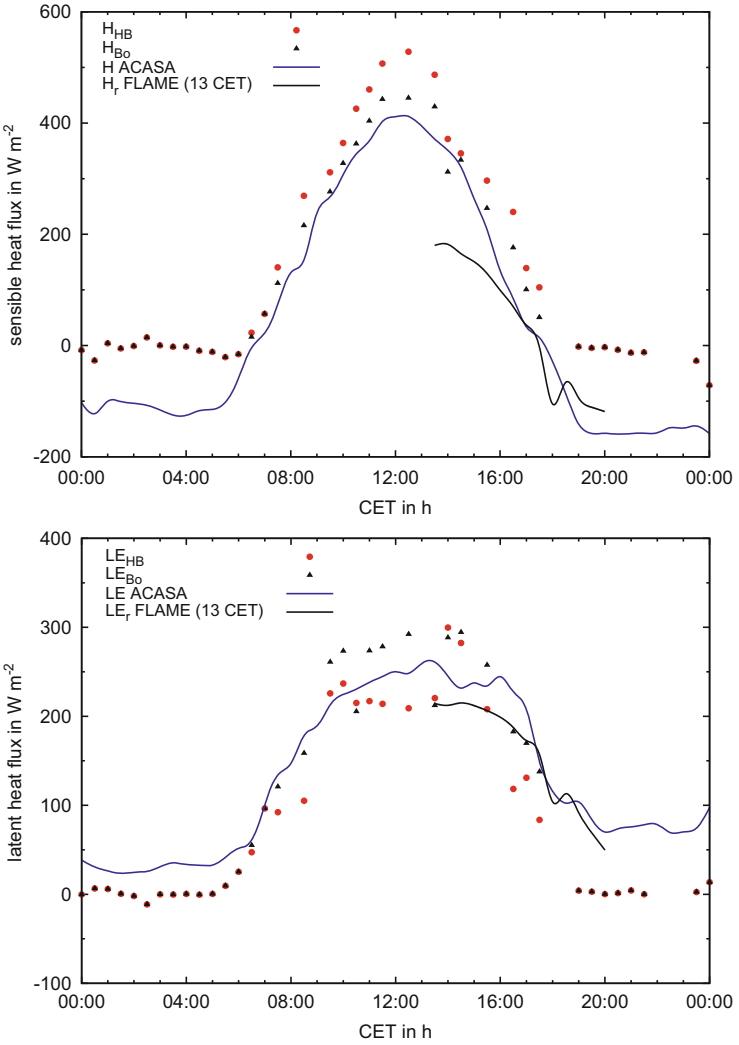

Fig. 16.6 Simulated and measured (above) sensible (*H*) and (below) latent heat (*LE*) fluxes for 8 August 1998 of the forest. The subscript "r" for the FLAME simulation indicates ABL initialization with radiosonde data

nighttime sensible heat fluxes (Fig. 16.6a). At daytime, an overall good agreement for the simulated sensible heat fluxes is found for ACASA. Only at noon can the peak of the measured fluxes not be covered by ACASA, especially not for the HB correction. Overall, ACASA overestimates the measured sensible heat fluxes, which leads to a slope higher than one for the regression. For both models, the intercepts are negative and the magnitudes are higher than at 14 July. For the latent heat fluxes, short duration FLAME simulations agree best with the HB-corrected

fluxes (Fig. 16.6b). ACASA underestimates the latent heat flux at night, which might be caused by the overestimation of the sensible heat flux. Therefore, this discrepancy is due to an incorrect partitioning of the available turbulent energy at night. At daytime, the simulated latent heat fluxes lie between the fluxes of the two correction methods (Fig. 16.6b). Overall, simulated and measured latent heat fluxes show a good correlation for ACASA, but for both models, the magnitudes of the positive intercepts are increased compared with those of 14 July.

Overall, both turbulence models simulate the turbulent exchange for the forest in good accordance with the eddy-covariance measurements. Different inputs are used for the initialization of the models, and this could be a criterion for model choice. This prognostic version of FLAME needs only a onetime input at the beginning of the model run. But the model domain reaches up to 3000 m above the ABL height; thus DWD regional model data or radiosonde data are required for model initialization. ACASA needs model input over the whole simulation time, but only for a limited measurement height in the range of the canopy height or—at most—twice the canopy height. Because of the continuous input, ACASA can also simulate for longer durations.

16.3.2 ACASA: 3D STANDFLUX Intercomparison

A detailed investigation of evapotranspiration at the Waldstein-Weidenbrunnen site, in measurements as well as model simulations, was the aim of a study by Staudt et al. (2011). For a 5-day fair weather period during the IOP1 of the EGER project (September, 20–24, 2007, DOY 263–267), eddy-covariance and sap flux measurements were available not only for the stand as a whole but also along vertical profiles within the canopy. This provided a sound database for an investigation of the performance of the ACASA model and the 3D model STANDFLUX, which not only simulate the partitioning of evapotranspiration between their components but also between canopy layers.

Ecosystem evapotranspiration (E_{eco}) is one of the most important components of the water budget in Central European forests, which can account for up to 60 % of precipitation for spruce forests (Frühauf et al. 1999; Rebmann et al. 2004). E_{eco} is made up of four components (Staudt et al. 2011):

$$E_{eco} = E_c + E_s + E_g + E_w \tag{16.1}$$

with transpiration from the canopy (E_c), transpiration from the understory vegetation (E_s), evaporation from the ground (E_g) (soil and standing water on understory vegetation), and evaporation from wet canopy surfaces such as from intercepted water (E_w).

The ACASA and STANDFLUX models simulate these four components. Also, E_c and E_w are simulated for several layers within the canopy. To measure the components of E_{eco}, no single measurement technique is available. However,

a combination of different measurement techniques was employed during the intensive observation period at our site, which covers most of the components. With the assumption of a dry canopy during the 5-day fair weather period and thus of zero evaporation from intercepted water (E_w), all components were represented by measurements in the following way: The latent heat flux (LE) from eddy-covariance measurements at the top of the Turbulence Tower (36 m) represented ecosystem evapotranspiration (E_{eco}). An eddy-covariance system within the trunk space of the forest (measurement height of 2.25 m) measured evapotranspiration of the soil and understory ($LE(2.25\ \text{m}) = E_s + E_g$). The remaining component, the transpiration from the canopy (E_c), can then be calculated from the latent heat fluxes measured above the canopy and within the trunk space ($E_c = E_{eco} - (E_s + E_g) = LE(36\,\text{m}) - LE(2.25\,\text{m})$). An alternative method to capture E_c was sap flux measurements, which were carried out at the "biotower" at six different heights above the forest floor. Here, the readings at the lowest measurement height (1.4 m) represented E_c of the canopy. Also, sap flux and eddy-covariance measurements at further heights within the canopy at the two towers provided estimations of E_c within the profile. However, one has to bear in mind that these different measurement techniques involve a range of specific assumptions and upscaling methods and thus have their own uncertainties and limitations (see Staudt et al. (2011) for more details).

Time series of E_{eco} and its components as measured by eddy-covariance and sap flux techniques and modeled by ACASA and STANDFLUX for the 5-day period are displayed in Fig. 16.7a. For additional comparisons, including scatter plots and tables for error measures, see Staudt et al. (2011). During daytime, E_{eco} was underestimated by both models (Fig. 16.7a). In particular, maximum daytime values were much larger in eddy-covariance measurements than in models, whereas the agreement of models and measurements was better in the morning hours. At nighttime, STANDFLUX largely underestimated E_{eco}, whereas ACASA estimates better-captured measured nighttime E_{eco}. Canopy transpiration E_c (Fig. 16.7b) measured by the eddy-covariance method reached larger daytime maximum values than when measured by the sap flux technique and simulated by the two models. However, toward the end of the 5-day period, model results moved closer to E_c from eddy-covariance measurements. For most of the days, the agreement of modeled E_c with sap flux measurements was good. During nighttime, both models underestimated measured E_c values. The ACASA model captured maximum daytime soil and understory evapotranspiration ($E_g + E_s$) as measured with the eddy-covariance system in the trunk space of the forest (Fig. 16.7c). However, nighttime values were overestimated. The STANDFLUX model on the other hand underestimated measured daytime $E_g + E_s$.

There are several reasons for the smaller daytime E_c values of the sap flux measurements and the model simulations compared to eddy covariance. First of all, uncertainties in the two measurement techniques, e.g., due to their underlying assumptions and upscaling of measurements, have to be considered. Secondly, the initial assumption of a dry canopy and thus negligible E_w may have been wrong. A rainy period ended more than 24 h before the 5-day period analyzed here, which was assumed to be long enough for drying of the canopy. However, fog may have delayed

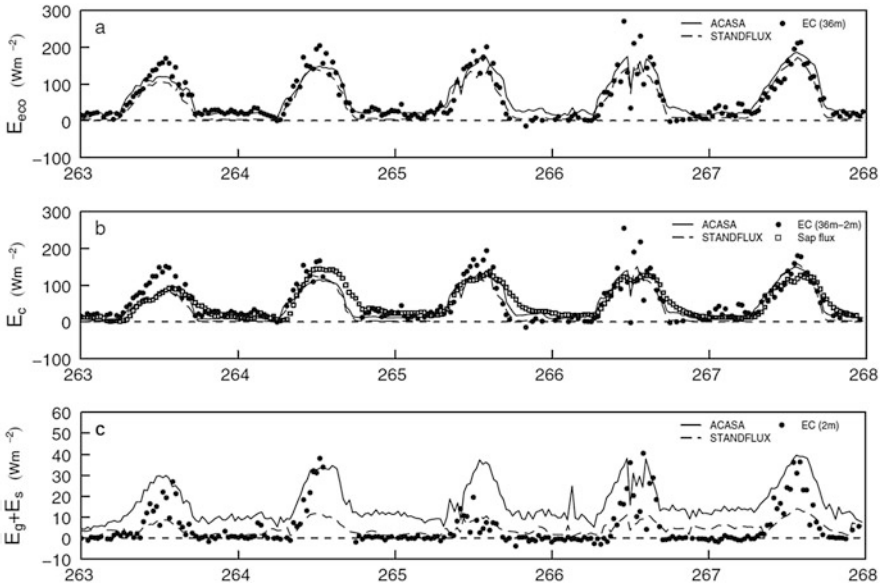

Fig. 16.7 Ecosystem evaporation (E_{eco}, **a**) for DOY 263–268 as measured by the eddy-covariance (EC) system at 36 m and modeled by ACASA and STANDFLUX. Canopy transpiration (E_c, **b**) as determined by the eddy-covariance systems (evapotranspiration from the forest floor as measured by the eddy-covariance system at 2.25 m was subtracted from the eddy-covariance measurements at 36 m) and the sap flux measurements and as modeled by ACASA and STANDFLUX. Evapotranspiration from soil and understory ($E_g + E_s$, **c**). (Adapted from Staudt et al. (2011), published with kind permission of © Elsevier, 2011. All Rights Reserved)

the drying of the canopy, and thus E_w may have played a role, at least during the first 2 days of the 5-day period, as in a separate simulation by the two models (not shown here). Unfortunately, no measurements of E_w were available. However, this can only partly explain the mismatch of E_c measured by the eddy-covariance technique on the one hand and E_c measured by sap flux, as well as modeled, on the other. As this mismatch was larger at the beginning than at the end of the 5-day period, and the wind direction changed on the evening of day 265, a simultaneous change in the footprint area preferentially sampled by the eddy-covariance measurements might be another explanation. The eddy-covariance footprint area is comprised mainly of conifer forest. However, clearings south and east of the study site contribute to the outer 20 % of the footprint area (see Chap. 2). During periods of southerly winds, as with the first 3 days, contributions from the clearings might have led to enhanced evapotranspiration rates measured at the "turbulence tower." Whereas the eddy-covariance flux footprint is dynamic, the area used for upscaling the sap flux measurements stays the same for every time step. This fenced area of the site is also the area modeled by the 3D model STANDFLUX, where each tree is represented individually and its exchange rates calculated. Plant morphological input parameters to run the ACASA model, such as the LAI and its profile, were

also derived for the fenced area. The area assumed in the ACASA model has a similar size to the flux footprint; however, it is covered with a uniform forest. Thus, the two models do not include any contribution from clearings. Areas represented in the models match the area used to upscale sap flux measurements, which probably explains the better agreement of models with sap flux measurements than with eddy-covariance measurements. The deviating areas of the eddy-covariance flux footprint and the areas represented in the models may also explain the underestimation of E_{eco} by the models. The smaller E_{eco} values of STANDFLUX compared to ACASA stem from the smaller $E_g + E_s$ estimations. However, keeping the uncertainties of the measurements in mind, the ACASA and STANDFLUX models simulated the partitioning of ecosystem evapotranspiration into its components reasonably well for our case study.

As both models also simulate the partitioning of evapotranspiration between several layers of the canopy, and measurements were also done at several heights within the canopy, we had the opportunity to also compare modeled and measured profiles of canopy evapotranspiration. Mean profiles for the 5-day period were calculated for daytime and nighttime (Fig. 16.8). According to the probable contribution of E_w to measured latent heat fluxes by the eddy-covariance technique, as discussed above,

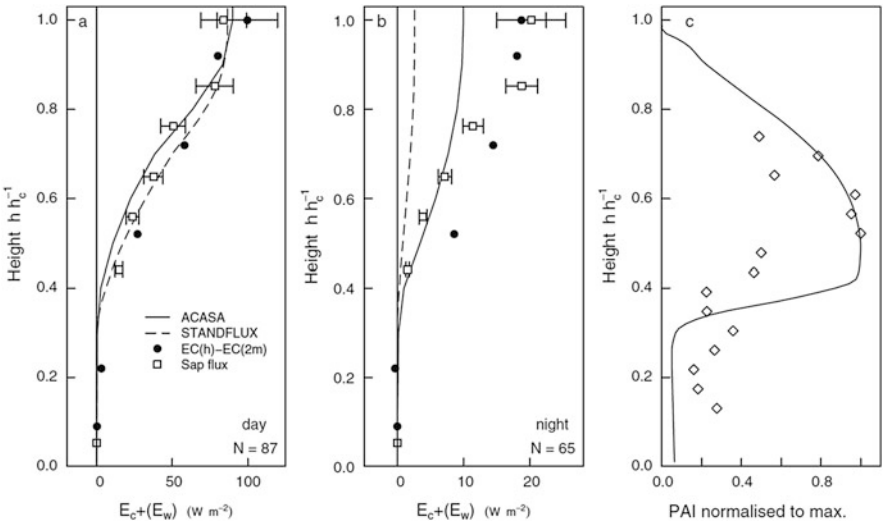

Fig. 16.8 Comparison of mean daytime (**a**) and nighttime (**b**) evapotranspiration ($E_c + E_w$; eddy-covariance measurements (EC), ACASA, STANDFLUX) and transpiration profiles (E_c; sap flux). Error estimates are included for sap flux measurements (mean of the individual measurement errors). For eddy-covariance measurements, an error of 20 % is added to the data of the uppermost height for comparison. Note the different ranges of the x-axis for daytime and nighttime. Plant area index profile (**c**) normalized to the maximum value. *Diamonds* mark measurements made in April 2008, the *line* represents the PAI profile as derived for STANDFLUX and used in ACASA. (Adapted from Staudt et al. (2011), published with kind permission of © Elsevier, 2011. All Rights Reserved)

model results also include E_w. Here, measurements of the highest eddy-covariance system, which was situated several meters above the canopy top, are displayed as canopy top values consistent with the assumption of a constant flux layer above the canopy as in the ACASA model. For daytime, sap flux measurements were also smaller than eddy-covariance measurements along the profile. However, the shape of the measured profiles was similar during daytime. During nighttime, the shape of the profiles of the two measurements deviated. Both models simulated daytime $E_c + E_w$ profiles that were in good agreement with eddy-covariance measurements. During nighttime, both models underestimated $E_c + E_w$ measurements throughout the canopy, with a larger underestimation for STANDFLUX than ACASA. From these profiles, the contributions of in-canopy layers to E_c $(+E_w)$ can be derived. During daytime, highest contributions were found in the upper layers of the canopy above the maximum of PAI (Fig. 16.8c), where radiative input is largest, and thus higher vapor pressure deficits and higher air temperatures occurred. Models and measurements agreed on this daytime distribution within the canopy.

These results proved the ability of the two models to not only simulate the partitioning of ecosystem evapotranspiration to its components but also to canopy layers. Performance of the models depended on the time of the day, with better agreement for daytime than for nighttime. The ACASA and STANDFLUX models largely differ in their setup. STANDFLUX includes a three-dimensional representation of the stand, whereas ACASA is a one-dimensional model but incorporates a better representation of turbulence by a third-order closure method. However, in this study, the two models performed equally well.

16.3.3 ACASA Annual Calculations: The Year 2003

In the year of 2003, Western and Central Europe was under the influence of a heat wave during the summer months (Schaer and Jendritzky 2004). Even at the Waldstein-Weidenbrunnen site, significantly higher temperatures were recorded, especially in June and August 2003 (see Chap. 3). These special weather conditions are related to obvious lower net ecosystem exchange rate measurements for carbon dioxide for many other ecosystems in Central Europe (Ciais et al. 2005). Therefore, the ACASA model was run to evaluate the quality of the modeling for a long-term period in general and to observe the modeling behavior under extreme climatic conditions for the carbon exchange.

For modeling the ecosystem behavior with ACASA, the meteorological conditions and all reference data have to be provided in continuous half-hourly time series to fit the requirements for the model run and the evaluation with in situ measurements. Therefore, it was a major challenge to fill all the gaps of missing data. Almost all input parameters and improvements in the model code of ACASA were transferred from the previous investigations (Staudt et al. 2010, 2011). The internal parameters for the plant physiological module and the parameters for leaves were taken from Falge et al. (1996). Regarding the wind profile, a factor was

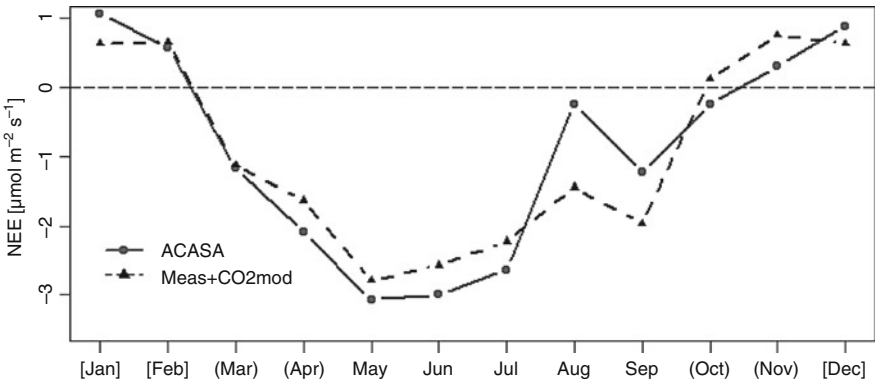

Fig. 16.9 Monthly mean of the net ecosystem exchange; gaps in the measured NEE time series (Meas) are filled with parameterized data (CO_2mod). The average values with the month's name in curved brackets are determined with less than 60 % measured values. Average values in square brackets are derived from more than 70 % parameterized data

added to the ACASA model code to extrapolate measured wind speed data to 32 m, because this value has to be in double canopy height at the top boundary of the model. The values for the root and microbe basal respiration rate, as well as the Near-IR leaf reflectivity from literature, were adjusted as well to improve the matching between simulated results and in situ measurements for 2003.

The simulated NEE was compared with eddy-covariance measurements and flux partitioning from the Main Tower (32 m, see Chap. 4). Hence, this time series was developed with measured and parameterized information mixed to obtain continuous data. As a result, the matching of simulated NEE and the NEE measurements is good for monthly means in 2003, except for the value for August (Fig. 16.9). In this month, the measured and especially the modeled mean NEE values show an obvious smaller net carbon uptake. The reason for this effect is the higher temperatures prevailing at the Waldstein site and an overestimated modeled respiration rate. In comparison to the long-term mean, it was about 5° warmer on average. In June, the difference between the measured and the climatological mean was in the same order, but the monthly mean was only 17.5 °C compared to 19.1 °C in August.

This behavior is also shown in cumulative sum graphs of NEE and its flux partitioning (Fig. 16.10). In August, the cumulated NEE curve shows a small peak due to the above-average temperatures. The cumulated assimilation and respiration rates show an overestimation in modeling values, both starting in August. The obvious difference in cumulated respiration between modeled and measured curves (-24.1 mol CO_2 m^{-2} $=$ -289 g CO_2 C m^{-2}) compared with the difference in assimilation (23.8 mol CO_2 m^{-2} $=$ 285 g CO_2 C m^{-2}) for the whole year 2003 leads to a significant underestimation of the net carbon uptake of the ecosystem (-0.3 mol CO_2 m^{-2} $=$ -4 g CO_2 C m^{-2}).

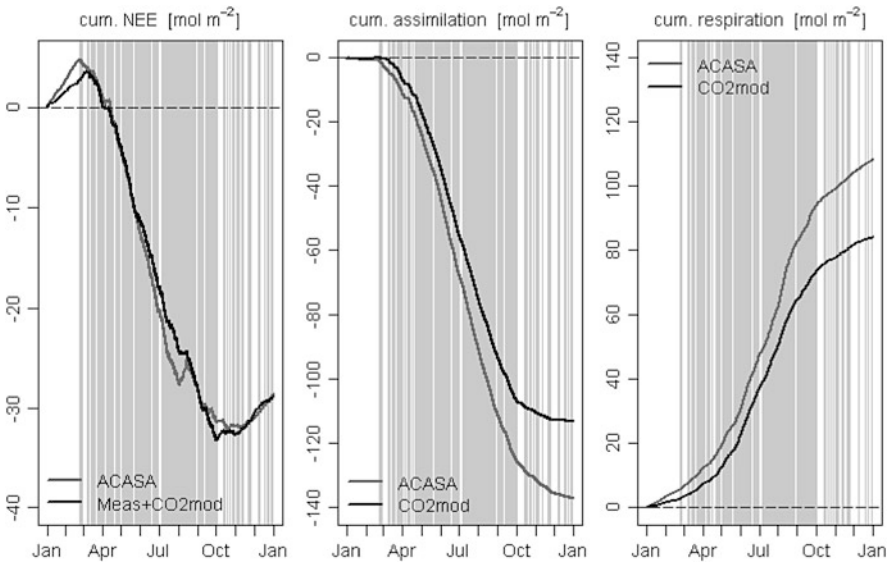

Fig. 16.10 Cumulative sum of NEE and its flux partitioning processes of assimilation and respiration for the year 2003; *gray areas* are related to those daily means based on more than 50 % measured values

16.3.4 ACASA Tile Approach for Forest and Clearing

ACASA was successfully adapted to the Weidenbrunnen site and applied to two intensive observation periods of the EGER project by Staudt et al. (2010, 2011). For the IOP3 of the EGER project, ACASA was once again applied to the Waldstein-Weidenbrunnen site and additionally adapted to the adjacent Köhlerloh clear-cut. The clear-cut contains multiple vegetation species with various canopy heights. The clearing includes mainly four plant genera *Vaccinium*, *Deschampsia*, *Calamagrostis*, *Juncus*, and one spruce species *Picea abies* (see Chap. 2). Therefore, a tile approach that includes parameterizations for the five types of vegetation and additionally for a mixture of deadwood, dead grassland, as well as bare soil was utilized. The individual model parameters for the five different vegetation types are listed in Table 16.1. The calculation of the internal boundary layer height with the criterion of Raabe (1983), utilizing the distance between forest and clearing for the fetch, has shown that the measurements at the clear-cut should be nearly unaffected by the footprint of adjacent forest area. Thus, the vegetation specific simulation results were weighted by the percentage of land cover for the individual vegetation type. With this method, the horizontal homogeneous ACASA model can be applied to the heterogeneous measurement area. For comparison, for the clearing,

two eddy-covariance systems existed at measurement heights 2.25 m and 5.5 m over the ground. The simulations are executed for both measurement heights, but in the following, only 2.25 m results are included.

Figure 16.11 displays the simulation results of the individual plant species for the NEE. The NEE exhibits the largest variations between the plant-specific simulations. The typical daily variation between positive fluxes at night (respiration) and negative fluxes at daytime (assimilation) is observed for all species, whereby *Calamagrostis* and *Picea abies* show enormous amplitudes. An exception is the deadwood, which respires all day and amounts to roughly one-third of the mean NEE values. The deadwood simulation also differs from the other model runs for the sensible and latent heat flux. The sensible heat flux has the smallest value and the latent heat flux the largest (not shown here). Thus, the uncultivated area cannot avoid the evaporation of water from the soil.

Overall, the simulated radiation balance accords to the measurements. However, deviations occur for the radiation amplitudes at daytime, which were slightly underestimated by ACASA. For the clearing, some major deviations exist at night. Thus, the long-wave radiative transfer shows a deficit for the clearing. This aspect could be caused by a lacking adjustment of the reflectivity and transmissivity parameters for the vegetation of the clear-cut. For the spruce forest, only one maximum deviation of 146 W m^{-2} occurs at the second golden day period. Thus, the radiation balance simulation is slightly more accurate for the spruce forest (Fig. 16.12).

Furthermore, the simulated sensible and latent heat fluxes were compared with the measurements. Therefore, it is mandatory to apply an energy balance correction method on the measured fluxes to partition the residual. According to Sect. 16.2.3, the methods by Twine et al. (2000) and Charuchittipan et al. (2014) were applied for energy balance closure. As anticipated, no clear difference between the correction methods can be observed at nighttime. During the day, the simulations agree better with the EBC-HB-corrected sensible heat fluxes for the forest as well as the clearing. This is indicated by lower absolute and relative deviations (not shown here). An exception is a 2-day period of the first golden day period (8 and 9 June—DOY 179/180) for the forest, where better accordance is achieved with the EBC-Bo-corrected sensible heat fluxes (Fig. 16.13). Markedly higher relative deviations occur for both correction methods during the second golden day period for the clearing (2.25 m). The discrepancy is caused by an overestimation of minor sensible heat fluxes in the morning hours.

For the latent heat flux, the mean absolute deviations at daytime are larger than at nighttime. At night, only long-wave radiation exists and the ground heat flux is directed into the ground. Thus, evaporation from the ground is limited, and transpiration is the main source of the nighttime latent heat flux. Overall, the absolute deviations are lower for the EBC-HB-corrected latent heat fluxes, but the relative deviations are smaller for the EBC-Bo-corrected heat fluxes. The lowest mean absolute deviations are achieved for the simulations of the clearing in 2.25 m

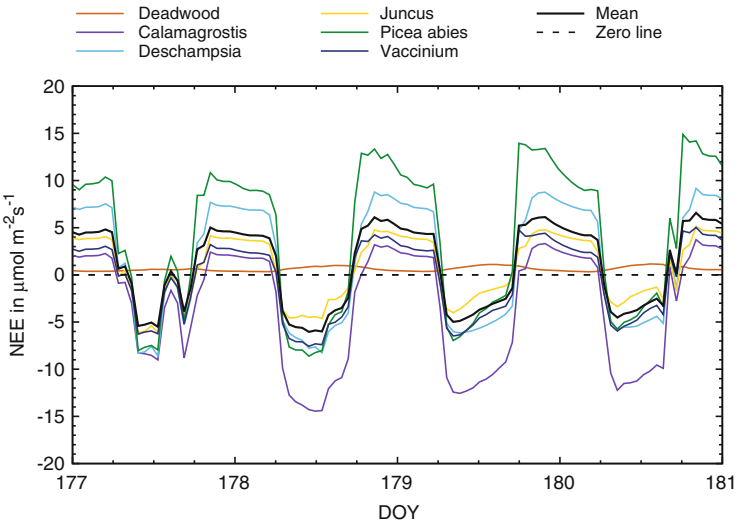

Fig. 16.11 Simulated net ecosystem exchange (NEE) with the tiled ACASA for the six land types found on the Köhlerloh clearing for the first golden day period (DOY 177–181, corresponding to 26–29 June 2011). The *black line*, labeled ("Mean"), indicates the averaged tile approach for the weighted land cover distribution of the entire clearing

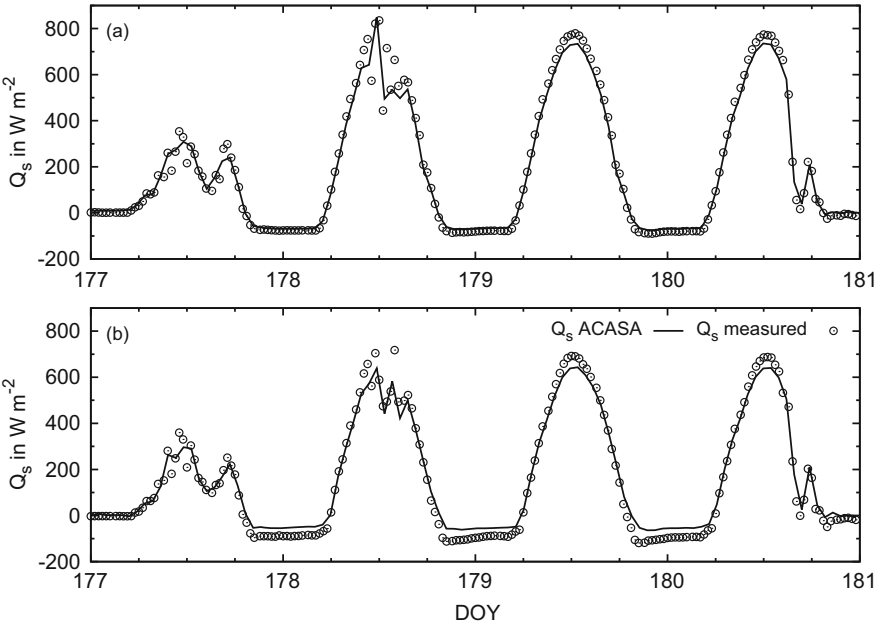

Fig. 16.12 Simulated and measured radiation balance (Q_s) for the first golden day period (DOY 177–181, corresponding to 26–29 June 2011) (**a**) of the forest and (**b**) of the clearing

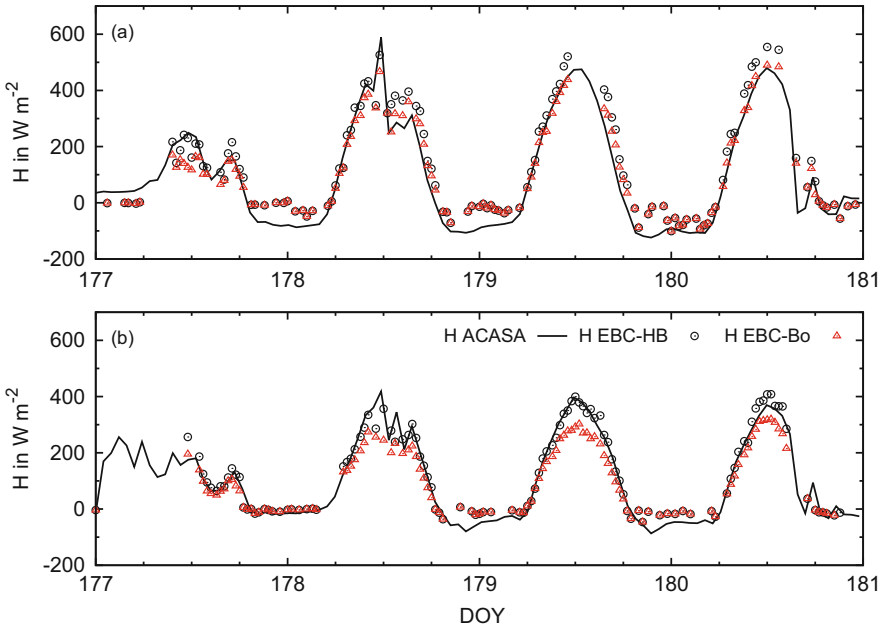

Fig. 16.13 Simulated and measured sensible heat flux (H) for the first golden day period (DOY 177–181, corresponding to 26–29 June 2011) (**a**) of the forest and (**b**) of the clearing. EBC-HB energy balance closure with buoyancy flux, ECB-Bo energy balance closure with Bowen ratio

height. A characteristic time delay between measurements and simulations can be observed for the forest in the first golden day period and the clearing (2.25 m) in the third golden day period (Fig. 16.14). In the simulations, the daily maxima are reached later, and ACASA overestimates the latent heat fluxes in the evening and at nighttime. This behavior could be explained by considering an unrealistic decrease in the stomata resistances simulated by ACASA for these times. In the input data, low relative humidity and a high air temperature can be observed at this date.

Furthermore, the net ecosystem exchange for both land surfaces was simulated. Therefore, the dark respiration at day was reduced by 50 % in ACASA for the leaves and needles, based on Falge et al. (1996). This circumstance is known as day respiration, which is constant if a certain temperature level is reached (Farquhar and von Caemmerer 1982). The latent heat flux is correlated with the NEE by the exchange of water vapor and CO_2 via the stomata. Thus, the measured NEE is corrected referring to the latent heat flux. For this purpose the ratio k between the corrected and the uncorrected latent heat fluxes is calculated for both correction methods: $k_{\mathrm{Bo}} = \frac{LE_{\mathrm{Bo}}}{LE}$ and $k_{\mathrm{HB}} = \frac{LE_{\mathrm{HB}}}{LE}$. The measured NEE value was then multiplied with the respective correction factor k_{Bo} or k_{HB}.

The simulations show that the net ecosystem exchange for the clearing reaches only half the daily value of the spruce forest (Fig. 16.15). One reason is the strong influence that deadwood has on the clearing. Investigations of Gough

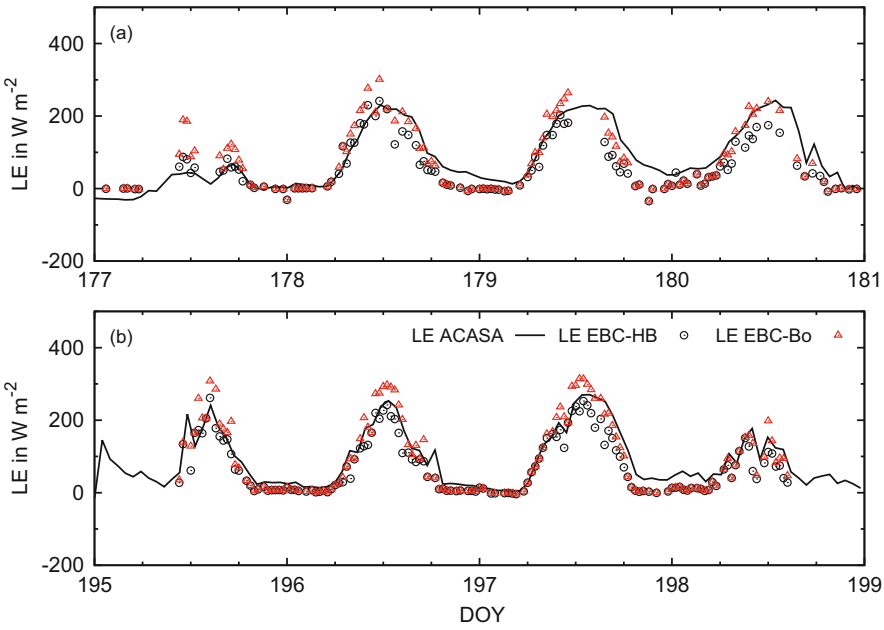

Fig. 16.14 Simulated and measured latent heat flux (LE) (**a**) for the first golden day period (DOY 177–181, corresponding to 26–29 June 2011) of the forest and (**b**) for the third golden day period (DOY 195–199, corresponding to 14–17 July 2011) of the clearing. The delayed latent heat fluxes for the forest occur at DOY 178/179 and for the clearing at DOY 197. EBC-HB energy balance closure with buoyancy flux, ECB-Bo energy balance closure with Bowen ratio

et al. (2007) point out that coarse woody debris emits CO_2 in the atmosphere over several years. Another explanation for the lower NEE is the lower leaf area index (LAI = 3.4 m^2 m^{-2}) of the clearing compared to the spruce forest (LAI = 5 m^2 m^{-2}). With respect to the measurements, ACASA reliably adjusts the amplitudes of the NEE (Fig. 16.15). The abovementioned delay for the latent heat fluxes of the forest in the first golden day period (DOY 178–180) also appears for the NEE. Generally, the absolute and relative deviations are very small for the simulations of the clearing. With respect to the correction method, the absolute deviations for the forest are lower for the EBC-HB-corrected fluxes, whereby this result is confirmed for the relative deviations of the clearing.

For both landscape structures, ACASA performs in good accordance with the eddy-covariance measurements. Thus, the tile approach serves as suitable description of the heterogeneous clearing area. Furthermore, secondary structures can cause increased turbulent mixing (Klaassen et al. 2002), which cannot be taken into account by ACASA and therefore could induce discrepancies between simulated and measured turbulent fluxes. Eder et al. (2013) refer to the existence of secondary structures at the Waldstein-Weidenbrunnen site.

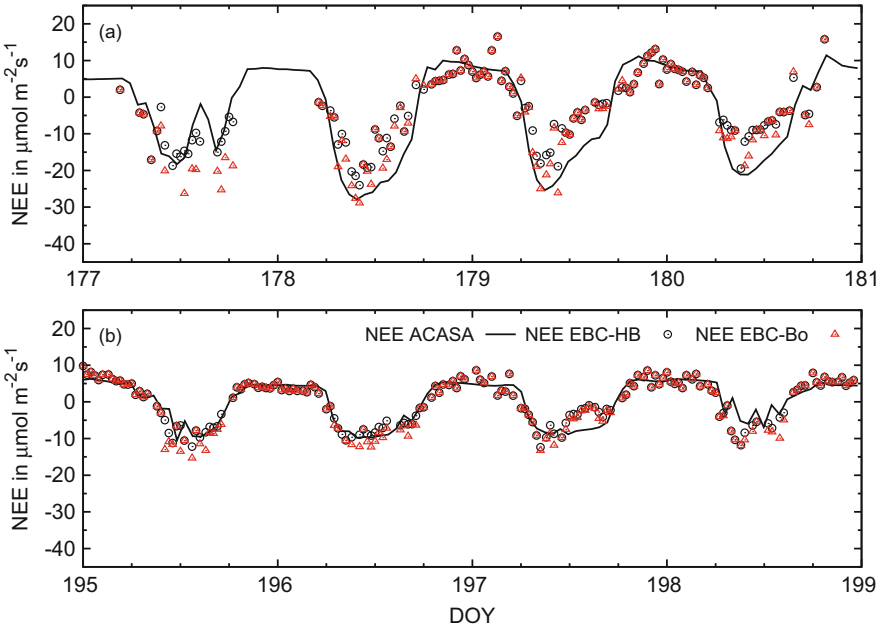

Fig. 16.15 Simulated and measured net ecosystem exchange (NEE) for the first golden day period (DOY 177–181, which corresponds to 26–29 June 2011) (**a**) of the forest and (**b**) of the clearing. The delayed net ecosystem exchange for the forest occurs at DOY 178/179. EBC-HB energy balance closure with buoyancy flux, ECB-Bo energy balance closure with Bowen ratio

16.3.5 3D SVAT-CN Simulation

To investigate the interactive effects of canopy structural and optical properties on vegetation/atmosphere exchange, validated models are necessary that allow for canopy heterogeneity in structure and physiological traits. We used a three-dimensional (3D) canopy light absorptance model to illustrate how spatial variability of canopy structure results in horizontal heterogeneities in light transmittance, transpiration, and net photosynthesis for the *Weidenbrunnen* site, a 54-year-old *Picea abies* (L.) Karst. stand of 1.4 ha, and the 4 km^2 target area of EGER II, a part of the Eger catchment.

In Staudt et al. (2011) and Foken et al. (2012), the 3D model was tested and validated at the plot scale. Hence, further 3D applications were performed to address the spatial heterogeneity of gas exchange at larger scales. The first application focused on the Norway spruce forest at Waldstein-Weidenbrunnen. Plant area index (PAI) estimates for the overstory tree canopy ranged from almost 0–12.0 m^2 m^{-2} (Fig. 16.16a). As canopy transpiration depends to a large degree on available transpiring surface (e.g., leaf area), modeled tree canopy transpiration varied between the single 1 m × 1 m squares and covaried with the measured PAI

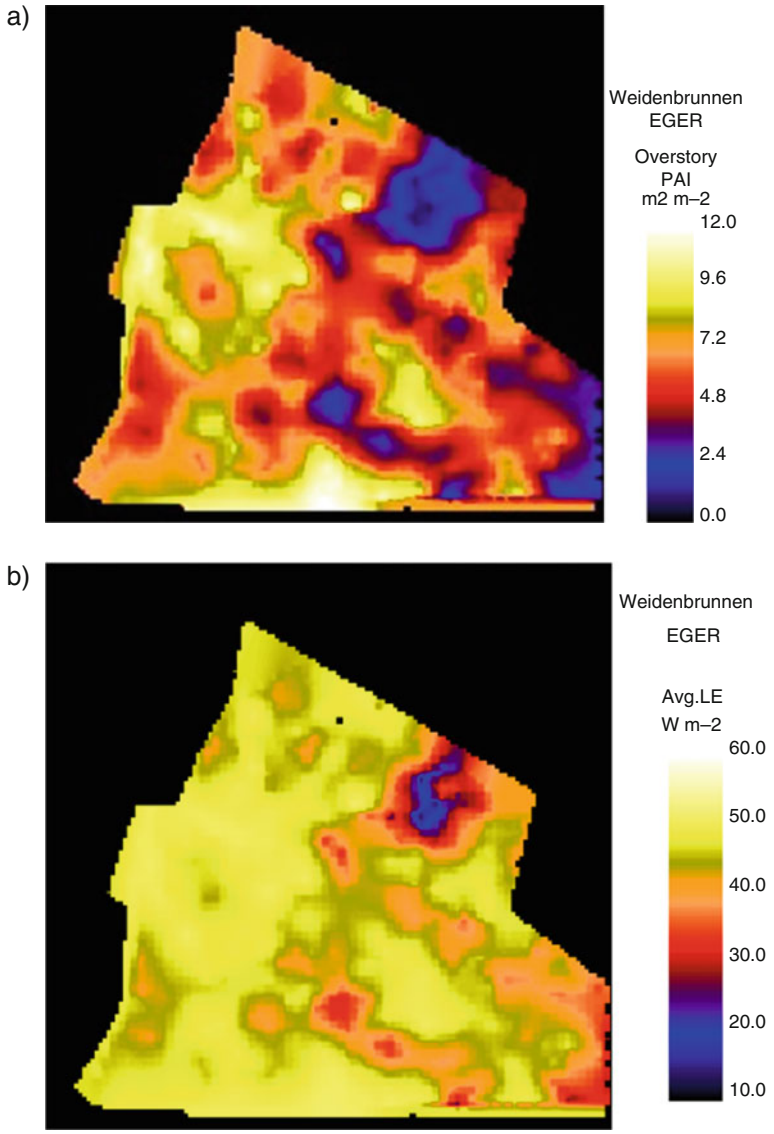

Fig. 16.16 (**a**) Map of the horizontal distribution of overstory PAI within the Weidenbrunnen research area in the Fichtelgebirge. (**b**) 3D application for assessment of the horizontal variability in average transpiration at the Weidenbrunnen for IOP2 (average for mid-May to beginning of July 2008)

distribution. The spatial heterogeneity in modeled transpiration (average over Julian Day 146–193 in 2008, IOP2) is shown in Fig. 16.16b. Probability density analyses of the model results from summer 2008 showed that in more than 60 % of the model

area of 1.4 ha, the average tree transpiration is homogeneous, ranging between 60 and 70 W m^{-2}, on average, for IOP2. Analyzing the remaining area reveals that in another third of the area, tree transpiration yields 40–60 W m^{-2}. In the remaining 6 %, tree transpiration may be as low as 10 W m^{-2}. With respect to the leaf area of the 1 × 1 m squares, the ratio between actual tree transpiration and maximum for the entire area increases with increasing LAI until an LAI of ca. 6; above this, the ratio shows saturation behavior.

The second 3D application was performed to address the spatial heterogeneity of latent heat exchange at the 4 km^2 target area of the EGER IOP3 project. Again, modeled latent heat exchange (Fig. 16.3b) covaried with the PAI distribution (Fig. 16.3a), derived from LIDAR and ground-truth data (see above), with a strong effect on the clear-cut/windthrow areas. It is planned to analyze the model results with respect to coupling stage for the tower sites on the extended target area of EGER II, to evaluate the role of secondary and local circulations on model performance.

In addition to the spatial analyses, the results from the 3D simulation experiment were analyzed by land cover type. In a first attempt we distinguished old forest stands (Norway spruce with tree heights above 4 m), young spruce forests, vegetated clearings, and roads. In general, old spruce forest stands show the largest latent heat exchange, followed by young spruce, and vegetated clearings. Roads show no latent heat exchange (no parameterization available). As expected, for sensible heat exchange the pattern is the opposite: vegetated clearing showed on average the largest sensible heat exchange, followed by young spruce, and old spruce stands.

Modeled net photosynthesis followed, in principle, the behavior described for latent heat, with the largest values for old spruce stands, followed by young spruce, and vegetated clearings. There were no obvious differences in predicted soil respiration of the different land-use types, because only a single parameterization (chamber data from the Waldstein-Weidenbrunnen spruce forest, see Falge et al. 2003; Subke et al. 2003) was available, and applied for all land uses.

16.4 Discussion and Conclusions

Obviously the Waldstein-Weidenbrunnen site was the only FLUXNET site where different types of soil-vegetation-atmosphere transfer models, having different complexities and closure approaches, were tested. These are the STANDFLUX and SVAT-CN models in 1D and 3D resolution, with a classical first-order closure according to the K-approach. For a better resolution of the in-canopy exchange processes, the 1,5-order FLAME with the transilient approach and the ACASA model with a third-order closure were applied. Also, a first application of a Large-Eddy-Simulation was done (see Chap. 17). As well, the widely used ORCHIDEE model (Organising Carbon and Hydrology In Dynamic Ecosystems, Ducoudré et al. 1993; Krinner et al. 2005), with a big-leaf approach and with the addition of a multilayer surface budget model, was applied recently to different FLUXNET sites including the Waldstein-Weidenbrunnen site (data set of EGER, IOP3, Chen et al.

2016). An important decision for all model application was to determine and use physical and plant physiological input parameters that were site and plant specific. No optimization algorithm for the model parameters was applied. A deficit of all these studies, which were made during the last 15 years, is the use of different data sets and model versions. With the data sets of the EGER project (see Chap. 2), the model validation was not only possible at the top of the canopy but also inside the canopy, even though the data used for this comparison were not energy balance closure corrected (Foken 2008, for more details, see discussion in Staudt et al. 2011).

From the presented comparison of model outputs and measured data, the agreement can be considered to be very satisfactory. Surprising was also the good agreement of the first-order closure models inside the canopy, also in comparison to sap flow data. Only at nighttime, with a low coupling between the canopy and the atmosphere, did the higher-order closure model ACASA have advantages in comparison to the other models (Foken et al. 2012). The application of the ACASA model on a clearing with low vegetation and a tile approach of the contribution of the different plant species were also positively evaluated with flux measurements. An additional application of a footprint model on the flux data is still in preparation but will show an even better agreement. Unfortunately the transilient approach, which would offer the parametrization of different coupling schema (Thomas and Foken 2007; and see Chap. 6), was not developed further. Obviously, the recently developed correction with the buoyancy flux (Charuchittipan et al. 2014), which has a larger contribution of the residual to the sensible heat flux in comparison to the Bowen ratio correction (Twine et al. 2000), gives a better energy balance closure and agreement with the ACASA results. The results of the model comparison study on partitioning of ecosystem evapotranspiration to its components and to canopy layers open up perspectives for new studies. The partitioning of CO_2 fluxes into components and separated in-canopy layers should be considered in future investigations, both in model representations and underpinned by detailed measurements.

The application of flux partitioning models shows not only deficits for low temperatures (see Chap. 4) but also for high temperatures. This was found by the application of the ACASA model to data of the year 2003, with its summer heat wave mainly in June and August. Monthly temperature departures from the climatological mean had little influence on the comparison between modeled and measured carbon fluxes except for the extremely high absolute temperatures in August. The measurements have already shown a decrease of NEE and an increase of respiration in this month. This was much stronger in the model output, because obviously the respiration parametrization was not well validated for such conditions because of missing data under extreme conditions. This reveals the risk of applying models for extreme conditions without a good validation—which of course is not easy—for such conditions.

The newly further-developed 3D model SVAT-CN provides a useful spatial tool for linking small to intermediate scale heterogeneity in vegetation type with soil/vegetation/atmosphere exchange of trace gases and energy, shown here exem-

plarily for latent and sensible heat exchange, and net photosynthesis. Set up for small to intermediate scale resolution (grid cell size of 1 and 25 m^2), it allows stand-scale and short-term (max. months to year) assessments. For larger grid cell sizes, the model provides a starting point for developing efficient tools for three-dimensional simulations of land surface exchange of nonreactive gases (H_2O, CO_2). The model design is favorable for validation with field observations. Model development in the area of in-canopy turbulent transport is viewed as critical over the long term in order to provide an efficient linkage between studies at the measurement sites and generalization via remote sensing/mesoscale modeling.

The goal of the study was to summarize insights gained from various model applications at the Waldstein-Weidenbrunnen site to provide guidance to future models selection for the analysis and evaluation of fluxes above tall vegetation. Exchange conditions in and over tall vegetation are characterized by the development of a mixing layer above the canopy which influences meteorological parameters in this zone, and the occurrence of counter-gradient fluxes, which violate the assumption of the classic K-approach, that is, that fluxes are proportional to local gradients. Nevertheless, and besides all the deficits described in this chapter, the study has shown the nearly unrestricted applicability of models like ACASA (1D third-order closure model) and SVAT-CN (3D first-order closure model) for the tall vegetation at the Waldstein-Weidenbrunnen site. In addition, it could be shown that these models are evenly applicable to low vegetation and tile approaches. This indicates that both model types included the appropriate theory and representation of the relevant processes to describe the data available. Similar findings are reported in other comparisons of closure schemes and discuss uncertainties in model coefficients as potential reasons for the unsuccessful attempt to proof the presumed superiority of higher-order closure schemes (Katul and Albertson 1998; Pinard and Wilson 2001; Juang et al. 2008). Furthermore, the study indicated that the data sets of the Waldstein-Weidenbrunnen site are qualified for the validation of the different types of models. Both model results and data from independent measurement techniques were adequate and suitable regarding accuracy and uncertainty for the scientific questions investigated. The described results helped to establish confidence in model output and their robustness for multiple purposes, such as to transfer process understanding and ecosystem functioning to a larger scale.

Acknowledgement This research was funded within the DFG projects FO 226/16-1 and ME 2100/4-1 as well the DFG PAK 446 project, mainly the subprojects ME 2100/5-1 and FO226/21-1, the fourth projects of BITÖK, PT BEO 51-0339476 D), and BaCaTeC (Bayerisch-Kalifornische Hochschulzentrum) "Modellierung des Energieaustausches zwischen der Atmosphäre und Waldökosystemen." Partial support came from a grant from the US National Science Foundation EF1137306 to the Massachusetts Institute of Technology, sub-award 5710003122 to the University of California Davis.

References

Baldocchi DD, Wilson KB, Gu L (2002) How the environment, canopy structure and canopy physiological functioning influence carbon, water and energy fluxes of a temperate broad-leaved deciduous forest-an assessment with the biophysical model CANOAK. Tree Phys 22:1065–1077

Berger M, Dlugi R, Foken T (2004) Modelling the vegetation atmospheric exchange with transilient model. In: Matzner E (ed) Biogeochemistry of forested catchments in a changing environment, a German case study, Ecological studies, vol 172. Springer, Berlin, pp 177–190

Charuchittipan D, Babel W, Mauder M, Leps J-P, Foken T (2014) Extension of the averaging time of the eddy-covariance measurement and its effect on the energy balance closure. Boundary Layer Meteorol 152:303–327

Chen Y, Ryder J, Bastrikov V, McGrath MJ, Naudts K, Otto J, Ottlé C, Peylin P, Polcher J, Valade A, Black A, Elbers JA, Moors E, Foken T, van Gorsel E, Haverd V, Heinesch B, Tiedemann F, Knohl A, Launiainen S, Loustau D, Ogée J, Vessala T, Luyssaert S (2016) Evaluating the performance of land surface model ORCHIDEE-CAN v1.0 on water and energy flux estimation with a single- and multi-layer energy budget scheme. Geosci Model Dev 9:2951–2972

Ciais P, Reichstein M, Viovy M, Granier A, Ogée J, Allard V, Aubinet M, Buchmann N, Bernhofer C, Carrara A, Chevallier F, De Noblet N, Friend AD, Friedlinstein P, Grünwald T, Heinesch B, Keronen P, Knohl A, Krinner G, Loustau D, Manca G, Matteucci G, Migglietta F, Ourcival JM, Papale D, Pilegaard K, Rambal S, Seufert G, Soussana JF, Sanz MJ, Schulze ED, Vesala T, Valentini R (2005) Europe-wide reduction in primary productivity caused by the heat and drought in 2003. Nature 437:529–533

Collatz GJ, Ball JT, Grivet C, Berry JA (1991) Regulation of stomatal conductance and transpiration, a physiological model of canopy processes. Agric For Meteorol 54:107–136

Constantin J, Inclan MG, Raschendorfer M (1998) The energy budget of a spruce forest: field measurements and comparison with the forest–land–atmosphere model (FLAME). J Hydrol 212–213:22–35

Deardorff JW (1966) The counter-gradient heat flux in the lower atmosphere and in the laboratory. J Atmos Sci 23:503–506

Denmead DT, Bradley EF (1985) Flux-gradient relationships in a forest canopy. In: Hutchison BA, Hicks BB (eds) The forest-atmosphere interaction. D. Reidel, Dordrecht, pp 421–442

Denmead DT, Bradley EF (1987) On scalar transport in plant canopies. Irrig Sci 8:131–149

Ducoudré NI, Laval K, Perrier A (1993) SECHIBA, a new set of parameterizations of the hydrologic exchanges at the land-atmosphere interface within the LMD atmospheric general circulation model. J Clim 6:248–273

Eder F, Serafimovich A, Foken T (2013) Coherent structures at a forest edge: properties, coupling and impact of secondary circulations. Boundary Layer Meteorol 148:285–308

Falge E, Graber W, Siegwolf R, Tenhunen JD (1996) A model of the gas exchange response of Picea abies to habitat conditions. Trees 10:277–287

Falge EM, Ryel RJ, Alsheimer M, Tenhunen JD (1997) Effects on stand structure and physiology on forest gas exchange: a simulation study for Norway spruce. Trees 11:436–448

Falge E, Tenhunen JD, Ryel R, Alsheimer M, Köstner B (2000) Modelling age- and density-related gas exchange of Picea abies canopies of the Fichtelgebirge, Germany. Ann Sci For 57:229–243

Falge E, Tenhunen J, Aubinet M, Bernhofer C, Clement R, Granier A, Kowalski A, Moors E, Pilegaard K, Rannik Ü, Rebmann C (2003) A model-based study of carbon fluxes at ten European forest sites. In: Valentini R (ed) Fluxes of carbon, water and energy of European forests, Ecological studies, vol 163. Springer, Berlin, pp 151–177

Falge E, Reth S, Brüggemann N, Butterbach-Bahl K, Goldberg V, Oltchev A, Schaaf S, Spindler G, Stiller B, Queck R, Köstner B, Bernhofer C (2005) Comparison of surface energy exchange models with eddy flux data in forest and grassland ecosystems of Germany. Ecol Mod 188:174–216

Falk M, Pyles RD, Ustin SL, Paw U KT, Xu L, Whiting ML, Sanden BL, Brown PH (2014) Evaluated crop evapotranspiration over a region of irrigated orchards with the improved ACASA-WRF model. J Hydrometeorol 15:744–758

Farquhar GD, von Caemmerer S (1982) Modeling photosynthetic response to environmental conditions. In: Lange OL et al (eds) Encyclopia of plant physiology II, vol 12b. Springer, Berlin

Farquhar GD, von Caemmerer S, Berry JA (1980) A biochemical of photosynthetic CO_2 assimilation in leaves of C_3 species. Planta 149:78–90

Finnigan J (2000) Turbulence in plant canopies. Ann Rev Fluid Mech 32:519–571

Foken T (2008) The energy balance closure problem—An overview. Ecolog Appl 18:1351–1367

Foken T, Mangold A, Rebmann C, Wichura B (2000) Characterization of a complex measuring site for flux measurements. 14th Symposium on Boundary Layer and Turbulence, Aspen, CO, 07–11 Aug 2000. Am Meteorol Soc, Boston, pp 388–389

Foken T, Meixner FX, Falge E, Zetzsch C, Serafimovich A, Bargsten A, Behrendt T, Biermann T, Breuninger C, Dix S, Gerken T, Hunner M, Lehmann-Pape L, Hens K, Jocher G, Kesselmeier J, Lüers J, Mayer JC, Moravek A, Plake D, Riederer M, Rütz F, Scheibe M, Siebicke L, Sörgel M, Staudt K, Trebs I, Tsokankunku A, Welling M, Wolff V, Zhu Z (2012) Coupling processes and exchange of energy and reactive and non-reactive trace gases at a forest site—results of the EGER experiment. Atmos Chem Phys 12:1923–1950

Frühauf C, Zimmermann L, Bernhofer C (1999) Comparison of forest evapotranspiration from ECEB-measurements over a spruce stand with the water budget of a catchment. Phys Chem Earth B 24:805–808

Garratt JR (1978) Flux profile relations above tall vegetation. Quart J Roy Meteorol Soc 104:199–211

Gough C, Vogel C, Kazanski C, Nagel L, Flower C, Curtis P (2007) Coarse woody debris and the carbon balance of a north temperate forest. For Ecol Manage 244:60–67

Harman IN, Finnigan JJ (2007) A simple unified theory for flow in the canopy and roughness sublayer. Boundary Layer Meteorol 123:339–363

Harman IN, Finnigan JJ (2008) Scalar concentration profiles in the canopy and roughness sublayer. Boundary Layer Meteorol 129:323–351

Inclán MG, Forkel R, Dlugi R, Stull RB (1996) Application of transilient turbulent theory to study interactions between the atmospheric boundary layer and forest canopies. Boundary Layer Meteorol 79:315–344

Inclán MG, Dlugi R, Richter SH, Foken T (1998) Vergleich zwischen LITFASS- und FLAME-(Forest-Land-Atmosphere-Model) Ergebnissen. Ann Meteorol 37:267–268

Inclán G, Schween J, Dlugi R (1999) Estimation of volatile organic compound fluxes using the forest-land-atmosphere model (FLAME). J Appl Meteorol 38:913–921

Juang JY, Katul G, Siqueira MB, Stoy PC, McCarthy HR (2008) Investigating a hierarchy of Eulerian closure models for scalar transfer inside forested canopies. Boundary Layer Meteorol 128:1–32

Katul GG, Albertson JD (1998) An investigation of higher-order closure models for a forested canopy. Boundary Layer Meteorol 89:47–74

Klaassen W, van Breugel PB, Moors EJ, Nieveen JP (2002) Increased heat fluxes near a forest edge. Theor Appl Climat 72:231–243

Krinner G, Viovy N, de Noblet-Ducoudré N, Ogée J, Polcher J, Friedlingstein P, Ciais P, Sitch S, Prentice IC (2005) A dynamic global vegetation model for studies of the coupled atmosphere-biosphere system. Global Biogeochem Cycles 19:GB1015

Leuning RFM (1990) Modeling stomatal behavior and photosynthesis of Eucalyptus grandis. Austr J Plant Phys 17:159–175

Meyers TP (1985) A simulation of the canopy microenvironment using higher order closure principles. PhD Thesis, Purdue University, Purdue, 153 pp

Meyers TP, Paw U KT (1986) Testing a higher-order closure model for modelling airflow within and above plant canopies. Boundary Layer Meteorol 37:297–311

Meyers TP, Paw U KT (1987) Modelling the plant canopy microenvironment with higher-order closure principles. Agric For Meteorol 41:143–163

Norman JM (1979) Modelling the complete crop canopy. In: Barfield B, Gerber J (eds) Modification of areal environment of crops, monograph 2. American Society of Agricultural Engineering, St. Joseph, pp 249–277

Paw U KT, Gao W (1988) Application of solutions to non-linear energy budget equations. Agric For Meteorol 43:121–145

Pinard JD, Wilson JD (2001) First- and second-order closure models for wind in a plant canopy. J Appl Meteorol 40:1762–1768

Pyles RD (2000) The development and testing of the UCD advanced canopy-atmosphere-soil algorithm (ACASA) for use in climate prediction and field studies. PhD, University of California, Davis, 194 pp

Pyles RD, Weare BC, Paw U KT (2000) The UCD Advanced Canopy-Atmosphere-Soil Algorithm: comparisons with observations from different climate and vegetation regimes. Quart J Roy Meteorol Soc 126:2951–2980

Pyles RD, Paw U KT, Falk M (2004) Directional wind shear within an old-growth temperate rainforest. Observations and model results. Agric For Meteorol 125:19–31

Raabe A (1983) On the relation between the drag coefficient and fetch above the sea in the case of off-shore wind in the near shore zone. Z Meteorol 33:363–367

Raupach MR, Finnigan JJ, Brunet Y (1996) Coherent eddies and turbulence in vegetation canopies: the mixing-layer analogy. Boundary Layer Meteorol 78:351–382

Rebmann C, Anthoni P, Falge E, Göckede M, Mangold A, Subke J-A, Thomas C, Wichura B, Schulze ED, Tenhunen J, Foken T (2004) Carbon budget of a spruce forest ecosystem. In: Matzner E (ed) Biogeochemistry of forested catchments in a changing enivironment, a German case study, Ecological studies, vol 172. Springer, Berlin, pp 143–160

Reichstein M (2001) Drought effects on ecosystem carbon and water exchange in three Mediterranean forest ecosytems-a combined top-down and bottom-up analysis. Bayreuther Forum Ökologie 89:1–150

Schaer C, Jendritzky G (2004) Climate change: hot news from summer 2003. Nature 432:559–560

Serafimovich A, Eder F, Hübner J, Falge E, Voß L, Sörgel M, Held A, Liu Q, Eigenmann R, Huber K, Duarte HF, Werle P, Gast E, Cieslik S, Liu H, Foken T (2011) ExchanGE processes in mountainous Regions (EGER)-Documentation of the Intensive Observation Period (IOP3) 13 June to 26 July 2011. Arbeitsergebn, Univ Bayreuth, Abt Mikrometeorol. ISSN 1614-8916, 47:135

Shaw RH, Schumann U (1992) Large-eddy simulation of turbulent flow above and within a forest. Boundary Layer Meteorol 61:47–64

Smirnova TG, Brown JM, Benjamin SG (1997) Performance of different soil model configurations in simulating ground surface temperature and surface fluxes. Monthly Weather Rev 125:1870–1884

Smirnova TG, Brown JM, Benjamin SG, Kim D (2000) Parameterization of cold-season processes in the MAPS land-surface scheme. J Geophys Res D 105:4077–4086

Staudt K, Falge E, Pyles RD, Paw U KT, Foken T (2010) Sensitivity and predictive uncertainty of the ACASA model at a spruce forest site. Biogeoscience 7:3685–3705

Staudt K, Serafimovich A, Siebicke L, Pyles RD, Falge E (2011) Vertical structure of evapotranspiration at a forest site (a case study). Agric For Meteorol 151:709–729

Stull RB (1984) Transilient turbulence theory, Part 1: the concept of eddy mixing across finite distances. J Atmos Sci 41:3351–3367

Stull R (1993) Review of non-local mixing in turbulent atmospheres: transilient turbulence theory. Boundary Layer Meteorol 62:21–96

Su H-B, Paw U KT, Shaw RH (1996) Development of a coupled leaf and canopy model for the simulation of plant-atmosphere interactions. J Appl Meteorol 35:733–748

Subke J-A, Reichstein M, Tenhunen J (2003) Explaining temporal variation in soil CO_2 efflux in a mature spruce forest in Southern Germany. Soil Biol Biochem 35:1467–1483

Tenhunen JD, Falge E, Ryel R, Manderscheid B, Peters K, Ostendorf B, Joss U, Lischeid G (2001) Modelling of fluxes in a spruce forest catchment of the Fichtelgebirge. In: Tenhunen JD et al

(eds) Ecosystem approaches to landscape management in Central Europe, Ecological studies, vol 147. Springer, Berlin, pp 417–462

Tenhunen J, Geyer R, Adiku S, Reichstein M, Tappeiner U, Bahn M, Cernusca A, Dinh NQ, Kolcun O, Lohila A, Otieno D, Schmidt M, Schmitt M, Wang Q, Wartinger M, Wohlfahrt G (2009) Influences of changing land use and CO_2 concentration on ecosystem and landscape level carbon and water balances in mountainous terrain of the Stubai Valley, Austria. Glob Planet Change 67:29–43

Thomas C, Foken T (2007) Flux contribution of coherent structures and its implications for the exchange of energy and matter in a tall spruce canopy. Boundary Layer Meteorol 123:317–337

Twine TE, Kustas WP, Norman JM, Cook DR, Houser PR, Meyers TP, Prueger JH, Starks PJ, Wesely ML (2000) Correcting eddy-covariance flux underestimates over a grassland. Agric For Meteorol 103:279–300

Wang Q, Tenhunen J, Schmidt M, Kolcun O, Droesler M (2006) A model to estimate global radiation in complex terrain. Boundary Layer Meteorol 119:409–429

Xu L, Pyles RD, Paw U KT, Chen S-H, Monier E (2014) Coupling the high-complexity land surface model ACASA to the mesoscale model WRF. Geosci Model Dev 7:2917–2932

Chapter 17
Complexity of Flow Structures and Turbulent Transport in Heterogeneously Forested Landscapes: Large-Eddy Simulation Study of the Waldstein Site

Farah Kanani-Sühring, Eva Falge, Linda Voß, and Siegfried Raasch

17.1 Introduction

When a turbulent flow comes along a transition from an unforested (clearing, grass- or farmland) to a forested surface patch, as present at the Waldstein–Weidenbrunnen site (see Chap. 2), the flow is strongly disturbed due to the abrupt change of the mechanical and thermodynamical surface conditions (e.g. Yang et al. 2006b,a; Dupont and Brunet 2009; Foken et al. 2012; Eder et al. 2013). This means that the mean flow as well as the turbulence statistics, and hence, the scalar transport of heat, humidity and chemical compounds, can be highly variable along this flow path, until each quantity or process has adjusted to the new surface conditions. Wherever forest patches are internally inhomogeneous due to small-scale gaps and changes in tree density, the flow disturbance can be larger than across more homogeneous forest edges, so that the three-dimensional flow becomes even more complex (Schlegel et al. 2012, 2015; Queck et al. 2015), and with that the advective and turbulent transports. Likewise, large hills can introduce similar effects to the mean flow and

F. Kanani-Sühring (✉) • S. Raasch
Leibniz Universität Hannover, Institute of Meteorology and Climatology, Herrenhäuser Straße 2, 30419 Hannover, Germany
e-mail: kanani@muk.uni-hannover.de

E. Falge
Thünen-Institute, Institute of Climate-Smart Agriculture, Bundesallee 50, 38116 Braunschweig, Germany

L. Voß
GEO-NET Umweltconsulting GmbH, Große Pfahlstraße 5a, 30161 Hannover, Germany

E. Falge, L. Voß: Affiliation during the work at the Waldstein sites: Max Planck Institute for Chemistry, Hahn-Meitner-Weg 1, 55128 Mainz, Germany

T. Foken (ed.), *Energy and Matter Fluxes of a Spruce Forest Ecosystem*,
Ecological Studies 229, DOI 10.1007/978-3-319-49389-3_17

turbulence statistics (e.g. Ross 2011; Ross and Baker 2013). As a consequence, the spatial variability of, e.g., momentum or heat fluxes complicates the interpretation of micrometeorological measurements in such disturbed ecosystems, concerning the question of the spatial representativity of an in situ flux measurement.

Previous experimental (e.g. Klaassen et al. 2002) and numerical (e.g. Sogachev et al. 2008; Kanani-Sühring and Raasch 2015) studies have revealed that momentum-, heat- and, e.g., CO_2-fluxes can be significantly enhanced above the forest at certain distances downstream of a forest edge. Klaassen et al. (2002) reported about enhanced sensible and latent heat fluxes downstream of a moorland-to-forest transition, which overshot the available energy by up to 16% of the net radiation, in a region of 20 tree heights from the forest edge. They attributed the flux enhancement to the advection of relatively warm and humid air from the moorland into the forest. Based on the results of a Reynolds-averaged Navier Stokes (RANS) study of an idealized neutrally stratified forest-edge flow, Sogachev et al. (2008) revealed that when a scalar like CO_2 is emitted from the Earth's surface (from soil respiration), CO_2-fluxes above the forest patch considerably over- and undershoot the actual net ecosystem exchange of CO_2. For a similar setup, but by means of idealized large-eddy simulations (LES), Kanani-Sühring and Raasch (2015) likewise found peaks in the streamwise concentration and flux distribution of a passive scalar. They identified the localized concentration enhancement to depend strongly on leaf area index (LAI) and wind speed, with highest peak concentrations at the largest LAI and the lowest wind speeds. Further, the scalar-flux enhancement was shown to noticeably vary with LAI, i.e., peak fluxes were higher and occurred closer to the forest edge for larger LAI, connected to the behaviour of the peak concentrations. Kanani-Sühring and Raasch (2015) reported flux overshoots of 20–280% (LAI of 1–8) of the net ecosystem exchange, in regions between 20 and 8 tree heights from the forest edge.

The few existing numerical studies dealing with this topic focused on the transport of passive scalars (no feedback on the flow) in idealized forest-edge flows with homogeneous forest patches and neutral atmospheric stratification. However, these studies already highlight how variable scalar concentrations and fluxes can be in a forest-edge-flow regime. Open questions are, how scalar transport behaves under convective conditions (i.e. considering active scalars such as temperature), and under consideration of a 3d-heterogeneous vegetation structure. The present LES study deals with these questions, and it is to be determined what consequences this might have for the spatial representativity of micrometeorological measurements.

For this purpose an LES was carried out, representing the Waldstein–Weidenbrunnen site under given experiment conditions, exemplarily for July 13th, 2011, a "Golden Day" of the third intensive observation period (IOP3) within the EGER project (ExchanGE processes in mountainous Regions; see Chap. 1). We selected a period of the daily cycle where the convective boundary layer (CBL) was fully developed and its properties such as the boundary-layer height were nearly stationary. Based on the given conditions an LES was created, where CBL properties remained quasi-stationary over the simulation period, which is helpful to enhance

the statistical reliability of the data. Background information on the meteorological situation such as wind speed/-direction, boundary-layer height and the heat sources near the surface were derived from on-site tower and SODAR data. Information on tree heights and plant area distribution (PAD) were derived from airborne laser scanning and terrestrial optical measuring techniques, respectively. It shall be noted that there was no intention to reproduce the physical and meteorological site conditions one-to-one, but rather to demonstrate possible effects of a realistic heterogeneous vegetation cover on the distribution of scalar concentrations and their respective turbulent fluxes, and finally, on the representativity of an in situ measurement. This LES study is one of the first of its kinds to study flow structures and turbulent transport in complex-heterogeneous forest environments.

17.2 Material and Methods

17.2.1 Large-Eddy Simulation Model

The Waldstein–Weidenbrunnen site was simulated using the parallelized LES model PALM, version 4.0 revision 1550.[1] PALM is based on the non-hydrostatic incompressible Boussinesq equations and the conservation equations of energy and mass. Advection terms are discretized by a fifth-order scheme (Wicker and Skamarock 2002), and a third-order Runge–Kutta scheme (Williamson 1980) is applied for time integration. Turbulence scales unresolved by the numerical grid are parametrized (Deardorff 1980), involving the solution of an additional prognostic equation for subgrid-scale turbulent kinetic energy. Incompressibility of the flow is obtained by solving a Poisson equation for pressure by means of fast Fourier transformation (Schumann and Sweet 1988). A detailed documentation of PALMs governing equations and applied numerics is given by Maronga et al. (2015).

With its embedded plant canopy model, PALM enables to account for the drag effects of a vertically extended vegetation canopy on a turbulent flow, as well as, e.g., for heat storage within the vegetation layer. PALMs canopy model treats vegetation as a porous viscous layer of drag elements that exert form - and viscous-drag forces on the flow, volume-averaged over each numerical grid box holding vegetation. Theory and numerics behind the plant canopy model in PALM are described in detail by Maronga et al. (2015). This method of modelling flows above vegetated surfaces has been successfully applied to study homogeneous (e.g. Shaw and Schumann 1992; Watanabe 2004) and heterogeneous canopy flows (e.g. Yang et al. 2006b; Cassiani et al. 2008; Dupont and Brunet 2009), and recently, to examine scalar transport in forest-edge-flow regimes (e.g. Ross and Baker 2013; Kanani-Sühring and Raasch 2015).

[1]The code can be accessed under http://palm.muk.uni-hannover.de/browser?rev=1550.

17.2.2 EGER-Case Selection and Simulation Setup

The aim was to simulate the Waldstein–Weidenbrunnen geometry for a daytime CBL scenario, in order to examine flow patterns and scalar transport in a complex-heterogeneous forested landscape. As illustrated by the areal picture in Fig. 17.1a, a $1 \times 1\,\mathrm{km}^2$ plot of land was selected as the simulation domain (SD) of interest, with the Waldstein–Weidenbrunnen site roughly centred in SD.

Tree distribution and vertical tree geometry were represented in the LES based on data of airborne laser scanning and terrestrial forest inventory, as will be explained in Sect. 17.2.3. A flat surface was assumed, neglecting the 3° average hill slope at the Waldstein measuring site (see Chap. 2), which has presumably no effect under convective windy conditions. For simplicity, a dry atmosphere was simulated. Two scalars were considered: potential temperature θ and a passive tracer C. A fine grid resolution was used, with $1 \times 1 \times 1\,\mathrm{m}^3$ grid volumes, in order to be able to explicitly resolve even small-scale flow patterns due to 3d-heterogeneous vegetation distribution, and to perform resolved-scale virtual flux measurements as close to the surface as possible. This high-resolution LES framework is highly demanding from the computational-resources perspective.

Because of that, this LES study was restricted to the simulation of one specific meteorological situation during EGER IOP3, desired to meet certain conditions: preferably clear-sky conditions; not too strong heating; moderate mean wind from SSW at 210 ± 15° (= wind direction perpendicular to the orientation of the forest

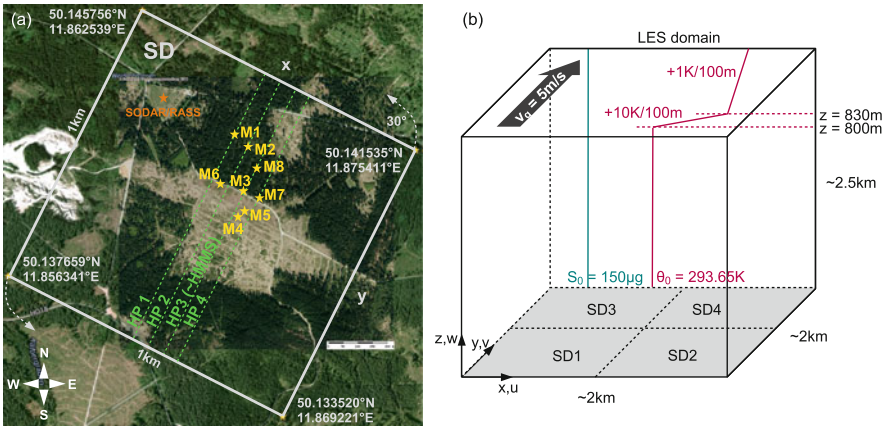

Fig. 17.1 (**a**) Aerial view of the Waldstein–Weidenbrunnen simulation domain (SD) and surroundings (collage of © Google 2013 satellite picture and aerial photograph printed with kind permission © Bayerische Vermessungsverwaltung 2011, All rights reserved). *Yellow stars* mark tower positions of EGER IOP3, where virtual tower measurements were performed in the LES; *green dashed lines* mark locations of additional horizontal-profile (HP) measurements, analogue to the horizontal mobile measuring system HMMS installed during EGER IOP3 on a segment of the marked HP3 path. (**b**) Sketch of LES model domain setup

edge); boundary-layer height $z_i < 1$ km. Only one time slot during EGER IOP3 fulfilled the listed conditions: July 13th 2011, 13:00 to 13:30 CEST.

The mean boundary-layer height during this time slot was estimated to 800 m, based on SODAR/RASS data of wind speed and temperature measured at the Waldstein–Pflanzgarten site (see Chap. 2). Based on this z_i, the LES domain was dimensioned $2 \times 2 \times 2.5\,\mathrm{km}^3$, and filled with four identical $1 \times 1\,\mathrm{km}^2$ SD plots, as sketched in Fig. 17.1b. The enlarged horizontal domain size is necessary to enable a free development of the large-scale convective flow structures, which scale with z_i. Imprinting four identical SD to the domain surface is insofar advantageous that statistics can be improved by ensemble averaging over the four SD. The large domain height assures together with a Rayleigh damping applied above $z = 1400$ m that gravity waves generated near the capping inversion do not reach the domain top, where they would be reflected back towards the boundary layer. In order to reduce the number of simulated grid points, and thus to save computational resources, grid boxes above $z = 1400$ m were gradually stretched in the vertical direction from 1 to 25 m.

Lateral boundaries were cyclic, resulting in a periodic repetition of the LES domain in the horizontal directions. At the domain top, free-slip conditions were set. No-slip conditions and zero vertical velocity were applied at the domain surface, and surface momentum fluxes were parametrized using Monin–Obukhov similarity theory (Monin and Obukhov 1954). On forest clearings, the surface roughness due to vegetation was simply represented by a homogeneous roughness length $z_0 = 0.145$ m, estimated following Monteith (1973) to be 10% of the tallest dominant vegetation found on the Köhlerloh clearing (Serafimovich et al. 2011a, p. 88). The surface roughness on forested ground is represented by a vertically extended viscous layer, with its vertical structure described by profiles of the local plant area density, as will be explained in Sect. 17.2.3.

The simulation was initialized and driven using 30-min averaged measuring data of the selected IOP3 time period. Dynamical flow forcing was steered in the LES by setting an appropriate geostrophic wind in the free-atmosphere part of the model domain. In order to reproduce the mean wind speed of $v = 2.9\,\mathrm{m\,s^{-1}}$, measured on "Turbulence Tower" M2 (Appendix A) at 36 m above ground approximately 8 m above tree top, the geostrophic wind components were prescribed to $v_g = 5\,\mathrm{m\,s^{-1}}$ and $u_g = 0.5\,\mathrm{m\,s^{-1}}$. The initial profiles of u and v were derived from a one-dimensional version of PALM steered with the same prescribed setup. Initial temperature profile started in the entire model domain with $\theta = 293.65$ K at the surface (see Fig. 17.1b) and constant up to $z = 800$ m, followed by a strong capping inversion and a weakly stable stratification above $z = 830$ m. This profile describes a well-mixed boundary layer at simulation start; the strong capping inversion helps to maintain $z_i \approx 800$ m throughout the simulation, mainly important for the data-analysis period.

Thermal forcing was steered by prescribing heat sources on the forest clearings as well as inside the vegetation, provided to PALM as kinematic heat fluxes (in $\mathrm{K\,m\,s^{-1}}$), which were derived from the measured heat fluxes (in $\mathrm{W\,m^{-2}}$) divided by air density $\rho = 1.2\,\mathrm{kg\,m^{-3}}$ and heat capacity $c_p = 1005\,\mathrm{J\,kg^{-1}\,K^{-1}}$ of air at

temperature $T = 20°C$. On clearings and all other tree-free surfaces, a constant sensible heat flux of $Q_H = 0.038\,K\,m\,s^{-1}$ based on the $45.5\,W\,m^{-2}$ measured at the clearing tower M4 at 5.5 m height (Appendix A). This assumes a solar zenith angle of zero, i.e., no shading of surfaces by trees except directly below the tree crowns, which is not too far from the actual zenith angle of 20° at this time of day and year, yielding maximal shadow lengths of 10 m for trees of up to 30 m height. At tree locations, no sensible heat flux was prescribed, instead, the heat source within the vegetation layer was defined based on the available net radiation at tree top, decaying exponentially with depth into the forest as a function of the cumulative plant area index (for details see Maronga et al. 2015), accounting for the shading of lower vegetation layers by the tree crown. The prescribed value of net radiation at tree top was $0.109\,K\,m\,s^{-1}$ corresponding to $130\,W\,m^{-2}$, being only a portion of the net radiation of $300\,W\,m^{-2}$ measured on "Main Tower" M1 at 30 m height (see Appendix A) as estimated based on the relation between sensible heat flux and total heat flux (sensible + latent) measured at M2 above tree top at 36 m height. This relative reduction of net radiation was necessary, since in the simulated dry atmosphere, the entire radiation energy is used for heating of the plant elements. Whereas in the field, the $300\,W\,m^{-2}$ net radiation transformed almost equally into sensible and latent heat. For the evaluation of the behaviour of scalars with different sources, a passive tracer was additionally considered, for simplicity with a time- and space-constant background concentration of $C = 150\,\mu g\,m^{-3}$. The tracer was constantly emitted at the domain surface via a horizontally homogeneous tracer flux $Q_C = 0.05\,\mu g\,m^{-2}\,s^{-1}$, and to yield the constant background concentration, tracer was removed through the upper domain boundary.

In the initial phase of the simulation, turbulence was triggered by imposing random perturbations to the horizontal velocity fields.

17.2.3 Determination of Tree Heights and Leaf Area Distribution

As described above, the heterogeneous plant distribution at the Waldstein–Weidenbrunnen site was to be represented in the LES. Required vegetation-height information were collected during EGER IOP3 by means of airborne lidar measurements (company Trimble/Toposys, www.toposys.com, Biberach), which supplied separate data of land surface elevation and vegetation height on 4 km^2-map at 1 m horizontal and 0.1 m vertical resolution. Georeferencing was performed using differential Global Positioning System with a virtual SAPOS reference station in the target area. For the local transformation of WGS84 to UTM32 standard parameters were used. The absolute accuracy for position is smaller than ±0.5 m, and for height smaller than ±0.15 m. Harrier 56 laser scanner point clouds were measured with a Riegl LMS-Q560 sensor head. First and last echo of the point clouds were extracted to generate a digital surface model (DSM-FE, from first echo) and a digital terrain

model (DTM, from last echo). The overflight took place in summer, on July 2, 2011 (12:28–13:04 UTC), ca. 600 m above ground over vegetated area. In such a case, last echo data might not always coincide with the soil surface. Therefore, the DTM was filtered to remove vegetation and buildings, and gaps interpolated, resulting in a filled digital terrain model (FDTM) which formed (together with the DSM-FE) the basis for the calculation of the vegetation heights. The original map was north-oriented; however, for technical reasons regarding the LES setup, the map was rotated by 30° in order to obtain a measuring site with west-east-oriented forest edge. Vegetation < 5 m in height as well as some unrealistic vegetation heights resulting from scanning errors was assumed as a simple surface roughness, described by the same roughness length $z_0 = 0.145$ m as estimated for the clearing (see Sect. 17.2.2). The final rotated tree-height map, as presented in Fig. 17.2a, was provided as input for PALM in ASCII file format.

Besides the tree heights, information about the vertical distribution of leaf or plant area per unit volume (plant area density PAD) was required for PALM. Unfortunately, PAD profiles were not available for the entire modelled domain, since this would require full wave form data and tools such as 3d terrestrial laser scanning (Schlegel et al. 2012) in order to efficiently survey the entire area, which could not be achieved during EGER. However, based on a set of forest inventory measurements on 25 forest plots, we were able to derive an empirical function for the determination of plant area index values (PAI: vertical integral of PAD) as a function of vegetation height. PAI estimates were derived from two different indirect methods: the commercially available LAI-2200 plant canopy analyzer [LI-COR Biosciences Inc., Lincoln, NE, USA; LI-COR 1992, Cutini et al. (1998)] and

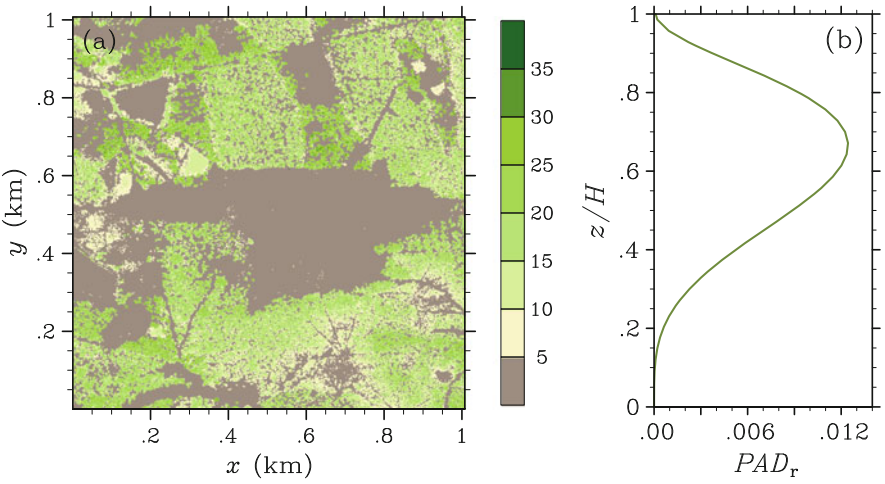

Fig. 17.2 (**a**) Map of tree heights (in m) derived by airborne laser scanning. *Grey shading* marks surfaces with vegetation height < 5 m, where the surface roughness is simply described by a uniform roughness length. (**b**) Generic PAD profile calculated as described by Eq. (17.1)

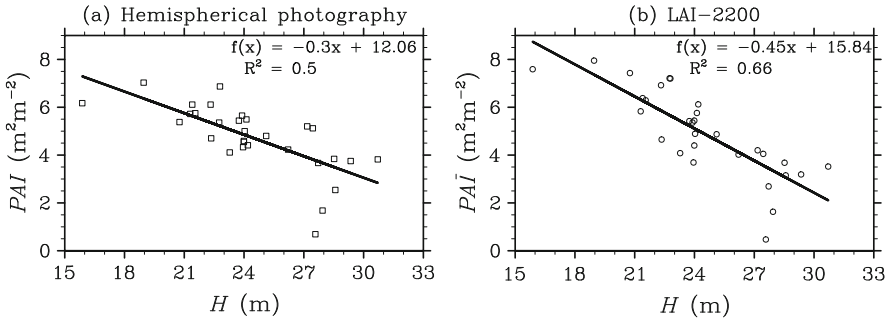

Fig. 17.3 Relation between tree height H and PAI, derived from two different techniques: (**a**) hemispherical photos, (**b**) LAI-2200

digital hemispherical photography (Ryu et al. 2012; Macfarlane et al. 2007). On nine locations at each forest plot, LAI-2200 readings and hemispherical photographs were taken. At each location, the first LAI-2200 sensor head was operated in manual below-mode right above the tripod for the digital camera. These below-canopy readings were combined (using the company software) with the second sensor head readings, recorded in remote above-mode with a logging interval of 30 s at a nearby forest clearing. Both sensor heads were equipped with 90° view caps, calibrated against each other and aligned in the same azimuthal direction. LAI-2200 measurements under direct sunlight conditions were discarded. The hemispherical photographs were taken with an upward-pointing Nikon D3100 SLR digital camera equipped with a Sigma 10/2.8 EX DC Fisheye HSM lens, mounted on a tripod. The images were post-processed using the image analysis software CAN-EYE V6.1. To minimize interference of multiple scattering and chromatic aberration, only the blue band of the images was used for the analyses (Zhang et al. 2005). Figure 17.3 presents scatter plots of PAI against tree height H, derived by hemispherical photos (a) and LAI-2200 (b). Generally, both methods deliver similar PAI values for the respective tree heights, and both reveal a linear relation between PAI and tree height. However, the slope as well as the y-intercept deviates between both methods, while data of the LAI-2200 measurements show a better match with the linear regression as indicated by the larger R^2 values.

Based on these results, the empirical PAI function derived by LAI-2200 was chosen to calculate a horizontal PAI array for the forested area based on the 1 m-resolution tree-height map. As for the vertical distribution of PAD, it was simply assumed that for all trees > 5 m the bulk of the plant elements are concentrated in the crown space. So we first define a relative PAD distribution, $\mathrm{PAD_r}$, given for each horizontal point by the following beta probability density function (Markkanen et al. 2003):

$$\mathrm{PAD_r}\left(\frac{z}{H},\alpha,\beta\right) = \frac{(\frac{z}{H})^{\alpha-1}\,(1-\frac{z}{H})^{\beta-1}}{\int_0^1 (\frac{z}{H})^{\alpha-1}\,(1-\frac{z}{H})^{\beta-1}\,d(\frac{z}{H})}\,, \tag{17.1}$$

as a function of height z, tree height H, as well as coefficients α and β. $\mathrm{PAD_r}$ integrates to unity between $z = 0$ and $z = H$. The form of the PAD distribution is steered by α and β, set to values of 5 and 3, respectively, creating a $\mathrm{PAD_r}$ profile with dense crown and sparse trunk space as presented in Fig. 17.2b. In order to obtain the actual PAD profiles at each horizontal location (x,y), $\mathrm{PAD_r}(x, y)$ is multiplied with the horizontal $\mathrm{PAI}(x, y)$ array.

17.2.4 Data Output and Analysis

The analysis phase of the simulation started after 2 h into the simulation, after boundary-layer dynamics had reached quasi-stationarity. Virtual measurements of velocity components u, v, w, potential temperature θ and passive tracer C were performed during this period at different measuring positions as illustrated in Fig. 17.1a. This measuring setup was equal in each of the four SD, allowing for improved statistics due to ensemble averaging over the four SD in addition to time-averaging over 30 min. Data was collected at 10 Hz over a 30-min period. Based on these measurements, 30 min- and ensemble-averaged turbulent scalar fluxes were calculated by means of the temporal eddy-covariance (EC) method, plus some corrections such as linear detrending of the timeseries and subtraction of the mean vertical wind. A set of virtual measurements of these averaged quantities was output in three-dimensional fields, covering the entire model domain, analogue to a SODAR/RASS measurement.

17.3 Results and Discussions

17.3.1 Mean Flow Structures

As a first picture of the simulated flow at the Waldstein–Weidenbrunnen site, Fig. 17.4 presents horizontal views of the mean prevailing streamwise wind v (a) and vertical wind w (b), exemplarily at 2 m above ground. For a simplified interpretation of the results, clusters of grey isolines mark regions with trees and black dots indicate the tower positions during EGER IOP3. Arrows locally illustrate magnitude and direction of the horizontal wind.

As expected and previously discussed by Schlegel et al. (2012, 2015); Queck et al. (2015), rather complex flow patterns are introduced by the 3d-heterogeneity of the forest, forming separated regions of higher and lower horizontal wind speeds, as well as distinct changes in wind direction (see arrows in Fig. 17.4). Large values of v are present on the relatively large Köhlerloh clearing, where due to the absent plant drag and the significant clearing size, the flow accelerates to higher velocities. Even larger wind speeds appear downstream of the Köhlerloh clearing within the first

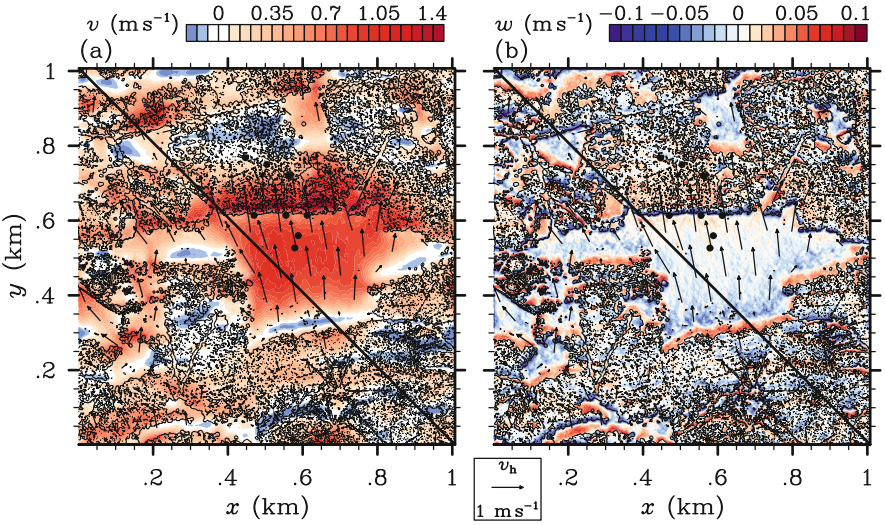

Fig. 17.4 Horizontal cross-sections of 30-min and ensemble-averaged flow at $z \approx 2\,\mathrm{m}$. (**a**) Horizontal velocity component v, perpendicular to surveyed forest edge, (**b**) vertical velocity component w. *Arrows* illustrate the 30-min and ensemble-averaged horizontal velocity vectors. Clusters of *grey isolines* mark regions with trees. *Black dots* indicate locations of the measuring towers

100 m into the surveyed forest stand, owing to reasons of continuity as the clearing flow is forced into the narrow trunk space. Deep inside the tree stands, v values are generally less than 20% of the maximum values on the clearing, and in some regions v even takes negative values (blue colouring), indicating zones with weak reversed flows. Such zones have been previously found in LES by Cassiani et al. (2008), occurring at similar distances downstream of a windward forest edge as observed here in Fig. 17.4a within the surveyed forest stand, and attributed to processes of pressure redistribution. For similar reasons reversed flows appear at most leeward forest edges connected to the phenomenon of flow separation in these regions, in agreement with findings of previous experimental and numerical studies (e.g. Bergen 1975; Cassiani et al. 2008; Detto et al. 2008; Queck et al. 2015). Another flow pattern that can be observed is flow channelling, i.e., the flow is diverted around small-scale forest patches (e.g. $0.0 < x < 0.2\,\mathrm{km}$, $0.2 < y < 0.4\,\mathrm{km}$) or forced through forest aisles (e.g. $x \approx 0.75\,\mathrm{km}$, $y \approx 0.7\,\mathrm{km}$; $x \approx 0.8\,\mathrm{km}$, $y \approx 0.6\,\mathrm{km}$). Looking closely at the surveyed forest edge, which forms the downstream end of the Köhlerloh clearing, this region can be separated into two parts: the left-hand-side ($0.4 < x < 0.6\,\mathrm{km}$), where the streamwise flow is gradually decelerated with depth into the forest to values close to zero followed by a reversed-flow zone; and the right-hand-side ($0.6 < x < 0.75\,\mathrm{km}$), where the flow maintains higher wind speeds further into the forest and into the adjacent clearing. The reason for this pronounced difference is not only the lower tree density in the right-hand-side forest patch, but also the fact that trees are taller here and thus have a more open trunk space.

Concerning the patterns of mean vertical wind w (Fig. 17.4b), one can see that the strongest upward and downward motions occur near transitions between forest and clearing. At this height level of 2 m, a mean downward motion is present at most windward forest edges and a mean upward motion at leeward forest edges. The latter might be attributed to the reversal of the streamwise flow near the surface (see Fig. 17.4a). The downward motion at windward edges occurs because the impinging streamwise flow is vertically deflected due to the drag forces of the trees, forming downward motions near the surface and mean upward motions above (not shown here), which will be further illustrated in the following paragraph. The locally non-zero mean w can especially affect the turbulence measurements directly at the forest edge (towers M3, M6, M7).

In addition to this horizontal view, Fig. 17.5 shows horizontal profiles (at locations HP1 to HP4 shown in Fig. 17.1a) of the mean wind vectors along the plane. The green colouring depicts non-zero PAD values to illustrate the tree distribution. The vectors represent well-known features of flows in and above fragmented forest canopies (as reviewed in parts by Belcher et al. 2012): the above-canopy flow descends into the larger forest gaps and clearings; small gaps are mainly overflown, while a weak vortex might develop inside the gap; further, some wave-like flow patterns appear above small gaps and undulating tree top height; at windward forest edges such as adjacent to the Köhlerloh clearing, the clearing flow is decelerated and deflected upward to overflow the roughness obstacle, except for the lowest levels where it descends and continues its path into the forest's open trunk space; here, a sub-canopy jet is present, i.e., the mean flow is significantly faster in the trunk than in the crown space; further into the tree stand, the jet vanishes and mean winds are generally low. Comparing the mean flow at the tower locations, it strikes that M1 and M2 seem to stand far enough from the forest edge to be in a sector of horizontal flow, while M8 and especially M7 (M3, M6) are located in sectors with a significant mean upwind.

Figure 17.6 presents vertical profiles of the mean horizontal wind v_h, simulated (purple curves) and measured (asterisks) at the forest towers M1, M2, M8 and the forest-edge towers M3, M7. Experiment data are from July 13th 2011, 13:00 to 13:30 MESZ, averaged over this half-hour period. Values of v_h are, respectively, normalized with reference wind $v_\mathrm{h,ref}$, being the mean wind measured or simulated at $z = 36\,\mathrm{m}$ on M2: $v_\mathrm{h,ref} = 2.4\,\mathrm{m\,s^{-1}}$ in LES; $v_\mathrm{h,ref} = 2.9\,\mathrm{m\,s^{-1}}$ in experiment. By the way of illustration, green curves depict an averaged relative PAD around the respective tower location. The simulated forest-tower profiles reflect the typical shape found in vegetation canopies: strong vertical shear and an inflection point near the tree tops; nearly constant vanishing wind speed in the crown layer; more or less pronounced secondary wind maximum (jet) in the trunk space. Simulated wind profiles at towers M3, M7 directly at the forest edge show more similarity to the standard logarithmic profiles found above rough surfaces, although at M7, the wind profile starts to bend towards a canopy-typical shape. The simulated profiles more or less fit to the experiment data. We can state that at M1, both profiles match satisfyingly well, besides the slight underestimation of the simulated trunk-layer flow against the experiment data. The few data points at M2 and M8 likewise show

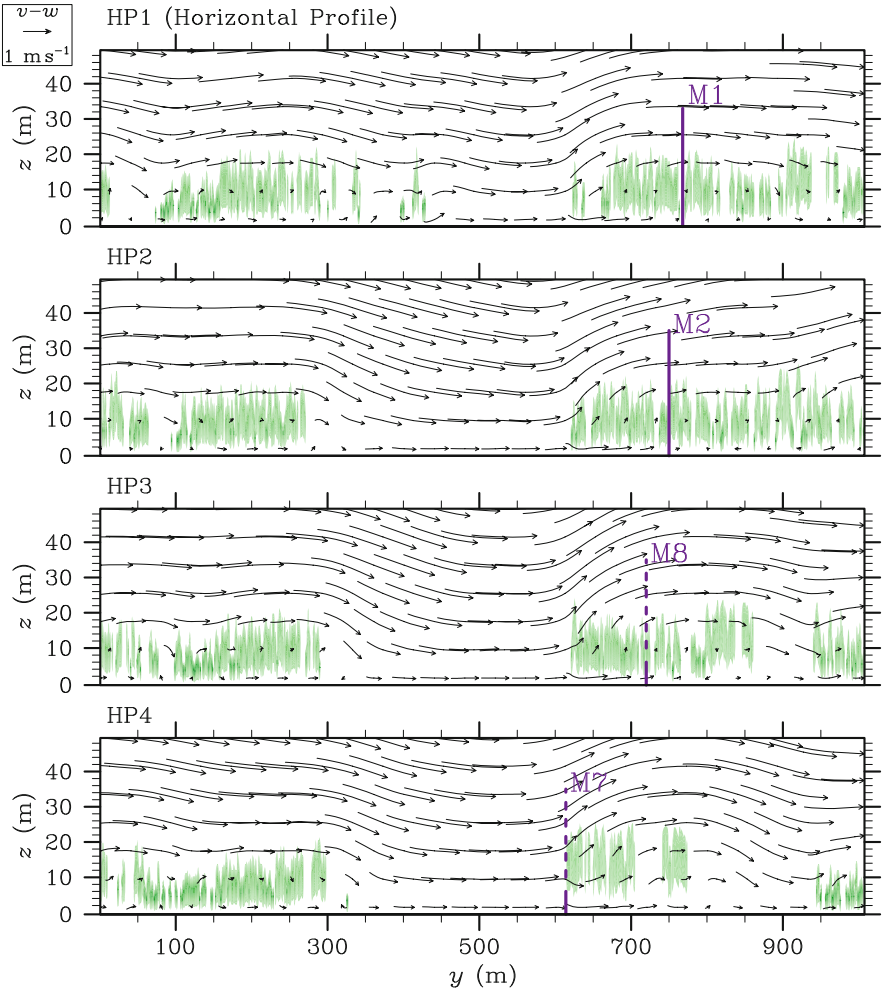

Fig. 17.5 Horizontal profiles (HP) of the v–w velocity vectors at locations of HP1 to HP4 (see Fig. 17.1a), 30 min and ensemble-averaged. *Green colouring* marks non-zero PAD values. Tower locations on HP paths are marked by *purple lines*. *Dashed purple lines* illustrate a virtual elongation of those experiment towers which were less than 10 m of height

that the simulated trunk-layer flow is weaker than observed in the measurement. This systematic deviation implies that the simulated PAD distribution might not sufficiently reflect the real forest structure of the trunk space. Overall, experiment and simulation data agree much better above the forest than within, indicating that a realistic description of the PAD distribution is more important for the representation of the in-canopy flow, which is in agreement with findings of Queck et al. (2015). Nevertheless, we have to be careful not to overinterpret this comparison, as we were not able to reproduce the meteorological and site conditions one-to-one.

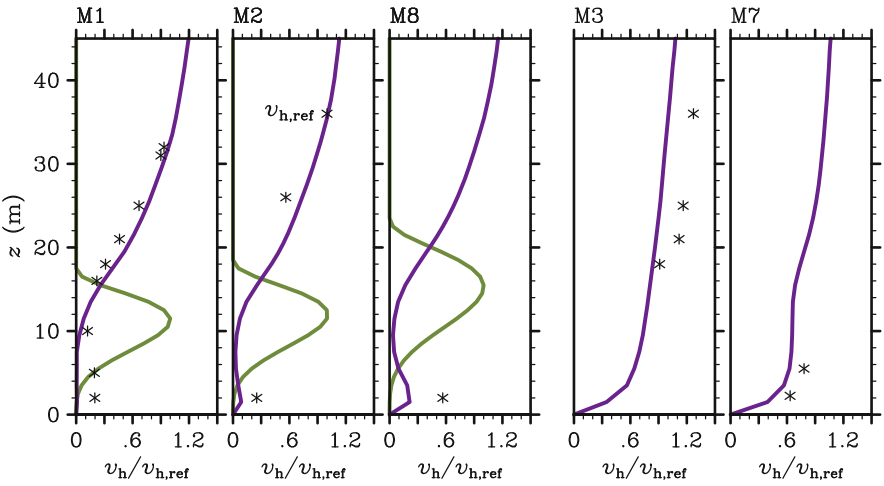

Fig. 17.6 Vertical profiles of mean horizontal wind speed v_h from LES (*purple curve*) and experiment data of July 13th 2011, 13:00 to 13:30 CEST (*asterisks*), exemplarily drawn for forest towers M1, M2, M8 and forest-edge towers M3, M7. Wind speed values are, respectively, normalized to the mean horizontal wind measured or simulated at $z = 36$ m on M2, denoted $v_{h,ref}$. The *green curve* depicts the PAD profile, averaged over all profiles in a 15 m radius around each tower, presented here in arbitrary values just to illustrate the vertical extension of the tree, crown and trunk layer

To summarize so far, mean flow structures can be arbitrarily complex in a 3d-heterogeneous forest landscape, and the formation of the flow patterns seems to depend strongly on the vegetation structure (see also Queck et al. 2015).

17.3.2 Temperature and Tracer Distributions

The horizontal distribution of mean scalar concentration, presented in Fig. 17.7 for potential temperature θ (a) and passive tracer C (b), likewise shows a complex horizontal structure as observed for the mean flow (see Sect. 17.3.1). Figure 17.7a illustrates for $z \approx 2$ m that the highest temperatures expectedly occur above forest clearings and smaller gaps directly warmed by the sun, while the shaded trunk space of the tree stands is generally cooler. Lowest temperatures are found in regions of greatest tree and plant area densities (e.g. $x \approx 0.35$ km, $y \approx 0.65$ km), hence, where shading is most efficient. Interestingly but not less anticipated, the overall highest temperatures appear in the lee of tree stands and in small gaps, where due to flow separation and decreased turbulent mixing, the heated air is trapped near the surface. Overall, the heterogeneous forest structure can induce small-scale horizontal temperature differences due to variations in canopy density and the resulting incident sunlight, forming local microclimates within the forest stand.

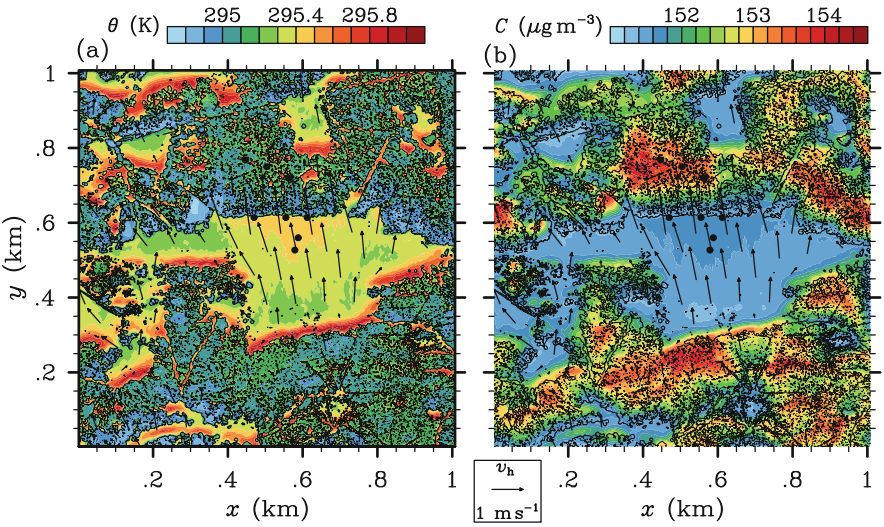

Fig. 17.7 Horizontal cross-sections of 30-min and ensemble-averaged scalar concentrations at $z \approx 2$ m. (**a**) Potential temperature θ, (**b**) passive tracer C. *Arrows* illustrate the 30-min and ensemble-averaged horizontal velocity vectors. Clusters of *grey isolines* mark regions with trees. *Black dots* indicate locations of the measuring towers

These microclimates might induce small-scale flow patterns that locally contribute to the transport of energy and mass. Similar horizontal temperature variations at daytime were observed during EGER IOP3 between clearing and forest by means of a horizontal mobile measuring system (HMMS) operated 1 m above ground (see Chap. 14).

In the distribution of the passive tracer in Fig. 17.7b, we find local tracer hotspots deep inside the forest, where concentrations are some μg higher than on the clearings or in other parts of the forest, keeping in mind that tracer sources were horizontally homogeneous. Local tracer accumulation inside a forest stand is a result of flow convergence and decreased turbulent mixing, tending to form at certain distances downstream of a forest edge as a result of flow-adjustment processes (see Kanani-Sühring and Raasch 2015). This mostly leads to a gradual increase of the tracer concentration between windward forest edges and the forest interior. Although, with the heterogeneous forest structure, we do not find a continuous accumulation along the entire length of the forest edge: e.g., between $0.6 < x < 0.75$ km at the surveyed forest edge, concentrations are lower than those observed further to the left, owing to the more efficient through-flow (see arrows and Fig. 17.4). This is different from findings for homogeneous forest patches, where a streak of high tracer concentration forms parallel to the edge at a certain distance into the forest, strongly depending on the prevailing PAI.

The horizontal profile of the averaged temperature and tracer field, presented in Fig. 17.8 exemplarily for location HP2 (see Fig. 17.1a), extends our view of

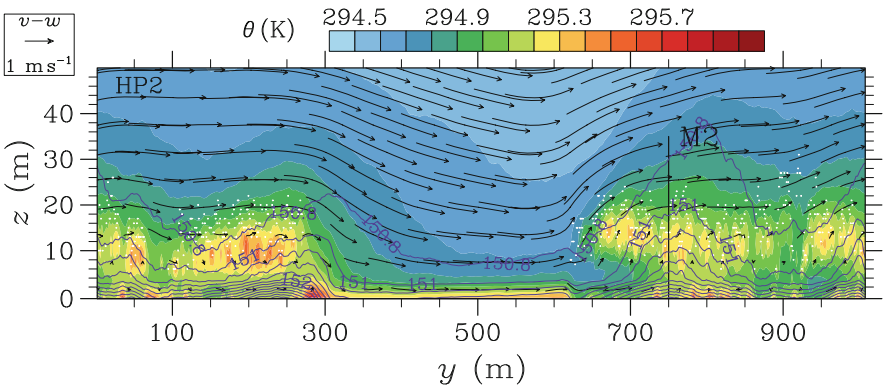

Fig. 17.8 Horizontal profile of 30-min and ensemble-averaged data at location of HP2 (see Fig. 17.1a): *coloured contours* illustrate potential temperature θ, *purple isolines* represent tracer concentration C, *arrows* visualize the mean flow along the plane. *White dots* mark the tree tops

the scalar distribution. Illustrated by the coloured contours, the mean potential temperature is largest near the clearing surface and within the tree's crowns, whereas the trunk space is generally 0.5 K cooler, forming a weakly stable stratification between trunk and crown. While the mean flow as marked by the arrows descends into the Köhlerloh clearing (centre of plot), it carries along cooler air from aloft, which is further advected into the open trunk space. This effect should be less pronounced in forests with dense understory vegetation. As mentioned earlier, overall largest temperatures occur in the lee of the upstream forest patch ($y \approx 275$ m) as well as in small gaps (e.g. $y \approx 75$ m; $y \approx 800$ m). The fact that the gap floors were heated in this LES at the same rate as the Köhlerloh clearing – and the forest is thoroughly interspersed with gaps – probably diminishes the temperature difference between trunk and crown or clearing, which can actually reach up to several Kelvin in nature (see, e.g., Chap. 14; Geiger et al. 2009). Regarding the tracer distribution, one can see that areas with tracer build-up and largest spatial concentration gradients exist near the surface in certain parts of the forest. We can further identify regions where tracer-poor air is obviously advected downward into gaps (e.g. $y \approx 75$ m), while tracer-enriched air is lifted upward in regions of flow convergence (e.g. $700 < y < 800$ m). Location and magnitude of tracer build-up depend strongly on PAI (e.g. Kanani-Sühring and Raasch 2015), and it significantly changes for scalars that are predominantly emitted/deposited on leaf surfaces (e.g. Sogachev et al. 2008; Ross and Harman 2015), or under the presence of hilly terrain (e.g. Ross 2011). As evident from Figs. 17.7 and 17.8, the heterogeneity of the forest adds arbitrary complexity to the distribution of scalars, as well as the temperature distribution itself. For example, in case of stable thermal stratification below the crown volume, gases or particles can be trapped in the trunk space.

Briefly overlooking the location of "Turbulence Tower" M2 concerning its spatial representativity to estimate forest-atmosphere exchange, we can assume based on the wind vectors that under situations with a mean background wind, sensors at the

higher tower levels might be capturing advective signals from the upstream clearing, while at lower levels sensors should be capturing signals originating from the forest.

17.3.3 Spatial Variability of Turbulent Transports

So far we have learned that mean flow structures and concentration distributions can be highly complex in heterogeneous forest stands. Turbulent transport processes are likely to be affected by this. Figure 17.9 presents horizontal profiles (at locations HP1 to HP4 shown in Fig. 17.1a) of the instantaneous potential temperature (*left*), as well as timeseries of temperature (*right*) measured at three heights on virtual towers M1, M2, M7, M8 in order to point out possible coupling events. This figure is a snapshot of an animated video (http://extras.springer.com/2017/978-3-319-49389-3), illustrating the temperature transport in a two-dimensional view over 600 s of simulated time. A few features are worth mentioning. Obviously, the crown layer is generally warmer than the trunk space. We can detect situations with warm air being locally ejected from the heated tree crown into the relatively cool air above, and other situations with relatively cool above-canopy air being swept into the tree stand, sometimes even down to the forest floor. This indicates that trunk, crown and the overlying atmosphere are at times coupled under the presently simulated conditions. However, the "fully coupled" events are not the majority, mostly only the crown layer is in exchange with the air above. This is in agreement with results of a coupling analysis for a part of EGER IOP3 (see Chap. 13), revealing that during daytime around noon, the forest is mostly coupled to the above atmosphere with roughly 20% "fully coupled" situations.

The mean turbulent flux of sensible heat $\overline{w'\theta'}$, calculated as described in Sect. 17.2.4 and depicted in Fig. 17.10, describes the mean heat exchange between earth's surface, vegetation and atmosphere by turbulent motions. Two horizontal layers are presented: one at 5 m above ground (Fig. 17.10a) and the other roughly 5 m above the tallest trees at 36 m above ground (Fig. 17.10b). Dots mark tower locations, and the values represent virtually measured fluxes at the respective height and horizontal location. As expected, there is a clear difference between clearing and forest, and significant horizontal variations on spatial scales of tens to hundreds of metres can also be detected above one and the same surface type. At 5 m height (a), heat-flux values above the Köhlerloh clearing are for the most part of similar magnitude as the prescribed surface-heating rate $Q_\mathrm{H} = 0.038\,\mathrm{K\,m\,s^{-1}}$ (derived from experiment data, see Sect. 17.2.2), as can be seen in the printed values at both clearing towers. Above smaller clearings and gaps, and especially in the lee of forest patches, $\overline{w'\theta'}$ values tend to be up to 40% larger than Q_H, most probably due to enhanced temperatures and increased vertical motions in these regions. The forest interior is characterized by uniformly low values of $\overline{w'\theta'}$ with magnitudes of roughly 10% of the values at the clearing towers, which might be attributed to the thermal stability within the trunk space as well as to turbulence damping by viscous drag forces within the vegetation. At 36 m height (b), the largest heat fluxes occur

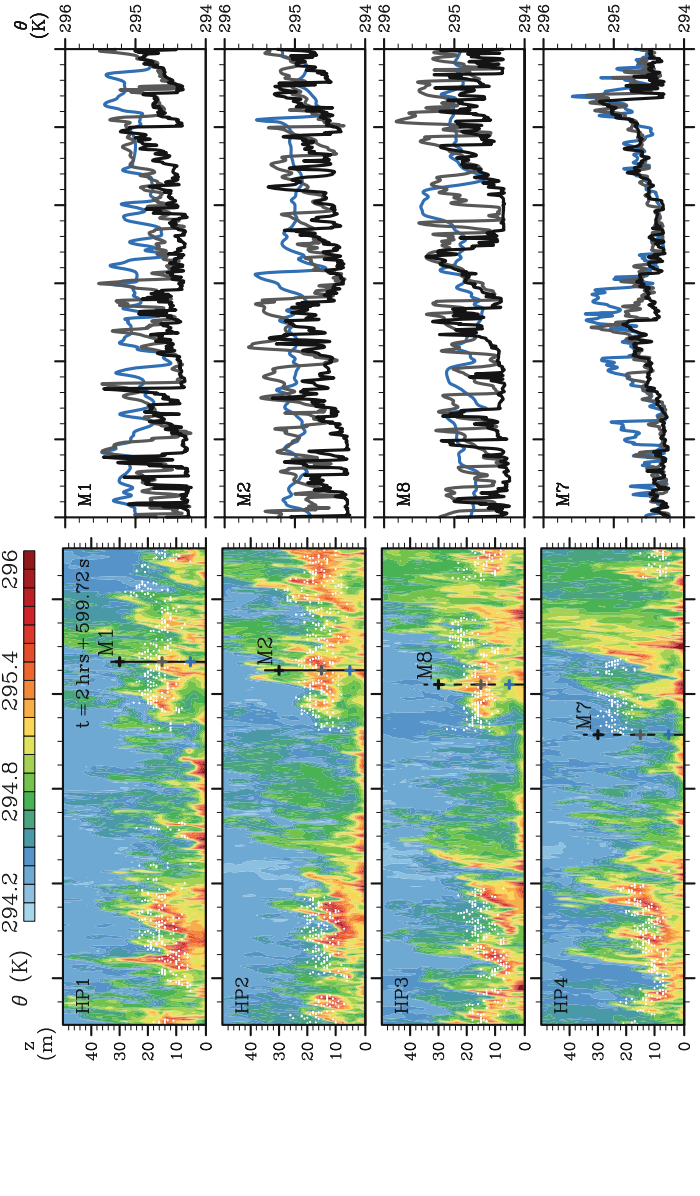

Fig. 17.9 *Left*: Vertical streamwise cross-sections of instantaneous potential temperature at locations of HP1 to HP4 (see Fig. 17.1a). *White dots* mark tree top height at respective locations. Tower locations on HP paths are marked by *purple lines*. *Right*: Timeseries of potential temperature for tower locations of M1, M2, M8 and M7 at three different heights as illustrated by the *coloured crosses* in the cross-sections, corresponding to the line colours in the timeseries plots. An animated video of the entire plot panel over 600 s of simulated time is available, http://extras.springer.com/2017/978-3-319-49389-3

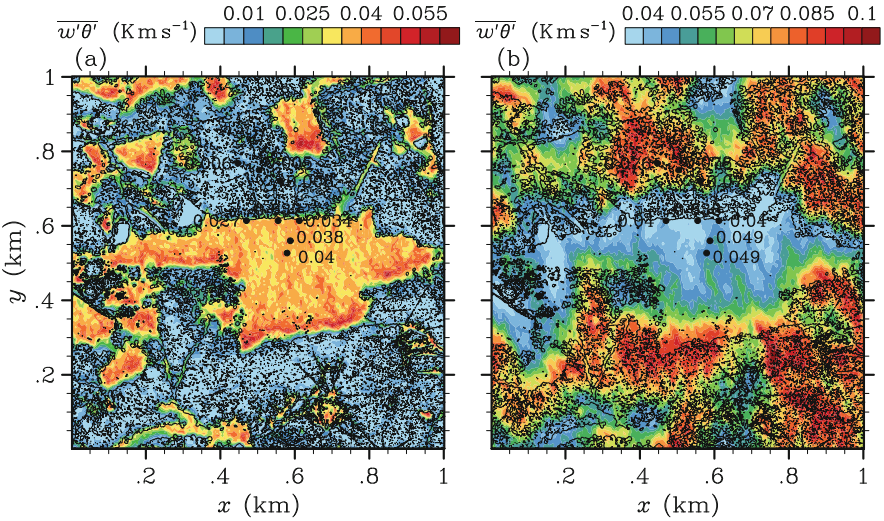

Fig. 17.10 Horizontal cross-sections of 30-min and ensemble-averaged sensible heat flux at (**a**) $z = 5$ m and (**b**) $z = 36$ m above ground. Clusters of *grey isolines* mark regions with trees. *Black dots* indicate locations of the measuring towers

above the tree stands, since these have experienced a stronger warming than clearing surfaces (based on the experiment data used for model setup, see Sect. 17.2.2). The value of $\overline{w'\theta'} = 0.078\,\mathrm{K\,m\,s^{-1}}$ measured at the virtual "Turbulence Tower" M2 is quite similar to the experimentally derived sensible heat flux at M2 being $\overline{w'\theta'} = 0.088\,\mathrm{K\,m\,s^{-1}}$ during the underlying IOP3 period. Virtually measured values at the other two forest towers are of similar magnitude, although the areal $\overline{w'\theta'}$ distribution indicates that values within distances of 100 m around the towers vary between $\overline{w'\theta'} = 0.035\,\mathrm{K\,m\,s^{-1}}$ and $\overline{w'\theta'} = 0.096\,\mathrm{K\,m\,s^{-1}}$, i.e., a difference of almost a factor of 3. This pronounced spatial variability together with the marked tower positions highlights the possible errors made by estimating a representative energy (or mass) exchange for a heterogeneously forested landscape based on single-point measurements. Explanations for this spatial variability – keeping in mind that the radiative forcing at tree top was equal everywhere – are arbitrarily complex, since the $\overline{w'\theta'}$ distribution depends on several physical and technical aspects, which are to date subject to ongoing experimental and numerical studies: heat storage capacity of the vegetation as a function of tree density, plant area distribution, hydrological factors; forest-atmosphere transport processes as a function of, e.g., wind speed, atmospheric stability, vegetation distribution (e.g. Jones 2013); limitations of the eddy-covariance approach under the presence of non-zero vertical velocities and other factors (e.g. Foken 2008). This paragraph highlights the need for more sophisticated joined measuring-modelling concepts, in order to tackle these aspects.

17.4 Conclusions

The purpose of this contribution was to demonstrate the complexity of flow structures and turbulent transports in heterogeneous forest landscapes, realized by means of a high-resolution large-eddy simulation of the Waldstein–Weidenbrunnen site. Due to the large computational demands of this proposal, the focus was deliberately set on simulating one clearly defined meteorological situation during the third intensive observation period (IOP3) within the EGER project (ExchanGE processes in mountainous Regions; see Chap. 1): a daytime cloudless convective boundary layer with moderate winds perpendicular to the transition from Köhlerloh clearing to Weidenbrunnen forest patch. Such conditions were rare during EGER IOP3, and best met during midday hours of "Golden Day" July 13th, 2011. The forest structure on site – namely forest height, plant area index, vertical plant area distribution – was represented in the simulation based on airborne laser scanning data and forest inventory measurements. There was no intention to reproduce the physical and meteorological site conditions one-to-one, but rather to demonstrate possible effects of a realistic heterogeneous vegetation cover on the distribution of scalar concentrations and their respective turbulent fluxes, and consequently, on the representativity of an in situ measurement.

It was found that due to patchiness of the forest and variations in PAI, individual horizontal and vertical flow patterns develop across and along forest edges, as well as in gaps and forest aisles. Flow structures can be arbitrarily complex in a 3d-heterogeneous forest landscape, and the formation of the flow patterns seems to depend strongly on the vegetation structure (e.g. Schlegel et al. 2012; Queck et al. 2015). These flow patterns directly affect the spatial distribution of scalars such as temperature and tracers. For example, a homogeneously emitted passive tracer locally accumulates to tracer hotspots in regions with flow convergence, while it is well-mixed in areas dominated by accelerated flows and strong turbulence. Further, the patchy forest cover causes a differential heating by solar radiation between clearings/gaps and forest, as well as internally within the forest due to variations in tree/crown density. Air above clearings and forest gaps is typically warmer than air in the trunk space of trees, owing to shading of the trunk by the tree's crown (see also Chap. 14). Lowest trunk temperatures are expectedly found in regions of greatest tree- and plant area density, which is also where highest crown temperatures occur. These local temperature differences can induce local microclimates and might generate small-scale flows in addition to the mechanically driven flow patterns. This can affect local transports of the various scalars, which needs to be accounted for in vegetation-land-atmosphere models (see Chap. 16). A visual coupling analysis – looking at the forest-atmosphere exchange of warmer and cooler air parcels – indicated that trunk, crown and overlying atmosphere are at times fully coupled. However, most of the time only the crown layer is in exchange with the air above. This agrees with results of a coupling analysis during EGER IOP3 (see Chap. 13), showing that around noon hours (as simulated here), the forest was mostly coupled to the above atmosphere with roughly 20% "fully coupled"

situations. Finally, horizontal views of the simulated turbulent flux of sensible heat expectedly showed a clear difference between clearing and forest, but also above the forest patches significant horizontal variations on spatial scales of tens to hundreds of metres were detected, owing to internal heterogeneities in plant distribution. Measured and simulated heat-flux values at the "Turbulence Tower" M2 agree quite well, however, simulated flux values in a 100-m perimeter around M2 vary by a factor of up to three from the flux at M2, highlighting the possible errors made by estimating a representative energy/mass exchange for a forested landscape based on single-point measurements.

Above results – not entirely new to the community – underline the value of LES to contribute to a better understanding of micrometeorological processes and the interpretation of their measurement. However, this study has also shown that not all aspects of the Waldstein–Weidenbrunnen meteorology were accordingly reproduced by the LES, e.g., the flow from the Köhlerloh clearing into the forest trunk space was much more pronounced in the LES than found in the measurements (Serafimovich et al. 2011b; Eder et al. 2013). The differences might be attributed to incorrect representation of the understory plant density due to lack of data (see also Chap. 19). That incorrect plant area distribution can have significant effects on the flow field was recently shown, e.g., by Schlegel et al. (2012), hence, for a realistic simulation of a site it is crucial to have detailed data of the forest structure. Recent efforts in determination of forest structure data have shown that 3D terrestrial laser scanning is a promising tool for this purpose (e.g. Schlegel et al. 2012, 2015; Queck et al. 2015).

Overall, there is a clear need for large-scale joint efforts combining experimental and model studies to improve our understanding of micrometeorological processes in complex landscapes.

Acknowledgements This study was supported by the German Research Foundation (DFG) under grant RA 617/23-1, and by the University of Bayreuth beyond the project funding period. All simulations were performed on the Cray XC30 at The North-German Supercomputing Alliance HLRN[2] in Hannover and Berlin. NCL[3] has been used for data processing and visualization.

References

Belcher S, Harman I, Finnigan J (2012) The wind in the willows: flows in forest canopies in complex terrain. Annu Rev Fluid Mech 44:479–504

Bergen J (1975) Air movement in a forest clearing as indicated by smoke drift. Agric Meteorol 15:165–179

[2]https://www.hlrn.de/home/view.

[3]The NCAR Command Language (Version 6.1.2) [Software]. (2013). Boulder, Colorado: UCAR/NCAR/CISL/VETS. http://dx.doi.org/10.5065/D6WD3XH5.

Cassiani M, Katul G, Albertson J (2008) The effects of canopy leaf area index on airflow across forest edges: large-eddy simulation and analytical results. Boundary-Layer Meteorol 126:433–460

Cutini A, Matteucci G, Mugnozza GS (1998) Estimation of leaf area index with the LI-COR LAI 2000 in deciduous forests. For Ecol Manage 105:55–65

Deardorff J (1980) Stratocumulus-capped mixed layers derived from a three-dimensional model. Boundary-Layer Meteorol 18:495–527

Detto M, Katull G, Siqueira M, Juang J, Stoy P (2008) The structure of turbulence near a tall forest edge: the backward-facing step flow analogy revisited. Ecol Appl 18(6):1420–1435

Dupont S, Brunet Y (2009) Coherent structures in canopy edge flow: a large-eddy simulation study. J Fluid Mech 630:93–128

Eder F, Serafimovich A, Foken T (2013) Coherent structures at a forest edge: properties, coupling and impact of secondary circulations. Boundary-Layer Meteorol 148:285–308

Foken T (2008) The energy balance closure problem – an overview. Ecol Appl 18:1351–1367

Foken T, Meixner F, Falge E, Zetzsch C, Serafimovich A, Bargsten A, Behrendt T, Biermann T, Breuninger C, Dix S, Gerken T, Hunner M, Lehmann-Pape L, Hens K, Jocher G, Kesselmeier J, Lüers J, Mayer J, Moravek A, Plake D, Riederer M, Rütz F, Scheibe M, Siebicke L, Sörgel M, Staudt K, Trebs I, Tsokankunku A, Welling M, Wolff V, Zhu Z (2012) Coupling processes and exchange of energy and reactive and non-reactive trace gases at a forest site – results of the EGER experiment. Atmos Chem Phys 12:1923–1950

Geiger R, Aron R, Todhunter P (2009) The climate near the ground. Rowman & Littlefield, Lanham

Jones H (2013) Plants and microclimate: a quantitative approach to environmental plant physiology. Cambridge University Press, Cambridge.

Kanani-Sühring F, Raasch S (2015) Spatial variability of scalar concentrations and fluxes downstream of a clearing-to-forest transition: an LES study. Boundary-Layer Meteorol 155:1–27

Klaassen W, Van Breugel P, Moors E, Nieveen J (2002) Increased heat fluxes near a forest edge. Theor Appl Climatol 72:231–243

Macfarlane C, Grigg A, Evangelista C (2007) Estimating forest leaf area using cover and fullframe fisheye photography: thinking inside the circle. Agric Forest Meteorol 146:1–12

Markkanen T, Rannik Ü, Marcolla B, Cescatti A, Vesala T (2003) Footprints and fetches for fluxes over forest canopies with varying structure and density. Boundary-Layer Meteorol 106:43–459

Maronga B, Gryschka M, Heinze R, Hoffmann F, Kanani-Sühring F, Keck M, Ketelsen K, Letzel M, Sühring M, Raasch S (2015) The parallelized large-eddy simulation model (PALM) version 4.0 for atmospheric and oceanic flows: model formulation, recent developments, and future perspectives. Geosci Model Dev 8:2515–2551

Monin AS, Obukhov A (1954) Basic laws of turbulent mixing in the atmosphere near the ground (in Russian). Trudy Academia Nauka SSR 24(151):163–187

Monteith J (1973) Principles of environmental physics. Edward Arnold, London

Queck R, Bernhofer C, Bienert A, Eipper T, Goldberg V, Harmansa S, Hildebrand V, Maas H, Schlegel F, Stiller J (2015) TurbEFA: an interdisciplinary effort to investigate the turbulent flow across a forest clearing. Meteorol Z 23:637–659

Ross A (2011) Scalar transport over forested hills. Boundary-Layer Meteorol 141:179–199

Ross A, Baker T (2013) Flow over partially forested ridges. Boundary-Layer Meteorol 146:375–392

Ross A, Harman I (2015) The impact of source distribution on scalar transport over forested hills. Boundary-Layer Meteorol 156:211–230

Ryu Y, Verfaillie J, Macfarlane C, Kobayashi H, Sonnentag O, Vargas R, Ma S, Baldocchi D (2012) Continuous observation of tree leaf area index at ecosystem scale using upward-pointing digital cameras. Remote Sens Environ 126:116–125

Schlegel F, Stiller J, Bienert A, Maas H, Queck R, Bernhofer C (2012) Large-eddy simulation of inhomogeneous canopy flows using high resolution terrestrial laser scanning data. Boundary-Layer Meteorol 142:223–243

Schlegel F, Stiller J, Bienert A, Maas H, Queck R, Bernhofer C (2015) Large-eddy simulation study of the effects on flow of a heterogeneous forest at sub-tree resolution. Boundary-Layer Meteorol 154:27–56

Schumann U, Sweet R (1988) Fast Fourier transforms for direct solution of Poisson's equation with staggered boundary conditions. J Comput Sci 75:123–137

Serafimovich A, Eder F, Hübner J, Falge E, Voß L, Sörgel M, Held A, Liu Q, Eigenmann R, Huber K, Duarte H, Werle P, Gast E, Cieslik S, Heping L, Foken T (2011a) Documentation of the Intensive Observation Period (IOP3). Arbeitsergebnisse Nr. 47, Bayreuth, Germany

Serafimovich A, Thomas C, Foken T (2011b) Vertical and horizontal transport of energy and matter by coherent motions in a tall spruce canopy. Boundary-Layer Meteorol 140:429–451

Shaw R, Schumann U (1992) Large-eddy simulation of turbulent flow above and within a forest. Boundary-Layer Meteorol 61:47–64

Sogachev A, Leclerc M, Zhang G, Rannik Ü, Vesala T (2008) CO_2 fluxes near a forest edge: a numerical study. Ecol Appl 18(6):1454–1469

Watanabe T (2004) Large-eddy simulation of coherent turbulence structures associated with scalar ramps over plant canopies. Boundary-Layer Meteorol 112:307–341

Wicker L, Skamarock W (2002) Time-splitting methods for elastic models using forward time schemes. Mon Weather Rev 130:2088–2097

Williamson J (1980) Low-storage Runge-Kutta schemes. J Comput Phys 35:48–56

Yang B, Morse A, Shaw R, Paw U KT (2006a) Large-eddy simulation of turbulent flow across a forest edge. Part II: momentum and turbulent kinetic energy budgets. Boundary-Layer Meteorol 121:433–457

Yang B, Raupach M, Shaw R, Paw U KT, Morse A (2006b) Large-eddy simulation of turbulent flow across a forest edge. part I: flow statistics. Boundary-Layer Meteorol 120:377–412

Zhang Y, Chen J, Miller J (2005) Determining digital hemispherical photograph exposure for leaf area index estimation. Agric Forest Meteorol 133:166–181

Chapter 18
Comparison of Meso-Scale Modelled Fluxes and Measurements

Andrei Serafimovich and Christoph Thieme

18.1 Introduction

The weather forecast is one of the most important practical applications in meteorology, because life and human activities are often directly dependent on different atmospheric phenomena. Agriculture, marine navigation, auto and air traffic are just a few examples of the great importance of weather forecasts. Since the first efforts to predict the weather, the accuracy and resolution of numerical forecasting models has been greatly improved due to the better understanding of physical processes in the atmosphere and the increase in computer performance.

One of the most commonly used models on the regional scale is the Weather Research and Forecasting (WRF) model. There have been numerous research studies conducted using the WRF model with a spatial resolution up to about 1 km (Loridan et al. 2010; Jiménez et al. 2010; Valkonen et al. 2010; LeMone et al. 2010). A high spatial resolution of the WRF model in the upper micro range

A. Serafimovich (✉)
Helmholtz Centre Potsdam, GFZ German Research Centre for Geosciences, Telegrafenberg, 14473 Potsdam, Germany
e-mail: andrei.serafimovich@gfz-potsdam.de

C. Thieme
Helmholtz Zentrum München, German Research Center for Environmental Health, Institute of Biochemical Plant Pathology, Ingolstädter Landstr. 1, 85764 Neuherberg, Germany

A. Serafimovich and C. Thieme: Affiliation during the work at the Waldstein sites- Department of Micrometeorology, University of Bayreuth, Bayreuth, Germany

T. Foken (ed.), *Energy and Matter Fluxes of a Spruce Forest Ecosystem*,
Ecological Studies 229, DOI 10.1007/978-3-319-49389-3_18

(2 km $\geq$ micro $\alpha \geq$ 200 m) makes investigation of micrometeorological phenomena possible. The WRF model can be used, for instance, in urban meteorology with special surface parametrizations to investigate energy fluxes (Loridan et al. 2010), to model surface fire behaviour (Mölders 2008) or to examine gravity wave characteristics on a fine scale of 0.9 km (Valkonen et al. 2010).

The aim of this work is to evaluate the prediction-accuracy of meteorological parameters and turbulent surface fluxes simulated by the WRF model over forest and grass-dominated ecosystems. These investigations are based on the modelled data for two measuring sites in the Fichtelgebirge (Germany) for the second intensive observation period (IOP2) of the EGER project (ExchanGE processes in mountainous Regions). This project aims to examine relevant processes in the soil-vegetation-atmosphere system by analysing transport of energy, water and trace gases in a spruce forest (see Chap. 1). Special emphasis is placed on the understanding of interactions between different scales and their contribution to the mass and energy balance (Foken et al. 2012).

The strategy is to evaluate the area-wide model forecast for turbulent surface fluxes and several meteorological parameters and compare them with point meteorological and micrometeorological measurements. For this purpose, it will be examined to what extent the increase of temporal and spatial resolutions for the selected meteorological parameters makes sense, which parameters are in good agreement with measurements, how large-scale weather patterns influence the WRF model performance and how well the model can be adapted to the topography to consider micrometeorological phenomena like katabatic flow.

18.2 Material and Methods

18.2.1 Measuring Site and Climatic Characteristics

For the comparison with the model data, two measuring stations are used: Waldstein–Weidenbrunnen and Voitsumra, located in the Fichtelgebirge. The site description can found in Chap. 2. The shape of the low mountain range can be described as an open, eastward-facing horseshoe (Gerstberger et al. 2004). The station Waldstein–Weidenbrunnen (775 m above sea level) is located between two peaks, and the station Voitsumra (624 m above sea level) is located 4 km south-southwest of the Waldstein Mountain in the upper Eger river valley (Fig. 2.1, Chap. 2).

The Waldstein area, classified as a forest ecosystem, is dominated by spruce (*Picea abies*). The ground vegetation of this coniferous forest consists of just a few species, such as woolly reed grass (*Calamagrostis villosa*), wood sorrel (*Oxalis acetosella*) and blueberry (*Vaccinium myrtillus*). The height of the forest canopy close to the measuring tower at the Waldstein–Weidenbrunnen station was, during the IOP2 measuring campaign in 2008, about 25 m and the Leaf Area Index was about 4.8 (see Chap. 2).

Table 18.1 Measurements and sensors used for the comparison of the WRF model data

Parameter	MT and Pflanzgarten[a], Waldstein Instruments	Measuring height
Temperature[a]	HMP45 Vaisala	2 m
Wind speed[b]	2D Ultra Thies	32.5 m
Wind direction[b]	2D Ultra Thies	32.5 m
Global radiation	CM 14 Kipp & Zonen	30 m
Sensible and latent heat fluxes	USA-1 Metek GmbH, LI-7000 LI-COR Biosciences	32 m
Parameter	*Voitsumra Instruments*	*Measuring height*
Temperature	HMP45a Vaisala	2 m
Global radiation	CNR1 Kipp& Zonen	2 m
Wind speed	A100R Vector Instruments	2 m
Wind direction	W200P Vector Instruments	2 m

[a] Temperature was measured at the Pflanzgarten site close to the MT
[b] Wind measurements were corrected to 10 m measuring height according to the logarithmic wind profile, assuming neutral stratification

The Voitsumra station area, classified as a grassland ecosystem, is about half a kilometer southeast from the village of the same name. The soil is gley influenced by groundwater (Mertens 2001). The land surrounding the measuring site is extensively used grassland. The common species are bistort (*Polygonum bistorta*), thread rush (*Juncus Filiformis*), white clover (*Trifolium repens*), great burnet (*Sanguisorba officinalis*), hairy lady's mantle (*Alchemilla monticola*) and meadow buttercup (*Ranunculus acris*). The climate data for the measuring sites are given in Chap. 3.

For the comparison of model data, the quality-controlled data from the IOP2 were used. The instruments and their locations are listed in Table 18.1. The WRF-model output provides the wind speed at 10 m above the surface, while the wind speed was measured at different heights. To overcome this inconsistency, the measured wind-speed data were corrected according to the logarithmic wind profile, assuming neutral stratification. For the comparison of the temperature, the data from the Pflanzgarten sites at a small clearing close to the MT were used. For more details see Chap. 2 and Appendix A.

18.2.2 Configuration and Evaluation of the WRF-ARW Model

The WRF model (Weather Research and Forecasting model) is a meso-scale numerical weather prediction model designed for the regional scale (Skamarock et al. 2008) and can be used for operational forecasting and atmospheric research needs. The WRF system contains two solvers: Advanced Research WRF (ARW) model developed by National Center for Atmospheric Research (NCAR) and Non-hydrostatic Meso-scale Model (NMM) developed by the National Centers of

Table 18.2 Configuration of the WRF model

Domains and physical parameterizations	
dx, dy [m]	9300 (D1); 3100 (D2); 1033,33 (D3)
Microphysics	Lin (Purdue) scheme (Lin et al. 1983)
Longwave radiation	Rapid Radiative Transfer Model (Mlawer et al. 1997)
Shortwave radiation	Goddard shortwave scheme (Chou and Suarez 1994)
Surface layer	MM5 similarity theory surface layer scheme (Paulson 1970; Dyer and Hicks 1970) (Webb 1970; Beljaars 1994)
Land surface	Noah Land Surface Model (Tewari et al. 2004)
Planetary boundary layer	Yonsei University scheme (Hong et al. 2006)
Cumulus parameterization	Kain–Fritsch scheme (Kain 2004)

Environmental Prediction (NCEP). This model is adaptable to a higher resolution (1 km or less) through use of a nested domains technique and zooming in to the area of interest.

For the analysis, the WRF-ARW version 3.1.1 was used and the configuration of the WRF model is given in Table 18.2. The WRF was initialized using three nested domains D1, D2 and D3 with spatial resolution 9.3 km, 3.1 km, 1.033 km and temporal resolution 3 h, 1 h and 30 min, respectively (Fig. 18.1). The results from the final operational global analysis of the National Centers for Environmental Prediction (NCEP FNL) were used as meteorological input data.

Input parameters and resulting simulated physical characteristics can vary greatly in complex terrain. Therefore, measured parameters were compared with simulated data at the so-called next and interpolated grid points. The "next" grid point is the closest grid point of the WRF model and the "interpolated" grid point represents an interpolation using the four grid points around the station. The interpolation was done according to the Cressman scheme (Cressman 1959) using a weighted mean, depending on the distance between interpolated and input grid points:

$$w_i = \frac{R^2 - d_i^2}{R^2 + d_i^2}, \tag{18.1}$$

$$x_{\text{interpol}} = \frac{\sum_{i=1}^{4} w_i x_i}{\sum_{i=1}^{4} w_i}, \tag{18.2}$$

where w_i is the weighting factor for the grid point i, d_i is the distance between observation and grid point i, R is the radius of influence, equal mean distance between grid points, x_i is WRF-simulated parameter at grid point i and x_{interpol} is the interpolated parameter at the observation point.

Fig. 18.1 Location of domains D1, D2 and D3

For comparison of modelled and observed atmospheric parameters, different quality indices can be used. The MBE [Mean Bias Error, Eq. (18.3)] is used to indicate overestimation or underestimation of measured parameters by model data.

$$\mathrm{MBE} = N^{-1} \sum_{i=1}^{N} (P_i - O_i), \tag{18.3}$$

However, a zero value of MBE does not necessarily mean that the measured values and the predictions are in good agreement. The Root Mean Square Error [RMSE, Eq. (18.4)] and Mean Average Error [MAE, Eq. (18.5)] do not have this deficiency:

$$\mathrm{RMSE} = \sqrt{\left| N^{-1} \sum_{i=1}^{N} (P_i - O_i)^2 \right|}, \tag{18.4}$$

$$\mathrm{MAE} = N^{-1} \sum_{i=1}^{N} |P_i - O_i| , \tag{18.5}$$

where P is predicted value, O is observed value and N is number of predicted and observed pairs. A deficiency of these error indices [Eqs. (18.3)–(18.5)] is that they do not provide any information about the relative magnitude of the error. For such cases, Willmott (1982) suggested the use of the Index of Agreement [IA, Eq. (18.6)]

$$\mathrm{IA} = 1 - \left[\sum_{i=1}^{N} (O_i - P_i)^2 / \sum_{i=1}^{N} (|P_i'| + |O_i'|)^2 \right], 0 \le \mathrm{IA} \le 1 \tag{18.6}$$

and Willmott et al. (2012) proposed the use of the Coefficient of Efficiency [E, Eq. (18.7)]

$$E = 1 - \left[\sum_{i=1}^{N} (P_i - O_i)^2 / \sum_{i=1}^{N} (O_i - \overline{O})^2 \right], \tag{18.7}$$

where $\overline{O}$ is averaged observed value, $P_i' = P_i - \overline{O}$ and $O_i' = O_i - \overline{O}$. Despite their advantages, the IA and E are sensitive to extreme values due to the squaring of differences between observations and predictions. The same applies to the RMSE. Therefore, before estimating these error indices the data quality has to be checked.

18.3 Results and Discussion

18.3.1 Predictive Quality of State Variables

18.3.1.1 Temperature

The error parameters for the temperature at Waldstein and Voitsumra are shown in Table 18.3. Positive MBE values mean that the modelled temperature is higher than actually measured. The lowest values of all parameters: MBE, MAE, RMSE, IA and E, indicate that the smallest errors are in the domain D3, with higher resolution than in the domains D2 and D1.

Table 18.3 Error indices for temperature at Waldstein and Voitsumra for three domains over the IOP2 period

	Waldstein					Voitsumra				
	MBE	RMSE	MAE	IA	E	MBE	RMSE	MAE	IA	E
	[K]	[K]	[K]			[K]	[K]	[K]		
Temperature (D1)	0.8	4.7	3.8	0.68	−0.1	1.4	5.2	4.2	0.68	−0.01
Temperature (D2)	0.7	3.2	2.5	0.86	0.5	1.4	3.9	2.9	0.84	0.48
Temperature (D3)	**0.7**	**1.8**	**1.4**	**0.96**	**0.83**	**1.4**	**2.6**	**1.9**	**0.93**	**0.77**

The lowest error indices are marked in bold

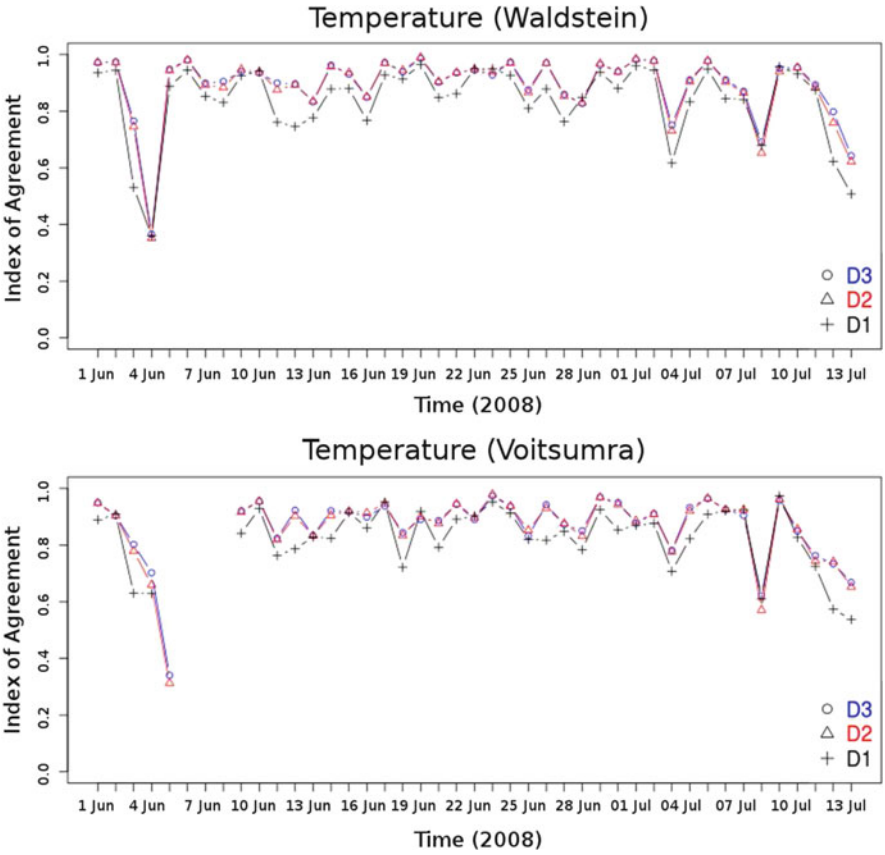

Fig. 18.2 Daily values of IA for temperature at the Waldstein and Voitsumra for the IOP2 period (*black*—domain D1, *red*—domain D2, *blue*—domain D3)

Daily values of the IA for temperature at Waldstein for three domains are shown in Fig. 18.2 (upper frame). IA exhibits large variability during IOP2 and demonstrates that temperature for the domain D3 is modelled with high quality.

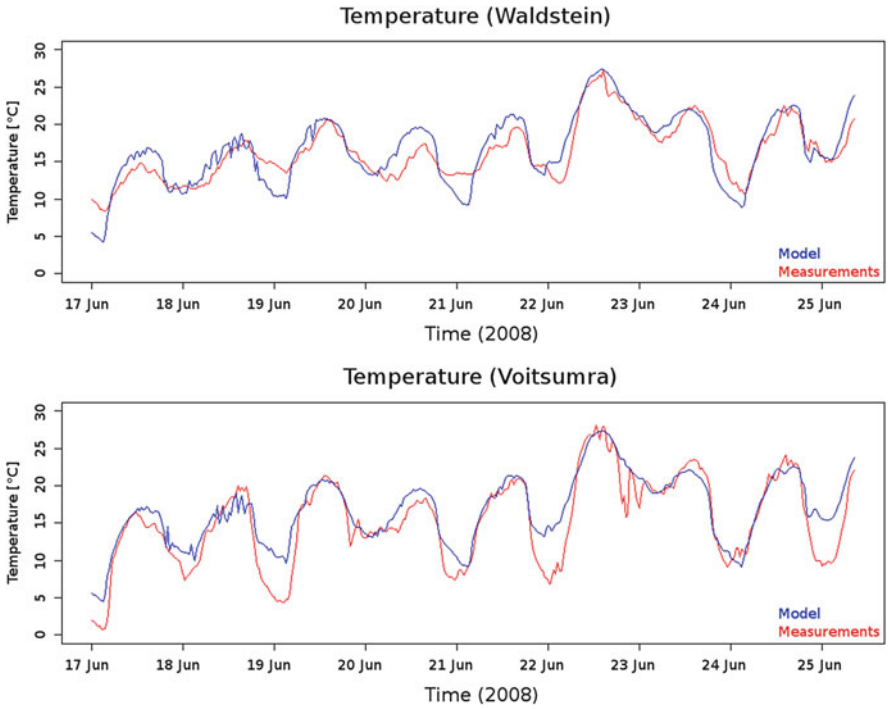

Fig. 18.3 Influence of nocturnal drainage flows between 17.06.2008 and 25.06.2008 on the modelled temperature. There are no noticeable differences between modelled (*blue*) and measured temperature (*red*) at the Waldstein site (*top frame*). It is rather temporal overestimation of measured values between 19.06.2008 and 21.06.2008. The measured values in Voitsumra (*bottom frame*) in more than half of the cases are significantly lower than the modelled values or slightly lower or similar in the other cases

The Waldstein forested site is not resolved in the input land-use map and is shown as "dryland cropland and pasture". The elevation of Waldstein above sea level given in terrestrial data is too low (∼590 m instead of 775 m). This leads to errors and overestimation of temperature at the Waldstein measuring site. Voitsumra, on the other hand, is well resolved in land-use map and terrestrial data.

The above-mentioned overestimation of the temperature by the model at the Waldstein due to the too-low topography and resulting too-high air pressure is shown in Fig. 18.3 (upper frame). The underestimation of the temperature by the model during night time in the mountains is due to night time inversions. Cold-air masses flow into the valley, in the highlands, however, there remains a warm residual layer (warmer temperature) under a free inversion (Stull 1988; Foken 2008b). These two opposite effects result in slight overestimation of the temperature at the Waldstein.

The MBE values in Voitsumra are too high. One explanation for this overestimation is, in this case, the lack of modelling of cold-air drainage. Voitsumra is located in the Eger valley. Such sites are preferred flow-paths of cold-air drainage.

Comparing calculated error parameters from other studies, one can see that the error parameters for the Fichtelgebirge are in a normal range for the WRF. For example, Jorba et al. (2008) showed that WRF simulations of temperature with a resolution of 12 km in June and July 2004 over whole Europe gave an average monthly MBE of −0.3 and −0.5 K. Mölders (2008) estimated an MBE value of −1.5 K for simulations of temperature over Alaska in June 2005 with a resolution of 4 km. The latter gave RMSE values of 2.8, which is close to what is found in the simulations in D2 and D3 at the Waldstein site and Voitsumra.

18.3.1.2 Global Radiation

The relative-error parameters for the global radiation at Waldstein site (IA and E) reveal almost no differences between different resolutions (Table 18.4). The absolute error parameters (MBE, RMSE and MAE) change slightly with increasing resolution. Figure 18.4 shows small differences in daily values of IA for the global radiation at the Waldstein and Voitsumra measuring sites.

The quality of modelling is generally good in the case of the global radiation. As shown in Figs. 18.4 and 18.5, the WRF model can predict the global radiation for days with a low degree of cloud cover sufficiently well (from 30.06.2008 to 02.06.2008). Some days with a high degree of cloud cover, nevertheless, reflect relatively poor quality of the forecast.

The MBE of the global radiation for the grassland ecosystem is less than the above-discussed MBE for the forested ecosystem and has values between 29.0 (D1) and 63.9 (D3) Wm^{-2}. The largest deviations in MBE are found in the domain D3, with the finest resolution. RMSE and MAE are relatively similar in all domains. The relative-error parameters IA and E show very similar forecast-quality in all three domains. The comparison of the three domains demonstrates that the global radiation is already modelled well enough in the domain D1. The quality of modelling is clearly better for the Voitsumra measuring site than for the Waldstein site, because small-scale events are difficult to model. The Waldstein area is characterized by frequent fog events (Foken 2003) and orographic-induced precipitation. Cloudiness occurs more frequently at the Waldstein than in Voitsumra, because Voitsumra is located on the lee side of hills during westerly winds (prevailing wind direction).

18.3.1.3 Wind Speed

The range of the wind-speed measurements was similar at Waldstein and Voitsumra during IOP2 (min = 0.3/0.0 ms^{-1}, max = 11.9/12.3 ms^{-1}). Nevertheless, the distribution of wind-speed values is shifted towards higher values in the mountain-

Table 18.4 Error indices for global radiation at Waldstein and Voitsumra for three domains and over IOP2 period

	Waldstein					Voitsumra				
	MBE	RMSE	MAE	IA	E	MBE	RMSE	MAE	IA	E
	[Wm^{-2}]	[Wm^{-2}]	[Wm^{-2}]			[Wm^{-2}]	[Wm^{-2}]	[Wm^{-2}]		
Global radiation (D1)	**69.9**	**196.6**	133.6	0.88	**0.40**	**29.0**	**177.9**	123.1	0.91	0.63
Global radiation (D2)	89.7	210.6	**123.0**	0.88	0.39	42.9	184.2	105.9	0.91	**0.65**
Global radiation (D3)	99.2	212.5	123.1	0.88	**0.40**	63.9	186.2	**104.1**	**0.92**	**0.65**

The lowest error indices are marked in bold

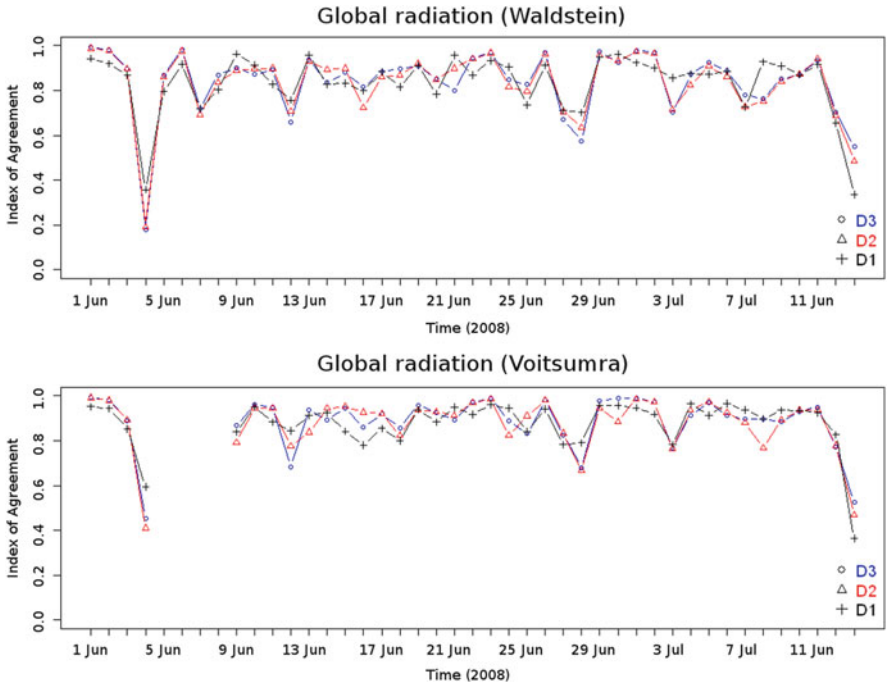

Fig. 18.4 Daily values of IA for global radiation at the Waldstein and Voitsumra for the IOP2 period (*black*—domain D1, *red*—domain D2, *blue*—domain D3). For extreme deviations see Sect. 18.3.1

ous Waldstein (median = 4.5 ms^{-1}) site compared to the valley-located Voitsumra (median = 2.3 ms^{-1}). Both locations could be modelled with a positive E in the finest resolution (E = 0.34/0.36, Table 18.5), which indicates that the predictions are useful, whereas the two coarser resolutions cannot be recommended. In general, a slight underestimation of the measurements at the Waldstein site is indicated by the negative MBE value of $-0.8\,ms^{-1}$ and a slight overestimation at the Voitsumra by a positive MBE value of $0.8\,ms^{-1}$ (Table 18.5). Figure 18.6 shows that this overestimation at Waldstein appears mostly during the day, and during the night in Voitsumra. The latter is in some cases seen as a consequence of a nocturnal decoupling of the valley from the main wind flow, which is not resolved in the model because of the poor resolution of the model orography for Fichtelgebirge. The underestimation of the daytime values at Waldstein is also attributed to the poor resolution of the orography.

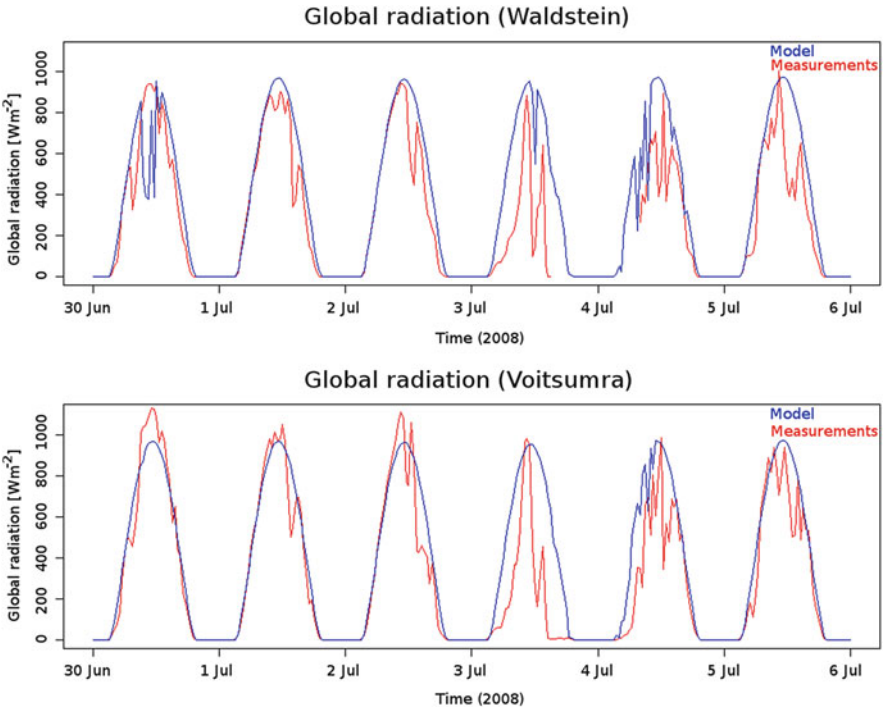

Fig. 18.5 Global radiation at Waldstein (*top frame*) and Voitsumra (*bottom frame*) from 30.06.2008 to 06.07.2008. The modelled values (*blue*) are close to measured (*red*) in Voitsumra from 30.06.2008 to 01.07.2008 and mostly underestimated for other periods. An overestimation occurs rarely

Table 18.5 Error indices for wind speed at Waldstein and Voitsumra for three domains and over IOP2 period

	Waldstein					Voitsumra				
	MBE	RMSE	MAE	IA	E	MBE	RMSE	MAE	IA	E
	[ms^{-1}]	[ms^{-1}]	[ms^{-1}]			[ms^{-1}]	[ms^{-1}]	[ms^{-1}]		
Wind speed (D1)	−0.6	2.6	2.1	0.35	−1.9	3.1	5.1	3.6	0.31	−1.3
Wind speed (D2)	**−0.1**	2.8	2.2	0.47	−0.62	2.7	4.5	3.2	0.35	−1.1
Wind speed (D3)	−0.8	**1.9**	**1.5**	**0.79**	**0.34**	**0.8**	**2.0**	**0.8**	**0.79**	**0.36**

The measurements were corrected according to the logarithmic wind profile (adequate to height of 10 m) . The lowest error indices are marked in bold

18.3.1.4 Wind Direction

To compare wind direction, a time window was chosen where wind prediction was challenging for the model due to changing wind directions. Overall, there is a significant difference in the forecast-quality between both locations. Figure 18.7 shows that wind direction was predicted more accurately on the mountainous site than in

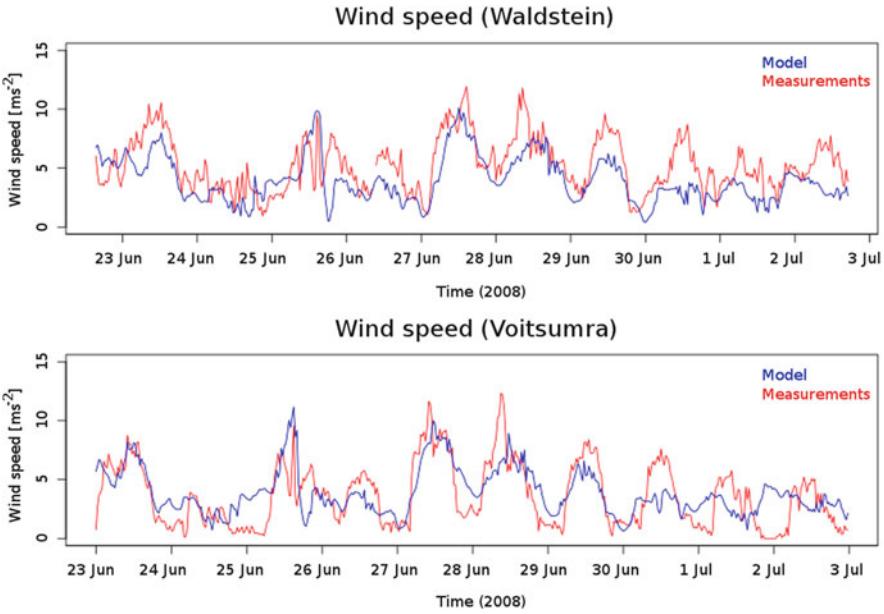

Fig. 18.6 Wind speed at Waldstein (*top frame*) and Voitsumra (*bottom frame*) from 23.06.2008 to 02.07.2008. The measurements were corrected according to the logarithmic wind profile (adequate to height of 10 m)

the valley, especially during night time. This is in accordance with recent findings of Jiménez and Dudhia (2013), who compared wind direction measurements of six mountaintops and 17 valleys. This is seen as a consequence of the decoupling of the valley from the main flow during night time on some days and orographic-induced cold-air drainage. Without finer orographic input, these micrometeorological phenomena in the Eger valley cannot be captured by the model.

18.3.2 Predictive Quality of Turbulent Energy Fluxes

To compare modelled and observed fluxes of sensible (Q_H) and latent heat (Q_E), only eddy covariance measurements from the Waldstein site were used, because flux measurements at the Voitsumra station were not performed. More details about turbulence measurements at the Waldstein site are given in Chap. 4.

The MBE-values for the sensible heat flux decrease with each domain and indicate an underestimation of the measured values in the order of $-32.4\,\mathrm{Wm}^{-2}$ in the domain D3 (Table 18.6). Also, E improves from 0.04 to 0.17, which is a better accuracy than the arithmetic mean of the data. All other error parameters change little. Even though the computational effort for smaller domain increases, IA and E show only small improvement in predictive values (Table 18.6). Figure 18.8 (upper frame) shows no difference between daily values of IA for all domains.

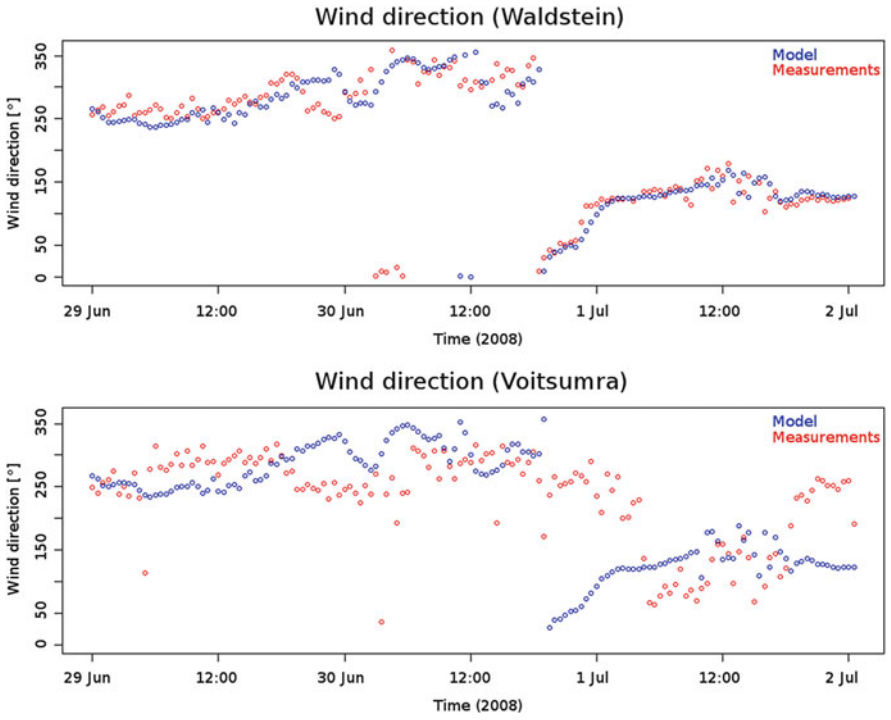

Fig. 18.7 Comparison of modelled (*blue*) and measured (*red*) wind direction at Waldstein (*top frame*) and Voitsumra (*bottom frame*)

Table 18.6 Error indices for sensible and latent heat fluxes at Waldstein site for three domains and over IOP2 period

	Sensible heat flux					Latent heat flux				
	MBE	RMSE	MAE	IA	E	MBE	RMSE	MAE	IA	*E*
	[Wm^{-2}]	[Wm^{-2}]	[Wm^{-2}]			[Wm^{-2}]	[Wm^{-2}]	[Wm^{-2}]		
D1	−47.1	**103.4**	**79.3**	0.63	0.04	108.0	**155.3**	**100.2**	0.46	−9.6
D2	36.9	109.7	82.5	0.64	0.09	108.1	160.6	113.5	0.50	−8.6
D3	**−32.4**	108.6	80.7	**0.65**	**0.17**	**107.9**	156.9	112.3	**0.52**	**−7.5**

The lowest error indices are marked in bold. Only positive fluxes were used for the model evaluation

The accuracy of prediction according to IA and MBE values is relatively good. However, considering just the MBE value can be misleading in this case because the overestimation and underestimation partially cancel each other out. For example, the absolute overestimation of sensible heat flux on 04.06.2008 by the model was more than 200 Wm^{-2}. On the other hand, the absolute underestimation on 01.06.2008

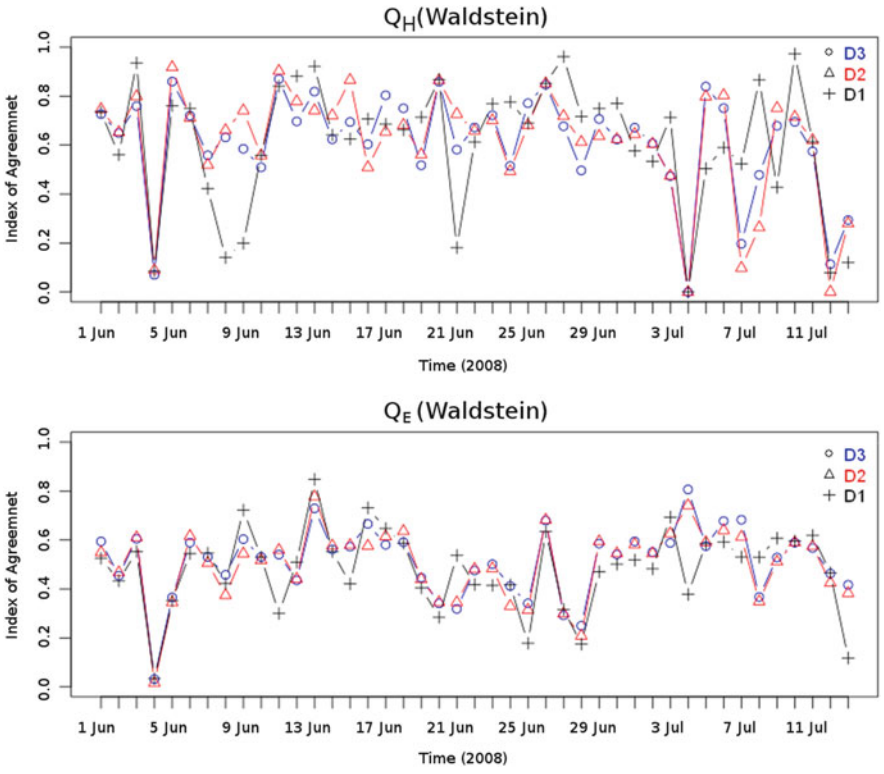

Fig. 18.8 Daily values of IA for sensible (*top frame*) and latent heat (*bottom frame*) fluxes at Waldstein for the IOP2 period (*black*—domain D1, *red*—domain D2, *blue*—domain D3)

by the model was approximately 200 Wm^{-2}. Especially in such cases, the RMSE and MAE are suitable error parameters because they do not count the sign of the deviation.

It is difficult to select the best resolution for the modelling of sensible heat flux, because the differences in error parameters are too small. The least errors are estimated for the domain D3. However, it should be noted that errors for the domains D1 and D2 are slightly worse and the coarse domain D1 has even lower RMSE values.

The fact that measured fluxes are higher than modelled fluxes can be explained by incorrect representation of forest and grassland in land-use input data. It is well known that forest absorbs more radiation than grassland and therefore the sensible heat flux measured over forested area will be higher. As shown by Teuling et al. (2010), forest emits 40 Wm^{-2} more sensible heat than grassland, but only the time period between 9:00 and 13:00 UTC was considered.

The forecast-quality of this study emphasizes the problem of incorrect land-use maps, which have to be fairly accurate for domains with 1km spatial resolution. In work at the "Southern Great Plains" field site in North America, it was shown that

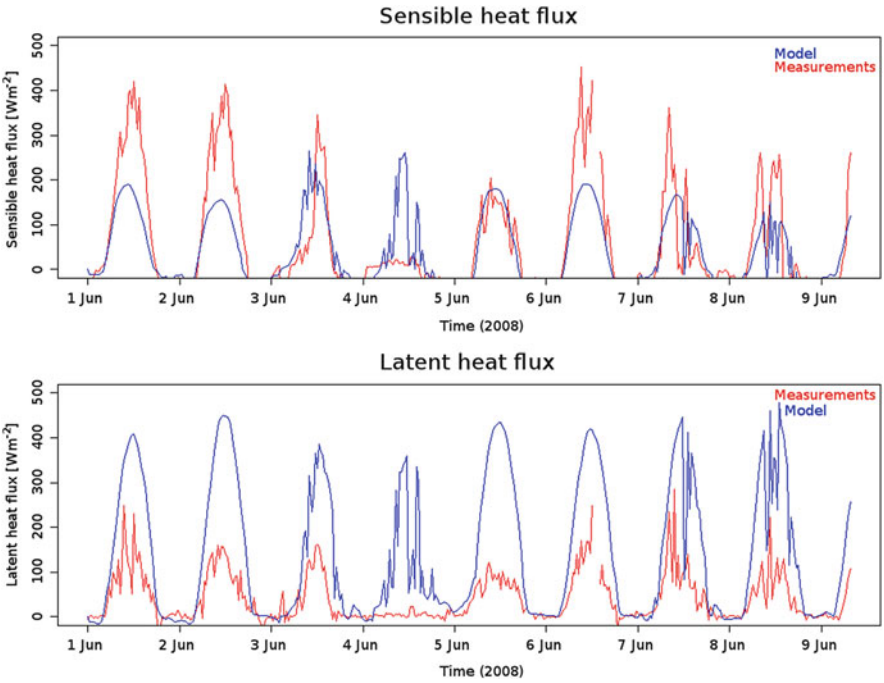

Fig. 18.9 Modelled values (*blue*) of the sensible heat (*top frame*) and the latent heat (*bottom frame*) and measured values (*red*) at Waldstein. There is a significant underestimation of the sensible heat flux and a significant overestimation of the latent heat flux by the WRF model

use of usual terrestrial WRF input parameters leads to RMSE values between 76.4 and 91.1 Wm^{-2} (Hong et al. 2009). The RMSE values of this study are between 79.3 and 83.2 Wm^{-2}.

The coefficient E for latent heat in all three domains is worse than for all other parameters. The model, according to the MBE, overestimated measured flux by about 108 Wm^{-2} in each domain, which is a high overestimation for a measured parameter in the order of 100 Wm^{-2}. Moreover, a yet higher overestimation occurs around noon (Fig. 18.9, bottom frame). The RMSE and MAE indicate deviations from observations in each domain of about 155 Wm^{-2} and 110 Wm^{-2}, respectively. The quality of the latent heat modelling as shown by parameters IA and E is worse than with all other parameters. A slight improvement, with higher spatial resolution, is observed. However, as in the case of sensible heat flux, the variability is small and the latent heat flux is always overestimated by the WRF model.

The overestimation of the latent heat flux by the WRF model is a well-known problem. Due to erroneous land-use classification of forest in the input model data (grassland instead of forest) an additional overestimation of the latent heat flux is assumed. The forecast-quality of our study is slightly higher than the ranges evaluated by Hong et al. (2009) from the study over three different areas in North

America. The values of RMSE in the model runs of Hong et al. (2009) vary strongly over all study areas (RMSE from 47.41 to 151.5 Wm^{-2}), whereas RMSE for the latent heat flux modelling in this study (160 Wm^{-2}) is slightly higher than the highest RMSE value assessed by Hong et al. (2009). The overestimation of latent heat is attributed to an overestimation of the vegetation transpiration by the WRF model and strong dependence of the latent and sensible heat fluxes on the spatial and temporal resolution of the vegetation was also shown by Hong et al. (2009). The WRF model in the study of Hong et al. (2009) and in this study uses the Noah Land Surface Model. In this model, the parameter "green vegetation fraction" plays a significant role in determination of the evapotranspiration. Thus, "green vegetation fraction" is required to be well parameterized with more compatible temporal and spatial resolution for improved model simulations.

From Figs. 18.5 and 18.9 it is apparent that the energy balance of the WRF model is obviously closed—even when the ground heat flux is not shown—but for the experimental data this is not the case, which is in agreement with the present knowledge (Foken 2008a; Kracher et al. 2009) and with the findings for the Waldstein–Weidenbrunnen site (see Chap. 12) of about 20% missing energy. Also typical is that the Bowen ratio of the model is lower than that of the experimental data. This effect will be still more pronounced after the correction of the energy balance closure with the Bowen ratio (Twine et al. 2000) or the buoyancy flux (Charuchittipan et al. 2014). Both methods would increase the sensible heat flux—the latter method much more—while the latent heat flux increases only a little bit. This is in agreement with too-high evaporation or cloudiness and too-low sensible heat fluxes or temperatures of the models (Liu et al. 2013; Wilmot et al. 2014).

18.3.3 Influence of Large-Scale Weather Patterns

Figure 18.10 shows daily values of IA of temperature (black), sensible heat flux (red), global radiation (blue) and large-scale weather patterns (source: German Meteorological Service, DWD). Time series of the forecast-quality reveals large variability during the period of investigation. Figure 18.10 also shows the temporal coincidence of worse prediction for all three physical parameters (o-shaped blue areas) resulting from their dependence on each other. The temperature depends on the sensible heat flux. On the other hand, the sensible heat flux (also the latent heat flux) is dependent on the excess of the net radiation. To check the influence of weather conditions on the quality of modelled parameters, the prevailing large-scale weather patterns during IOP2 are highlighted (see Fig. 18.10). It is expected that during large-scale weather patterns associated with cyclones, meteorological parameters can be predicted to be generally poor.

For example, for the period from 01.06.2008 to 07.06.2008, Germany was under the influence of cyclonic flow. During that time the worst modelling quality according to the IA was found. The value of IA for global radiation on 04.06.2008 dropped to about 0.2. The weather front during these days crossed Germany and

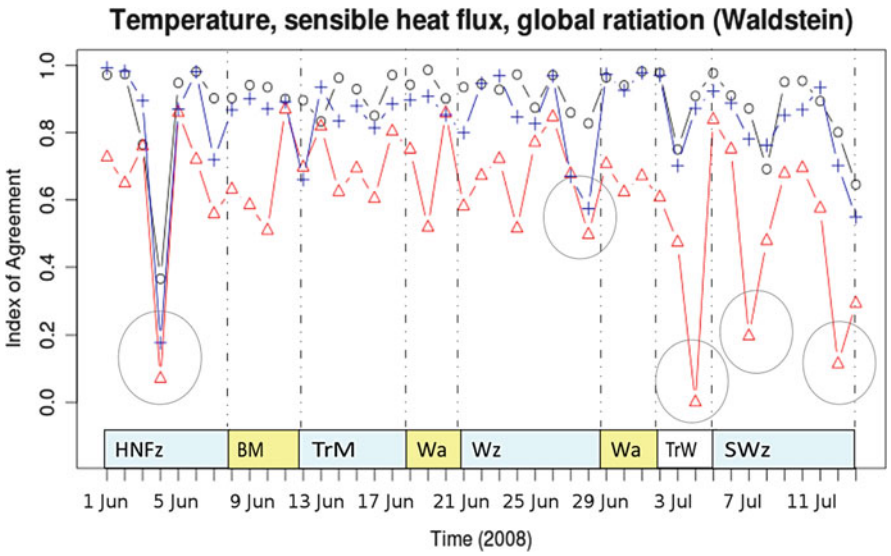

Fig. 18.10 Large-scale weather patterns and daily values of IA of temperature (*black*), sensible heat flux (*red*) and global radiation (*blue*). Large-scale weather patterns are shown at the bottom axis (HNFz—high pressure centre, North Sea and Fennoscandia, cyclonic flow; BM—high-pressure ridge across Central Europe; TrM—surface trough, Central Europe; Wa—westerly flow, anticyclonic; Wz—westerly flow, cyclonic; TrW—surface trough, Western Europe; SwZ—south westerly flow, cyclonic). Large-scale weather patterns associated with cyclones are highlighted in *cyan* and with anticyclones in *yellow*

dry air flowed from the north-east. In other parts of Germany, moist air in an unstable stratification prevailed. In the period from 01.06.2008 to 04.06.2008, this front moved from south-west through the Mittelgebirge to eastern Germany. However, no clouds and thunderstorms were observed in Franconia on 01.06.2008 and 02.06.2008. The model was able to simulate these days quite well (Fig. 18.10). However, on 03.06.2008 and 04.06.2008 the global radiation, sensible heat flux and temperature were overestimated by the model. The dense cloud cover could not be adequately reproduced by the model. This effect was observed through the whole period of IOP2: dense cloud cover and the resulting low global radiation were never simulated with good quality during IOP2, and very low values of global radiation were always overestimated. In contrast, all three parameters were predicted well during the large-scale weather patterns associated with anticyclones.

18.4 Conclusions

Turbulent surface fluxes are the most important interactions between land surface and atmosphere. Modelling of these fluxes is widely used to extend our understanding of turbulent flux observations. The prediction-accuracy of fluxes and different

meteorological parameters simulated by the WRF model over forest and grass-dominated ecosystems was examined in this study through use of three nested domains zooming in to the area of interest.

Within a domain comparison, temperature, wind speed, wind direction, sensible and latent heat fluxes performed best, having the finest resolution out of three model resolutions at both locations. Global radiation was the same in all three domains. Based on statistical analyses, predictions of temperature, global radiation, wind speed and wind direction can be considered as reasonable. A tendency for better temperature and radiation predictions was observed in Voitsumra because of a better representation of this site in the geographical input data. On the other hand, wind speed and wind direction were better at the Waldstein site because of a stronger coupling to the main flow of the mountain site. The accuracy of the modelled latent and sensible heat fluxes was worse. One possible reason is the influence of too-low-resolution land-use data in the model input data.

Presented results show the ability of the meso-scale WRF model to simulate meteorological parameters as boundary conditions for the hydrological and groundwater models (see Chap. 15), soil-vegetation-atmosphere transfer models (see Chap. 16) and large-eddy simulation (LES)-based turbulence models (see Chap. 17). However, the accuracy of the modelled fluxes has to be improved.

The study also shows that the prediction quality depends on different scale processes from the micro- to the macro-scale. For an accurate forecast, all relevant processes have to be described adequately in the model. An observation with regard to large-scale weather patterns showed that the worst predictions always occur during cyclonal weather patterns. Also caution must be taken when selecting the points for comparison. The weighted interpolation of surrounding grid points can lead to a higher accuracy if the nearest grid point is not representative of the point of observation.

For future simulation improvements, the orographic resolution of the model has to be enhanced in order to capture processes on the micrometeorological scale, as terrain-induced processes can only be modelled with an adequate representation of the topography in the model input. This is especially true for temperature, pressure, wind speed and wind direction. Observations from mountain sites have rarely been compared with model data. The data should be analyzed during other seasons and over other areas to confirm the findings of this study. The micro-scale models described in this book can be used to increase the knowledge about the effects produced by the unresolved topography over the resolved flow.

To improve the shifted Bowen ratio and thus the flux prediction, the spatial and temporal resolution of the land use has to be improved. Vegetation is a key parameter in modelling surface energy fluxes. With a changed vegetation, much better simulations of latent and sensible heat fluxes can be expected.

References

Beljaars ACM (1994) The parameterization of surface fluxes in large-scale models under free convection. Q J R Meteorol Soc 121:255–270

Charuchittipan D, Babel W, Mauder M, Leps JP, Foken T (2014) Extension of the averaging time of the eddy-covariance measurement and its effect on the energy balance closure. Boundary-Layer Meteorol 152:303–327

Chou MD, Suarez MJ (1994) An efficient thermal infrared radiation parameterization for use in general circulation models. NASA Tech Memo 104606 3:85

Cressman GP (1959) An operational objective analysis system. Mon Weather Rev 87:367–374

Dyer AJ, Hicks BB (1970) Fluxgradient relationships in the constant flux layer. Q J R Meteorol Soc 96:715–721

Foken T (2003) Lufthygienisch-bioklimatische Kennzeichnung des oberen Egertales (Fichtelgebirge bis Karlovy Vary). Bayreuther Forum Ökologie, 100. ISSN:0944-4122

Foken T (2008a) The energy balance closure problem - an overview. Ecolog Appl 18:1351–1367

Foken T (2008b) Micrometeorology. Springer, Berlin, Heidelberg

Foken T, Meixner F, Falge E, Zetzsch C, Serafimovich A, Bargsten A, Behrendt T, Biermann T, Breuninger C, Dix S, Gerken T, Hunner M, Lehmann-Pape L, Hens K, Jocher G, Kesselmeier J, Lüers J, Mayer JC, Moravek A, Plake D, Riederer M, Rütz F, Scheibe M, Siebicke L, Sörgel M, Staudt K, Trebs I, Tsokankunku A, Welling M, Wolff V, Zhu Z (2012) Coupling processes and exchange of energy and reactive and non-reactive trace gases at a forest site – results of the EGER experiment. Atmos Chem Phys 12:1923–1950. doi:10.5194/acp-12-1923-2012

Gerstberger P, Foken T, Kalbitz K (2004) The Lehstenbach and Steinkreuz chatchments in NE Bavaria, Germany. In: Matzner E (ed) Biogeochemistry of forested catchments in a changing environment: ecological studies, vol 172. Springer, Heidelberg, pp 15–41

Hong SY, Noh Y, Dudhia J (2006) A new vertical diffusion package with an explicit treatment of entrainment processes. Mon Weather Rev 134:2318–2341

Hong S, Lakshmi V, Small EE, Chen F, Tewari M, Manning KW (2009) Effects of vegetation and soil moisture on the simulated land surface processes from the coupled WRF/Noah model. J Geophys Res 114:D18118. doi:10.1029/2008JD011249

Jiménez PA, Dudhia J (2013) On the ability of the WRF model to reproduce the surface wind direction over complex terrain. J Appl Meteor Climatol 52:1610–1617

Jiménez PA, González-Rouco JF, García-Bustamante E, Navarro J, Montávez JP, de Arellano JVG, Dudhia J, Muñoz-Roldan A (2010) Surface wind regionalization over complex terrain: evaluation and analysis of a high-resolution WRF simulation. J Appl Meteor Climatol 49:268–287

Jorba O, Loridan T, Jiménez-Guerrero P, Baldasano JM (2008) Annual evaluation of WRF-ARW and WRF-NMM meteorological simulations over Europe. In: 9th annual WRF users workshop, 23–27 June 2008, Boulder, CO

Kain JS (2004) The KainFritsch convective parameterization: an update. J Appl Meteorol 43:170–181

Kracher D, Mengelkamp HT, Foken T (2009) The residual of the energy balance closure and its influence on the results of three SVAT models. Meteorol Z 18:647–661

LeMone MA, Chen F, Tewari M, Dudhia J, Geerts B, Miao Q, Coulter RL, Grossman RL (2010) Simulating the IHOP 2002 fair-weather CBL with the WRF-ARW-Noah modeling system. part II: structures from a few kilometers to 100 km across. Mon Weather Rev 138:745–764

Lin Y-L, Farley RD Orville HD (1983) Bulk parameterization of the snow field in a cloud model. J Appl Meteorol Climatol 86:9707–9714

Lindzen RS (1981) Turbulence and stress owing to gravity wave and tidal breakdown. J Geophys Res 22:1065–1092

Liu G, Liu Y, Endo S (2013) Evaluation of surface flux parameterizations with long-term ARM observations. Mon Weather Rev 141:773–797. doi:10.1175/MWR-D-12-00095.1

Loridan T, Grimmond CSB, Grossman-Clarke S, Chen F, Tewari M, Manning K, Martilli A, Kusaka H, Best M (2010) Trade-offs and responsiveness of the single-layer urban canopy parametrization in WRF: an offline evaluation using the MOSCEM optimization algorithm and field observations. Q J R Meteorol Soc 136:997–1019

Mertens M (2001) Die Anwendung der Fuzzy-Set-Theorie auf die Modellierung von Stickstoffbilanzen im Weißenstädter Becken. Bayreuther Forum Ökologie 85:215

Mlawer EJ, Taubman SJ, Brown PD, Iacono MJ, Clough SA (1997) Radiative transfer for inhomogeneous atmosphere: RRTM, a validated correlated-k model for the longwave. J Geophys Res 102 (D14):16663–16682

Mölders N (2008) Suitability of the weather research and forecasting (WRF) model to predict the June 2005 fire weather for interior Alaska. Wea Forecasting 23:953–973

Paulson CA (1970) The mathematical representation of wind speed and temperature profiles in the unstable atmospheric surface layer. J Appl Meteorol 9:857–861

Skamarock WC, Klemp JB, Dudhia J, Gill DO, Barker DM, Huang XY, Wang W, Powers JG (2008) A description of the advanced research WRF version 3. NCAR Technical Note NCAR/TN475 + STR, p 113

Stull RB (1988) An introduction to boundary layer meteorology. Kluwer Acad. Publ., Dordrecht, Boston, London

Teuling AJ, Seneviratne SI, Stöckli R, Reichstein M, Moors E, Ciais P, Luyssaert S, Hurk B van den, Ammann C, Bernhofer C, Dellwik E, Gianelle D, Gielen B, Grünwald T, Klumpp K, Montagnani L, Moureaux C, Sottocornola M, Wohlfahrt G (2010) Contrasting response of European forest and grassland energy exchange to heatwaves. Nature Geosci 3:722–727

Tewari M, Chen F, Wang W, Dudhia J, LeMone MA, Mitchell K, Ek M, Gayno G, Wegiel J, Cuenca RH (2004) Implementation and verification of the unified NOAH land surface model in the WRF model. In: 20th conference on weather analysis and forecasting/16th conference on numerical weather prediction, pp 11–15

Twine TE, Kustas WP, Norman JM, Cook DR, Houser PR, Meyers TP, Prueger JH, Starks PJ, Wesely ML (2000) Correcting eddy-covariance flux underestimates over a grassland. Agric For Meteorol 103:279–300

Valkonen T, Vihma T, Kirkwood S, Johansson M (2010) Fine-scale model simulation of gravity waves generated by Basen nunatak in antarctica. Tellus 62:319–332

Webb EK (1970) Profile relationships: the log-linear range, and extension to strong stability. Q J R Meteorol Soc 96:67–90

Willmott CJ (1982) Some comments on the evaluation of model performance. Bull Am Meteorol Soc 63:1309–1313

Willmott CJ, Robeson SM, Matsuura K (2012) A refined index of model performance. Int J Climatol 32:2088–2094

Wilmot CSM, Rappenglück B, Li X, Cuchiara G (2014) MM5 v3.6.1 and WRF v3.5.1 model comparison of standard and surface energy variables in the development of the planetary boundary layer. Geosci Model Dev 7:2693–2707

Part V
Conclusions

Chapter 19
What Can We Learn for a Better Understanding of the Turbulent Exchange Processes Occurring at FLUXNET Sites?

Thomas Foken

19.1 Introduction

The present book is not the first about the Waldstein measuring sites. A monograph (Matzner 2004) covering the funding period of the Bayreuth Institute of Terrestrial Ecosystem Research (BITÖK, see Chap. 1) up to 2004 has already been written, and large parts of other books from the EUROFLUX period are about this site (Schulze et al. 1989; Tenhunen et al. 2001; Valentini 2003). As shown in Chap. 1, the funding of the research was not continuous, and also a clear shift from complex ecological research to soil science and micrometeorology can be seen. Nevertheless, a certain continuity is apparent, due mainly to the long time series of air pollution, meteorological, and flux measurements. The theme of this book is therefore much more closely related to the atmosphere and its interaction with the ecosystem, and the main topic is energy and matter fluxes and the process studies related to these fluxes. But funding and administrative issues can still be considered "metadata" of a site and are reflected, for example, in the availability of high-quality data (see Chap. 4) and the point of time of the application of technical progress.

Since long-term data sets of FLUXNET sites are available, principally the LaThuile data set, many papers have been published which analyze and compare these data and link them to ecosystems, regions, and climate (Baldocchi 2008; Williams et al. 2012; Keenan et al. 2013; Kutsch and Kolari 2015). From the

T. Foken (✉)
Am Herrgottsbaum 28, 96120 Bischberg, Germany

Bayreuth Center of Ecology and Environmental Research, University of Bayreuth, Bayreuth, Germany
e-mail: foken@micrometeorology.de

Affiliation during the work at the Waldstein sites – University of Bayreuth, Department of Micrometeorology, Bayreuth, Germany

T. Foken (ed.), *Energy and Matter Fluxes of a Spruce Forest Ecosystem*,
Ecological Studies 229, DOI 10.1007/978-3-319-49389-3_19

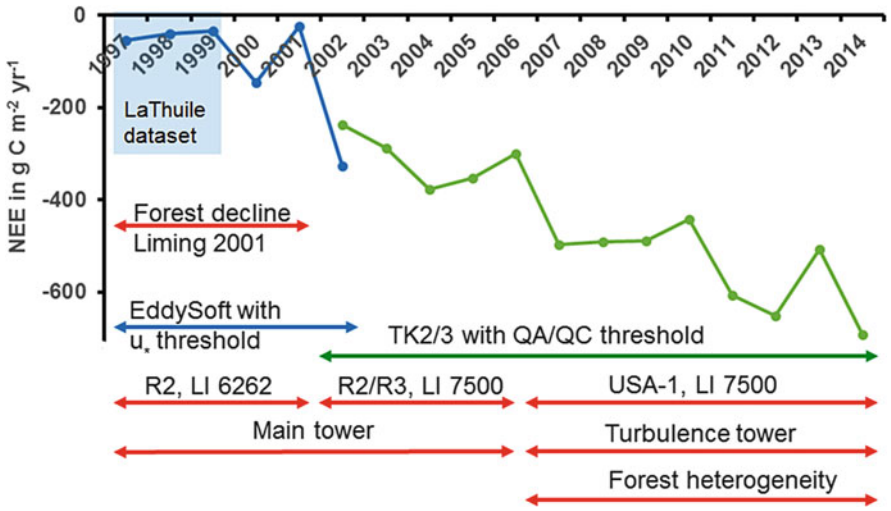

Fig. 19.1 Net ecosystem exchange at the Waldstein-Weidenbrunnen site from 1997 to 2014 (see Chap. 4), with periods of influence by forest decline and a significant heterogeneity and different sensor applications and data handling (Adapted from Foken and Babel 2016, with kind permission of © Authors, All rights reserved)

Waldstein site, only the years 1997–1999 are included in this data set. The lack of funding for the data analysis and also the visible gaps and jumps in the time series were the reasons that only these few years, or some selected data thereof, were published in overview papers (Appendix C). But this book should make the data set more public. The intensified work with the data and many methodical studies have shown that the Waldstein data set is influenced by so many factors that a simple presentation of sums and trends would not be possible. Furthermore, the analysis has shown that there are so many factors affecting the ecosystem fluxes that the many simple conclusions drawn in overview papers probably need some revision.

In Chap. 4, it was shown that there is a strong increase of net ecosystem exchange (NEE) over the nearly 20-year time series, which is in agreement with findings at other sites (Keenan et al. 2013). But it is still an open question as to whether this is linked to climate change or if there are also other relevant factors that generate a similar trend. This increase is introduced into this chapter through Fig. 19.1, which shows the time series of NEE together with typical changes in the instrumentation and the structure and properties of the site. The effect of forest decline up to the end of the 1990s is not a specific Waldstein problem, because all sites in Central, Northern, and Eastern Europe are affected in a similar way. Also, the progress in instrumentation and data calculation (most of the data were recalculated in the same manner as the Waldstein-Weidenbrunnen data) is similar for most of the FLUXNET sites. And it is likely that the change from a homogeneous forest at the time of the installation of the site to a more heterogeneous forest, which is due to several reasons, is not site specific; only the significant change in 2007 may be unique. Therefore, in the first part of this chapter, these possible effects are addressed in the

light of the results presented in this book. For uncertainties of the eddy covariance method, see Chap. 4 and the relevant references (Hollinger and Richardson 2005; Mauder et al. 2006; Foken et al. 2012a; Richardson et al. 2012; Mauder et al. 2013).

In contrast to the structure of the other book chapters, the results of the book are discussed, and conclusions are drawn here in terms of four aspects related to spruce forest – or at least to tall vegetation – and on a time scale from a tenth of a second up to hours and monthly and annual sums:

- Flux measurements in a changing environment
- The linking of atmospheric turbulence and air chemistry
- Progress toward an optimal data quality protocol
- Recommendations for the future of FLUXNET sites

The aim of these focuses is to make the specific results of the Waldstein sites available for a general discussion and to give researchers hints for their own measuring sites. Therefore, this chapter links and condenses the results and conclusions of all other chapters and of available publications and has the character of a final conclusion.

19.2 Flux Measurements in a Changing Environment

19.2.1 Climate Change

The availability of long-term carbon and moisture flux measurements, along with the visible climate change or change of the carbon dioxide concentration, provides the possibility of linking climate and flux changes (Keenan et al. 2013). Indeed, climate has changed at the Waldstein site (see Chap. 3) as is apparent not only in the 40 ppm increase of the carbon dioxide concentration in the last 15–20 years but also in the significant temperature increase of 0.4 K per decade and even, for April, of 0.8 K per decade. While annual precipitation sum shows no trend, April shows a trend of −4 mm per decade and September of +8 mm per decade. Drought periods occur more often and last longer. And recent years – in particular 2014 and 2015 – were the warmest in the region in more than 150 years. Heat waves like the summer of 2003 have also shown effects on the ecosystem (Ciais et al. 2005), however, not during the period of high deviation from the climatological normal value in June but rather during the extreme high temperatures in August. This was the hottest August for the region, with a decrease of the carbon uptake and probably also an influence on the functioning of the ecosystem as could be seen from the modeling results (see Chap. 16). Furthermore, the dimming and brightening effect on carbon uptake are discussed (Wild et al. 2012; Cescatti 2009, personal communication), with an increase of the uptake related to an increase of the diffuse radiation. More direct radiation may be possible in spring and more diffuse in summer, but possible effects on carbon exchange are too small to allow separation of these from other

influences. Climate change has some more indirect effects: the warm and dry spring provides a good environment for the development of the bark beetle population. Some trees in and around the Waldstein-Weidenbrunnen site have had to be felled in the last years. Other trees had to be felled because the crown snapped off after wet and heavy snowfall. Such trees would have been vulnerable to beetle infestation. The most significant influence was had by strong storm events, which affected the structure of the whole forested area in the Fichtelgebirge mountains (see Chap. 2).

Even though the sulfur dioxide concentration has dramatically decreased since the beginning of the 1990s, and acid rain is no longer relevant (see Chap. 3), an increase of the ozone concentrations must be considered, as well as generally high NO_x concentrations. Both may have an influence on the health of the forest. Although the sulfur concentration in the soil has decreased slowly and was, at the end of the 1990s, already significantly lower in the upper soil layers (Matzner et al. 2004), the sulfur discharge in the Lehestenbach catchment, although also reduced, remains high (LfU 2015).

The possible effect of climate change cannot be downplayed, but it is probably not the direct effects (temperature, precipitation, etc.) that have the strongest influence on the increase of carbon uptake and evapotranspiration (see Chap. 4) but indirect factors like the change of the forest structure or even the effects of changing instrumentation. It must also be remembered that the liming in 2001 of a heavily declined Waldstein-Weidenbrunnen site had an extremely strong effect on the fluxes. Under these circumstances, the consideration of climate influence on the increase of the carbon uptake (Keenan et al. 2013) must be seen under a different light. All sites were selected in the 1990s as homogeneous and healthy forests. In the last 20 years, most of the sites have been affected by pests, windthrow, thinning, etc., all of which may have had an influence on fluxes. These changes must be taken into account to isolate the real climate effect. The main problem is that the necessary information is often missing in the databases.

Concluding Remarks Climate and even air pollution measurements are essential for characterization of a measuring site – not only according to trends but also single special or extreme events.

19.2.2 Instrumental Problems

The instrumentation of not only the Waldstein-Weidenbrunnen site but all FLUXNET sites has changed dramatically, mainly at the beginning of the 2000s (see Fig. 19.1). At this time, the first commercial open-path instruments for carbon dioxide (and water vapor) measurements became available. Before 2000 only closed-path instruments were used. These had only a 12-bit signal resolution, while later on all devices had 16-bit or more. This possible problem of the effect of amplitude resolution on small fluxes had already been addressed by Vickers and Mahrt (1997). The problem is more significant for carbon dioxide than for

water vapor because the carbon dioxide fluctuations are much smaller in relation to the mean concentration than are those of water vapor. This effect is visible in the Waldstein-Weidenbrunnen data: the closed-path LiCor 6262 instrument was replaced in early 2002 by the open-path LiCor 7500 gas analyzer. The observed increase of the fluxes may have been caused by the liming in 2001, but the increase is much higher for carbon dioxide than for water vapor. Therefore, the amplitude resolution must be taken into account as one possible reason for this increase. Of course, the effect should be relevant only for low fluxes, but may also have an influence on the gap filling of the respiration and on cumulative fluxes.

Up to spring 2003, the sonic anemometer Solent R2 was used, followed by the sonic anemometer R3 up to summer 2007. After this, the METEK USA1 was utilized (Appendix A). The normalized standard deviation of the vertical wind velocity was shown in Chap. 4 to have decreased in 2007. This may result from the stronger heterogeneity of the forest (see Sect. 19.2.3) but may also be an effect of the change of the sonic anemometer. The R2/R3 sonic anemometers had, up to 2003, digitalization problems (Foken et al. 2004) in such a way that R2 did not measure vertical wind velocities of $w = -0.01$ ms^{-1}, but added these values to the digitalization step 0.00 ms^{-1}. For R3 there was a similar effect every 0.07 ms^{-1} for negative values and every 0.14 ms^{-1} for positive values. If the flux is large enough, the problem is not relevant, but for low turbulent conditions together with the amplitude resolution problem of the gas analyzer, this effect may be relevant. The number of comparison experiments with the Solent R2 is limited compared to other instruments. Available reports are very limited: Wieser et al. (2001) concluded "because the simple correction procedure increases the variance and covariance of the wind components disproportionally it is advisable to use the sensor in uncalibrated mode" and Högström and Smedman (2004) found a very large scatter in the data. Such a large scatter can be seen where the data were corrected with a mean calibration function in the firmware. Foken et al. (1997) found an underestimation of the friction velocity by the Solent instrument. Similar results were also shown by Christen et al. (2000), with a large scatter of different anemometers of this type. All these results would support the findings in Chap. 4.

The change from the closed-path system to the open-path system should not have a significant influence (Ocheltree and Loescher 2007; Haslwanter et al. 2009; Järvi et al. 2009), if all corrections were done appropriately. Both used software packages that were well compared with other commonly used packages (Mauder et al. 2008).

Concluding Remarks Unfortunately, no systematic investigations of these sensor effects are available. Therefore, investigations of older data sets (>10–15 years) should be undertaken with care. Because of the high relevance of long time series for carbon fluxes, systematic investigations of possible errors in older data are urgently recommended.

19.2.3 Influence of the Heterogeneity

The influence of the heterogeneity was, in the past, only discussed in relation to the footprint of the measurements in a patchy area (Göckede et al. 2008). The specific application of the footprint investigations was made for the carbon fluxes in 1997–1999 (Rebmann 2003). The idea behind this was to always measure above the same area. Because the footprint under stable stratification is much larger than under neutral and unstable stratifications, measurements at 22 m (canopy height 18–19 m) were used for stable stratification and those at 32 m height for all other situations. Using this combination, the respiration was higher than given in Chap. 4 and Appendix B, and therefore the cumulative NEE is significantly higher, with 116.4 g C m^{-2} (1997), 111.1 g C m^{-2} (1998), and 138.0 g C m^{-2} (1999). The reasons were not investigated, and further investigations of this method were not undertaken because the method found no application in the FLUXNET community. For the FLUXNET database, only the data set from 32 m was reported.

The footprint findings in this book have shown that an inner heterogeneity of the forest has been significantly changed, while the footprint is nearly identical (see Chap. 2). This means that the area, with the exception of the clearing, is still classified as spruce forest and yields nearly the same footprint; however, the inner structure of the forest has changed. Typical changes are the large clearing "Köhlerloh" south of the site and the thinning in the area between Pflanzgarten and Weidenbrunnen (west of the site, see Chap. 7, Fig. 7.1) due to the storm "Kyrill" on Jan. 18, 2007, as well as a thinning due to bark beetle infestation and windthrow in the whole area located mainly northeast of the main tower. In this area, we observed a growth of the understory (see Chap. 2, Figs. 2.4 and 2.5).

The investigations of the coherent structure (see Chap. 6) around the Weidenbrunnen site and at the edge to the Köhlerloh clearing (see Chap. 13) have shown that the strongest coherent structures were observed at the interface between the closed forest and a clearing or gap in the canopy. This may generate higher fluxes and – as the sum of many heterogeneities – a larger NEE for the whole site. This is in agreement with the larger fluxes of carbon dioxide and water vapor and a larger carbon use efficiency after 2007 (Fig. 19.1) found in Chap. 4.

In large eddy simulation studies at a forest edge, it was found that a maximum flux occurs at a distance from the edge of about ten times the canopy height (Dupont and Brunet 2009; Finnigan et al. 2009; Kanani-Sühring and Raasch 2015). This was also found for a model study for the Waldstein-Weidenbrunnen site (see Chap. 17, Fig. 17.7). But such studies show an inflow from the clearing into the trunk space (Fig. 17.8). This disagrees with the low coupling between the clearing and the trunk space that is probably due to a denser understory in this area (Serafimovich et al. 2011; Eder et al. 2013). Therefore the relationship between canopy height and the distance for the flux maximum may be different in a heterogeneous forest (Schlegel et al. 2015). For the Waldstein-Weidenbrunnen site, due to the dominating westerly winds, the edge between the Waldstein-Pflanzgarten site and the Weidenbrunnen site may be important. Directly at the edge, the density of the trees was significantly

reduced in 2007 (see above), and furthermore, the distance from this edge to the main tower (the FLUXNET station up to 2007) and the turbulence tower (the FLUXNET station since 2007) changed from 200 to 240 m. This means that the tower position is now closer to a possible maximum of the fluxes. Therefore, the change of the tower and of the sonic anemometer (see above) could also have had an influence on the fluxes. Note that the data quality for turbulence measurements at both towers for the USA1 sonic anemometer is identical.

Because the energy balance closure was nearly unchanged, being 80 % over the whole period of investigation covering the end of the 1990s (Aubinet et al. 2000), 2007/2008 (Foken et al. 2012b), and longer periods (Chaps. 4 and 12), heterogeneities with a size of <200–500 m, as discussed above, cannot be a reason for this phenomenon. As heterogeneities were identified as a reason for energy balance closure (Foken 2008), these should be characterized by the distribution of forest and agricultural land in the area, which did not change over the time period.

The heterogeneity of the measuring site also had an influence on the local climate. It was shown in Chap. 14 that the general behavior of meteorological elements in the forest is in agreement with the textbook knowledge. However, significant modification could be found due to the heterogeneity, especially near the forest edge, and due to the different coupling stages.

Concluding Remarks Several factors of the surface heterogeneity may explain increasing fluxes. It is absolutely impossible to separate the influence of different effects or to separate these effects from the climatological effects discussed above. But it should be assumed that similar changes of the site conditions might be possible at other FLUXNET sites as well.

19.2.4 Influences of the Atmospheric Boundary Layer

As reported in the literature (Karipot et al. 2006), gravity waves and low-level jets (LLJ) have a significant influence on nighttime fluxes, which are increased for short periods. First results were already published by Foken et al. (2012b). These phenomena are related to a local wind system with easterly wind through the Lehestenbach valley at night. When the wind changes from westerly to easterly, for a short time, a northerly wind that passes the small mountain "Bergkopf" is observed (see Chap. 2). At the Waldstein-Weidenbrunnen site, this flow generates breaking gravity waves. In the period of easterly winds at night, LLJ were always observed. Both phenomena were investigated in greater depth in Chap. 11. Because during summer time these situations occur on about one third of all nights, it may have an influence on the determination of the respiration fluxes and some fluxes of chemical species. Because these events occur mainly during the night with low

wind velocities near the ground, in the widely used gap-filling procedure using an u_*-criterion, these events are deleted.

Concluding Remarks High fluxes for a short time due to low-level jets or breaking gravity waves should not be gap filled. A permanent investigation of the boundary layer structure would be desirable.

19.3 Linking Atmospheric Turbulence and Air Chemistry

Because the Waldstein-Weidenbrunnen site is well equipped and, at the Pflanzgarten site, the concentrations of relevant trace gases are measured, several research groups have tested their instruments and methods in the last 20 years at both sites, and they have also provided the basis for larger experiments (see Chap. 1). During the BITÖK period, two large chemical experiments, BEWA 2001 and 2002, were realized (Steinbrecher et al. 2004; Klemm et al. 2006) and again during the EGER project, with two measuring campaigns in 2007 and 2008 (Foken et al. 2012b). The EGER projects had a stronger link between turbulence and atmospheric chemistry, with a focus on coupling effects and a changing Damköhler number. All results are summarized in Chaps. 8 and 9.

Besides basic studies of aerosol flux (Held et al. 2003) and reactive trace gas flux measurements, mainly ozone (Klemm et al. 2004; Zhu et al. 2009) and nitrogen oxides NO–NO_2 (Tsokankunku 2014), remarkable progress was achieved by combining the canopy–atmosphere coupling schema by Thomas and Foken (2007) with trace gas concentrations and fluxes (Sörgel et al. 2011; Foken et al. 2012b). It was possible to explain the concentration changes of reactive trace gases by a dependence on the length of stay in a certain layer due to decoupling or strong turbulent mixing. Besides this coupling between trunk space, crown, and atmosphere, a second coupling process was detected near the forest floor in the lowest meter (see Chap. 8). Therefore, profile measurements having high resolution in height were carried out. Important was the combination of the profile of the noble gas radon, which is not affected by biological processes, and a hydrodynamic model (Foken 1979; Foken 1984), which was able to calculate from given fluxes the properties at the surface. If these modeled properties are equal to the measured surface concentrations, the forest floor was coupled with the trunk space. Periods could be identified with and without coupling. The periods are identical for radon, carbon dioxide, and water vapor; however, the concentrations of carbon dioxide and water are slightly biased due to the biological activities.

Concluding Remarks With the investigation of coupling processes, significant progress was made in better understanding the chemical processes in the turbulent atmosphere, especially in tall vegetation.

19.4 Further Remarkable Results

Even though not all models were applied and compared using the same data set, the number of models used at the Waldstein sites is remarkable, and the results and the comparison with experimental data are surprisingly good, even under the circumstances of a very complex site (see Chap. 16). Therefore, it is possible to conclude that a family of models is available for application at this site and probably also for many other sites. The application of models in all measuring periods was helpful in showing that the data were – at least at daytime – in agreement with the meteorological and plant physiological drivers. But it was also shown that a mesoscale modeling with the WRF model often gives unrealistic flux data, because the generally available land use map which was applied is not in agreement with the hilly terrain and local meteorological effects cannot be isolated (see Chap. 18). However, hydrological modeling was also realized (see Chaps. 7 and 15).

Not only did the models constitute a tool for the independent verification of the flux measurements, but the sap flow measurements (see Chap. 5) also had this function. These witnessed solely an increase of the evapotranspiration between the beginning of the measurements and recent years. They also served as an additional parameter of the water fluxes within the canopy. A similar function – but on a much larger scale – was provided by the investigation of the catchment runoff dependent on precipitation and evapotranspiration (see Chap. 15). Besides some deficiencies, like the correction of the precipitation measurements or the measurement of the evapotranspiration at only one point – and probably the point with the highest evapotranspiration – the result is quite interesting. It could be shown that in dry years, the water storage in the ground is reduced, while in wet years, a regeneration of the groundwater was indicated. This study and the study of water fluxes in the soil on a small scale (see Chap. 7) were the first hydrological studies in the Lehestenbach catchment that were linked to atmospheric flux measurements.

At the end of the 1990s, we had the great hope of using ^{13}C-isotope fluxes for a better understanding of plant physiological functions and turbulent transport. Two measuring systems were developed, and a few measurements were realized at the Waldstein-Weidenbrunnen site in 2000 and 2003; however, the measurements were too personnel-intensive and complicated, and the turbulence structure did not allow the drawing of simple conclusions. Therefore, these measurements cannot be classified as successful (see Chap. 10). But the related investigations, such as a scale analysis for tall vegetation (Ruppert et al. 2006), were helpful for further investigations. And finally, the method was successfully applied over meadows for flux partitioning (Riederer et al. 2014).

19.5 Relevant Results for the FLUXNET Network

19.5.1 Optimal Data Quality Control

In Chap. 12 of this volume, it was shown that the Waldstein-Weidenbrunnen site was used to develop data quality tools which are now standard for many national and international networks. Main components are the tests according to Foken and Wichura (1996), the application of footprint models (Göckede et al. 2008; Leclerc and Foken 2014), and the data flagging according to quality (Foken et al. 2004). These tools are now in most of the available software packages (Mauder et al. 2008; Foken et al. 2012a).

The results of this book have shown that at least two aspects of the data quality control should be included in the data quality network:

1. The investigations have shown that the internal heterogeneity of the forest and the forest edge has a significant influence on fluxes (Chaps. 4, 6, and 13). This problem cannot be solved with the present footprint technique. But it is possible to indicate whether a forest edge is in the footprint. The heterogeneity of a forest should be mainly detected using the number and position of significant jumps in the plant area index, which are one cause of the generation of significant coherent structures. This could be the number of jumps or edges weighted with the footprint function for all wind directions. This parameter could be listed for different stability classes in a lookup table similar to the footprint analyses (Göckede et al. 2004). But the generation of such a parameter, the application of the parameter at different sites, and the interpretation of the parameter together with the measured fluxes are still an ongoing process.
2. In Chap. 6 of this volume, the importance of the coupling between the atmosphere and the tall vegetation was documented. The requirement for such an investigation is, of course, at least the installation of a second sonic anemometer measuring complex in the trunk space. A tool for the calculation of the degree of the coupling could easily be applied. The number of coupling classes could also be reduced to coupled, partly coupled (upper canopy), and not coupled, as demonstrated by Foken et al. (2012b). The detection of coupling does not require mandatory flux measurements at three levels (Thomas and Foken 2007); two levels already supply (Thomas et al. 2013; Jocher et al. 2017) significant information. Such a characterization is not only relevant for chemical measurements in and above the forest (Chaps. 8 and 9) but could also help to develop better parameterizations for the respiration as dependent on the coupling and investigate the influence of the subcanopy. Such a coupling indicator could be added to lookup tables (Papale 2012) for gap filling and flux partitioning.

The available data set of the Waldstein-Weidenbrunnen site and the experiences of the authors of the relevant chapters could support investigations into both of these aspects. An application of a better characterization of heterogeneities was already carried out achieved in the paper of Stoy et al. (2012).

Chapter 17 has demonstrated that large eddy simulations are a helpful tool for studying the heterogeneity of a site. However, the model needs to be qualified in several points: the horizontal interaction at the forest edge, the effect of coupling and coherent structures, and the realistic fields of scalars dependent on the stratification in and above the canopy. Such a more realistic model could help to optimize tower positions and interpret the data sets. But there is still a long way to go to achieve this aim.

19.5.2 Recommendations for FLUXNET Data Analysis

The findings of this book may be relevant for FLUXNET and other national and international programs like NEON and ICOS. Two points may have high relevance:

1. The data sets of FLUXNET sites are highly complex regarding specific information in the data and influences on the data. It is not possible to easily make simple correlations to the increase of the carbon dioxide concentration or to global warming. It must be seen that many environmental parameters are correlated and are not statistically independent. Such investigations are highly important and must be taken into account.
2. It must be seen that each measuring site has a history. They were first installed in nearly homogeneous ecosystems. In each ecosystem the heterogeneity has increased through time, with the possible effect of an increasing uptake. This is a similar effect to the stable and high carbon uptake of old forests (Baldocchi 2008; Herbst et al. 2015) and may even be important in the discussion of a necessary carbon sink. But measuring sites should not only be selected according to ecological requirements but also according to micrometeorological requirements, which will guarantee a good flux quality and representativeness. None of these factors should have a priority above the others.

This chapter has also shown the necessity for some further research, which could be initiated by FLUXNET and other programs. The importance of old data sets is undoubted, but this means that sensor and digitalization problems of the 1990s should be investigated to determine their relevance (see Sect. 19.2.2). The recently used quality classification program should be supplemented by factors that characterize the heterogeneity of a site and the coupling within and above the canopy (see Sect. 19.2.3 and Sect. 19.5.1). This needs research activities at more than one site. And finally, large eddy simulation should be accepted as a tool for characterizing sites and for helping to interpret data sets. But this path may be a long one.

Concluding Remarks Long-term measuring programs should not be understood as time independent. Instrumentations and sites are changing and need further research

to understand how this influences the results. Furthermore, the programs should be open to the application of new findings of research studies.

Acknowledgment Because most of the conclusions have been made above, I would like to highlight some personal feelings regarding this book. The book is highly interdisciplinary; not only did experimentalists and modelers come together but also micrometeorologists, climatologists, atmospheric chemists, ecologists, and hydrologists. As well, groups that have been operating for a long time in the Waldstein area have brought their research together and compared their data under the subject of fluxes on short time scales. In this context, Chaps. 5, 7, and 15 are remarkable. Therefore, I want to acknowledge all scientists who were responsible for the 18 chapters and three appendixes or supported these, as well as all agencies (for details see the relevant chapters) and the University of Bayreuth with the Bayreuth Center of Ecology and Environmental Research (BayCEER), who supported the research at the Waldstein sites and this book.

References

Aubinet M, Grelle A, Ibrom A, Rannik Ü, Moncrieff J, Foken T, Kowalski AS, Martin PH, Berbigier P, Bernhofer C, Clement R, Elbers J, Granier A, Grünwald T, Morgenstern K, Pilegaard K, Rebmann C, Snijders W, Valentini R, Vesala T (2000) Estimates of the annual net carbon and water exchange of forests: the EUROFLUX methodology. Adv Ecol Res 30:113–175

Baldocchi D (2008) 'Breathing' of the terrestrial biosphere: lessons learned from a global network of carbon dioxide flux measurement systems. Aust J Bot 56:1–26

Christen A, van Gorsel E, Andretta M, Calanca M, Rotach M, Vogt R (2000) Intercomparison of ultrasonic anemometers during the MAP-Riviera project. In: 9th conference on mountain meteorology, Aspen, CO2000. AMS, pp 130–131

Ciais P, Reichstein M, Viovy M, Granier A, Ogée J, Allard V, Aubinet M, Buchmann N, Bernhofer C, Carrara A, Chevallier F, De Noblet N, Friend AD, Friedlinstein P, Grünwald T, Heinesch B, Keronen P, Knohl A, Krinner G, Loustau D, Manca G, Matteucci G, Migglietta F, Ourcival JM, Papale D, Pilegaard K, Rambal S, Seufert G, Soussana JF, Sanz MJ, Schulze ED, Vesala T, Valentini R (2005) Europe-wide reduction in primary productivity caused by the heat and drought in 2003. Nature 437:529–533

Dupont S, Brunet Y (2009) Coherent structures in canopy edge flow: a large-eddy simulation study. J Fluid Mech 630:93–128

Eder F, Serafimovich A, Foken T (2013) Coherent structures at a forest edge: properties, coupling and impact of secondary circulations. Bound-Lay Meteorol 148:285–308

Finnigan JJ, Shaw RH, Patton EG (2009) Turbulence structure above a vegetation canopy. J Fluid Mech 637:687–424

Foken T (1979) Vorschlag eines verbesserten Energieaustauschmodells mit Berücksichtigung der molekularen Grenzschicht der Atmosphäre. Z Meteorol 29:32–39

Foken T (1984) The parametrisation of the energy exchange across the air-sea interface. Dynam Atmos Ocean 8:297–305

Foken T (2008) The energy balance closure problem – an overview. Ecol Appl 18:1351–1367

Foken T, Babel W (2016) Are trend analyses from FLUXNET station data realistic? Paper presented at 22nd symposium on boundary layers and turbulence, Salt Lake City, June 20–24, 2016. https://ams.confex.com/ams/32AgF22BLT3BG/webprogram/Paper294622.html

Foken T, Wichura B (1996) Tools for quality assessment of surface-based flux measurements. Agric For Meteorol 78:83–105

Foken T, Jegede OO, Weisensee U, Richter SH, Handorf D, Görsdorf U, Vogel G, Schubert U, Kirzel H-J, Thiermann V (1997) Results of the LINEX-96/2 Experiment. Dt Wetterdienst, Forsch. Entwicklung, Arbeitsergebnisse. 48:75 pp

Foken T, Göckede M, Mauder M, Mahrt L, Amiro BD, Munger JW (2004) Post-field data quality control. In: Lee X et al (eds) Handbook of micrometeorology: a guide for surface flux measurement and analysis. Kluwer, Dordrecht, pp 181–208

Foken T, Leuning R, Oncley SP, Mauder M, Aubinet M (2012a) Corrections and data quality. In: Aubinet M et al (eds) Eddy covariance: a practical guide to measurement and data analysis. Springer, Dordrecht, pp 85–131

Foken T, Meixner FX, Falge E, Zetzsch C, Serafimovich A, Bargsten A, Behrendt T, Biermann T, Breuninger C, Dix S, Gerken T, Hunner M, Lehmann-Pape L, Hens K, Jocher G, Kesselmeier J, Lüers J, Mayer JC, Moravek A, Plake D, Riederer M, Rütz F, Scheibe M, Siebicke L, Sörgel M, Staudt K, Trebs I, Tsokankunku A, Welling M, Wolff V, Zhu Z (2012b) Coupling processes and exchange of energy and reactive and non-reactive trace gases at a forest site – results of the EGER experiment. Atmos Chem Phys 12:1923–1950

Göckede M, Rebmann C, Foken T (2004) A combination of quality assessment tools for eddy covariance measurements with footprint modelling for the characterisation of complex sites. Agric For Meteorol 127:175–188

Göckede M, Foken T, Aubinet M, Aurela M, Banza J, Bernhofer C, Bonnefond J-M, Brunet Y, Carrara A, Clement R, Dellwik E, Elbers JA, Eugster W, Fuhrer J, Granier A, Grünwald T, Heinesch B, Janssens IA, Knohl A, Koeble R, Laurila T, Longdoz B, Manca G, Marek M, Markkanen T, Mateus J, Matteucci G, Mauder M, Migliavacca M, Minerbi S, Moncrieff JB, Montagnani L, Moors E, Ourcival J-M, Papale D, Pereira J, Pilegaard K, Pita G, Rambal S, Rebmann C, Rodrigues A, Rotenberg E, Sanz MJ, Sedlak P, Seufert G, Siebicke L, Soussana JF, Valentini R, Vesala T, Verbeeck H, Yakir D (2008) Quality control of CarboEurope flux data – part 1: coupling footprint analyses with flux data quality assessment to evaluate sites in forest ecosystems. Biogeosciences 5:433–450

Haslwanter A, Hammerle A, Wohlfahrt G (2009) Open-path vs. closed-path eddy covariance measurements of the net ecosystem carbon dioxide and water vapour exchange: a long-term perspective. Agric For Meteorol 149:291–302

Held A, Hinz K-P, Trimborn A, Spengler B, Klemm O (2003) Towards direct measurement of turbulent vertical fluxes of compounds in atmospheric aerosol particles. Geophys Res Lett 30:8/1–8/4

Herbst M, Mund M, Tamrakar R, Knohl A (2015) Differences in carbon uptake and water use between a managed and an unmanaged beech forest in central Germany. For Ecol Manage 355:101–108

Högström U, Smedman A (2004) Accuracy of sonic anemometers: Laminar wind-tunnel calibrations compared to atmospheric in situ calibrations against a reference instrument. Bound-Lay Meteorol 111:33–54

Hollinger DY, Richardson AD (2005) Uncertainty in eddy covariance measurements and its application to physiological models. Tree Phys 25:873–885

Järvi L, Mammarella I, Eugster W, Ibrom A, Siivola E, Dellwik E, Keronen P, Burba G, Vesala T (2009) Comparison of net CO_2 fluxes measured with open- and closed-path infrared gas analyzers in urban complex environment. Boreal Environ Res 14:499–514

Jocher G, Ottosson Löfvenius M, De Simon G, Hörnlund T, Linder S, Lundmark T, Marshall J, Nilsson MB, Näsholm T, Tarvainen L, Öquist M, Peichl M (2017) Apparent winter CO_2 uptake by a boreal forest due to decoupling. Agric For Meteorol 232:23–34

Kanani-Sühring F, Raasch S (2015) Spatial variability of scalar concentrations and fluxes downstream of a clearing-to-forest transition: a large-eddy simulation study. Bound-Lay Meteorol 155:1–27

Karipot A, Leclerc MY, Zhang G, Martin T, Starr D, Hollinger D, McCaughey H, Hendrey GM (2006) Nocturnal CO_2 exchange over tall forest canopy associated with intermittent low-level jet activity. Theor Appl Climatol 85:243–248

Keenan TF, Hollinger DY, Bohrer G, Dragoni D, Munger JW, Schmid HP, Richardson AD (2013) Increase in forest water-use efficiency as atmospheric carbon dioxide concentrations rise. Nature 499:324–327

Klemm O, Mangold A, Held A (2004) Turbulent deposition of ozone to a mountainous forest ecosystem. In: Matzner E (ed) Biogeochemistry of forested catchments in a changing enivironment, a German case study, Ecological studies, vol 172. Springer, Berlin, pp 203–213

Klemm O, Held A, Forkel R, Gasche R, Kanter H-J, Rappenglück B, Steinbrecher R, Müller K, Plewka A, Cojocariu C, Kreuzwieser J, Valverde-Canossa J, Schuster G, Moortgat GK, Graus M, Hansel A (2006) Experiments on forest/atmosphere exchange: climatology and fluxes during two summer campaigns in NE Bavaria. Atmos Environ 40(1):3–20

Kutsch WL, Kolari P (2015) Data quality and the role of nutrients in forest carbon-use efficiency. Nat Clim Chang 5:959–960

Leclerc MY, Foken T (2014) Footprints in micrometeorology and ecology. Springer, Heidelberg, XIX, 239 pp

LfU (2015) 25 Jahre Versauerungsmonitoring in Bayern. Bayerisches Landesamt für Umwelt, München, 90 pp

Matzner E (ed) (2004) Biogeochemistry of forested catchments in a changing environment, a German case study. Springer, Berlin, 498 pp

Matzner E, Zuber T, Lischeid G (2004) Response of soil solution chemistry and solute fluxes to changig deposition rates. In: Matzner E (ed) Biogeochemistry of forested catchments in a changing environment, a German case study, Ecological studies, vol 172. Springer, Berlin, pp 339–260

Mauder M, Liebethal C, Göckede M, Leps J-P, Beyrich F, Foken T (2006) Processing and quality control of flux data during LITFASS-2003. Bound-Lay Meteorol 121:67–88

Mauder M, Foken T, Clement R, Elbers J, Eugster W, Grünwald T, Heusinkveld B, Kolle O (2008) Quality control of CarboEurope flux data - part 2: inter-comparison of eddy-covariance software. Biogeosciences 5:451–462

Mauder M, Cuntz M, Drüe C, Graf A, Rebmann C, Schmid HP, Schmidt M, Steinbrecher R (2013) A strategy for quality and uncertainty assessment of long-term eddy-covariance measurements. Agric For Meteorol 169:122–135

Ocheltree TW, Loescher HW (2007) Design of the AmeriFlux portable eddy covariance system and uncertainty analysis of carbon measurements. J Atmos Ocean Technol 24:1389–1406

Papale D (2012) Data gap filling. In: Aubinet M et al (eds) Eddy covariance: a practical guide to measurement and data analysis. Springer, Dordrecht, pp 159–172

Rebmann C (2003) Kohlendioxid-, Wasserdampf- und Energieaustausch eines Fichtenwaldes in Mittelgebirgslage. Dissertation, Universität Bayreuth, Bayreuth, 149 pp

Richardson AD, Aubinet M, Barr AG, Hollinger DY, Ibrom A, Lasslop G, Reichstein M (2012) Uncertainty quantification. In: Aubinet M et al (eds) Eddy covariance: a practical guide to measurement and data analysis. Springer, Berlin, pp 173–209

Riederer M, Hübner J, Ruppert J, Brand WA, Foken T (2014) Prerequisites for application of hyperbolic relaxed eddy accumulation on managed grasslands and alternative net ecosystem exchange flux partitioning. Athmos Meas Tech 7:4237–4250

Ruppert J, Thomas C, Foken T (2006) Scalar similarity for relaxed eddy accumulation methods. Bound-Lay Meteorol 120:39–63

Schlegel F, Stiller J, Bienert A, Maas H-G, Queck R, Bernhofer C (2015) Large-eddy simulation study of the effects on flow of a heterogeneous forest at sub-tree resolution. Bound-Lay Meteorol 154:27–56

Schulze E-D, Lange OL, Oren R (eds) (1989) Forest decline and air pollution. Springer, Berlin, XVIII, 475 pp

Serafimovich A, Thomas C, Foken T (2011) Vertical and horizontal transport of energy and matter by coherent motions in a tall spruce canopy. Bound-Lay Meteorol 140:429–451

Sörgel M, Trebs I, Serafimovich A, Moravek A, Held A, Zetzsch C (2011) Simultaneous HONO measurements in and above a forest canopy: influence of turbulent exchange on mixing ratio differences. Atmos Chem Phys 11:841–855

Steinbrecher R, Rappenglück B, Hansel A, Graus M, Klemm O, Held A, Wiedensohler A, Nowak A (2004) Vegetation-atmospheric interactions: the emissions of biogenic volatile organic compounds (BVOC) and their relevance to atmospheric particle dynamics. In: Matzner E (ed) Biogeochemistry of forested catchments in a changing enivironment, a German case study, Ecological studies, vol 172. Springer, Berlin, pp 215–235

Stoy PC, Mauder M, Foken T, Marcolla B, Boegh E, Ibrom A, Arain MA, Arneth A, Aurela M, Bernhofer C, Cescatti A, Dellwik E, Duce P, Gianelle D, van Gorsel E, Kiely G, Knohl A, Margolis H, McCaughey H, Merbold L, Montagnani L, Papale D, Reichstein M, Serrano-Ortiz P, Sottocornola M, Saunders M, Spano D, Vaccari F, Varlagin A (2012) A data-driven analysis of energy balance closure across FLUXNET research sites: the role of landscape-scale heterogeneity. Agric For Meteorol 171–172:137–152

Tenhunen JD, Lenz R, Hantschel R (eds) (2001) Ecosystem approaches to landscape management in Central Europe, ecological studies, vol 147. Springer, Berlin, 652 pp

Thomas C, Foken T (2007) Flux contribution of coherent structures and its implications for the exchange of energy and matter in a tall spruce canopy. Bound-Lay Meteorol 123:317–337

Thomas CK, Martin JG, Law BE, Davis K (2013) Toward biologically meaningful net carbon exchange estimates for tall, dense canopies: multi-level eddy covariance observations and canopy coupling regimes in a mature Douglas-fir forest in Oregon. Agric For Meteorol 173:14–27

Tsokankunku A (2014) Fluxes of the NO-O3-NO_2 triad above a spruce forest canopy in south-eastern Germany. PhD Thesis, University of Bayreuth, Bayreuth, 184 pp

Valentini R (ed) (2003) Fluxes of carbon, water and energy of European forests, Ecological studies, vol 163. Springer, Berlin, 270 pp

Vickers D, Mahrt L (1997) Quality control and flux sampling problems for tower and aircraft data. J Atmos Ocean Technol 14:512–526

Wieser A, Fiedler F, Corsmeier U (2001) The influence of the sensor design on wind measurements with sonic anemometer systems. J Atmos Ocean Technol 18:1585–1608

Wild M, Roesch M, Ammann C (2012) Global dimming and brightening – evidence and agricultural implications. CAP Rev 7(003):1–17

Williams CA, Reichstein M, Buchmann N, Baldocchi DD, Beer C, Schwalm C, Wohlfahrt G, Hasler N, Bernhofer C, Foken T, Papale D, Schymanski S, Schaefer K (2012) Climate and vegetation controls on the surface water balance: synthesis of evapotranspiration measured across a global network of flux towers. Water Resour Res 48:W06523

Zhu Z, Tsokankunku A, Plake D, Falge E, Foken T, Meixner FX (2009) Multi-level eddy covariance measurements for ozone fluxes above, within and below spruce forest canopy. In: Lüers J, Foken T (eds) Proceedings of the international conference of atmospheric transport and chemistry in forest ecosystems. Arbeitsergebn, Univ Bayreuth, Abt Mikrometeorol, No. 40, Bayreuth, p 32. ISSN 1614-8916

Appendices

Appendix A
Instrumentation of the Permanent and Periodic Measuring Programs of the Waldstein Measuring Sites

Compiled by Thomas Foken, Johannes Lüers, Andreas Held, Christoph K. Thomas, and Andrei Serafimovich

For site description, see Chap. 2, and for project description, see Chap. 1. Where there is no special remark, the instruments were operated by the University of Bayreuth.

T. Foken (ed.), *Energy and Matter Fluxes of a Spruce Forest Ecosystem*,
Ecological Studies 229, DOI 10.1007/978-3-319-49389-3

Table A1 Waldstein-Pflanzgarten site, automatic air quality and weather station, with permanent measurement routine since 1994. Data recording: 10-min values, 765 m a.s.l

Operating since	Operating until	Short descriptions (altitudes are in meter above ground, depth information in cm)	Measurement device	Phys. unit
02/1994		Air temperature 2 m (not ventilated)	HMP45, PT 100	°C
02/1994		Relative humidity 2 m (not ventilated)	HMP45, capacitive	%
02/1994	12/2010	Incoming shortwave (global) radiation 4 m (container roof)	EQ07	Wm^{-2}
07/1997	12/2010	Diffuse incoming shortwave (diffuse) radiation 4 m (container roof)	EQ07, shadow ring	Wm^{-2}
02/2008		Incoming shortwave (global) radiation 4 m (container roof)	SDE 9	Wm^{-2}
02/2008		Direct incoming shortwave (direct) radiation 4 m (container roof)	SDE 9	Wm^{-2}
02/2008		Sunshine duration 4 m (container roof)	SDE 9	s
02/1994		Wind speed 10 m	Thies cup anemometer	ms^{-1}
02/1994		Wind direction 10 m	Thies wind vane	degree
02/1994		Precipitation 1 m (tipping bucket rain gauge)	Observator Instruments OMC 212	mm
07/2012		Precipitation 1 m (weighing rain gauge)	Ott Pluvio^2 (II)	mm
02/1994		Air pressure (at station's altitude)	Ammonit AB60	hPa
01/2008		Wet-only precipitation collector	Eigenbrodt, NSA 181/KHS	mm
05/1994	01/2008	Ozone analyzer 3 m (air inlet container roof)	MLU ML 8810 M	ppb, μgm^{-3}
01/2008	07/2012	New ozone analyzer 3 m (air inlet container roof)	MLU-400 (API Inc.)	ppb
07/2012		New ozone analyzer 3 m (air inlet container roof)	MLU Model 49i (Thermo Scientific)	ppb
05/1994	01/2008	SO_2 analyzer 3 m (air inlet container roof)	MLU ML 8850 S	ppb, μgm^{-3}
01/2008	07/2012	New SO_2 analyzer (air inlet container roof)	Thermo Fisher Sci. 43C	ppb
05/1994	12/2008	NO_x analyzer 3 m, NO NO_x analyzer 3 m, NO_2 (air inlet container roof)	Eco Physics CLD 700AL	ppb, μgm^{-3}

Table A2 Waldstein-Weidenbrunnen site, accessible 32 m tall scaffold tower (Main Tower, MT), automatic weather and energy, and matter flux station (FLUXNET station DE-Bay), with permanent measurement routine partly since 1998. Data recording: 10-min values (fluxes 30-min values), 775 m a.s.l

Operating since	Operating until	Short descriptions (altitudes are in meter above ground, depth information in cm)	Measurement device	Phys. unit
04/2004		Air temperature 0 m (dry, ventilated)	Frankenberger psychrometer PT 100 (Frankenberger 1951)	°C
04/2004		Air temperature 0 m (wet, ventilated) only month 04–10	Frankenberger psychrometer PT 100	°C
12/1998		Air temperature 2 m (not ventilated)	HMP45, PT 100	°C
12/1998		Relative humidity 2 m (not ventilated)	HMP45, capacitive	%
04/1998		Air temperature 2 m (dry, ventilated)	Frankenberger psychrometer PT 100	°C
04/1998		Air temperature 2 m (wet, ventilated) only month 04–10	Frankenberger psychrometer PT 100	°C
04/2004		Air temperature 5 m (dry, ventilated)	Frankenberger psychrometer PT 100	°C
04/2004		Air temperature 5 m (wet, ventilated) only month 04–10	Frankenberger psychrometer PT 100	°C
04/2004		Air temperature 12 m (dry, ventilated)	Frankenberger psychrometer PT 100	°C
04/2004		Air temperature 12 m (wet, ventilated) only month 04–10	Frankenberger psychrometer PT 100	°C
12/1998		Air temperature 21 m (not ventilated)	HMP45, PT 100	°C
12/1998		Relative humidity 21 m (not ventilated)	HMP45, capacitive	%
04/1998		Air temperature 21 m (dry, ventilated)	Frankenberger psychrometer PT 100	°C
04/1998		Air temperature 21 m (wet, ventilated) only month 04–10	Frankenberger psychrometer PT 100	°C
12/1998		Air temperature 31 m (not ventilated)	HMP45, PT 100	°C
12/1998		Relative humidity 31 m (not ventilated)	HMP45, capacitive	%
04/1998		Air temperature 31 m (dry, ventilated)	Frankenberger psychrometer PT 100	°C
04/1998		Air temperature 31 m (wet, ventilated) only month 04–10	Frankenberger psychrometer PT 100	°C
05/1996	08/2007	Air temperature 31 m	Thies hair hygrometer	°C
05/1996	08/2007	Relative humidity 31 m	Thies hair hygrometer	%
09/2007		Soil temperature −02 cm	PT 100	°C

(continued)

Table A2 (continued)

Operating since	Operating until	Short descriptions (altitudes are in meter above ground, depth information in cm)	Measurement device	Phys. unit
04/1998		Soil temperature −05 cm (old replaced with new one 09/2007)	PT 100	°C
04/1998		Soil temperature −10 cm (old replaced with new one 09/2007)	PT 100	°C
04/1998		Soil temperature −20 cm (old replaced with new one 09/2007)	PT 100	°C
04/1998		Soil temperature −50 cm (old replaced with new one 09/2007)	PT 100	°C
09/2007		Soil temperature −70 cm (new)	PT 100	°C
09/2007		Soil temperature −100 cm (new)	PT 100	°C
09/2007		Soil temperature −200 cm (new)	PT 100	°C
09/2007		Soil humidity −10 cm	TDR (Nr. 1)	%
09/2007		Soil humidity −50 cm	TDR (Nr. 2)	%
05/1999	08/2007	Soil heat flux 1 between −5 cm and −2 cm (all three plates)	Hukseflux HFP01	Wm^{-2}
05/1999		Soil heat flux 2 –10 cm (HFP replaced since 09/2007)	RIMCO CN3	Wm^{-2}
05/1999		Soil heat flux 3 –10 cm (HFP replaced since 09/2007)	RIMCO CN3	Wm^{-2}
04/1998		Incoming shortwave (global) radiation 30 m (above canopy)	Kipp & Zonen CM 14 (ventilated)	Wm^{-2}
04/1998		Outgoing shortwave (reflected) radiation 30 m (above canopy)	Kipp & Zonen CM 14 (ventilated)	Wm^{-2}
04/1998		Incoming longwave (back) radiation 30 m (above canopy)	Kipp & Zonen CG 2 (ventilated)	Wm^{-2}
04/1998		Outgoing longwave (emitted) radiation 30 m (above canopy)	Kipp & Zonen CG 2 (ventilated)	Wm^{-2}
04/1998		Internal device temperature 30 m (back radiation)	PT100 CG 2	°C
04/1998		Internal device temperature 30 m (emission)	PT100 CG 2	°C

(continued)

Table A2 (continued)

Operating since	Operating until	Short descriptions (altitudes are in meter above ground, depth information in cm)	Measurement device	Phys. unit
04/2000		Wind speed 2 m	Friedrich cup anemometer	ms^{-1}
08/2007		Wind speed 5 m (new 08/2007)	Friedrich cup anemometer	ms^{-1}
04/2000		Wind speed 10 m	Friedrich cup anemometer	ms^{-1}
04/2000		Wind speed t 16 m	Friedrich cup anemometer	ms^{-1}
08/2000		Wind speed 18 m	Friedrich cup anemometer	ms^{-1}
04/1998		Wind speed 21 m	Friedrich cup anemometer	ms^{-1}
04/1998		Wind speed 25 m	Friedrich cup anemometer	ms^{-1}
07/1997		Wind speed 32 m	Friedrich cup anemometer	ms^{-1}
07/1997		Wind direction 32 m	Skye W200P	Grad
11/2000		Wind speed 32 m	Thies 2D ultrasonic	ms^{-1}
11/2000		Wind direction 32 m	Thies 2D ultrasonic	degree
01/2000		Precipitation 32 m (top, funnel)	Eigenbrodt, ship rain gauge SRM 450	mm
01/2000		Precipitation 32 m (side, vertical collector)	Eigenbrodt, ship rain gauge SRM 450	mm
09/2000		Visibility 21 m	Vaisala, PWD 11	m
11/2002		Weather code 21 m	Vaisala, PWD 11	–
01/1997	05/2003	Wind vector, sonic temperature 22 m (33 m until 05/2003)	Gill 3D-ultrasonic R2	ms^{-1}, °C
05/2003	08/2007	Wind vector, sonic temperature 33 m	Gill 3D-ultrasonic R3-50	ms^{-1}, °C
04/2002	08/2007	CO_2/H_2O flux/concentration 33 m (temporary used again for short-term campaigns)	LiCor 7500 (open path)	mmol m^{-2} s^{-1}, mmol m^{-3}, g m^{-2} s^{-1}, g m^{-3}
01/1997	04/2002	CO_2/H_2O flux/concentration 22 m (33 m until 04/2002)	LiCor 6262 (closed path)	mmol m^{-2} s^{-1}, mmol m^{-3}, g m^{-2} s^{-1}, g m^{-3}
09/2007		Wind vector, turbulent fluxes 33 m	Metek 3D-ultrasonic USA 1	ms^{1}, °C
09/2007		CO_2/H_2O flux/concentration 33 m	LiCor 7000 (closed path)	mmol m^{-2} s^{-1}, mmol m^{-3}, g m^{-2} s^{-1}, g m^{-3}

Table A3 Waldstein-Weidenbrunnen site, accessible 36 m tall slim tower (Turbulence Tower, MT), energy, and matter flux station (FLUXNET station DE-Bay), with permanent measurement routine since 09/2007, 773 m a.s.l

Operating since	Operating until	Short descriptions (altitudes are in meter above ground)	Measurement device	Phys. unit
09/2007		Wind vector, turbulent fluxes 36 m	Metek 3D-ultrasonic USA 1	ms^{-1}, °C
09/2007		CO_2/H_2O flux/concentration 33 m	LiCor 7500 (open path)	mmol m^{-2} s^{-1}, mmol m^{-3}, g m^{-2} s^{-1}, g m^{-3}

Table A4 Waldstein-Weidenbrunnen site, instrumentation at Main Tower during the experiments BEWA 2001 and 2002. For further instrumentation, see Tables A1 and A2, and for more details, see Klemm et al. (2006)

Operating since	Operating until	Short descriptions (altitudes are in meter above ground)	Measurement device	Phys. unit
For all instruments				
09.07.2001 24.06.2002	03.08.2001 02.08.2002	NO_2 photolysis rate 22 m	Filter radiometer	s^{-1}
		O_3 photolysis rate 31 m	Filter radiometer	s^{-1}
		Leaf wetness 13 m	Leaf wetness sensors (Klemm et al. 2002)	–
		O_3 flux 32 m	Ozonesonde OSG-2 (Güsten and Heinrich 1996)	nmol m^{-2} s^{-1}
		VOC fluxes and mixing ratios (C5–C10) 17, 30 m[b,c]	Relaxed eddy accumulation (Grabmer et al. 2006; Graus et al. 2006)	nmol m^{-2} s^{-1}ppb
		Peroxide fluxes and mixing ratios, 14, 32 m[d]	Relaxed eddy accumulation (Valverde-Canossa et al. 2006)	nmol m^{-2} s^{-1}ppb
		Carbonyls (C1–C5), alcohols (C1–C4), VOC (C5–C10) emission fluxes, and mixing ratios 12 m[e]	Cuvette measurements (Kreuzwieser et al. 2002)	nmol m^{-2} s^{-1}ppb
		Aerosol size distributions 22 m[f]	Twin differential mobility particle sizer (Held et al. 2004)	cm^{-3}
		Aerosol number fluxes 22 m	Eddy covariance (Held and Klemm 2006)	m^{-2} s^{-1}
		Aerosol chemical composition 12, 24 m[g]	Impactor sampling for inorganic ions, elemental carbon, organic carbon, organic acids, aldehydes (Plewka et al. 2006)	ng m^{-3}
		Aerosol carbonyl mixing ratios (C1–C12) 12, 24 m[g]	DNPH cartridge sampling (Müller et al. 2006)	ppb
		Fog chemical composition 25 m	Heatable active strand cloud water collector (Klemm et al. 2008)	μeq L^{-1}

(continued)

Table A4 (continued)

Operating since	Operating until	Short descriptions (altitudes are in meter above ground)	Measurement device	Phys. unit
		NH_3 mixing ratios 3 m[a]	Continuous wet denuder (Wyers et al. 1993)	ppb
		Aerosol chemical composition 1 m[a,g]	High-volume sampler Sierra Anderson	$\mu g\ m^{-3}$

[a]At Waldstein-Pflanzgarten site
[b]Operated by IFU, Garmisch-Partenkirchen, Germany
[c]Operated by University of Innsbruck, Innsbruck, Austria
[d]Operated by Max-Planck-Institute (MPI) for Chemistry Mainz, Germany
[e]Operated by University of Freiburg, Freiburg, Germany
[f]In collaboration with Leibniz Institute for Tropospheric Research, Leipzig, Germany
[g]Operated by Leibniz Institute for Tropospheric Research, Leipzig, Germany

Table A5 Waldstein-Weidenbrunnen site, instrumentation at Main Tower, and other positions during the experiments WALDATEM 2003. For further instrumentations, see Tables A1 and A2, and for more details, see Thomas et al. (2004)

Operating since	Operating until	Short descriptions (altitudes are in meter above ground)	Measurement device	Phys. unit
Main Tower				
21.05.2003	31.07.2003	Wind vector, sonic temperature 22 m	Gill 3D-ultrasonic R2 with 2D inclinometer	ms^{-1}, °C
04.06.2003	20.07.2003	CO_2/H_2O flux/concentration 22 m	LiCor 6262 (closed path)	mmol m^{-2} s^{-1}, mmol m^{-3}, g m^{-2} s^{-1}, g m^{-3}
21.05.2003	31.07.2003	Wind vector, sonic temperature 17 m	Young 3D-ultrasonic 8100	ms^{-1}, °C
24.05.2003	31.07.2003	Wind vector, sonic temperature 13 m	Young 3D-ultrasonic 8100	ms^{-1}, °C
24.06.2003	17.07.2003	Wind vector, turbulent fluxes 5.5 m	Metek 3D-ultrasonic USA 1-FHN	ms^{-1}, °C
16.06.2003	01.08.2003	Wind vector, turbulent fluxes 2.25 m	Metek 3D-ultrasonic USA 1-FHN	ms^{-1}, °C
16.06.2003	01.08.2003	CO_2/H_2O flux/concentration 2.25 m	LiCor 7500 (open path)	mmol m^{-2} s^{-1}, mmol m^{-3}, g m^{-2} s^{-1}, g m^{-3}
26.,28.06.; 06.-08., 23.07.2003		^{13}C isotope fluxes	Whole-air REA system (Ruppert 2005; Ruppert et al. 2012)	µmol m^{-2} s^{-1}
13.06.2003	13.08.2003	CO_2 concentration profile, 33, 22, 15, 5.25, 2.25, 0.9, 0.03 m	CO_2 and ^{13}C isotope profile system (installed by J. Ruppert)	ppm
26.,28.06.; 06.-08., 23.07.2003, selected periods		^{13}C isotope profile, 33, 22, 15, 5.25, 2.25, 0.9, 0.03 m		‰VPDB[a]
05.07.2003	02.08.2003	CO_2 concentration profile 2.25 m	Hydra-system (A.C. Delany, NCAR, USA)	ppm
25.06.2003	23.09.2003	Air temperature 5.5 and 12.5 m (dry, ventilated)	Frankenberger psychrometer PT 100	°C

(continued)

Table A5 (continued)

Operating since	Operating until	Short descriptions (altitudes are in meter above ground)	Measurement device	Phys. unit
25.06.2003	23.09.2003	Air temperature 5.5 and 12.5 m (wet, ventilated)	Frankenberger psychrometer PT 100	°C
25.06.2003	23.09.2003	Net radiation (four components) 4.6 m	Kipp & Zonen CNR1	W m^{-2}
Small tower, 50 m NE of the Main Tower				
20.06.2003	04.08.2003	Wind speed 6.0, 2.26, 1.0 m	Climatronics cup anemometer F460	ms^{-1}
20.06.2003	04.08.2003	Wind direction 1.6 m	Vector Instruments W200P	degree
05.07.2003	02.08.2003	CO_2 concentration profile 1 m, 2.25 m, 2.25 m (between NE-tower and Main Tower)	Hydra-system (A.C. Delany, NCAR, USA)	ppm
Small tower, 50 m S of the Main Tower				
20.06.2003	04.08.2003	Wind speed 2.2, 1.1 m	Climatronics cup anemometer F460	ms^{-1}
20.06.2003	04.08.2003	Wind direction 1.55 m	Vector Instruments W200P	Grad
05.07.2003	02.08.2003	CO_2 concentration profile 1 m, 2.25 m, 2.25 m (between S-tower and Main Tower)	Hydra-system (A.C. Delany, NCAR, USA)	ppm
Small tower, 50 m W of the Main Tower				
20.06.2003	04.08.2003	Wind speed 2.25, 1.05 m	Climatronics cup anemometer F460	ms^{-1}
20.06.2003	04.08.2003	Wind direction 1.85 m	Vector Instruments W200P	Grad
05.07.2003	02.08.2003	CO_2 concentration profile 1 m, 2.25 m	Hydra-system (A.C. Delany, NCAR, USA)	ppm

(continued)

Table A5 (continued)

Operating since	Operating until	Short descriptions (altitudes are in meter above ground)	Measurement device	Phys. unit
Waldstein-Pflanzgarten				
09.05.2003	16.07.2003	Wind speed, wind direction, and temperature profile in the boundary layer	Metek DSDPA.90/64 Sodar with 1290 MHz RASS extension	ms^{-1}, degree, °C

[a]VDPB: Vienna Pee Dee Belemnite

Table A6 Waldstein-Weidenbrunnen site, instrumentation at Main Tower, and other positions during the experiments EGER, IOP1 2007. For further instrumentation, see Tables A1, A2, and A3 and for more details, see Serafimovich et al. (2008a) and Foken et al. (2012)

Operating since	Operating until	Short descriptions (altitudes are in meter above ground)	Measurement device	Phys. unit
Main Tower M1				
14.09.2007	07.10.2007	Wind vector, sonic temperature 32 m[a]	Gill 3D-ultrasonic R2	ms^{-1}, °C
14.09.2007	05.10.2007	O_3 flux 32 m[a]	Ozonesonde OSG-2 (Güsten and Heinrich 1996)	nmol m^{-2} s^{-1}
26.08.2007	03.10.2007	Wind speed 31.3, 26.3, 24.3, 19.8, 13.3, 7.6 m[a]	Cup anemometer, Vector Instruments	ms^{-1}
26.08.2007	03.10.2007	Air temperature 30.9, 26.6, 24.4, 19.5 15.9, 9.9., 4.9 m (dry, ventilated)[a]	MPI psychrometer PT 100	°C
26.08.2007	03.10.2007	Air temperature 30.9, 26.6, 24.4, 19.5 15.9, 9.9., 4.9 m (wet, ventilated)[a]	MPI psychrometer PT 100	°C
28.08.2007	03.10.2007	CO_2, H_2O, O_3, NO, NO_2 concentration 31.0, 24.2 m[a]	RETGAP-System (CLD TR-780, BLC TEI 49i, LiCor 840 from 01.10.2007 LiCor-7000)	ppm mmol mol^{-1}ppb
28.08.2007	03.10.2007	CO_2, H_2O, O_3, NO, NO_2 concentration 24.2, 16.0, 10.0, 5.0 m[a]	RETGAP-System (CLD TR-780, BLC TEI 49c, LiCor-7000, from 01.10.2007 LiCor-840)	ppm mmol mol^{-1}ppb
26.08.2007	03.10.2007	NH_3, HNO_3, HONO, SO_2, HCl, NH_4^+,NO_3^-, SO_4^{2-}, Cl^- concentration 24,2 m[a]	GRAEGOR (GRadient of AErosol and Gases Online Registrator; ECN, Petten, NL)	µg m^{-3}
30.08.2007	25.09.2007	NH_3, HNO_3, HONO, SO_2, HCl, NH_4^+,NO_3^-, SO_4^{2-}, Cl^- concentration 30.4 m[a]	GRAEGOR (GRadient of AErosol and Gases Online Registrator; ECN, Petten, NL)	µg m^{-3}
07.09.2007	30.09.2007	Up- and downwelling NO_2 photolysis rate, j(NO_2), global radiation 28 m[a]	Airchem/BGC sensor (LiCor)	s^{-1}, Wm^{-2}

(continued)

Table A6 (continued)

Operating since	Operating until	Short descriptions (altitudes are in meter above ground)	Measurement device	Phys. unit
14.09.2007 24.09.2007 01.10.2007	22.09.2007 25.09.2007 03.10.2007	Particle size distribution 28 m[a]	Scanning mobility particle sizer (SMPS)	cm^{-3}
04.09.2007 13.09.2007	08.09.2007 25.09.2007	HONO concentration 24.5 m[a]	LOPAP (Kleffmann et al. 2002)	ppt
06.09.2007	07.10.2007	NO, NO_2, O_3, CO_2, H_2O exchange measurements on spruce branches 13 m[a]	dynamic cuvette (Breuninger et al. 2013)	ppb mmol mol^{-1},ppm
07.09.2007	01.10.2007	Leaf surface wetness, stomata resistance/leaf temperature, moisture, PHAR 13 m[a]	RESI, Typ R500-01; Gademann Instruments GmbH, Würzburg	S, °C, %, µmol m^{-2} s^{-1}
24.09.2007	09.10.2007	Air pressure 0.3 m	Ammonit AB60	hPa
05.09.2007	09.10.2007	Incoming shortwave (global) radiation 2 m	Kipp & Zonen CM 24 (ventilated)	Wm^{-2}
05.09.2007	09.10.2007	Outgoing shortwave (reflected) radiation 2 m	Kipp & Zonen CM 24 (ventilated)	Wm^{-2}
05.09.2007	09.10.2007	Incoming longwave (back) radiation 2 m	Eppley PIR (ventilated)	Wm^{-2}
05.09.2007	09.10.2007	Outgoing longwave (emitted) radiation 2 m	Eppley PIR (ventilated)	Wm^{-2}
05.09.2007	09.10.2007	Radon concentration 0.2, 0.5 m	Alpha Guard, Radim 2P	Bq m^{-3}
Forest floor mast about 20 m west of M1				
25.08.2007	12.09.2007	Wind vector, sonic temperature 1 m[a]	Gill 3D-ultrasonic R2	ms^{-1}, °C
29.08.2007	04.09.2007	O_3 flux 1 m[a]	Ozonesonde OSG-2 (Güsten and Heinrich 1996)	nmol m^{-2} s^{-1}
10.09.2007	03.10.2007	Wind vector (2D) 2.0, 1.0, 0.3, 0.04 m[a]	Vaisala 2D sonic anemometer, WS425	degree, ms^{-1}
10.09.2007	03.10.2007	Air temperature 2.16, 0.62 m (ventilated)[a]	Rotronic MP 100 A	°C
10.09.2007	03.10.2007	Air temperature 2.05, 1.0, 0.26, 0.09 m (dry, ventilated)[a]	MPI psychrometer PT 100	°C

(continued)

Table A6 (continued)

Operating since	Operating until	Short descriptions (altitudes are in meter above ground)	Measurement device	Phys. unit
10.09.2007	03.10.2007	Air temperature 2.05, 1.0, 0.26, 0.09 m (wet, ventilated)[a]	MPI psychrometer PT 100	°C
10.09.2007	03.10.2007	Air temperature 0.32, 0.16, 0.08, 0.04, 0.02, 0.01 m (not ventilated)[a]	thermocouple	°C
28.08.2007	03.10.2007	CO_2, H_2O, O_3, NO, NO_2 concentration 2.0, 1.0, 0.3, 0.05 m[a]	RETGAP-System (CLD TR-780, BLC TEI 49c, LiCor-7000, from 01.10.2007 Licor-840)	ppm mmol mol^{-1}ppb
10.09.2007	03.10.2007	^{220}Rn and ^{222}Rn concentration 0.27, 0.0 m[a]	Alpha Guard	Bq m^{-3}
13.09.2007	03.10.2007	HONO concentration 1 m[a]	LOPAP (Kleffmann et al. 2002)	ppt
26.09.2007	03.10.2007	HONO concentration 1 m[a]	LOPAP (Kleffmann et al. 2002)	ppt
10.09.2007	03.10.2007	^{222}Rn and CO_2 soil emission[a]	Static chamber, Alpha Guard, Vaisala GMP 343	Bq m^{-3} ppm
26.08.2007	03.10.2007	NO, NO_2 soil flux[a]	Chamber, Thermo Ti42c	nmol m^{-2} s^{-1}
26.08.2007	03.10.2007	O_3 soil flux[a]	Chamber, Thermo Ti49i	nmol m^{-2} s^{-1}
26.08.2007	03.10.2007	CO_2, H_2O soil flux[a]	Chamber, LiCor 840	mmol m^{-2} s^{-1}
10.09.2007	03.10.2007	Barometric pressure 1 m[a]	Vaisala PTA427	hPa
10.09.2007	03.10.2007	Soil temperature −0.1,–0.16, −0.2, −0.32, −0.4, −0.64 –0.8 m [a]	MPI thermocouple	°C
10.09.2007	03.10.2007	Soil temperature −0.02, −0.04, −0.08, −0.12, −0.16 m [a]	Campbell Sci. TP107	°C
10.09.2007	03.10.2007	Soil temperature (depth integrated) –0.01, −0.02, −0.04, −0.08 m[a]	Campbell Sci. special wired thermocouple	°C
10.09.2007	03.10.2007	Soil heat flux −0.08 (2x)[a]	Campbell Sci. HFT	Wm^{-2}

(continued)

Table A6 (continued)

Operating since	Operating until	Short descriptions (altitudes are in meter above ground)	Measurement device	Phys. unit
10.09.2007	03.10.2007	Net radiation 2 m[a]	Kipp & Zonen NRLite	Wm^{-2}
10.09.2007	03.10.2007	Global radiation 2 m[a]	SKYE	Wm^{-2}
10.09.2007	03.10.2007	Downwelling NO_2 photolysis rate, $j(NO_2)$ 2.0[a]	BGC sensor 686, 404, Meteorologie Consult	s^{-1}
10.09.2007	03.10.2007	Precipitation	ARG100	mm
Turbulence Tower M2		Position: see Fig. A1		
08.09.2007	07.10.2007	Wind vector, sonic temperature 23 m	Campbell CSAT3	ms^{-1}, °C
08.09.2007	07.10.2007	CO_2/H_2O flux/concentration 23 m	LiCor 7500 (open path)	mmol m^{-2} s^{-1}, mmol m^{-3}, g m^{-2} s^{-1}, g m^{-3}
14.09.2007	07.10.2007	Wind vector, sonic temperature 18 m[a]	Gill 3D-ultrasonic R2	ms^{-1}, °C
14.09.2007	07.10.2007	CO_2/H_2O flux/concentration 18 m[a]	LiCor 7500 (open path)	mmol m^{-2} s^{-1}, mmol m^{-3}, g m^{-2} s^{-1}, g m^{-3}
08.09.2007	07.10.2007	Wind vector, sonic temperature 13 m	Campbell CSAT3	ms^{-1}, °C
08.09.2007	07.10.2007	H_2O flux/concentration 13 m	Campbell KH20	g m^{-3}
14.09.2007	07.10.2007	Wind vector, sonic temperature 5.5 m[a]	Gill 3D-ultrasonic R2	ms^{-1}, °C
14.09.2007	07.10.2007	CO_2/H_2O flux/concentration 5.5 m[a]	LiCor 7500 (open path)	mmol m^{-2} s^{-1}, mmol m^{-3}, g m^{-2} s^{-1}, g m^{-3}
08.09.2007	13.11.2007	Wind vector, sonic temperature 2.25 m	Campbell CSAT3	ms^{-1}, °C
08.09.2007	13.11.2007	CO_2/H_2O flux/concentration 2.25 m	LiCor 7500 (open path)	mmol m^{-2} s^{-1}, mmol m^{-3}, g m^{-2} s^{-1}, g m^{-3}
Tower M3		Position: see Fig. A1		
14.09.2007	04.10.2007	Wind speed and direction 36 m[a]	Vector Instruments A100ML, WP200P	ms^{-1}, degree
07.09.2007	04.10.2007	Air temperature 22.6, 20.2, 17.2, 14.8, 11.7, 9.3 m (ventilated) [a]	Vaisala HMT337	°C

(continued)

Table A6 (continued)

Operating since	Operating until	Short descriptions (altitudes are in meter above ground)	Measurement device	Phys. unit
07.09.2007	04.10.2007	Relative humidity 22.6, 20.2, 17.2, 14.8, 11.7, 9.3 m (ventilated) [a]	Vaisala HMT337	%
14.09.2007	04.10.2007	Air temperature and humidity (not ventilated) 36 m [a]	Rotronic MP100A	°C, %
07.09.2007	04.10.2007	Net radiation 22.8, 17.4, 11.9 m[a]	Kipp & Zonen CNR1	Wm^{-2}
14.09.2007	04.10.2007	Net radiation 36 m[a]	Kipp & Zonen NRLite	Wm^{-2}
06.09.2007	06.10.2007	Sap flow (2 trees) 22.6, 20.2, 17.2, 14.8, 11.7, 1.4 m[a]	ICT HMR-30	$L\ tree^{-1}\ h^{-1}$
17.09.2007	02.10.2007	CO_2 and H_2O needle gas exchange[a]	Portable gas exchange system Walz GFS3000	$\mu mol\ m^{-2}\ s^{-1}$ $mmol\ m^{-2}\ s^{-1}$
Modified Bowen ratio M4		Position: clearing, 200 m ENE from Main Tower	According to Liu and Foken (2001)	
07.09.2007	07.10.2007	Wind vector, sonic temperature 3.0 m	METEK USA-1	ms^{-1}, °C
07.09.2007	07.10.2007	Air temperature 0.85, 2.1 m (dry, ventilated)	Frankenberger psychrometer PT 100	°C
07.09.2007	07.10.2007	Air temperature 0.85, 2.1 m (wet, ventilated)	Frankenberger psychrometer PT 100	°C
Small tower M5		Position: see Fig. A1		
07.09.2007	13.11.2007	Wind speed 1.0 m	Climatronics cup anemometer F460	ms^{-1}
07.09.2007	13.11.2007	Air temperature 1.0 m (dry, ventilated)	Frankenberger psychrometer PT 100	°C
07.09.2007	13.11.2007	Air temperature 1.0 m (wet, ventilated)	Frankenberger psychrometer PT 100	°C
07.09.2007	13.11.2007	Wind vector, sonic temperature 2.25 m [a]	METEK USA-1	ms^{-1}, °C
07.09.2007	13.11.2007	CO_2 concentration profile 2.25 m	CO_2 profile system (Ruppert 2005)	ppm
Small tower M6		Position: see Fig. A1		
07.09.2007	13.11.2007	Wind speed 1.0 m	Climatronics cup anemometer F460	ms^{-1}
07.09.2007	13.11.2007	Air temperature 1.0 m (dry, ventilated)	Frankenberger psychrometer PT 100	°C

(continued)

Table A6 (continued)

Operating since	Operating until	Short descriptions (altitudes are in meter above ground)	Measurement device	Phys. unit
07.09.2007	13.11.2007	Air temperature 1.0 m (wet, ventilated)	Frankenberger psychrometer PT 100	°C
07.09.2007	13.11.2007	Wind vector, sonic temperature 2.25 m[a]	METEK USA-1	ms^{-1}, °C
07.09.2007	13.11.2007	CO_2 concentration profile 2.25 m	CO_2 profile system (Ruppert 2005)	ppm
Small tower M7		Position: see Fig. A1		
07.09.2007	13.11.2007	Wind speed 1.0 m	Climatronics cup anemometer F460	ms^{-1}
07.09.2007	13.11.2007	Air temperature 1.0 m (dry, ventilated)	Frankenberger psychrometer PT 100	°C
07.09.2007	13.11.2007	Air temperature 1.0 m (wet, ventilated)	Frankenberger psychrometer PT 100	°C
07.09.2007	13.11.2007	Wind vector, sonic temperature 2.25 m[a]	METEK USA-1	ms^{-1}, °C
07.09.2007	13.11.2007	CO_2 concentration profile 2.25 m	CO_2 profile system (Ruppert 2005)	ppm
Small tower M8 (M2)		Position: see Fig. A1		
07.09.2007	13.11.2007	Wind speed 1.0 m	Climatronics cup anemometer F460	ms^{-1}
07.09.2007	13.11.2007	Air temperature 1.0 m (dry, ventilated)	Frankenberger psychrometer PT 100	°C
07.09.2007	13.11.2007	Air temperature 1.0 m (wet, ventilated)	Frankenberger psychrometer PT 100	°C
07.09.2007	13.11.2007	CO_2 concentration profile 2.25 m	CO_2 profile system (Ruppert 2005)	ppm
Small tower M9		position: see Fig. A1		
07.09.2007	13.11.2007	CO_2 concentration profile 2.25 m	CO_2 profile system (Ruppert 2005)	ppm
Waldstein-Pflanzgarten				
09.09.2007	03.10.2007	Wind speed, wind direction, and temperature profile in the boundary layer[a]	Metek DSDPA.90/64 Sodar with 1290 MHz RASS extension	ms^{-1}, degree, °C
20.09.2007 01.10.2007	26.09.2007 05.10.2007	Wind speed, wind direction profile in the boundary layer[a]	Scintec flat array sodar (SFAS)	ms^{-1}, degree
07.09.2007	05.10.2007	Wind speed and direction 2.9 m[a]	Vector Instruments A100ML, WP200P	ms^{-1}, degree

(continued)

Table A6 (continued)

Operating since	Operating until	Short descriptions (altitudes are in meter above ground)	Measurement device	Phys. unit
07.09.2007	05.10.2007	Air temperature and humidity (not ventilated) 2.8, 1.1 m[a]	Rotronic MP100A	°C, %
07.09.2007	05.10.2007	Barometric pressure 1 m[a]	Vaisala PTB101B	hPa
07.09.2007	05.10.2007	Precipitation intensity 1 m[a]	Campbell Sci. ARG 100	mm

[a]Operated by Max-Planck-Institute (MPI) for Chemistry Mainz, Germany

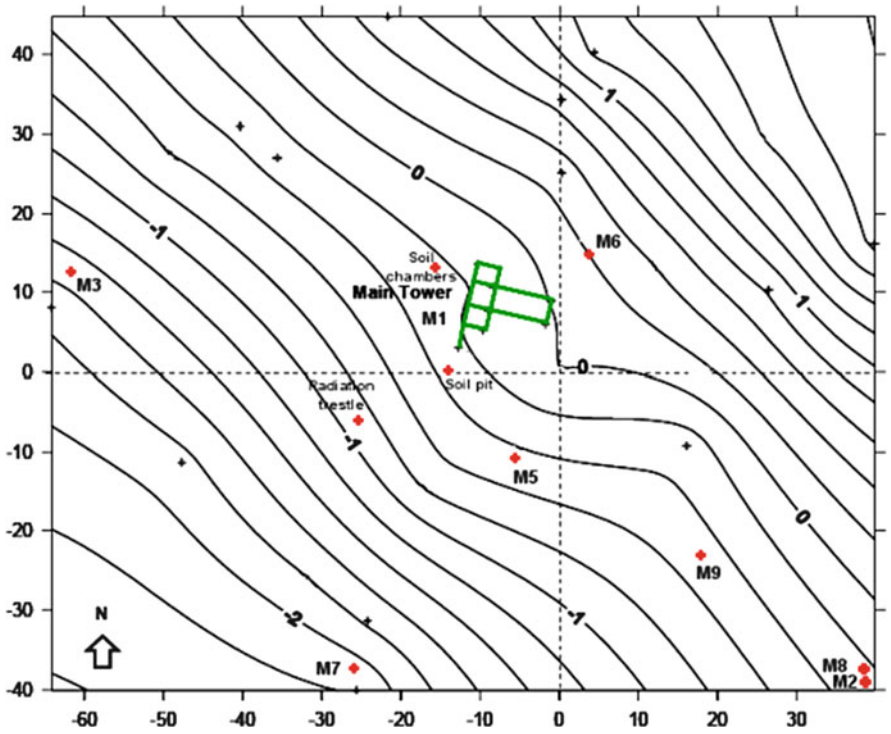

Fig. A1 Tower positions during the experiments EGER, IOP1, 2007, 0-line is 775 m a.s.l. (Serafimovich et al. 2008a, Published with kind permission © Authors 2008, All rights reserved)

Table A7 Waldstein-Weidenbrunnen site, instrumentation at Main Tower, and other positions during the experiments EGER, IOP2 2008. For further instrumentation, see Tables A1, A2, and A3 and for more details, see Serafimovich et al. (2008b) and Foken et al. (2012)

Operating since	Operating until	Short descriptions (altitudes are in meter above ground, depth information in cm)	Measurement device	Phys. unit
Main Tower M1				
01.06.2008	15.07.2008	Wind vector, sonic temperature 32 m[a]	Gill 3D-ultrasonic R2	ms^{-1}, °C
01.06.2008	15.07.2008	Wind vector, sonic temperature 31.5 m[a]	Campbell CSAT3	ms^{-1}, °C
04.06.2008	14.07.2008	O_3 flux 31.5 m[a]	Ozonesonde NOAA/ATDD	nmol m^{-2} s^{-1}
01.06.2008	15.07.2008	NO, NO_2 flux 31.5 m[a]	CLD 790SR2, Ecophysics	nmol m^{-2} s^{-1}
01.06.2008	15.07.2008	CO_2/H_2O flux/concentration 31.5 m[a]	LiCor-7000	mmol m^{-2} s^{-1}, mmol m^{-3}, g m^{-2} s^{-1}, g m^{-3}
01.06.2008	15.07.2008	Wind vector, sonic temperature 24.5 m[a]	Gill 3D-ultrasonic R2	ms^{-1}, °C
04.06.2008	14.07.2008	O_3 flux 24.5 m [a]	Ozonesonde Enviscope	nmol m^{-2} s^{-1}
01.06.2008	15.07.2008	CO_2/H_2O flux/concentration 24.5 m[a]	LiCor-7000	mmol m^{-2} s^{-1}, mmol m^{-3}, g m^{-2} s^{-1}, g m^{-3}
01.06.2008	15.07.2008	wind vector, sonic temperature 17 m [a]	Gill 3D-ultrasonic R2	ms^{-1}, °C
04.06.2008	15.07.2008	O_3 flux 17 m[a]	Ozonesonde Enviscope	nmol m^{-2} s^{-1}
01.06.2008	15.07.2008	Wind speed 31.3, 26.3, 24.3, 19.8, 13.3, 7.6 m [a]	Vector instruments cup anemometer	ms^{-1}
01.06.2008	15.07.2008	Air temperature 30.9, 26.6, 24.4, 19.5 15.9, 9.9., 4.9 m (dry, ventilated)[a]	MPI psychrometer, thermocouple	°C
01.06.2008	15.07.2008	Air temperature 30.9, 26.6, 24.4, 19.5 15.9, 9.9., 4.9 m (wet, ventilated)[a]	MPI psychrometer, thermocouple	°C

(continued)

Table A7 (continued)

Operating since	Operating until	Short descriptions (altitudes are in meter above ground, depth information in cm)	Measurement device	Phys. unit
01.06.2008	15.07.2008	CO_2, H_2O, O_3, NO, NO_2 concentration 31.5, 25.0, 20.5, 16.5 m[a]	RETGAP-System (CLD TR-780, BLC TEI 49i, Licor-7000)	ppm mmol mol^{-1}ppb
01.06.2008	15.07.2008	CO_2, H_2O, O_3, NO, NO_2 concentration 16.5, 10.0, 3.0 m[a]	RETGAP-System (CLD TR-780, BLC TEI 49c, Licor-840)	ppm mmol mol^{-1}ppb
26.05.2008	14.07.2008	Air pressure 0.3 m	Ammonit AB60	hPa
26.05.2008	14.07.2008	Incoming shortwave (global) radiation 2 m	Kipp & Zonen CM 24 (ventilated)	Wm^{-2}
26.05.2008	14.07.2008	Outgoing shortwave (reflected) radiation 2 m	Kipp & Zonen CM 24 (ventilated)	Wm^{-2}
26.05.2008	14.07.2008	Incoming longwave (back) radiation 2 m	Eppley PIR (ventilated)	Wm^{-2}
26.05.2008	14.07.2008	Outgoing longwave (emitted) radiation 2 m	Eppley PIR (ventilated)	Wm^{-2}
03.07.2008	10.07.2008	Leaf surface wetness, stomata resistance/leaf temperature, moisture, PHAR 13 m[a]	RESI, Typ R500-01; Gademann Instruments GmbH, Würzburg	S, °C, %, $\mu mol\ m^{-2}\ s^{-1}$
26.05.2008	14.07.2008	Radon concentration 0.2, 0.5 m	Alpha Guard, Radim 2P	Bq m^{-3}
26.05.2008	14.07.2008	Soil temperature −2, −5. –10, −20 cm	PT 100	°C
26.05.2008	02.07.2008	Soil humidity −5, −20 cm	IMKO TDR	%
03.07.2008	14.07.2008	Soil humidity −5, −20 cm	IMKO TDR	%
26.05.2008	14.07.2008	Soil heat flux 2x −10 cm	CN3	Wm^{-2}
01.06.2008	15.07.2008	NO, NO_2 soil flux [a]	Chamber, Thermo Ti42c (Bargsten et al. 2010; Behrendt et al. 2014)	nmol $m^{-2}\ s^{-1}$

(continued)

Table A7 (continued)

Operating since	Operating until	Short descriptions (altitudes are in meter above ground, depth information in cm)	Measurement device	Phys. unit
01.06.2008	15.07.2008	O_3 soil flux [a]	Chamber, Thermo Ti49i	nmol m^{-2} s^{-1}
01.06.2008	15.07.2008	CO_2, H_2O soil flux [a]	Chamber, LiCor 7000, LiCor 6262	mmol m^{-2} s^{-1}
05.06.2008	05.11.2008	Array 50 m around M1: soil temperature −0.01, −0.02, −0.04, −0.08, −0.16 m[a]	Solid state temperature sensor TP107	°C
05.06.2008	05.11.2008	Array 50 m around M1: soil moisture −0.3–0.0 m[a]	FDR	%
05.06.2008	05.11.2008	Array 50 m around M1: soil heat flux −0.08 m [a]	HTF	Wm^{-2}
Forest floor mast about 20 m west of M1				
01.06.2008	15.07.2008	Wind vector, sonic temperature 1 m[a]	Gill 3D-ultrasonic R2	ms^{-1}, °C
01.06.2008	15.07.2008	O_3 flux 1 m[a]	Ozonesonde GEFAS	nmol m^{-2} s^{-1}
01.06.2008	15.07.2008	Global radiation 2 m[a]	LiCor 200SZ	Wm^{-2}
01.06.2008	15.07.2008	Global radiation 2 m[a]	SKYE	Wm^{-2}
01.06.2008	15.07.2008	Net radiation 2 m[a]	Kipp & Zonen NR-Lite	Wm^{-2}
01.06.2008	15.07.2008	Precipitation intensity 0.66 m[a]	Campbell Sci. ARG 100	mm
01.06.2008	15.07.2008	Wind vector (2D) 2.0, 1.0, 0.3, 0.04 m[a]	Vaisala 2D sonic anemometer, WS425	degree, ms^{-1}
01.06.2008	15.07.2008	Air temperature 2.16, 0.62 m (ventilated)[a]	Rotronic MP 100 A	°C
01.06.2008	15.07.2008	Air temperature 2.05, 1.0, 0.26, 0.09 m (dry, ventilated)[a]	MPI psychrometer, thermocouple	°C
01.06.2008	15.07.2008	Air temperature 2.05, 1.0, 0.26, 0.09 m (wet, ventilated)[a]	MPI psychrometer, thermocouple	°C
01.06.2008	14.07.2008	Air temperature 0.32, 0.16, 0.08, 0.04, 0.02, 0.01 m (not ventilated)[a]	MPI, thin-wire thermocouple	°C

(continued)

Table A7 (continued)

Operating since	Operating until	Short descriptions (altitudes are in meter above ground, depth information in cm)	Measurement device	Phys. unit
01.06.2008	15.07.2008	CO_2, H_2O, O_3, NO, NO_2 concentration 0.9, 0.3, 0.1, 0.03, 0.005 m[a]	RETGAP-System (CLD TR-780, BLC TEI 49c, Licor-840)	ppm mmol mol^{-1}ppb
01.06.2008	15.07.2008	Up- and downwelling NO_2 photolysis rate, j(NO_2) 1.0, 0.3 m[a]	Meteorologie Consult filter radiometer	s^{-1}
01.06.2008	15.07.2008	^{220}Rn and ^{222}Rn concentration 0.3, 0.1, 0.03, 0.00 m[a]	Alpha Guard, Vaisala GMP 343	Bq m^{-3}
01.06.2008	15.07.2008	^{222}Rn and CO_2 soil emission[a]	Static chamber, Alpha Guard, Vaisala GMP 343	Bq m^{-2} s^{-1}
01.06.2008	15.07.2008	HONO concentration 1.0 m	LOPAP (Kleffmann et al. 2002)	ppt
01.06.2008	15.07.2008	Barometric pressure 1 m[a]	Vaisala PTA427	hPa
01.06.2008	15.07.2008	Soil temperature −0.1, −0.16, −0.2, −0.32, −0.4, −0.8 m[a]	MPI thermocouple	°C
01.06.2008	15.07.2008	Soil temperature −0.02, −0.04, −0.08, −0.12, −0.16 m[a]	Campbell Sci. TP107	°C
01.06.2008	15.07.2008	Soil temperature (depth integrated) –0.01, −0.02, −0.04, −0.08 m[a]	Campbell Sci. special wired thermocouple	°C
01.06.2008	15.07.2008	Soil heat flux −0.08 (2x)[a]	Campbell Sci. HFT	W m^{-2}
Turbulence Tower M2		Position: see Fig. A2		
01.06.2008	14.07.2008	Wind vector, sonic temperature 23 m	Campbell CSAT3	ms^{-1}, °C
01.06.2008	14.07.2008	CO_2/H_2O flux/concentration 23 m	LiCor 7500 (open path)	mmol m^{-2} s^{-1}, mmol m^{-3}, g m^{-2} s^{-1}, g m^{-3}
01.06.2008	15.07.2008	Wind vector, sonic temperature 18 m	Gill 3D-ultrasonic R3	ms^{-1}, °C

(continued)

Table A7 (continued)

Operating since	Operating until	Short descriptions (altitudes are in meter above ground, depth information in cm)	Measurement device	Phys. unit
01.06.2008	15.07.2008	CO_2/H_2O flux/concentration 18 m[a]	LiCor 7500 (open path)	mmol m^{-2} s^{-1}, mmol m^{-3}, g m^{-2} s^{-1}, g m^{-3}
01.06.2008	14.07.2008	Wind vector, sonic temperature 13 m	Campbell CSAT3	ms^{-1}, °C
01.06.2008	14.07.2008	CO_2/H_2O flux/concentration 13 m	LiCor 7500 (open path)	mmol m^{-2} s^{-1}, mmol m^{-3}, g m^{-2} s^{-1}, g m^{-3}
06.06.2008	03.07.2008	Wind vector, sonic temperature 5.5 m	Campbell CSAT3	ms^{-1}, °C
06.06.2008	03.07.2008	CO_2/H_2O flux/concentration 5.5 m[a]	LiCor 7500 (open path)	mmol m^{-2} s^{-1}, mmol m^{-3}, g m^{-2} s^{-1}, g m^{-3}
01.06.2008	14.07.2008	wind vector, sonic temperature 2.25 m	Campbell CSAT3	ms^{-1}, °C
01.06.2008	14.07.2008	CO_2/H_2O flux/concentration 2.25 m	LiCor 7500 (open path)	mmol m^{-2} s^{-1}, mmol m^{-3}, g m^{-2} s^{-1}, g m^{-3}
Tower M3		Position: see Fig. A2		
16.06.2008	07.07.2008	CO_2 concentration profile 36.0, about 29, 24.1, 21.4, 18.7, 16.0, 1.0, 0.03 m	CO_2 profile system (Ruppert 2005)	ppm
29.05.2008	12.07.2008	Wind speed and direction 36 m[a]	Vector Instruments A100ML, WP200P	ms^{-1}, degree
01.06.2008	11.07.2008	Air temperature 22.6, 20.2, 17.2, 14.8, 11.7, 9.3 m (ventilated)[a]	Vaisala HMT337	°C
01.06.2008	11.07.2008	Relative humidity 22.6, 20.2, 17.2, 14.8, 11.7, 9.3 m (ventilated)[a]	Vaisala HMT337	%
29.05.2008	12.07.2008	Air temperature and humidity (not ventilated) 36 m[a]	Rotronic MP100A	°C, %
01.06.2008	11.07.2008	Net radiation 22.8, 17.4, 11.9 m [a]	Kipp & Zonen CNR1	Wm^{-2}
29.05.2008	12.07.2008	Net radiation 36 m[a]	Kipp & Zonen NRLite	Wm^{-2}

(continued)

Table A7 (continued)

Operating since	Operating until	Short descriptions (altitudes are in meter above ground, depth information in cm)	Measurement device	Phys. unit
01.06.2008	11.07.2008	Sap flow (1 tree):22.6, 20.2, 17.2, 14.8, 11.7, sap flow (8 trees) 1.4 m[a]	ICT HMR-30	L tree^{-1} h^{-1}
01.06.2008	11.07.2008	CO_2 and H_2O needle gas exchange[a]	Portable gas exchange system Walz GFS3000	μmol m^{-2} s^{-1} mmol m^{-2} s^{-1}
Modified Bowen ratio M4		Position: clearing, 200 m ENE from Main Tower	According to Liu and Foken (2001)	
01.06.2008	14.07.2008	Wind vector, sonic temperature 3.0 m	METEK USA-1	ms^{-1}, °C
01.06.2008	14.07.2008	Air temperature 0.85, 2.1 m (dry, ventilated)	Frankenberger psychrometer PT 100	°C
01.06.2008	14.07.2008	Air temperature 0.85, 2.1 m (wet, ventilated)	Frankenberger psychrometer PT 100	°C
27.05.2008	10.07.2008	Wind speed, and wind direction in the boundary layer[a]	Scintec flat array sodar (SFAS)	ms^{-1}, degree
31.05.2008	14.07.2008	Wind speed and direction 2.9 m[a]	Vector Instruments A100ML, WP200P	ms^{-1}, degree
31.05.2008	14.07.2008	Air temperature and humidity (not ventilated) 2.8, 1.1 m[a]	Rotronic MP100A	°C, %
31.05.2008	14.07.2008	Barometric pressure 1 m[a]	Vaisala PTB101B	hPa
31.05.2008	14.07.2008	Precipitation intensity 1 m[a]	Campbell Sci. ARG 100	mm
Small tower M5		Position: see Fig. A2		
23.05.2008	03.09.2008	Wind speed 1.0 m	Climatronics cup anemometer F460	ms^{-1}
23.05.2008	03.09.2008	Air temperature 1.0 m (dry, ventilated)	Frankenberger psychrometer PT 100	°C
23.05.2008	03.09.2008	Air temperature 1.0 m (wet, ventilated)	Frankenberger psychrometer PT 100	°C
23.05.2008	03.09.2008	Wind vector, sonic temperature 2.25 m [a]	METEK USA-1	ms^{-1}, °C

(continued)

Table A7 (continued)

Operating since	Operating until	Short descriptions (altitudes are in meter above ground, depth information in cm)	Measurement device	Phys. unit
11.06.2008	03.09.2008	CO_2 concentration profile 2 m	CO_2 profile system (Siebicke et al. 2011)	ppm
Small tower M6		Position: see Fig. A2		
23.05.2008	03.09.2008	Wind speed 1.0 m	Climatronics cup anemometer F460	ms^{-1}
23.05.2008	03.09.2008	Air temperature 1.0 m (dry, ventilated)	Frankenberger psychrometer PT 100	°C
23.05.2008	03.09.2008	Air temperature 1.0 m (wet, ventilated)	Frankenberger psychrometer PT 100	°C
23.05.2008	03.09.2008	Wind vector, sonic temperature 2.25 m[a]	METEK USA-1	ms^{-1}, °C
11.06.2008	03.09.2008	CO_2 concentration profile 2.25 m	CO_2 profile system (Siebicke et al. 2011)	ppm
Small tower M7		Position: see Fig. A2		
23.05.2008	03.09.2008	Wind speed 1.0 m	Climatronics cup anemometer F460	ms^{-1}
23.05.2008	03.09.2008	Air temperature 1.0 m (dry, ventilated)	Frankenberger psychrometer PT 100	°C
23.05.2008	03.09.2008	Air temperature 1.0 m (wet, ventilated)	Frankenberger psychrometer PT 100	°C
23.05.2008	03.09.2008	Wind vector, sonic temperature 2.25 m[a]	METEK USA-1	ms^{-1}, °C
11.06.2008	15.07.2008	CO_2/H_2O flux/concentration 2.25 m	LiCor 7500 (open path)	mmol m^{-2} s^{-1}, mmol m^{-3}, g m^{-2} s^{-1}, g m^{-3}
11.06.2008	03.09.2008	CO_2 concentration profile 2 m	CO_2 profile system (Siebicke et al. 2011)	ppm
Small tower M8 (M2)		Position: see Fig. A2		
01.06.2008	27.08.2008	Wind speed 1.0 m	Climatronics cup anemometer F460	ms^{-1}
01.06.2008	27.08.2008	Air temperature 1.0 m (dry, ventilated)	Frankenberger psychrometer PT 100	°C

(continued)

Table A7 (continued)

Operating since	Operating until	Short descriptions (altitudes are in meter above ground, depth information in cm)	Measurement device	Phys. unit
01.06.2008	27.08.2008	Air temperature 1.0 m (wet, ventilated)	Frankenberger psychrometer PT 100	°C
11.06.2008	03.09.2008	CO_2 concentration profile 2 m	CO_2 profile system (Siebicke et al. 2011)	ppm
Small tower M9		Position: see Fig. A2		
23.05.2008	03.09.2008	Wind speed 1.0 m	Climatronics cup anemometer F460	ms^{-1}
23.05.2008	03.09.2008	Air temperature 1.0 m (dry, ventilated)	Frankenberger psychrometer PT 100	°C
23.05.2008	03.09.2008	Air temperature 1.0 m (wet, ventilated)	Frankenberger psychrometer PT 100	°C
03.06.2008	03.09.2008	Wind vector, sonic temperature 2.25 m	METEK USA-1A	ms^{-1}, °C
11.06.2008	03.09.2008	CO_2 concentration profile 2 m	CO_2 profile system (Siebicke et al. 2011)	ppm
Small tower M10		Position: see Fig. A2		
23.05.2008	31.07.2008	Wind vector, sonic temperature 2.25 m[a]	METEK USA-1	ms^{-1}, °C
11.06.2008	03.09.2008	CO_2 concentration profile 2 m	CO_2 profile system (Siebicke et al. 2011)	ppm
Small tower M11		Position: see Fig. A2		
11.06.2008	03.09.2008	CO_2 concentration profile 2 m	CO_2 profile system (Siebicke et al. 2011)	ppm
Small tower M12		Position: see Fig. A2		
11.06.2008	03.09.2008	CO_2 concentration profile 2 m	CO_2 profile system (Siebicke et al. 2011)	ppm
Small tower M13		Position: see Fig. A2		
11.06.2008	03.09.2008	CO_2 concentration profile 2 m	CO_2 profile system (Siebicke et al. 2011)	ppm

(continued)

Table A7 (continued)

Operating since	Operating until	Short descriptions (altitudes are in meter above ground, depth information in cm)	Measurement device	Phys. unit
Small tower M14		Position: see Fig. A2		
11.06.2008	03.09.2008	CO_2 concentration profile 2 m	CO_2 profile system (Siebicke et al. 2011)	ppm
Waldstein-Pflanzgarten				
02.06.2008	15.07.2008	Wind speed, wind direction, and temperature profile in the boundary layer	Metek DSDPA.90/64 Sodar with 1290 MHz RASS extension	ms^{-1}, degree, °C

[a]Operated by Max-Planck-Institute (MPI) for Chemistry Mainz, Germany

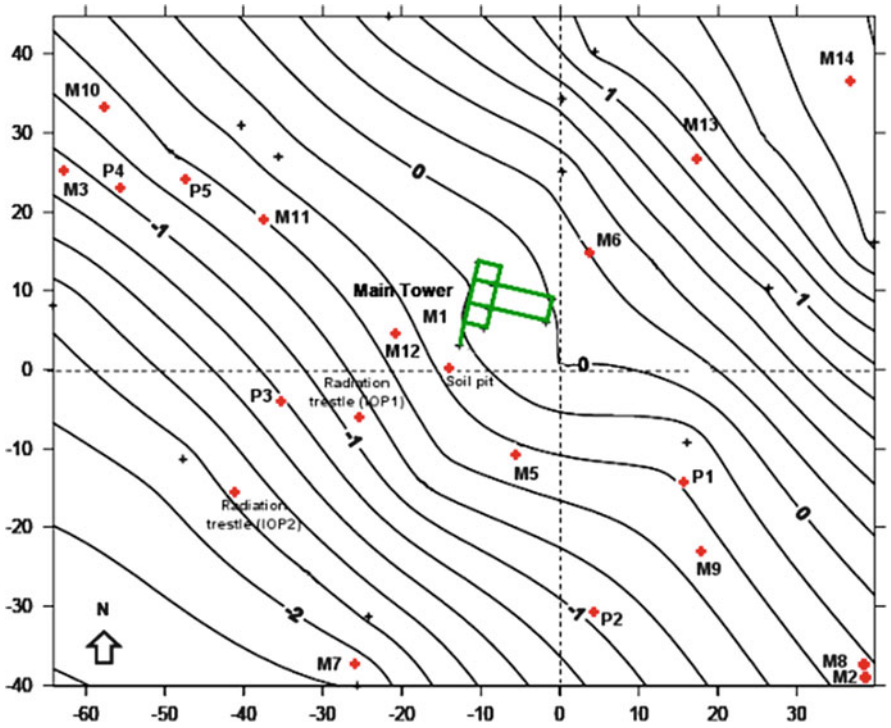

Fig. A2 Tower positions during the experiments EGER, IOP2, 2008, 0-line is 775 m a.s.l. (Serafimovich et al. 2008b, Published with kind permission of © Authors 2008, All rights reserved)

Table A8 Waldstein-Weidenbrunnen site, instrumentation at Main Tower, and other positions during the experiments EGER, IOP3, 2011. For further instrumentation, see Tables A1, A2, and A3 and for more details, see Serafimovich et al. (2011)

Operating since	Operating until	Short descriptions (altitudes are in meter above ground, depth information in cm)	Measurement device	Phys. unit
Main Tower M1				
14.06.2011	27.07.2001	O_3 flux, 32 m[a]	Enviscope	nmol m^{-2} s^{-1}
14.06.2011	27.07.2001	O_3 concentration, 32 m[a]	2B Technologies	ppb
Turbulence Tower M2		Position: see Fig. A3		
18.06.2011	26.07.2001	Wind vector, sonic temperature 26 m	METEK USA-1	ms^{-1}, °C
18.06.2011	26.07.2001	Wind vector, sonic temperature 2.25 m	METEK USA-1	ms^{-1}, °C
Tower M3		Position: see Fig. A3		
01.07.2011	25.07.2011	CO_2 concentration profile 36, 26, 13, 8, 5, 2.25, 1.0, 0.5 m	CO_2 profile system (Ruppert 2005)	ppm
15.06.2001	19.07.2011	Wind speed 39, 25, 21, 18, 13, 5 m	Climatronics cup anemometer F460	ms^{-1}
15.06.2001	19.07.2011	Air temperature 39, 25, 18, 13, 5 m (dry, ventilated)	Frankenberger psychrometer PT 100	°C
15.06.2001	19.07.2011	Air temperature 39, 25, 18, 13, 5 m (wet, ventilated)	Frankenberger psychrometer PT 100	°C
13.06.2011	26.07.2011	Air temperature 41 m (not ventilated)	HMP45, PT 100	°C
13.06.2011	26.07.2011	Relative humidity 41 m (not ventilated)	HMP45, capacitive	%
13.06.2011	26.07.2011	Wind vector, sonic temperature 41 m	Campbell CSAT3	ms^{-1}, °C
13.06.2011	26.07.2011	CO_2/H_2O flux / concentration 41 m	LiCor 7500 (open path)	mmol m^{-2} s^{-1}, mmol m^{-3}, g m^{-2} s^{-1}, g m^{-3}
13.06.2011	09.07.2011	Wind vector, sonic temperature 27 m[b]	METEK USA-1	ms^{-1}, °C
13.06.2011	09.07.2011	CO_2/H_2O flux/concentration 27 m[b]	LiCor 7500 (open path)	mmol m^{-2} s^{-1}, mmol m^{-3}, g m^{-2} s^{-1}, g m^{-3}
13.06.2011	09.07.2011	O_3 flux, 32 m[b]	Ozonesonde OSG-2 (Güsten and Heinrich 1996)	nmol m^{-2} s^{-1}

(continued)

Table A8 (continued)

Operating since	Operating until	Short descriptions (altitudes are in meter above ground, depth information in cm)	Measurement device	Phys. unit
13.06.2011	09.07.2011	O_3 concentration, 32 m[b]	2B Technologies	nmol
13.06.2011	13.06.2011	Wind vector, sonic temperature 2.25 m	Gill HS	ms^{-1}, °C
13.06.2011	13.06.2011	CO_2/H_2O flux/concentration 2.25 m	LiCor 7000 (closed path)	mmol m^{-2} s^{-1}, mmol m^{-3}, g m^{-2} s^{-1}, g m^{-3}
27.06.2011	26.07.2011	Wind vector, sonic temperature 2.25 m[c]	Campbell CSAT3	ms^{-1}, °C
27.06.2011	26.07.2011	CO_2/H_2O flux/concentration 2.25 m[c]	LiCor 7500 (open path)	mmol m^{-2} s^{-1}, mmol m^{-3}, g m^{-2} s^{-1}, g m^{-3}
13.06.2011	26.07.2011	Net radiation (four components) 2 m (north of M3)	Kipp & Zonen CNR1	W m^{-2}
13.06.2011	26.07.2011	Soil temperature −2, −5. –10, −20 cm (north of M3)	PT 100	°C
13.06.2011	26.07.2011	Soil humidity −10, −20 cm (north of M3)	IMKO TDR	%
13.06.2011	26.07.2011	Soil heat flux 2x −10 cm (north of M3)	CN3	Wm^{-2}
13.06.2011	26.07.2011	Net radiation (four components) 2 m (south of M3)	Kipp & Zonen CNR4 (ventilated)	W m^{-2}
13.06.2011	26.07.2011	Soil temperature −2, −5. –10, −20 cm (south of M3)	PT 100	°C
13.06.2011	26.07.2011	Soil humidity −10, −20 cm (south of M3)	IMKO TDR	%
13.06.2011	26.07.2011	Soil heat flux 2x −10 cm (south of M3)	CN3	Wm^{-2}
Small tower M4		Position: see Fig. A3		
13.06.2011	26.07.2011	Wind vector, sonic temperature 5.5 m	Campbell CSAT3	ms^{-1}, °C
13.06.2011	26.07.2011	CO_2/H_2O flux/concentration 5.5 m	LiCor 7500 (open path)	mmol m^{-2} s^{-1}, mmol m^{-3}, g m^{-2} s^{-1}, g m^{-3}
14.06.2011	26.07.2011	O_3 flux, 5.5 m[a]	Enviscope	nmol m^{-2} s^{-1}

(continued)

Table A8 (continued)

Operating since	Operating until	Short descriptions (altitudes are in meter above ground, depth information in cm)	Measurement device	Phys. unit
14.06.2011	26.07.2011	O_3 concentration, 5.5 m[a]	2B Technologies	nmol
13.06.2011	26.07.2011	Wind vector, sonic temperature 2.25 m	Campbell CSAT3	ms^{-1}, °C
13.06.2011	21.06.2011	CO_2/H_2O flux/concentration 2.25 m[d]	LiCor 7000 (closed path)	mmol m^{-2} s^{-1}, mmol m^{-3}, g m^{-2} s^{-1}, g m^{-3}
21.06.2011	26.07.2011	CO_2/H_2O flux/concentration 2.25 m[c]	LiCor 7200 (closed path)	mmol m^{-2} s^{-1}, mmol m^{-3}, g m^{-2} s^{-1}, g m^{-33}
18.06.2011	26.07.2011	Net radiation (four components) 2 m (south of M3)	Kipp & Zonen CNR4 (ventilated)	W m^{-2}
13.06.2011	26.07.2011	Incoming shortwave (global) radiation 30 m (above canopy)	Kipp & Zonen CM 24 (ventilated)	Wm^{-2}
13.06.2011	26.07.2011	Outgoing shortwave (reflected) radiation 30 m (above canopy)	Kipp & Zonen CM 24 (ventilated)	Wm^{-2}
13.06.2011	26.06.2011	Incoming longwave (back) radiation 30 m (above canopy)	Eppley PIR (ventilated)	Wm^{-2}
13.06.2011	26.06.2011	Outgoing longwave (emitted) radiation 30 m (above canopy)	Eppley PIR (ventilated)	Wm^{-2}
13.06.2011	26.07.2011	Soil temperature −2, −5. –10, −20, −50, −70, −100 cm	PT 100	°C
13.06.2011	26.07.2011	Soil humidity −5, −20 cm	IMKO TDR	%
13.06.2011	26.07.2011	Soil heat flux 2x −15 cm	HP3	Wm^{-2}
Modified Bowen ratio M5		Position: see Fig. A3	According to Liu and Foken (2001)	
14.07.2011	26.07.2011	Wind vector, sonic temperature 3.0 m	METEK USA-1	ms^{-1}, °C
14.07.2011	26.07.2011	Air temperature 0.6, 2.3 m (dry, ventilated)	Frankenberger psychrometer PT 100	°C
14.07.2011	26.07.2011	Air temperature 0.6, 2.3 m (wet, ventilated)	Frankenberger psychrometer PT 100	°C

(continued)

Table A8 (continued)

Operating since	Operating until	Short descriptions (altitudes are in meter above ground, depth information in cm)	Measurement device	Phys. unit
Small tower M6		Position: see Fig. A3		
20.06.2011	26.07.2011	Wind vector, sonic temperature 5.5 m[c]	Campbell CSAT3	ms^{-1}, °C
27.06.2011	26.07.2011	CO_2/H_2O flux/concentration 5.5 m[c]	LiCor 7500A (open path)	mmol m^{-2} s^{-1}, mmol m^{-3}, g m^{-2} s^{-1}, g m^{-3}
20.06.2011	26.07.2011	Wind vector, sonic temperature 2.25 m	METEK USA-1	ms^{-1}, °C
Small tower M7		Position: see Fig. A3		
20.06.2011	26.07.2011	Wind vector, sonic temperature 5.5 m[c]	Campbell CSAT3	ms^{-1}, °C
27.06.2011	26.07.2011	CO_2/H_2O flux/concentration 5.5 m[c]	LiCor 7500A (open path)	mmol m^{-2} s^{-1}, mmol m^{-3}, g m^{-2} s^{-1}, g m^{-3}
20.06.2011	26.07.2011	Wind vector, sonic temperature 2.25 m[c]	Campbell CSAT3	ms^{-1}, °C
Small tower M8		Position: see Fig. A3		
13.06.2011	26.07.2011	Wind vector, sonic temperature 2.25 m	METEK USA-1	ms^{-1}, °C
24.06.2011	26.07.2011	O_3 concentration, 1 m	Thermo 49i	ppb
Small tower CM		Position: see Fig. A3		
14.06.2011	26.07.2011	Leaf wetness, < 0.4 m	Leaf wetness sensors (Klemm et al. 2002)	–
14.06.2011	26.07.2011	Air temperature 1.0 m (dry, ventilated)	MPI psychrometer PT 100	°C
14.06.2011	26.07.2011	Air temperature 1.0 m (wet, ventilated)	MPI psychrometer PT 100	°C
14.06.2011	26.07.2011	NO_2 photolysis rate, 2 m	filter radiometer	s^{-1}
14.06.2011	26.07.2011	O_3 mixing ratio, 0.1–1.6 m (Lift)	Thermo 49i	ppb
14.06.2011	26.07.2011	NO_x mixing ratio, 0.1–1.6 m (Lift)	Thermo 42i TL	ppb
14.06.2011	26.07.2011	HONO mixing ratio, 0.1–1.6 m (Lift)	LOPAP-03 (Kleffmann et al. 2002)	ppt

(continued)

Table A8 (continued)

Operating since	Operating until	Short descriptions (altitudes are in meter above ground, depth information in cm)	Measurement device	Phys. unit
HMMS		Position: see Fig. A3	According to Hübner et al. (2014)	
24.06.2011	19.07.2011	O_3 concentration, 1 m	Enviscope	ppb
13.06.2011	19.07.2011	CO_2 concentration 1 m	Edinburgh Instr. Ltd. Gascard NG	ppm
13.06.2011	19.07.2011	Air temperature 1 m (ventilated)	HMP45, PT 100	°C
13.06.2011	19.07.2011	Relative humidity 1 m (ventilated)	HMP45, capacitive	%
13.06.2011	19.07.2011	Incoming shortwave (global) radiation 1 m	Kipp & Zonen CMP 3	Wm^{-2}
13.06.2011	19.07.2011	Outgoing shortwave (reflected) radiation 1 m	Kipp & Zonen CMP 3	Wm^{-2}
13.06.2011	19.07.2011	Incoming longwave (back) radiation 1 m	Kipp & Zonen CGR 3	Wm^{-2}
13.06.2011	19.07.2011	Outgoing longwave (emitted) radiation 1 m	Kipp & Zonen CGR 3	Wm^{-2}
Köhlerloh clearing		Position: see Fig. A3		
14.06.2011	26.07.2011	CO_2 and H_2O needle/leaf gas exchange for six representative species[a]	Portable gas exchange system Walz GFS3000	$\mu mol\ m^{-2}\ s^{-1}$ $mmol\ m^{-2}\ s^{-1}$
30.06.2011	26.07.2011	Momentum and sensible heat flux[d]	Scintillometer SLS-40	ms^{-1}, Wm^{-2}
24.06.2011	26.07.2011	Wind speed, wind direction, and temperature profile in the boundary layer[e]	Scintec mini sodar	ms^{-1}, degree, °C
Waldstein-Pflanzgarten				
13.06.2011	26.07.2011	Wind speed, wind direction, and temperature profile in the boundary layer	Metek DSDPA.90/64 Sodar with 1290 MHz RASS extension	ms^{-1}, degree, °C
18.05.2011	18.09.2011	Aerosol size distribution 2.5 m	Scanning mobility particle spectrometer	cm^{-3}

[a]Operated by Max-Planck-Institute (MPI) for Chemistry Mainz, Germany
[b]Operated by Joined Research Institute, Ispra, Italy
[c]Operated by Washington State University, Pullman, USA
[d]Operated by Karlsruhe Institute of Technology, IFU, Garmisch-Partenkirchen, Germany
[e]Operated by University of Georgia, Griffin, USA

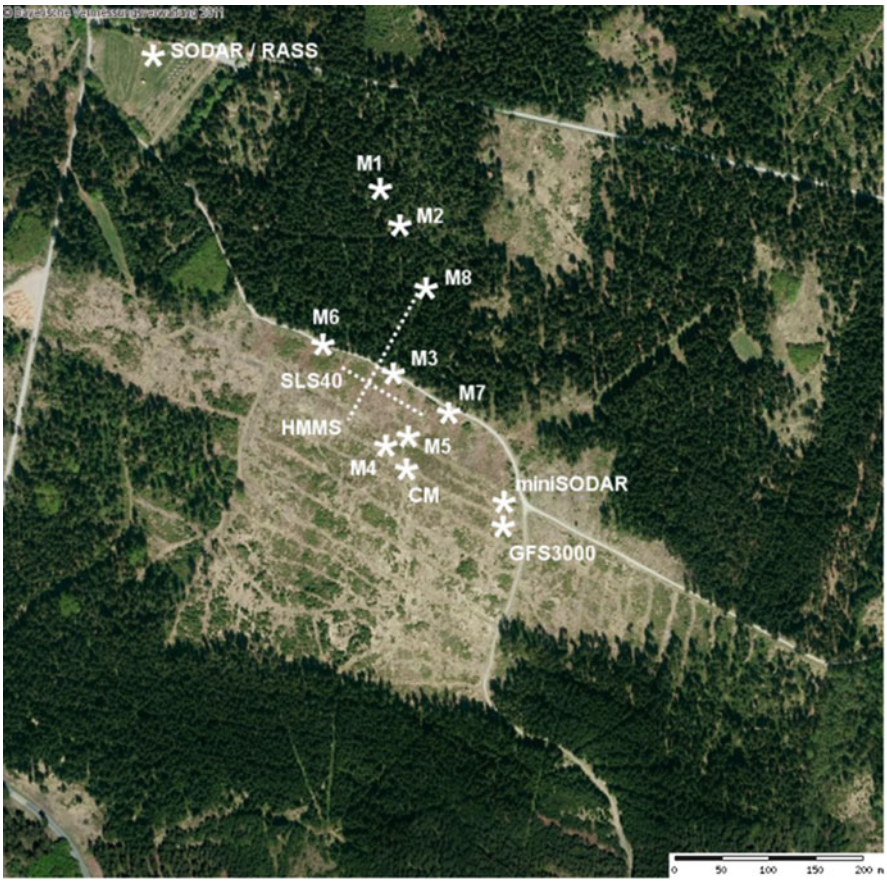

Fig. A3 Tower positions during the experiments EGER, IOP3, 2011 (Serafimovich et al. 2011, Published with kind permission of © Authors, Bayerische Vermessungsverwaltung 2011, All rights reserved)

References

Bargsten A, Falge E, Pritsch K, Huwe B, Meixner FX (2010) Laboratory measurements of nitric oxide release from forest soil with a thick organic layer under different understory types. Biogeosciences 7:1425–1471

Behrendt T, Veres PR, Ashuri F, Song G, Flanz M, Mamtimin B, Bruse M, Williams J, Meixner FX (2014) Characterisation of NO production and consumption: new insights by an improved laboratory dynamic chamber technique. Biogeosciences 11:5463–5492

Breuninger C, Meixner FX, Kesselmeier J (2013) Field investigations of nitrogen dioxide (NO_2) exchange between plants and the atmosphere. Atmos Chem Phys 13:773–790

Foken T, Meixner FX, Falge E, Zetzsch C, Serafimovich A, Bargsten A, Behrendt T, Biermann T, Breuninger C, Dix S, Gerken T, Hunner M, Lehmann-Pape L, Hens K, Jocher G, Kesselmeier J, Lüers J, Mayer JC, Moravek A, Plake D, Riederer M, Rütz F, Scheibe M, Siebicke L, Sörgel M, Staudt K, Trebs I, Tsokankunku A, Welling M, Wolff V, Zhu Z (2012) Coupling processes

and exchange of energy and reactive and non-reactive trace gases at a forest site—results of the EGER experiment. Atmos Chem Phys 12:1923–1950

Frankenberger E (1951) Untersuchungen über den Vertikalaustausch in den unteren Dekametern der Atmosphäre. Ann Meteorol 4:358–374

Grabmer W, Kreuzwieser J, Wisthaler A, Cojocariu C, Graus M, Rennenberg H, Steigner D, Steinbrecher R, Hansel A (2006) VOC emissions from Norway spruce (*Picea abies* L. [Karst]) twigs in the field—results of a dynamic enclosure study. Atmos Environ 40:S128–S137

Graus M, Hansel A, Wisthaler A, Lindinger C, Forkel R, Hauff K, Klauer M, Pfichner A, Rappenglück B, Steigner D, Steinbrecher R (2006) A relaxed-eddy-accumulation (REA) method using an online gas-chromatographic technique and PTR-MS for the measurement of isoprenoid canopyfluxes. Atmos Environ 40:S43–S54

Güsten H, Heinrich G (1996) On-line measurements of ozone surface fluxes: Part I. Methodology and instrumentation. Atmos Environ 30:897–909

Held A, Nowak A, Birmili W, Wiedensohler A, Forkel R, Klemm O (2004) Observations of particle formation and growth in a mountainous forest region in central Europe. J Geophys Res D109:D23204

Held A, Klemm O (2006) Direct measurement of turbulent particle exchange with a twin CPC eddy covariance system. Atmos Environm 40(Supplement 1):92–102

Hübner J, Olesch J, Falke H, Meixner FX, Foken T (2014) A horizontal mobile measuring system for atmospheric quantities. Atmos Meas Tech 7:2967–2980

Kleffmann J, Heland J, Lörzer JC, Wiesen P (2002) A new instrument (LOPAP) for the detection of nitrous acid (HONO). Environ Sci Pollut Res 9:48–54

Klemm O, Milford C, Sutton MA, Spindler G, van Putten E (2002) A climatology of leaf surface wetness. Theor Appl Climatol 71:107–117

Klemm O, Held A, Forkel R, Gasche R, Kanter H-J, Rappenglück B, Steinbrecher R, Müller K, Plewka A, Cojocariu C, Kreuzwieser J, Valverde-Canossa J, Schuster G, Moortgat GK, Graus M, Hansel A (2006) Experiments on forest/atmosphere exchange: climatology and Fluxes during two summer campaigns in NE Bavaria. Atmos Environ 40(Supplement 1):3–20

Klemm O, Wrzesinsky T, Gerchau J, Griessbaum F (2008) A collector for fog water and interstitial aerosol. J Atmos Ocean Technol 25:335–340

Kreuzwieser J, Cojocariu C, Jüssen V, Rennenberg H (2002) Elevated atmospheric CO_2 causes seasonal changes in carbonyl emissions from a Mediterranean oak species. New Phytol 154:327–333

Liu H, Foken T (2001) A modified Bowen ratio method to determine sensible and latent heat fluxes. Meteorol Z 10:71–80

Müller K, Haferkorn S, Grabmer W, Wisthaler W, Hansel A, Kreuzwieser J, Cojocariu C, Rennenberg H, Herrmann H (2006) Biogenic carbonyl compounds from a coniferous forest in Germany. Atmos Environ 40:S81–S91

Plewka A, Gnauk T, Brüggemann E, Herrmann H (2006) Biogenic contributions to the chemical composition of airborne particles in a coniferous forest in Germany. Atmos Environ 40:S103–S115

Ruppert J (2005) ATEM software for atmospheric turbulent exchange measurements using eddy covariance and relaxed eddy accumulation systems and Bayreuth whole-air REA system setup. Arbeitsergebn, Univ Bayreuth, Abt Mikrometeorol, ISSN 1614–8916. 28:27

Ruppert J, Riederer M, Brand WA and Foken T (2012) Whole-air relaxed eddy accumulation for the measurement of isotope and trace-gas fluxes. Arbeitsergebn, Univ Bayreuth, Abt Mikrometeorol, ISSN 1614–8916. 51:27

Serafimovich A, Siebicke L, Staudt K, Lüers J, Biermann T, Schier S, Mayer J-C and Foken T (2008a) ExchanGE processes in mountainous Regions (EGER): Documentation of the Intensive Observation Period (IOP1), September, 6th to October, 7th 2007. Arbeitsergebn, Univ Bayreuth, Abt Mikrometeorol, ISSN 1614–8916. 36:145 pp

Serafimovich A, Siebicke L, Staudt K, Lüers J, Hunner M, Gerken T, Schier S, Biermann T, Rütz F, Buttlar Jv, Riederer M, Falge E, Mayer J-C and Foken T (2008b) ExchanGE processes in mountainous Regions (EGER): Documentation of the Intensive Observation Period (IOP2)

June, 1st to July, 15th 2008. Arbeitsergebn, Univ Bayreuth, Abt Mikrometeorol, ISSN 1614–8916. 37:180 pp

Serafimovich A, Eder F, Hübner J, Falge E, Voß L, Sörgel M, Held A, Liu Q, Eigenmann R, Huber K, Duarte HF, Werle P, Gast E, Cieslik S, Liu H and Foken T (2011) ExchanGE processes in mountainous Regions (EGER)-Documentation of the Intensive Observation Period (IOP3) June, 13th to July, 26th 2011. Arbeitsergebn, Univ Bayreuth, Abt Mikrometeorol, ISSN 1614–8916. 47:135

Siebicke L, Steinfeld G, Foken T (2011) CO_2-gradient measurements using a parallel multi-analyzer setup. Atmos Meas Tech 4:409–423

Thomas C, Ruppert J, Lüers J, Schröter J, Mayer J-C and Bertolini T (2004) Documentation of the WALDATEM-2003 Experiment April, 28th to August, 03rd 2003. Arbeitsergebn, Univ Bayreuth, Abt Mikrometeorol, ISSN 1614–8916. 24:57

Valverde-Canossa J, Ganzeveld L, Rappenglück B, Steinbrecher R, Klemm O, Schuster G, Moortgat GK (2006) First Measurements of H_2O_2 and organic peroxides surface fluxes by the relaxed eddy accumulation technique. Atmos Environ 40:S55–S67

Wyers GP, Otjes RP, Slanina J (1993) A continuous-flow denuder for the measurement of ambient concentrations and surface-exchange fluxes of ammonia. Atmos Environ Part A 27:2085–2090

Appendix B
Important Measurements at Waldstein-Pflanzgarten and Waldstein-Weidenbrunnen Sites

Compiled by Johannes Lüers, Wolfgang Babel, and Corinna Rebmann

For site description, see Chap. 2, and for instrumentation, see Appendix A.

T. Foken (ed.), *Energy and Matter Fluxes of a Spruce Forest Ecosystem*,
Ecological Studies 229, DOI 10.1007/978-3-319-49389-3

Table B1 Mean monthly air temperature at 2 m above ground in °C at Waldstein-Pflanzgarten site, 765 m a.s.l., for the period 1994–2015, extreme values are typed shown in italic and bold. For climate analysis, see Chap. 3

Year	Jan	Feb	Mar	Apr	May	Jun	Jul	Aug	Sep	Oct	Nov	Dec	Annual mean
1994	−0.7	−3.2	3.2	4.4	9.8	13.6	19.0	15.3	10.7	4.9	3.7	0.1	6.8
1995	−4.0	0.9	−0.4	5.4	9.5	***11.0***	17.9	15.6	9.6	9.1	−1.5	−4.8	5.7
1996	***−6.6***	−5.4	−2.5	5.2	***8.1***	13.3	12.5	14.3	***7.5***	6.5	1.1	−6.0	***4.0***
1997	−4.5	0.4	2.9	***2.9***	10.2	12.9	14.1	17.1	11.7	4.3	0.7	−1.6	6.0
1998	−1.0	1.0	0.9	6.1	11.1	14.1	13.4	14.1	10.2	5.4	***−1.7***	−2.5	6.0
1999	−1.4	−3.9	1.9	5.6	11.1	12.2	15.9	14.1	14.1	5.5	0.0	−1.9	6.2
2000	−3.4	0.1	1.5	7.5	***12.4***	14.7	***12.2***	15.6	11.0	7.8	2.7	−0.5	6.8
2001	−3.0	−0.9	1.1	3.7	11.8	11.4	15.7	16.4	8.4	***9.9***	0.2	−3.7	6.0
2002	−2.0	***1.9***	2.6	5.2	11.8	15.7	15.6	16.5	10.4	5.6	2.9	−2.6	7.0
2003	−3.6	−4.8	3.0	5.1	12.0	***17.7***	16.1	***19.0***	11.5	***3.0***	3.4	−1.2	6.8
2004	−3.7	−0.9	0.8	6.6	8.6	13.0	14.6	15.8	11.4	7.5	1.4	−2.3	6.1
2005	−1.5	−4.9	0.3	6.9	10.7	14.2	15.8	13.4	12.8	8.4	0.9	−2.4	6.3
2006	−5.3	−3.2	−1.4	5.4	10.6	14.7	19.8	***12.5***	***14.2***	9.6	3.9	1.6	6.9
2007	***1.3***	1.5	3.4	9.3	12.2	15.0	14.9	14.5	9.7	5.8	−0.1	−1.2	7.2
2008	0.3	1.2	0.9	5.1	12.1	15.2	15.6	15.0	9.9	6.7	2.4	−1.9	6.9
2009	−4.9	−2.9	0.8	***10.0***	11.4	12.2	15.4	16.6	12.6	5.3	***4.5***	−2.4	6.6
2010	−6.6	−3.5	0.7	6.2	8.2	14.4	18.1	14.1	9.5	5.0	2.1	***−6.1***	5.2
2011	−1.7	−2.9	3.0	9.2	11.8	14.2	13.6	15.9	13.2	6.9	2.5	0.5	7.2
2012	−1.5	***−6.6***	4.5	5.7	12.3	13.8	15.1	16.3	11.3	5.8	2.2	−1.5	6.5
2013	−4.1	−4.2	***−3.2***	5.2	8.9	14.0	***20.0***	17.1	12.7	8.3	1.8	0.5	6.5
2014	−0.3	0.7	***4.8***	8.5	9.5	13.8	16.9	13.3	12.3	9.7	4.5	0.6	7.9
2015	0.1	−1.4	3.4	6.7	10.9	13.9	18.2	18.7	10.3	5.7	4.5	***3.9***	***8.0***

Waldstein-Pflanzgarten long-term values 1994–2015:													
Coldest one	−6.6	−6.6	−3.2	2.9	8.1	11.0	12.2	12.5	7.5	3.0	−1.7	−6.1	**4.0**
Mean	**−2.6**	**−1.9**	**1.5**	**6.2**	**10.7**	**13.9**	**15.9**	**15.5**	**11.1**	**6.7**	**1.9**	**−1.6**	**6.5**
Warmest one	1.3	1.9	4.8	10.0	12.4	17.7	20.0	19.0	14.2	9.9	4.5	3.9	**8.0**

Table B2 Monthly sum of precipitation in mm at Waldstein-Pflanzgarten site, 765 m a.s.l., for the period 1994–2015, extreme values are typed italic and bold. For climate analysis, see Chap. 3

Year	Jan	Feb	Mar	Apr	May	Jun	Jul	Aug	Sep	Oct	Nov	Dec	Annual sum
1994	149.0	54.5	166.1	92.7	77.9	69.2	86.8	159.2	99.0	113.7	100.3	179.6	***1348***
1995	183.2	123.7	81.8	***101.3***	52.9	***164.9***	157.8	121.5	123.4	***16.8***	62.8	71.6	1262
1996	***2.9***	45.6	36.3	38.4	124.4	64.0	***190.1***	118.4	57.0	49.5	36.2	***21.5***	784
1997	10.3	76.0	41.6	26.8	26.5	27.0	95.7	24.0	***14.5***	79.9	25.2	96.6	***544***
1998	73.0	29.9	102.0	67.1	64.9	117.1	178.5	96.4	***197.6***	***242.1***	97.6	37.5	1304
1999	91.4	78.1	86.0	47.7	119.4	108.6	156.8	114.8	105.5	73.7	78.6	122.7	1183
2000	83.5	81.1	133.4	47.9	46.5	105.7	185.8	53.6	65.8	73.5	44.5	61.0	982
2001	73.6	44.0	***169.0***	95.1	***22.8***	107.1	128.5	27.8	171.4	53.3	121.8	182.5	1197
2002	113.9	***215.3***	88.7	40.1	59.8	63.4	49.6	139.1	68.9	144.1	147.4	86.8	1217
2003	93.7	34.3	18.3	41.7	74.3	39.0	93.2	***18.5***	58.9	83.9	33.1	63.8	653
2004	93.8	42.7	51.9	54.9	94.2	81.9	134.2	107.2	108.4	74.8	122.1	62.3	1028
2005	154.4	109.8	52.2	38.7	79.6	62.0	122.5	137.6	116.2	25.1	47.8	107.3	1053
2006	33.9	58.4	127.7	93.4	171.2	44.0	***42.8***	150.6	31.0	96.3	67.7	55.8	973
2007	166.9	82.0	76.9	***8.4***	162.8	159.0	117.1	120.4	143.4	17.7	147.6	97.3	1300
2008	75.6	59.0	167.0	82.0	32.2	30.9	111.9	109.7	80.6	145.2	83.3	76.0	1053
2009	50.7	74.6	86.9	81.4	93.6	89.7	116.9	40.6	66.3	82.2	95.8	108.0	987
2010	70.2	66.3	73.5	31.0	107.2	67.3	93.9	***264.0***	85.1	34.8	140.9	140.6	1175
2011	114.5	30.9	14.6	35.7	48.0	113.3	120.5	62.8	105.2	82.0	***1.5***	***214.9***	944
2012	***201.0***	49.6	***13.2***	38.7	54.4	101.3	171.7	47.9	67.8	77.3	97.4	147.1	1067
2013	109.8	70.0	39.5	48.0	***198.8***	121.8	43.4	71.5	125.5	68.4	120.5	35.2	1052

2014	44.1	37.1	30.1	53.9	129.6	***25.2***	146.7	102.5	88.5	74.9	39.2	112.3	884
2015	121.6	***17.6***	85.2	54.4	28.2	88.7	70.5	58.5	35.5	34.4	***170.5***	78.3	843
Mean long-term sums:													
Waldstein-Pfg. 1994–2015	96	67	79	55	85	84	119	98	92	79	86	98	**1038**

Table B3 Monthly sum of evapotranspiration in mm above the spruce forest at Waldstein-Weidenbrunnen site, 775 m a.s.l., for the period 1997–2014, for details see Rebmann (2004, period 1997–2001) and Chap. 4 (period 2002–2014), light-shaded data: more than 50 % are modelled; dark-shaded data (only available for 2002–2014): more than 95 % are modelled

year	Jan	Feb	Mar	Apr	May	Jun	Jul	Aug	Sep	Oct	Nov	Dec	annual sum
1997	7.0	7.7	10.1	32.4	45.9	44.9	45.9	53.9	34.2	13.8	3.0	2.6	301
1998	1.4	5.1	9.2	27.0	39.1	59.7	53.1	66.9	23.3	8.1	2.2	3.8	299
1999	5.5	4.3	11.5	28.3	49.8	53.4	57.4	55.3	40.0	9.9	4.2	1.2	320
2000	1.6	3.8	10.8	24.6	43.7	51.7	32.1	49.2	21.3	8.7	3.7	2.4	254
2001	1.0	4.0	5.6	15.1	40.0	33.0	44.2	36.6	11.9	14.0	4.4	0.9	211
2002	4.0	6.2	19.2	28.7	45.5	64.6	63.3	50.2	37.5	20.0	9.8	3.2	352
2003	2.3	14.1	18.1	38.3	58.1	72.7	72.1	61.3	39.7	17.7	9.4	9.2	413
2004	4.3	8.5	18.2	44.9	52.2	68.2	66.7	67.1	45.4	26.7	5.8	7.0	415
2005	4.5	7.1	24.0	40.6	58.3	62.0	73.9	61.9	45.1	22.4	8.5	4.0	412
2006	4.5	7.1	17.0	39.1	58.2	70.9	75.6	41.6	50.7	23.3	12.1	6.9	407
2007	3.4	9.1	26.3	63.8	65.8	70.7	73.9	59.9	32.5	22.3	6.0	9.1	443
2008	14.5	17.2	19.6	37.2	65.4	67.3	77.7	59.2	40.7	23.8	8.9	3.3	435
2009	4.9	6.6	20.9	50.4	70.8	73.2	85.4	78.1	42.6	24.1	26.8	7.4	491
2010	2.3	17.0	26.7	47.2	47.2	71.0	77.2	43.1	31.1	23.8	17.3	4.2	408
2011	3.9	10.4	21.4	41.3	69.0	74.2	79.0	83.0	52.0	30.0	14.0	9.5	488
2012	4.3	10.3	31.7	53.0	79.5	86.8	98.3	83.6	58.5	35.1	17.4	11.8	570
2013	3.3	8.0	22.7	39.8	63.5	71.9	81.7	80.3	48.4	43.0	16.1	18.3	497
2014	12.7	22.5	39.2	53.8	64.5	84.6	93.8	80.5	45.8	34.4	15.0	15.0	562

Table B4 Monthly sum of potential evapotranspiration (Priestley-Taylor) in mm above the spruce forest at Waldstein-Weidenbrunnen site, 775 m a.s.l., for the period 2002–2014. For details, see Chap. 4

Year	Jan	Feb	Mar	Apr	May	Jun	Jul	Aug	Sep	Oct	Nov	Dec	Annual sum
2002	10.5	16.1	49.0	76.1	110.6	153.5	133.0	106.0	71.9	27.6	11.9	7.4	774
2003	7.5	28.8	58.5	90.7	128.9	185.2	148.5	159.2	83.6	31.0	15.2	9.1	946
2004	7.8	17.5	45.7	94.2	100.7	134.9	135.1	119.3	83.0	37.1	9.8	9.1	794
2005	8.4	15.3	49.5	84.9	128.7	151.6	131.6	100.9	70.4	48.6	12.9	5.4	808
2006	10.7	16.7	37.8	70.1	121.9	168.3	193.1	83.1	107.3	42.8	14.6	11.4	878
2007	7.9	20.3	58.1	138.8	142.5	151.2	140.8	117.4	61.4	37.7	11.4	9.3	897
2008	10.6	29.0	43.3	79.7	143.7	158.1	138.9	121.7	67.0	36.1	15.6	7.3	851
2009	11.6	15.8	35.8	114.3	135.4	123.1	136.1	146.3	87.6	27.3	11.4	6.7	852
2010	5.7	5.9	47.6	98.9	79.8	151.6	164.1	91.7	66.6	41.2	10.6	7.2	771
2011	8.4	18.2	49.6	89.8	123.1	142.3	122.4	128.1	93.5	45.7	7.2	6.8	835
2012	10.0	19.4	66.5	76.2	68.8	124.2	67.1	111.6	89.1	43.7	12.7	7.5	697
2013	6.8	12.7	41.4	74.7	77.5	129.8	176.1	129.4	48.9	39.0	10.3	10.9	757
2014	9.2	22.8	61.2	81.7	107.5	152.1	149.6	75.2	63.1	37.8	14.0	5.4	780

Table B5 Monthly sum of carbon NEE in g C m^{-2} above the spruce forest at Waldstein-Weidenbrunnen site, 775 m a.s.l., for the period 1997–2014, for details see Rebmann (2004, period 1997–2001) and Chap. 4 (period 2002–2014), light-shaded data: more than 50 % are modelled; dark-shaded data (only available for 2002–2014): more than 95 % are modelled

year	Jan	Feb	Mar	Apr	May	Jun	Jul	Aug	Sep	Oct	Nov	Dec	annual sum
1997	26.1	15.4	3.4	-34.8	-66.8	-42.6	-22.0	14.2	-18.2	10.9	28.5	31.2	-55
1998	24.9	15.0	5.4	-47.1	-55.5	-55.4	-18.4	-21.1	29.3	33.6	24.0	24.2	-41
1999	25.4	17.8	-6.1	-36.3	-51.0	-55.5	-14.0	-9.5	16.7	23.6	29.5	24.6	-35
2000	19.1	3.0	-15.5	-46.9	-84.7	-73.4	-59.2	-17.3	11.3	40.4	31.4	45.9	-146
2001	23.5	7.3	14.0	-37.1	-52.9	-43.1	-39.4	-9.3	23.9	34.0	32.3	22.5	-24
2002	21.8	29.6	0.4	-33.6	-86.3	-109.7	-71.4	-39.9	-18.4	0.4	44.0	25.6	-238
2003	21.0	20.9	-5.8	-41.1	-89.7	-82.0	-71.6	-49.3	-61.1	4.3	38.3	28.2	-288
2004	18.3	16.9	5.4	-66.5	-104.7	-125.2	-81.8	-39.3	-45.7	-13.0	30.0	28.9	-377
2005	22.5	15.4	-15.1	-66.2	-85.4	-102.2	-75.4	-56.4	-10.0	-20.0	16.7	22.6	-354
2006	16.0	18.2	15.7	-40.7	-107.3	-93.9	-39.9	-60.3	-57.9	-14.4	30.1	33.2	-301
2007	35.5	30.0	-30.0	-124.1	-117.3	-108.9	-90.1	-79.2	-58.6	-18.4	28.4	35.3	-497
2008	21.5	20.5	18.4	-37.7	-129.5	-148.2	-109.8	-83.1	-60.5	-20.1	5.9	31.0	-492
2009	17.3	17.1	29.5	-91.3	-125.1	-126.6	-104.1	-90.9	-67.8	0.6	27.0	23.8	-490
2010	12.5	20.4	-2.4	-73.5	-95.6	-124.1	-65.7	-54.3	-62.0	-33.8	23.2	12.4	-443
2011	26.0	17.2	-16.9	-98.9	-119.9	-131.3	-117.2	-101.0	-72.5	-25.7	3.3	28.6	-608
2012	26.7	34.9	-40.3	-35.4	-138.8	-145.7	-142.1	-104.5	-101.6	-54.0	29.3	20.0	-652
2013	22.0	13.8	14.4	-46.4	-125.3	-109.8	-97.9	-114.2	-73.8	-33.7	14.8	28.3	-508
2014	15.3	19.8	-27.6	-78.3	-100.6	-164.1	-104.4	-121.0	-66.8	-63.0	-30.9	29.3	-692

Table B6 Monthly sum of carbon respiration in g C m^{-2} above the spruce forest at Waldstein-Weidenbrunnen site, 775 m a.s.l., for the period 1997–2014. For details, see Rebmann (2004, period 1997–2001) and Chap. 4 (period 2002–2014)

Year	Jan	Feb	Mar	Apr	May	Jun	Jul	Aug	Sep	Oct	Nov	Dec	Annual sum
1997	30.9	33.1	58.9	55.6	108.5	172.9	175.3	252.6	145.7	81.8	51.7	36.0	1203
1998	43.0	52.1	54.5	90.4	154.7	171.6	173.8	186.9	150.4	80.4	34.1	32.4	1224
1999	34.8	22.8	56.8	79.8	145.9	148.6	223.3	191.3	206.3	92.6	45.5	31.3	1279
2000	35.2	45.7	65.2	152.1	235.1	265.9	200.4	276.1	207.3	163.5	87.5	67.7	1802
2001	38.7	47.1	67.7	85.0	206.0	202.0	283.6	303.4	140.0	170.9	60.4	33.9	1639
2002	24.8	37.7	45.5	59.1	126.9	155.0	169.6	164.9	101.4	70.7	51.1	26.3	1033
2003	22.7	23.3	49.6	70.1	124.5	180.9	163.9	180.2	107.1	56.2	54.5	35.4	1068
2004	21.6	30.2	38.6	76.4	88.2	117.7	154.5	165.2	113.1	79.5	40.7	34.2	960
2005	30.5	16.8	41.9	73.8	108.8	137.6	149.1	134.4	131.1	90.7	39.0	25.6	979
2006	17.0	19.6	30.0	61.7	107.1	142.6	202.7	116.0	138.7	93.9	55.6	42.6	1027
2007	40.3	34.0	49.7	91.8	119.6	152.5	167.1	151.6	91.6	72.3	31.7	44.7	1047
2008	37.3	48.3	36.1	58.0	120.4	148.3	159.4	147.4	102.4	81.8	46.0	33.1	1018
2009	17.3	22.9	39.9	98.9	120.9	128.1	166.5	171.1	119.5	89.8	66.5	30.7	1072
2010	12.5	32.2	46.7	69.3	85.3	133.5	181.3	133.6	88.8	74.3	62.2	15.6	935
2011	27.7	22.1	48.1	88.2	123.5	136.1	145.8	164.5	126.2	80.5	51.6	36.7	1051
2012	27.2	36.6	57.5	70.2	132.9	143.1	160.4	162.7	112.3	80.1	58.5	33.1	1075
2013	24.0	20.7	29.1	66.4	125.5	142.9	175.1	159.8	128.1	104.6	55.8	64.5	1097
2014	41.0	36.8	68.4	90.1	113.5	141.1	177.0	142.4	129.9	102.9	62.1	44.7	1150

Table B7 Monthly sum of carbon assimilation in g C m^{-2} above the spruce forest at Waldstein-Weidenbrunnen site, 775 m a.s.l., for the period 1997–2014. For details, see Rebmann (2004, period 1997–2001) and Chap. 4 (period 2002–2014)

Year	Jan	Feb	Mar	Apr	May	Jun	Jul	Aug	Sep	Oct	Nov	Dec	Annual sum
1997	−4.8	−17.7	−55.5	−90.4	−175.2	−215.5	−197.4	−238.4	−163.8	−70.8	−23.2	−4.8	−1257
1998	−18.2	−37.1	−49.0	−137.5	−210.2	−227.1	−192.2	−208.0	−121.1	−46.8	−10.0	−8.2	−1265
1999	−9.5	−5.0	−62.9	−116.2	−196.9	−204.0	−237.3	−200.8	−189.6	−69.0	−15.9	−6.7	−1314
2000	−16.1	−42.7	−80.7	−199.0	−319.7	−339.3	−259.5	−293.4	−196.0	−123.0	−56.1	−21.8	−1947
2001	−15.2	−39.9	−53.7	−122.1	−258.9	−245.1	−322.9	−312.7	−116.1	−136.9	−28.1	−11.4	−1663
2002	−3.0	−8.1	−45.1	−92.7	−213.2	−264.7	−241.0	−204.8	−119.8	−70.3	−7.1	−0.7	−1271
2003	−1.7	−2.4	−55.4	−111.2	−214.2	−262.9	−235.5	−229.5	−168.2	−51.9	−16.2	−7.2	−1356
2004	−3.3	−13.3	−33.2	−142.9	−192.9	−242.9	−236.3	−204.5	−158.8	−92.5	−10.7	−5.3	−1336
2005	−8.0	−1.4	−57.0	−140.0	−194.2	−239.8	−224.5	−190.8	−141.1	−110.7	−22.3	−3.0	−1333
2006	−1.0	−1.4	−14.3	−102.4	−214.4	−236.5	−242.6	−176.3	−196.6	−108.3	−25.5	−9.4	−1329
2007	−4.8	−4.0	−79.7	−215.9	−236.9	−261.4	−257.2	−230.8	−150.2	−90.7	−3.3	−9.4	−1544
2008	−15.8	−27.8	−17.7	−95.7	−249.9	−296.5	−269.2	−230.5	−162.9	−101.9	−40.1	−2.1	−1510
2009	0.0	−5.8	−10.4	−190.2	−246.0	−254.7	−270.6	−262.0	−187.3	−89.2	−39.5	−6.9	−1562
2010	0.0	−11.8	−49.1	−142.8	−180.9	−257.6	−247.0	−187.9	−150.8	−108.1	−39.0	−3.2	−1378
2011	−1.7	−4.9	−65.0	−187.1	−243.4	−267.4	−263.0	−265.5	−198.7	−106.2	−48.3	−8.1	−1660
2012	−0.5	−1.7	−97.8	−105.6	−271.7	−288.8	−302.5	−267.2	−213.9	−134.1	−29.2	−13.1	−1726
2013	−2.0	−6.9	−14.7	−112.8	−250.8	−252.7	−273.0	−274.0	−201.9	−138.3	−41.0	−36.2	−1604
2014	−25.7	−17.0	−96.0	−168.4	−214.1	−305.2	−281.4	−263.4	−196.7	−165.9	−93.0	−15.4	−1842

Reference

Rebmann C, Anthoni P, Falge E, Göckede M, Mangold A, Subke J-A, Thomas C, Wichura B, Schulze ED, Tenhunen J, Foken T (2004) Carbon budget of a spruce forest ecosystem. In: Matzner E (ed) Biogeochemistry of forested catchments in a changing environment, a German case study, Ecological studies, vol 172. Springer, Berlin, Heidelberg, pp 143–160

Appendix C
FLUXNET Overview Papers in Which Data Sets of the Waldstein-Weidenbrunnen Site Are Used

Compiled by Thomas Foken

The data of the EUROFLUX and later on of the FLUXNET sites were used in several overview publications. In 2007, after a workshop in La Thuile, a data set of all available FLUXNET data was generated, including the DE-Bay data from 1997 to 1999. Furthermore, several overview papers were initiated. In the following overview, papers before and after the La Thuile initiative are listed. Scientists who worked at the Waldstein-Weidenbrunnen site are only listed as coauthors if they made a significant contribution to the paper. Data from 2000 onward, or even from special experiments, were also included; however, only where there were coauthors from Bayreuth. In the following – probably incomplete – list are all papers where data from the Waldstein-Weidenbrunnen site were used together with data from other stations and compared with them. The papers are listed according to the year of issue. Scientists from the University of Bayreuth are highlighted.

References

Aubinet M, Grelle A, Ibrom A, Rannik Ü, Moncrieff J, **Foken T**, Kowalski AS, Martin PH, Berbigier P, Bernhofer C, Clement R, Elbers J, Granier A, Grünwald T, Morgenstern K, Pilegaard K, **Rebmann C**, Snijders W, Valentini R, Vesala T (2000) Estimates of the annual net carbon and water exchange of forests: the EUROFLUX methodology. Adv Ecol Res 30:113–175

Baldocchi D, **Falge E**, Gu L, Olson R, Hollinger D, Running S, Anthoni P, Bernhofer C, Davis K, Evans R, Fuentes J, Goldstein A, Katul G, Law B, Lee XH, Malhi Y, Meyers T, Munger W, Oechel W, Paw U KT, Pilegaard K, Schmid HP, Valentini R, Verma S, Vesala T (2001) FLUXNET: a new tool to study the temporal and spatial variability of ecosystem-scale carbon dioxide, water vapor, and energy flux densities. Bull Am Meteorol Soc 82:2415–2434

Falge E, Baldocchi D, Olson R, Anthoni P, Aubinet M, Bernhofer C, Burba G, Ceulemans R, Clement R, Dolman H, Granier A, Gross P, Grunwald T, Hollinger D, Jensen NO, Katul G,

T. Foken (ed.), *Energy and Matter Fluxes of a Spruce Forest Ecosystem*,
Ecological Studies 229, DOI 10.1007/978-3-319-49389-3

Keronen P, Kowalski A, Lai CT, Law BE, Meyers T, Moncrieff H, Moors E, Munger JW, Pilegaard K, Rannik U, Rebmann C, Suyker A, Tenhunen J, Tu K, Verma S, Vesala T, Wilson K, Wofsy S (2001) Gap filling strategies for defensible annual sums of net ecosystem exchange. Agric For Meteorol 107:43–69

Falge E, Baldocchi D, Olson R, Anthoni P, Aubinet M, Bernhofer C, Burba G, Ceulemans R, Clement R, Dolman H, Granier A, Gross P, Grunwald T, Hollinger D, Jensen NO, Katul G, Keronen P, Kowalski A, Lai CT, Law BE, Meyers T, Moncrieff H, Moors E, Munger JW, Pilegaard K, Rannik U, **Rebmann C**, Suyker A, **Tenhunen J**, Tu K, Verma S, Vesala T, Wilson K, Wofsy S (2001) Gap filling strategies for long term energy flux data sets. Agric For Meteorol 107:71–77

Law BE, **Falge E**, Gu L, Baldocchi DD, Bakwin P, Berbigier P, Davis K, Dolman AJ, Falk M, Fuentes JD, Goldstein A, Granier A, Grelle A, Hollinger D, Janssens IA, Jarvis P, Jensen NO, Katul G, Mahli Y, Matteucci G, Meyers T, Monson R, Munger W, Oechel W, Olson R, Pilegaard K, Paw U KT, Thorgeirsson H, Valentini R, Verma S, Vesala T, Wilson K and Wofsy S (2002) Environmental controls over carbon dioxide and water vapor exchange of terrestrial vegetation. Agric For Meteorol. 113:97–120. (Norbert Gerbier-MUMM International Award 2004)

Wilson KB, Goldstein AH, **Falge E**, Aubinet M, Baldocchi D, Berbigier P, Bernhofer C, Ceulemans R, Dolman H, Field C, Grelle A, Law B, Meyers T, Moncrieff J, Monson R, Oechel W, **Tenhunen J**, Valentini R, Verma S (2002) Energy balance closure at FLUXNET sites. Agric For Meteorol 113:223–234

Aubinet M, Clement R, Elbers J, **Foken T**, Grelle A, Ibrom A, Moncrieff H, Pilegaard K, Rannik U, **Rebmann C** (2003) Methodology for data acquisition, storage and treatment. In: Valentini R (ed) Fluxes of carbon, water and energy of European forests, Ecological studies, vol 163. Springer, Berlin, Heidelberg, pp 9–35

Bernhofer C, Aubinet M, Clement R, Grelle A, Grünwald T, Ibrom A, Jarvis P, **Rebmann C**, Schulze E-D, **Tenhunen JD** (2003) Spruce forests (Norway and Sitka spruce, including Douglas fir): carbon and water fluxes and balances, eco-logical and ecophysiological determinants. In: Valentini R (ed) Fluxes of carbon, water and energy of European forests. Ecological studies series 163. Springer, Berlin, Heidelberg, pp 99–123

Rebmann C, **Göckede M**, **Foken T**, Aubinet M, Aurela M, Berbigier P, Bernhofer C, Buchmann N, Carrara A, Cescatti A, Ceulemans R, Clement R, Elbers J, Granier A, Grünwald T, Guyon D, Havránková K, Heinesch B, Knohl A, Laurila T, Longdoz B, Marcolla B, Markkanen T, Miglietta F, Moncrieff H, Montagnani L, Moors E, Nardino M, Ourcvial J-M, Rambal S, Rannik U, Rotenberg E, Sedlak P, Unterhuber G, Vesala T, Yakir D (2005) Quality analysis applied on eddy covariance measurements at complex forest sites using footprint modelling. Theor Appl Climatol 80:121–141

Foken T (2008) The energy balance closure problem—An overview. Ecol Appl 18:1351–1367

Göckede M, **Foken T**, Aubinet M, Aurela M, Banza J, Bernhofer C, Bonnefond J-M, Brunet Y, Carrara A, Clement R, Dellwik E, Elbers JA, Eugster W, Fuhrer J, Granier A, Grünwald T, Heinesch B, Janssens IA, Knohl A, Koeble R, Laurila T, Longdoz B, Manca G, Marek M, Markkanen T, Mateus J, Matteucci G, **Mauder M**, Migliavacca M, Minerbi S, Moncrieff JB, Montagnani L, Moors E, Ourcival J-M, Papale D, Pereira J, Pilegaard K, Pita G, Rambal S, **Rebmann C**, Rodrigues A, Rotenberg E, Sanz MJ, Sedlak P, Seufert G, **Siebicke L**, Soussana JF, Valentini R, Vesala T, Verbeeck H and Yakir D (2008) Quality control of CarboEurope flux data—Part 1: Coupling footprint analyses with flux data quality assessment to evaluate sites in forest ecosystems. Biogeosciences. 5:433–450. (CarboEurope-IP, Best Paper Award 2008)

Mauder M, **Foken T**, Clement R, Elbers J, Eugster W, Grünwald T, Heusinkveld B, Kolle O (2008) Quality control of CarboEurope flux data—Part 2: Inter-comparison of eddy-covariance software. Biogeosciences 5:451–462

Thomas C, Martin JG, Göckede M, Siqueira MB, **Foken T**, Law BE, Loescher HW, Katul G (2008) Estimating daytime subcanopy respiration from conditional sampling methods applied to multi-scalar high frequency turbulence time series. Agric For Meteorol 148:1210–1229

Stoy PC, Richardson AD, Baldocchi DD, Katul GG, Stanovick J, Mahecha MD, Reichstein M, Detto M, Law BE, Wohlfahrt G, Arriga N, Campos J, McCaughey JH, Montagnani L, Paw

U KT, Sevanto S, Williams M (2009) Biosphere-atmosphere exchange of CO_2 in relation to climate: a cross-biome analysis across multiple time scales. Biogeosciences 6:2297–2312

Franssen HJH, Stöckli R, Lehner I, Rotenberg E, Seneviratne SI (2010) Energy balance closure of eddy-covariance data: a multisite analysis for European FLUXNET stations. Agric For Meteorol 150:1553–1567

Yi C, Ricciuto D, Li R, Wolbeck J, Xu X, Nilsson M, Aires L, Albertson JD, Ammann C, Arain MA, de Araujo AC, Aubinet M, Aurela M, Barcza Z, Barr A, Berbigier P, Beringer J, Bernhofer C, Black AT, Bolstad PV, Bosveld FC, Broadmeadow MSJ, Buchmann N, Burns SP, Cellier P, Chen J, Chen J, Ciais P, Clement R, Cook BD, Curtis PS, Dail DB, Dellwik E, Delpierre N, Desai AR, Dore S, Dragoni D, Drake BG, Dufrêne E, Dunn A, Elbers J, Eugster W, Falk M, Feigenwinter C, Flanagan LB, **Foken T**, Frank J, Fuhrer J, Gianelle D, Goldstein A, Goulden M, Granier A, Grünwald T, Gu L, Guo H, Hammerle A, Han S, Hanan NP, Haszpra L, Heinesch B, Helfter C, Hendriks D, Hutley LB, Ibrom A, Jacobs C, Johansson T, Jongen M, Katul G, Kiely G, Klumpp K, Knohl A, Kolb T, Kutsch WL, Lafleur P, Laurila T, Leuning R, Lindroth A, Liu H, Loubet B, Manca G, Marek M, Margolis HA, Martin TA, Massman WJ, Matamala R, Matteucci G, McCaughey H, Merbold L, Meyers T, Migliavacca M, Miglietta F, Misson L, Mölder M, Moncrieff J, Monson RK, Montagnani L, Montes-Helu M, Moors E, Moureaux C, Mukelabai MM, Munger JW, Myklebust M, Nagy Z, Noormets A, Oechel W, Oren R, Pallardy SG, Paw U KT, Pereira JS, Pilegaard K, Pintér K, Pio C, Pita G, Powell TL, Rambal S, Randerson JT, von Randow C, **Rebmann C**, Rinne J, Rossi F, Roulet N, Ryel RJ, Sagerfors J, Saigusa N, Sanz MJ, Mugnozza GS, Schmid HP, Seufert G, Siqueira M, Soussana J-F, Starr G, Sutton MA, **Tenhunen J**, Tuba Z, Tuovinen J-P, Valentini R, Vogel CS, Wang J, Wang S, Wang W, Welp LR, Wen X, Wharton S, Wilkinson M, Williams CA, Wohlfahrt G, Yamamoto S, Yu G, Zampedri R, Zhao B and Zhao X (2010) Climate control of terrestrial carbon exchange across biomes and continents. Environmental Research Letters. 5:034007. (Norbert Gerbier-MUMM International Award 2012)

Stoy PC, Mauder M, **Foken T**, Marcolla B, Boegh E, Ibrom A, Arain MA, Arneth A, Aurela M, Bernhofer C, Cescatti A, Dellwik E, Duce P, Gianelle D, van Gorsel E, Kiely G, Knohl A, Margolis H, McCaughey H, Merbold L, Montagnani L, Papale D, Reichstein M, Serrano-Ortiz P, Sottocornola M, Saunders M, Spano D, Vaccari F, Varlagin A (2012) A data-driven analysis of energy balance closure across FLUXNET research sites: The role of landscape-scale heterogeneity. Agric For Meteorol 171–172:137–152

Williams CA, Reichstein M, Buchmann N, Baldocchi DD, Beer C, Schwalm C, Wohlfahrt G, Hasler N, Bernhofer C, **Foken T**, Papale D, Schymanski S and Schaefer K (2012) Climate and vegetation controls on the surface water balance: synthesis of evapotranspiration measured across a global network of flux towers. Water Resour Res. 48: W06523

Vuichard N, Papale D (2015) Filling the gaps in meteorological continuous data measured at FLUXNET sites with ERA-Interim reanalysis. Earth Syst Sci Data 7:157–171

Chen Y, Ryder J, Bastrikov V, McGrath MJ, Naudts K, Otto J, Ottlé C, Peylin P, Polcher J, Valade A, Black A, Elbers JA, Moors E, **Foken T**, van Gorsel E, Haverd V, Heinesch B, Tiedemann F, Knohl A, Launiainen S, Loustau D, Ogée J, Vessala T, Luyssaert S (2016) Evaluating the performance of land surface model ORCHIDEE-CAN v1.0 on water and energy flux estimation with a single- and multi-layer energy budget scheme. Geosci Model Dev 9:2951–2972

Index

T. Foken (ed.), *Energy and Matter Fluxes of a Spruce Forest Ecosystem*,
Ecological Studies 229, DOI 10.1007/978-3-319-49389-3